1 of 3

$\frac{10}{2}$ 14-94 *SC* (1)

SANDIA REPORT

Hydraulic Testing of Salado Formation Evaporites at the Waste Isolation Pilot Plant Site: Second Interpretive Report

Richard L. Beauheim, Randall M. Roberts, Timothy F. Dale,
Michael D. Fort, Wayne A. Stensrud

HYDRAULIC TESTING OF SALADO FORMATION EVAPORITES AT THE WASTE ISOLATION PILOT PLANT SITE: SECOND INTERPRETIVE REPORT

Richard L. Beauheim
Geohydrology Department
Sandia National Laboratories
Albuquerque, New Mexico 87185-1324

Randall M. Roberts, Timothy F. Dale, Michael D. Fort, and Wayne A. Stensrud
INTERA Inc.
6850 Austin Center Boulevard, Suite 300
Austin, Texas 78731

ABSTRACT

Pressure-pulse, constant-pressure flow, and pressure-buildup tests have been performed in bedded evaporites of the Salado Formation at the Waste Isolation Pilot Plant (WIPP) site to evaluate the hydraulic properties controlling brine flow through the Salado. Transmissivities ranging from about 7×10^{-15} to 5×10^{-13} m^2/s have been interpreted from six sequences of tests conducted on five stratigraphic intervals within 15 m of the WIPP underground excavations. The corresponding vertically averaged hydraulic conductivities of the intervals range from about 1×10^{-14} to 2×10^{-12} m/s (permeabilities of 2×10^{-21} to 3×10^{-19} m^2). Storativities of the tested intervals range from about 1×10^{-8} to 2×10^{-6}, and values of specific storage range from 9×10^{-8} to 1×10^{-5} m^{-1}. Pore pressures in eight stratigraphic intervals range from about 2.5 to 12.5 MPa, and appear to be affected by stress relief around the excavations. Anhydrite interbeds appear to be one or more orders of magnitude more permeable than the surrounding halite, primarily because of subhorizontal bedding-plane fractures present in the anhydrites. Interpretations of the tests revealed no apparent hydrologic boundaries within the radii of influence of the tests, which were calculated to range from about 2 to 20 m from the test holes. An assumption of Darcy flow through the evaporites is thought to be a reasonable interpretive approach because Darcy-flow models are able to replicate the flow and pressure behavior observed during entire testing sequences involving different types of tests performed with different hydraulic gradients.

MASTER

ACKNOWLEDGEMENTS

TABLE OF CONTENTS

Figures

Tables

1. INTRODUCTION

This report presents interpretations of hydraulic tests conducted in bedded evaporites of the Salado Formation from mid-1989 through mid-1992 at the Waste Isolation Pilot Plant (WIPP) site in southeastern New Mexico (Figure 1-1). The WIPP is a U.S. Department of Energy research and development facility designed to demonstrate safe disposal of transuranic wastes from the nation's defense programs. The WIPP disposal horizon is located in the lower portion of the Permian Salado Formation. The hydraulic tests discussed in this report were performed in the WIPP underground facility by INTERA Inc., Austin, Texas, under the technical direction of Sandia National Laboratories, Albuquerque, New Mexico.

Hydraulic testing is being performed in the Salado Formation to provide quantitative estimates of the hydraulic properties controlling brine flow through the Salado Formation. The specific objectives of the tests are:

- To determine transmissivities and storativities of different stratigraphic intervals in the Salado Formation around the WIPP facility;

- To determine formation pore pressures within different stratigraphic intervals in the Salado Formation around the facility;

- To determine the radii of influence of the tests in order to define the scales at which the interpreted properties are representative;

- To determine how and to what distance(s) excavation effects around the WIPP facility

have affected hydraulic properties and/or formation pore pressures in the surrounding rock; and

- To provide data to allow evaluation of the mechanisms controlling brine flow through evaporites.

This report represents a continuation of the work described by Beauheim et al. (1991). That report presented preliminary interpretations of pressure-pulse tests completed in nine isolated borehole intervals between September 1988 and February 1990. Two problems associated with pressure-pulse tests were identified by Beauheim et al. (1991). First, estimation of transmissivity requires knowledge of the aggregate compressibility of everything contained within a test zone in a borehole, which is not always well defined. Second, pressure-pulse tests provide no information on the storage properties of the medium being tested. To remedy these problems, the testing program was expanded to include constant-pressure flow and pressure-buildup testing. Constant-pressure flow tests provide estimates of transmissivity independent of test-zone compressibility. Pressure-buildup tests (the recovery of fluid pressure after a constant-pressure flow test is terminated) provide direct information on both test-zone compressibility and transmissivity. Conjunctive analysis of pulse, flow, and buildup tests also allows determination of formation storativity.

This report discusses testing completed between May 1990 and July 1992. The hydraulic testing reported herein consists of pressure-pulse, constant-pressure flow, and/or pressure-buildup tests of five stratigraphic intervals at locations

1
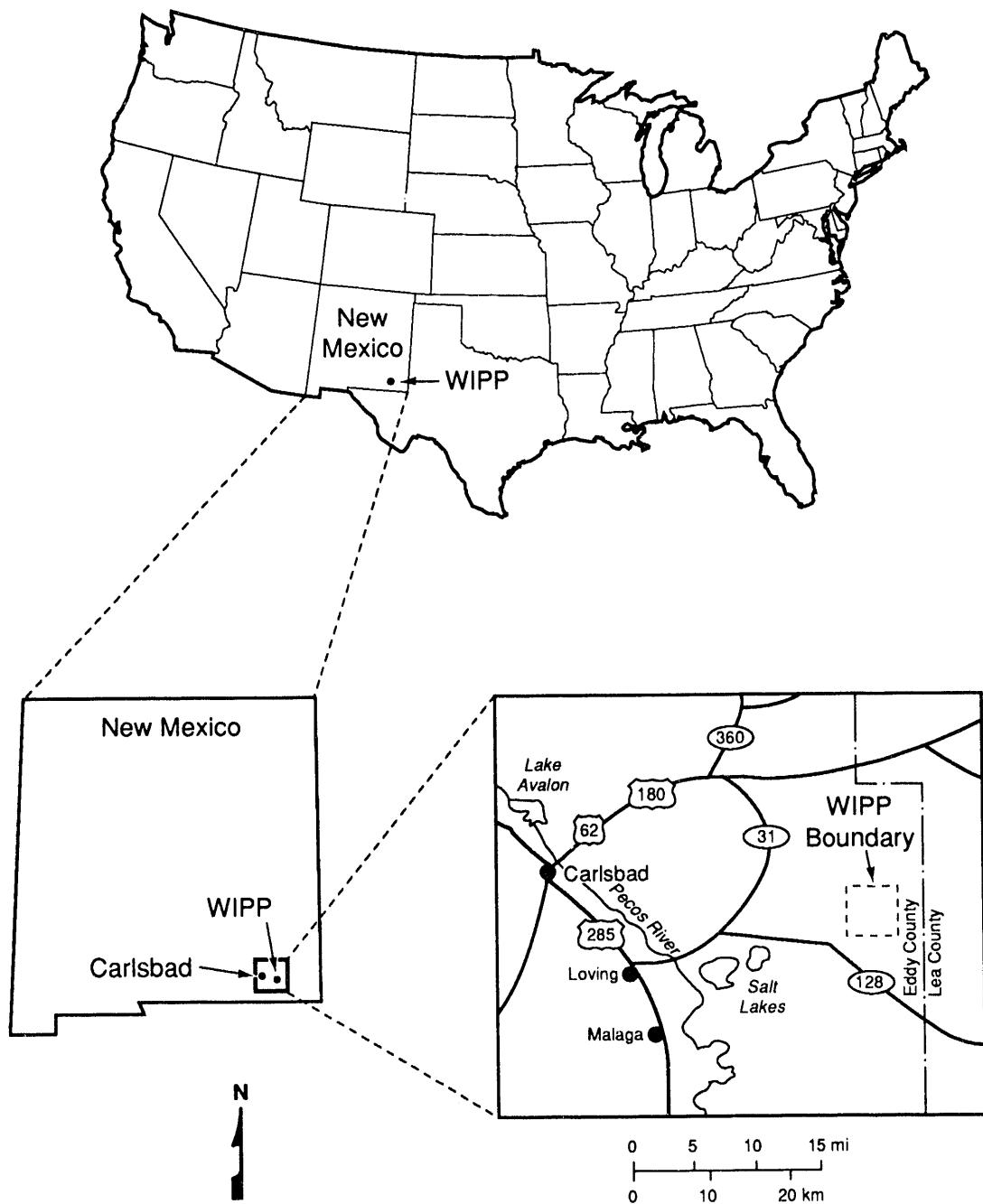
Figure 1-1. Location of the WIPP site.

TRI-6330-3-5

within 15 m of the WIPP excavations. The stratigraphic intervals tested included halite (both pure and impure) and anhydrite (with associated clay seams). Eight sets of pressure-pulse tests were completed in different intervals in six boreholes. Constant-pressure flow tests were also performed in six intervals, all but one of which were followed by pressure-buildup tests. Tests of two stratigraphic intervals containing anhydrite interbeds were attempted in one of the boreholes, but the intervals were apparently connected by fractures and/or roof-bolt holes to the room below, and could not be pressurized.

The hydraulic-test analyses presented in this report and in the report of Beauheim et al. (1991) were performed under assumptions that Darcy's law adequately describes flow through low-permeability evaporites, and that the transient fluid pressures observed during the tests were not affected by inelastic or nonlinearly elastic deformation of the rock. These assumptions are evaluated in light of the data provided by the testing. The hydraulic-test analyses also included an assumption of cylindrical flow to vertical boreholes. In reality, three of the six boreholes considered in this report were drilled at acute angles to the subhorizontal bedding, which could result in elliptical and vertical flow components. Modeling studies were performed, therefore, to determine the effects of borehole orientation (slant) on the test interpretations, and the results of these studies are included in this report. Modeling studies were also performed to attempt to develop an understanding of the pressure depletion observed while testing an anhydrite layer exhibiting two-phase behavior.

2. GEOLOGIC SETTING AND LOCAL STRATIGRAPHY

The WIPP site is located in the northern part of the Delaware Basin in southeastern New Mexico. WIPP-site geologic investigations have concentrated on the upper seven formations typically found in that part of the Delaware Basin. These are, in ascending order, the Bell Canyon Formation, the Castile Formation, the Salado Formation, the Rustler Formation, the Dewey Lake Red Beds, the Dockum Group, and the Gatuña Formation (Figure 2-1). All of these formations are of Permian age, except for the Dockum Group, which is of Triassic age, and the Gatuña, which is a Quaternary deposit.

The WIPP underground facility lies in the lower part of the Salado Formation at an approximate depth of 655 m below ground surface. The Salado Formation is approximately 600-m thick at the WIPP site, and is composed largely of halite, with minor amounts of interspersed clay and polyhalite. The Salado also contains interbeds of anhydrite, polyhalite, clay, and siltstone. Many of these interbeds are traceable over most of the Delaware Basin. Jones et al. (1960) designated 45 of the continuous anhydrite and/or polyhalite interbeds as "Marker Beds", and numbered these "Marker Beds" from 100 to 144, increasing downward. The WIPP facility horizon (the stratigraphic location of the underground excavations) lies between Marker Beds 138 and 139.

A typical stratigraphic section of the Salado Formation in the vicinity of the WIPP underground facility, adapted from Deal et al. (1989), is shown in Figure 2-2. Deal et al. (1989) present a detailed description of stratigraphic units that correlate throughout most of the underground facility (Appendix A). The

description covers a 41.2-m interval of the Salado, centered approximately at the stratigraphic midpoint of the excavations. This description delineates 16 "map units" numbered 0 to 15 and 23 other map units. The majority of the units are composed primarily of halite, and are differentiated principally on the basis of differing clay and polyhalite contents. The halite units lacking integer map-unit designations are identified by H (pure halite), AH (argillaceous halite), or PH (polyhalitic halite) prefixes, followed by a number representing that unit's position with respect to the base of the sequence, which was arbitrarily defined as the halite unit immediately underlying anhydrite "c" and clay B. For example, AH-4 is the fourth argillaceous halite unit above the base of the sequence. The remainder of the units are anhydrite interbeds such as Marker Beds 138 and 139. Thinner anhydrite interbeds and a number of the more continuous clay seams have also been given letter designations (e.g., anhydrite "a", clay B) to facilitate consistent referencing. These units are shown on Figure 2-2. The stratigraphic positions of the WIPP excavations with respect to the designated map units are shown in Figure 2-3. The testing and guard-zone monitoring discussed in this report were carried out in Marker Bed 138, Marker Bed 139, anhydrites "a", "b", and "c", map unit 0, polyhalitic halite 4, argillaceous halite 1 (clay J), and halite 2.

The halitic units described by Deal et al. (1989) are not encountered by all boreholes, however. As shown in detailed geologic maps of drift and room ribs (walls) throughout the underground facility (e.g., Westinghouse, 1989, 1990), the halitic map units are locally crosscut by syndepositional dissolution pits (Powers and

System	Series	Group	Formation	Member
Recent	Recent		Surficial Deposits	
Quater-nary	Pleisto-cene		Mescalero Caliche	
			Gatuña	
Triassic		Dockum	Undivided	
Permian	Ochoan		Dewey Lake Red Beds	
			Rustler	Forty-niner
				Magenta Dolomite
				Tamarisk
				Culebra Dolomite
				unnamed
			Salado	
			Castile	
	Guadalupian	Delaware Mountain	Bell Canyon	
			Cherry Canyon	
			Brushy Canyon	

TRI-6330-89-5

Figure 2-1. WIPP site stratigraphic column.

ANHYDRITE (MB-137)
21.61
21.21
POLYHALITIC HALITE (MAP UNIT PH-7)
20.12
20
HALITE (MAP UNIT H-9)
19.29

POLYHALITIC HALITE (MAP UNIT PH-6)
ANHYDRITE — CLAY N
17.47
16.83
ARGILLACEOUS HALITE (MAP UNIT AH-4)

— CLAY M-2
15.55
(MAP UNIT H-8)
15

14.17
— CLAY M-1
POLYHALITIC HALITE (MAP UNIT PH-5)
13.05
— CLAY L
ARGILLACEOUS HALITE (MAP UNIT AH-3)
11.58
HALITE (MAP UNIT H-7)
10
HALITE (MAP UNIT H-6)
9.18
ANHYDRITE (MB-138)
8.96
— CLAY K
ARGILLACEOUS HALITE (MAP UNIT AH-2)
7.62
HALITE (MAP UNIT H-5)
6.71
ARGILLACEOUS HALITE (MAP UNIT AH-1)
— CLAY J
HALITE (MAP UNIT 15)
— CLAY I
5.09
HALITE (MAP UNIT 14)
5
HALITE (MAP UNIT 13)

POLYHALITIC HALITE (MAP UNIT 12)
2.29
ANHYDRITE "a" (MAP UNIT 11)
2.07
— CLAY H
— HALITE (MAP UNIT 10)
HALITE (MAP UNIT 9)
0.06
0
0.0
ANHYDRITE "b" (MAP UNIT 8)
HALITE (MAP UNIT 7) CLAY G
HALITE (MAP UNIT 6)

HALITE (MAP UNIT 5)
— CLAY F
ARGILLACEOUS HALITE (MAP UNIT 4)
2.74
HALITE (MAP UNIT 3)
4.18
ARGILLACEOUS HALITE (MAP UNIT 2)
4.27
4.42
— HALITE (MAP UNIT 1)
5
5.03
HALITE (MAP UNIT 0)

POLYHALITIC HALITE (MAP UNIT PH-4)

7.71
ANHYDRITE (MB-139)
8.57
— CLAY E
HALITE (MAP UNIT H-4)

10
POLYHALITIC HALITE (MAP UNIT PH-3)

10.97
— CLAY D
HALITE (MAP UNIT H-3)

POLYHALITIC HALITE (MAP UNIT PH-2)

HALITE (MAP UNIT H-2)

15
POLYHALITIC HALITE (MAP UNIT PH-1)
16.25
ANHYDRITE "c"
16.31
— CLAY B
HALITE (MAP UNIT H-1)
m

DISTANCE FROM CLAY G (METERS)

EXPLANATION

ROCK TYPE

HALITE   ANHYDRITE   POLYHALITIC   ARGILLACEOUS
                        HALITE   HALITE

ACCESSORY CONSTITUENTS

POLYHALITE   CLAY SEAM
                          >0.6 cm THICK

ARGILLACEOUS   ANHYDRITE
MATERIAL   STRINGERS

LITHOLOGIC CONTACTS

SHARP   GRADATIONAL   DIFFUSE

NOTES:

1. DISTANCES IN METERS ARE MEASURED FROM
THE BASE OF ANHYDRITE "b"(CLAY G) AND ARE
AVERAGED FROM REPRESENTATIVE COREHOLE
LOGS, SHAFT AND TEST-ROOM MAPPING. ACTUAL
DISTANCE AND UNIT THICKNESSES MAY VARY
LOCALLY FROM THOSE SHOWN.

2. DESCRIPTIONS OF UNITS ARE BASED ON
COREHOLE DATA, SHAFT MAPPING AND VISUAL
INSPECTION OF EXPOSURES IN UNDERGROUND
DRIFTS AND ROOMS.

ADAPTED FROM DEAL ET AL. (1989)

Figure 2-2. Detailed stratigraphy near the WIPP underground facility.

CLAY	MAP UNITS		SALADO FORMATION LITHOLOGY	DISTANCES FROM CLAY G (METERS)

Top to bottom stratigraphic column labels:

- H-6 — CLEAR TO REDDISH-ORANGE HALITE, TRACE POLYHALITE — 10.36
- K — GREY ANHYDRITE UNDERLAIN BY CLAY SEAM, MARKER BED 138 — 9.17 / 8.96
- AH-2 — ARGILLACEOUS HALITE, BROWN TO GREY CLAY UP TO 5% — CLAY K
- H-5 — CLEAR COARSELY CRYSTALLINE HALITE — 7.62
- J / AH-1 — CLAY J, OR ARGILLACEOUS HALITE, OR 1.25cm REDDISH-BROWN CLAY SEAM, AND SCATTERED CLAY BREAKS — 7.01
- 15 — CLEAR TO GRAYISH ORANGE-PINK HALITE, TRACE OF DISPERSED POLYHALITE AND INTERCRYSTALLINE CLAY — 6.40
- 14 — 5.09 / 4.82
- 13 — CLEAR TO GRAYISH ORANGE-PINK HALITE, TRACE POLYHALITE AND DISCONTINUOUS CLAY STRINGERS
- CLEAR TO MODERATE REDDISH-BROWN HALITE, TRACE TO SOME POLYHALITE AND TRACE OF CLAY
- 12 — CLEAR TO MODERATE REDDISH-BROWN HALITE, TRACE TO SOME POLYHALITE, ANHYDRITE STRINGERS NEAR BOTTOM OF UNIT — 3.51
- H / 11 — ANHYDRITE "a" UNDERLAIN BY CLAY SEAM — 2.29 / 2.07
- 10 — CLEAR TO MODERATE REDDISH-BROWN HALITE, TRACE TO SOME POLYHALITE AND DISCONTINUOUS CLAY STRINGERS — 1.68
- 9 — CLEAR TO GRAYISH ORANGE-PINK HALITE
- ANHYDRITE "b" UNDERLAIN BY CLAY G — 0.06
- G / 8 — 0.00
- 7 — CLEAR TO MODERATE REDDISH-BROWN TO MEDIUM GRAY HALITE, TRACE POLYHALITE AND SOME CLAY STRINGERS — -0.67
- 6 — CLEAR TO REDDISH-ORANGE HALITE, TRACE POLYHALITE
- 5 — CLEAR HALITE TRACE ARGILLACEOUS MATERIAL — -2.13
- F — -2.74
- 4 — CLEAR TO REDDISH-BROWN ARGILLACEOUS HALITE WITH DISCONTINUOUS CLAY PARTINGS IN UPPER HALF
- 3 — CLEAR TO REDDISH-ORANGE HALITE, TRACE POLYHALITE — -3.47
- 2 — -4.18 / -4.27
- 1 — REDDISH-ORANGE HALITE TRACE POLYHALITE — -4.42
- REDDISH-BROWN TO BLUISH GRAY ARGILLACEOUS HALITE
- 0 — CLEAR TO REDDISH-ORANGE AND REDDISH-BROWN HALITE, ARGILLACEOUS IN UPPER PART, TRACE POLYHALITE
- PH-4 — CLEAR TO REDDISH-ORANGE POLYHALITIC HALITE, LOCALLY GRADING DOWNWARD TO POLYHALITE — -6.71
- ANHYDRITE UNDERLAIN BY CLAY SEAM MARKER BED (MB) 139 — -7.71
- E / H-4 — -8.60 / -9.51
- CLEAR TO GRAY AND REDDISH-ORANGE HALITE, TRACE POLYHALITE AND ARGILLACEOUS MATERIAL — CLAY E
- D / PH-3 / H-3 — CLAY D (LOCALLY OVERLAIN BY 0.01m ANHYDRITE) — -10.97
- PH-2 — CLEAR TO GRAY AND REDDISH-ORANGE HALITE, TRACE POLYHALITE (AND ARGILLACEOUS) MATERIAL — -11.52
- H-2 — -13.01
- PH-1 — ANHYDRITE "c" — -14.42 / -16.25
- B / H-1 — CLAY B — -16.31 / -20.03

Figures shown:
- TYPICAL 5.5-m HIGH SIMULATED-WASTE EXPERIMENTAL ROOM
- GRAY CLAY SEAM LOCALLY WITH ANHYDRITE
- TYPICAL 4.0-M HIGH WASTE-STORAGE ROOM
- TOP OF ORANGE BAND
- NOTE: NOT TO SCALE

Figure 2-3. Schematic of typical WIPP underground rooms showing stratigraphic positions.

Hassinger, 1985). These pits range in depth and width from a few centimeters to a few meters, and may completely crosscut one or several map units at any given location. The pits are typically filled by relatively pure, coarsely crystalline halite.

As mentioned above, the halitic map units designated by Deal et al. (1989) were defined on the basis of relatively consistent differences in clay content and/or color and polyhalite content that are apparent in macroscopic examination, rather than on sedimentological differences. Holt and Powers (1990) present a detailed discussion of the sedimentology of the Salado Formation. They provide descriptions of lithofacies commonly found within the Salado, and discuss syndepositional alteration processes. Salado textures and lithofacies distributions are highly variable both laterally (at a local scale) and vertically, as they are the products of repeated episodes of dissolution and alteration over a large areal scale.

DISTANCE FROM CLAY G (METERS)

21.61 — ANHYDRITE (MB-137)
21.21 — POLYHALITIC HALITE (MAP UNIT PH-7)
20 — 20.12 — HALITE (MAP UNIT H-9)
19.29 —
— POLYHALITIC HALITE (MAP UNIT PH-6)
17.47 — ANHYDRITE — CLAY N
16.83 — ARGILLACEOUS HALITE (MAP UNIT AH-4)
— CLAY M-2
15.55 — (MAP UNIT H-8)
15 —
14.17 — CLAY M-1
13.05 — POLYHALITIC HALITE (MAP UNIT PH-5) — CLAY L
— ARGILLACEOUS HALITE (MAP UNIT AH-3)
11.58 —
— HALITE (MAP UNIT H-7)
10 —
9.18 — HALITE (MAP UNIT H-6)
8.96 — ANHYDRITE (MB-138) — CLAY K
— ARGILLACEOUS HALITE (MAP UNIT AH-2)
7.62 — HALITE (MAP UNIT H-5)
6.71 — ARGILLACEOUS HALITE (MAP UNIT AH-1) — CLAY J
— HALITE (MAP UNIT 15) — CLAY I
5.09 — HALITE (MAP UNIT 14)
5 — HALITE (MAP UNIT 13)
— POLYHALITIC HALITE (MAP UNIT 12)
2.29 — ANHYDRITE "a" (MAP UNIT 11)
2.07 — CLAY H — HALITE (MAP UNIT 10)
— HALITE (MAP UNIT 9)
0.06 — ANHYDRITE "b" (MAP UNIT 8)
0 — 0.0 — HALITE (MAP UNIT 7) CLAY G
— HALITE (MAP UNIT 6)
— HALITE (MAP UNIT 5)
2.74 — CLAY F
— ARGILLACEOUS HALITE (MAP UNIT 4)
4.18 — HALITE (MAP UNIT 3)
4.27 — ARGILLACEOUS HALITE (MAP UNIT 2)
4.42 — HALITE (MAP UNIT 1)
5 — 5.03 — HALITE (MAP UNIT 0)
— POLYHALITIC HALITE (MAP UNIT PH-4)
7.71 — ANHYDRITE (MB-139)
8.57 — CLAY E
— HALITE (MAP UNIT H-4)
10 — POLYHALITIC HALITE (MAP UNIT PH-3)
10.97 — CLAY D
— HALITE (MAP UNIT H-3)
— POLYHALITIC HALITE (MAP UNIT PH-2)
— HALITE (MAP UNIT H-2)
15 — POLYHALITIC HALITE (MAP UNIT PH-1)
16.25 — ANHYDRITE "c"
16.31 — CLAY B
— HALITE (MAP UNIT H-1)
m

EXPLANATION

ROCK TYPE

HALITE   ANHYDRITE   POLYHALITIC HALITE   ARGILLACEOUS HALITE

ACCESSORY CONSTITUENTS

POLYHALITE   CLAY SEAM >0.6 cm THICK

ARGILLACEOUS MATERIAL   ANHYDRITE STRINGERS

LITHOLOGIC CONTACTS

SHARP   GRADATIONAL   DIFFUSE

NOTES:

1. DISTANCES IN METERS ARE MEASURED FROM THE BASE OF ANHYDRITE "b"(CLAY G) AND ARE AVERAGED FROM REPRESENTATIVE COREHOLE LOGS, SHAFT AND TEST-ROOM MAPPING. ACTUAL DISTANCE AND UNIT THICKNESSES MAY VARY LOCALLY FROM THOSE SHOWN.

2. DESCRIPTIONS OF UNITS ARE BASED ON COREHOLE DATA, SHAFT MAPPING AND VISUAL INSPECTION OF EXPOSURES IN UNDERGROUND DRIFTS AND ROOMS.

ADAPTED FROM DEAL ET AL. (1989)

Figure 2-2. Detailed stratigraphy near the WIPP underground facility.

SALADO FORMATION LITHOLOGY

DISTANCES FROM CLAY G (METERS)

CLAY UNITS	MAP UNITS	Lithology description	Distance

H-6 — CLEAR TO REDDISH-ORANGE HALITE, TRACE POLYHALITE — 10.36

K — GREY ANHYDRITE UNDERLAIN BY CLAY SEAM, MARKER BED 138 — 9.17 — CLAY K — 8.96

AH-2 — ARGILLACEOUS HALITE, BROWN TO GREY CLAY UP TO 5%

H-5 — CLEAR COARSELY CRYSTALLINE HALITE — 7.62 / 7.01

J / AH-1 — CLAY J, OR ARGILLACEOUS HALITE, OR 1.25cm REDDISH-BROWN CLAY SEAM, AND SCATTERED CLAY BREAKS — 6.40

15 — CLEAR TO GRAYISH ORANGE-PINK HALITE, TRACE OF DISPERSED POLYHALITE AND INTERCRYSTALLINE CLAY — 5.09

14 — 4.82

CLEAR TO GRAYISH ORANGE-PINK HALITE, TRACE POLYHALITE AND DISCONTINUOUS CLAY STRINGERS.

13 — CLEAR TO MODERATE REDDISH-BROWN HALITE, TRACE TO SOME POLYHALITE AND TRACE OF CLAY.

GRAY CLAY SEAM LOCALLY WITH ANHYDRITE

— 3.51

12 — CLEAR TO MODERATE REDDISH-BROWN HALITE, TRACE TO SOME POLYHALITE, ANHYDRITE STRINGERS NEAR BOTTOM OF UNIT.

TYPICAL 5.5-m HIGH SIMULATED-WASTE EXPERIMENTAL ROOM

— 2.29

11 — ANHYDRITE "a" UNDERLAIN BY CLAY SEAM — 2.07

H

10 — CLEAR TO MODERATE REDDISH-BROWN HALITE, TRACE TO SOME POLYHALITE AND DISCONTINUOUS CLAY STRINGERS — 1.68

9 — CLEAR TO GRAYISH ORANGE-PINK HALITE

ANHYDRITE "b" UNDERLAIN BY CLAY G — 0.06

G / 8 — 0.00

7 — CLEAR TO MODERATE REDDISH-BROWN TO MEDIUM GRAY HALITE, TRACE POLYHALITE AND SOME CLAY STRINGERS.

— -0.67

6 — CLEAR TO REDDISH-ORANGE HALITE, TRACE POLYHALITE

— -2.13

5 — CLEAR HALITE TRACE ARGILLACEOUS MATERIAL — -2.74

F

4 — CLEAR TO REDDISH-BROWN ARGILLACEOUS HALITE WITH DISCONTINUOUS CLAY PARTINGS IN UPPER HALF

TYPICAL 4.0-M HIGH WASTE-STORAGE ROOM

3 — CLEAR TO REDDISH-ORANGE HALITE, TRACE POLYHALITE. — -3.47

TOP OF ORANGE BAND

2 — -4.18 / -4.27

1 — REDDISH-ORANGE HALITE, TRACE POLYHALITE — -4.42

— REDDISH-BROWN TO BLUISH-GRAY ARGILLACEOUS HALITE

0 — CLEAR TO REDDISH-ORANGE AND REDDISH-BROWN HALITE, ARGILLACEOUS IN UPPER PART, TRACE POLYHALITE. — -6.71

PH-4 — CLEAR TO REDDISH-ORANGE POLYHALITIC HALITE, LOCALLY GRADING DOWNWARD TO POLYHALITE. — -7.71

ANHYDRITE UNDERLAIN BY CLAY SEAM MARKER BED (MB) 139

E / H-4 — -8.60 / -9.51

CLEAR TO GRAY AND REDDISH-ORANGE HALITE, TRACE POLYHALITE AND ARGILLACEOUS MATERIAL. CLAY E

PH-3 — -10.97

D / H-3 — CLAY D (LOCALLY OVERLAIN BY 0.01m ANHYDRITE). — -11.52

PH-2 — CLEAR TO GRAY AND REDDISH-ORANGE HALITE, TRACE POLYHALITE AND ARGILLACEOUS MATERIAL.

H-2 — -13.01 / -14.42

PH-1 — ANHYDRITE "c" — -16.25

B / H-1 — CLAY B — -16.31

NOTE: NOT TO SCALE — -20.03

Figure 2-3. Schematic of typical WIPP underground rooms showing stratigraphic positions.

8

Hassinger, 1985). These pits range in depth and width from a few centimeters to a few meters, and may completely crosscut one or several map units at any given location. The pits are typically filled by relatively pure, coarsely crystalline halite.

As mentioned above, the halitic map units designated by Deal et al. (1989) were defined on the basis of relatively consistent differences in clay content and/or color and polyhalite content that are apparent in macroscopic examination, rather than on sedimentological differences. Holt and Powers (1990) present a detailed discussion of the sedimentology of the Salado Formation. They provide descriptions of lithofacies commonly found within the Salado, and discuss syndepositional alteration processes. Salado textures and lithofacies distributions are highly variable both laterally (at a local scale) and vertically, as they are the products of repeated episodes of dissolution and alteration over a large areal scale.

10

3. TESTING EQUIPMENT

The following sections briefly describe the equipment used in the permeability-testing program in the WIPP underground facility. The equipment includes multipacker test tools, data-acquisition systems, pressure transducers, thermocouples, linear variable-differential transformers, a differential-pressure-transmitter panel, and a system to separate gas and brine and measure the production of each. More detailed descriptions of the testing equipment and the procedures and methods used to calibrate the equipment are presented in Stensrud et al. (1992).

NOTE: The use of brand names in this report is for identification only, and does not imply endorsement of specific products by Sandia National Laboratories.

3.1 Multipacker Test Tool

The multipacker test tool designed for this testing program, shown on Figures 3-1 and 3-2, has two sliding-end, 9.5-cm outside diameter (O.D.) inflatable packers mounted on a 4.83-cm O.D. mandrel and oriented with the packers' fixed ends toward the bottom-hole end of the test tool. The packers have 0.92-m-long inflatable elastic elements composed of natural rubber and synthetic materials. The packer elements have approximately 0.84-m seal lengths when inflated in 4-inch (10.2-cm) diameter boreholes. For some tests, the test tool was restrained using a cross made of 1-m lengths of 2-inch (5.08-cm) square tubular steel which is clamped onto the mandrel or its extension and anchored to the floor or wall using 61-cm-long rock bolts. For other tests, a set of radially oriented tapered jaws or slips that tighten on the test-tool mandrel as the tool attempts to move out of the borehole

in response to pressure buildup was used to restrain the tool.

Each multipacker test tool is equipped with three sets of ports to the bottom-hole test zone and the guard zone between the packers. One set of ports is used to transmit pressures from the test and guard zones to the transducers, which are mounted outside of the boreholes. A second set of ports is used to dissipate "squeeze" pressures created during packer inflation and to vent fluid from the isolated intervals during withdrawal tests. These two sets of ports are accessed by continuous lengths of 3/16-inch (0.48-cm) O.D. stainless-steel tubing. The third set of ports provides access for 1/8-inch (0.32-cm) diameter Type E thermocouples to measure temperatures in the test and guard zones. Packer-inflation pressures are monitored with transducers attached to the packer-inflation lines.

The test-interval section of each test tool is equipped with linear variable-differential transformers (LVDTs) to measure borehole deformation and test-tool movement during the testing period. Three radially oriented LVDTs are located below the test-interval packer, and one axially oriented LVDT is mounted at the bottom end of the multipacker test tool (Figure 3-2) to measure tool movement relative to the bottom of the hole during testing.

3.2 Data-Acquisition System

A computer-controlled data-acquisition system (DAS) monitors the progress of each test and records pressure, temperature, and borehole-deformation data (Figure 3-3). Each DAS consists of an IBM PS/2 Model 50 desktop computer for system control and data storage,
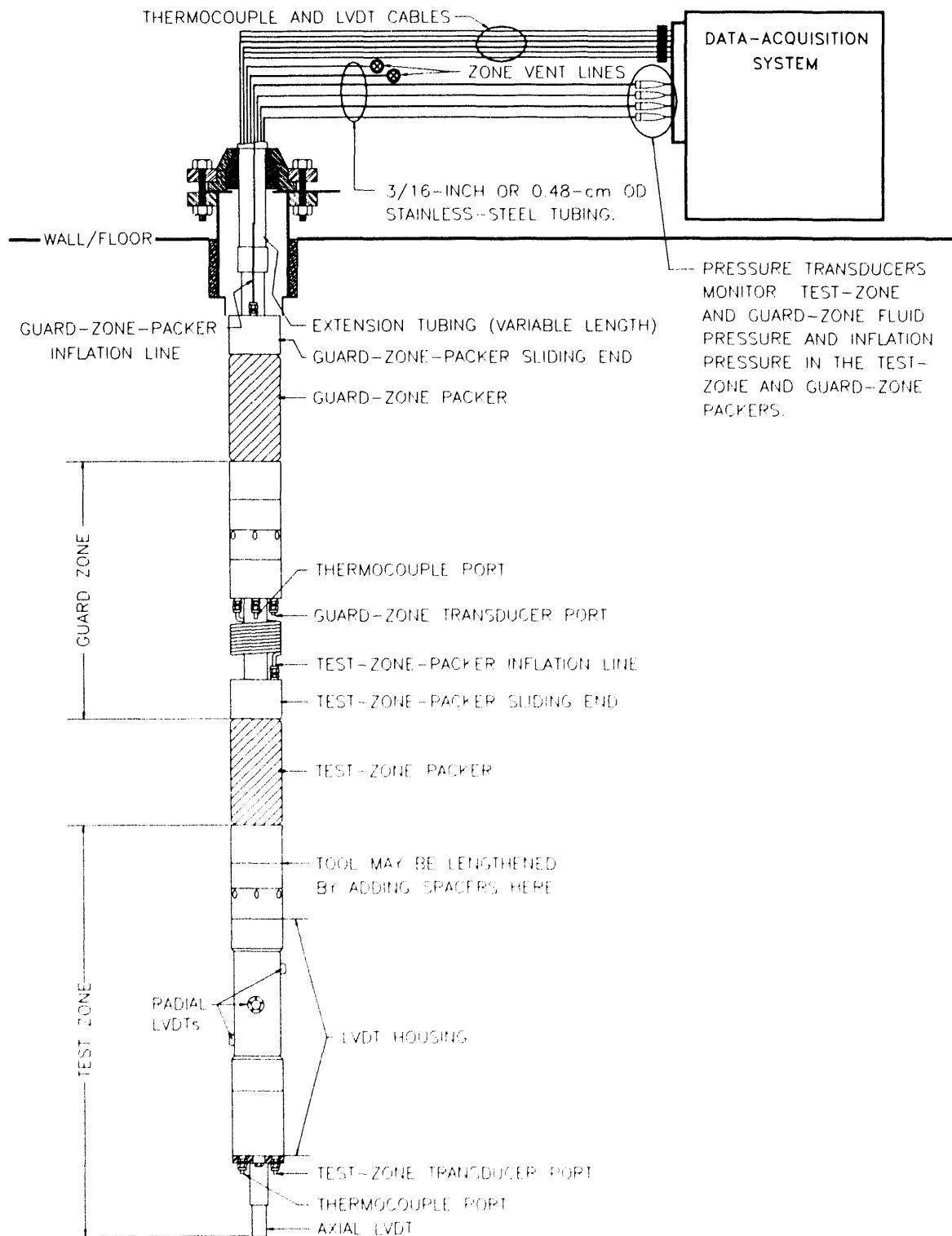
Figure 3-1. Typical configuration of the multipacker test tool used for hydraulic testing.

GUARD−ZONE−PACKER ELEMENT

R=4.754 cm

0.56 m

GUARD ZONE

236.0 cm STAINLESS−
STEEL INFLATION TUBING
R=0.238 cm

VENT/INJECTION PORTS AND
TRANSDUCER/THERMOCOUPLE
ACCESS

R=2.413 cm

0.15 m

0.25 m

TEST−ZONE−PACKER ELEMENT

R=4.754 cm

0.44 m

R=4.413 cm

RADIAL LVDTs

0.33 m

LVDT
HOUSING

TEST ZONE

AXIAL LVDT HOUSING

0.41 m

VENT/INJECTION PORTS AND
TRANSDUCER/THERMOCOUPLE
ACCESS
AXIAL LVDT
PLUNGER HOUSING

R=2.238 cm
R=1.796 cm

AXIAL LVDT PLUNGER

0.18 m

0.10 m

NOTE:
TEST−ZONE AND GUARD−ZONE PACKER ELEMENTS≈0.92 m LONG.

Figure 3-2. Detail of test- and guard-zone sections of the multipacker test tool.

13
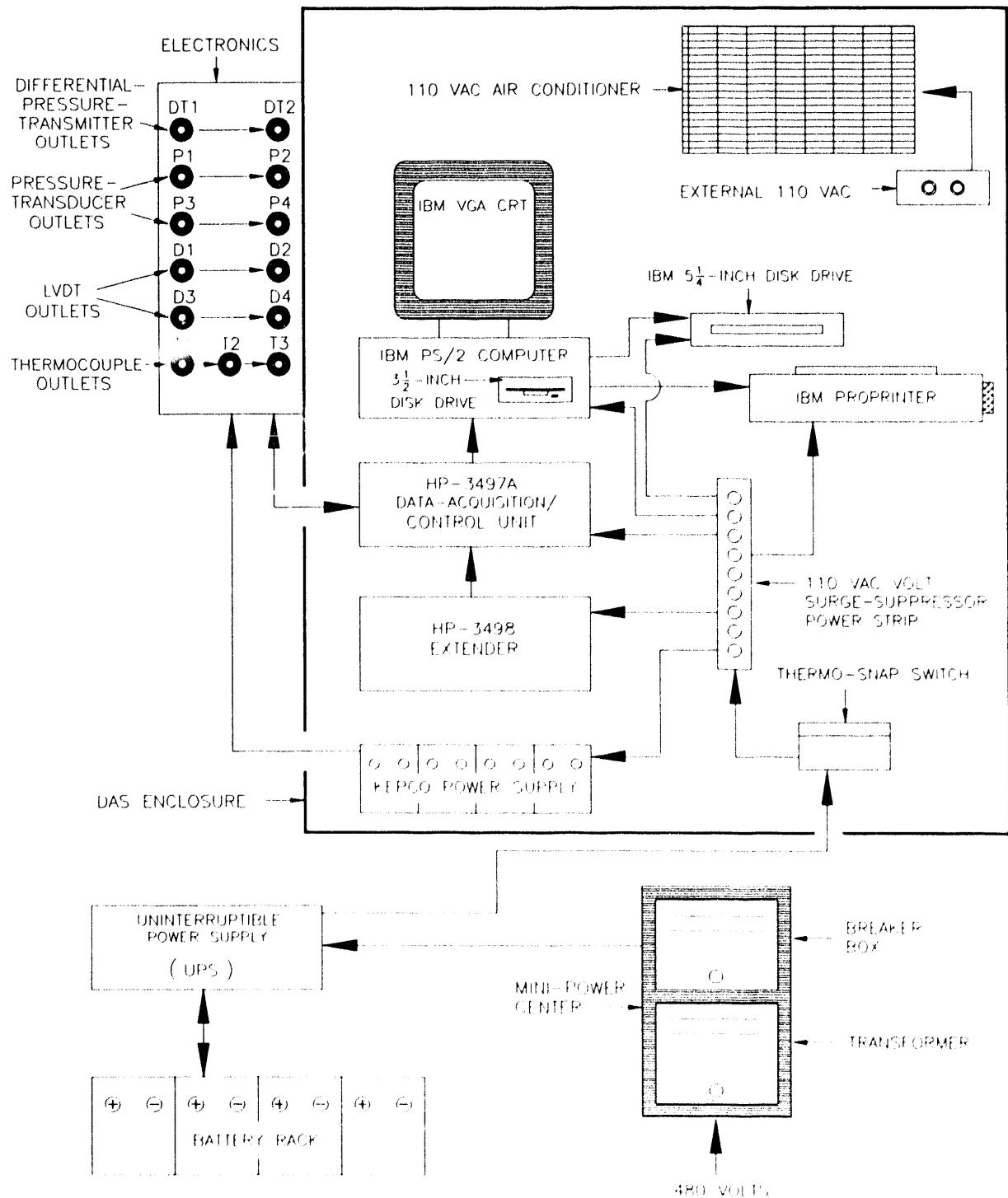
Figure 3-3. Schematic illustration of the data-acquisition system.

and a Hewlett Packard (HP) 3497A Data-Acquisition/Control Unit containing: power supplies to excite the transducers, thermocouples, and LVDTs; a signal scanner to switch and read channels; and a 5-1/2 digit voltmeter to measure the output from the transducers, thermocouples, and LVDTs. The data-acquisition software allows sampling of the sensors' outputs at user-specified time intervals ranging from 15 seconds to 24 hours. As data are acquired, they are stored both on the computer's hard disk and on either 3.5-inch or 5.25-inch diskettes. Real-time listing of the data on an auxiliary printer and screen and/or printer plots of the accumulated data are also possible.

3.3 Pressure Transducers

Pressures in the test and guard zones and in the packers are monitored with Druck PDCR-830 strain-gage pressure transducers rated to monitor pressures from 0 to 2000 psi (0 to 13.8 MPa). The transducers are mounted on instrument panels outside the boreholes and are connected to the isolated zones and the packers through 3/16-inch (0.48-cm) O.D. stainless-steel tubing which passes into and through the packer mandrels (Figure 3-2). The manufacturer's stated accuracy of the transducers is ± 0.1% of full scale, or ± 2 psi (0.014 MPa).

Transducers are calibrated before and after each installation of a multipacker test tool according to procedures described in Stensrud et al. (1992) to determine their accuracies and to evaluate the magnitude of transducer drift during the testing periods. For the tests discussed in this report, the pre-test calibrations showed that the test-zone pressure transducers were accurate to within ± 0.02 MPa over the pressure ranges observed during the tests. The post-test calibrations showed that drift caused the

transducers used during testing in boreholes S1P71 and S1P73 to have maximum errors of about 0.04 MPa by the ends of the tests, while the error in the transducer used for testing in borehole L4P51-B increased to 0.11 MPa. The accuracies of the test-zone transducers used during testing in the other boreholes improved slightly during the tests. Small errors in the third or fourth significant digits of the transducer readings are considered to have insignificant effects on interpretations of transmissivities from the pressure data. The sensitivity coefficients derived from the calibration of the transducers used during the permeability testing discussed in this report are tabulated in Stensrud et al. (1992).

3.4 Thermocouples

Type E Chromel-Constantan thermocouples are used to monitor temperatures within the test and guard zones during the permeability tests. The thermocouples are 1/8 inch (0.32 cm) in diameter and are sheathed in Inconel 600. The thermocouples are reported to be accurate to within ± 0.06 °C by the manufacturer, ARI Industries. The thermocouples are calibrated by Sandia National Laboratories.

3.5 Linear Variable-Differential Transformers

Open boreholes, rooms, and drifts in the underground facility exhibit closure, deformation, and differential movement between halite and anhydrite beds (Bechtel, 1986). Measurable borehole closure (on the order of a few tenths-of-a-millimeter change in borehole diameter) in a shut-in, fluid-filled test interval could raise the pressure in the hole. Axial movement of the multipacker test tool can be caused by changes in packer-inflation pressure, pressure buildup or withdrawal in the isolated intervals, and hole

elongation resulting from creep closure of the excavations. The rate of rock creep decreases with increasing distance from an excavation (Westinghouse, 1990), causing boreholes drilled from an excavation to elongate. Axial movement of the test tool can change the test-zone volume, which, in low-permeability media, can affect the observed pressure response in an isolated borehole interval. Three Trans-Tek Model 241 LVDTs are radially mounted, with 120° separation, on the test-interval part of the multipacker test tool to measure radial borehole deformation (Figures 3-1 and 3-2). These LVDTs can each measure a range of motion of 0.5 cm. An axially mounted Trans-Tek Model 245 LVDT on the bottom of the test tool measures tool movement along the borehole axis (Figures 3-1 and 3-2). This LVDT has a range of motion of 10 cm. The LVDT responses are reported by Trans-Tek to be linear within $\pm$ 0.5% over their working ranges. Jensen (1990) discusses in detail the design, calibration, and use of the LVDTs.

3.6 Differential-Pressure-Transmitter Panel

Fluid volumes produced during constant-pressure flow tests were measured using a differential-pressure-transmitter panel (Figure 3-4). The panel consists of a differential-pressure transmitter (DPT) and injection/withdrawal columns. Rosemount Alphaline Model 1151DP DPTs are used in the WIPP permeability-testing program. The DPTs are calibrated from 0 to 100 cm of water (0-9.8 kPa). The manufacturer's stated accuracy of the DPTs is $\pm$ 0.2% of the calibrated span, including the combined effects of hysteresis, repeatability, and independent linearity.

The DPT panel includes five cylindrical columns: 4-inch (10.16-cm), 1-inch (2.54-cm), 1/2-inch (1.27-cm), and 3/8-inch (0.95-cm) O.D. stainless-steel columns, and a 1/4-inch (6.35-mm) Lexan-column manometer (Figure 3-4). As fluid from the test zone enters and fills a column, voltage measurements are taken by the DAS from the DPT. The DPT measures the difference in the pressure exerted on two sides of a sensing diaphragm. On one side of the diaphragm is the ambient test pressure. On the other side of the diaphragm is the pressure exerted by the fluid in the column, plus the ambient pressure. The difference, or differential pressure, is equal to the pressure exerted by the fluid in the column. As the fluid level in the column changes (a change in fluid-column height corresponds to a linear change in the volume), the voltage output changes proportionally.

During constant-pressure flow tests, the pressure inside the injection/withdrawal column is maintained under near constant-pressure conditions. To maintain constant pressure, the injection/withdrawal column is connected to a nitrogen-gas reservoir. Before testing, the reservoir pressure is set to the designated test pressure. During a constant-pressure withdrawal test, fluid (and sometimes gas) enters a designated column from the test zone, but little change in the gas pressure in the column occurs due to the buffering capacity of the gas reservoir.

3.7 Gas-Brine Separation and Measurement System

Fluid volumes produced during constant-pressure flow tests in borehole S1P72 were measured using the gas-brine separation and measurement system shown in Figure 3-5. The system
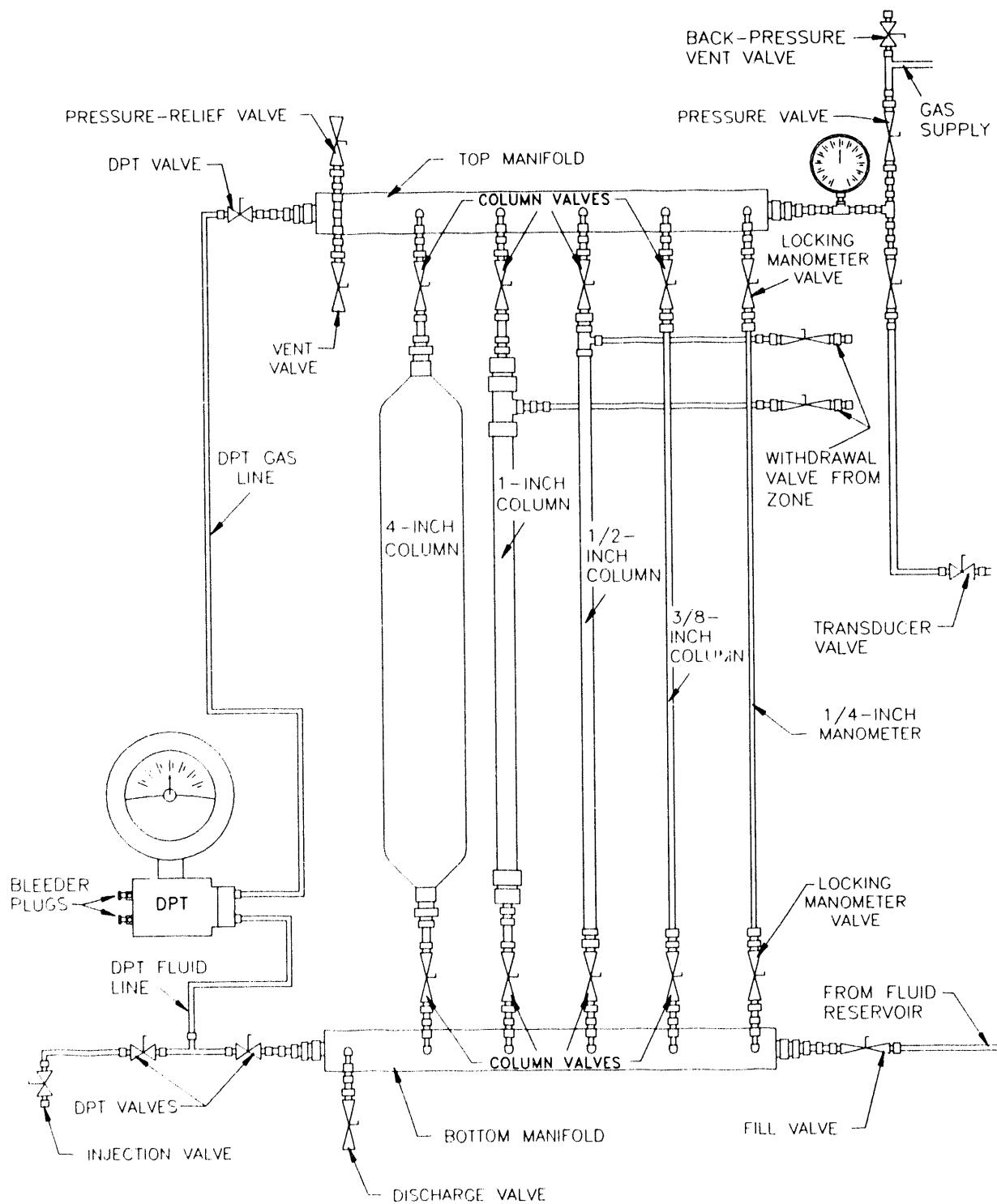
Figure 3-4. Differential-pressure-transmitter panel.

17
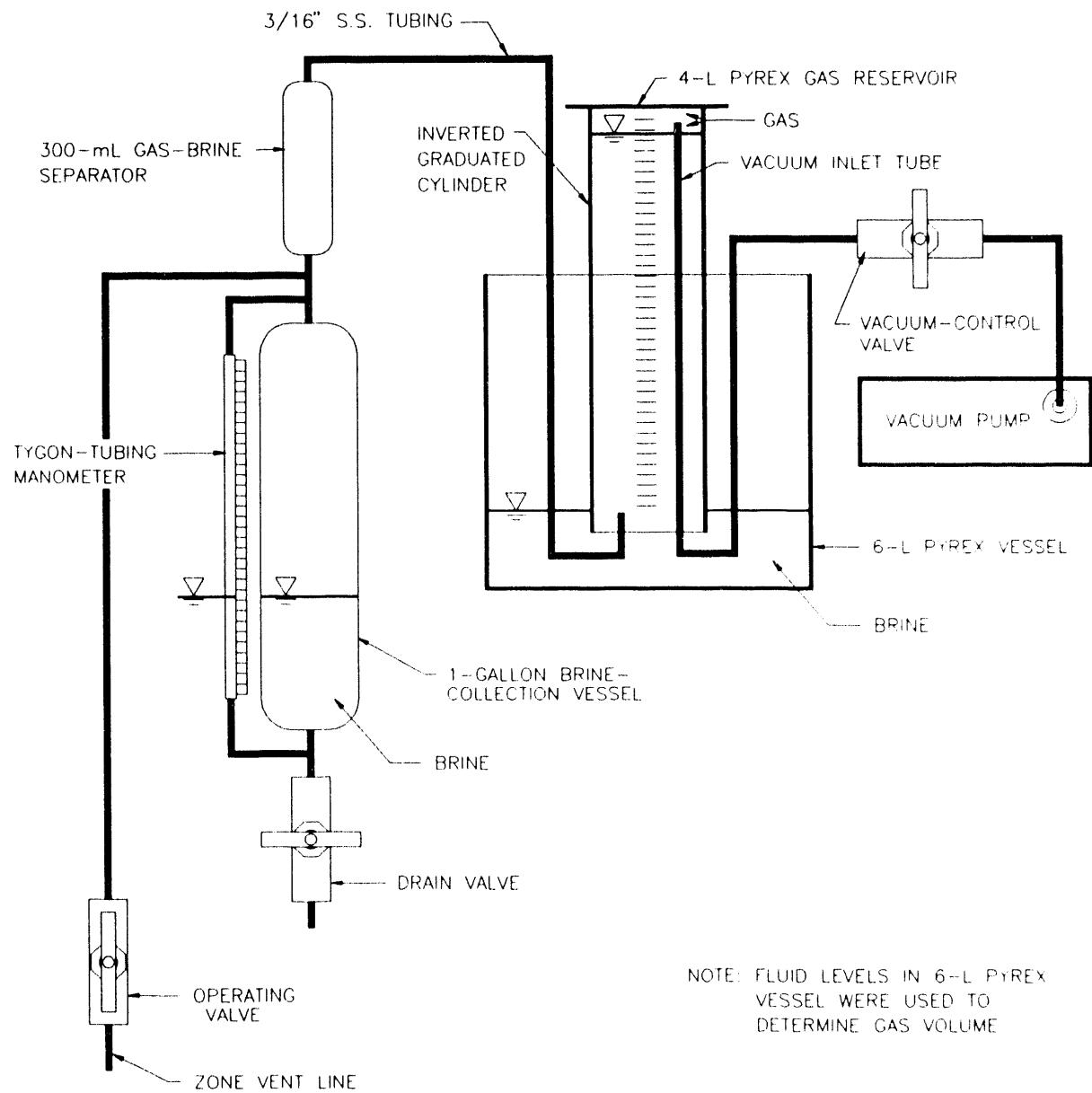
Figure 3-5. Gas-brine separation and measurement system.

consisted of a 1-gallon (3.785-L) stainless-steel brine-collection vessel coupled with a tygon-tubing manometer, a 300-mL stainless-steel gas-brine separator, a 4-L graduated cylinder (gas reservoir) inverted in a water-filled 6-L Pyrex vessel, and a vacuum pump. Brine and gas flowing from the test zone through the zone vent line were collected in the 1-gallon brine-collection vessel and in the gas reservoir, respectively. The 300-mL gas-brine separator prevented brine from flowing into the 6-L Pyrex vessel where it could not be measured.

The S1P72 constant-pressure flow tests were performed with the flow line open to atmospheric pressure at the surface. However, the pressure in the test zone did not remain constant during these tests, but cycled between about 0.05 MPa and about 0.08 MPa. The test-zone pressure varied because both brine and gas were produced during the flow test. Brine and gas traveled from the test zone to the gas-brine separation and measurement system through the test-zone vent line (Figure 3-5). The downhole end of the vent line was located between 0.09 and 0.18 m (depending on test-tool rotation) vertically above the lowest point in the test zone. Given the low pressures in the test zone (0.05 - 0.08 MPa), the gas in the test zone was probably present as a separate phase and collected at the top of the test zone above the brine. When the brine level in the test zone was high enough to cover the end of the vent line, the flow of brine and gas from the formation into the test zone would cause the gas pressure above the brine to increase. The gas pressure would continue to increase until enough brine had flowed to the gas-brine separation and measurement system to cause the brine level to fall below the bottom of the vent line. The gas would then vent to the gas-brine separation and measurement system, decreasing the gas pressure in the test zone until

brine again covered the end of the vent line, and the process would repeat.

The volume of brine that flowed into the brine-collection vessel over a given period of time was calculated from changes in the height of the brine in the manometer. Calibration of the brine-collection vessel before the test provided a correlation between a change in the height of the brine in the manometer and the corresponding volume of brine that had flowed into the brine-collection vessel. Manometer readings were manually entered in the test log book and were not recorded by the DAS.

The volume of gas produced from the test zone over several hours during the constant-pressure flow tests exceeded the volume of the gas reservoir, preventing continuous direct measurement of gas flow. To calculate the total gas flow, several gas-flow cycles were measured directly using the gas-brine separation and measurement system and a correlation was developed between the change in test zone pressure during each cycle and the volume of gas produced. Total gas production during each constant-pressure flow test was then determined by multiplying the pressure change during each cycle as recorded by the DAS by the correlation coefficient. This correlation was developed in the following manner. Gas flowing from the test zone first entered the gas-brine separator. From there the gas flowed through 3/16-inch (4.76-mm) stainless-steel tubing into the gas reservoir which was inverted in a 6-L Pyrex vessel partially filled with water (Figure 3-5). A vacuum pump was used before each flow cycle to decrease the pressure in the gas reservoir, causing the water to rise in the gas reservoir. Gas flowing into the gas reservoir displaced the water and the volume of gas produced during each cycle was calculated from the volume of water displaced.

Two corrections were made to the gas volumes directly measured in the gas reservoir. Brine flowing into the 1-gallon brine-collection vessel during each cycle displaced a corresponding volume of gas which then flowed into the gas reservoir. This volume was subtracted from the measured volume of gas at the end of each cycle. Also, the gas pressure in the gas reservoir at the end of each cycle was usually above or below atmospheric pressure depending on the relative positions of the water levels in the gas reservoir and in the 6-L Pyrex vessel (Figure 3-5). The remaining volume of gas was adjusted to reflect the volume it would occupy at atmospheric pressure.

3.8 Packer-Pressure-Maintenance System

Packer pressures steadily declined during some testing sequences, potentially jeopardizing the isolation of test and/or guard zones. For testing in borehole L4P52, a pressure-maintenance system (Figure 3-6) was attached to the guard-zone packer to hold the packer pressure nearly constant during testing. A 1-gallon cylinder was filled approximately half-full with water and then pressurized with nitrogen to the desired packer pressure. The control valve between the cylinder and the nitrogen tank was closed when the desired pressure in the cylinder was achieved, and the control valve between the cylinder and the packer was opened, allowing the pressures in the packer and in the cylinder to equilibrate. The nitrogen in the cylinder served to increase

the compressibility in the packer/cylinder system. Subsequent losses of fluid from the packer and/or changes in packer volume thereafter resulted in smaller changes in packer pressure than would have otherwise occurred (see Figure F-3).

3.9 Compliance-Testing Equipment

Pickens et al. (1987) have shown that test-tool movement in response to packer inflation and fluid injection or withdrawal can affect pressure responses in isolated intervals in boreholes in low-permeability media. Figure 3-7 illustrates how packer movement due to packer inflation can cause the packer element to displace fluid in isolated intervals, causing changes in pressure. Changes in the shape, volume, or position of the test tool which affect pressure responses during testing are referred to as compliance. To evaluate the magnitude of compliance for the multipacker test tool, preinstallation compliance tests were conducted in the underground facility on all test tools according to procedures outlined in Section 4.1. Compliance tests were conducted in sealed and pressure-tested sections of 4.5-inch (11.43-cm) O.D. stainless-steel casing to differentiate test-tool-related phenomena from formation-related pressure responses observed in boreholes. The casing was intended to simulate a borehole with effectively zero permeability. The casing was placed in a borehole to minimize temperature fluctuations and associated pressure changes (Figure 3-8).

PRESSURE
REGULATOR

CONTROL
VALVE

VENT VALVE

1-GAL WHITEY
SAMPLE CYLINDER

PRESSURE-RELIEF
VALVE

NITROGEN
TANK

NITROGEN

FLUID

CONTROL VALVE
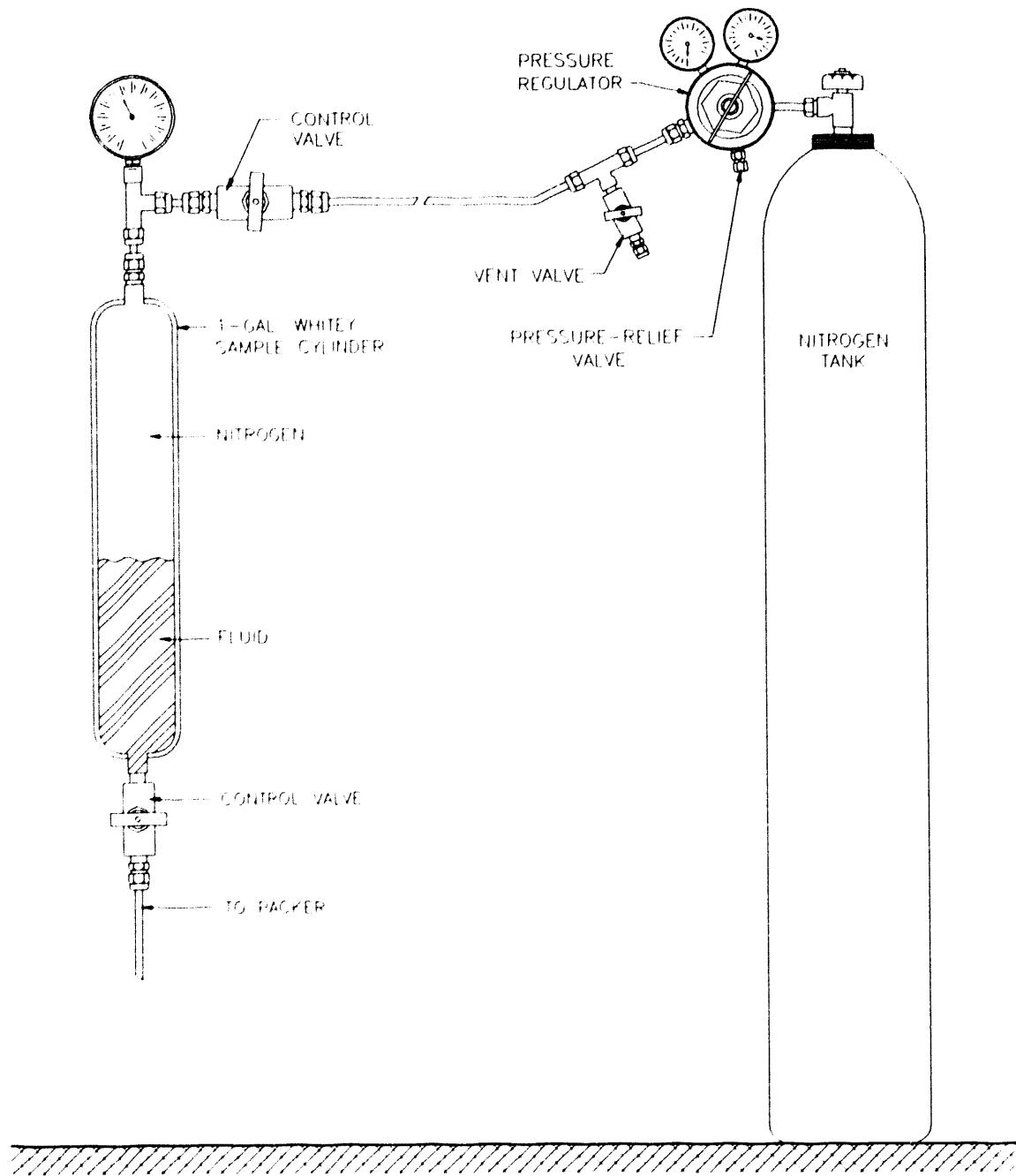
TO PACKER

Figure 3-6. Packer-pressure-maintenance system.

21

BEFORE INFLATION

VENT LINE

INJECTION LINE

INFLATION LINE

INFLATION LINE
(TEST–ZONE
PACKER)

SLIDING END

3/16–INCH (0.48 cm) O.D.
STAINLESS–STEEL TUBING
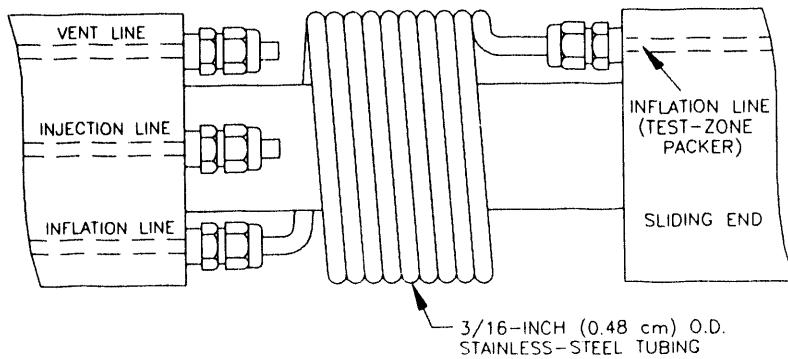
AFTER INFLATION

SLIDING END OF TEST–ZONE PACKER
MOVES ALONG BOREHOLE WHEN INFLATED

VENT LINE

INJECTION LINE

INFLATION LINE

INFLATION LINE
(TEST–ZONE
PACKER)
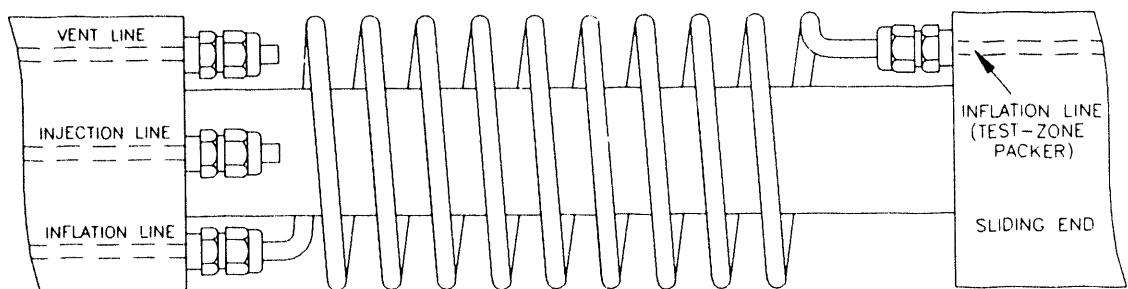
SLIDING END

Figure 3-7. Movement of the sliding-end sub in the guard zone during packer inflation.

COMPLIANCE FACTORS

- PACKER DEFORMATION
- TOOL MOVEMENT
- GAS ENTRAPMENT IN ZONES

5.5" O.D. BOREHOLE

WALL

FLOOR

GUARD ZONE

BEFORE
AFTER

MOVEMENT OF SLIDING END DURING INFLATION

GUARD-ZONE PACKER

BEFORE
AFTER

MOVEMENT OF SLIDING END DURING INFLATION

TEST-ZONE PACKER

TEST ZONE

3 RADIAL LVDTs SPACED AT 120°

STAINLESS-STEEL COMPLIANCE-TEST CHAMBER

NOTE: NOT TO SCALE

AXIAL LVDT
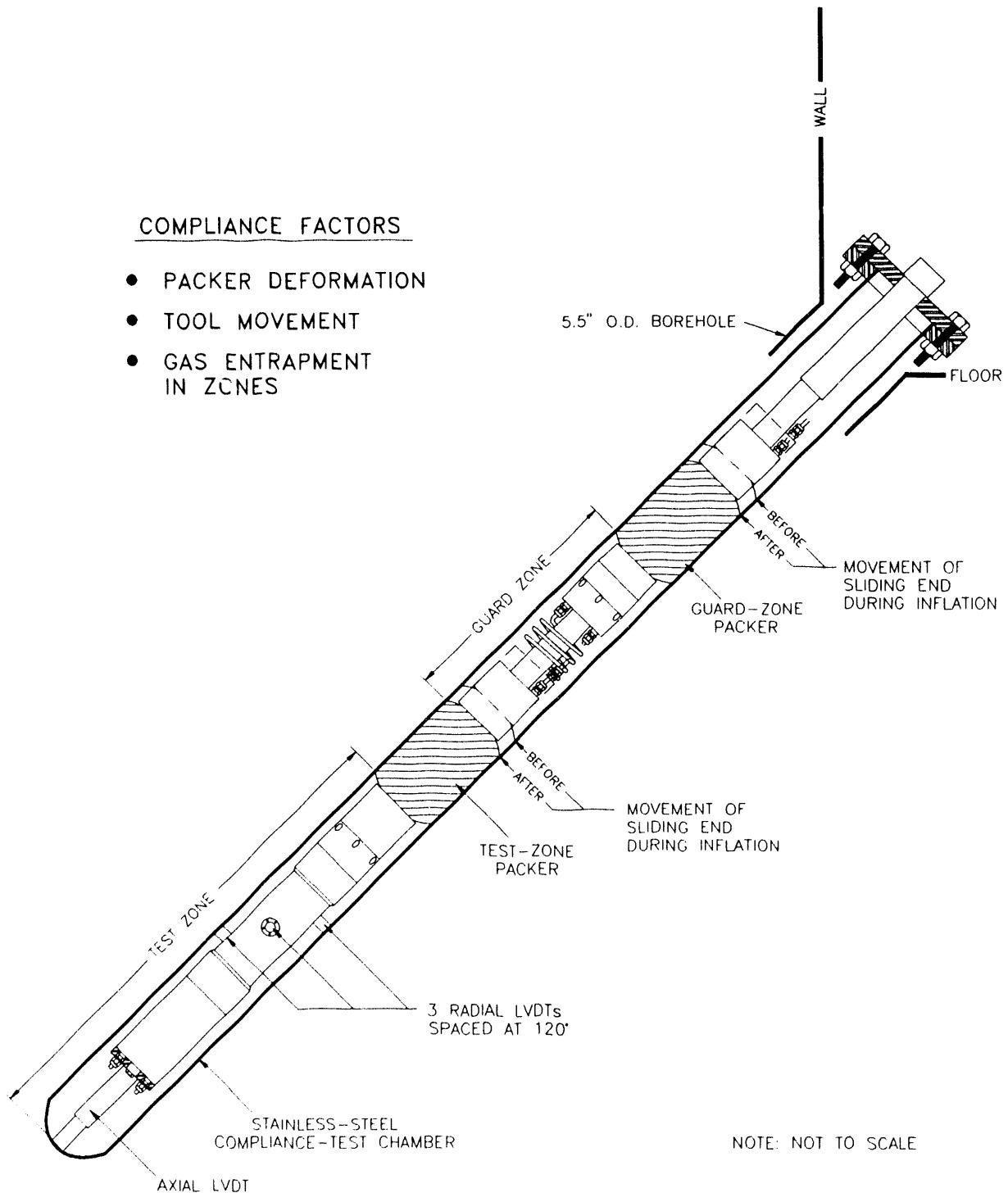
Figure 3-8. Cross-section view of the stainless-steel compliance-testing chamber in borehole P4P30.

4. TESTING PROCEDURES

The multipacker test tools are used to conduct hydraulic tests in boreholes drilled from the underground excavations. In low-permeability formations such as the Salado, changes in the volume or temperature of the test-zone fluid and/or the test tool can affect observed pressure responses, as described in Pickens et al. (1987). In addition, pressure changes in isolated sections of boreholes in low-permeability media can cause physical movement of the test tool. Pressures in test intervals may also be affected by changes in packer-inflation pressures, and vice versa, as when a pulse injection in a test zone increases the forces acting against the outside of the test-zone packer, causing the packer-inflation pressure to increase.

Changes in the volume and pressure of the test-zone fluid that are not due to the formation's hydraulic response but instead to changes in the position of the test tool or deformation of the test tool or borehole are included under the term "compliance". Pickens et al. (1987) showed that compliance-related pressure changes during hydraulic tests of formations with hydraulic conductivities less than 10^{-12} m/s can obscure and/or dominate actual formation-related pressure changes and result in incorrect estimates of the formation's hydraulic properties. Test-tool-related compliance can be empirically estimated by subjecting the testing equipment to simulated test conditions and observing the resulting pressure responses. These "compliance tests" provide data to understand and/or compensate pressure changes resulting from compliance during actual hydraulic testing.

The multipacker test tool to be used for hydraulic testing in any borehole undergoes compliance testing in a compliance-test chamber (Section 3.8) before being installed in the test borehole. Compliance testing quantifies the response of the test tool to the types and magnitudes of pressure changes anticipated during hydraulic testing. After compliance testing is completed, the test tool is installed in the test borehole. A hydraulic testing sequence is then performed, consisting of a shut-in pressure buildup followed by one or two pressure-pulse tests and in some cases a constant-pressure flow test followed by a buildup test. Compliance- and hydraulic-testing procedures are discussed below.

4.1 Compliance Testing

Compliance tests are performed for each test tool before the tool is installed in a test borehole. The purposes of the compliance testing are to (1) establish that the test tools have been properly assembled and that all seals and fittings are performing as designed; and (2) evaluate test-tool responses to packer inflation and applied pressure pulses in the intervals isolated by the inflated packers. For compliance tests, the test tools with all monitoring instruments are installed in test chambers in the same manner employed when installing the test tool in a borehole. The compliance chambers consist of stainless steel well casing sealed at one end. The DAS is used to monitor and record the results of the compliance testing.

The test tool's packers are sequentially inflated, starting with the test-zone packer. Both packers are inflated to between 8 and 10 MPa, after which the pressures are monitored for 24 to 48 hours for evidence of leaks or improper performance. Packer pressures usually decrease

during this period due to the elasticity of the packer-element material, air that may have been entrapped during inflation going into solution, and other compliance-related phenomena. After monitoring this pressure decline for the initial 24- to 48-hour period, packer-inflation pressures are usually increased to 8 to 10 MPa and monitored for an additional 24 to 48 hours.

After the leak-check/packer-pressure-adjustment periods, the test zone is subjected to a pressure-injection pulse of at least 3.5 MPa. The pressure responses of both the test and guard zones are then monitored for evidence of leaks, and the associated packer-pressure responses are also monitored. After evaluation of test-zone integrity is completed, the same procedure is followed to evaluate the integrity of the guard zone.

In some instances, the test- and guard-zone pressures are increased and/or decreased in a series of step pressure-injection and/or pressure-withdrawal pulses to provide a range of test-zone and packer-pressure responses to pressure changes in neighboring zones and packers. During the withdrawals, the volume of fluid released during each pressure drop is measured to provide data with which to evaluate test-tool or system compressibility.

Figures 4-1 to 4-5 display the results of a typical compliance-test sequence. Figure 4-1 shows the pressures in the test and guard zones; Figure 4-2 shows the pressures in the test-zone and guard-zone packers; Figure 4-3 shows the fluid temperatures in the test and guard zones; Figure 4-4 shows the relative movement of the radial LVDTs; and Figure 4-5 shows the relative movement of the axial LVDT.

During the compliance test depicted on Figures 4-1 to 4-5, the pressure in the test zone was increased from approximately 0 MPa to 7 MPa on Day 223 by injecting a small quantity of brine. The peak pressure quickly dissipated to about 4 MPa and then slowly decreased due to compliance effects, such as packer readjustment as stresses were redistributed through the entire test-tool string and axial test-tool movement. Figure 4-1 also shows that the guard zone received a pulse injection on Day 227 when the pressure was increased from 0 MPa to 5 MPa. The guard-zone pressure displayed similar behavior to that of the test zone. The pulse injections into the test and guard zones caused pressure changes throughout the system. As the pressure in a zone is increased, the adjacent packer(s) is compressed, causing its internal pressure to increase (Figure 4-2). The packer(s) also deforms slightly away from the zone being pressurized, which can cause the pressure in the adjacent zone to rise slightly. This pressure increase can in turn be transmitted to another packer.

Figure 4-3 shows the temperatures measured in the test and guard zones during compliance testing. Temperatures were stable throughout the testing period except for short-lived increases in the guard-zone temperature following the pulse injections.

Figures 4-4 and 4-5 show the LVDT responses during compliance tests. The radial LVDTs (Figure 4-4) show that the test chamber's diameter in the test zone increased by about 0.04 mm during the pulse injection. This increase is consistent with the predicted diameter increase calculated from the material properties of the test chamber. Note that because of the LVDTs' orientation (see Section 3.5), the actual increase in diameter must be estimated by integrating the responses of all three radial LVDTs. Figure 4-5 shows that the axial LVDT
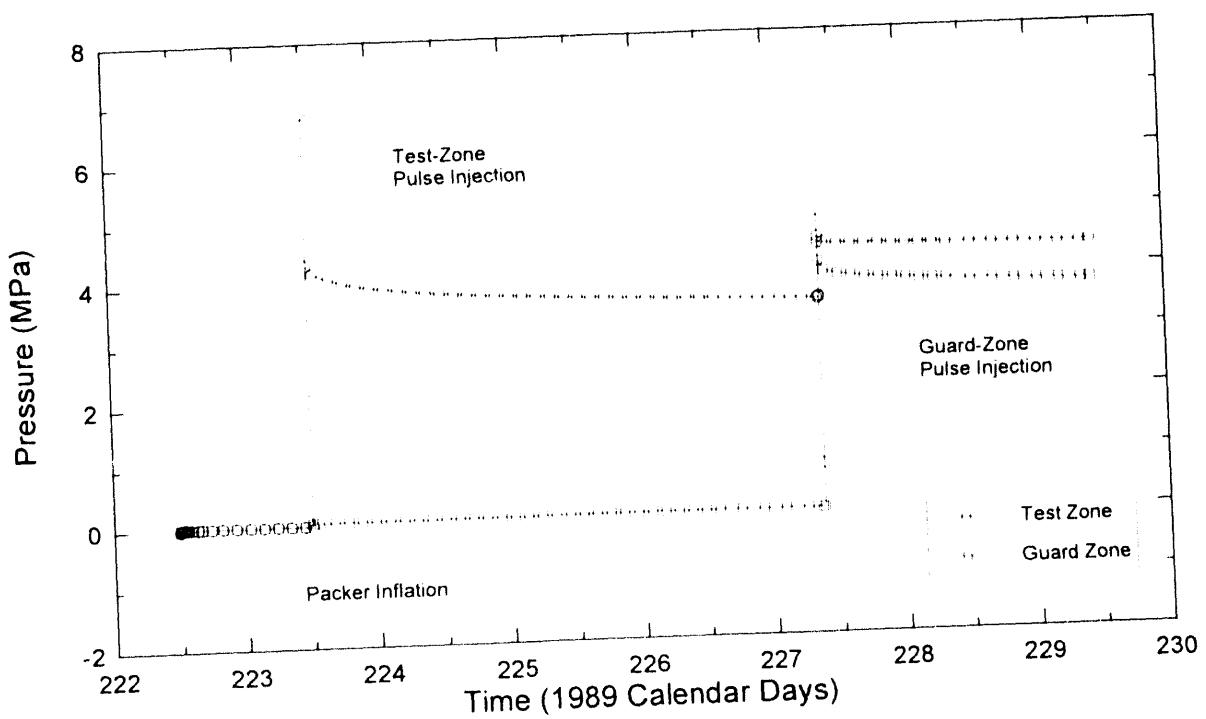
Figure 4-1. Zone pressures for compliance test COMP 16, multipacker test tool #5.
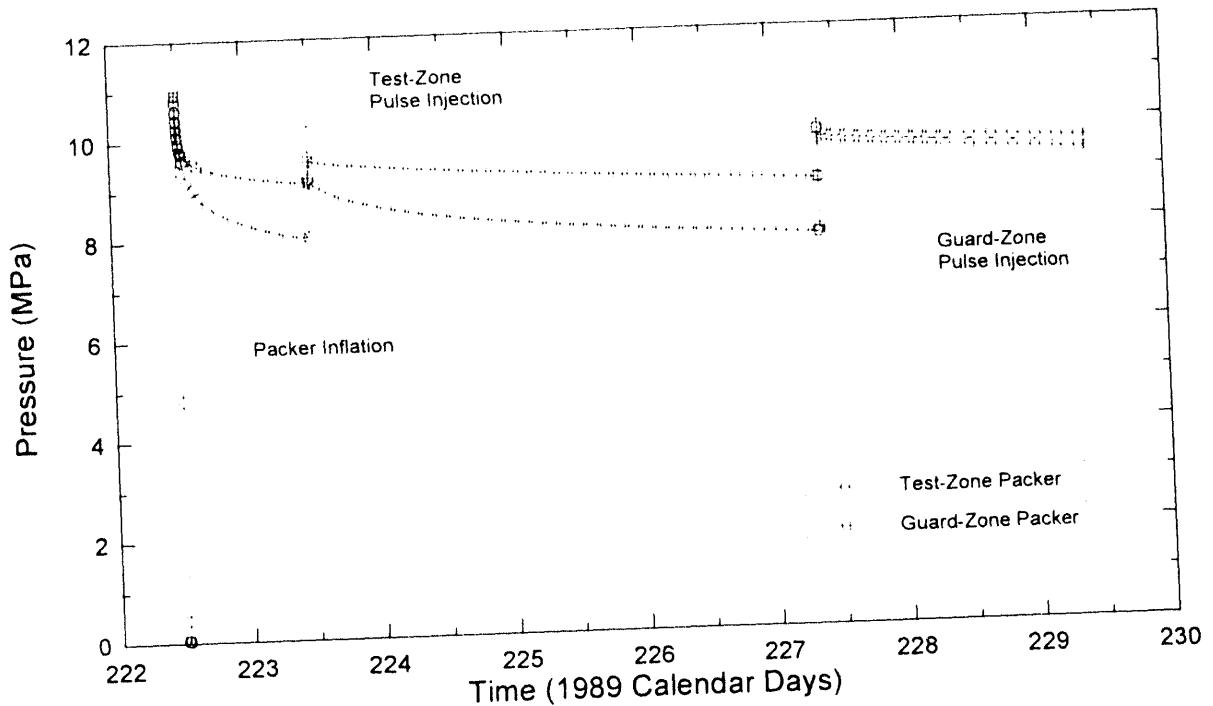
Figure 4-2. Packer pressures for compliance test COMP 16, multipacker test tool #5.

Figure 4-5. Axial-LVDT data for compliance test COMP 16, multipacker test tool #5.

was compressed (shortened) when the test-zone packer was inflated, but tended to lengthen as the test-zone-packer pressure declined. This response is probably due to some elastic response of the packer element. During the pulse injection in the test zone, the axial LVDT lengthened as the increase in test-zone pressure forced the test tool upward in the compliance-testing chamber. The guard-zone pulse injection did not have the same effect on the axial LVDT response. Stensrud et al. (1992) present complete plots and tabulated data for the compliance tests performed before the hydraulic tests analyzed in this report.

4.2 Hydraulic Testing

A hydraulic-testing sequence begins with the drilling of a nominal 4-inch (10.2-cm) diameter borehole. Downward-drilled boreholes are filled with brine shortly after drilling is completed.

Upward-drilled boreholes are filled after a test tool is installed and the packers are inflated by injecting brine through an injection line until brine discharges from a vent line located at the top of the isolated interval. The brine used is collected from boreholes in the WIPP underground facility and, therefore, should already be in chemical equilibrium with the Salado strata (Deal et al., 1991). A multipacker test tool is installed in each test borehole as soon after drilling as possible to minimize pretest borehole history under non-shut-in conditions. The packers are sequentially inflated to approximately 11 MPa, starting with the lower-most packer. The packers are inflated with fresh water using a positive-displacement pressure-intensifier pump. The packer-inflation pressures are monitored closely for 24 to 48 hours after inflation. If compliance-related reductions in the packer-inflation pressures of greater than 3 MPa are

29

observed, the packer-inflation pressures are increased to 11 MPa and observed for an additional 24 hours. After the initial transient decreases in packer pressures occur and the packer-inflation pressures approach relative stability, valves on the test- and guard-zone vent lines are closed to shut in the test and guard zones. Once the test and guard zones are shut in, the pressures in the two zones increase as they equilibrate with the formation pore pressure in the vicinity of the borehole. After the rate of pressure increase in the test zone decreases and the pressure-recovery curve appears to be on an asymptotic trend (Figure 4-6), hydraulic testing begins.

4.2.1 PRESSURE-PULSE TESTING. Pressure-pulse testing as described by Bredehoeft and Papadopulos (1980) is the first type of hydraulic test performed in a test interval. Pulse-withdrawal rather than pulse-injection tests were generally chosen for the Salado permeability testing because: they do not force fluids into the formation that may not be in complete chemical equilibrium with the rock; they do not overpressurize the formation, a process which could potentially open existing fractures or create new fractures by hydrofracture; and they more closely represent the hydraulic conditions expected shortly after closure of the WIPP underground facility when brine may be flowing
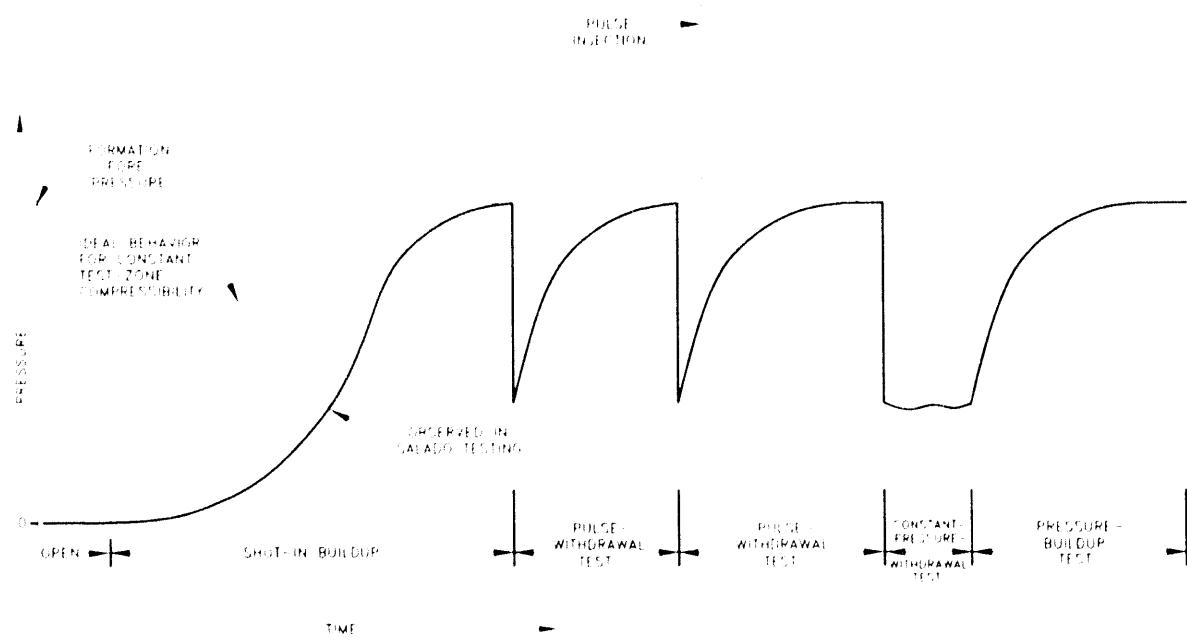
Figure 4-6. Typical permeability-testing sequence.

from the host rock towards the relatively underpressurized rooms.

Pulse-withdrawal tests are initiated in a test or guard zone by opening the zone's vent valve and allowing fluid to flow from the zone until the desired fraction of the shut-in pressure has dissipated. After the desired pressure decrease has been achieved, the valve is then closed to shut in the zone. The volume of fluid released from the vent line during each pulse withdrawal is measured and recorded. Following the pulse withdrawal, the reequilibration of the zone's pressure and the formation pore pressure is monitored with the DAS. After the zone's pressure has recovered to approximately its pre-pulse value, the test is usually repeated (Figure 4-6) to provide assurance that the observed pressure responses are reproducible and are representative of formation responses.

Pulse-injection tests were performed when little pressure buildup occurred in a shut-in interval to determine whether the lack of pressurization was caused by low pore pressure in the formation or by low permeability. A pulse-injection test was also performed in the L4P51-B guard zone (see Section 7.1.2.2) to evaluate the integrity of the test tool. Pulse-injection tests are initiated by injecting brine until the desired pressure increase has been achieved. The zone is then shut in and the reequilibration of the zone's pressure and the formation pore pressure is monitored.

4.2.2 CONSTANT-PRESSURE FLOW TESTING. Constant-pressure flow tests are performed after pressure recovery from a pressure-pulse test is complete and the fluid pressure in the zone to be tested is relatively constant. The test zone is opened to one of the columns on the DPT panel (Section 3.6) which is pressurized to the constant pressure at which the

test is to be conducted. The flow tests discussed in this report were all withdrawal tests, and were conducted at constant pressures between 0.2 and 3 MPa below the pretest zone pressures. As a constant-pressure flow test proceeds, the increase in fluid volume in the column is measured by the DPT. If free gas is also produced, it is captured and its volume measured as described in Section 3.7. The test is terminated by shutting in the test zone after adequate flow data have been collected for analysis.

4.2.3 PRESSURE-BUILDUP TESTING.
Pressure-buildup testing consists of monitoring the pressure recovery after terminating a constant-pressure flow test and shutting in the test zone. A pressure-buildup test should generally last longer than the preceding flow test to provide adequate data for analysis. In low-permeability systems, buildup periods between two and ten times as long as the preceding flow periods are often required, and are always preferred.

5. TEST LOCATIONS AND BOREHOLES

Figure 5-1 shows the locations of all of the boreholes drilled to date for the underground hydraulic-testing program. Boreholes have been drilled in the experimental area, the operations area, and the waste-storage area. Borehole locations are chosen to provide access to different Salado Formation lithologies (Figure 2-3), to investigate whether or not the ages of excavations affect permeability in similar stratigraphic intervals, and to provide a representative distribution of data from a wide area of the underground facility. The tests discussed in this report were performed in boreholes L4P51, L4P52, S1P71, S1P72, S1P73, and SCP01.

In some instances, holes are deepened and additional testing is performed after testing of the initial borehole configuration has been completed. In such a case, the first testing sequence performed in a borehole is given an "A" suffix, as in L4P51-A, and subsequent testing sequences are given "B", "C", etc. suffixes, as in L4P51-B and L4P51-C. Note that the "A" testing for boreholes L4P51 (test zone only) and S1P71 was reported in Beauheim et al. (1991).

All of the boreholes were cored and/or drilled to a nominal 4-inch (10.2-cm) diameter. The boreholes were cored, when possible, to allow sample recovery. In most cases, compressed air was used as the circulation medium during drilling to remove drill cuttings from the holes. When visible quantities of formation brine were encountered in association with clay and/or anhydrite layers, brine saturated with respect to sodium chloride was used as the drilling fluid and conventional, non-coring drill bits were used. To provide an anchoring assembly for a test tool, a

5-inch (12.7-cm) I.D., 20-inch (51-cm) long, steel borehole collar was grouted to the formation in the top of each of the holes. The multipacker test tools were then bolted or otherwise anchored to the collars as described in Section 3.1 to reduce test-tool movement in response to packer inflation and pressure buildup in the guard and test zones.

Core samples were recovered from 95 percent of the drilled lengths of the test boreholes. The lithologies, fracturing, penetration times, and fluid occurrences noted in each borehole were recorded on core sample logs presented by Stensrud et al. (1992). The lithologies are referenced to the standard WIPP map units listed in Appendix A.

Descriptions of the drilling locations and individual boreholes are presented below. A summary of the configuration information for each test is presented in Table 5-1.

5.1 Room L4

Room L4 was excavated in February 1989 (Westinghouse, 1990) to nominal dimensions of 10.1 m wide, 3.7 m high, and 59.7 m long. Borehole L4P51 was drilled and cored vertically downward to a depth of 4.75 m below the floor of the room (Figure 5-2) from October 18 to 19, 1989 (Calendar Days 290 and 291). The borehole was drilled to allow testing of Marker Bed 139 and the underlying halite, polyhalitic halite, and clay D during test sequence L4P51-A. Marker Bed 139 (including clay E) was encountered from 1.50 to 2.36 m below the floor of the room, and clay D was encountered from 4.55 to 4.57 m deep (Figure 5-2).
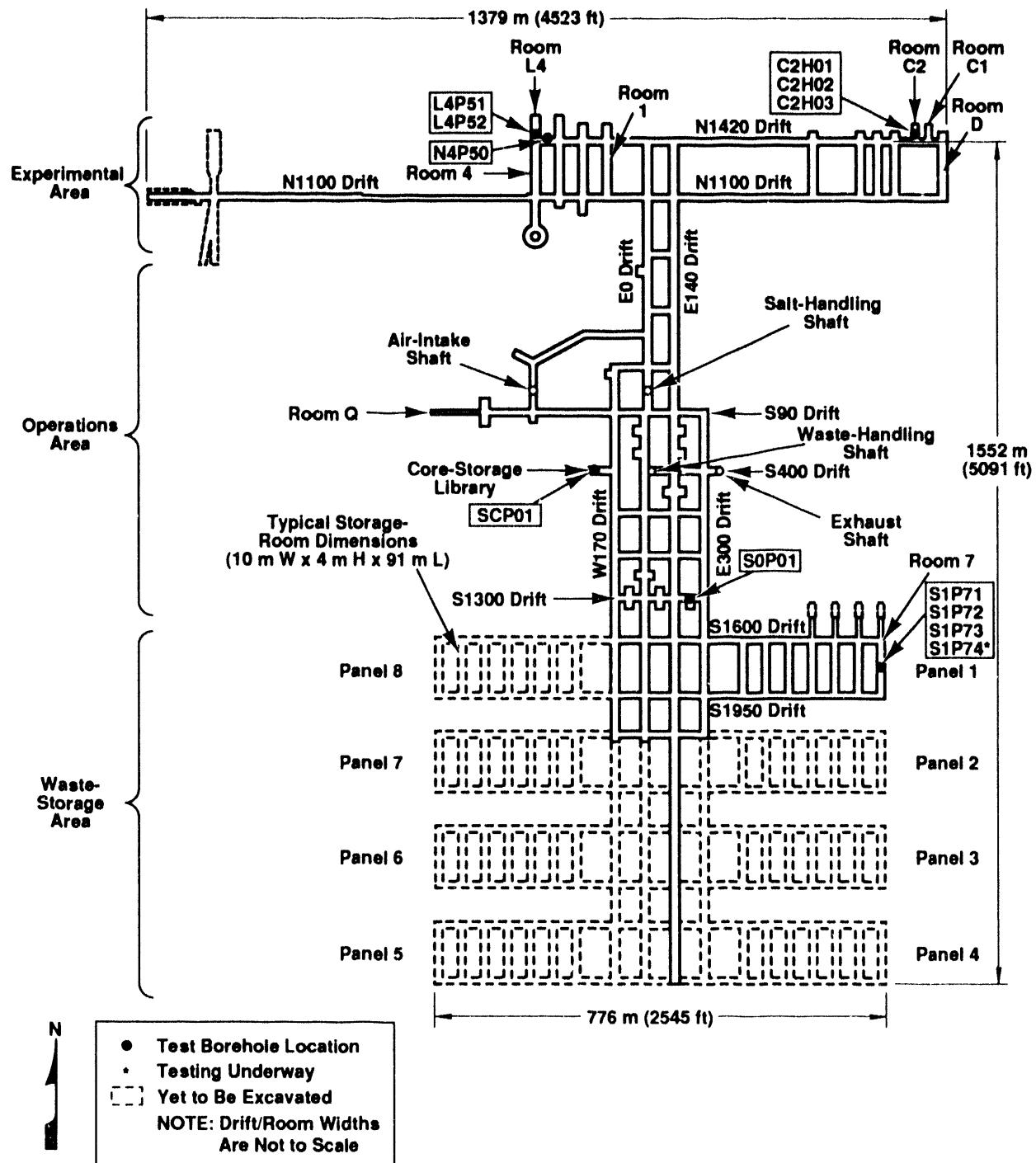
Figure 5-1. Map of the WIPP underground facility showing test locations.

Table 5-1. Summary of Test-Configuration Information

| Hole	Orientation	Radius (cm)	Zone	Fluid Volume (cm³)	Isolated Interval (m)	Map Units Tested
L4P51-A	vertical down	5.297	guard	2927	1.45-2.49	PH-4, MB139, clay E, H-4
L4P51-B	vertical down	5.340	test	4532	8.63-10.06	PH-1, anhydrite "c", clay B, H-1
	vertical down	5.340	guard	2906	6.75-7.79	H-2
L4P52-A	up 50°	5.163	test	3403	4.14-5.56	11 (anhydrite "a"), 10 (halite), 9 (halite)
	up 50°	5.163	guard	2201	2.27-3.32	9 (halite), 8 (anhydrite "b"), 7 (halite)
S1P71-B	vertical down	5.296	test	4418	8.70-10.15	PH-1, anhydrite "c", clay B, H-1
	vertical down	5.296	guard	2813	6.82-7.87	H-2
S1P72-A	down 32°	5.265	test	5009	4.01-6.05	PH-4, MB139, clay E, H-4
	down 32°	5.265	guard	2522	2.15-3.18	0 (halite), PH-4
S1P73-A	vertical up	5.269	test	3964	3.38-4.80	12 (polyhalitic halite), 11 (anhydrite "a"), 10 (halite), 9 (halite)
	vertical up	5.269	guard	2599	0.85-2.49	9 (halite), 8 (anhydrite "b"), 7 (halite)
S1P73-B	vertical up	5.253	test	3868	9.92-11.32	H-6, MB138, clay K, AH-2
	vertical up	5.253	guard	2637	8.04-9.09	H-5, AH-1 (clay J), 15 (halite)
SCP01-A	down 13°	5.197	test	8734	10.68-15.39	PH-4, MB139, H-4
	down 13°	5.197	guard	2454	8.80-9.85	PH-4
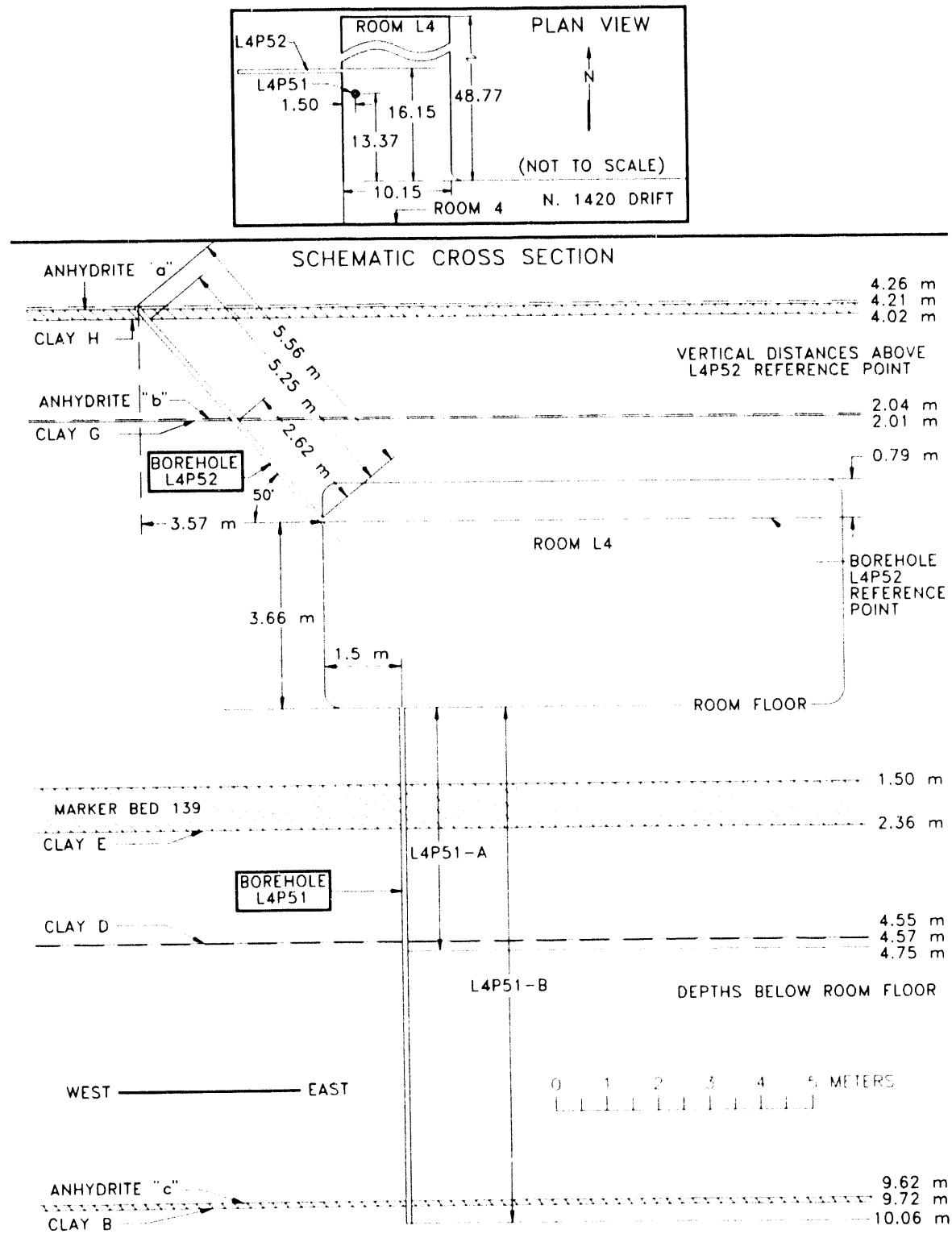
Figure 5-2. Schematic illustration of boreholes L4P51 and L4P52 in Room L4.

L4P51 was deepened on October 1 and 2, 1990 (Calendar Days 274 and 275) to 10.06 m below the floor of Room L4. The deepening allowed testing of anhydrite "c" and clay B during test sequence L4P51-B. Anhydrite "c" was encountered from 9.62 to 9.72 m deep. Clay B directly underlies anhydrite "c" and is only about 0.005 m thick at L4P51.

Borehole L4P52 was drilled on April 1 and 2, 1991 (Calendar Days 91 and 92). The hole was drilled into the upper part of the west rib of Room L4 at an angle 40° below vertical to a distance of 5.56 m (Figure 5-2). The borehole was drilled to allow testing of anhydrites "a" and "b" during test sequence L4P52-A. Anhydrite "b" was encountered from 2.62 to 2.66 m along the hole (including up to 0.01 m of clay G) and anhydrite "a" was encountered from 5.25 to 5.50 m (including 0.005 m of clay H).

5.2 Room 7 of Waste Panel 1

Room 7 of Waste Panel 1 was excavated in March 1988 to nominal dimensions of 10.1 m wide, 4.1 m high, and 91.4 m long (Westinghouse, 1989). Borehole S1P71 was drilled vertically downward into the floor of Room 7 (Figure 5-3) on November 10, 1988 (Calendar Day 315) to a depth of 4.56 m. After the S1P71-A testing sequence reported in Beauheim et al. (1991) was completed, the hole was deepened to 10.15 m between July 20 and 24, 1989 (Calendar Days 201 to 205). The hole was deepened to allow testing of anhydrite "c" during test sequence S1P71-B. Anhydrite "c" was encountered from 9.75 to 9.80 m below the floor of Room 7 and an additional anhydrite layer was encountered from 9.48 to 9.51 m (Figure 5-3).

Borehole S1P72 was drilled downward into the east rib of Room 7 at an angle of 58° from vertical on December 12 and 13, 1989 (Calendar Days 346 and 347). The hole was drilled to a total length of 6.05 m, and encountered Marker Bed 139 from 4.40 to 6.00 m along its length (Figure 5-3).

Borehole S1P73 was drilled vertically upward into the back (roof) of Room 7 on December 10 and 21, 1990 (Calendar Days 344 and 355) to a length of 4.80 m. Anhydrite "b" was encountered from 1.84 to 1.90 m along the hole (including 0.003 m of clay G) and anhydrite "a" was encountered from 3.94 to 4.09 m. After attempted testing of these anhydrites (testing sequence S1P73-A), the hole was extended to a length of 11.32 m on January 14 and 15, 1991 (Calendar Days 14 and 15). The hole encountered clay K from 10.86 to 10.89 m along its length and Marker Bed 138 from 10.89 to 11.03 m (Figure 5-3).

5.3 Core-Storage Library

The core-storage library west of the West 170 drift at South 400 (Figure 5-1) was excavated in April and May 1989 to nominal dimensions of 7.9 m wide, 4.1 m high, and 45.7 m long (Westinghouse, 1990). Figure 5-4 shows the location of borehole SCP01 in the core-storage library. The borehole was drilled downward into the south rib of the room angled 45° to the west (S 45° W) and inclined 77° from vertical. The hole was drilled from March 26 to 30, 1990 to a total depth of 15.39 m. Marker Bed 139 was encountered from 10.50 to 14.78 m along the hole (Figure 5-4).

PLAN VIEW

ROOM 7

N

(NOT TO SCALE)

S1P73
S1P72
3.43
S1P71
1.50
64.38
62.60
10.10
59.60
S. 1950 DRIFT

SCHEMATIC CROSS SECTION

MARKER BED 138
CLAY K

11.32 m
11.03 m
10.86 m

BOREHOLE S1P73

DISTANCES ABOVE ROOM CEILING

S1P73-B

4.80 m

ANHYDRITE "a"
CLAY H

4.09 m
3.94 m

S1P73-A

ANHYDRITE "b"
CLAY G

1.90 m
1.84 m

ROOM CEILING

3.43

ROOM 7

1.50

BOREHOLE S1P72 REFERENCE POINT

5.13

37

0.75 m

ROOM FLOOR

4.40
6.06
6.00

BOREHOLE S1P72

1.40 m

2.33 m

MARKER BED 139

2.25 m
CLAY E

3.18 m
3.21 m

S1P71-A

BOREHOLE S1P71

4.56 m

S1P71-B

DEPTHS BELOW ROOM FLOOR

WEST ——————— EAST

VERTICAL DEPTHS BELOW S1P72 REFERENCE POINT

0 1 2 3 4 5 METERS

9.75 m   ANHYDRITE "c"
9.80 m   CLAY B
10.15 m

Figure 5-3. Schematic illustration of boreholes S1P71, S1P72 and S1P73 in Room 7 of Waste Panel 1.

PLAN VIEW

BOREHOLE
SCP01

45°

7.77 m

CORE-STORAGE LIBRARY

44.01 m

45.72 m

N

W. 90 DRIFT

(NOT TO SCALE)

SCHEMATIC CROSS SECTION

CORE-STORAGE LIBRARY

15.00 m

BOREHOLE
SCP01
REFERENCE
POINT

15.39 m

14.78 m

10.50 m

13°

0.70 m

BOREHOLE
SCP01

10.99 m

2.36 m

MARKER BED 139

3.32 m

CLAY E

3.46 m

DEPTHS BELOW SCP01
REFERENCE POINT

0 1 2 3 4 5 METERS

SOUTHWEST ————— NORTHEAST
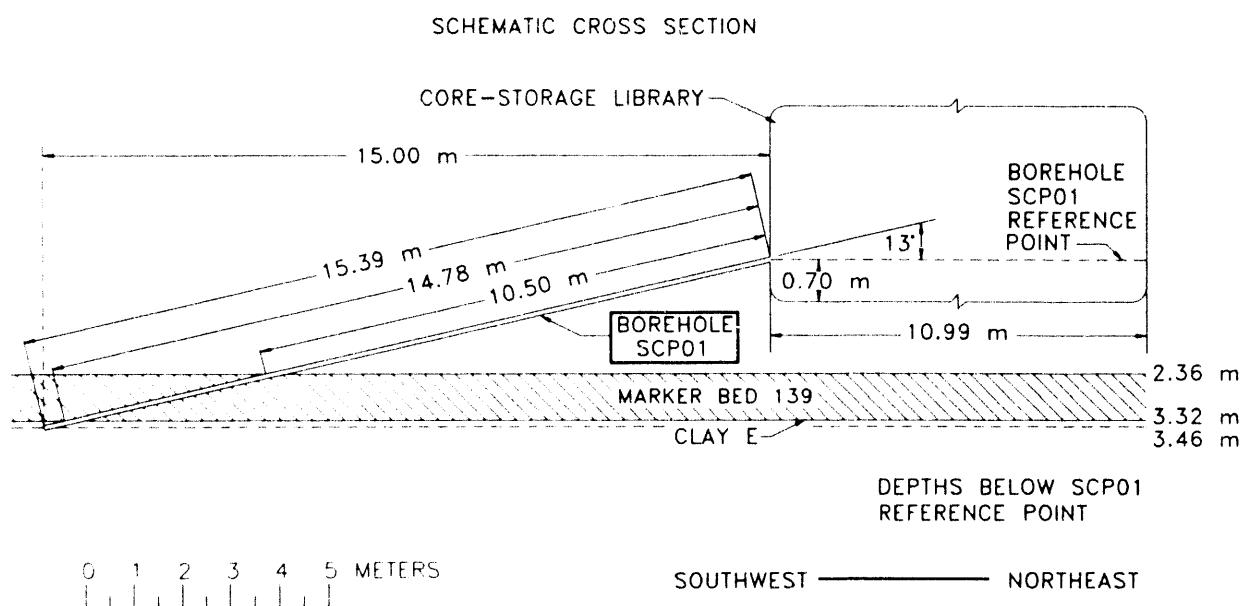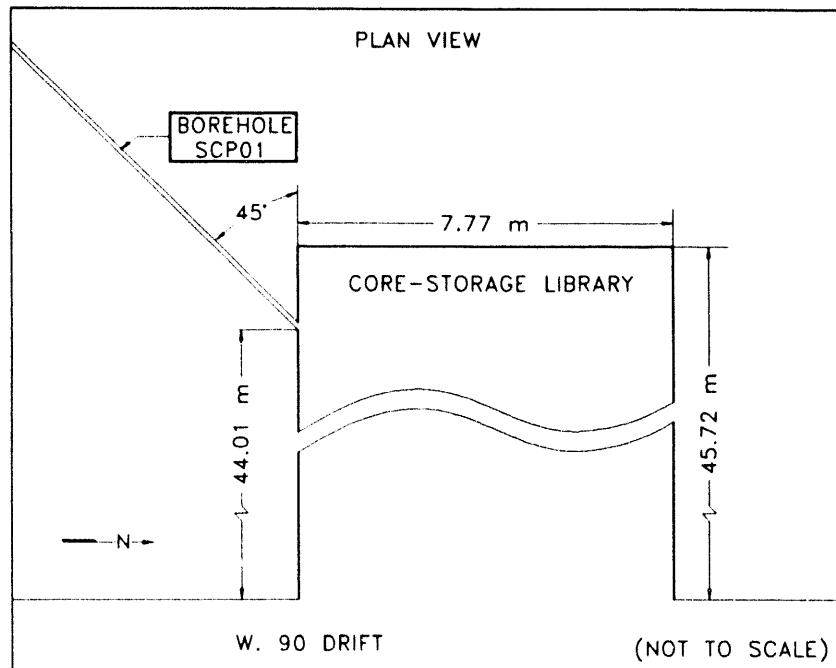
Figure 5-4. Schematic illustration of borehole SCP01 in the core-storage library.

6. INTERPRETATION METHODOLOGY AND OBJECTIVES

Both analytical and numerical methods were used to interpret the hydraulic tests discussed in this report. These methods and the objectives of the interpretations are discussed in Section 6.1. Section 6.2 summarizes the major assumptions underlying the test interpretations. Section 6.3 discusses the values of material properties and experimental parameters needed as input in the test interpretations and how those values were determined.

6.1 Interpretive Methods

Interpretation of hydraulic tests is essentially an inverse problem. During a hydraulic test, one or more known stresses are applied to the system being studied, and the responses of the system are measured. Interpretation of the test consists of inferring the properties of the system from its measured responses. Typically, a unique set of properties cannot be inferred from a single test. As noted by Gringarten et al. (1979), however, increasing the number and types of stresses applied to a system provides an increase in information gained from the measured responses. By solving the inverse problem simultaneously or iteratively for a variety of different testing conditions, the number of viable alternative solutions can be greatly reduced.

The three types of tests discussed in this report are amenable to interpretation using different techniques, providing the opportunity for cross-checking and cross-validation among results. Both analytical and numerical methods can be used. Pressure-pulse tests (also referred to as "shut-in" or "modified" slug tests) can be interpreted using type curves developed from an

analytical solution by Bredehoeft and Papadopulos (1980). Constant-pressure flow tests can be interpreted using type curves based on an analytical solution for the decay in flow rate as a function of time developed by Jacob and Lohman (1952). Pressure-buildup tests can be interpreted using standard analytical solutions for wells with wellbore storage and skin, such as those of Gringarten et al. (1979). Details about the derivations of the analytical solutions are presented in Appendix B. All three types of tests can also be interpreted using numerical simulations. Brief discussions about the application of the analytical solutions and about the numerical techniques used to interpret the tests discussed in this report are presented below. The objectives of the different types of interpretations are also presented.

6.1.1 ANALYTICAL METHOD FOR PRESSURE-PULSE TESTS.
Bredehoeft and Papadopulos (1980) derived an analytical solution to describe the response of a shut-in test interval to an instantaneous pressure pulse (Appendix B), and used that solution to construct a family of type curves to be used for pulse-test interpretation (Figure 6-1). Each type curve represents a plot of one lumped parameter, β, on a logarithmic x-axis versus the normalized pressure change, H/H_o, on a linear y-axis for a specific value of a second lumped parameter, α, where α and β are given by:

$$\alpha = \frac{\pi r_s^2 S}{V_w C_{tz} \rho_w g} \qquad (6\text{-}1)$$

$$\beta = \frac{\pi T t}{V_w C_{tz} \rho_w g} \qquad (6\text{-}2)$$

41
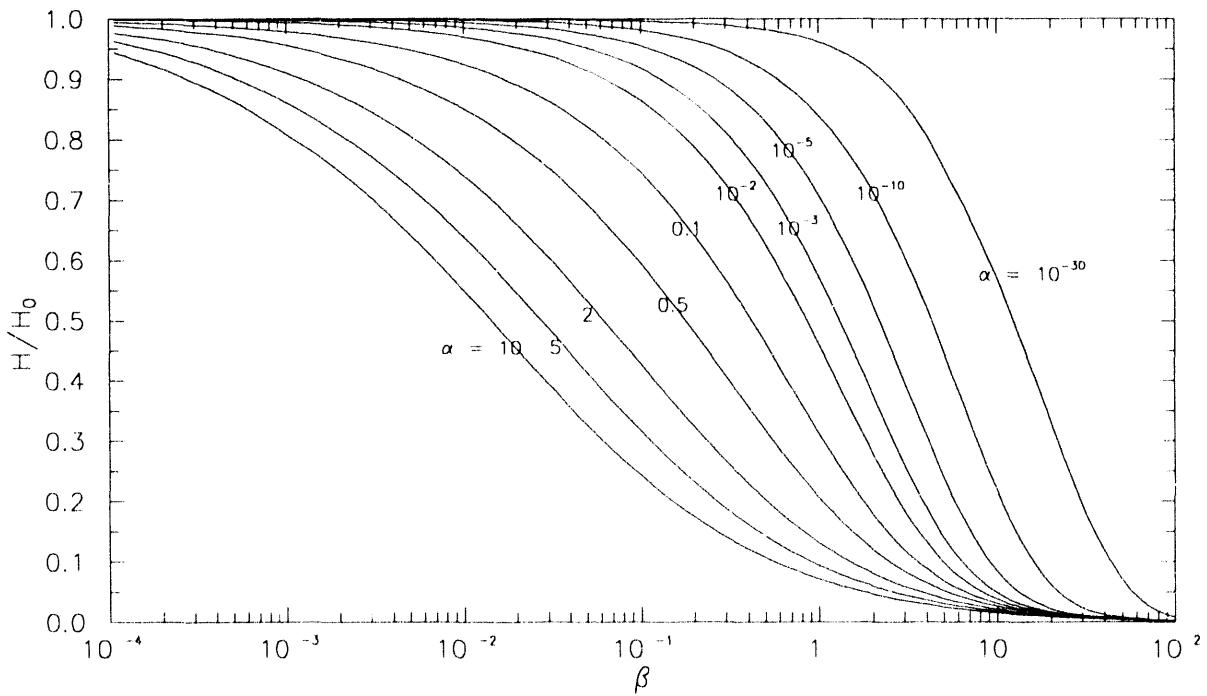
Figure 6-1. Type curves for pressure-pulse tests.

where: H = change from pretest pressure at time t, M/LT^2

H_o = pulse change in pressure, M/LT^2

r_s = radius of well, L

S = storativity, dimensionless

T = transmissivity, L^2/T

t = time since pressure pulse, T

V_w = volume of water within shut-in interval or test zone, L^3

C_{tz} = compressibility of test zone, LT^2/M

ρ_w = density of water, M/L^3

g = gravitational acceleration, L/T^2

Pulse-test data are plotted as elapsed time (t) on a logarithmic x-axis versus H/H_0 on a linear y-axis. If the analysis is to be performed manually, the data plot is placed over the type-curve plot and translated in the x direction, while keeping the x-axes overlapping, until the best possible match between the data and one of the type curves is obtained. In this position, an arbitrary match point is chosen and the corresponding values of t and β are read from the data and type-curve plots, respectively. The curve-matching procedure can also be carried out on a computer.

The transmissivity (T) of the tested interval is calculated from the following rearrangement of Eq. 6-2, using the t and β values from the match point:

$$T = \frac{V_w \, C_{tz} \, \rho_w \, g \, \beta}{\pi \, t} \qquad (6\text{-}3)$$

Using petroleum terminology for dimensionally consistent units, Eq. 6-3 can be written as:

$$kh = \frac{V_w \, C_{tz} \, \mu \, \beta}{\pi \, t} \qquad (6\text{-}4)$$

where: k = permeability, L^2

h = test-interval thickness, L

μ = fluid viscosity, M/LT

and other symbols are as defined above.

Pressure-pulse tests are conducted because they represent the fastest, simplest technique available to estimate transmissivity in low-permeability media. Equipment requirements and, hence, costs are small relative to other types of tests. However, of the tests discussed in this report, the pressure-pulse tests are the tests least amenable to analytic interpretation. Because pressure-pulse tests involve less of a stress on the tested system than do flow and buildup tests, non-ideal antecedent conditions have more of an effect on pressure-pulse test responses. Such non-ideal antecedent conditions in fact precluded analytic interpretation of many of the pressure-pulse tests considered in this report.

The transmissivity interpreted from a pressure-pulse test also tends to be less definitive than that derived from a constant-pressure flow test or a pressure-buildup test. Pulse tests have smaller radii of influence than flow or buildup tests. Therefore, pulse tests may be more sensitive to drilling-induced changes in permeability around a borehole than are the other types of tests. Pressure responses observed during pulse tests in low-permeability media may also be dominated

by wellbore-storage effects and provide little information on formation properties. Also, as can be seen from Eq. 6-3, error in the estimation of test-zone compressibility results in linearly proportional error in interpreted transmissivity. Interpretation of constant-pressure flow tests and pressure-buildup tests does not depend on knowledge of test-zone compressibility. Despite their limitations, however, pressure-pulse tests are useful in obtaining rough estimates of transmissivity in a relatively short period of time that can then be used to design more definitive tests.

6.1.2 ANALYTICAL METHODS FOR CONSTANT-PRESSURE FLOW TESTS. Jacob and Lohman (1952) provided the first analytical solution to interpret constant-pressure flow tests in the field of groundwater hydrology (Appendix B). In the petroleum literature (e.g., Fetkovich, 1980; Uraiet and Raghavan, 1980; Ehlig-Economides and Ramey, 1981), Jacob and Lohman's (1952) solution is represented by a type curve of dimensionless time, t_D, plotted versus dimensionless flow rate, q_D, on a log-log graph (Figure 6-2). Test data are then plotted as elapsed flow time, t, versus flow rate, q, on a similarly scaled graph. The data can be matched to the type curve manually by placing the data plot on top of the type-curve plot, and shifting the data plot, keeping both sets of axes parallel, until the data overlie the type curve as much as possible. The curve-fitting procedure can also be carried out on a computer.

Once a match is obtained, an arbitrary point is selected and the coordinates of that point are read on both plots. The permeability-thickness product (transmissivity) of the tested interval is calculated from the following equation:

43
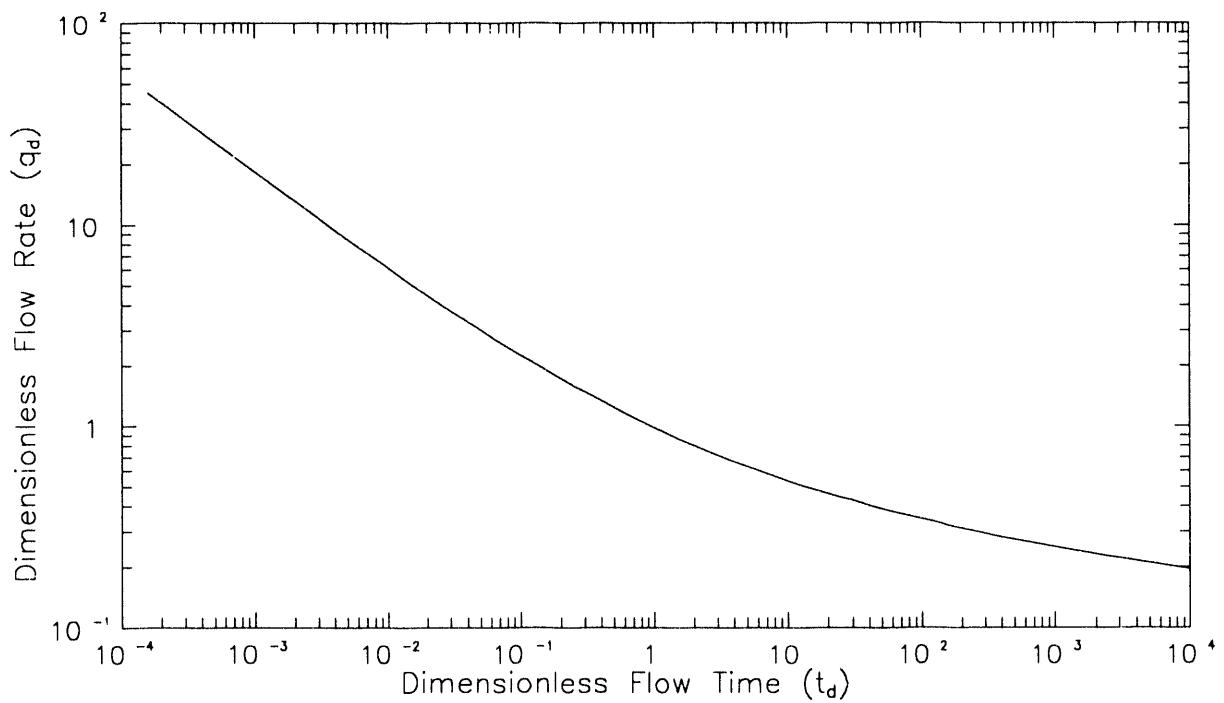
Figure 6-2. Type curves for radial constant-pressure flow.

$$kh = \frac{q\mu}{2\pi q_D(p_i - p_{wf})} \qquad (6\text{-}5)$$

where: k = permeability, L^2

h = test-interval thickness, L

q = flow rate at match point on data plot, L^3/T

μ = fluid viscosity, M/LT

q_D = dimensionless flow rate at match point on type curve

p_i = initial pressure before flow began, M/LT^2

p_{wf} = constant pressure at which well flowed, M/LT^2

If hydraulic boundaries are encountered during constant-pressure flow testing, flow-rate data will deviate from the type curve. Once the effects of the flow test reach the boundary, a constant-pressure (or increased permeability) boundary will cause the flow rate to stabilize, and a no-flow (or decreased permeability) boundary will cause the flow rate to decrease more rapidly than predicted by the type curve.

Uncertainty or inaccuracy in the estimation of transmissivity from matching of constant-pressure flow data to type curves arises primarily from poor definition (non-uniqueness) of the match between the data and the type curve. Definition of a type-curve match typically improves as more data become available. Therefore, uncertainty in transmissivity generally decreases as the test duration increases. A secondary source of

uncertainty in transmissivity estimation is uncertainty in the driving pressure differential (see Eq. 6-5). When a constant-pressure flow test is only one in a sequence of hydraulic tests, the initial pressure before flow begins (p_i) may be different from the stabilized pressure that existed throughout the formation before the sequence of tests began. When a transient pressure distribution already exists within a formation at the start of a constant-pressure flow test, the driving pressure differential will include another transient component in addition to that caused by the flow test itself. If this additional transient component is ignored, the transmissivity estimate may be in error by a factor not greater than the percentage difference between the pressure difference between the actual initial pressure and the flowing pressure and the pressure difference between the pre-test stabilized pressure and the flowing pressure. However, transient pressure conditions existing at the start of a constant-pressure flow test may also affect the quality of the match between the flow data and the type curve, because the analytical solution underlying the type curve assumes stabilized pressure conditions at the start of the test. Again, the significance of this problem correlates with the magnitude of the difference between the assumed and actual initial pressure differentials. Estimation of transmissivity from constant-pressure flow tests is entirely independent of test-zone compressibility because those tests do not involve transient pressures in the test zone.

6.1.3 ANALYTICAL METHODS FOR PRESSURE-BUILDUP TESTS.

Many authors in the fields of groundwater hydrology and petroleum reservoir engineering have studied the buildup of pressure in a well following a constant-rate flow period. The early studies of Theis (1935), Cooper and Jacob (1946), and Horner (1951) considered only the behavior of a well

acting as a line source, with no wellbore storage or skin. Gringarten et al. (1979) included wellbore storage and skin in their analytical solution when they devised a new set of type curves for flow- and buildup-test interpretation (Appendix B). Each type curve is characterized by a distinct value of $C_D e^{2s}$ and is plotted as p_D versus t_D/C_D on a log-log graph (Figure 6-3), where:

C_D = dimensionless wellbore-storage coefficient

s = dimensionless wellbore skin

p_D = dimensionless pressure change

t_D = dimensionless elapsed time

Test data are plotted as pressure change, Δp, versus elapsed flow time, t, on a log-log graph of the same scale as the type curves. The data can be matched to a type curve manually by placing the data plot on top of the type-curve plot and shifting the data plot, keeping both sets of axes parallel, until the best match possible is obtained between the data and one of the type curves. After a match is obtained, an arbitrary point is selected and the coordinates of that point are read on both plots. Using the ordinate values for the match point (the pressure match), the permeability-thickness product (transmissivity) of the tested interval is calculated from the following equation:

$$kh = \frac{q\mu\, p_D}{2\pi\, \Delta p} \qquad (6\text{-}6)$$

where: k = permeability, L^2

h = test-interval thickness, L

q = flow rate, L^3/T

μ = fluid viscosity, M/LT

Δp = pressure change, M/LT^2

The wellbore-storage coefficient (C) can then be calculated from the abscissa values of the match point (the time match) as:

45
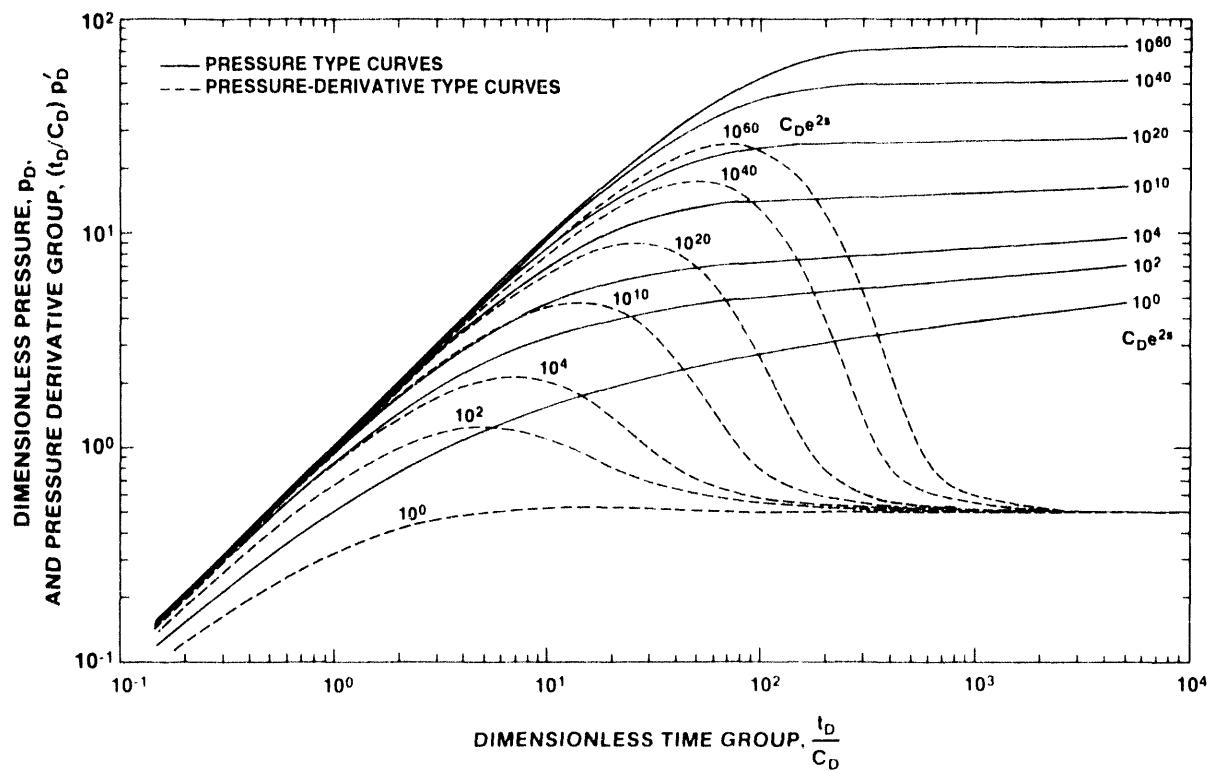
Figure 6-3. Pressure and pressure-derivative type curves for wells with wellbore storage and skin.

$$C = \frac{2\pi kht}{\mu(t_D/C_D)} \qquad (6\text{-}7)$$

The apparent wellbore skin (s) can be calculated using the value of $C_D e^{2s}$ for the type curve that matched the data and the value of C_D determined from the following equation:

$$C_D = \frac{C}{2\pi\phi c_t h r_w^2} \qquad (6\text{-}8)$$

where: ϕ = porosity, dimensionless

c_t = total system compressibility, LT^2/M

r_w = wellbore radius, L

Note that calculation of the skin value requires knowledge of the porosity-compressibility product (equivalent to specific storage divided by fluid density). Earlougher (1977) relates skin to an effective wellbore radius (r_e) by the following equation:

$$r_e = r_w \, e^{-s} \qquad (6\text{-}9)$$

Although the solution of Gringarten et al. (1979) was developed for the drawdown response of a well producing at a constant rate, it can be extended to analysis of the pressure buildup following a constant-rate flow period through linear superposition of the buildup response on the continuing drawdown response. The solution can be further extended to apply to the buildup response following a constant-pressure flow test by subdividing the constant-pressure flow period into a number of shorter periods having constant, but different, rates and using linear superposition to combine the effects of all of the flow periods. This approach was verified theoretically by Ehlig-Economides (1979).

The analytical solution of Gringarten et al. (1979) is included in the Interpret/2 well-test-interpretation code developed by Scientific Software-Intercomp. Interpret/2 also includes numerous analytical solutions for systems other than the infinite single-porosity system considered by Gringarten et al. (1979). These include analytical solutions for double-porosity systems, fractured systems, bounded systems, radially heterogeneous systems, and leaky systems, as well as for wells that are horizontal or only partially penetrate a permeable layer. The pressure-derivative analysis techniques developed by Bourdet et al. (1989) are also included in Interpret/2. The pressure derivative serves a diagnostic role by providing insight into the nature of the system being tested, such as the presence (or absence) of hydraulic boundaries, fractures, leakage, or double-porosity effects, which aids in selection of an appropriate model. Once a particular well and system model is selected within Interpret/2, the code generates pressure and pressure-derivative type curves for that model (Figure 6-3). Built-in regression techniques allow optimization of the fit between type curves and data. Simultaneous type-curve matching to pressure data and pressure-derivative data provides much more definitive results than matching to pressure data alone. In addition to automated log-log type-curve matching, Interpret/2 also provides matching to semilog Horner (1951) plots and simple linear-linear pressure-versus-time plots. Horner plots are particularly useful in defining the pressure towards which a system is stabilizing.

The interpretation of each pressure-buildup test had five principal objectives. First, we wanted to determine the transmissivity of the tested interval. Second, we wanted an estimate of the wellbore-storage coefficient to compare to the test-zone compressibility measurements made during pulse

tests. Third, we wanted to define the stabilized pore pressure in the tested stratum at the time of testing. Fourth, we wanted to know the approximate radius of influence of the constant-pressure flow and buildup tests. Fifth, we wanted information on whether the tested stratum behaved hydraulically as infinite (on the scale of testing) or bounded, fully confined or leaky, and as a single-porosity medium or a double-porosity medium.

Estimation of transmissivity from pressure-buildup tests is independent of test-zone compressibility. Instead of needing a value of test-zone compressibility as model input, log-log analysis of pressure-buildup tests provides an estimate of the wellbore-storage coefficient (the product of the test-zone compressibility and the shut-in test-zone volume) as output. Stabilized pore pressure is readily determined by extrapolating the late-time pressure trend on a Horner plot to infinite recovery time. Information on the nature of the system tested comes from the pressure-derivative data and the final model fit to the data by Interpret/2.

The radius of influence of a flow or buildup test is given by different authors as some multiple of the parameter group $(kt/\phi\mu c_t)^{1/2}$. For instance, Earlougher (1977) defines the radius of drainage of a test, using SI units, as:

$$r_d = 1.786 \sqrt{\frac{kt}{\phi\mu c_t}} \qquad (6\text{-}10)$$

where: t = test duration, T

and other parameters are as defined above. Oliver (1990) examined how the properties of a formation at different radial distances from a well contributed to the permeability interpreted from a well test. He found that fifty percent of the

permeability information was from the region between $r = 0.67$ $(kt/\phi\mu c_t)^{\frac{1}{2}}$ and $r = 1.35$ $(kt/\phi\mu c_t)^{\frac{1}{2}}$, and less than one percent of the information came from beyond $r = 2.34$ $(kt/\phi\mu c_t)^{\frac{1}{2}}$. Both Earlougher (1977) and Oliver (1990) ignored wellbore storage and skin in their formulations. These factors would tend to reduce the radius of influence of a test. Interpret/2 uses Eq. 6-10 to calculate the radius of influence of well tests.

6.1.4 NUMERICAL METHODS.

A major limitation encountered when interpreting hydraulic tests with analytical solutions is that actual pretest conditions do not entirely match the idealized boundary conditions and initial conditions that underlie the analytical solutions. For this reason, a numerical model capable of dealing with complex pretest borehole history and variable boundary conditions was also used to interpret the Salado hydraulic tests. The numerical model chosen, GTFM (Graph Theoretic Field Model; Pickens et al., 1987), simulates the hydraulic response of a single-phase, one-dimensional, radial-flow regime to boundary conditions applied at a borehole located at the center of the modeled flow system. The problem domain is discretized by dividing the radial-flow system into a series of concentric rings centered on the borehole, with each ring represented by a node. A constant multiplicative factor is used to increase the spacing between nodes with increasing distance from the origin (borehole). For the simulations presented in this report, 250 radial nodes were used. The model assumes that the formation has a constant thickness with vertically homogeneous hydraulic properties. Formations may have single or double porosity, and may include a single radially centered heterogeneity to simulate the presence of a "skin" zone adjacent to the borehole. The skin zone may have properties

different from those of the remainder of the formation.

GTFM can be used with assigned conditions of either fixed pressure or zero flow at the external boundary of the model. Selection between the two boundary conditions is made on a test-specific basis, depending on whether or not the test data show boundary effects. If no boundary effects are indicated by the test data, a fixed-pressure boundary condition is specified at a distance from the borehole such that the type of boundary has no effect on the calculated pressure response in the borehole. The adequacy of the specified distance is verified by ensuring that the pressure in the node adjacent to the fixed-pressure boundary node does not change over the duration of the test simulation. In cases where boundary effects are indicated by the test data, the type of and distance to the boundary are parameters selected and fitted as part of the test interpretation.

The model has wellbore (inner) boundary conditions which can be used to simulate pulse-injection/withdrawal tests, specified borehole-pressure conditions, specified formation flow rates, and slug-injection/withdrawal tests. The cumulative effects of consecutive tests are incorporated in the simulations. The model can also incorporate test-zone pressure changes resulting from temperature variations in the test zone as well as from test-equipment- and/or formation-induced changes in the test-zone volume. The model output consists of simulated pressure responses in the borehole and at selected radial distances from the borehole. The model can also calculate formation flow rates and cumulative production based on the formation's estimated hydraulic properties.

The primary input parameters to GTFM include the formation's hydraulic properties (hydraulic conductivity, pore pressure, and specific storage or its constituent parameters), fluid properties (density, compressibility, and thermal-expansion coefficient), test-zone parameters (radius, length, contained fluid volume, and compressibility), and, if used, skin properties (radial thickness, hydraulic conductivity, and specific storage). For test interpretation, all of the input parameters except for the formation's hydraulic (and skin) properties and test-zone compressibility are fixed. Values for test-zone compressibility are determined and assigned as discussed below in Section 6.3.2. Different combinations of the hydraulic properties are then investigated by creating a matrix of values and graphically comparing the simulated and observed pressure responses for each combination. The graphical comparisons can involve linear-linear, semilog, and/or log-log plots of individual tests or of the entire testing sequence. The parameters yielding the simulated responses that most closely match the observed pressure responses are considered to be representative estimates of the actual formation parameters. The matching procedure is entirely subjective. That is, no goodness-of-fit evaluations or fitting algorithms are available within GTFM. GTFM can be used, however, to perform parameter-sensitivity studies to obtain an estimate of the uncertainty associated with a particular simulation.

For the interpretations presented in this report, the individual testing periods were subdivided into discrete time intervals, called sequences. Sequences are differentiated by the wellbore boundary conditions in effect during those time periods. Sequences during which borehole pressures are prescribed in the model are referred to as **history** sequences. History sequences were used to represent: (1) the pressure in a test zone

(often zero, or atmospheric) during the period between drilling and initial shut-in of the test zone; (2) time periods when external factors, such as changes in packer pressures, affected the observed test-zone pressures; and (3) test-zone pressures during constant-pressure flow tests. The pressures specified for history sequences are taken directly from the DAS records. Model output during history sequences consists of flow rates between the test zone and the surrounding formation and transient formation pore pressures. Sequences during which a test zone is shut in, and pressures in the test zone and the surrounding formation are equilibrating, are referred to as **pulse** sequences. Pulse sequences were used to represent: (1) periods immediately after test zones were shut in for the first time; (2) pressure-recovery periods following individual pulse injections and pulse withdrawals; and (3) pressure-buildup (recovery) periods following constant-pressure flow tests. Model output during pulse sequences consists of transient pressures in both the test zone and formation, as well as flow rates.

GTFM can be used to define a radius of influence of a test or testing sequence. This is accomplished by successively decreasing the distance to the external boundary in the model until boundary effects alter the test simulation. For the tests discussed in this report, a change of one percent in the simulated pressure at the end of a test was established as the criterion for defining the radius of influence. A one-percent deviation from a best-fit simulation is readily apparent in simulation plots and would ordinarily induce the analyst to alter the model parameters to try to achieve a better fit.

A complete description of the methodology, appropriate boundary conditions, and governing equations of GTFM can be found in Pickens et al.

49

(1987). GTFM was verified by comparing its results to analytical solutions for pulse tests, slug tests, constant-pressure flow tests, and constant-flow-rate pumping tests (Pickens et al., 1987).

6.2 Assumptions Used in Test Analysis

The expressions "Darcy flow" or "Darcian behavior" usually refer to a flow system in which the flow rate is linearly proportional to the hydraulic gradient. The empirical observation of this proportionality by Darcy (1856) formed the basis for what is today known as Darcy's law. Most equations used in hydraulic-test analyses to describe the flow of groundwater assume this linear proportionality found in Darcy's law. However, systematic studies of the validity of Darcy's law have not been performed over wide ranges of hydraulic conductivities and hydraulic gradients. Data from Stearns (1927) support Darcy's law over a range of gradients between 0.0009 and 0.05 for hydraulic conductivities on the order of 10^{-4} m/s. Conversely, Davis et al. (1992) adduce evidence from Darcy's (1856) own experiments, performed with hydraulic gradients between 1.9 and 19, that Darcy's law is not valid under those high-gradient conditions.

Neuzil (1986) performed a comprehensive review of information pertaining to flow through low-permeability media. He could find no determinations of hydraulic conductivities less than 10^{-8} m/s from experiments conducted with hydraulic gradients less than one. In addition, all determinations of hydraulic conductivities less than 10^{-10} m/s involved gradients between 100 and 1,000,000. He concluded that the validity of Darcy's law remains to be demonstrated in situations where hydraulic gradients are much less than one, as are commonly found in natural environments, and hydraulic conductivities are less than 10^{-9} m/s. However, he could find no compelling evidence that Darcy's law is not valid under those conditions.

Other researchers (e.g., Swartzendruber, 1962; Pascal, 1981; Remson and Gorelick, 1982) have suggested that there may be threshold gradients for low-permeability media with small pores below which no flow occurs. Possible causes of the threshold gradients include electrical interactions between polarized water molecules and charged clay particles and resistance to flow caused by capillarity or surface-tension effects in very small pores.

The testing discussed in this report was not performed under low-gradient conditions, but in an environment where both high hydraulic gradients already existed and where high hydraulic gradients were created during the tests. For example, a shut-in pressure of nearly 12 MPa was measured in borehole SCP01 in a test zone lying only 10.7 to 15.4 m from an excavation at atmospheric pressure. A 12-MPa pressure differential over a distance of 10.7 m corresponds to a hydraulic gradient of about 94 (m of brine per m distance). Pressure differentials between 1 and 4 MPa were typically induced for each pressure-pulse test, creating high pressure gradients in the immediate vicinities of the test boreholes. Hydraulic conductivities of Salado evaporites reported by Beauheim et al. (1991) are generally less than 10^{-11} m/s. Under these conditions, Darcian behavior cannot be considered a given. Nevertheless, interpretation of the tests discussed in this report assumed Darcian behavior as a working hypothesis. The extent to which this hypothesis resulted in acceptable test interpretations is discussed in Section 7.2.2.

In analyzing each of the tests discussed in this report, we assumed that the only factor causing transient pressure and flow responses was the pressure disequilibrium between the borehole and surrounding formation induced by the testing sequence. Transient responses caused by ongoing stress redistribution around the excavations, by creep of halite towards the excavations, by dilation of the rock, or by any other deformation mechanisms related to the rock response to the presence of the excavations were not considered in the test interpretations. These processes, if acting, could cause progressive changes in hydraulic properties and/or pore pressures during long testing sequences. However, because the hydraulic tests were all performed around excavations that were several years old, residual transient responses due to excavation effects were assumed to be occurring on time scales much longer than the hydraulic tests and, therefore, not affecting the hydraulic-test responses. An inability to simulate an entire testing sequence adequately might indicate that processes such as these that are not included in GTFM were affecting the observed responses.

For all tests considered, our initial working model also assumed cylindrical flow towards the borehole through a continuous porous medium. In reality, three of the six boreholes considered in this report were drilled at acute angles to the bedding, which may have resulted in elliptical and vertical flow components. The elliptical opening created by an inclined cylindrical borehole passing through a horizontal plane can be considered as an equivalent circular opening to simplify test interpretation. Kucûk and Brigham (1981) compared several methods of determining effective circular radii of elliptical openings. They examined averaging elliptical axes, calculating the

radius of a circle with the same perimeter as the ellipse, and calculating the radius of a circle with the same area as the ellipse. They concluded that the area-based method led to the greatest errors, that the perimeter-based method gave the best results at early time, and that the axis-averaging method gave the best results at intermediate and late time. Abbaszadeh and Hegeman (1990) recommend the following refinement of the axis-averaging method to define an effective circular borehole radius (r_w'):

$$ r_w' = \left[\frac{r_w}{2}\right] \left[1 + 1/\sqrt{\cos^2\theta_w + \frac{k_v}{k_h}\sin^2\theta_w}\right] $$

(6-11)

where: θ_w = borehole slant from vertical
k_v = vertical permeability
k_h = horizontal (radial) permeability

In the absence of prior knowledge about the ratio of vertical to horizontal permeability, the axis-averaging method of calculating effective circular radii of slanted holes was used for the interpretations presented in this report. That method represents the limiting case of Eq. 6-11 in which k_v goes to zero, and results in a maximum circular radius.

The value for borehole radius used in analyzing a hydraulic test has no effect on the interpreted transmissivity, but does affect the interpreted storativity. In the definition of dimensionless time (see Eq. B-22 in Appendix B), storativity (porosity-compressibility-thickness product) appears with the borehole radius squared in the denominator. Thus, any combination of storativity and radius squared having the same product will result in identical well behavior. Error in the estimation of

one term, therefore, translates directly into error in the estimation of the other. Because the uncertainty in the exact effective radius of any hole may be a significant fraction of that radius, estimation of storativity from single-hole tests is inherently less reliable than estimation from multihole tests in which the uncertainty in the distance between holes is a small fraction of the distance.

Cinco et al. (1975) examined the effects of borehole inclination on pressure responses during flow and buildup tests. They considered the case in which a slanted hole fully penetrated a horizontal permeable layer with impermeable upper and lower boundaries. They found that the pressure response in a slanted hole during a constant-rate flow period goes through three phases: an early-time radial-flow phase, a transition phase, and a late-time pseudo-radial-flow phase. During the early-time radial-flow phase, data plotted as pressure versus log time define a straight line having a slope proportional to the (vertical) permeability-thickness of the formation multiplied by the factor $cos\ \theta_w'$. During the late-time pseudo-radial-flow phase, this slope is proportional only to the permeability-thickness of the formation, just as if the hole were vertical. θ_w' represents an apparent borehole slant that compensates for the presence of anisotropy between vertical and horizontal permeability. The apparent borehole slant is given by:

$$\theta_w' = \tan^{-1}\left[\sqrt{\frac{k_v}{k_h}}\ \tan\ \theta_w\right] \qquad (6\text{-}12)$$

By Eq. 6-12, as the vertical-to-horizontal permeability ratio decreases, pressure responses around slanted holes become more similar to those observed around vertical holes. For instance, an anisotropy ratio of 0.01 makes a borehole inclined 77° from vertical (such as SCP01) behave like a borehole inclined only 23° in an isotropic system. Thus, as vertical permeability decreases relative to horizontal permeability, the first radial-flow phase observed in a slanted hole differs less and less from the late-time pseudo-radial-flow phase which is the only phase observed in a vertical hole.

As an approximation, the interpretations presented in this report of tests conducted in slanted holes treated the holes as if they were vertical. The actual fluid volumes present in the slanted test intervals were specified in all GTFM simulations involving equivalent vertical test intervals. As shown by Eq. 6-12, the reasonableness of the vertical approximation depends on the anisotropy of the tested strata. Evidence for anisotropy is discussed in the appropriate sections of Chapter 7 for each relevant test.

In summary, interpretations of the tests conducted in slanted holes treated the test intervals as vertical cylindrical sections having thicknesses equal to the vertical thicknesses of the tested strata, and effective radii calculated by averaging elliptical axes. To evaluate the potential errors associated with these geometrical idealizations, numerical modeling studies were performed. These studies used the finite-difference code SWIFT II (Reeves et al., 1986) to model hydraulic testing in slanted boreholes in three dimensions. The idealized geometries used for test interpretation were also modeled, and the results were compared to those from the fully three-dimensional simulations. The general conclusions of the study are that: 1) slant angles ≤15° have insignificant effects on test results for any

magnitude of anisotropy; 2) at slant angles up to 30°, idealized vertical geometries match the slant behavior well for any magnitude of anisotropy; and 3) at slant angles $\geq 45°$, vertical geometries match the slant behavior well as long as the vertical-to-horizontal permeability ratio is ≤ 0.1. Full details of the modeling studies are presented in Appendix C, and their application to individual test interpretations is discussed in the appropriate sections of Chapter 7.

Another assumption made for test interpretation was that the pore pressure in each test horizon was static (constant with time), and radially and longitudinally (parallel to the borehole axis) invariant before drilling began. Evidence from a limited number of holes indicates that the pressures under the floor and in the roof of an excavation are less than the pressures under and over the ribs (walls). The resulting pressure gradients may reflect an increase in pore volume above and below excavations and/or flow to the excavations. These gradients appear to persist over longer time scales than those of the hydraulic tests. Thus, the pressure responses to the hydraulic tests may be superimposed on a relatively static pressure field. In any case, lacking reliable two-dimensional definition of the pressure distribution over time within a tested horizon, our initial assumption in modeling was that a single constant pressure existed throughout a tested horizon when testing began. As more data on pressure distributions become available, two-dimensional modeling may be performed to evaluate the influence of this assumption on the test interpretations.

Considering the proximity of excavations at atmospheric pressure to the test intervals, longitudinal pressure gradients through the test intervals toward the excavations should be present. The pressures observed during testing,

therefore, probably represent the average pore pressures over the entire tested intervals. Treating these average pressures as if they were uniformly distributed over the tested 1- to 2-m thicknesses is not expected to lead to significant errors in test interpretation.

Other assumptions specific to the interpretation of individual tests are discussed in Section 7.1 under the headings of the individual tests.

6.3 Material Properties and Experimental Parameters Used in Test Interpretations

To interpret hydraulic tests using either analytical solutions or GTFM, a number of material properties and experimental parameters must be specified. The specific properties and parameters required vary among the interpretive methods. These properties include the porosity and elastic moduli (drained bulk modulus, solids modulus, shear modulus, Young's modulus, and Poisson's ratio) of the lithology(ies) being tested, and the compressibility, density, viscosity, and thermal-expansion coefficient of the test-zone and formation brine. Porosity, elastic moduli, and brine compressibility are used to calculate the total system compressibility (c_t) used in Interpret/2, and are combined with brine density to calculate the specific storage of the formation for GTFM. Brine viscosity is required to convert between hydraulic conductivity and permeability. The thermal-expansion coefficient of brine is used to incorporate the effects of variations in test-zone temperatures on test-zone pressures in GTFM. The thermal expansion of other materials present in test zones, such as stainless-steel tool components, is neglected because the thermal-expansion coefficients of these materials are all more than an order of magnitude lower than the thermal-expansion coefficient of brine.

Experimental parameters important in test interpretation include the radius and length of each test zone, the volume of water contained within each test zone, and the aggregate compressibility of everything within each test zone.

6.3.1 MATERIAL PROPERTIES.

Most of the values of the material properties necessary for test interpretation can be reliably estimated to within an order of magnitude or less. For a given rock type, estimates of specific storage based on values of its constituent parameters range over several orders of magnitude. However, because specific storage is treated as a fitting parameter in GTFM simulations rather than as a fixed parameter, the calculated ranges are used only to provide an initial focus for the GTFM simulations. Beauheim et al. (1991) presented base-case values and ranges of values for the necessary input parameters, along with rationales for their selection. These parameters and their values are shown in Table 6-1.

The only parameter whose base-case value and range differ from that given by Beauheim et al. (1991) is brine compressibility. Based on correlations between brine dissolved-solids concentration, gas saturation, and compressibility published in Earlougher (1977), Beauheim et al. (1991) estimated that the brine used in Salado hydraulic testing had a compressibility of 3.1×10^{-10} Pa^{-1}, and performed sensitivity studies using a range from 2.9×10^{-10} to 3.3×10^{-10} Pa^{-1}. McTigue et al. (1991) calculated the compressibilities of six Salado brine samples from acoustic-velocity measurements performed at 25 °C. Their values ranged from 2.40×10^{-10} to 2.50×10^{-10} Pa^{-1}. As discussed by Beauheim et al. (1991), the compressibility of brine saturated with nitrogen could be as much as ten percent higher than the compressibility of brine without gas.

Therefore, Salado brine compressibility is now estimated to be 2.7×10^{-10} Pa^{-1}, with a range of uncertainty from 2.5×10^{-10} to 2.9×10^{-10} Pa^{-1}. The reduction in the estimated value of brine compressibility also resulted in a slight reduction in estimated values of specific storage compared to those used by Beauheim et al. (1991). Base-case values of specific storage and ranges of uncertainty for halite and anhydrite are given in Table 6-1.

6.3.2 EXPERIMENTAL PARAMETERS.

The experimental parameters needed for test interpretation include the dimensions of the borehole and test zone and the test-specific compressibility of each test zone. The radius of a test zone is determined from the radial-LVDT measurements made after a test tool is installed, the packers are inflated, and the test zone is shut in. Test-zone length is determined from the position of a test tool in a borehole, knowing the dimensions of the test-tool components. The volume of water contained within a test zone includes the water contained in injection and vent lines (tubing) between the test zone and valves positioned outside of the hole. The volume is calculated from the dimensions of the hole and tubing, and the known displacement volume of the test tool. Beauheim et al. (1991) discuss the calculation of test-zone volume in greater detail.

Test-zone compressibility is an important factor in permeability testing performed under shut-in conditions because, given the volume of a test zone, the test-zone compressibility governs the pressure change resulting from the flow of a given amount of fluid into or out of the test zone. In an ideal system, characterized by a pressure-invariant test-zone volume completely filled with a homogeneous fluid, the test-zone compressibility would be equal to that of the test-zone fluid. However, in real systems test-zone compressibility

Table 6-1. Material Properties Used in Test Interpretations*

Material	Parameter	Base-Case Value	Range of Uncertainty
halite	porosity	0.01	0.001 - 0.03
	Young's modulus	31.0 GPa	20.7 - 36.5 GPa
	Poisson's ratio	0.25	0.17 - 0.31
	drained bulk modulus	20.7 GPa	15.0 - 21.7 GPa
	solids modulus	23.4 GPa	22.8 - 24.0 GPa
	shear modulus	12.4 GPa	8.1 - 15.6 GPa
	specific storage	9.0×10^{-8} m^{-1}	2.8×10^{-8} - 3.5×10^{-7} m^{-1}
anhydrite	porosity	0.01	0.001 - 0.03
	Young's modulus	75.1 GPa	59.0 - 78.9 GPa
	Poisson's ratio	0.35	0.31 - 0.42
	drained bulk modulus	83.4 GPa	68.1 - 85.0 GPa
	shear modulus	27.8 GPa	21.4 - 30.4 GPa
	specific storage	1.3×10^{-7} m^{-1}	9.7×10^{-8} - 2.3×10^{-7} m^{-1}
Salado brine	density	1220 kg/m^3	1200 - 1250 kg/m^3
	compressibility (gas saturated)	2.7×10^{-10} Pa^{-1}	2.5×10^{-10} - 2.9×10^{-10} Pa^{-1}
	viscosity	1.6 cp	--
	thermal-expansion coefficient	4.6×10^{-4} $°C^{-1}$	--

*Data and rationales in Beauheim et al. (1991)

represents the aggregate compressibility of the fluid in a test zone and everything with which that fluid is in contact. The fluid is in contact with the metal components of the test tool, injection and vent tubing, one or two packers, the borehole wall, and, in some cases, a free gas phase. All of these items deform in response to changes in test-zone pressure, which makes test-zone compressibility higher than the compressibility of brine alone. Test and test-simulation results further indicate that test-zone compressibility is pressure dependent and may have a transient component.

Neuzil (1982) observed test-zone compressibilities a factor of six larger than water compressibility during pressure-pulse testing of the Pierre Shale. He evaluated the possible factors that could be responsible for the observed high test-zone compressibilities and concluded that test-tool compliance and air entrapment were probably the most important influences. Because interpreted transmissivity and storativity are directly proportional to test-zone compressibility, Neuzil also emphasized the importance of **measuring** test-zone compressibility rather than simply assuming that it would be equal to fluid compressibility. Hsieh et al. (1983) also report test-zone compressibilities a factor of five greater than water compressibility and relate the higher test-zone compressibilities to test-tool compliance.

Six factors that could contribute to high test-zone compressibilities in the Salado permeability-testing program were identified and described by Beauheim et al. (1991). These include: 1) non-packer test-tool-component compressibility; 2) borehole-wall compressibility; 3) axial test-tool movement; 4) test-zone-packer deformation; 5) entrapped gas or gas generated in the test zone; and 6) creep closure of the borehole. Test-zone compressibilities calculated for the tests in this

report include the effects due to the first five factors listed above in a single compressibility coefficient. The sixth factor, creep closure, occurs too slowly to affect test-zone compressibility and was therefore not included in the calculations.

Whenever fluid was injected into or removed from a test zone, the volume of fluid and the resulting change in test-zone pressure were measured. From these data, the test-zone compressibility was calculated using:

$$C_{tz} = \frac{1}{V_{tz}} \frac{V_w}{\Delta P} \qquad (6\text{-}13)$$

where: C_{tz} = test-zone compressibility
V_{tz} = test-zone volume
V_w = volume of brine withdrawn/injected
ΔP = change in test-zone pressure due to withdrawal/injection

Data collected from shut-in tests performed in the Salado indicate that test-zone compressibility is pressure dependent. The pressure buildups observed after shut in are not characteristic of ideal shut-in buildups. Figure 6-4 shows pressure data collected during testing in SCP01-A along with an idealized shut-in pressure buildup. As discussed in Beauheim et al. (1991), the non-ideal buildup could be caused by a varying test-zone compressibility that decreased with increasing pressure.

Two methods were used to measure the instantaneous component of compressibility at various pressures. In the first method, a discrete volume of brine was withdrawn from the test zone and measured in a graduated cylinder. The change in pressure corresponding to the withdrawal was measured using a pressure

56
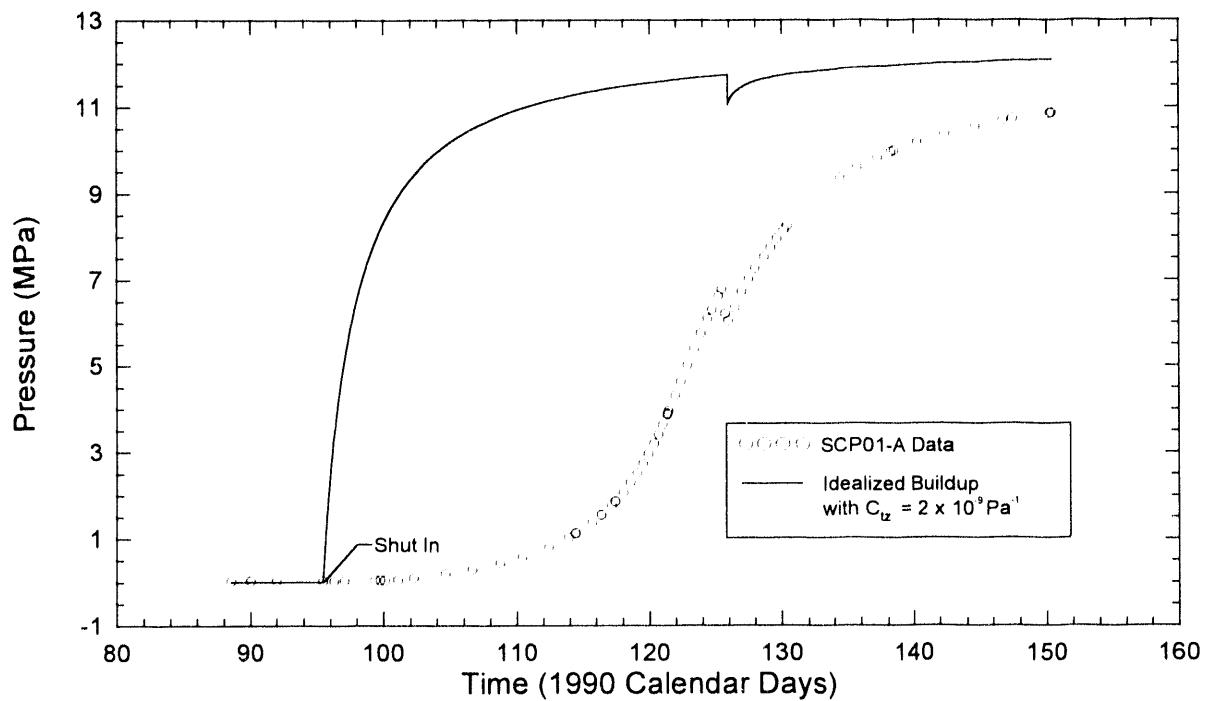
Figure 6-4.   Comparison of observed SCP01-A pressure buildup with simulated buildup using a constant test-zone compressibility.

transducer and compressibility was then calculated using Eq. 6-13. This method gives the average test-zone compressibility over the particular pressure range used in the calculation. In the second method, brine was continuously injected into the test zone using a DPT panel (Section 3.6). The volume injected was measured by the DPT and the corresponding pressure change was measured using a pressure transducer. When using the continuous-injection method, the compressibility is calculated by first computing the numerical derivative of the measured volume-versus-pressure curve and then dividing this derivative by the test-zone volume. This technique gives a more continuous representation of compressibility versus pressure than the discrete-volume method. Both methods for measuring compressibility are performed

rapidly and, therefore, capture only the instantaneous component of compressibility.

Compressibility calculations utilizing both methods have been made using data from tests performed in the stainless-steel compliance-test chamber and in actual boreholes. Compressibilities calculated using data from pulse withdrawals and constant-pressure withdrawals performed during permeability-testing sequences and depressurization steps performed after testing was completed are presented in Table 6-2.

Figure 6-5 shows calculated test-zone compressibilities for L4P52-A testing and also for a similar test tool installed in the stainless-steel compliance-test chamber. This figure shows that test-zone compressibility decreases as pressure

57

Table 6-2. Summary of Test-Zone and Guard-Zone Compressibility Information

Test Sequence	Zone	Event	Initial Pressure (MPa)	Final Pressure (MPa)	Volume Produced (cm^3)	Zone Fluid Volume (cm^3)	Zone Compressibility (Pa^{-1})	Gas Observations
L4P51-A	guard	CPW	0.235	0.207	40	2927	4.88 x 10^{-7}	not observable
L4P51-B	test	PW1	4.750	3.663	6.2	4532	1.26 x 10^{-9}	no record
	test	PW2	4.829	2.784	12.0	4532	1.29 x 10^{-9}	none
	test	CPW	4.978	3.345	6.8	4532	9.19 x 10^{-10}	not observable
	guard	PW1	2.300	1.256	5.4	2908	1.78 x 10^{-9}	none
	guard	PW2	3.152	1.983	5.6	2908	1.65 x 10^{-9}	none
	guard	PI	3.249	4.469	6.9	2908	1.94 x 10^{-9}	not observable
L4P52-A	test	PW	6.187	4.888	15.8	3403	3.57 x 10^{-9}	in solution
	test	CPW	6.162	3.957	18.1	3403	2.41 x 10^{-9}	not observable
	test	DP1	0.829	0.710	9.7	3403	2.40 x 10^{-8}	none
	test	DP2	0.710	0.497	24.6	3403	3.39 x 10^{-8}	in solution
	test	DP3	0.499	0.389	22.4	3403	5.98 x 10^{-8}	in solution
S1P71-B	test	DP1	3.898	2.596	6.8	4418	1.18 x 10^{-9}	no record
	test	DP2	1.679	0.338	8.6	4418	1.45 x 10^{-9}	no record
	guard	DP1	4.120	2.804	155	2813	4.19 x 10^{-8}	in solution
	guard	DP2	2.830	1.436	405	2813	1.03 x 10^{-7}	free gas
S1P72-A	test	PW1	1.184	0.832	1379.6	5009	7.82 x 10^{-7}	in solution
	test	PW2	1.211	0.038	3085	5009	5.25 x 10^{-7}	free gas
	test	CPW2	0.912	0.670	975	5009	8.04 x 10^{-7}	free gas
	test	DP	0.677	0.665	46	5009	7.65 x 10^{-7}	in solution
	guard	DP1	3.175	2.243	5	2522	2.13 x 10^{-9}	in solution
	guard	DP2	2.377	1.475	5.25	2522	2.31 x 10^{-9}	in solution
	guard	DP3	1.656	0.667	5.5	2522	2.21 x 10^{-9}	in solution
	guard	DP4	1.392	0.039	9.5	2522	2.78 x 10^{-9}	in solution
S1P73-B	test	PW1	4.070	3.158	4.1	3868	1.16 x 10^{-9}	no record
	test	PW2	4.163	3.147	9.4	3868	2.39 x 10^{-9}	none
	test	CPW	4.237	2.892	10.4	3868	2.00 x 10^{-9}	not observable

Table 6-2. Summary of Test-Zone and Guard-Zone Compressibility Information (Continued)

Test Sequence	Zone	Event	Initial Pressure (MPa)	Final Pressure (MPa)	Volume Produced (cm^3)	Zone Fluid Volume (cm^3)	Zone Compressibility (Pa^{-1})	Gas Observations
S1P73-B	test	DP1	2.913	2.099	11.9	3868	3.78 x 10^{-9}	none
	test	DP2	2.133	1.417	15.8	3868	5.71 x 10^{-9}	none
	test	DP3	1.484	0.858	35.2	3868	1.01 x 10^{-8}	none
	test	DP4	0.876	0.261	95.1	3868	4.00 x 10^{-8}	in solution
	guard	PW	2.098	1.405	57	2637	3.12 x 10^{-8}	free gas
	guard	DP1	1.640	1.044	100	2637	6.36 x 10^{-8}	in solution
	guard	DP2	1.058	0.385	395	2637	2.23 x 10^{-7}	in solution
	guard	DP3	0.401	-0.040	865	2637	7.44 x 10^{-7}	in solution
SCP01-A	test	PW1	10.860	8.833	46	8734	2.60 x 10^{-9}	in solution
	test	PW2	11.130	7.009	76	8734	2.11 x 10^{-9}	no record
	test	CPW1	11.032	8.458	38.1	8734	1.69 x 10^{-9}	not observable
	test	CPW2	11.381	8.260	32.7	8734	1.12 x 10^{-9}	not observable
	test	DP1	11.818	8.419	42	8734	1.41 x 10^{-9}	in solution
	test	DP2	8.882	4.292	57	8734	1.42 x 10^{-9}	in solution
	test	DP3	5.155	0.133	121	8734	2.76 x 10^{-9}	in solution
	guard	DP1	2.260	1.472	32	2454	1.65 x 10^{-8}	in solution
	guard	DP2	1.478	0.775	75	2454	4.35 x 10^{-8}	in solution
	guard	DP3	0.775	0.121	500	2454	3.12 x 10^{-7}	in solution

Key: CPW = constant-pressure withdrawal
PW = pulse withdrawal
PI = pulse injection
DP = depressurization
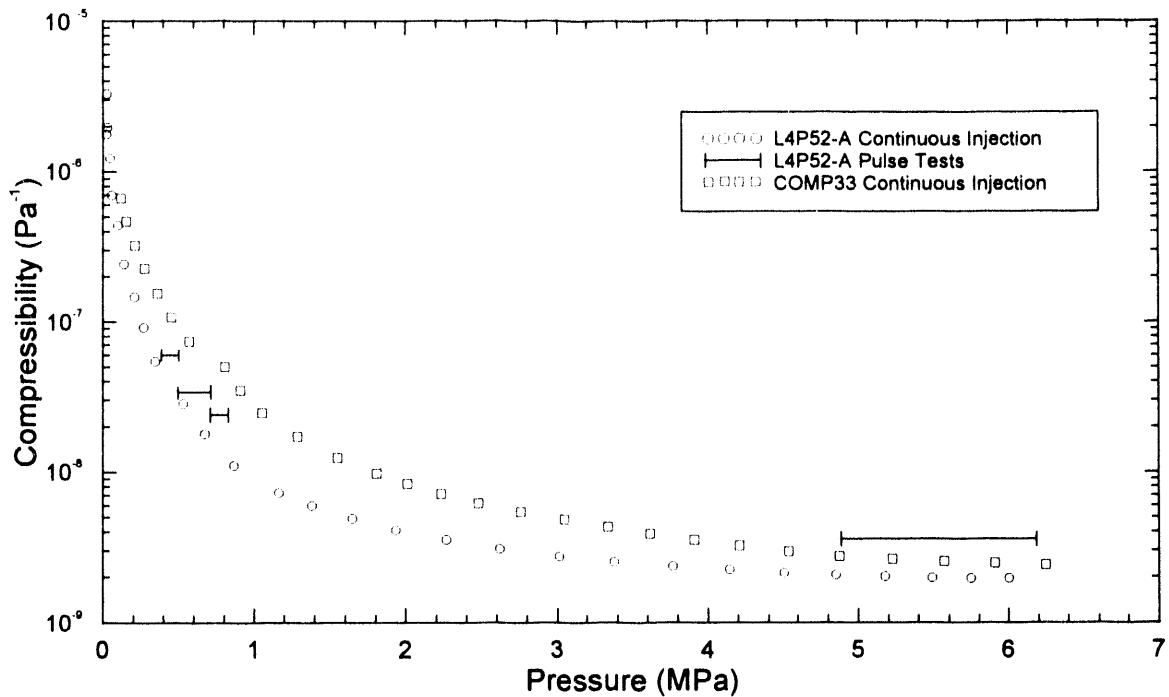
Figure 6-5.   Comparison of test-zone compressibilities observed during K4P52-A testing and compliance testing.

increases, i.e., test-zone compressibility is pressure dependent. Compressibilities calculated from tests performed in the compliance chamber are comparable to those calculated from permeability-test data, suggesting that compressibility is test-tool dominated. Both the compliance and permeability-test data show that test-zone compressibility asymptotically approaches some value greater than 1×10^{-9} Pa^{-1} as pressure increases. As discussed above, the compressibility of the brine used in these tests is estimated to be about 2.7×10^{-10} Pa^{-1}. Therefore, most of the compressibility in a test zone must be provided by the test tool itself. Also shown on Figure 6-5 are test-zone compressibilities calculated from pulse withdrawals during L4P52-A testing. Both the pulse and continuous-injection techniques used to estimate test-zone compressibility yielded similar results although the

compressibilities calculated from pulse-withdrawal data tended to be higher than those calculated from continuous-injection data. Pressures change rapidly during pulse withdrawals and the DAS is not likely to capture the extreme lowest pressure reached by scanning every 15 seconds. This measurement uncertainty probably results in calculated test-zone compressibilities from pulse withdrawals that are slightly high. Figure 6-6 shows similar results for compressibilities calculated for both the test zone and the guard zone during compliance-testing sequence COMP33.

As stated previously, entrapped gas could result in a high test-zone compressibility and could also result in pressure-dependent compressibility. The amounts of gas necessary to yield the observed variations in test-zone compressibilities during

60
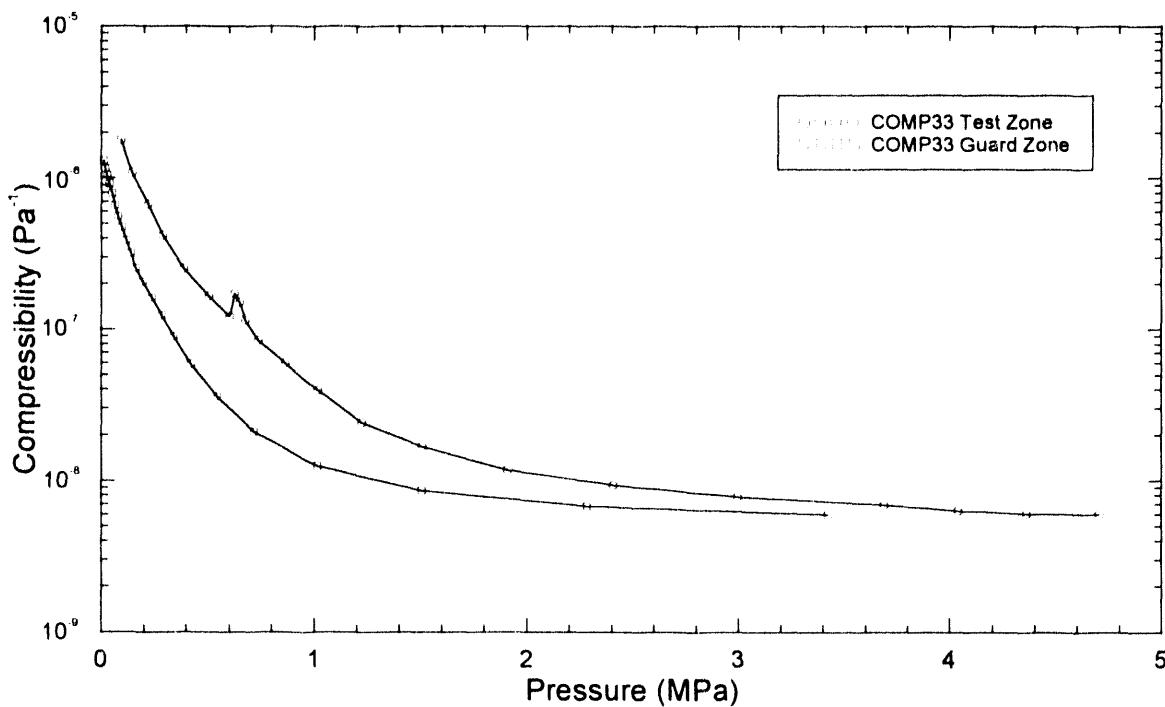
Figure 6-6.   Comparison of test-zone and guard-zone compressibilities observed during compliance testing.

testing sequences COMP33 and L4P52-A were calculated using the following equation, derived using the ideal gas law:

$$V_g = \frac{P \ (C_{tz} - C_b)}{1 - PC_b} \qquad (6\text{-}14)$$

where: V_g = volume fraction of gas in test zone

P = test-zone pressure

C_{tz} = test-zone compressibility

C_b = brine compressibility

Using Eq. 6-14, scoping calculations indicate that, at atmospheric pressure, 10% or more of the test-zone volume would have to be filled with gas to

account for the observed high test-zone compressibilities. These volumes of gas could not be trapped in the test zones during tool installation because of the procedures followed. Therefore, the measured compressibilities cannot be attributed to the presence of gas alone and must reflect additional factors such as packer compressibility and other forms of test-tool compliance.

The test-zone-compressibility calculations described above result from specific test conditions such as particular packer-inflation pressures, test- and guard-zone pressure differentials, and pressure histories. Although these factors are not expected to affect the calculated compressibilities greatly, the combined effects of these factors preclude the direct use of

61

calculated compressibilities in simulations. The calculated compressibilities serve as a guide to the variations in test-zone compressibilities needed to simulate observed test results but must be adjusted to provide a more definitive simulation.

To incorporate variations in test-zone compressibility in GTFM simulations, they must be input as compressibility versus time for a given pressure history. Calculated test-zone compressibilities, initially defined as a function of pressure, and the observed pressure history from the test to be simulated are used as input by a GTFM utility code to generate a compressibility-versus-time sequence to be used during that test simulation. Figure 6-7 shows an unadjusted (or raw) compressibility-versus-time sequence generated for testing in SCP01-A and the final compressibility-versus-time sequence adjusted to fit the simulation to the observed data. These compressibility sequences were generated using the calculated compressibilities from compliance test COMP33 and the pressure history observed during SCP01-A testing. Test-zone compressibilities calculated from compliance test COMP33 were used because sufficient data were not available from either the SCP01-A tests or compliance test COMP21 (the compliance test performed on the test tool used in SCP01-A) to generate a compressibility-versus-time sequence for the full range of pressures observed during the test. Figure 6-7 shows that the adjusted compressibility-versus-time sequence has a
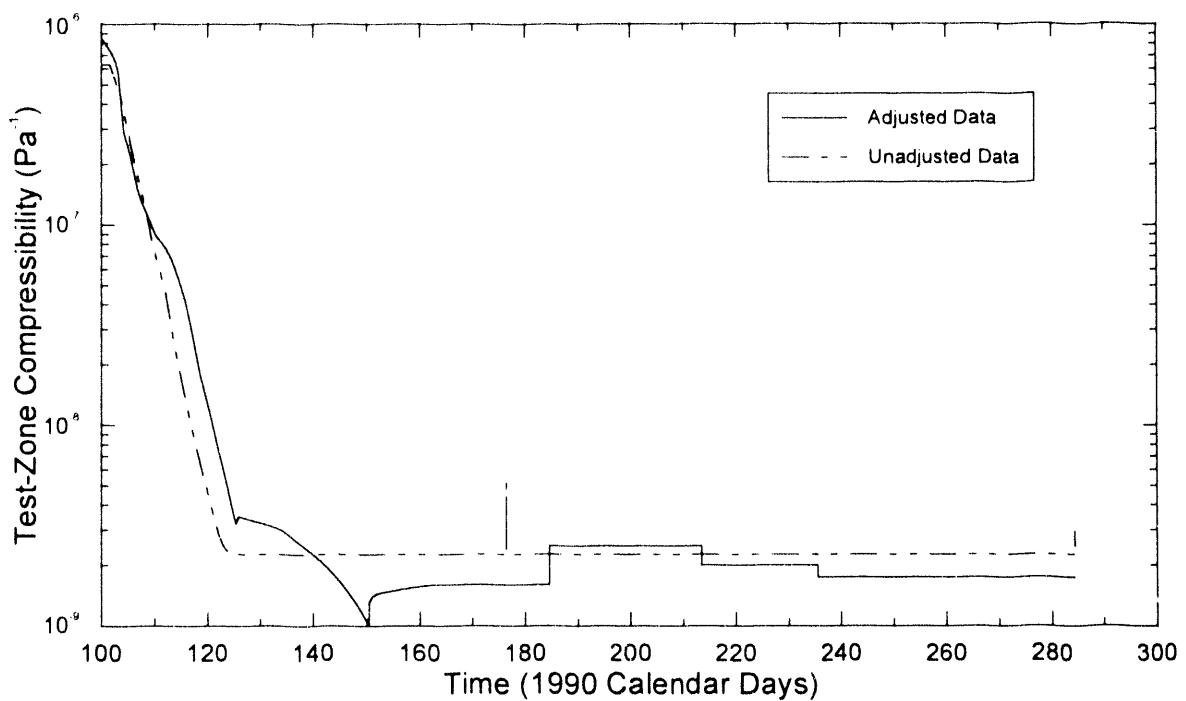
Figure 6-7. Comparison of test-zone compressibility versus time function derived by fitting to SCP01-A data and function derived from compliance testing.

reasonable basis provided by compliance-testing data.

In addition to instantaneous compressibility responses, test tools may also exhibit transient compressibility or compliance effects. Constant-pressure flow tests and pulse tests were performed in the stainless-steel compliance chamber to quantify the amount of transient compliance that could be attributed to the test tool. Figure 6-8 shows the pressure drop and subsequent buildup after a pulse withdrawal performed in the compliance chamber. The pressure buildup results from the transient component of compliance. If there were no transient component, there would be no pressure recovery. That is, the pulse test in the compliance chamber would resemble a step function. A pressure buildup of about 0.093 MPa,

which was about eight percent of the magnitude of the imposed pulse, occurred during the first 4 hr (0.1667 day) after the pulse. About two-thirds of the pressure buildup occurred in the first 7 minutes (0.0049 day) after the pulse and the other one-third occurred over the next 3.9 hr (0.1618 day). No further pressure buildup was observed after that time. Figure 6-9 shows the fluid production from a constant-pressure-withdrawal test performed in the compliance chamber. This figure shows that the transient production from test-tool compliance after the initial instantaneous response is only about 0.55 cm³. About two-thirds of this production came in the first 16 minutes (0.0111 day) of the test and the remaining one-third occurred over the next 12.5 hr (0.5208 day). No further production was observed after that time.
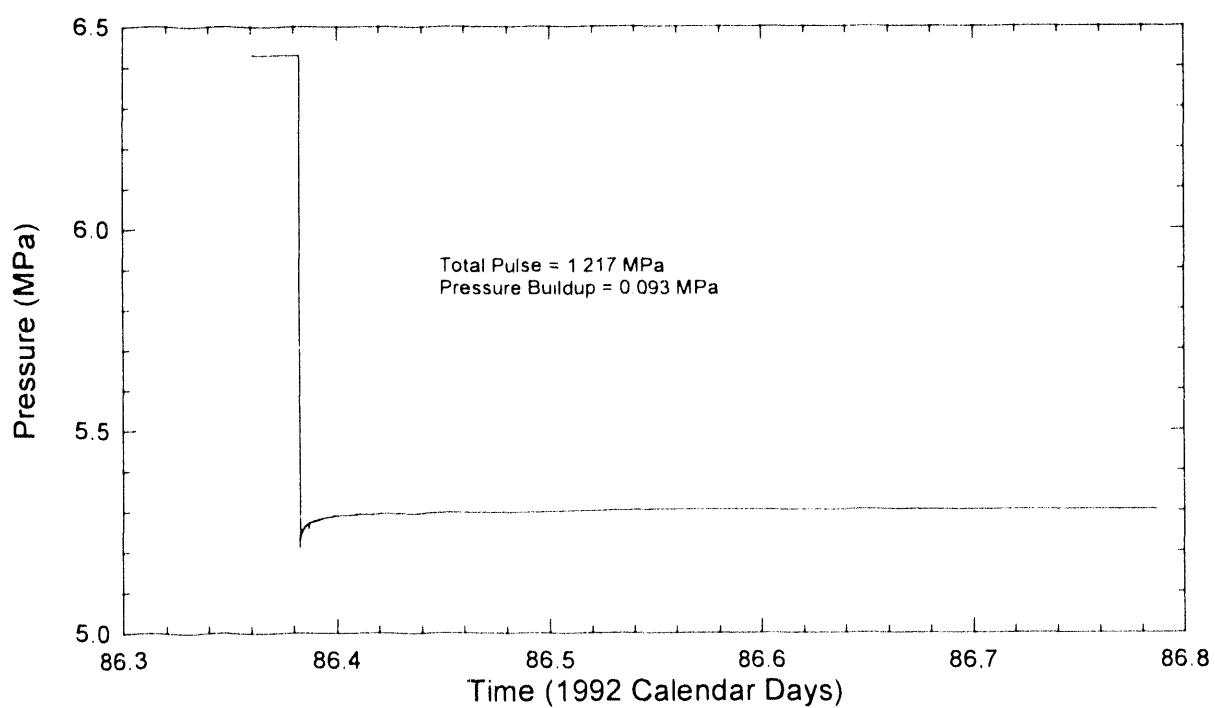

Figure 6-8. Pressure recovery following a pulse withdrawal from the compliance chamber.

63
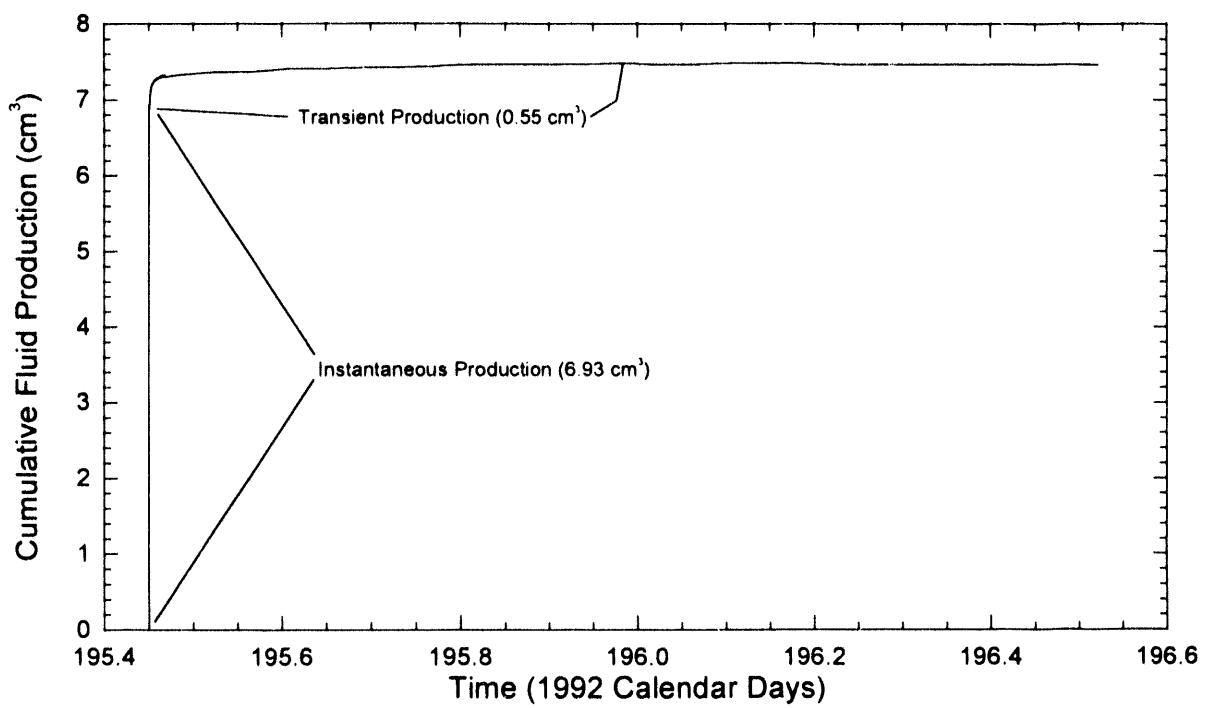
Figure 6-9. Fluid production during a constant-pressure withdrawal from the compliance chamber.

7. ESTIMATION OF HYDRAULIC PROPERTIES

This chapter presents individual interpretations of the pressure-pulse, constant-pressure flow, and pressure-buildup tests conducted in the boreholes discussed in Chapter 5. Section 7.1 presents both analytical and numerical (GTFM) interpretations of the tests and estimates of the hydraulic parameters of the tested intervals. Section 7.2 presents a discussion of the results of the interpretations and an evaluation of various assumptions made in test interpretation.

7.1 Individual Test Interpretations

The tests performed in the individual boreholes are discussed and interpreted in the following sections. The pressure responses observed in untested guard zones during the testing in the test zones are also examined to see if any conclusions can be drawn about the hydraulic properties of the guard-zone intervals. A summary of the interpreted results is presented in Table 7-1.

The interpreted values of the parameters listed in Table 7-1 are given to two significant figures, with the exception of formation pore pressure, which is given to three significant figures. The number of significant figures presented reflects the sensitivity of the interpretive models used rather than real knowledge of the parameter values. That is, the values listed are the actual values used to generate the best-fit simulations. Changes in the last digits of those values cause noticeable degradation of the fit of simulated versus observed pressure responses. Because of measurement uncertainty (see Chapter 3), most of the interpreted values are probably accurate to only one significant figure.

Formation pore pressures are thought to be accurate to about ±0.25 MPa.

7.1.1 L4P51-A. Borehole L4P51 was originally drilled vertically downward into the floor of Room L4 in October 1989 (Section 5.1). Because the hole has since been deepened twice to allow testing of anhydrite "c" and Marker Bed 140, the testing performed with the original hole configuration is given an "A" suffix. The test-tool configuration for the L4P51-A testing is shown in Figure 7-1. The guard zone extended from 1.45 to 2.49 m deep and included the lower 0.05 m of polyhalitic halite 4, Marker Bed 139, clay E, and the upper 0.13 m of halite 4. The test zone extended from 3.33 to 4.75 m deep and included the lower 1.22 m of polyhalitic halite 3, clay D, and the upper 0.18 m of halite 3.

Figure 7-2 shows a plot of the pressure data from the test and guard zones collected during the L4P51-A testing. The pressure values presented in Figure 7-2 have been compensated for the elevation differences between the locations of the pressure transducers and the centers of the tested units in the test and guard zones. The test-zone and guard-zone pressures were compensated by adding 0.060 and 0.035 MPa, respectively, to the pressures measured by the pressure transducers and reported by Stensrud et al. (1992). In the test zone, the testing sequence consisted of an initial buildup period followed by two pulse-withdrawal tests. Interpretations of the pulse-withdrawal tests in the test zone and discussion of the pressures observed in the guard zone during those tests are presented in Beauheim et al. (1991). A constant-pressure flow test was conducted in the

Table 7-1. Summary of Test-Interpretation Results

Hole	Zone	Map Unit	Test	Analysis Method	Transmissivity T (m^2/s)	Permeability-Thickness kh (m^3)	Storativity S	Map Unit Thickness h (m)	Average Hydraulic Conductivity K (m/s)	Average Permeability k (m^2)	Average Specific Storage S_s (m^{-1})	Formation Pore Pressure p_i (MPa)	Skin Factor or Thickness	Radius of Influence r_i (m)
L4P51-B	test	anhydrite "c"	PB	Interpret/2	3.8×10^{14}	5.1×10^{21}	--	0.10	3.8×10^{13}	5.1×10^{20}	--	5.17	-1.84	11
			all	GTFM	4.8×10^{14}	6.4×10^{21}	1.0×10^8	0.10	4.8×10^{13}	6.4×10^{20}	1.0×10^7	5.21	15 cm	18
	guard	H-2	SI	--	--	--	--	--	1.04	--	--	--	>3.25	--	--
L4P52-A	test	anhydrite "a"	PB	Interpret/2	9.1×10^{14}	1.2×10^{20}	--	0.19	4.8×10^{13}	6.4×10^{20}	--	6.50	0.37	16
			all	GTFM	8.5×10^{14}	1.1×10^{20}	2.6×10^8	0.19	4.5×10^{13}	6.0×10^{20}	1.0×10^7	6.75	none	15
	guard	anhydrite "b"	SI	--	--	--	--	--	0.03	--	--	--	>3.5	--	--
S1P71-B	test	anhydrite "c"	all	GTFM	4.8×10^{14}	6.4×10^{71}	1.0×10^8	0.08	6.0×10^{13}	8.0×10^{20}	1.25×10^7	5.12	15 cm	20
	guard	H-2	SI	--	--	--	--	--	1.06	--	--	--	>4.2	--	--
S1P72-A	guard	0, PH-4	all	GTFM	7.4×10^{15}	1.0	10^8	0.55	1.4×10^{14}	1.8×10^{21}	9.2×10^8	4.08	none	4
S1P73-A	test	anhydrite "a"	SI	--	--	--	--	--	0.15	--	--	--	0	--	--
	guard	anhydrite "b"	SI	--	--	--	--	--	0.06	--	--	--	0	--	--
S1P73-B	test	MB138	PW2	type curve	3.7×10^{13}	4.9×10^{20}	--	0.17	2.2×10^{12}	2.9×10^{19}	--	-	-	-
			CPW	type curve	1.3×10^{13}	1.8×10^{20}	--	0.17	7.6×10^{13}	1.1×10^{19}	--	--	--	--
			PB	Interpret/2	3.7×10^{13}	4.9×10^{20}	--	0.17	2.2×10^{12}	2.9×10^{19}	--	4.29	-0.08	2
			all	GTFM	3.7×10^{13}	4.9×10^{20}	1.7×10^6	0.17	2.2×10^{12}	2.9×10^{19}	1.0×10^5	4.37	none	3
	guard	AH-1	SI	Horner	-	-	-	1.05			-	2.55	-	-
SCP01-A	test	MB139	CPW2	type curve	4.3×10^{13}	5.8×10^{20}	--	0.96	4.5×10^{13}	6.0×10^{20}	--	-	-	-
			PB2	Interpret/2	3.8×10^{13}	5.1×10^{20}	--	0.96	4.0×10^{13}	5.3×10^{20}	--	12.40	-0.62	5
			all	GTFM	5.3×10^{13}	7.1×10^{20}	1.9×10^7	0.96	5.5×10^{13}	7.4×10^{20}	1.95×10^7	12.55	none	12

Key: PB = pressure-buildup test; SI = shut-in pressure buildup; PW = pulse-withdrawal test; CPW = constant-pressure withdrawal test

99

L4P51−A
TEST−TOOL CONFIGURATION
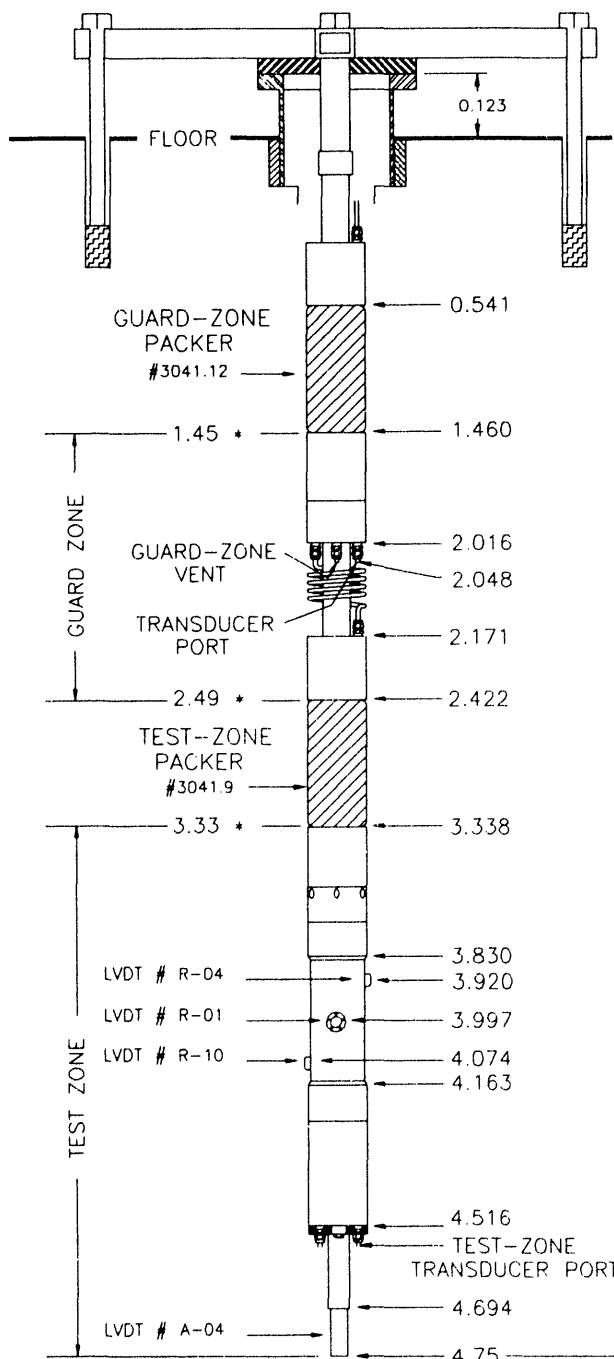
BOREHOLE: L4P51   DATE: 10/23/89
TEST TOOL: #3   DEPTH OF HOLE: 4.75m.

BOREHOLE STRATIGRAPHY

NOTE: MEASUREMENTS IN METERS FROM FLOOR BEFORE PACKER INFLATION.
* ESTIMATED POSITION AFTER PACKER INFLATION.

Figure 7-1. Test-tool configuration for permeability-testing sequence L4P51-A.

Figure 7-2. Test- and guard-zone pressures during L4P51-A testing.

guard zone from March 1, 1990 (1989 Calendar Day 425) to June 4, 1990 (1989 Calendar Day 520). A discussion of that flow test is presented below.

7.1.1.1 Test Zone. The second pulse-withdrawal test in the L4P51-A test zone was initiated on December 20, 1989 (Calendar Day 354), when the test-zone pressure was decreased from 2.24 to 1.14 MPa. The subsequent pressure buildup reached a peak of about 2.30 MPa on February 22, 1990 (1989 Calendar Day 418). By the start of the constant-pressure flow test in the L4P51-A guard zone on March 1, 1990 (1989 Calendar Day 425), the pressure in the test zone had decreased to about 2.26 MPa. During the flow test in the guard zone, the L4P51-A test-zone pressure oscillated between about 2.23 and 2.27 MPa (Figure 7-2).

7.1.1.2 Guard Zone. The L4P51-A guard zone was first shut in on October 27, 1989 (Calendar Day 300), eight days after drilling was completed. A pulse injection was performed about 30 minutes after shut in, increasing the guard-zone pressure to about 4.25 MPa. Within 24 minutes, the guard-zone pressure had decreased to about 1.22 MPa. The guard-zone pressure was then reduced to about 0.13 MPa by removing a total of 190 cm^3 of brine from the guard zone in two steps. Within a few hours of the brine withdrawal, the guard-zone pressure had stabilized at about 0.32 MPa. The guard-zone pressure then decreased slowly during the pulse-withdrawal testing in the test zone. A constant-pressure withdrawal test was initiated in the guard zone on March 1, 1990 (1989 Calendar Day 425) when the guard-zone pressure was about 0.24 MPa. The test was

68

terminated 95 days later on June 4, 1990 (1989 Calendar Day 520).

The back pressure in the DPT panel was maintained at about 0.076 MPa during the constant-pressure withdrawal test. The pressure in the guard zone, however, did not remain constant during the flow test, but instead cycled between about -0.01 MPa (as measured at the control panel in the drift) and about 0.07 MPa (Figure 7-3). The guard-zone pressure varied because both brine and gas were produced during the flow test. Brine and gas traveled from the guard zone to the DPT panel through the guard-zone vent line. The downhole end of the vent line was located 0.432 m above the bottom of the 1.04-m long guard zone (Figure 7-1). Given the low back pressure in the DPT panel (0.076 MPa), the gas in the guard zone was probably present as a separate phase and collected at the top of the guard zone above the brine. When the brine level in the guard zone

was high enough to cover the end of the vent line, the flow of brine and gas from the formation into the guard zone would cause the gas pressure above the brine to increase. The gas pressure would continue to increase until enough brine had flowed to the DPT panel to cause the brine level to fall below the bottom of the vent line. The gas would then vent to the DPT panel, decreasing the gas pressure in the guard zone until brine again covered the end of the vent line, and the process would repeat.

The gas flowing from the guard zone displaced brine in the guard-zone vent line and in the measurement columns in the DPT panel, disrupting brine-flow measurements. After several attempts to separate gas and brine, the DPT panel was modified to provide separation of gas and brine. The new design separated the brine and gas at the top of the DPT measurement columns, allowing uninterrupted measurements of brine production. However,
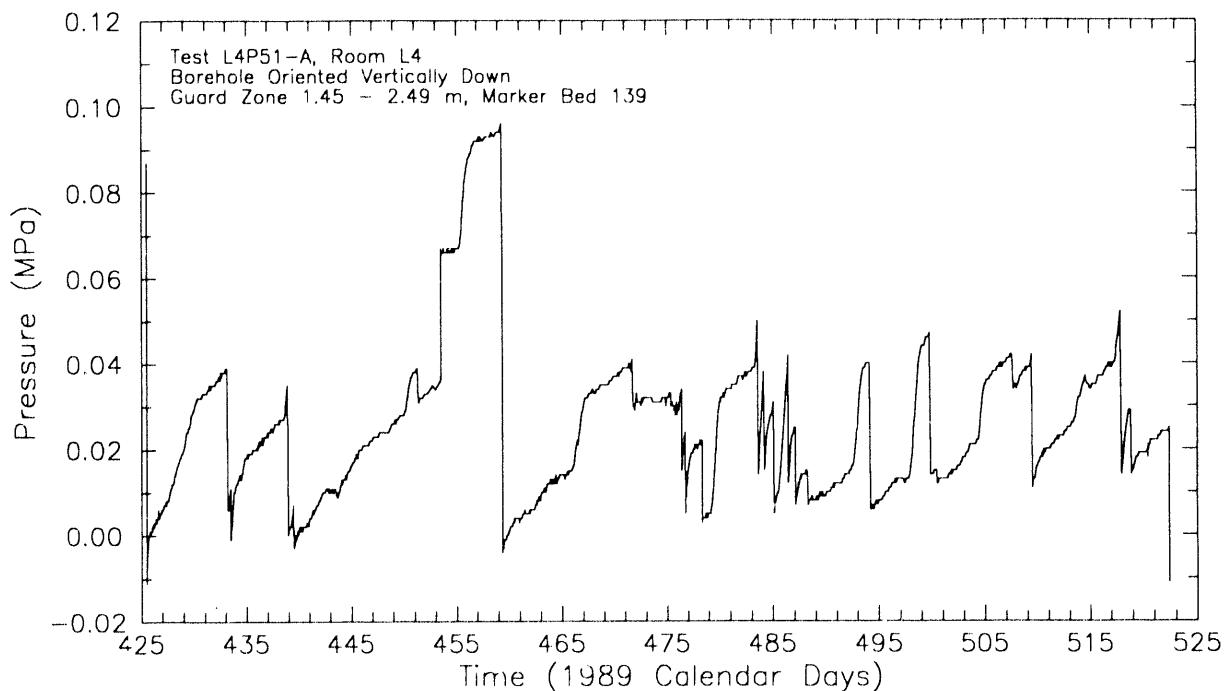
Figure 7-3. Guard-zone pressures during L4P51-A constant-pressure withdrawal test.

69

gas-flow measurements were not possible with this system and brine production was not continuous due to the pressure cycling occurring in the guard zone. The gas-brine separation and measurement system discussed in Section 3.7 was developed after completion of the L4P51-A testing to address the problems discussed above.

Figure 7-4 shows the brine flow measured during the flow test. A total of about 717 cm³ of brine was produced during the 95-day flow period (Table 7-2). Because the observed brine flow rates were affected by gas flow rates that were not measured, no analytical or numerical interpretations of the flow test were attempted. No pressure-buildup test was performed following the flow test because no quantitative interpretation of a buildup test is possible without reliable flow-rate data. The constant-pressure flow test in the L4P51-A guard zone served

primarily as a learning exercise, allowing better preparation for subsequent flow tests performed in other boreholes.

7.1.2 L4P51-B. Borehole L4P51 was deepened from 4.75 m to 10.06 m below the floor of Room L4 on October 1 and 2, 1990 (Calendar Days 274 and 275). The hole was deepened to allow testing of anhydrite "c" and clay B. Figure 7-5 shows the configuration of the test tool in L4P51 for the L4P51-B testing. The L4P51-B guard zone extended from 6.75 to 7.79 m below the floor of Room L4 and included only a portion of halite 2. The test zone extended from 8.63 to 10.06 m deep and included the lower 0.99 m of polyhalitic halite 1, the combined 0.10-m thickness of anhydrite "c" and clay B, and the upper 0.34 m of halite 1.

L4P51-B testing in the test zone consisted of a 6-day open-borehole period, an initial pressure-
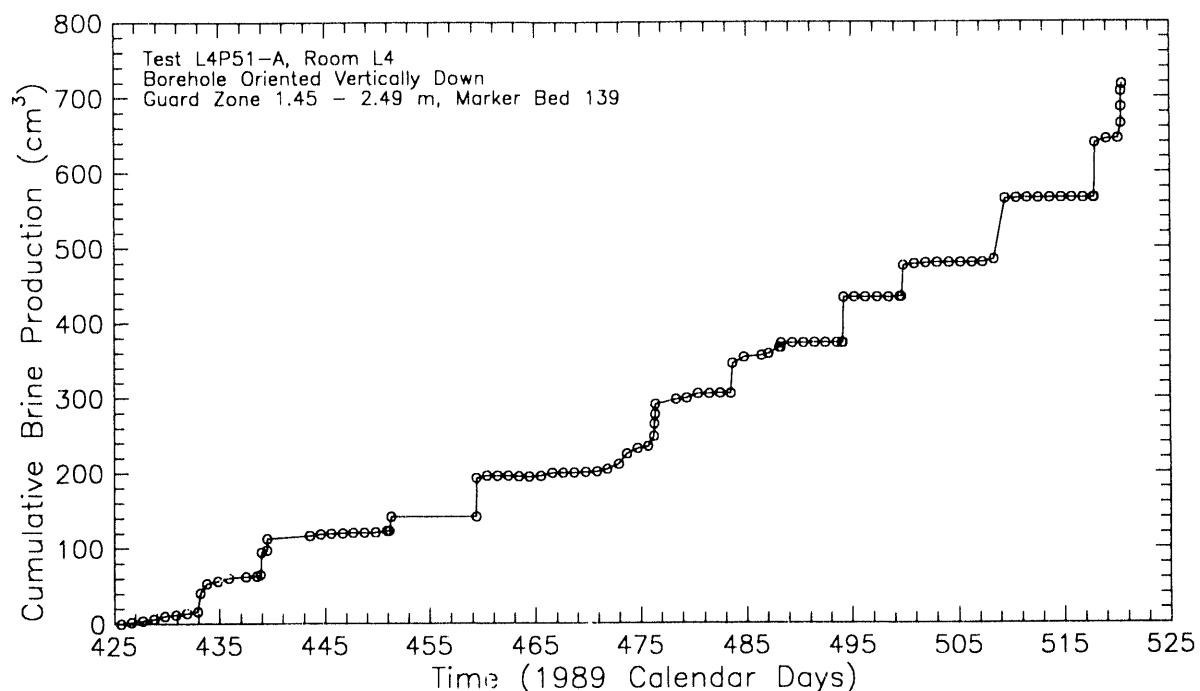
Figure 7-4. Cumulative brine production during L4P51-A guard zone constant-pressure withdrawal test.

70

Table 7-2. Summary of Constant-Pressure Flow Test Data

Test	Stratum	ΔP (MPa)	Duration (days)	Total Flow (cm³)
L4P51-A	MB139	0.20	95	717
L4P51-B #1	anhydrite "c"	1.60-2.25	0.9	18
L4P51-B #2	anhydrite "c"	1.22	44.9	37
L4P52-A	anhydrite "a"	2.21	53.1	165.5
S1P72-A #1	MB139	1.10	7.0	10,350 (brine) 124,400 (gas)
S1P72-A #2	MB139	0.84	27.0	22,000 (brine) 274,400 (gas)
S1P73-B	MB138	1.39	9.9	133
SCP01-A #1	MB139	2.57	12.0	282.2
SCP01-A #2	MB139	3.12	10.1	344.6

buildup period, two pulse-withdrawal tests, a constant-pressure withdrawal test, and a pressure-buildup test. The constant-pressure withdrawal test was interrupted after one day due to a leak in the injection panel. The test was restarted five days later. Testing in the guard zone consisted of a 6-day open-borehole period, an initial pressure-buildup period, two pulse-withdrawal tests, and one pulse-injection test. The guard-zone testing was terminated when a leak was found in the guard-zone injection panel. The pressures in the test and guard zones during the L4P51-B testing are shown in Figure 7-6. The test-zone and guard-zone pressure data shown in Figure 7-6 and subsequent figures were adjusted by adding 0.103 and 0.083 MPa, respectively, to the values recorded by the DAS and reported by Stensrud et al. (1992) to account for the elevation differences between the measuring points of the pressure transducers and the midpoints of the hydrologic units tested.

7.1.2.1 Test Zone. The test zone in L4P51-B was shut in on October 8, 1990 (Calendar Day 281). The first pulse-withdrawal test was initiated on November 27, 1990 (Calendar Day 331) and the second pulse-withdrawal test was initiated on December 17, 1990 (Calendar Day 351). A constant-pressure withdrawal test was initiated on March 13, 1991 (1990 Calendar Day 437), but was terminated the next day when a leak was discovered in the flow-control panel. The test resumed on March 19, 1991 (1990 Calendar Day 443) and continued until May 3, 1991 (1990 Calendar Day 488), producing a total of 37 cm³ of brine over that 45-day period (Table 7-2). The test-zone pressure was about 4.98 MPa before the flow test began, and was reduced to about 3.77 MPa for the duration of the test. Figure 7-7 shows cumulative brine production plotted as a function of time during this test. The pressure-buildup test began on May 3, 1991 (1990 Calendar Day 488) and
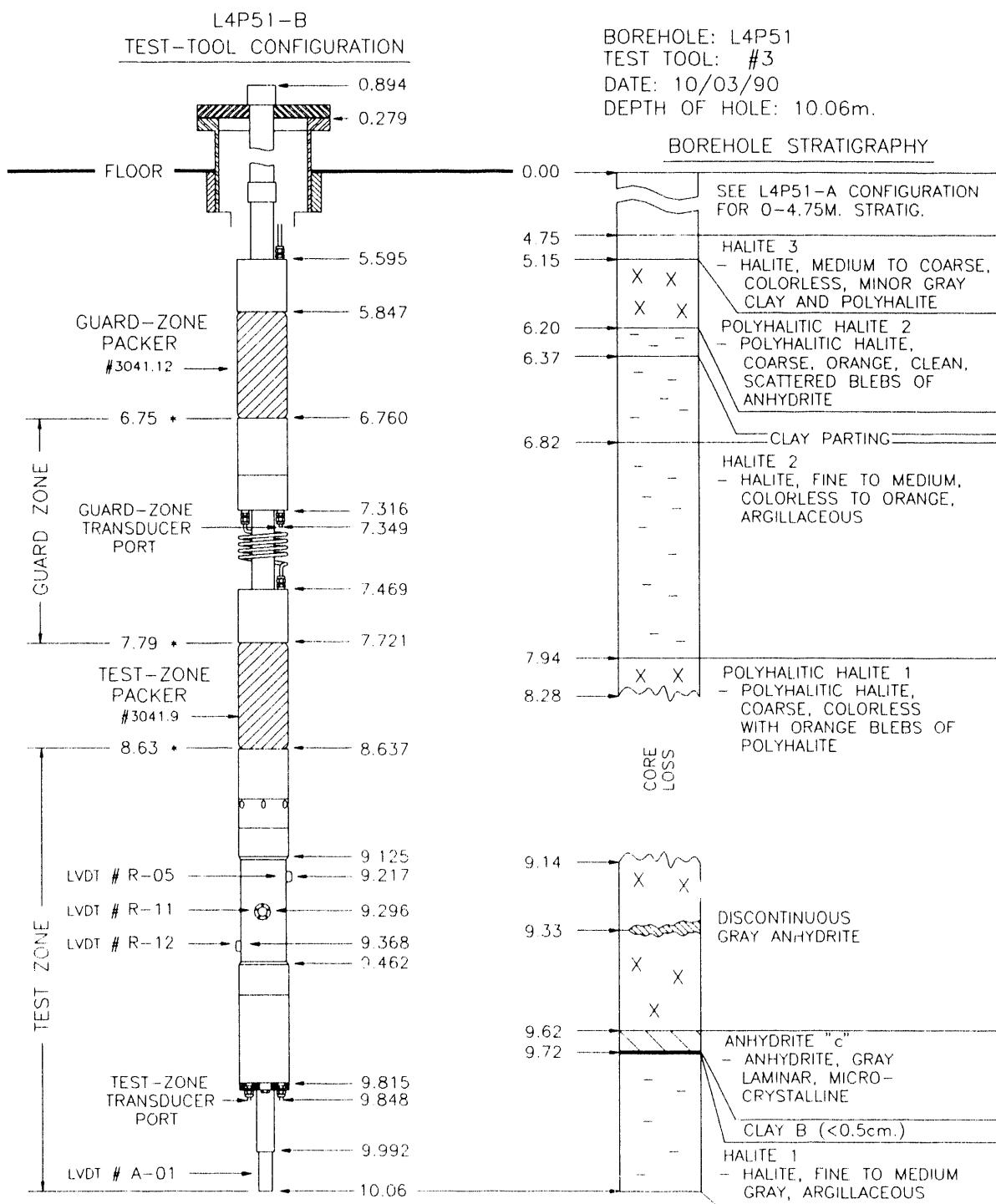
L4P51-B
TEST-TOOL CONFIGURATION

BOREHOLE: L4P51
TEST TOOL: #3
DATE: 10/03/90
DEPTH OF HOLE: 10.06m.

BOREHOLE STRATIGRAPHY

NOTE: MEASUREMENTS IN METERS FROM FLOOR BEFORE PACKER INFLATION.
  * ESTIMATED POSITION AFTER PACKER INFLATION.

Figure 7-5. Test-tool configuration for permeability-testing sequence L4P51-B.

72
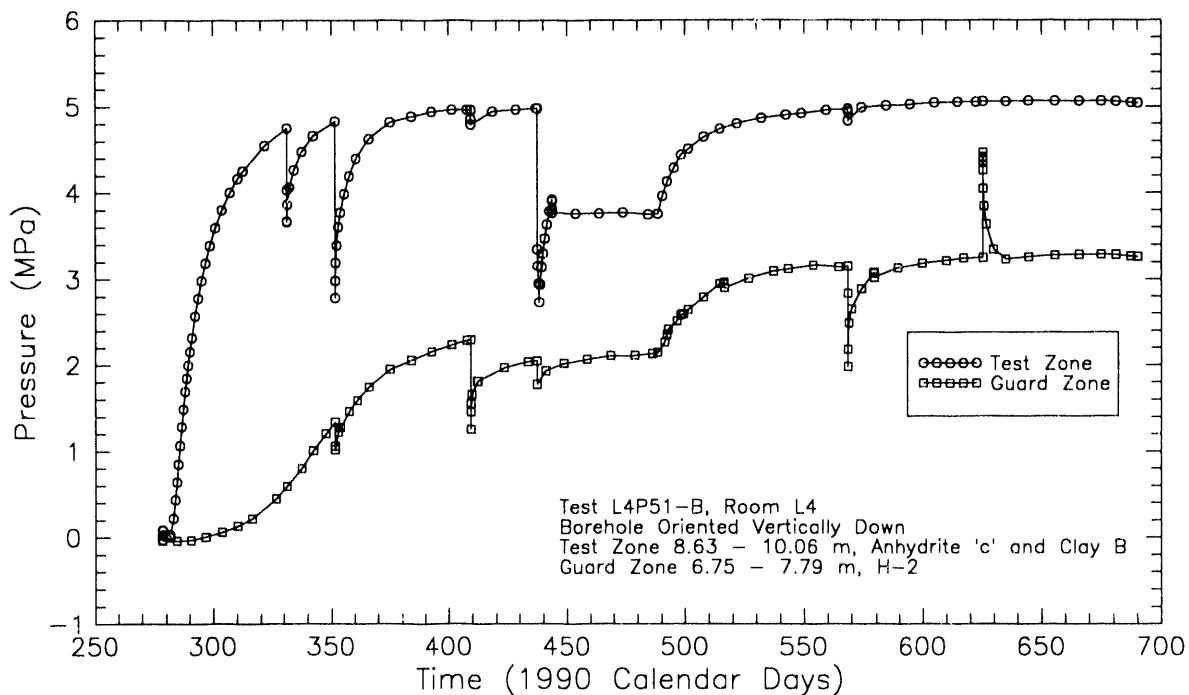
Figure 7-6. Test- and guard-zone pressures during L4P51-B testing.
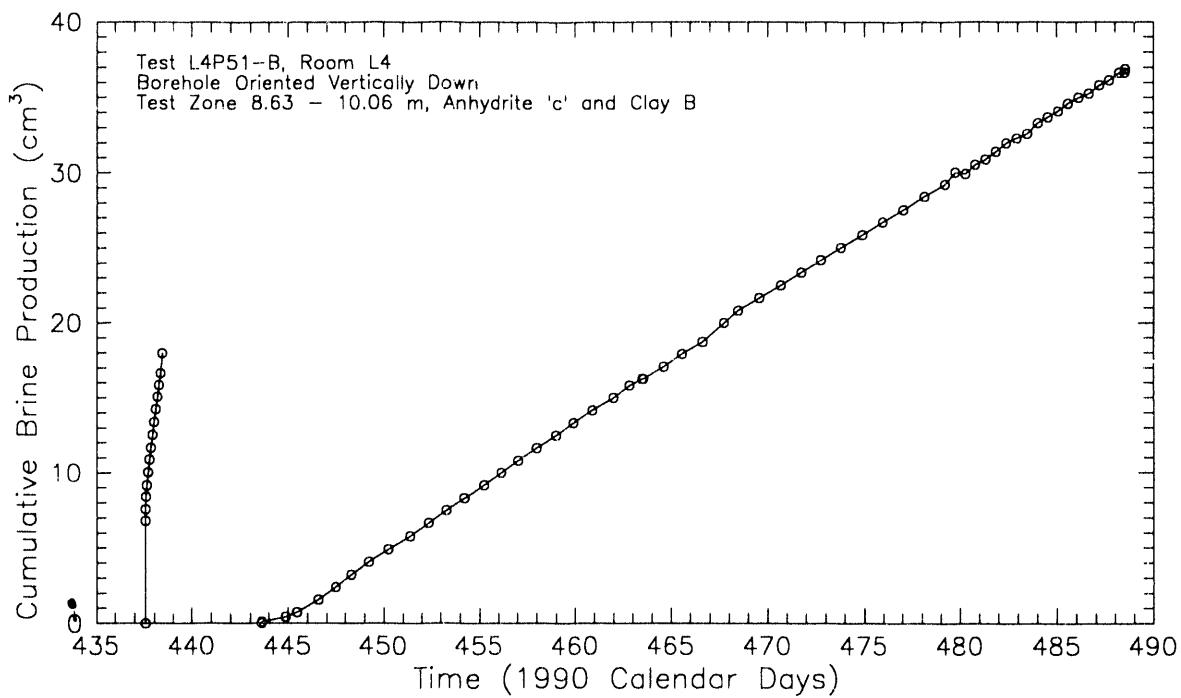
Figure 7-7. Cumulative brine production during L4P51-B constant-pressure withdrawal test.

continued until the end of testing on November 21, 1991 (1990 Calendar Day 690). However, the pressure behavior in the test zone changed after power outages shut down the DAS on September 6, 1991 (1990 Calendar Day 614) and October 10, 1991 (1990 Calendar Day 648) and after a pulse injection into the guard zone on September 17, 1991 (1990 Calendar Day 625). The pressure-buildup trend decreased or became erratic after each of these events, ultimately becoming a pressure-decrease trend after the last power outage. This erratic behavior is thought to be related to equipment problems and, therefore, the data collected after September 6, 1991 (1990 Calendar Day 614) are not considered representative of the true tested formation's response.

Test-zone compressibility values were calculated using data from the two pulse withdrawals and Eq. 6-13. A test-zone compressibility of 1.26×10^{-9} Pa^{-1} was calculated from the first pulse withdrawal and a value of 1.29×10^{-9} Pa^{-1} was calculated from the second pulse withdrawal (Table 6-2). Free gas was not observed during either of the pulse withdrawals.

Analytical Interpretations. Attempts to match the L4P51-B pulse-withdrawal data with type curves were unsuccessful. The pressure recoveries early in the tests were more rapid than predicted by the type curves and no definitive matches to the late-time data could be obtained because of uncertainty as to the formation pore pressure the recoveries were trending toward. The flow-rate data from the constant-pressure withdrawal test could also not be fit to a type curve because the first aborted phase of the flow test disrupted the single pressure-step conditions assumed in the analytical solution.

For analysis of the pressure-buildup test using Interpret/2, the two segments of the constant-pressure withdrawal test were divided into seven separate flow periods having constant rates ranging from 10,000 to 0.23 cm^3/day. The best fit obtained between log-log pressure and pressure-derivative type curves and the pressure-buildup data is shown in Figure 7-8. The late-time stabilization of the pressure derivative is indicative of single-porosity conditions with no evidence of double-porosity, leakage, or hydraulic boundaries (Bourdet et al., 1989). The best dimensionless Horner match is shown in Figure 7-9, and the best linear-linear match is shown in Figure 7-10. The simulations match the observed data well in all cases. The same match parameters were used for all of the fits in Figures 7-8 through 7-10, providing the following estimated parameters: a transmissivity of 3.8×10^{-14} m^2/s (permeability-thickness product of 5.1×10^{-21} m^3), a formation pore pressure of 5.17 MPa, a wellbore-storage coefficient of 5.89 cm^3/MPa (corresponding to a test-zone compressibility of 1.30×10^{-9} Pa^{-1}), and a wellbore skin of -1.84. As described by Eq. 6-9, a wellbore skin of -1.84 implies that the effective wellbore radius is over six times as large as the actual wellbore radius. This effect may be caused by fracturing of the rock immediately around the wellbore or by some other type of permeability enhancement. Assuming a total system compressibility of 8.37×10^{-10} Pa^{-1} (derived from a GTFM storativity estimate of 1.0×10^{-8}), the radius of influence of the constant-pressure withdrawal and pressure-buildup tests was about 11 m.

Numerical Interpretations. The L4P51-B testing was preceded by a 6-day period during which the borehole was open at atmospheric pressure. This open-borehole period was
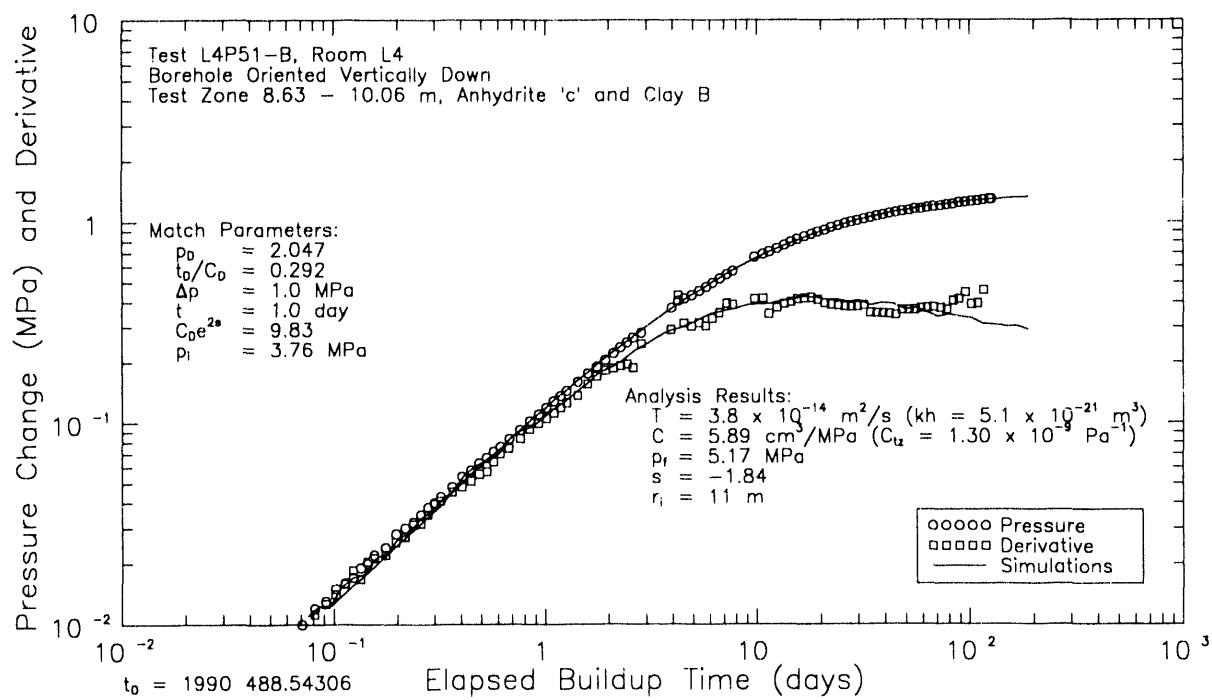
Figure 7-8. Log-log plot of Interpret/2 simulation of L4P51-B pressure-buildup test.
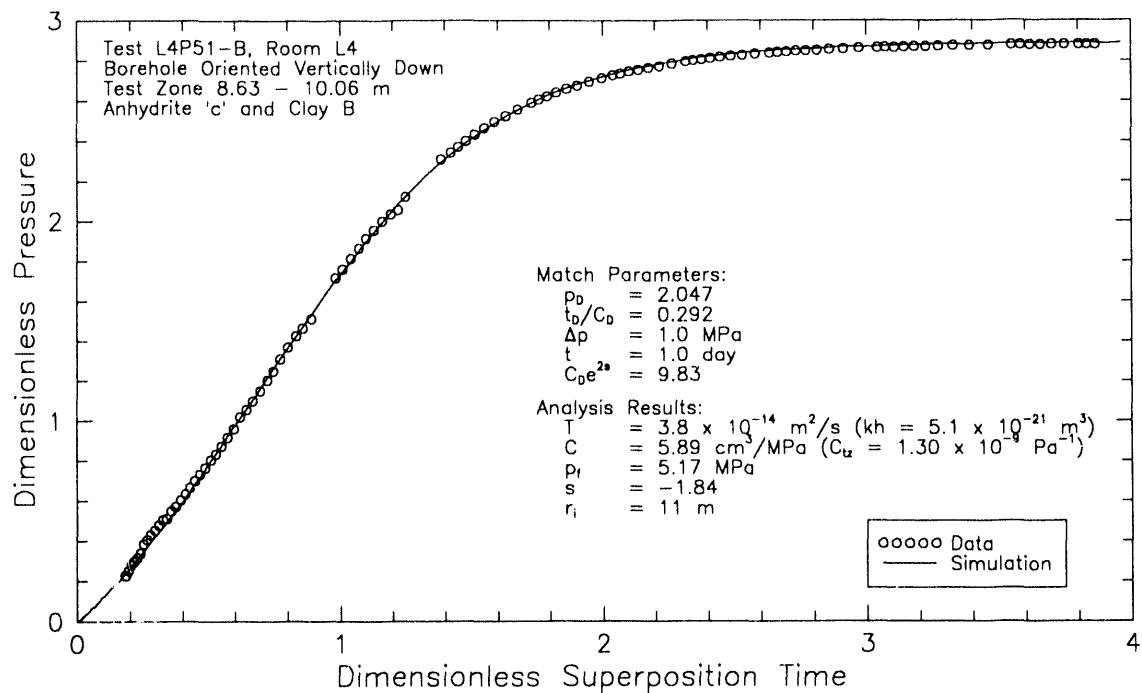

Figure 7-9. Horner plot of Interpret/2 simulation of L4P51-B pressure-buildup test.

75
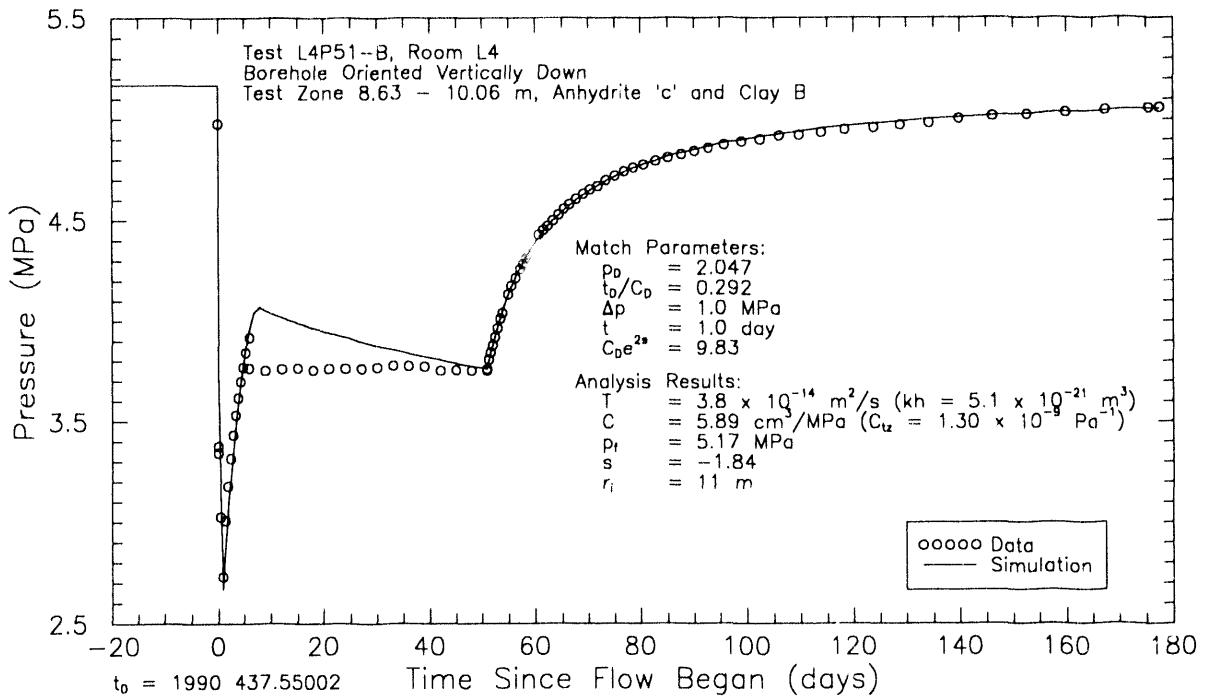
Figure 7-10. Linear-linear plot of Interpret/2 simulation of L4P51-B constant-pressure flow and pressure-buildup tests.

included in all GTFM simulations as a specified-pressure history sequence. History sequences were also used to represent the test-zone pressure offsets caused by pulse withdrawals from the guard zone and the test-zone pressure during constant-pressure withdrawal testing. Temperatures measured in the L4P51-B test zone during the monitoring period are shown in Figure E-1 of Appendix E. Also shown is the smoothed representation of the temperature data used as input to GTFM to compensate the simulated pressures for the temperature fluctuations. The specified parameters for all of the L4P51-B GTFM simulations were a borehole radius of 5.340 cm and a test-zone fluid volume of 4532 cm^3.

Figures 7-11 and 7-12 show semilog plots of the best-fit GTFM simulations and the observed pressure data for the first and second pulse-withdrawal tests, respectively. A constant test-zone compressibility of 1.10×10^{-9} Pa^{-1} was used for the simulations. The fitted parameters for these simulations were a transmissivity of 4.8×10^{-14} m^2/s (permeability-thickness product of 6.4×10^{-21} m^3), a storativity of 1.0×10^{-8}, and a formation pore pressure of 5.21 MPa (Table 7-1). In addition to these formation parameters, matching the early-time responses during the pulse tests required the inclusion of a skin zone around the borehole in the simulations. The fitted parameters for the skin zone were a radial thickness of 15 cm, a transmissivity of 5.0×10^{-13} m^2/s (permeability-thickness product of 6.7×10^{-19} m^3), and a storativity of 7.0×10^{-8}.

Figure 7-13 shows the best-fit simulation and observed fluid-flow data for the constant-pressure withdrawal test. The data are well matched using the same parameters as were

76
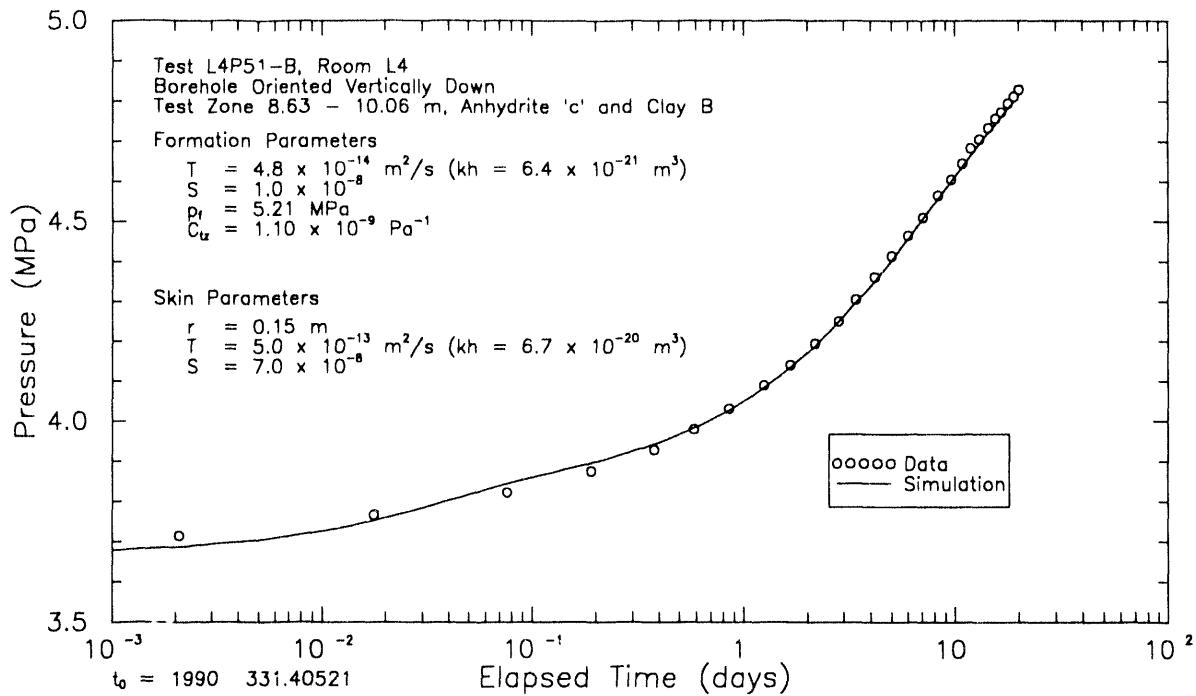
Figure 7-11. Semilog plot of GTFM simulation of L4P51-B pulse-withdrawal test #1.
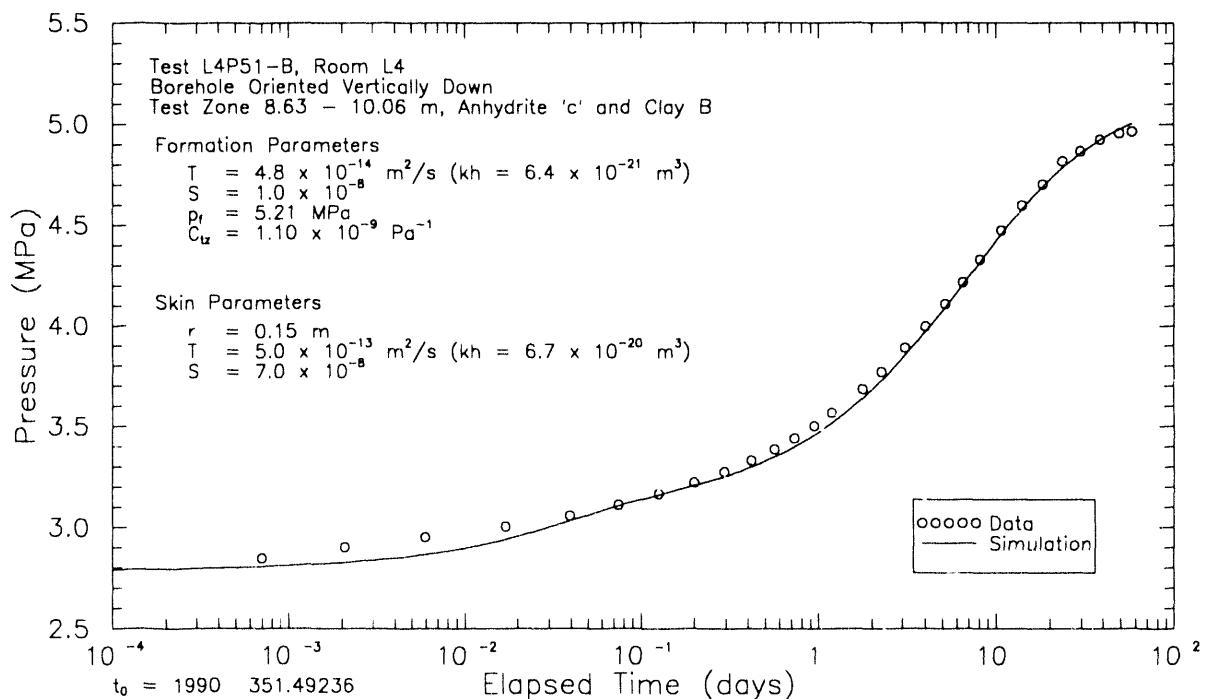
Figure 7-12. Semilog plot of GTFM simulation of L4P51-B pulse-withdrawal test #2.

77
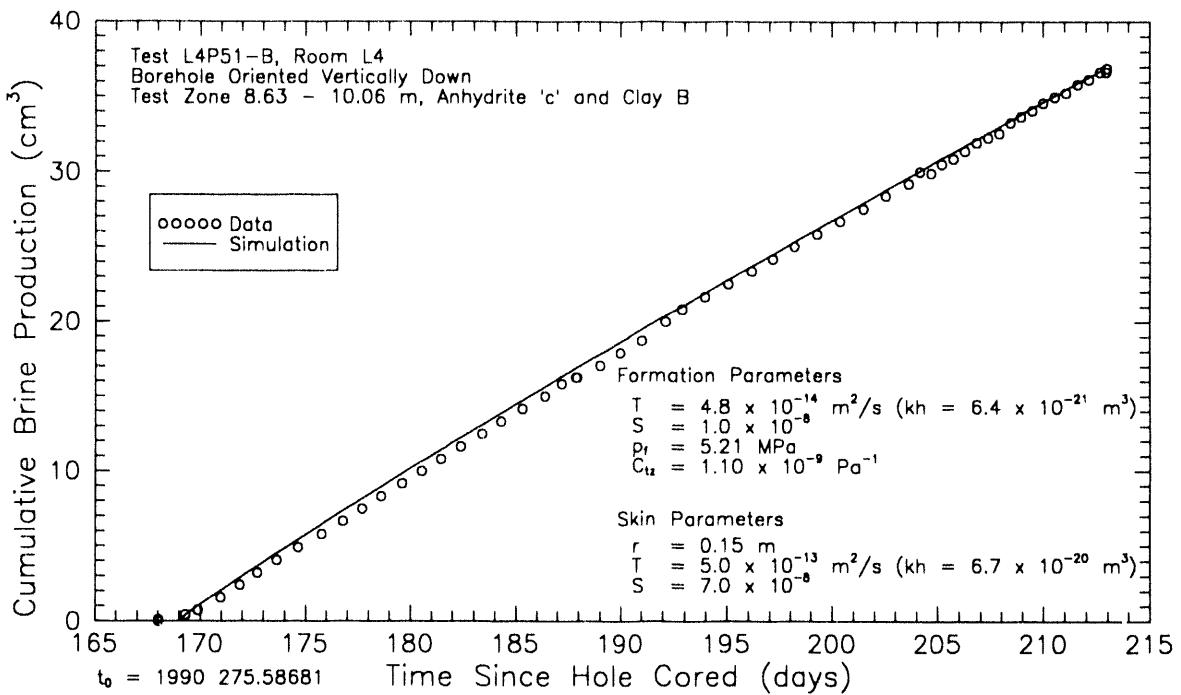
Figure 7-13. Linear-linear plot of GTFM simulation of brine production during L4P51-B constant-pressure withdrawal test.

used to simulate the pulse-withdrawal tests. Figure 7-14 is a Horner plot of the pressure-buildup test data and GTFM simulation using the same simulation parameters. Again, the observed data are well matched. Figure 7-15 shows the match between the GTFM simulation and the observed data over the entire testing sequence. In this instance, using a single constant value of test-zone compressibility of 1.10×10^{-9} Pa^{-1} for the entire testing sequence provided a good simulation of the data except during the initial buildup period. A higher test-zone compressibility is needed to match the initial pressure buildup. The radius of influence of the entire testing sequence calculated using GTFM with a one-percent pressure-change criterion was 18 m.

Summary. The analytical and numerical interpretations of the L4P51-B tests provided estimates of transmissivity of 3.8×10^{-14} and 4.8

$\times 10^{-14}$ m^2/s (permeability-thickness products of 5.1×10^{-21} and 6.4×10^{-21} m^3), respectively. Interpret/2 and GTFM interpretations provided similar estimates of formation pore pressure, ranging from 5.17 to 5.21 MPa. GTFM provided good simulations of all of the tests using a storativity of 1.0×10^{-8}. Using this value of storativity (expressed as total system compressibility), Interpret/2 calculates a radius of influence for the constant-pressure withdrawal and pressure-buildup tests of about 11 m and the radius of influence of the entire testing sequence calculated using GTFM was 18 m. Both interpretations also indicated the presence of a skin zone of increased permeability around the borehole.

Vertically averaged values of hydraulic conductivity (permeability) and specific storage can be calculated for the L4P51-B test zone by assuming that fluid was produced only by the
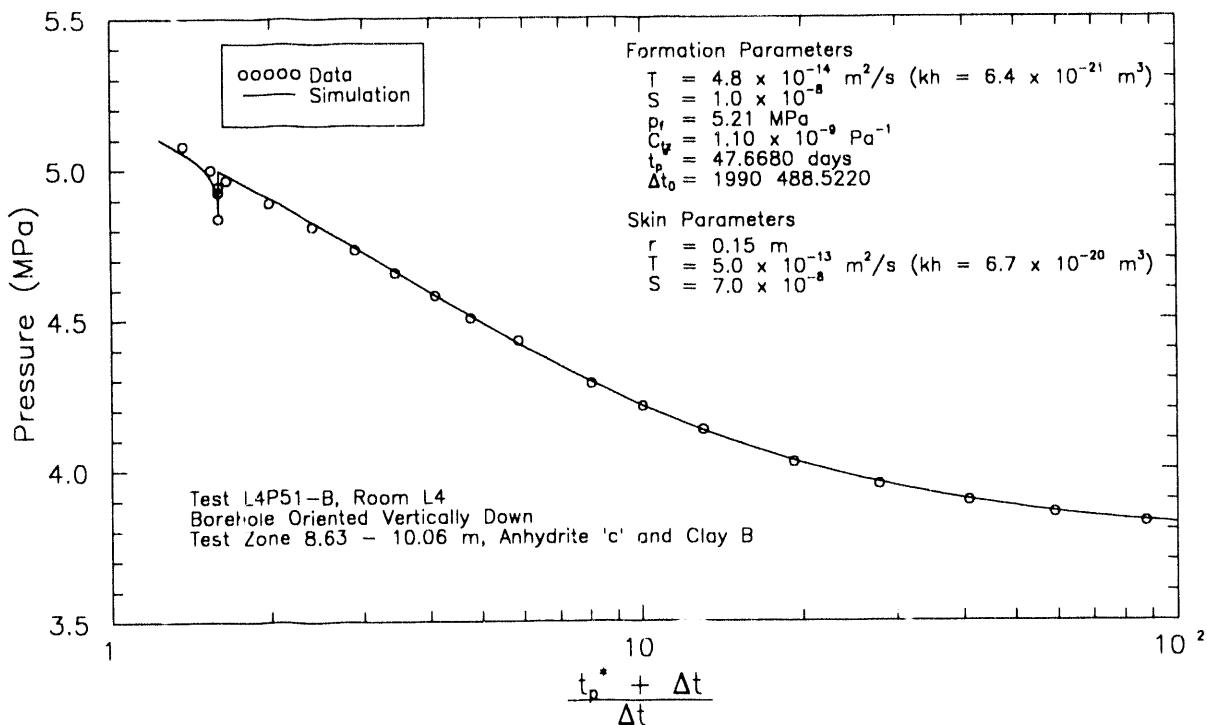
Figure 7-14. Horner plot of GTFM simulation of L4P51-B pressure-buildup test.
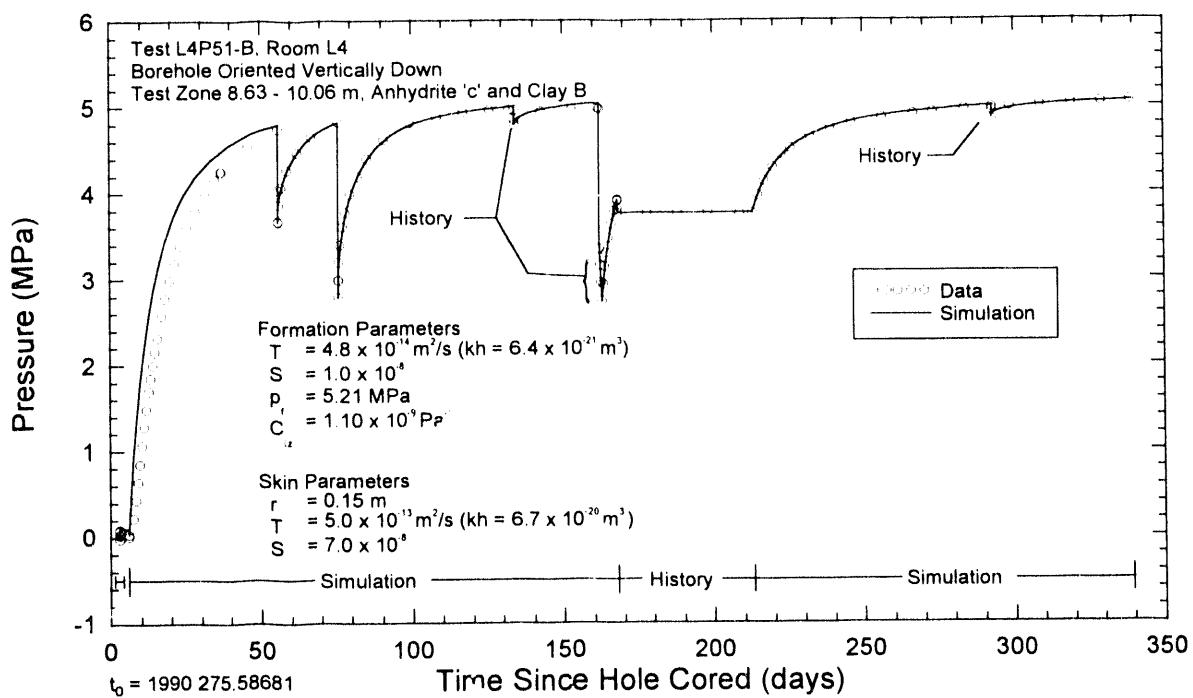
Figure 7-15. Linear-linear plot of GTFM simulation of entire L4P51-B testing sequence.

79
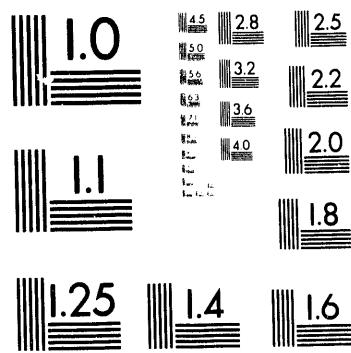
0.10-m interval containing anhydrite "c" and clay B. The average hydraulic conductivity of this interval is 3.8 x 10^{-13} to 4.8 x 10^{-13} m/s (permeability of 5.1 x 10^{-20} to 6.4 x 10^{-20} m^2) and the specific storage is 1.0 x 10^{-7} m^{-1}.

7.1.2.2 Guard Zone. Figure 7-6 is a plot of the pressure data for the test-zone and guard-zone intervals for testing sequence L4P51-B. The guard zone in L4P51-B was shut in on October 8, 1990 (Calendar Day 281). The first pulse-withdrawal test was initiated on February 13, 1991 (1990 Calendar Day 409) and the second pulse-withdrawal test was initiated on July 22, 1991 (1990 Calendar Day 568). The pulse-injection test was initiated on September 17, 1991 (1990 Calendar Day 625). The pressure response during the first pulse-withdrawal test was anomalous in that the pressure did not appear to be recovering to the pre-pulse-withdrawal value until the constant-pressure flow test in the test zone was terminated. The pressure responses to the next two pulse tests were also anomalous in that unexplained oscillations in the pressure trends were observed. The L4P51-B testing sequence was stopped on November 21, 1991 (1990 Calendar Day 690) when a leak was detected in the test apparatus. Evaluation of the data from the L4P51-B guard zone indicates that the data are not interpretable. The guard zone may not have been completely shut in during the testing sequence. The only conclusion that can be drawn from the L4P51-B guard-zone monitoring is that the formation pore pressure of halite 2 at that location was at least 3.25 MPa.

7.1.3 L4P52-A. Borehole L4P52 was drilled on April 1 and 2, 1991 (Calendar Days 91 and 92) into the upper part of the west rib (wall) of Room

L4 at an angle of 40° below vertical (Figure 5-2) to allow testing of anhydrites "a" and "b" at a location not immediately above an existing excavation. Figure 7-16 shows the configuration of the test tool in L4P52, and indicates the lengths and stratigraphic locations of the test and guard zones. The test zone included the lower 0.06 m of map unit 12 (polyhalitic halite), the combined 0.25-m thickness of anhydrite "a" and clay H, the 0.40-m thickness of map unit 10 (halite), and the upper 0.71 m of map unit 9 (halite). The guard zone included the lower 0.66 m of map unit 9 (halite), the combined 0.04-m thickness of anhydrite "b" and clay G, and the upper 0.35 m of map unit 7 (halite). (All thicknesses listed above are as measured along the inclined borehole.)

Figure 7-17 illustrates the test- and guard-zone pressure responses recorded by the DAS during the monitoring period. The pressure values presented in Figure 7-17 and subsequent figures have been compensated for the elevation differences between the locations of the pressure transducers and the centers of the tested units in the test and guard zones. The test-zone and guard-zone pressures were compensated by subtracting 0.078 and 0.057 MPa, respectively, from the pressures measured by the pressure transducers and reported by Stensrud et al. (1992).

The test and guard zones in L4P52-A were shut in and subsequently depressurized several times before the "final" shut-in occurred on June 26, 1991 (Calendar Day 177; Stensrud et al., 1992). Following a pressure-buildup period, pulse-withdrawal, constant-pressure flow, and pressure-buildup tests were conducted in the test zone. No testing was successfully completed in
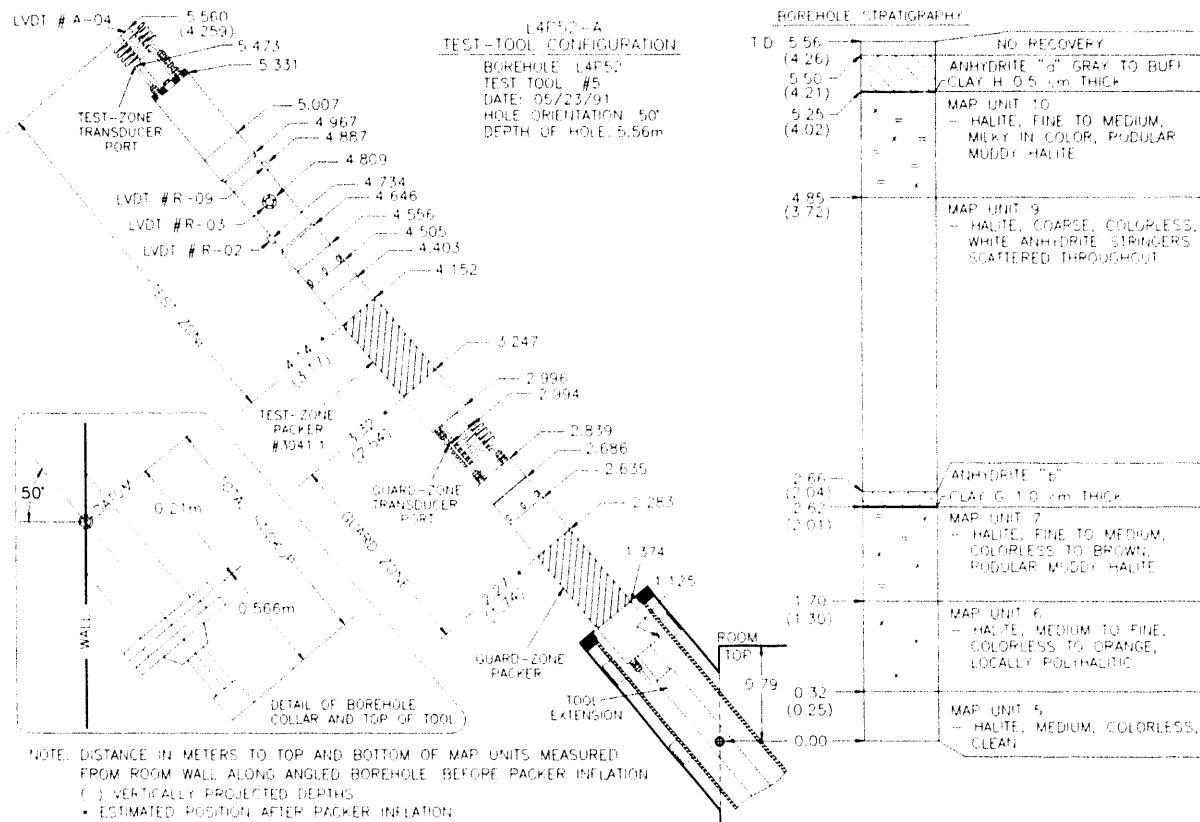
Figure 7-16. Test-tool configuration for permeability-testing sequence L4P52-A.
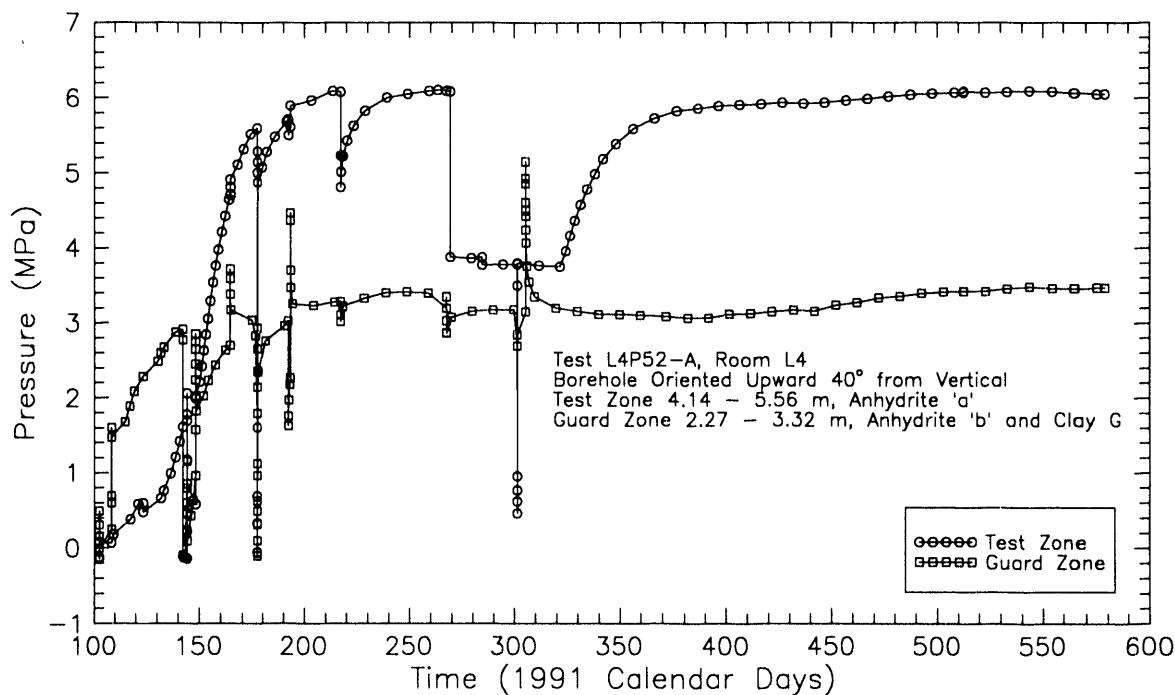
Figure 7-17. Test- and guard-zone pressures during L4P52-A testing.

81

the guard zone because of recurring problems maintaining pressure in the guard-zone packer (Appendix F, Figure F-3). On November 1, 1991 (Calendar Day 305), both the guard-zone and test-zone packer-inflation pressures were increased to 10.6 MPa. On January 15, 1992 (1991 Calendar Day 380), during the pressure-buildup test in the test zone, a gas-buffered fluid reservoir (Section 3.8) was attached to the guard-zone packer to maintain the packer-inflation pressure at a constant value of about 7.5 MPa.

7.1.3.1 Test Zone. The testing sequence in the L4P52-A test zone consisted of an open borehole period lasting from April 2, 1991 (Calendar Day 92) to April 12, 1991 (Calendar Day 102), an initial shut-in period from April 12 to May 22, 1991 (Calendar Days 102 to 142), a 2-day depressurized period, a second shut-in period from May 24 to June 26, 1991 (Calendar Days 104 to 177), a 40-minute depressurized period, a third shut-in period beginning on June 26, 1991 (Calendar Day 177), a pulse-withdrawal test initiated on August 5, 1991 (Calendar Day 217), a constant-pressure withdrawal test lasting from September 26, 1991 (Calendar Day 269) to November 18, 1991 (Calendar Day 322), and a pressure-buildup test lasting until July 31, 1992 (1991 Calendar Day 578). The pressures observed in the L4P52-A test zone during the testing sequence are shown in Figure 7-17. During the pressure-buildup test, the test-zone pressure rose smoothly only until about January 1, 1992 (1991 Calendar Day 366). For the balance of the test, the pressure fluctuated without a clear trend.

The fluid-production data from the constant-pressure withdrawal test are shown in Figure 7-18. A total of about 166 cm^3 of brine was produced during the 53-day test (Table 7-2).

The DPT column was drained four times during the constant-pressure withdrawal test. While draining the column on October 28, 1991 (Calendar Day 301), the pressure in the test zone was inadvertently lowered to about 0.54 MPa. The design constant pressure of 3.87 MPa was restored by injecting brine into the test zone.

The compressibility of the L4P52-A test zone was evaluated both during testing and after testing was complete. Calculations of test-zone compressibility were made using the pressure-change-versus-volume-removed data collected at the initiation of the pulse withdrawal and constant-pressure withdrawal tests and during depressurization of the system at the conclusion of testing. The values of test-zone compressibility calculated from these events ranged from 2.41 x 10^{-9} to 5.98 x 10^{-8} Pa^{-1} and exhibited an inverse relationship with respect to pressure (Table 6-2). A separate procedure was also performed at the end of testing to provide a continuous measure of test-zone compressibility as test-zone pressure increased from 0 to 6 MPa (Figure 6-6). Test-zone compressibilities calculated from these data over given pressure ranges were slightly lower than those calculated using data from the discrete depressurization events.

The L4P52-A tests were analyzed using an idealized test-zone geometry as described in Section 6.2. Flow from anhydrite "a" to the borehole was assumed to be horizontal only, and the test zone was modeled as a vertical cylindrical borehole with a radius of 5.951 cm. The assumption of horizontal flow to the borehole is considered reasonable because video examination of anhydrite "a" in L4P52 showed fluid being produced only from bedding-plane fractures.
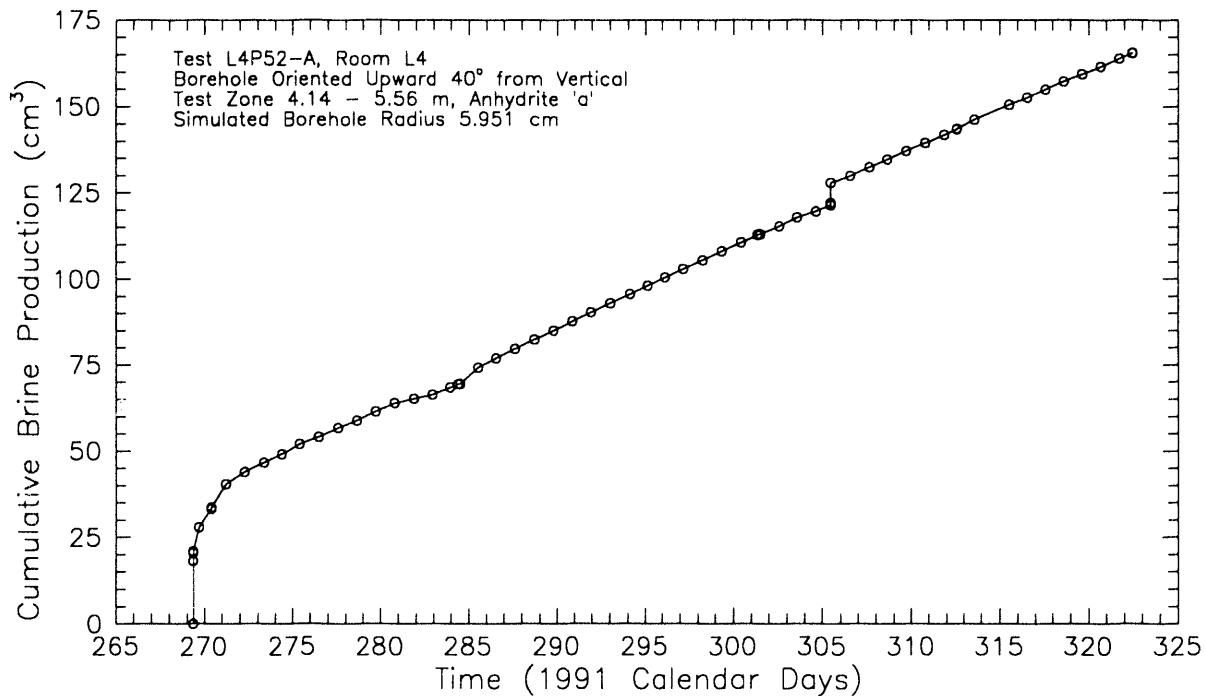
Figure 7-18. Cumulative brine production during L4P52-A constant-pressure withdrawal test.

Analytical Interpretations. Attempts to match the L4P52-A pulse-withdrawal data with type curves were unsuccessful because the pressure recovered more rapidly at early time than predicted by the type curves. Also, the pressure trend became erratic after approximately the first 22 days of the test (after Calendar Day 239), making it impossible to determine what formation pore pressure the recovery was trending toward. No type-curve analysis could be performed of the data from the constant-pressure withdrawal test because of excessive noise in the data. All attempts at calculating flow rates from the accumulated-brine data (Figure 7-18) resulted in erratic data to which no definitive type-curve match could be obtained.

For analysis of the pressure-buildup test using Interpret/2, the constant-pressure withdrawal test was divided into five separate flow periods having constant rates ranging from 280 to 2.4

cm³/day. Because of fluctuations in the test-zone pressure during the final seven months of the pressure-buildup test, a definitive interpretation of the test was difficult to obtain. The transition between the "good" data and the fluctuating data is more evident on a dimensionless Horner plot than on a log-log or linear-linear plot, so the strategy adopted for interpretation was to obtain the best fit possible to the "good" data on the dimensionless Horner plot. The dimensionless Horner plot and the best match obtained are shown in Figure 7-19. The data having dimensionless pressures less than 1.2 were not used during the fitting procedure.

Using the parameters derived from the dimensionless Horner match, the fit obtained between log-log pressure and pressure-derivative type curves and the pressure-buildup data is shown in Figure 7-20. The linear-linear match is shown in Figure 7-21. In all cases, the

83
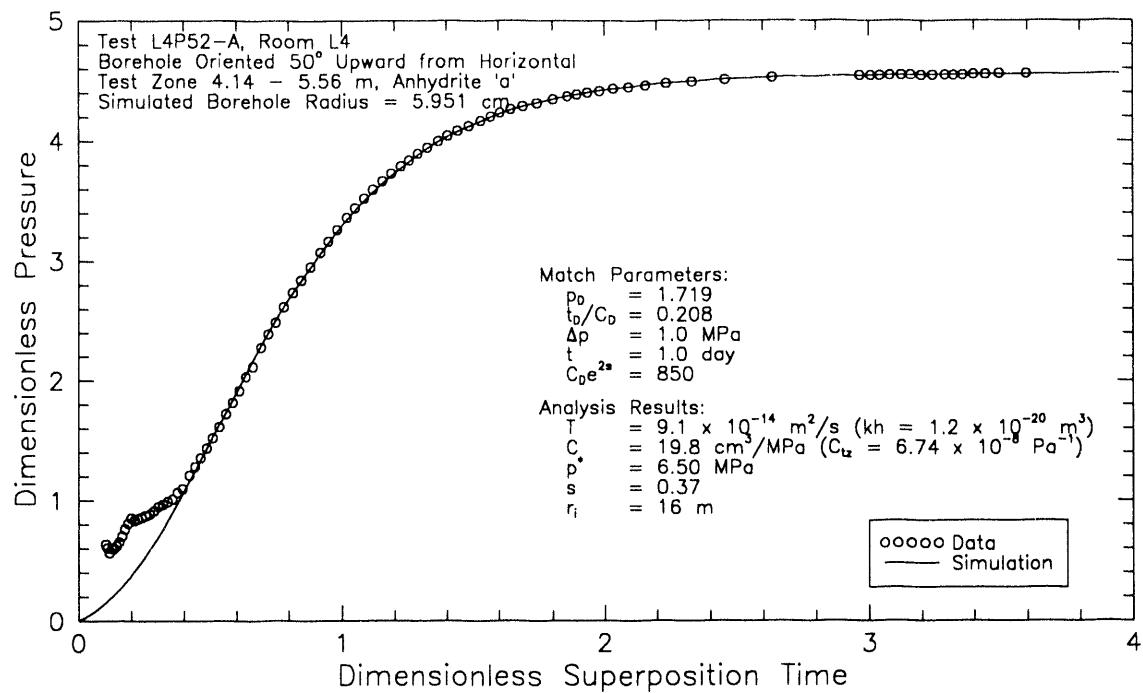
Figure 7-19. Horner plot of Interpret/2 simulation of L4P52-A pressure-buildup test.
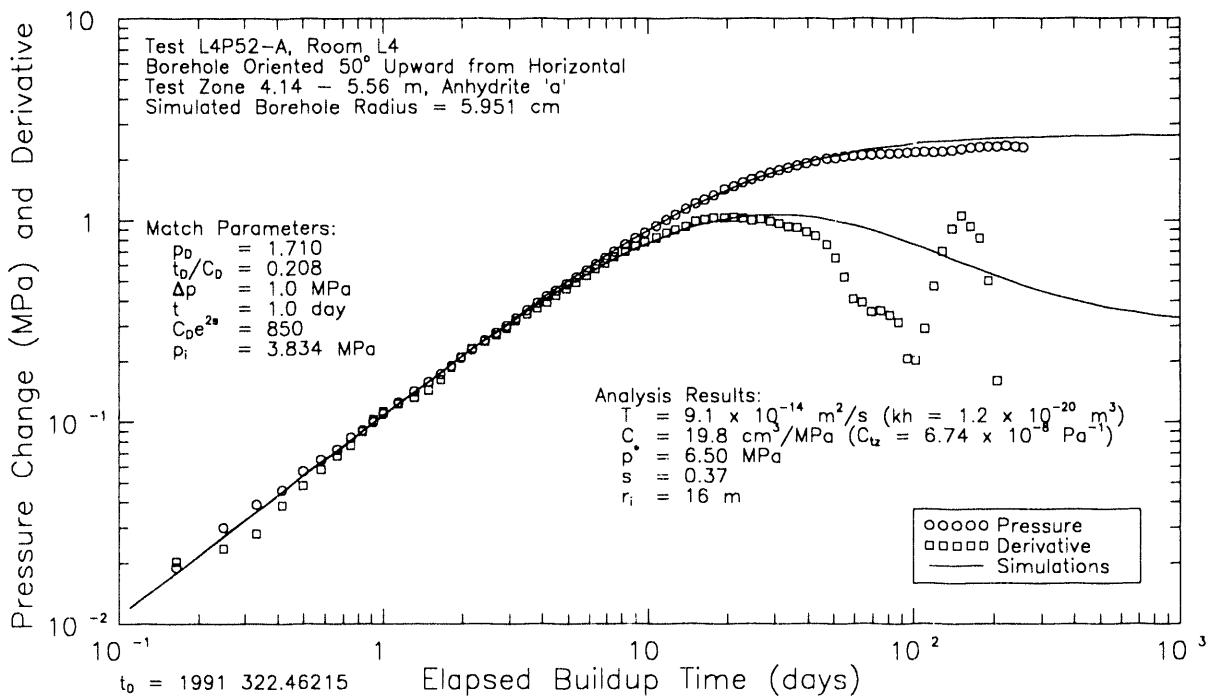
Figure 7-20. Log-log plot of Interpret/2 simulation of L4P52-A pressure-buildup test.
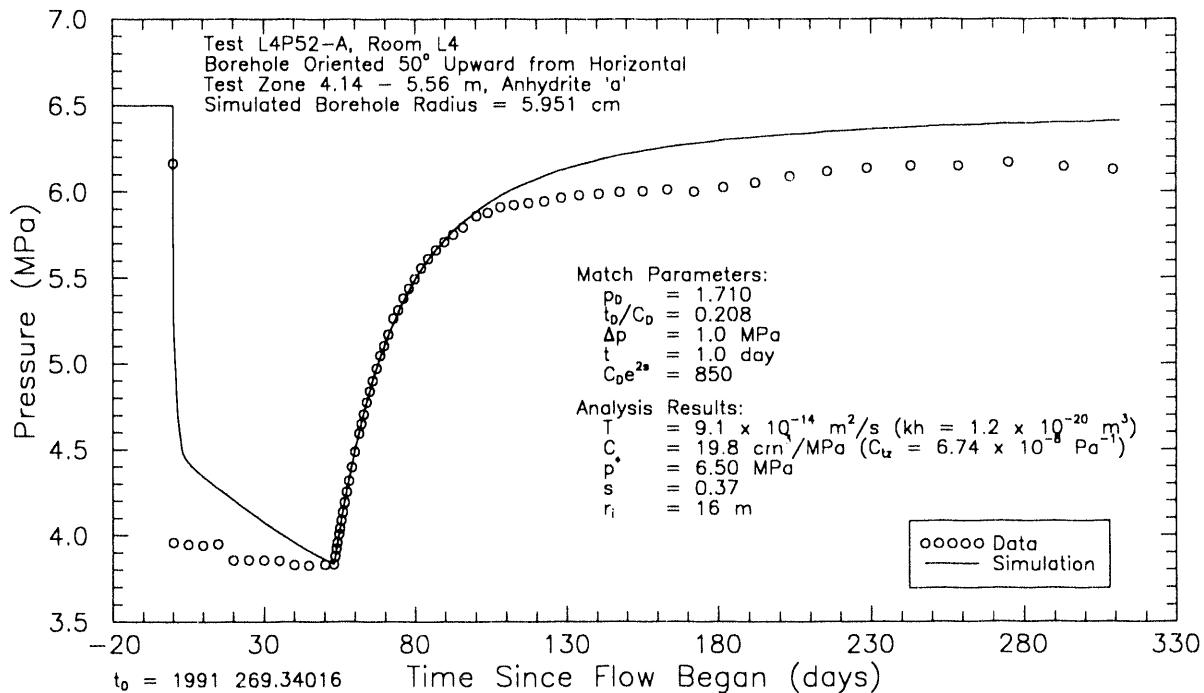
Figure 7-21. Linear-linear plot of Interpret/2 simulation of L4P52-A constant-pressure flow and pressure-buildup tests.

simulations match the observed data well for about the first 40 days of the buildup test. After that time, the simulations predict higher pressures than those observed.

The parameters derived from the dimensionless Horner analysis were a transmissivity of 9.1 x 10^{-14} m^2/s (permeability-thickness product of 1.2 x 10^{-20} m^3), a formation pore pressure of 6.50 MPa, a wellbore-storage coefficient of 19.8 cm^3/MPa (corresponding to a test-zone compressibility of 5.82 x 10^{-9} Pa^{-1}), and a wellbore skin of 0.37 (Table 7-1). As described by Eq. 6-9, a positive wellbore skin of 0.37 implies that the effective wellbore radius is only 69 percent of the actual wellbore radius. This effect is commonly caused by the wellbore being poorly connected to the permeable portion of the formation (Earlougher, 1977). Assuming a total system compressibility of 1.15 x 10^{-9} Pa^{-1}

(derived from a GTFM storativity estimate of 2.6 x 10^{-8}), the radius of influence of the constant-pressure withdrawal and pressure-buildup tests was about 16 m.

Numerical Interpretations. The L4P52-A testing was preceded by a 10-day period during which the borehole was at atmospheric pressure. This open-borehole period was included in the GTFM simulations as a specified-pressure history sequence, as were other periods when the test zone was depressurized or affected by changes in packer pressures. A history sequence was also used to represent the test-zone pressure during the constant-pressure flow test. Temperatures measured in the L4P52-A test zone during the monitoring period are shown in Figure E-2 of Appendix E. Also shown is the smoothed representation of the temperature data used as input to GTFM to compensate

the simulated pressures for the temperature fluctuations. The specified parameters used in the L4P52-A GTFM simulations were a borehole radius of 5.951 cm and a test-zone fluid volume of 3403 cm³.

Initial attempts at simulating the L4P52-A tests using a single value of test-zone compressibility were unsatisfactory. Therefore, test-zone compressibility was varied as a function of pressure during the simulations using a function derived from the values determined during and after testing (Table 6-2). The final test-zone-compressibility-versus-time function used in the simulations is shown in Figure D-1 of Appendix D.

Figure 7-22 shows a semilog plot of the best-fit GTFM simulation of the L4P52-A pulse-withdrawal test. The simulation matches the observed data well until near the end of the test when the simulation appears to be trending towards a higher pressure than the observed data. Figure 7-23 shows the GTFM simulation of the brine production during the constant-pressure withdrawal test. The observed production during the first two days of the test could not be matched by GTFM. The observed initial flow rates were probably caused, in part, by packer expansion into the test zone and borehole closure after the decrease in test-zone pressure. Flow rates during the latter part of the test, when the test tool and borehole had completely
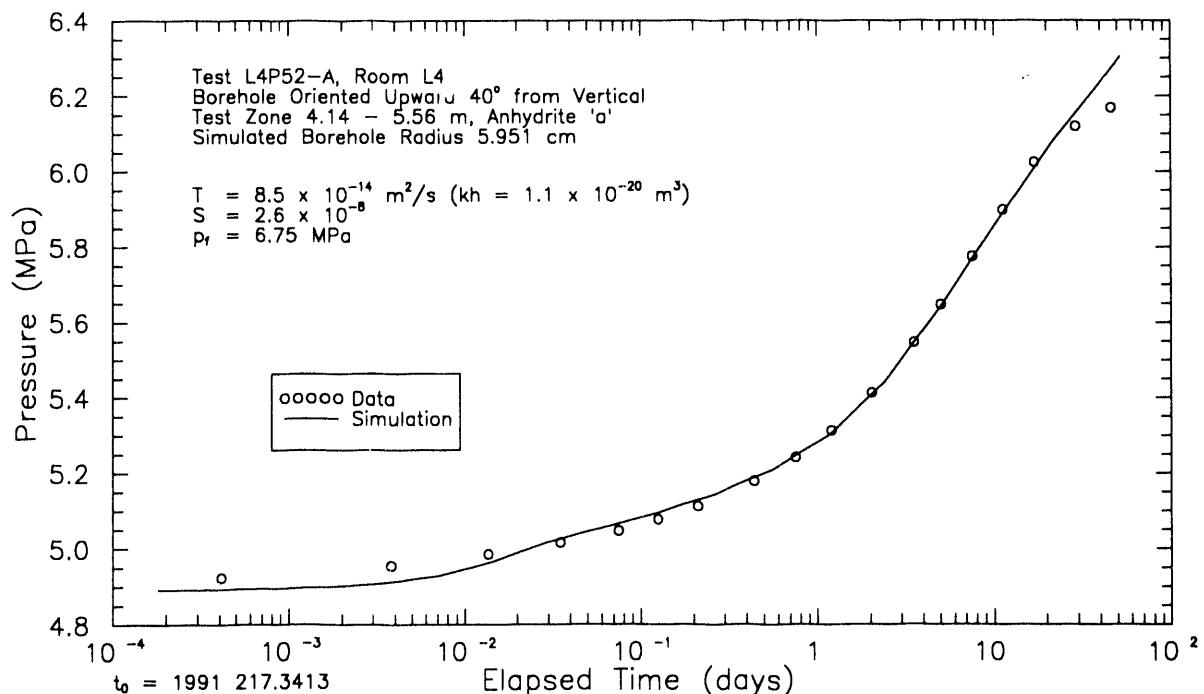
Figure 7-22. Semilog plot of GTFM simulation of L4P52-A pulse-withdrawal test.
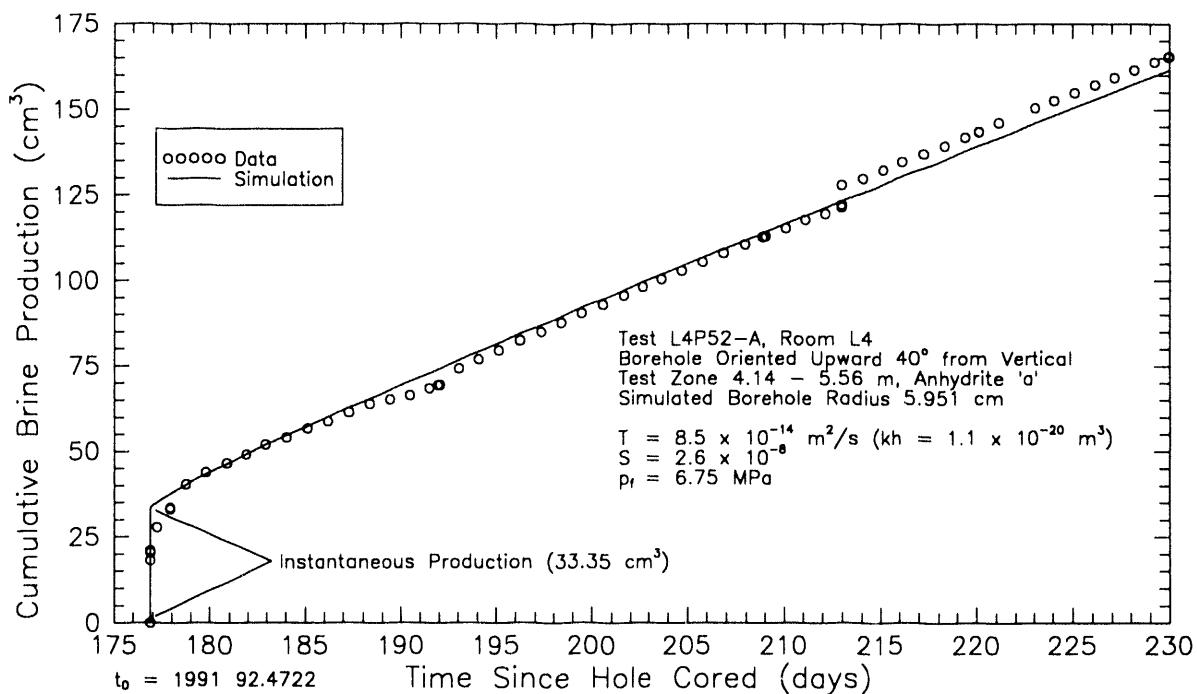
Figure 7-23. Linear-linear plot of GTFM simulation of brine production during L4P52-A constant-pressure withdrawal test.

adjusted to the relatively constant test-zone pressure, were well matched by GTFM. In the simulation shown in Figure 7-23, 33 cm^3 of instantaneous brine production was added at the start of the test to allow better visual comparison of the simulated and observed production during the test.

Figure 7-24 shows a Horner plot of the best-fit GTFM simulation for the L4P52-A pressure-buildup test. A modified production time of 76.523 days was calculated for the Horner plot based on a flow rate of about 2.16 cm^3/day at the end of the constant-pressure withdrawal test and a total of about 165.45 cm^3 of fluid produced during the test. Figure 7-25 shows the GTFM simulation and observed pressures for the entire L4P52-A testing period. The fitted parameters used in the simulations shown in Figures 7-22

through 7-25 were a transmissivity of 8.5 x 10^{-14} m^2/s (permeability-thickness product of 1.1 x 10^{-20} m^3), a storativity of 2.6 x 10^{-8}, and a formation pore pressure of 6.75 MPa. The radius of influence of the entire L4P52-A testing sequence up to the time when the pressure recovery became erratic during the pressure-buildup test was calculated as 15 m using a one-percent pressure-change criterion.

Summary. The analytical and numerical interpretations of the L4P52-A tests provided estimates of transmissivity of 9.1 x 10^{-14} and 8.5 x 10^{-14} m^2/s (permeability-thickness products of 1.2 x 10^{-20} and 1.1 x 10^{-20} m^3), respectively. Interpret/2 and GTFM interpretations provided similar estimates of formation pore pressure, ranging from 6.50 to 6.75 MPa. GTFM provided good simulations of all of the tests using a
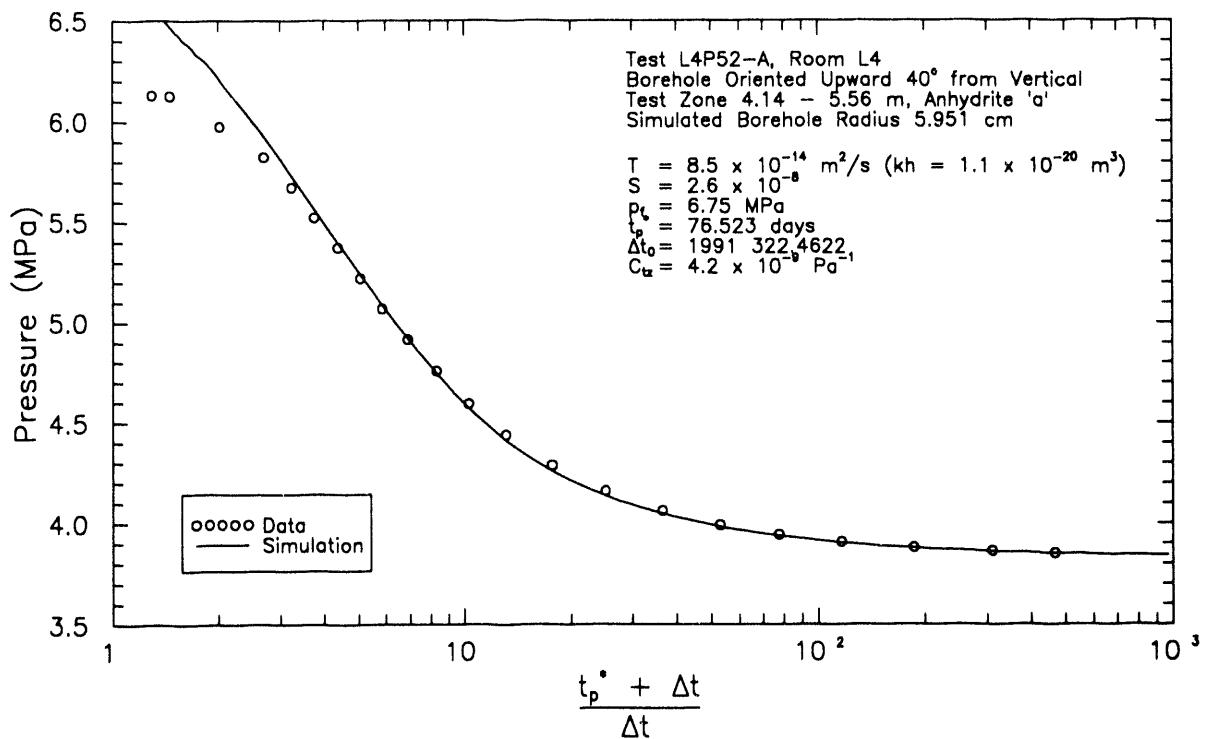
Figure 7-24. Horner plot of GTFM simulation of L4P52-A pressure-buildup test.
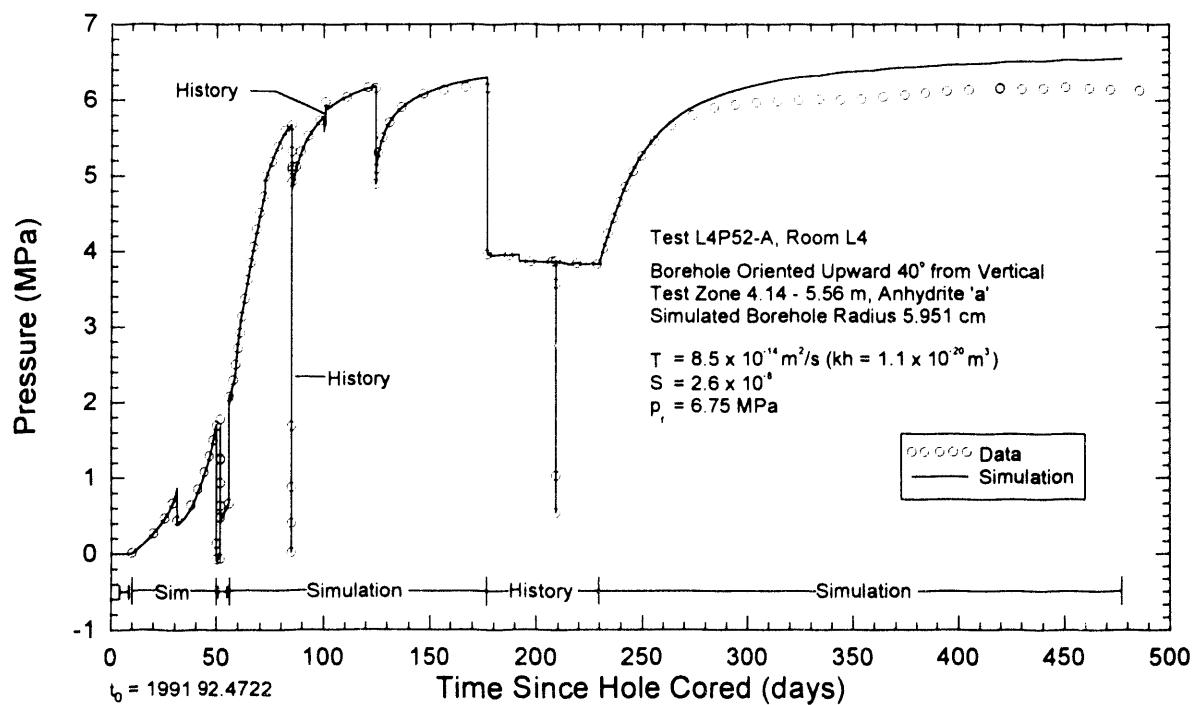
Figure 7-25. Linear-linear plot of GTFM simulation of entire L4P52-A testing sequence.

storativity of 2.6×10^{-8}. Using this value of storativity (expressed as total system compressibility), Interpret/2 calculates a radius of influence for the constant-pressure withdrawal and pressure-buildup tests of about 16 m. The radius of influence of the entire testing sequence excluding the last seven months of the pressure-buildup test was calculated by GTFM as 15 m.

Vertically averaged values of hydraulic conductivity (permeability) and specific storage can be calculated for the L4P52-A test zone by assuming that fluid was produced only by the 0.19-m interval containing anhydrite "a" and clay H. The average hydraulic conductivity of this interval is 4.5×10^{-13} to 4.8×10^{-13} m/s (permeability of 6.0×10^{-20} to 6.4×10^{-20} m^2) and the specific storage is 1.0×10^{-7} m^{-1}.

We are uncertain whether the fluctuating pressures observed during the last seven months of the pressure-buildup test reflect a failure of the test tool to maintain an adequate seal or changing conditions in anhydrite "a" around Room L4.

7.1.3.2 Guard Zone. No testing could be performed in the L4P52-A guard zone due to problems maintaining pressure in the guard-zone packer. However, the monitoring performed in the guard zone (Figure 7-17) provided an indication that the formation pore pressure of anhydrite "b" at L4P52 is at least 3.5 MPa.

7.1.4 S1P71-B. Borehole S1P71 was drilled vertically downward into the floor of Room 7 in Waste Panel 1 (Figure 5-3) to a depth of 4.55 m in November 1988 for testing sequence S1P71-A (Beauheim et al., 1991). S1P71 was deepened to 10.15 m on July 20, 1989 (Calendar Day 201) for testing sequence S1P71-B. Figure 7-26 shows the test-tool configuration for S1P71-B,

and indicates the lengths and stratigraphic locations of the guard and test zones. The test zone consisted of the lower 1.05 m of polyhalitic halite 1 (including a 0.03-m band of orange anhydrite), the 0.05-m-thick anhydrite "c", and the upper 0.35 m of halite 1. The guard zone (1.06 m) was contained entirely within halite 2.

Figure 7-27 is a plot of the test- and guard-zone pressure data collected by the DAS during the monitoring period from July 25, 1989 to May 24, 1990 (1989 Calendar Days 206 to 509). The pressure values presented in Figure 7-27 and subsequent figures have been compensated for the elevation differences between the locations of the pressure transducers and the centers of the tested units in the test and guard zones. The test-zone and guard-zone pressures were compensated by adding 0.131 and 0.102 MPa, respectively, to the pressures measured by the pressure transducers and reported by Stensrud et al. (1992). Two pulse-withdrawal tests were conducted in the S1P71-B test zone. No testing was conducted in the guard zone.

7.1.4.1 Test Zone. The test zone of S1P71-B was shut in initially on July 26, 1989 (Calendar Day 207). The test-zone pressure had increased to 1.59 MPa on August 3, 1989 (Calendar Day 215) when the test-zone pressure began to decrease. After injecting brine into the test zone in an attempt to increase the pressure, the test tool was removed on August 7, 1989 (Calendar Day 219) to inspect for leaks and then reinstalled on August 21, 1989 (Calendar Day 233). The test zone was shut in on August 24, 1989 (Calendar Day 236). The test-zone pressure increased much more slowly than it had during the first shut-in period from July 26 to August 3, 1989 (Calendar Days 207 to 215), reaching only 0.59 MPa by November 30, 1989 (Calendar Day 334). On that date, brine was injected into the

S1P71-B TEST-TOOL CONFIGURATION

BOREHOLE: S1P71
TEST TOOL: #2
DATE: 02/28/90
HOLE DEPTH: 10.15m.

TOOL EXTENSION

GUARD-ZONE
PACKER
3041.4

GUARD-ZONE
TRANSDUCER
PORT

TEST-ZONE
PACKER
3041.7

LVDT # R-05
LVDT # R-11
LVDT # R-12

TEST-ZONE
TRANSDUCER
PORT

LVDT # A-01

GUARD ZONE

TEST ZONE

5.917
6.826

7.382

7.546
7.798

8.710

9.207
9.293
9.373
9.448
9.537

9.890

10.15

6.82 *
7.87 *
8.70 *

BOREHOLE STRATIGRAPHY

0.46	MAP UNIT 0 — HALITE, COARSE, COLORLESS
0.46	POLYHALITIC HALITE 4 — POLYHALITIC HALITE, COARSE, COLORLESS TO ORANGE POLYHALITE INCREASES WITH DEPTH
1.40	MARKER BED 139 — ANHYDRITE, MICROCRYSTALLINE, ORANGE
2.25	HALITE 4 — HALITE, COARSE, COLORLESS, ARGILLACEOUS
3.20	POLYHALITIC HALITE 3 — POLYHALITIC HALITE, COARSE, COLORLESS TO ORANGE
4.53 / 4.55	CLAY D
	HALITE 3 — HALITE, MEDIUM TO COARSE, ARGILLACEOUS
5.10	POLYHALITIC HALITE 2 — POLYHALITIC HALITE, COARSE, COLORLESS TO ORANGE
6.20	HALITE 2 — HALITE, MEDIUM TO FINE, COLORLESS TO BROWN, ARGILLACEOUS, MINOR POLYHALITE
7.97	POLYHALITIC HALITE 1 — POLYHALITIC HALITE, COARSE, ORANGE
	9.48 – 9.51 BAND OF ORANGE ANHYDRITE
9.75 / 9.80	ANHYDRITE "c" — ANHYDRITE, GRAY, LAMINAR
	HALITE 1 — HALITE, FINE TO MEDIUM, COLORLESS ARGILLACEOUS

NOTE: MEASUREMENTS IN METERS FROM FLOOR BEFORE PACKER INFLATION.
  * ESTIMATED POSITION AFTER PACKER INFLATION.

Figure 7-26. Test-tool configuration for permeability-testing sequence S1P71-B.

90
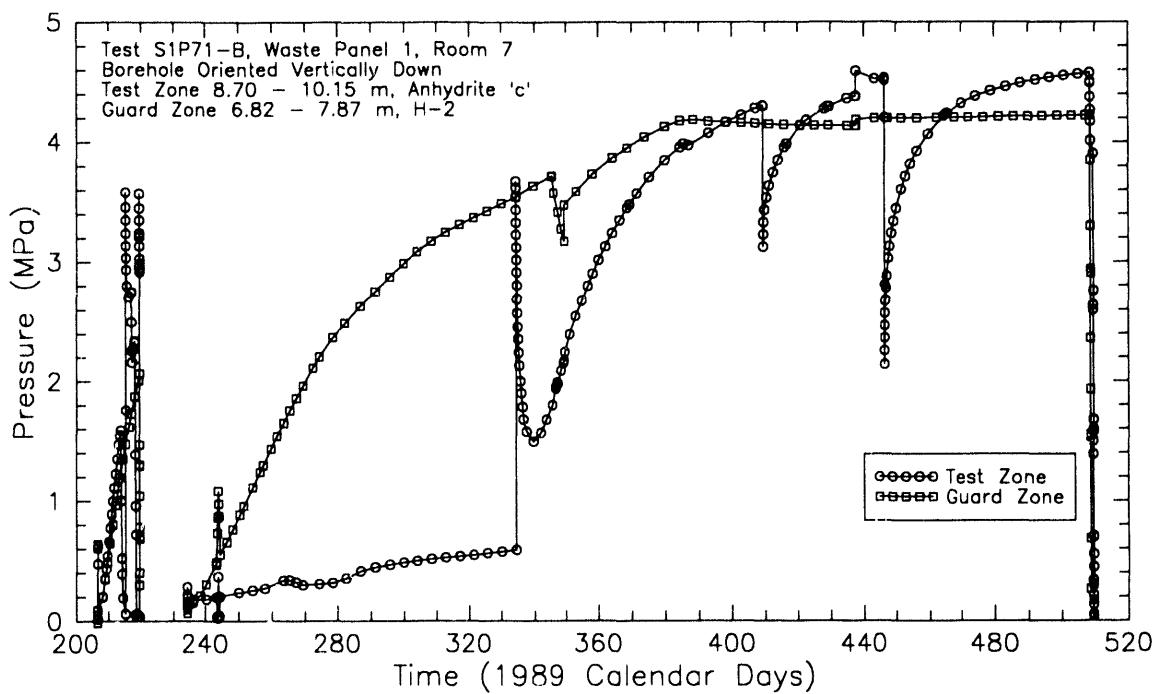
Figure 7-27. Test- and guard-zone pressures during S1P71-B testing.

test-zone and the pressure was increased to 3.67 MPa. The pressure response observed thereafter was similar to that observed during the first shut-in period. The slow rate of pressure buildup from August 24 to November 30, 1989 (Calendar Days 236 to 334) may have been caused by incomplete shut-in of the test zone.

On January 21, 1990 (1989 Calendar Day 386), the pressure in the test zone decreased slightly due to a decrease in the guard-zone packer-inflation pressure (Appendix F, Figure F-4). A pulse-withdrawal test was initiated on February 13, 1990 (1989 Calendar Day 409) by decreasing the test-zone pressure approximately 1.1 MPa. Towards the end of the pulse-withdrawal test on March 13, 1990 (1989 Calendar Day 437), the pressure in the test zone increased when the guard-zone packer-inflation pressure was increased (Figure F-4). The second pulse-

withdrawal test was initiated on March 22, 1990 (1989 Calendar Day 446) by lowering the test-zone pressure by approximately 2.4 MPa.

The fluid removed from the test zone during the two pulse withdrawals was collected in evacuated sample cylinders, preventing measurement of the fluid volumes and subsequent calculations of test-zone compressibility. Two test-zone-compressibility measurements were made at the end of testing before the test tool was removed from the borehole. Values of 1.18×10^{-9} and 1.45×10^{-9} Pa^{-1} were determined for pressure decreases from about 3.90 to 2.60 MPa and 1.68 to 0.34 MPa, respectively (Table 6-2).

Analytical Interpretations. An attempt was made to fit a type curve to the data from the second S1P71-B pulse-withdrawal test. No

good match could be obtained, however, because the observed pressure recovery at early time was more rapid than predicted by the type curves, perhaps indicating the presence of a negative skin around the borehole. Therefore, no analytical interpretations of the S1P71-B hydraulic tests were completed.

Numerical Interpretations. The GTFM simulation of the S1P71-B test-zone testing included specified-pressure sequences from the open-borehole period beginning July 24, 1989 (Calendar Day 205) until December 15, 1989 (Calendar Day 349) when the rate of pressure buildup began to decrease, and from the test-zone pressure increase caused by the guard-zone packer-pressure increase on March 13, 1990 (1989 Calendar Day 437) to the start of the second pulse-withdrawal test. Initial attempts at simulating the observed pressure responses using a constant value for test-zone compressibility were unsatisfactory (see below). Therefore, test-zone compressibility was used as another fitting parameter during the simulations, with its values constrained by the measurements listed in Table 6-2. The final test-zone-compressibility function used in the simulations is presented in Figure D-2 of Appendix D. Temperatures measured in the S1P71-B test zone during the monitoring period are shown in Figure E-3 of Appendix E. Also shown is the smoothed representation of the temperature data used as input to GTFM to compensate the simulated pressures for the temperature fluctuations. The specified parameters for the S1P71-B GTFM simulations were a borehole radius of 5.296 cm and a test-zone fluid volume of 4418 cm^3.

Figures 7-28 and 7-29 show semilog plots of the best-fit GTFM simulations and the observed pressure data for the first and second pulse-withdrawal tests, respectively. The fitted parameters for these simulations were a transmissivity of 4.8 x 10^{-14} m^2/s (permeability-thickness product of 6.4 x 10^{-21} m^3), a storativity of 1.0 x 10^{-8}, and a formation pore pressure of 5.12 MPa. In addition to these formation parameters, matching the early-time responses during the pulse tests required the inclusion of a skin zone around the borehole in the simulations. The fitted parameters for the skin zone were a radial thickness of 15 cm, a transmissivity of 5.8 x 10^{-13} m^2/s (permeability-thickness product of 7.7 x 10^{-20} m^3), and a storativity of 9.6 x 10^{-8}. Figure 7-30 shows the excellent match between the GTFM simulation and the observed data over the entire testing sequence. The radius of influence of the entire S1P71-B testing sequence calculated by GTFM using a one-percent pressure-change criterion was 20 m.

Figures 7-28 and 7-30 show simulations performed with both constant and varying values of test-zone compressibility, with other parameters held the same. The simulations with a constant value of test-zone compressibility do not match the observed data as well as the simulations using varying values of test-zone compressibility.

Summary. No analytical interpretations of the S1P71-B pulse-withdrawal tests could be performed because of anomalous early-time behavior. The numerical interpretations of the tests required inclusion of a skin zone with transmissivity and storativity increased relative to that in the surrounding formation to match the early-time pulse-test data. The numerical interpretations also required that test-zone compressibility vary during the tests. GTFM provided an estimated transmissivity of 4.8 x 10^{-14} m^2/s (permeability-thickness product of 6.4 x 10^{-21} m^3) for the S1P71-B test zone. Assuming
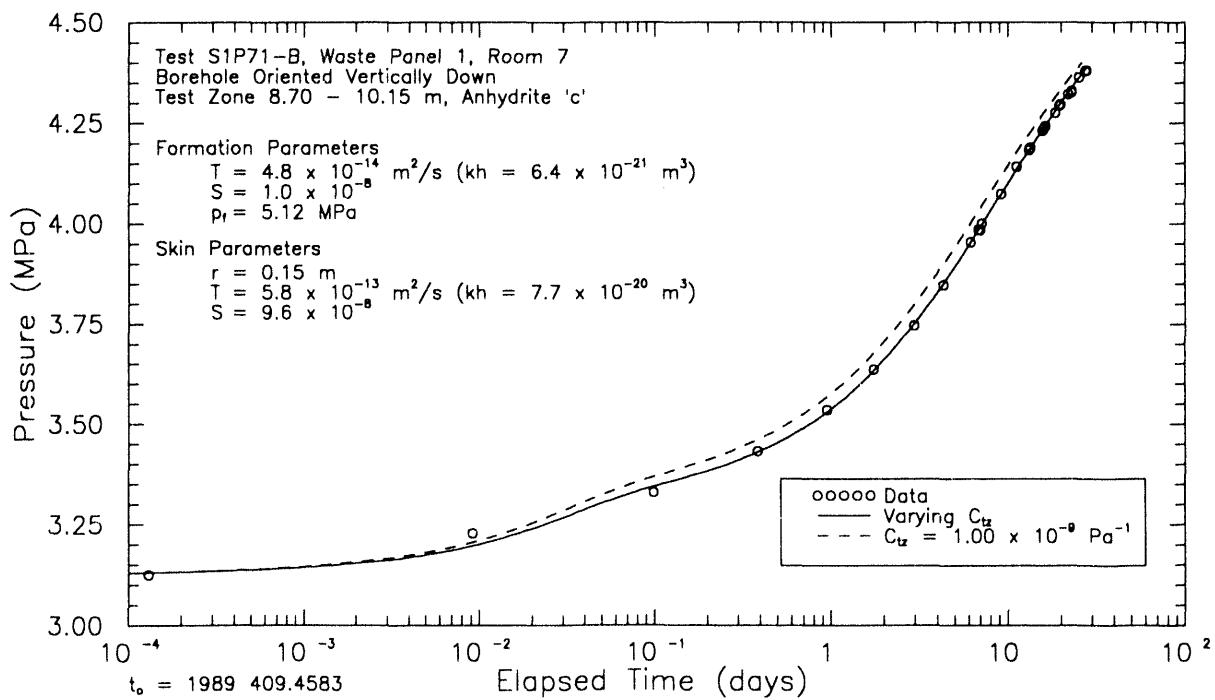
Figure 7-28. Semilog plot of GTFM simulations of S1P71-B pulse-withdrawal test #1.
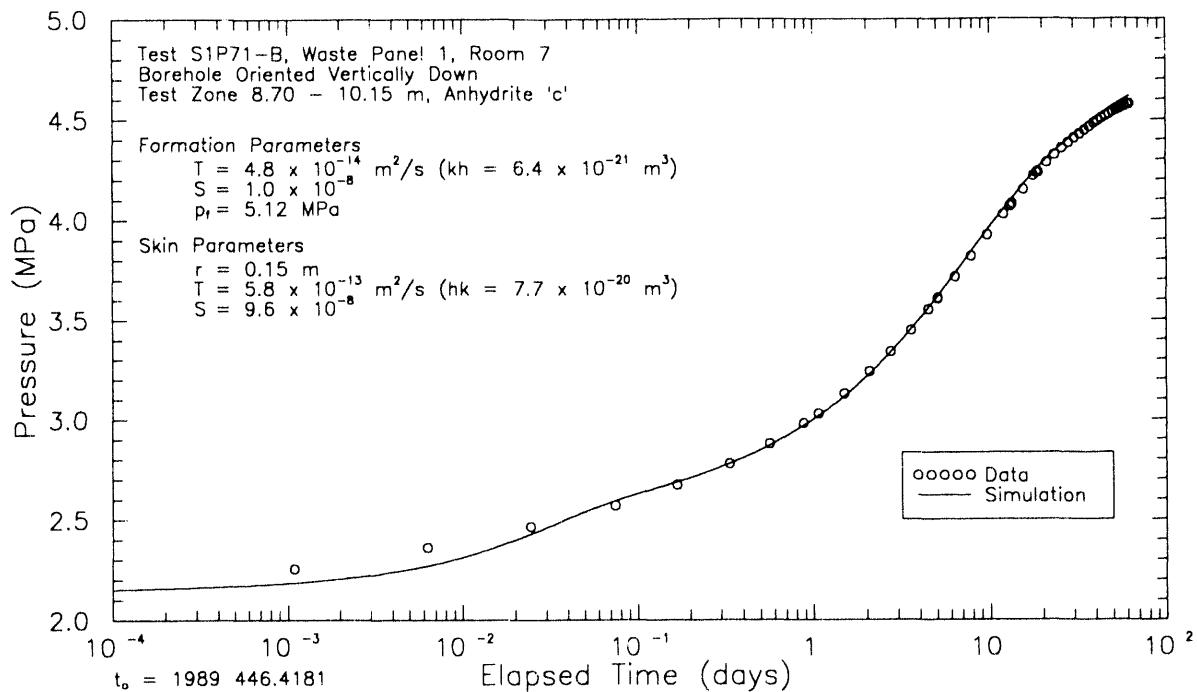
Figure 7-29. Semilog plot of GTFM simulation of S1P71-B pulse-withdrawal test #2.

93
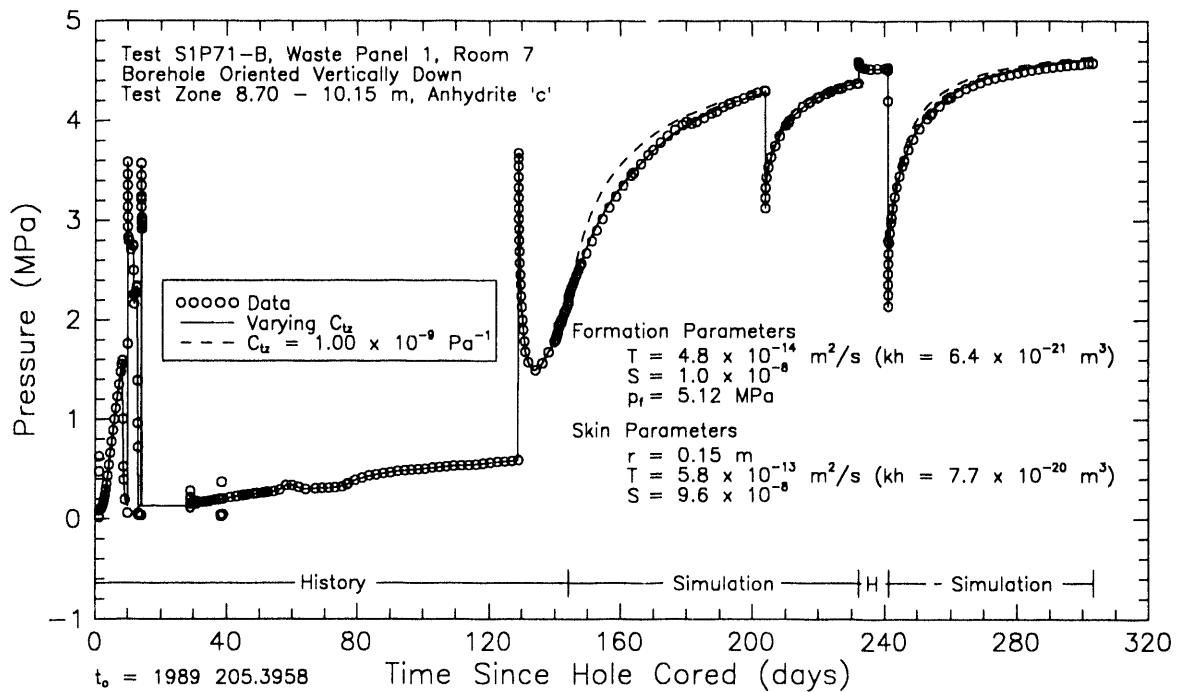
Figure 7-30. Linear-linear plot of GTFM simulations of entire S1P71-B testing sequence.

that fluid was produced only by the 0.08-m thickness of anhydrite "c", the average hydraulic conductivity of the anhydrite is 6.0 x 10⁻¹³ m/s (permeability of 8.0 x 10⁻²⁰ m²). Likewise, the estimated storativity of 1.0 x 10⁻⁸ converts to an average specific storage of 1.25 x 10⁻⁷ m⁻¹. The formation pore pressure of anhydrite "c" was estimated as 5.12 MPa, and the radius of influence of the testing was about 20 m.

7.1.4.2 Guard Zone. The S1P71-B guard zone was initially shut in from July 26, 1989 (Calendar Day 207) to August 7, 1989 (Calendar Day 219), when the test tool was removed from the borehole to repair a leak from the test zone. The guard-zone pressure increased from 0 to 2.07 MPa during this period (Figure 7-27). The test tool was reinstalled on August 21, 1989 (Calendar Day 233), and the guard zone was shut in on August 24, 1989 (Calendar Day

236) to begin the second buildup period. The guard-zone pressure built up to about 3.72 MPa as of December 11, 1989 (Calendar Day 345), when it began to decrease due to a decrease in the guard-zone packer-inflation pressure (Appendix F, Figure F-4). The inflation pressure in the guard-zone packer was increased on December 15, 1989 (Calendar Day 349), causing an immediate increase in the guard-zone pressure. The guard-zone pressure then resumed its earlier buildup behavior until January 21, 1990 (1989 Calendar Day 386), when the guard-zone packer-inflation pressure again began to decrease. From that time on, no sustained buildup in the guard-zone pressure was observed, even after the guard-zone packer-inflation pressure was increased on March 13, 1990 (1989 Calendar Day 437). The pressure in the guard zone ranged between 4.13 and 4.22 MPa for the remainder of the S1P71-B testing

sequence, as if some part of the test tool was acting as a pressure-relief valve to prevent the guard-zone pressure from exceeding about 4.2 MPa. Permeability testing was not performed in the guard zone because of this anomalous pressure behavior.

7.1.5 S1P72-A Borehole S1P72 was drilled downward at an angle of 58° from vertical to test Marker Bed 139 beneath the east rib of Room 7 of Waste Panel 1 (Figure 5-3). Figure 7-31 shows the test-tool configuration for the S1P72-A testing, and indicates the lengths and stratigraphic locations of the guard and test zones. S1P72 was drilled on December 12 and 13, 1989 (Calendar Days 346 and 347), and the test tool was installed on December 20, 1989 (Calendar Day 354). The test zone extended from 4.01 to 6.05 m and included the

1.60-m-thick Marker Bed 139, 0.39 m of overlying polyhalitic halite 4, 0.01 m of clay E, and 0.04 m of underlying halite 4. The guard zone extended from 2.15 to 3.18 m and included the lower 0.35 m of map unit 0 (halite) and 0.68 m of polyhalitic halite 4 overlying Marker Bed 139.

Figure 7-32 is a plot of the test- and guard-zone pressure data collected by the DAS during the monitoring period from December 20, 1989 to January 30, 1991 (1989 Calendar Days 354 to 760). The pressure values presented in Figure 7-32 and subsequent figures have been compensated for the elevation differences between the locations of the pressure transducers and the centers of the tested units in the test and guard zones. The test-zone and guard-zone pressures were compensated by
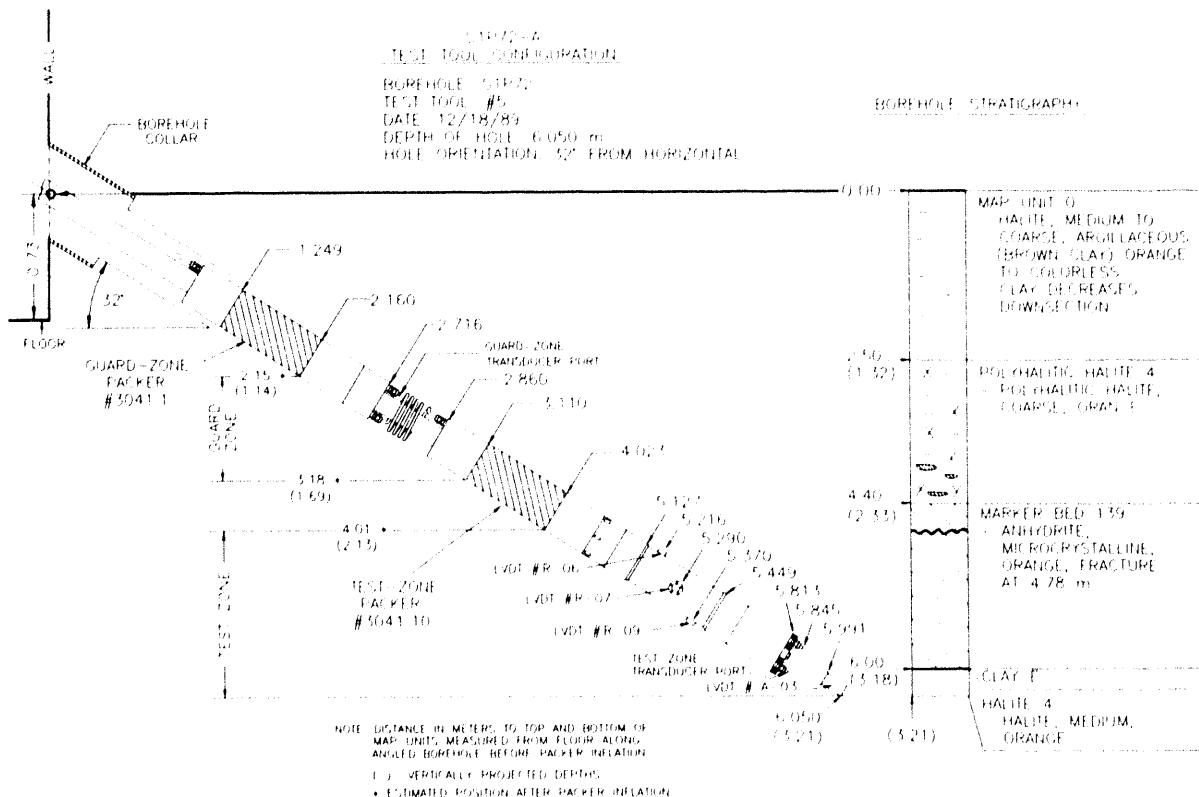
Figure 7-31. Test-tool configuration for permeability-testing sequence S1P72-A.

95
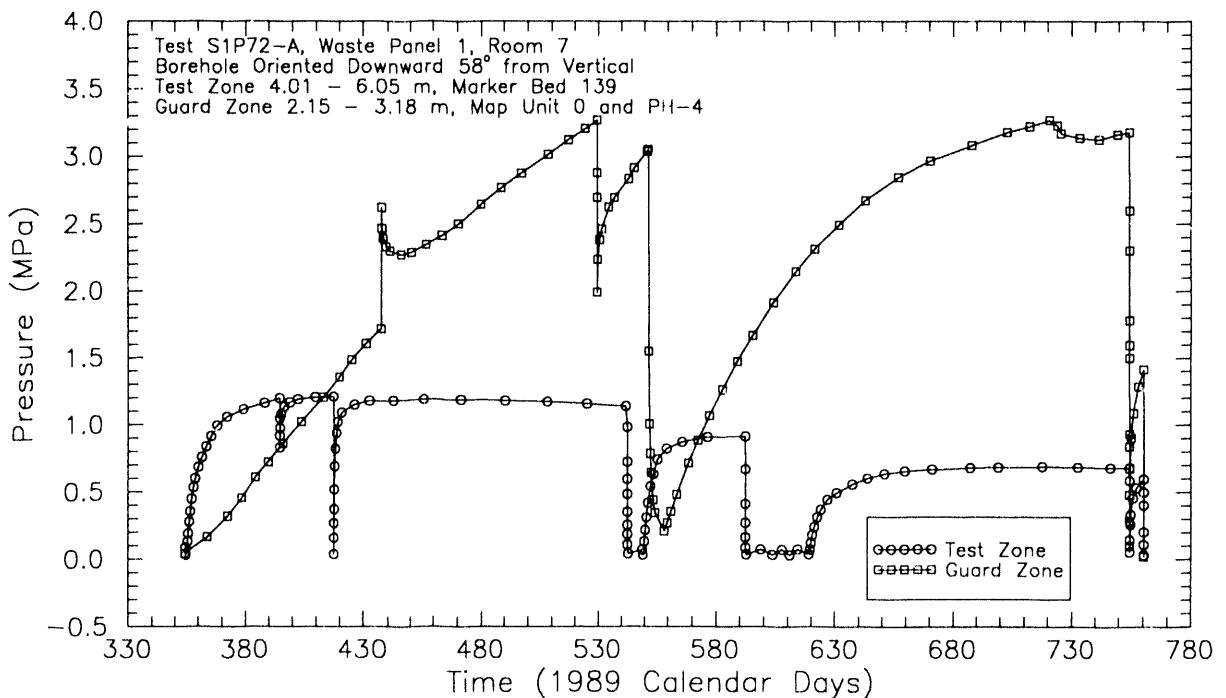
Figure 7-32. Test- and guard-zone pressures during S1P72-A testing.

adding 0.039 and 0.023 MPa, respectively, to the pressures measured by the pressure transducers and reported by Stensrud et al. (1992). The testing sequence in the test zone consisted of approximately seven days of open-borehole conditions, an initial pressure-buildup period, two pulse-withdrawal tests, and two constant-pressure withdrawal tests with subsequent pressure-buildup tests. The testing sequence in the guard zone consisted of an open-borehole period, an initial pressure-buildup period, an increase in the guard-zone pressure due to an increase in the guard-zone packer-inflation pressure, a pulse-withdrawal test, a decrease in the guard-zone pressure caused by a leaky fitting, and the subsequent pressure buildup after the leak was stopped. Interpretations of the tests performed in both the test and guard zones are discussed below.

The slanted S1P72 borehole was treated as an equivalent vertical borehole for test interpretation, following the procedure described in Section 6.2. The test interpretations assumed an equivalent cylindrical borehole radius of 7.60 cm for both the test and guard zones.

7.1.5.1 Test Zone. The S1P72-A test zone was shut in on December 21, 1989 (1989 Calendar Day 355). The first pulse-withdrawal test was initiated on January 29, 1990 (1989 Calendar Day 394) and the second pulse-withdrawal test was initiated on February 21, 1990 (1989 Calendar Day 417). After the pulse withdrawals indicated the presence of abundant gas in the test zone, a measurement device was attached to the test-zone vent line to monitor both gas and brine production (Figure 3-5) during constant-pressure withdrawal tests. Manual readings of manometers were required to obtain the data

96

needed to calculate brine production volumes (Stensrud et al., 1992). The first constant-pressure withdrawal test started on June 26, 1990 (1989 Calendar Day 542) and involved lowering the test-zone pressure from 1.15 MPa to approximately 0.08 MPa and maintaining that pressure for 7.0 days. The test zone was then shut in and the post-test pressure buildup was monitored. Figure 7-33 presents the cumulative brine production and Figure 7-34 presents the cumulative gas production during the first constant-pressure withdrawal test. Approximately 10,350 cm^3 of brine and 124,400 cm^3 of gas (at atmospheric pressure) were produced during the first test.

The second S1P72-A constant-pressure withdrawal test began on August 15, 1990 (1989 Calendar Day 592) and consisted of lowering the

test-zone pressure from 0.91 MPa to approximately 0.07 MPa and maintaining that pressure for 26.9 days. The test zone was then shut in and the pressure buildup was monitored. Figures 7-35 and 7-36 present the cumulative brine and gas volumes, respectively, produced during the constant-pressure withdrawal test. Approximately 22,000 cm^3 of brine and 343,000 cm^3 of gas (at atmospheric pressure) were produced during the second test.

Test-zone compressibility values were determined for each of the test-zone pulse withdrawals, during the second constant-pressure withdrawal test, and during the test-zone depressurization at the end of the testing period (Table 6-2). The test-zone compressibilities at these times ranged from 5.25 x 10^{-7} to 8.04 x 10^{-7} Pa^{-1}, over three orders of magnitude higher
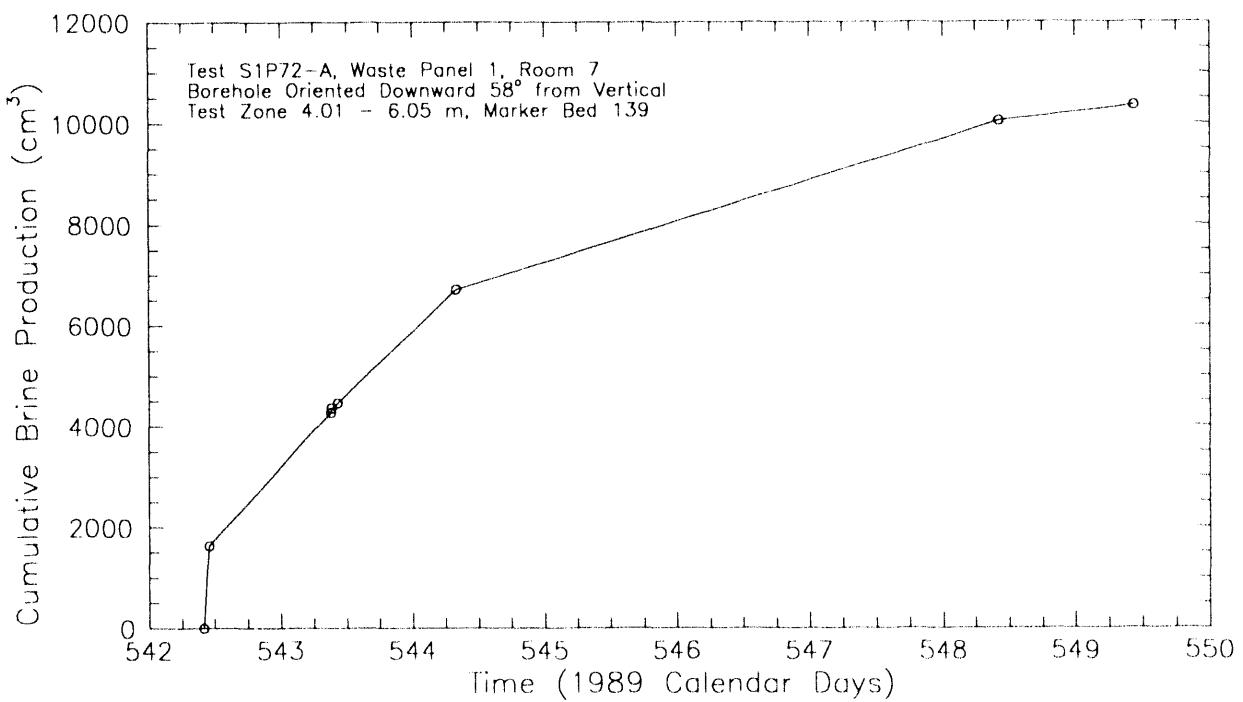
Figure 7-33. Cumulative brine production during S1P72-A test-zone constant-pressure withdrawal test #1.

97
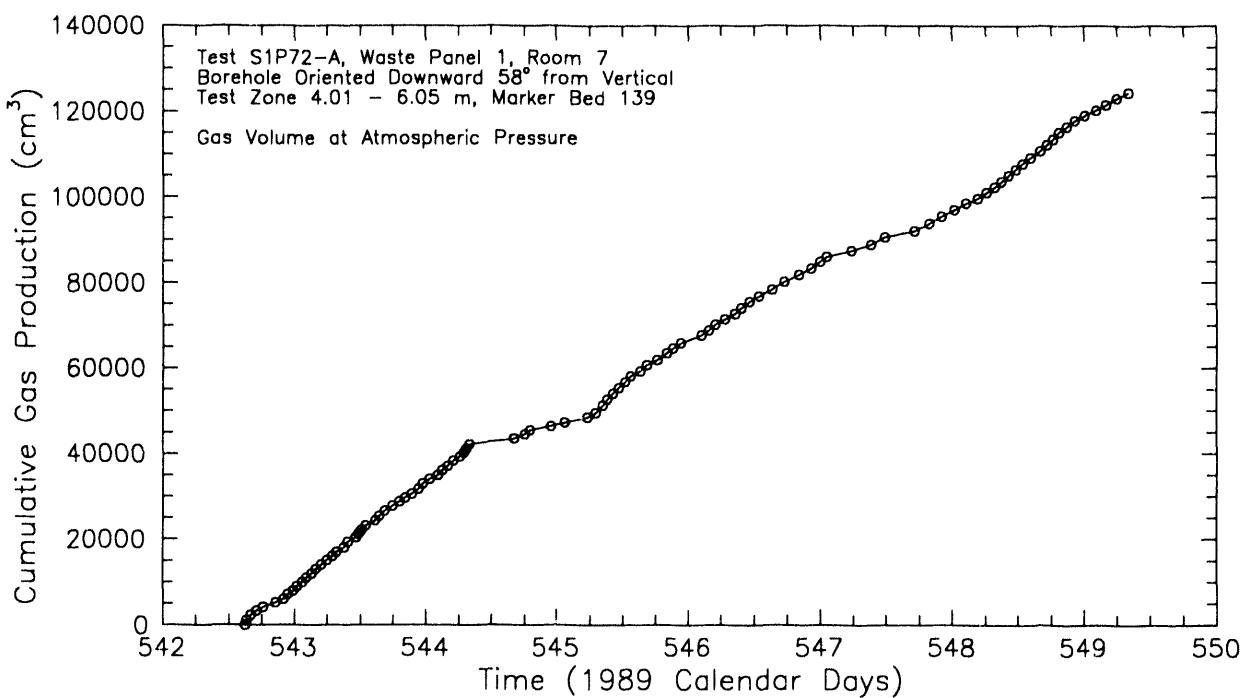
Figure 7-34. Cumulative gas production during S1P72-A test-zone constant-pressure withdrawal test #1.
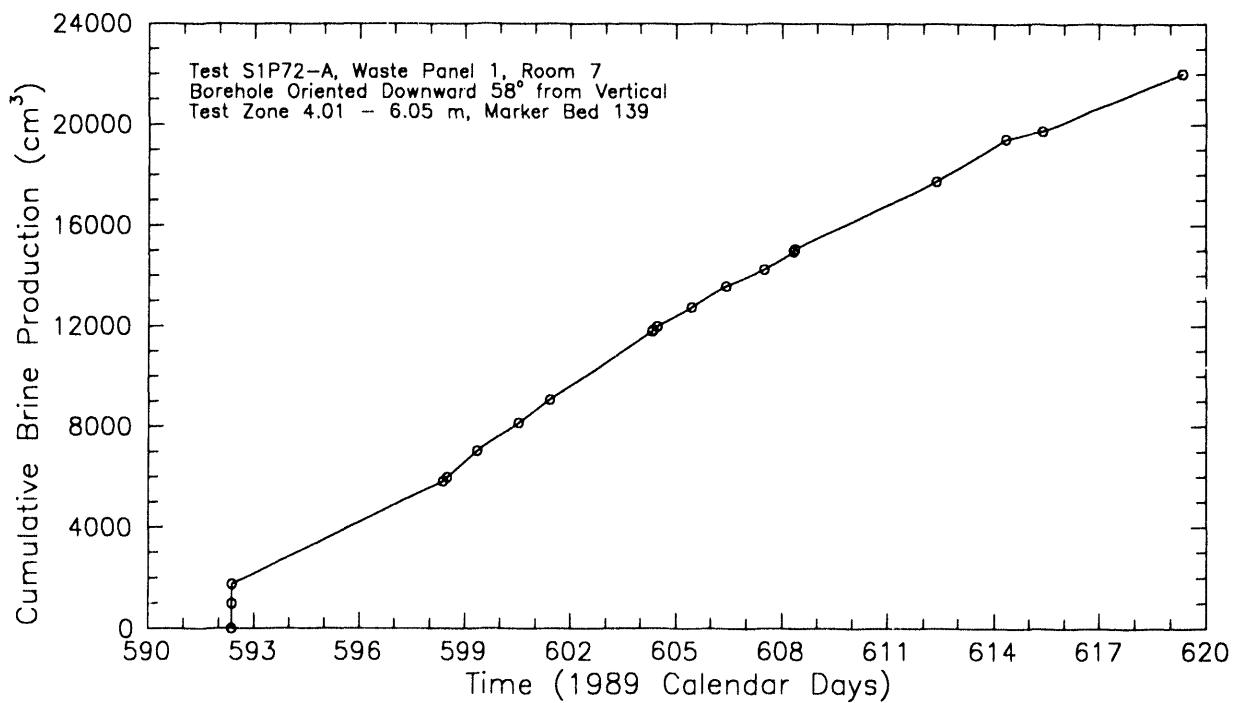
Figure 7-35. Cumulative brine production during S1P72-A test-zone constant-pressure withdrawal test #2.
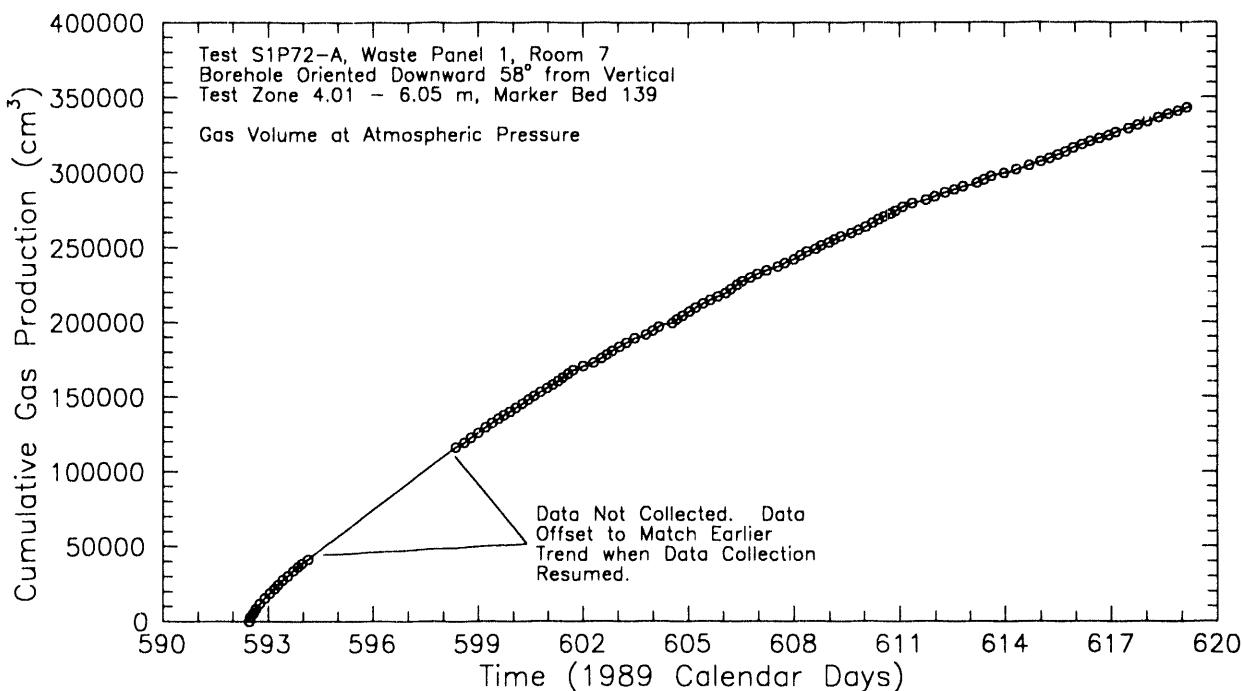
Figure 7-36. Cumulative gas production during S1P72-A test-zone constant-pressure withdrawal test #2.

than the estimated compressibility of brine alone (Section 6.3.1). These high values of test-zone compressibility are attributed to the presence of free gas in the test zone, which was observed during the second pulse withdrawal, during both constant-pressure withdrawal tests, and during depressurization of the test zone at the end of testing.

Figure 7-32 shows that the test-zone pressure recovered to successively lower values following each episode of fluid removal and actually declined after reaching peaks during the second pulse-withdrawal and pressure-buildup tests. S1P71-A testing showed that Marker Bed 139 was at atmospheric pressure beneath the floor in Room 7 (Beauheim et al., 1991). Therefore, a pressure difference of approximately 1.24 MPa existed in Marker Bed 139 between the S1P72

location under the east rib of Room 7 and the S1P71 location under the floor of the room at the initiation of the S1P72-A testing, resulting in flow toward the room from the east. As S1P72-A testing progressed, continued flow toward the room could have decreased the formation pore pressure in Marker Bed 139 underneath the east rib of the room. This type of depressurization would be expected to continue indefinitely and, in fact, pressure-monitoring data reported by Stensrud et al. (1992) show that the pressure in Marker Bed 139 at S1P72 was continuing to decrease a year and a half after the S1P72-A testing was completed.

Analytical Interpretations. No analytical interpretations of the S1P72-A tests were attempted because of the complications presented by the gas evident during the tests.

99

Numerical Interpretations. Because of the two-phase flow conditions apparent during the S1P72-A tests, a two-phase flow model was required to attempt to interpret the tests. The finite-difference model TOUGH2 (Preuss, 1991) was selected for this purpose. Input parameters for TOUGH2 include intrinsic permeabilities, relative-permeability curves, capillary-pressure curves, initial saturations, specific storage, and the initial pressure distribution. Because measured values of few of these parameters were available, scoping simulations were performed to try to define ranges of values of parameters that could produce flow and pressure behavior similar to that observed. These scoping simulations are presented in Appendix G.

The scenario envisioned in the scoping simulations assumed that excavation of Room 7 caused the permeability to increase and the pressure to decrease in Marker Bed 139 directly below the room. The pressure gradient created thereby caused flow toward the room from the far field. Marker Bed 139 was assumed to be completely saturated with brine, containing gas in solution, prior to the excavation. As the pore pressure decreased along the direction of flow, gas came out of solution. The simulations attempted to match, first, the pressure observed in Marker Bed 139 at boreholes S1P71 and S1P72 at the time testing began and, second, the pressure and gas- and brine-flow behavior observed in S1P72 during testing. The first of these objectives was met, but the second was not. The overall pressure behavior during the entire S1P72-A testing sequence could not be matched using any of the combinations of parameters attempted. Calculated brine-production volumes were only about 25 to 35 percent of the observed volumes, and no gas production at all was calculated because gas

never reached the assumed critical saturation in the model.

The simulations presented in Appendix G serve mainly to demonstrate the need for additional information to interpret the S1P72-A tests. The values of one or two unknown parameters could be interpreted from the tests if all the other parameters were known. But inasmuch as initial and/or time-dependent distributions of intrinsic permeability, specific storage, pore pressure, and relative saturations are all unknown, as well as relative-permeability and capillary-pressure curves, no reliable interpretations of the tests are possible.

Summary. The tests performed in the S1P72-A test zone cannot be interpreted because of inadequate constraints on, or knowledge of, the testing conditions. A gradual decline in the formation pore pressure in Marker Bed 139 at S1P72 was observed during the testing sequence, which may be caused by continuing flow from the far field toward Room 7.

7.1.5.2 Guard Zone. The guard zone in S1P72-A was shut in on December 21, 1989 (Calendar Day 355). An almost linear increase in the guard-zone pressure followed the shut-in (Figure 7-32). On February 13, 1990 (1989 Calendar Day 437), the guard-zone packer-inflation pressure was increased (Appendix F, Figure F-5) resulting in a 1.0-MPa increase in the guard-zone pressure. After an initial decrease, the guard-zone pressure resumed a nearly linear increase, but at a lower rate than before the increase in packer-inflation pressure. On June 13, 1990 (1989 Calendar Day 529), a pulse-withdrawal test was initiated in the guard zone. A compressibility of 1.24×10^{-8} Pa^{-1} was determined for a decrease in guard-zone

pressure from 3.27 to 1.99 MPa (Table 6-2). On June 26, 1990 (1989 Calendar Day 542), the guard-zone pressure decreased slightly in response to the initiation of the first constant-pressure withdrawal test in the test zone. On July 5, 1990 (1989 Calendar Day 551), a leak occurred in a valve connected to the guard-zone vent tubing, causing the guard zone to lose most of its pressure. The leak was corrected seven days later on July 12, 1990 (1989 Calendar Day 558), after which the guard-zone pressure began to increase. Immediate correction of the leak was not possible because Room 7 was inaccessible from July 5 to July 11, 1990 (1989 Calendar Days 551 to 557). On August 15, 1990 (1989 Calendar Day 592), the guard-zone pressure decreased slightly in response to the start of the second constant-pressure withdrawal test in the test zone. On December 23, 1990 (1989 Calendar Day 722) the guard-zone pressure decreased due to a decrease in the guard-zone packer-inflation pressure (Appendix F, Figure F-5).

On January 24, 1991 (1989 Calendar Day 754), the guard-zone pressure was decreased incrementally to make guard-zone-compressibility determinations. A three-step pressure drawdown was performed with pressure decreases to 2.243, 1.475, and 0.667 MPa, yielding guard-zone compressibilities of 2.13×10^{-9}, 2.31×10^{-9}, and 2.21×10^{-9} Pa^{-1}, respectively (Table 6-2). The guard zone was then shut in. On January 30, 1991 (1989 Calendar Day 760), the guard zone was depressurized and a guard-zone compressibility of 2.78×10^{-9} Pa^{-1} was determined for a pressure decrease from 1.39 to 0.04 MPa.

Analytical Interpretations. No analytical interpretations were attempted of the S1P72-A guard-zone tests. The pulse-withdrawal test was terminated prematurely by a leak in the vent line, and no flow-rate information is available for the period of the leak with which to perform a quantitative interpretation of the subsequent pressure buildup.

Numerical Interpretations. The factors mentioned above that prevented analytical interpretations of the S1P72-A guard-zone tests presented no obstacles to interpretation using GTFM. Three history sequences were used in simulating the pressure responses observed in the S1P72-A guard zone during testing. The periods with prescribed pressure histories were the 9-day period between the time the guard zone was cored and when it was shut in, a 15-day period during which the guard-zone pressure was responding to an increase in the guard-zone packer pressure, and the nearly 7-day period during which the guard-zone vent line was leaking. Initial attempts at simulating the observed pressure responses using a constant value for guard-zone compressibility were unsuccessful. Therefore, guard-zone compressibility was used as another fitting parameter during the simulations, with its values constrained by the measurements listed in Table 6-2. Temperatures measured in the S1P72-A guard zone during the monitoring period are shown in Figure E-4 of Appendix E. Also shown is the smoothed representation of the temperature data used as input to GTFM to compensate the simulated pressures for the temperature fluctuations. The specified parameters used in the simulations were a borehole radius of 7.60 cm and a guard-zone fluid volume of 2522 cm^3.

Figure 7-37 shows a semilog plot of the best-fit simulation and the observed pressure for the pulse-withdrawal test, and Figure 7-38 shows a
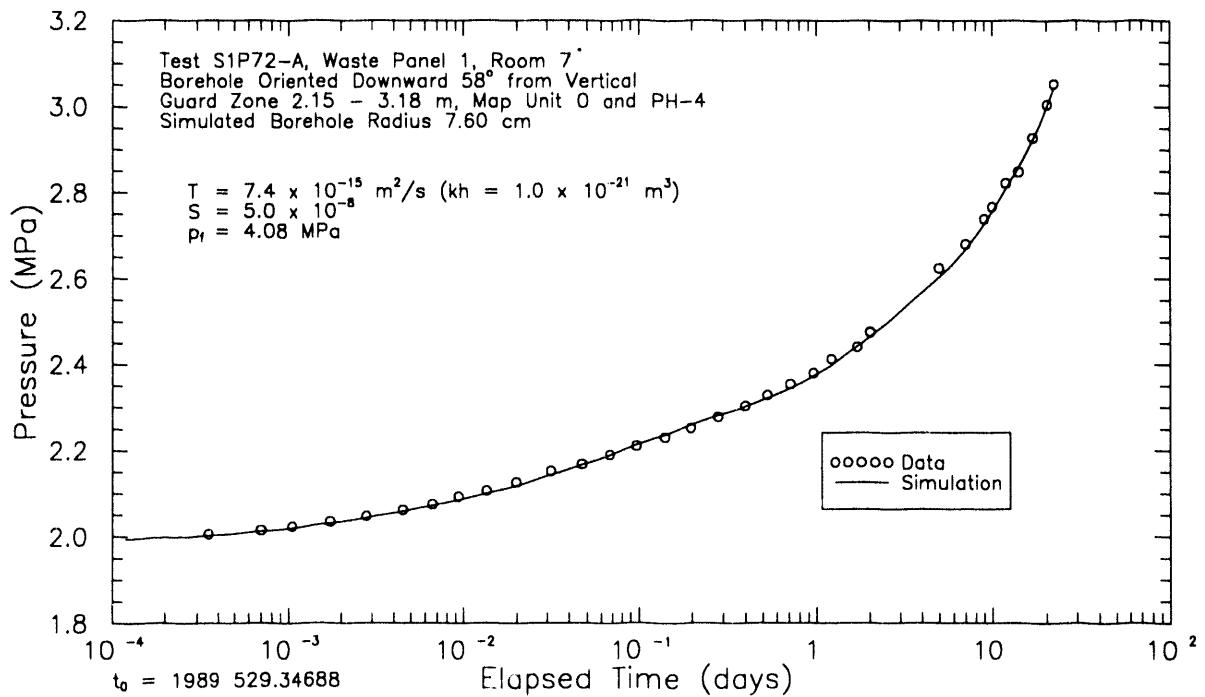
Figure 7-37. Semilog plot of GTFM simulation of S1P72-A guard-zone pulse-withdrawal test.
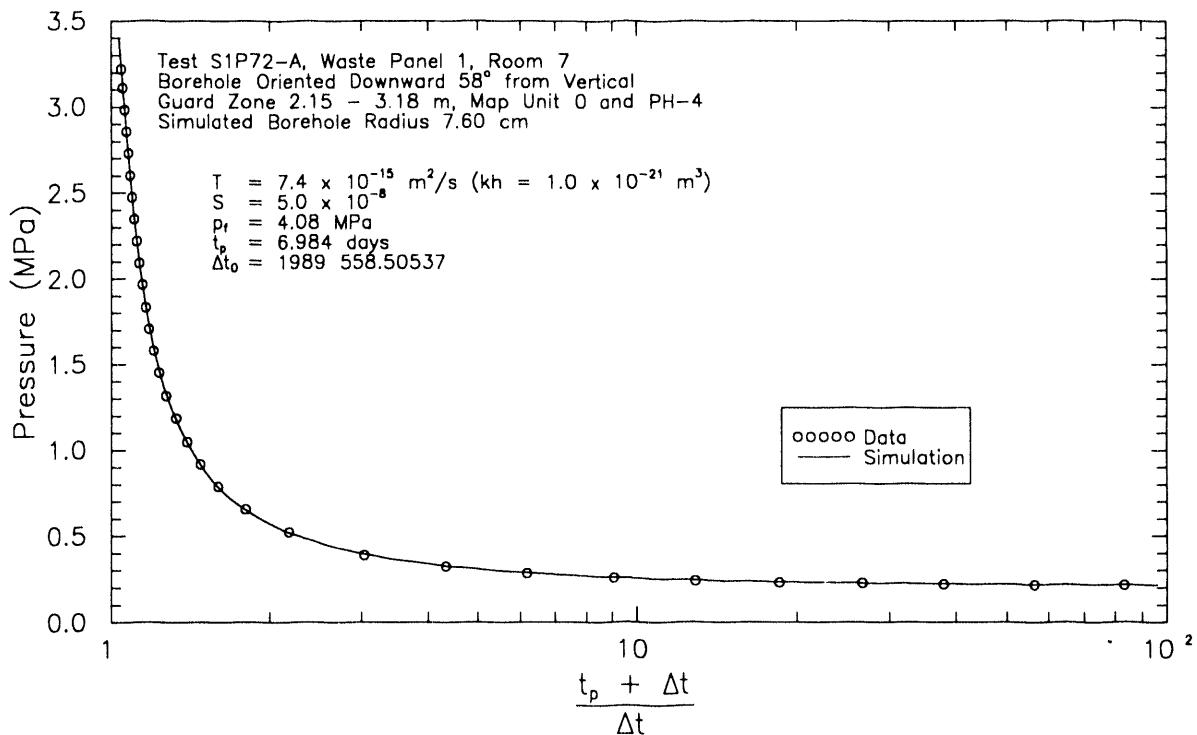

Figure 7-38. Horner plot of GTFM simulation of S1P72-A guard-zone pressure recovery.

Horner plot of the pressure buildup following the repair of the leak in the guard-zone vent line.

Figure 7-39 shows the match between the best-fit simulation and the entire testing sequence. The fitted parameters were a transmissivity of 7.4 x 10^{-15} m^2/s (permeability-thickness product of 1.0 x 10^{-21} m^3), a storativity of 5.0 x 10^{-8}, and a formation pore pressure of 4.08 MPa (Table 7-1). The guard-zone-compressibility function used in the simulations is presented in Figure D-3 of Appendix D. The radius of influence of the S1P72-A guard-zone testing sequence was calculated by GTFM as 4 m using a one-percent pressure-change criterion.

Summary. As discussed in Section 7.1.5, the slanted S1P72 borehole was treated as an equivalent vertical borehole with a radius of 7.60 cm for test interpretation. Assuming that the entire 0.546-m vertical thickness of halite within the guard zone contributed equally to the

observed pressure responses, the average hydraulic conductivity of the interval is 1.4 x 10^{-14} m/s (permeability of 1.8 x 10^{-21} m^2) and the average specific storage is 9.2 x 10^{-8} m^{-1}. No information is available, however, pertaining to possible differences between vertical and horizontal permeability in halite. If no anisotropy exists, the S1P72-A guard-zone tests would be better interpreted in terms of radial flow towards a slanted borehole than towards an equivalent vertical borehole. In this case, the actual borehole radius of 5.265 cm and the actual guard-zone length of 1.03 m should be used to calculate hydraulic properties. As discussed in Section 6.2, the borehole radius used in a test simulation can be changed without altering the simulation as long as the product of the radius squared and storativity ($r^2 S$) does not change. Therefore, the simulations shown in Figures 7-37 through 7-39 are also representative of radial flow to the actual S1P72-A guard-zone geometry with a formation storativity of 1.0 x 10^{-7} and
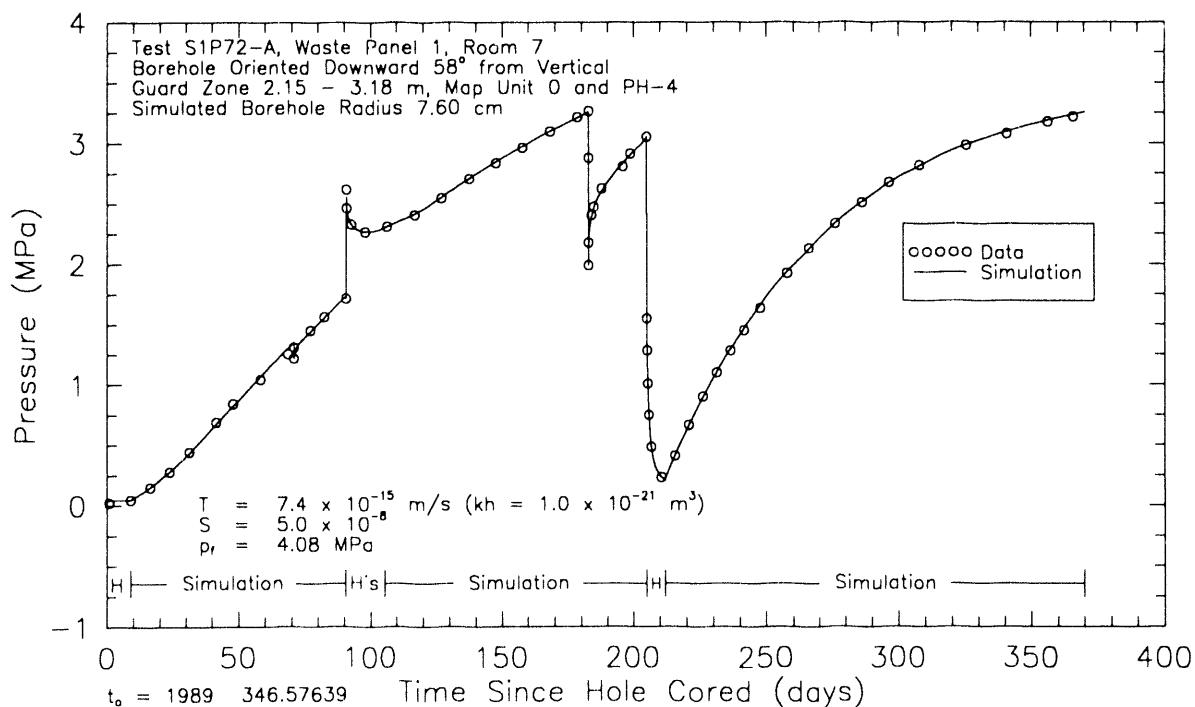

Figure 7-39. Linear-linear plot of GTFM simulation of entire S1P72-A guard-zone testing sequence.

103

transmissivity and pore pressure unchanged. With this geometry, the average hydraulic conductivity would be 7.2 x 10^{-15} m/s (permeability of 9.6 x 10^{-22} m^2) and the average specific storage would be 1.0 x 10^{-7} m^{-1}. The radius of influence of the testing would also be less than the 4 m calculated for the equivalent vertical geometry.

7.1.6 S1P73-A. Borehole S1P73 was drilled vertically upward 4.80 m into the back (ceiling) of Room 7 in Waste Panel 1 in December 1990. Figure 7-40 shows the configuration of the test tool in borehole S1P73 for S1P73-A testing, and indicates the lengths and stratigraphic locations of the guard and test zones. The guard zone for the S1P73-A test configuration extended from 1.51 to 2.55 m above the back of Room 7 and included the upper 0.33 m of map unit 7 (argillaceous halite), anhydrite "b", and the lower 0.65 m of map unit 9 (halite). The test zone extended from 3.38 to 4.80 m above the back of the room and included the upper 0.32 m of map unit 9 (halite), map unit 10 (halite), anhydrite "a", and the lower 0.71 m of map unit 12 (polyhalitic halite). (No core samples were recovered from 4.37 to 4.80 m, but the typical thickness of map unit 12 (see Appendix A) suggests that it extends beyond the terminus of the borehole.)

Brine was injected into the test and guard zones, including anhydrites "a" and "b", respectively. Neither zone completely filled with brine, and brine was observed coming out of a nearby roof-bolt hole during injection into the guard zone. The roof bolts in Room 7 penetrate anhydrite "b" but not anhydrite "a". Therefore, anhydrite "b" is probably connected to the underlying room through roof-bolt holes and possibly fractures, and anhydrite "a" may be connected to anhydrite "b" and possibly the room through fractures. Because the test and guard zones could not be

filled with brine and consequently could not be pressurized for permeability testing, the test tool was removed from S1P73 on January 9, 1991 (1990 Calendar Day 374). The pressures measured in the S1P73-A test and guard zones while the test tool was in the borehole are shown in Figure 7-41. The pressure values presented in Figure 7-41 have been compensated for the elevation differences between the locations of the pressure transducers and the centers of the tested units in the test and guard zones. The test-zone and guard-zone pressures were compensated by subtracting 0.085 and 0.060 MPa, respectively, from the pressures measured by the pressure transducers and reported by Stensrud et al. (1992).

7.1.7 S1P73-B. Borehole S1P73 was deepened from 4.80 m to 11.32 m above the back of Room 7 on January 14 and 15, 1991 (Calendar Days 14 and 15). The hole was deepened to allow testing of clay J in the guard zone and clay K and Marker Bed 138 in the test zone. Figure 7-42 shows the configuration of the test tool in S1P73 for the S1P73-B testing, and indicates the lengths and stratigraphic locations of the guard and test zones. The guard zone for the S1P73-B testing extended from 8.04 to 9.09 m above the back of Room 7 and included the upper 0.11 m of map unit 15 (halite), argillaceous halite 1 (clay J), and 0.39 m of halite 5 above clay J. The test zone extended from 9.92 to 11.32 m above the top of the room and included the upper 0.94 m of argillaceous halite 2, clay K, Marker Bed 138, and the lower 0.29 m of halite 6.

S1P73-B testing in the test zone consisted of a shut-in period, followed by two pulse-withdrawal tests, a constant-pressure withdrawal test, and a pressure-buildup test. A pulse-withdrawal test was attempted in the guard zone during the
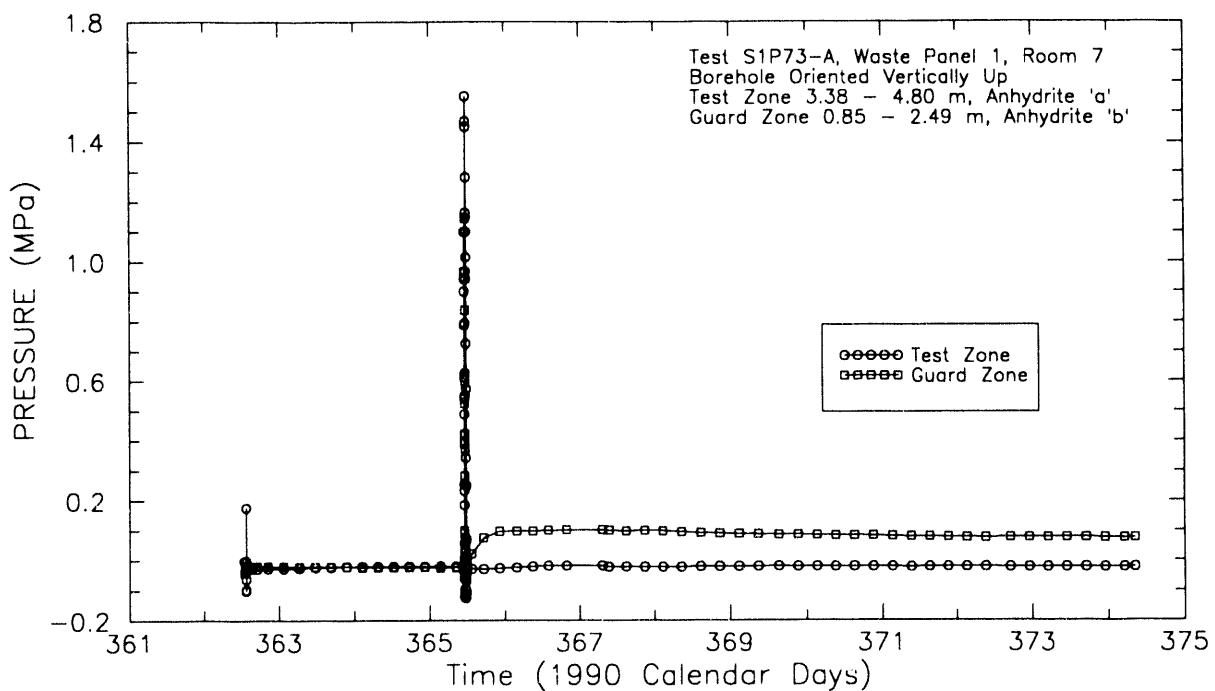
Figure 7-41. Test- and guard-zone pressures during S1P73-A testing.

pressure-buildup test in the test zone. Shortly after the pulse-withdrawal test began, a leak developed in the test tool forcing the termination of the test. The pressures in the test and guard zones during S1P73-B testing are shown in Figure 7-43. The pressure values presented in Figure 7-43 and subsequent figures have been compensated for the elevation differences between the locations of the pressure transducers and the centers of the tested units in the test and guard zones. The test-zone and guard-zone pressures were compensated by subtracting 0.168 and 0.140 MPa, respectively, from the pressures measured by the pressure transducers and reported by Stensrud et al. (1992).

7.1.7.1 Test Zone. The test zone in S1P73-B was shut in on January 21, 1991 (Calendar Day 21). The first pulse-withdrawal test was initiated on February 26, 1991 (Calendar Day 57) and the second pulse-withdrawal test was initiated on March 19, 1991 (Calendar Day 78). A 10-day constant-pressure withdrawal test was conducted

between May 7 and 17, 1991 (Calendar Days 127 to 137). The pressure was reduced from 4.24 to 2.89 MPa for this test, which produced a total of 133 mL of brine (Table 7-2). Figure 7-44 shows cumulative brine production plotted as a function of time during this test. The pressure-buildup test began on May 17, 1991 (Calendar Day 137) and continued until the end of testing on July 3, 1991 (Calendar Day 184).

The compressibility of the S1P73-B test zone could be evaluated with data collected during both pulse withdrawals, at the beginning of the constant-pressure withdrawal test, and during the depressurization of the test zone at the end of testing. The test-zone compressibilities calculated using these data ranged from 1.16×10^{-9} Pa^{-1} to 4.00×10^{-8} Pa^{-1} (Table 6-2).

Analytical Interpretations. Type-curve analysis was performed on the data from the second S1P73-B pulse-withdrawal test. The second test was selected for analysis in preference to the first test because the test-zone pressure was

S1P73-B
TEST-TOOL CONFIGURATION

LVDT # A-02 ———— 11.322

TEST-ZONE
TRANSDUCER ———— 11.106
PORT

TEST ZONE

LVDT # R-17 ———— 10.662
LVDT # R-16 ———— 10.585
LVDT # R-15 ———— 10.512

———— 9.92* ———— 9.928

TEST-ZONE
PACKER
#3041.6

———— 9.09* ———— 9.017

———— 8.765

GUARD ZONE

GUARD-ZONE ———— 8.639
TRANSDUCER ———— 8.609
PORT

———— 8.04* ———— 8.053

GUARD-ZONE
PACKER
#3041.11

———— 7.149

TOOL EXTENSION

ROOM TOP ———— 0.00

BOREHOLE: S1P73   DATE: 01/17/91
TEST TOOL: #4   DEPTH OF HOLE: 11.32 m

BOREHOLE STRATIGRAPHY

11.18 — NO RECOVERY

11.15 — HALITE 6
— HALITE, MEDIUM CRYSTALLINE, ORANGE,
ANHYDRITE LAMINA AT 11.15m

11.03 — MARKER BED 138
— ANHYDRITE, GRAY

10.89 —
10.86 — CLAY K, GRAY
ARGILLACEOUS HALITE 2
— ARGILLACEOUS HALITE,
PODULAR, FINE TO COARSELY
CRYSTALLINE, COLORLESS TO BROWN,
BROWN CLAY. CORE IS VERY
ARGILLACEOUS FROM 10.2m TO
CONTACT WITH CLAY K

9.30 — HALITE 5
— HALITE, MEDIUM CRYSTALLINE,
COLORLESS, TRACE ANHYDRITE

8.70 — ARGILLACEOUS HALITE 1 (CLAY J)
— ARGILLACEOUS HALITE,
PODULAR, FINE TO COARSELY
CRYSTALLINE, COLORLESS TO BROWN

8.15 — MAP UNIT 15
— HALITE, FINE TO MEDIUM CRYSTALLINE,
COLORLESS; WHITE PLANAR
ANHYDRITE LAMINAE SCATTERED
THROUGHOUT

6.97 — ANHYDRITE, GRAY
6.96 —
6.95 — CLAY I, BROWN
MAP UNITS 13 AND 14
— HALITE, COARSELY CRYSTALLINE,
GRAY TO ORANGE.

5.30 — MAP UNIT 12
— HALITE, MEDIUM CRYSTALLINE,
COLORLESS TRACE OF POLYHALITE

4.80 —

(SEE FIGURE 7-40 FOR REMAINDER OF DESCRIPTION.)

NOTE: MEASUREMENTS IN METERS FROM ROOM
CEILING BEFORE PACKER INFLATION.
* ESTIMATED POSITION AFTER PACKER INFLATION.

Figure 7-42. Test-tool configuration for permeability-testing sequence S1P73-B.

107
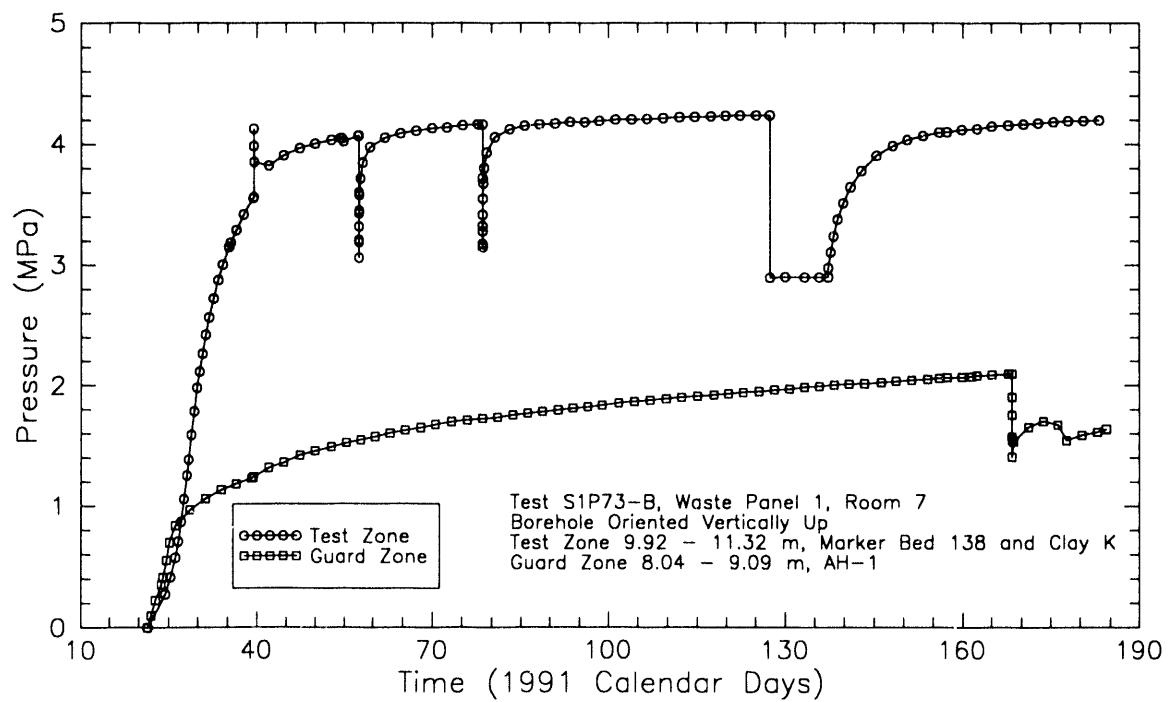
Figure 7-43. Test- and guard-zone pressures during S1P73-B testing.
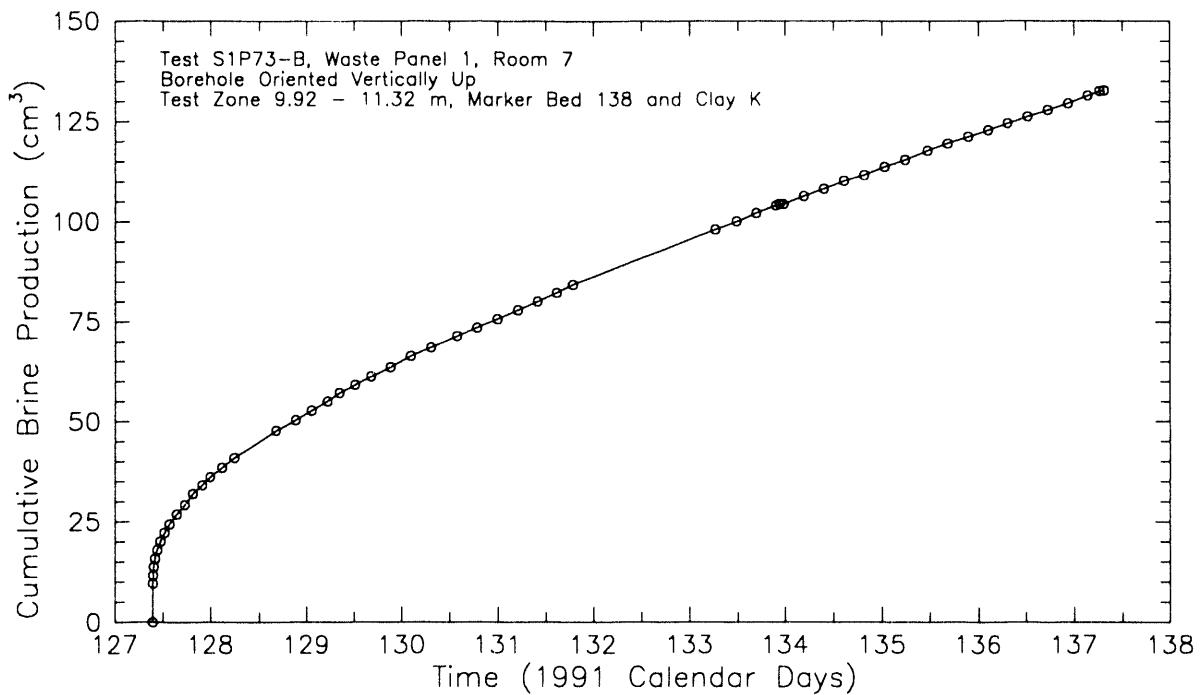
Figure 7-44. Cumulative brine production during S1P73-B test zone constant-pressure withdrawal test.

changing less rapidly just before the second test than just before the first test, and the second test had a longer duration than the first test. The test-zone pressure immediately before the second pulse withdrawal was performed was 4.163 MPa, and was increasing at a rate of about 0.002 MPa/day. The pulse withdrawal decreased the test-zone pressure to 3.147 MPa. At the end of the test 49 days later, the test-zone pressure was 4.239 MPa. To compensate for the increasing pressure trend that was superimposed on the pulse-test response, a linear correction factor of -0.0017 MPa/day was applied to the pulse-test data beginning at the start of the test.

The compensated data from the second pulse-withdrawal test are plotted as normalized pressure versus elapsed time in Figure 7-45. Also shown is the best match obtained to one of the type curves of Bredehoeft and Papadopulos

(1980). Assuming a test-zone compressibility of 2.39×10^{-9} Pa^{-1} (Table 6-2), the type-curve match provides a transmissivity estimate of 3.7×10^{-13} m^2/s (permeability-thickness product of 5.0×10^{-20} m^3; Table 7-1).

Figure 7-46 shows the best-fit match of the flow-rate data from the S1P73-B constant-pressure withdrawal test to the radial-flow type curve for constant-pressure flow tests developed by Jacob and Lohman (1952). After approximately the first 4 hr of the test, the data fit the type curve well. The flow rate at early time decreased more rapidly than predicted by the type curve. This behavior is probably related to test-tool and borehole compliance. When the test-zone pressure was decreased to start the constant-pressure flow test, the test-tool components should have expanded slightly and the hole radius should have decreased slightly, driving brine from the hole in addition to that being
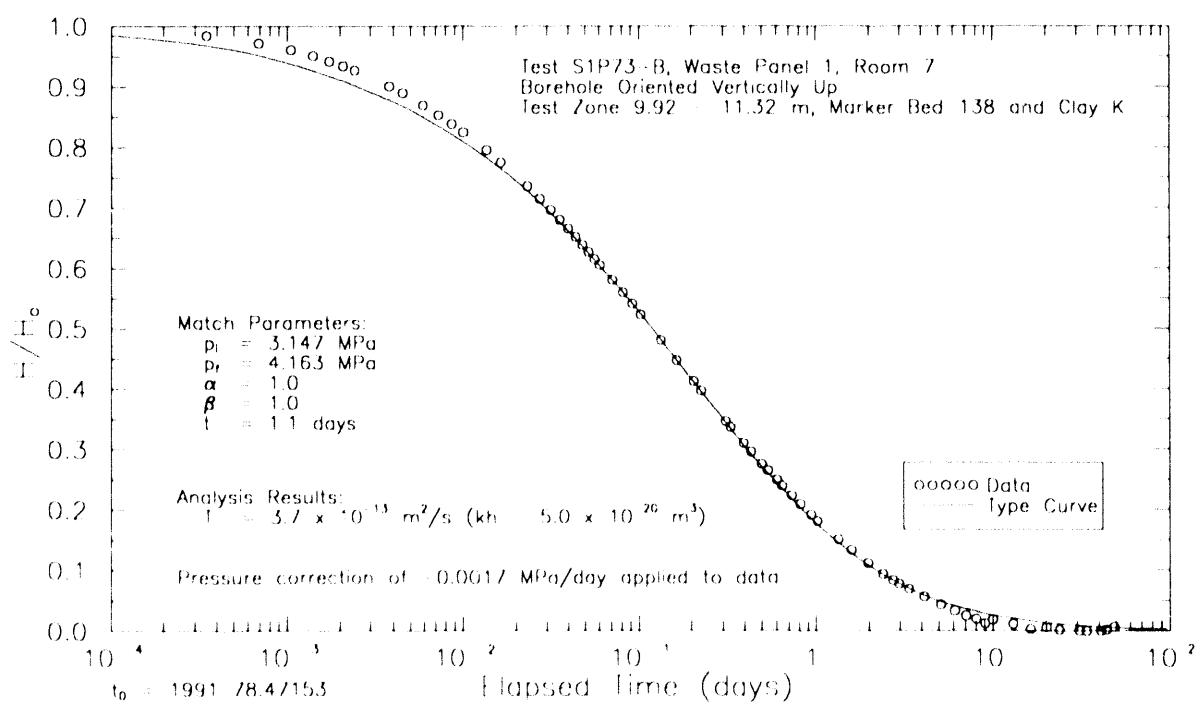
Figure 7-45 Semilog type-curve match to S1P73-B pulse-withdrawal test #2

109
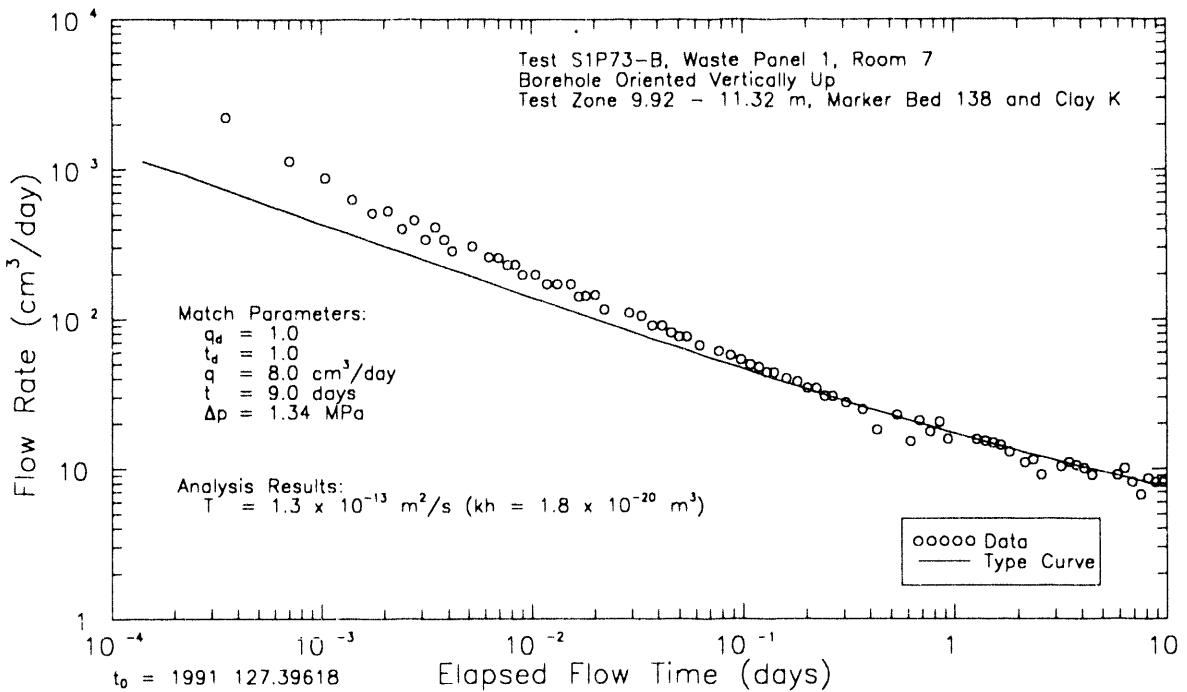
Figure 7-46. Log-log type-curve match to flow rates during S1P73-B constant-pressure withdrawal test.

produced from the formation. After a few hours, the materials in the test zone should have equilibrated with the new pressure, at which time all of the continued brine production should have come from the formation. The match to the radial-flow type curve shown in Figure 7-46 provides a transmissivity estimate of 1.3×10^{-13} m^2/s (permeability-thickness product of 1.7×10^{-20} m^3; Table 7-1).

For analysis of the pressure-buildup test using Interpret/2, the constant-pressure withdrawal test was divided into 34 separate flow periods having constant rates ranging from 27,400 to 8.14 cm^3/day. The best fit obtained between log-log pressure and pressure-derivative type curves and the pressure-buildup data is shown in Figure 7-47. The best Horner match is shown in Figure 7-48, and the best linear-linear match is shown in Figure 7-49. All of these matches provided the same estimated parameters: a transmissivity

of 3.7×10^{-13} m^2/s (permeability-thickness product of 4.9×10^{-20} m^3), a formation pore pressure of 4.29 MPa, a wellbore-storage coefficient of 19.9 cm^3/MPa (corresponding to a test-zone compressibility of 5.14×10^{-9} Pa^{-1}), and a slightly negative wellbore skin of -0.08. Assuming a total system compressibility of 8.37×10^{-8} Pa^{-1} (derived from a GTFM storativity estimate of 1.7×10^{-6}), the radius of influence of the constant-pressure withdrawal and pressure-buildup tests was about 2 m.

Numerical Interpretations. The S1P73-B testing was preceded by a 6-day period during which the borehole was at atmospheric pressure. This open-borehole period was included in the GTFM simulations as a specified-pressure sequence. The pressure buildup observed after initially shutting in the test zone on January 21, 1991 (Calendar Day 21) exhibited increasing-rate behavior (Figure 7-43) indicative of pressure-

110
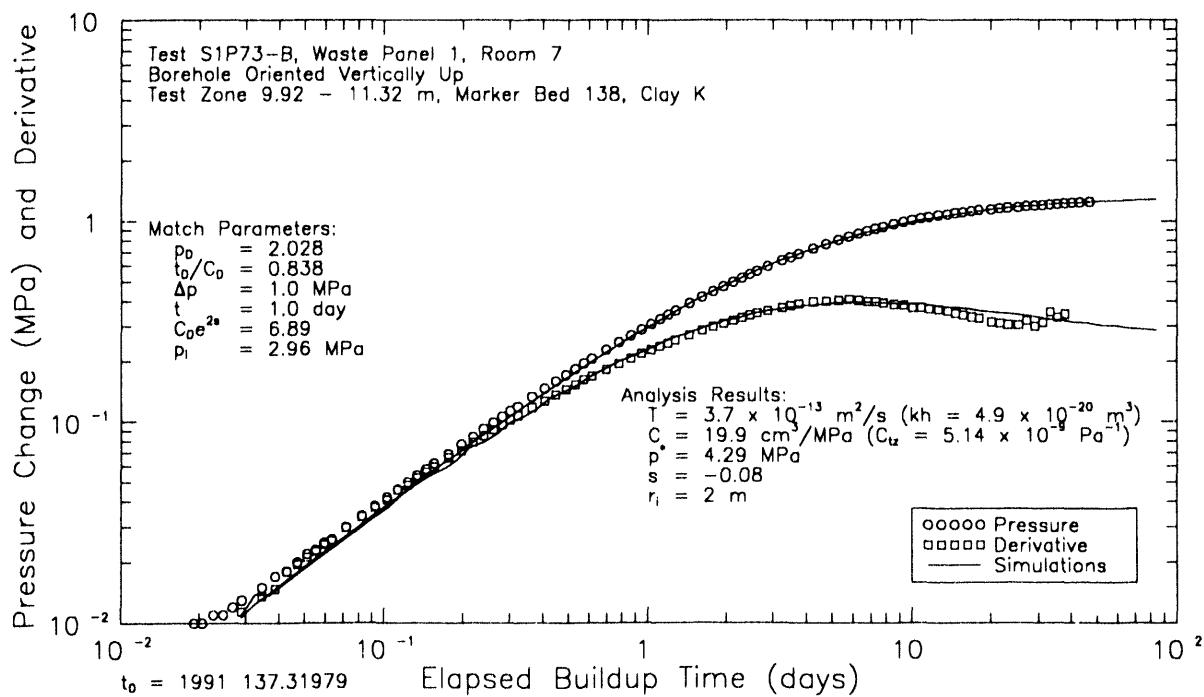
Figure 7-47. Log-log plot of Interpret/2 simulation of S1P73-B pressure-buildup test.
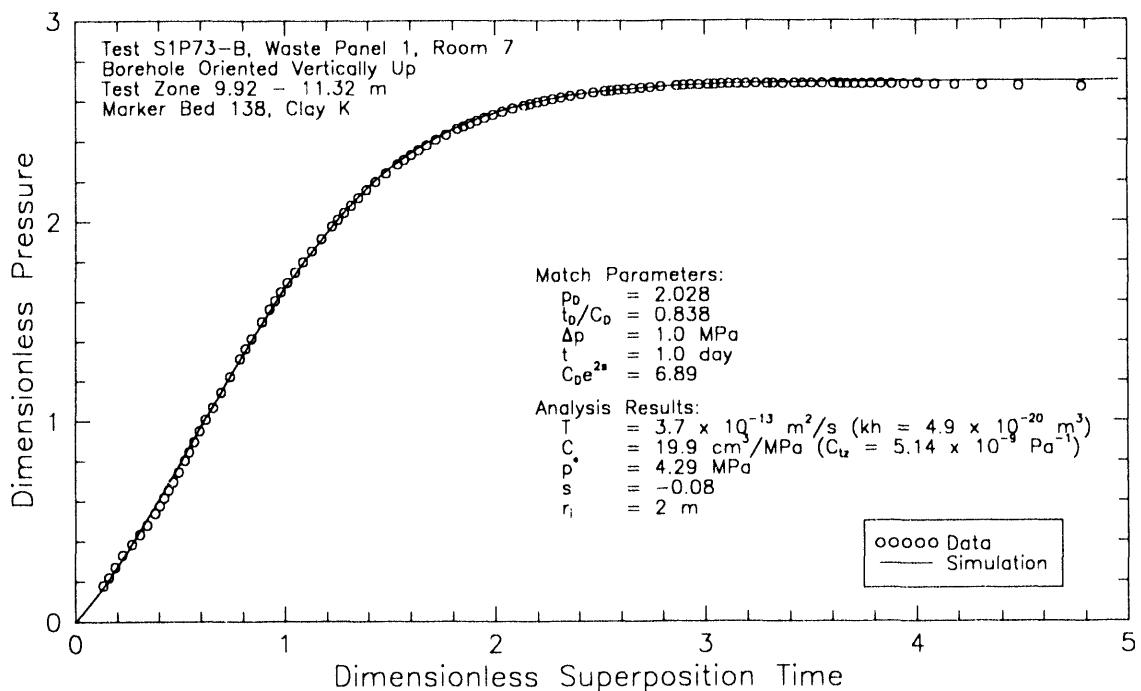
Figure 7-48. Horner plot of Interpret/2 simulation of S1P73-B pressure-buildup test.
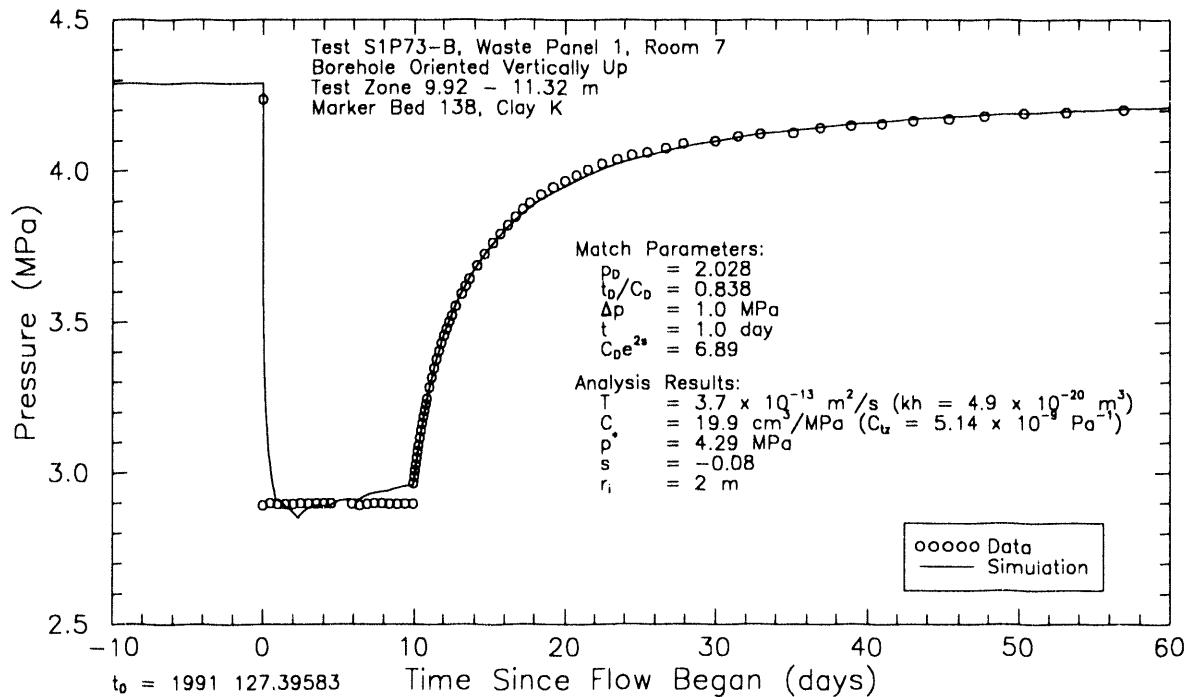
Figure 7-49.   Linear-linear plot of Interpret/2 simulation of S1P73-B constant-pressure flow and pressure-buildup test.

dependent test-zone compressibility (Beauheim et al., 1991). Because compliance testing suggests that test-zone compressibility is most nonlinear at low test-zone pressures (Section 6.3.2), the early portion of the shut-in period was simulated using a specified-pressure sequence. The test-zone packer-inflation pressure (Appendix F, Figure F-7) was increased on February 8, 1991 (Calendar Day 39), causing an increase in the test-zone pressure. The test-zone pressure response to this increase in packer-inflation pressure was related to test-tool compliance and was also treated as a specified-pressure sequence in the simulations. Temperatures measured in the S1P73-B test zone during the monitoring period are shown in Figure E-5 of Appendix E. Also shown is the smoothed representation of the temperature data used as input to GTFM to compensate the simulated pressures for the temperature

fluctuations. The specified parameters used in the S1P73-B GTFM simulations were a test-zone radius of 5.253 cm and a test-zone fluid volume of 3868 cm^3.

Figure 7-50 shows a semilog plot of the best-fit GTFM simulation compared to the observed pressures for the first S1P73-B pulse-withdrawal test. A test-zone compressibility of 1.16 x 10^{-9} Pa^{-1} was specified for this test based on data collected during the pulse withdrawal (Table 6-2). The fitted parameters were a transmissivity of 3.7 x 10^{-13} m^2/s (permeability-thickness product of 5.0 x 10^{-20} m^3), a storativity of 1.7 x 10^{-6}, and a formation pore pressure of 4.37 MPa (Table 7-1).

Figure 7-51 shows a semilog plot of the best-fit GTFM simulation and the observed pressures for the second pulse-withdrawal test. Although a test-zone compressibility of 2.39 x 10^{-9} Pa^{-1} was
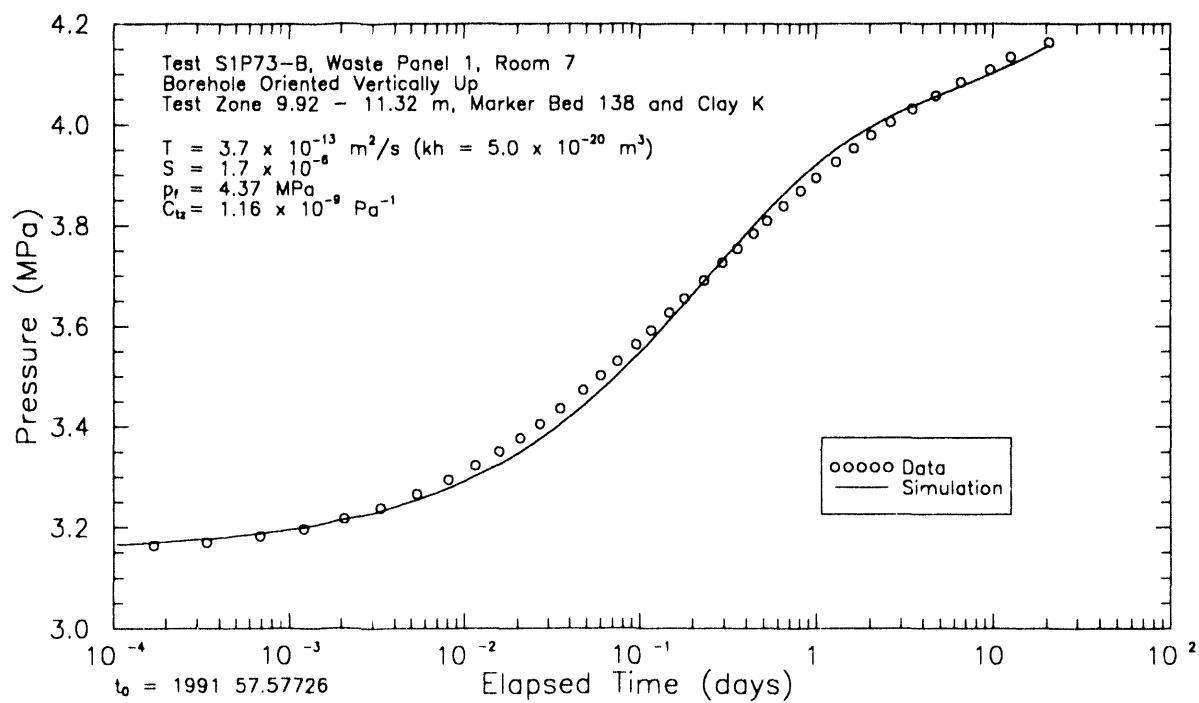
Figure 7-50. Semilog plot of GTFM simulation of S1P73-B pulse-withdrawal test #1.
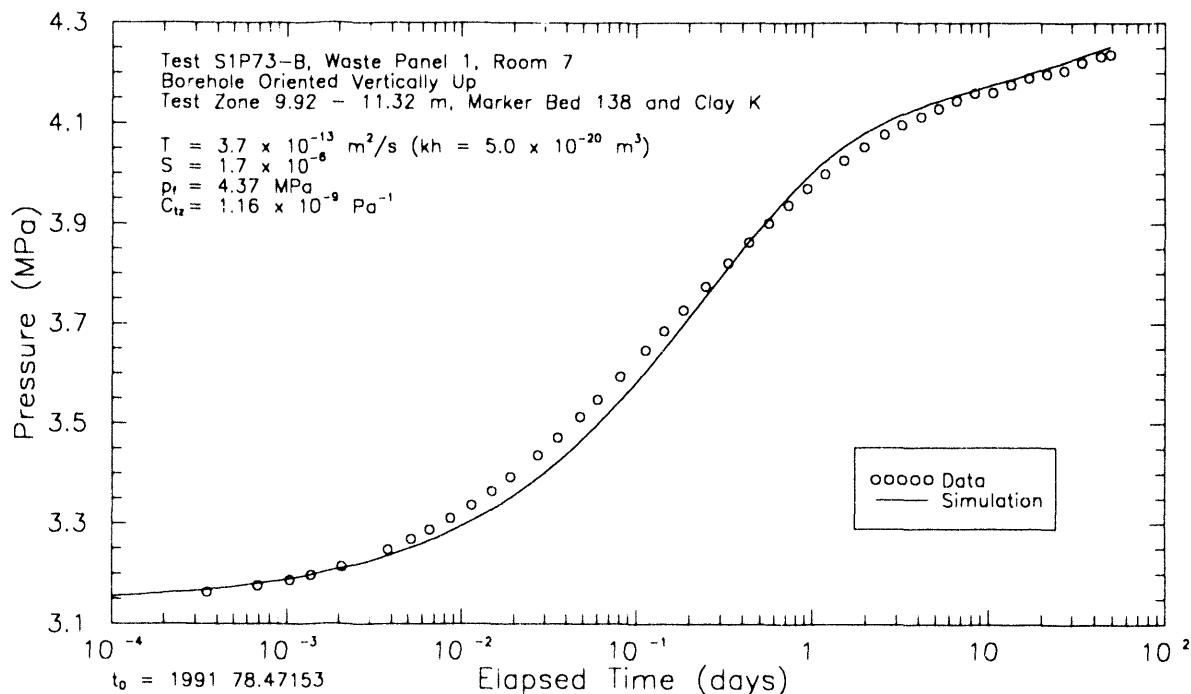
Figure 7-51. Semilog plot of GTFM simulation of S1P73-B pulse-withdrawal test #2.

113

calculated from the second pulse withdrawal, the simulation using this value of test-zone compressibility did not provide as good a match as the simulation using the compressibility (1.16 x 10^{-9} Pa^{-1}) calculated from the first pulse withdrawal. The calculated test-zone compressibility from the second pulse withdrawal may have been larger than that calculated from the first pulse withdrawal because of differences in the lengths of time the test-zone vent was open during the two pulses. Although similar pressure decreases were produced, the first pulse withdrawal lasted approximately 1.5 minutes and the second lasted approximately 3 minutes. The additional fluid produced during the second pulse withdrawal relative to that produced during the first pulse withdrawal may have resulted from increased compliance over the longer vent period. The fitted parameters used to simulate the second pulse-withdrawal test were the same as for the simulation of the

first pulse-withdrawal test: a transmissivity of 3.7 x 10^{-13} m^2/s (permeability-thickness product of 5.0 x 10^{-20} m^3), a storativity of 1.7 x 10^{-6}, and a formation pore pressure of 4.37 MPa (Table 7-1).

Figure 7-52 shows the best-fit GTFM simulation compared to the observed flow for the constant-pressure withdrawal test. The fitted parameters required to match the simulated and observed data for the constant-pressure withdrawal test were exactly the same as those used to simulate the two pulse-withdrawal tests. However, GTFM simulations could not match the flow rates during the first 2 to 3 days of the constant-pressure withdrawal test. The simulation shown in Figure 7-52 includes 28.4 cm^3 of fluid production added at the start of the test beyond what GTFM calculated to bring the simulated and observed total productions into agreement after about 3 days of testing. The observed initial flow rates may have been caused, at least in part, by
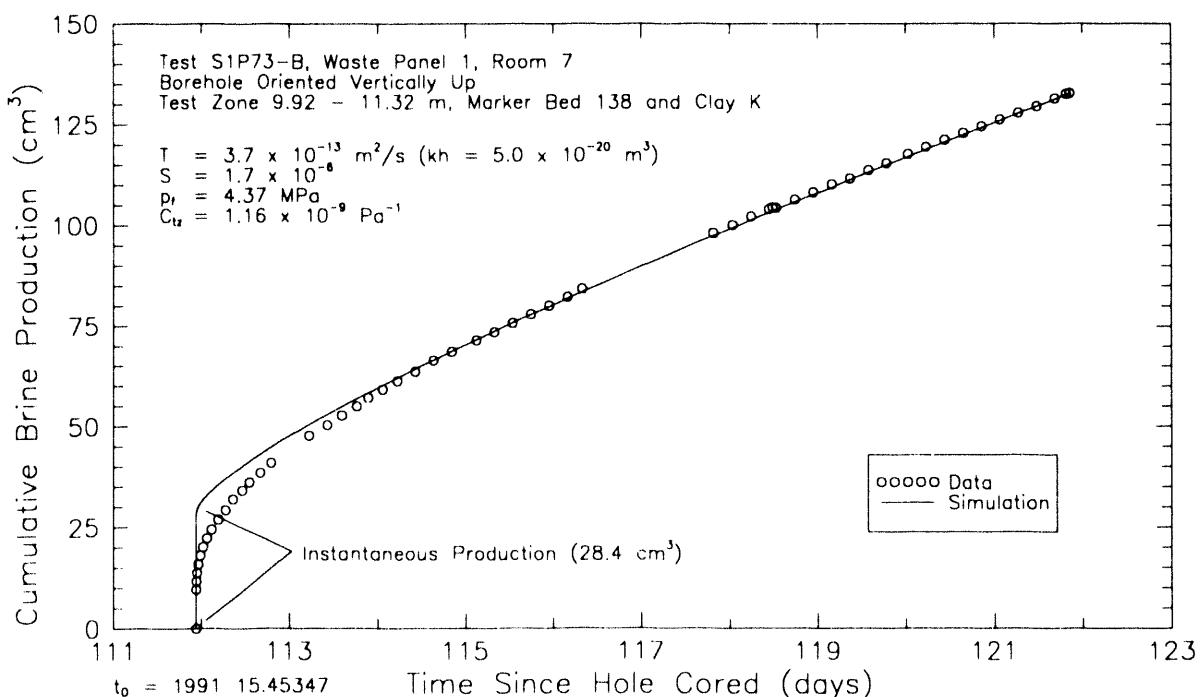
Figure 7-52. Linear-linear plot of GTFM simulation of brine production during S1P73-B constant-pressure withdrawal test.

114

borehole closure after the decrease in test-zone pressure or by production from a skin zone around the hole. Flow rates during the latter part of the test, when the test tool and borehole had completely adjusted to the relatively constant test-zone pressure, were well matched by GTFM.

Figure 7-53 shows a Horner plot of the best-fit GTFM simulation for the S1P73-B pressure-buildup test. The fitted parameters used in the simulation were a transmissivity of 3.7×10^{-13} m²/s (permeability-thickness product of 4.9×10^{-20} m³), a storativity of 1.7×10^{-6}, a formation pore pressure of 4.37 MPa, and a test-zone compressibility of 4.2×10^{-9} Pa⁻¹. This test-zone compressibility is higher than the values calculated from the pulse-withdrawal and constant-pressure withdrawal data (Table 6-2), but is close to the value of 4.74×10^{-9} Pa⁻¹ suggested by Interpret/2 analysis of the pressure-buildup test. The test-zone

compressibility might have increased if a small amount of gas came out of solution while the test zone was depressurized for the duration of the flow test.

Figure 7-54 shows GTFM simulations and observed pressures for the entire S1P73-B testing period using the parameters determined 1) from fitting to the pulse-withdrawal tests and constant-pressure flow test, and 2) from fitting to the pressure-buildup test. The only difference between the simulations is the values of test-zone compressibility used. The high value of test-zone compressibility determined from the pressure-buildup test provides a good match to the initial pressure-buildup period, but causes the pressure recoveries from the two pulse withdrawals to occur more slowly than suggested by the data. The low value of test-zone compressibility determined from the pulse-withdrawal and constant-pressure flow tests
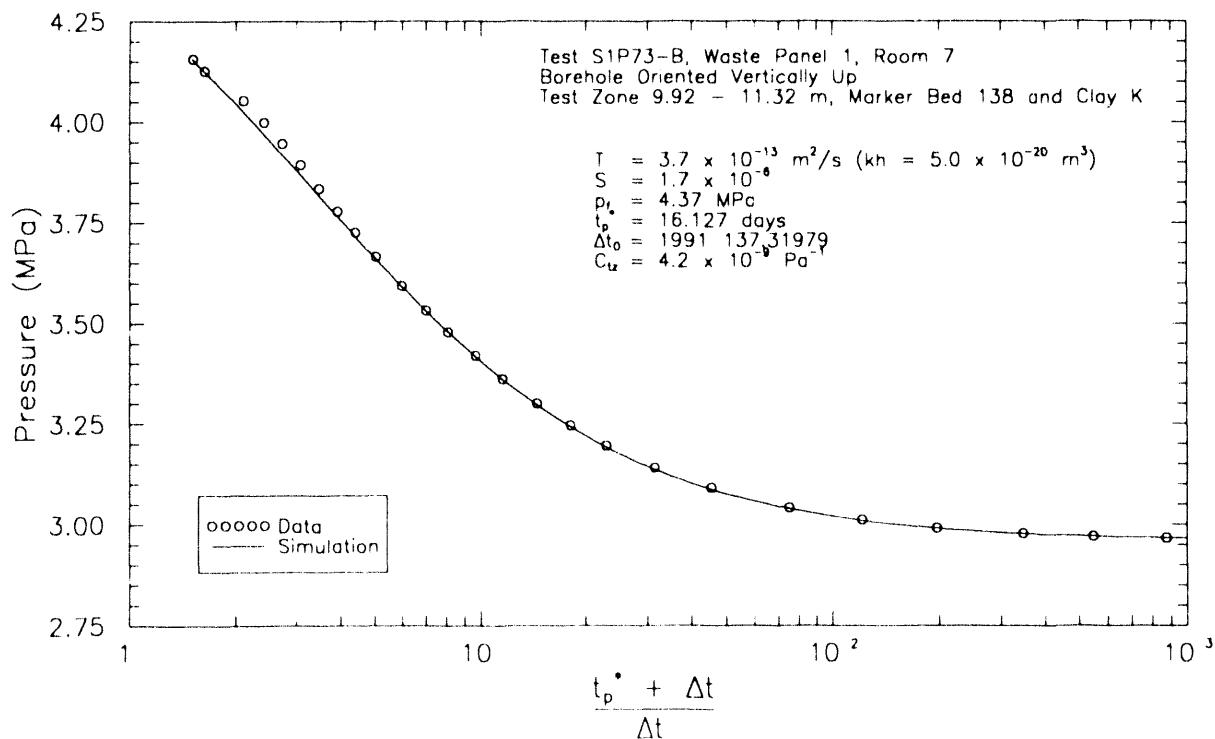
Figure 7-53. Horner plot of GTFM simulation of S1P73-B pressure-buildup test.

115
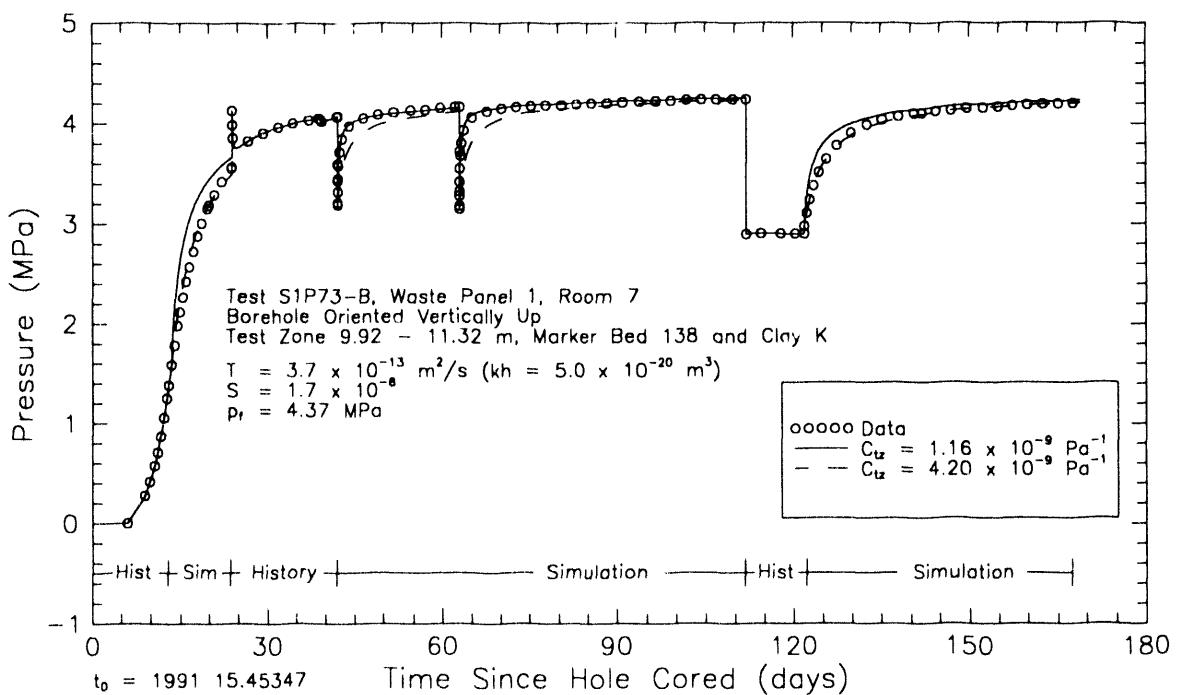
Figure 7-54. Linear-liner plot of GTFM simulations of entire S1P73-B testing sequence.

causes the simulated initial and final pressure buildups to occur more rapidly than was observed. These differences highlight the importance of quantifying test-zone compressibility throughout a test sequence. Using a one-percent pressure-change criterion, GTFM calculated the radius of influence of the entire S1P73-B testing sequence to be 3 m.

Summary. All of the analytical and numerical interpretations of the S1P73-B tests provided estimates of transmissivity of 3.7×10^{-13} m²/s (permeability-thickness products of 4.9×10^{-20} m³) except for the analytical interpretation of the constant-pressure flow test, which provided a transmissivity estimate of 1.3×10^{-13} m²/s (permeability-thickness product of 1.7×10^{-20} m³). The early-time data from the flow test appeared to be strongly influenced by compliance, and

could not be well matched by either a type curve or GTFM. Therefore, the transmissivity derived from the type-curve match to the flow-rate data is probably not as reliable as the transmissivity values derived from the other tests. Both Interpret/2 and GTFM interpretations provided similar estimates of formation pore pressure, ranging from 4.29 to 4.37 MPa. GTFM provided good simulations of all of the tests using a storativity of 1.7×10^{-6}. Using this value of storativity (expressed as total system compressibility), Interpret/2 calculates a radius of influence for the constant-pressure withdrawal and pressure-buildup tests of about 2 m. The radius of influence of the entire testing sequence calculated by GTFM using a one-percent pressure-change criterion was 3 m. Neither Interpret/2 nor GTFM simulations indicated the presence of significant wellbore skin.

116

Vertically averaged values of hydraulic conductivity (permeability) and specific storage can be calculated for the S1P73-B test zone by assuming that fluid was produced only by the 0.17-m interval containing Marker Bed 138 and clay K. The average hydraulic conductivity of this interval is 2.2×10^{-12} m/s (permeability of 2.9×10^{-19} m^2) and the specific storage is 1.0×10^{-5} m^{-1}.

7.1.7.2 Guard Zone. During most of the testing in the S1P73-B test zone, the guard zone was shut in and a pressure buildup was monitored (Figure 7-43). A Horner plot of this buildup is shown in Figure 7-55. The Horner superposition time was calculated using the time from when the middle of the guard zone was cored to when the guard zone was shut in as the flow-period duration. The buildup data extrapolate to a formation pore pressure of about 2.55 MPa at

infinite recovery time (1.0 on the time axis). A pulse-withdrawal test was initiated in the guard zone on June 17, 1991 (Calendar Day 168). On June 24, 1991 (Calendar Day 175), a leak developed in the test tool. The pulse-withdrawal test was abandoned 9 days later. No interpretation was attempted of the pressure response observed before the leak occurred.

7.1.8 SCP01-A. Borehole SCP01 was drilled downward at an angle of 77° from vertical to allow testing of Marker Bed 139 beneath the south rib in the core-storage library (Figure 5-4). Figure 7-56 shows the test-tool configuration for SCP01-A testing, and indicates the lengths and stratigraphic locations of the guard and test zones. SCP01 was drilled from March 26 to 30, 1990 (Calendar Days 85 to 89) to a total depth of 15.39 m. The test tool was installed on April 5, 1990 (Calendar Day 95). The test zone
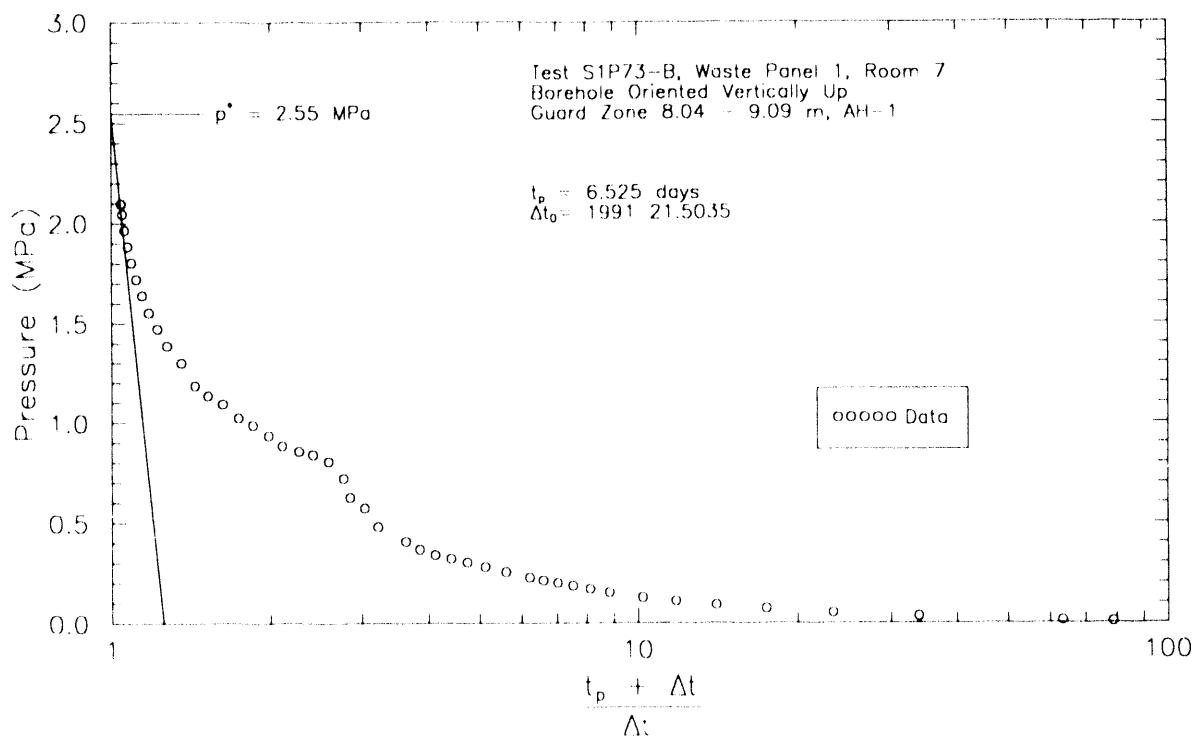
Figure 7-55. Horner plot of S1P73-B guard-zone shut-in pressure buildup.

117
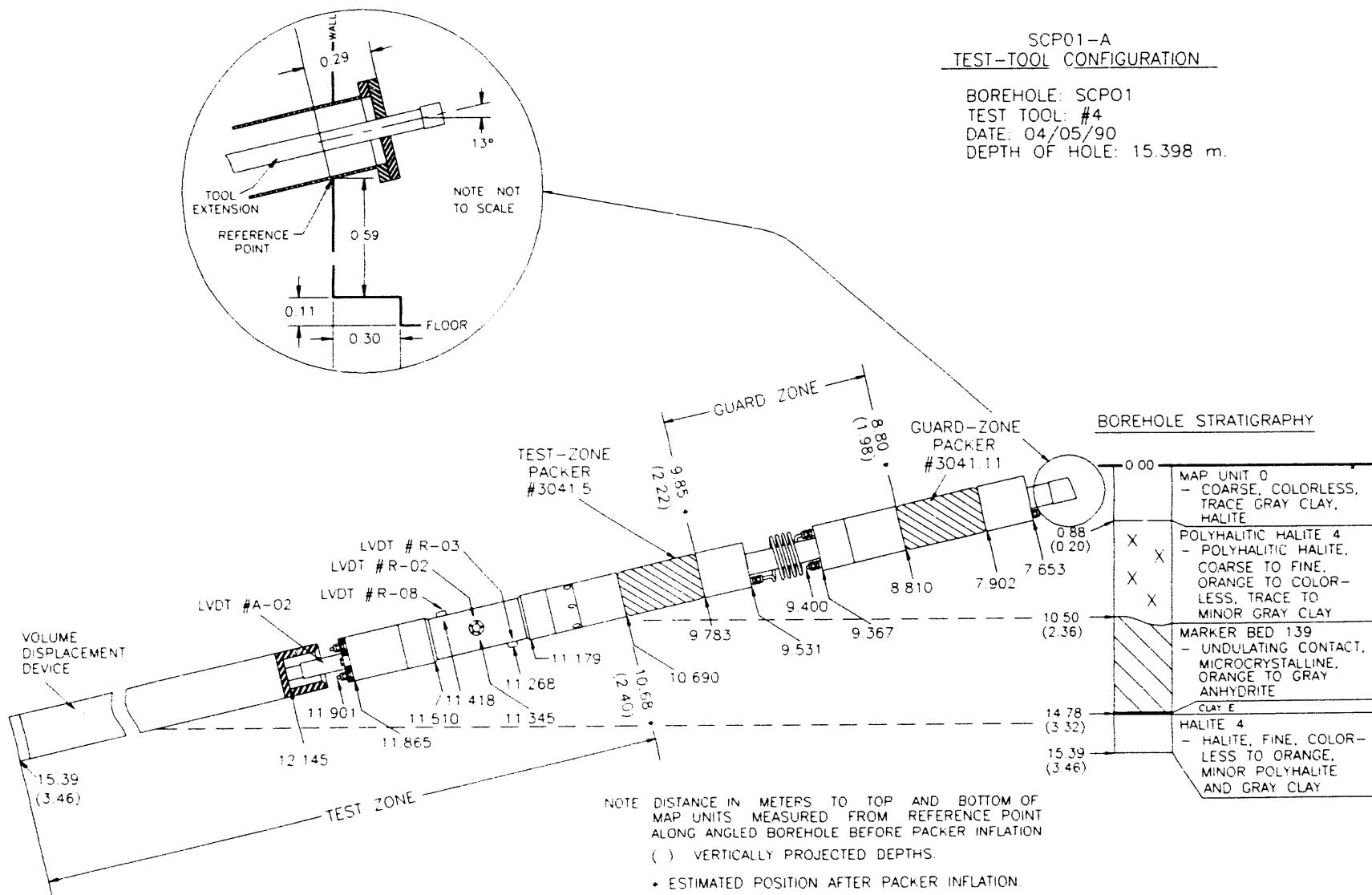
Figure 7-56   Test-tool configuration for permeability-testing sequence SCP01-A.

extended from 10.68 to 15.39 m along the borehole and included 4.28 m of Marker Bed 139 and the underlying clay E, and 0.51 m of halite 4 underlying clay E. The entire guard zone consisted of 1.05 m of polyhalitic halite 4 which overlies Marker Bed 139. A volume-displacement device was inserted into the bottom of the borehole to decrease the overall fluid volume in the test-zone interval (Figure 7-56). The test tool was inserted into the borehole until the axial LVDT was slightly depressed against the top of the volume-displacement device.

Figure 7-57 presents the test- and guard-zone pressure data collected by the DAS during the monitoring period of April 10 to October 11, 1990 (Calendar Days 100 to 284). The pressure values presented in Figure 7-57 and subsequent figures have been compensated for the elevation differences between the locations of the pressure

transducers and the centers of the tested units in the test and guard zones. The test-zone and guard-zone pressures were compensated by adding 0.040 and 0.031 MPa, respectively, to the pressures measured by the pressure transducers and reported by Stensrud et al. (1992). The testing sequence in the test zone consisted of 12 days under open-borehole conditions, an initial pressure-buildup period, two pulse-withdrawal tests, two constant-pressure withdrawal tests, and two pressure-buildup tests. On August 1, 1990 (Calendar Day 213), the test and guard zones and the test- and guard-zone packers were depressurized and the test tool was rotated to correct a depressurization problem in the test zone. After reinflating the packers and shutting in the test and guard zones, brine was injected into the test zone to accelerate recovery to formation pore pressure. The last tests conducted in the test zone consisted of a
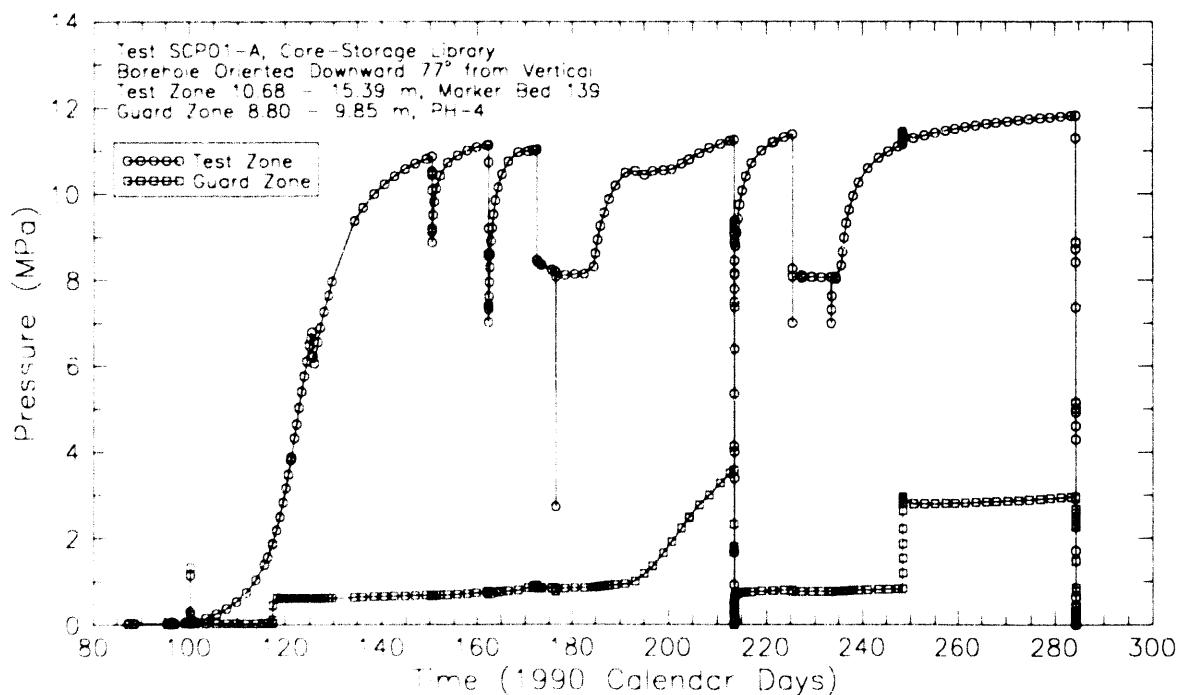
Figure 7-57. Test- and guard-zone pressures during SCP01-A testing.

119

constant-pressure withdrawal test and subsequent pressure-buildup test. The testing sequence in the guard zone consisted of 13 days of open borehole conditions, an initial shut-in period, and two pulse-injection tests. The increase in guard-zone pressure between the two pulse-injection tests was probably due to pressure leaking from the test zone past the test-zone packer and into the guard zone. After the test tool was rotated to stop the pressure leak, fluid was injected into the guard zone to increase the pressure, and then the guard zone was shut in.

The slanted test borehole SCP01 was treated as an equivalent vertical borehole for test interpretation. The borehole geometry for SCP01 was modified according to the procedure described in Section 6.2. The test interpretations assumed an equivalent cylindrical borehole radius of 14.15 cm.

7.1.8.1 Test Zone. The test zone of SCP01-A was shut in on April 10, 1990 (Calendar Day 100). On May 5, 1990 (Calendar Day 125), the test-zone pressure decreased probably due to a slip in the position of the test-zone packer, an event correlated to a corresponding increase in the test-zone packer-inflation pressure. The first pulse-withdrawal test was initiated on May 30, 1990 (Calendar Day 150) by lowering the test-zone pressure from 10.86 to 8.83 MPa. The second pulse-withdrawal test was initiated on June 11, 1990 (Calendar Day 162) by lowering the pressure in the test zone from 11.13 to 7.01 MPa. The test-zone pressure increased steadily until June 17, 1990 (Calendar Day 168), at which time it decreased slightly and thereafter increased at a lower rate for the duration of the pulse-withdrawal test than seemed consistent with its earlier behavior. At the same time, the rate of pressure increase in the guard zone

increased (Figure 7-57). This behavior, which is similar to that observed during the pressure buildup after the first constant-pressure withdrawal test, is explained below.

The first constant-pressure withdrawal test was initiated on June 21, 1990 (Calendar Day 172). The pressure in the test zone decreased steadily instead of remaining constant until a valve was inadvertently opened on June 25, 1990 (Calendar Day 176), causing a rapid drop in pressure. After the valve was closed, the pressure was increased to approximately 8.1 MPa by injecting brine. The pressure remained nearly constant at about 8.1 MPa until the constant-pressure withdrawal test was terminated on July 3, 1990 (Calendar Day 184). Figure 7-58 shows the cumulative brine volume produced from the test zone during the first constant-pressure withdrawal test. A total of about 280 cm^3 of brine was produced during the test (Table 7-2). On July 11, 1990 (Calendar Day 192), during the pressure-buildup test following the first constant-pressure withdrawal test, the test-zone pressure decreased and fluctuated for several days before increasing. Because the decrease in the test-zone pressure was coincident with a rise in guard-zone pressure, a leak from the test zone to the guard zone was suspected. A similar leak is suspected of being the cause of the anomalous pressure behavior observed during the later stages of the second pulse-withdrawal test. The test and guard zones and the test- and guard-zone packers were depressurized and the tool was rotated on August 1, 1990 (Calendar Day 213) to obtain a better test-zone packer seal.

The second constant-pressure withdrawal test was initiated on August 13, 1990 (Calendar Day 225) by lowering the test-zone pressure from 11.38 to 8.08 MPa and maintaining it at
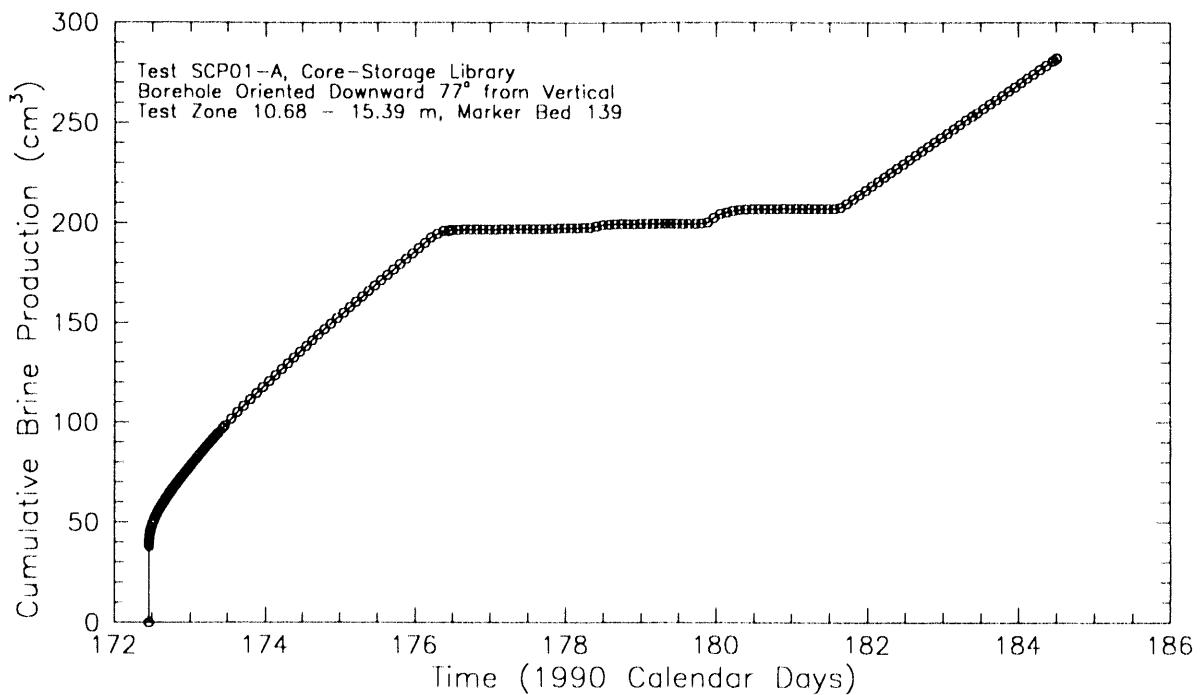
Figure 7-58. Cumulative brine production during SCP01-A constant-pressure withdrawal test #1.

approximately that pressure for 10 days. Figure 7-59 shows the cumulative brine volume produced from the test zone during this test. A total of about 345 cm³ of brine was produced (Table 7-2). The flow test was terminated and a pressure-buildup test begun on August 23, 1990 (Calendar Day 235). The increase in the test-zone pressure on September 5, 1990 (Calendar Day 248) evident on Figure 7-57 occurred in response to a pulse injection performed in the guard-zone interval.

Values of test-zone compressibility were calculated from the two pulse withdrawals, the two constant-pressure withdrawal tests, and from data collected during the incremental depressurization of the test zone at the end of the SCP01-A testing. The compressibilities calculated for these events ranged from 1.12

x 10^{-9} to 2.76 x 10^{-9} Pa^{-1}, increasing as the test-zone pressure decreased (Table 6-2).

Analytical Interpretations. Figure 7-60 shows the best-fit match of the flow-rate data from the second SCP01-A constant-pressure withdrawal test to the radial-flow type curve for constant-pressure flow tests developed by Jacob and Lohman (1952). The data match the type curve well even though the hole is inclined 77° from vertical. The absence of non-radial flow effects caused by the inclination of the hole (see Figure C-40) may indicate that flow to the hole occurs through subhorizontal bedding-plane fractures that do not communicate vertically. The match to the type curve provides a transmissivity estimate of 4.3 x 10^{-13} m²/s (permeability-thickness product of 5.8 x 10^{-20} m³).
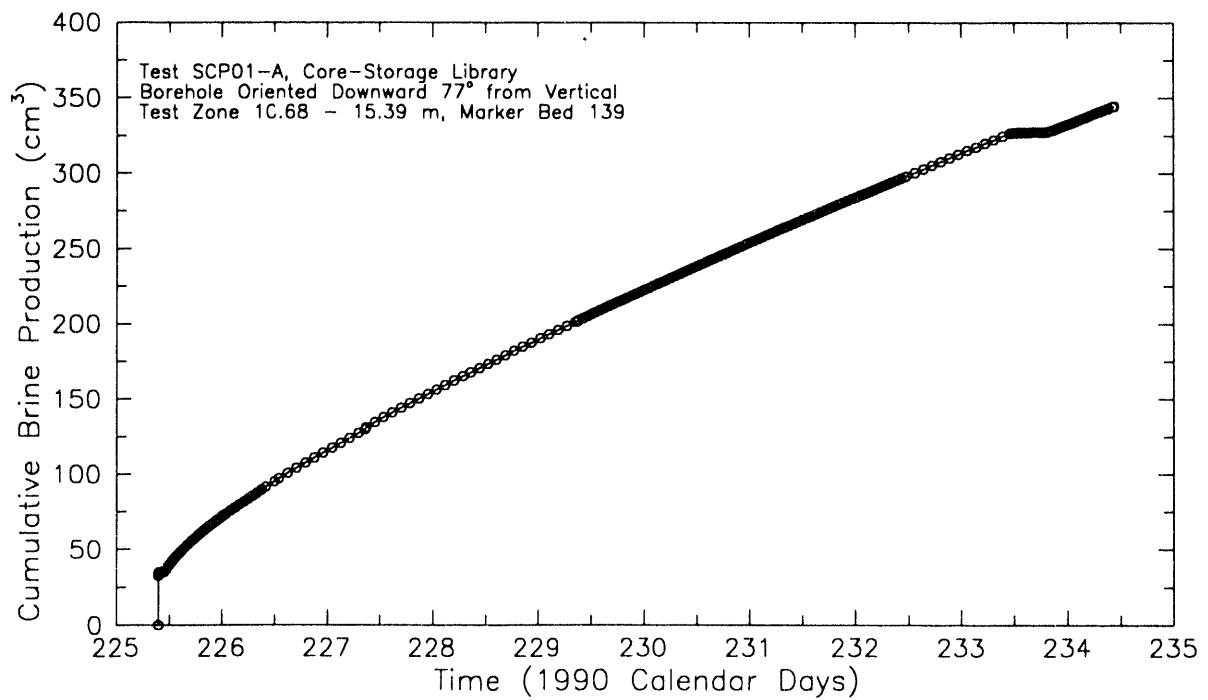
Figure 7-59. Cumulative brine production during SCP01-A constant-pressure withdrawal test #2.
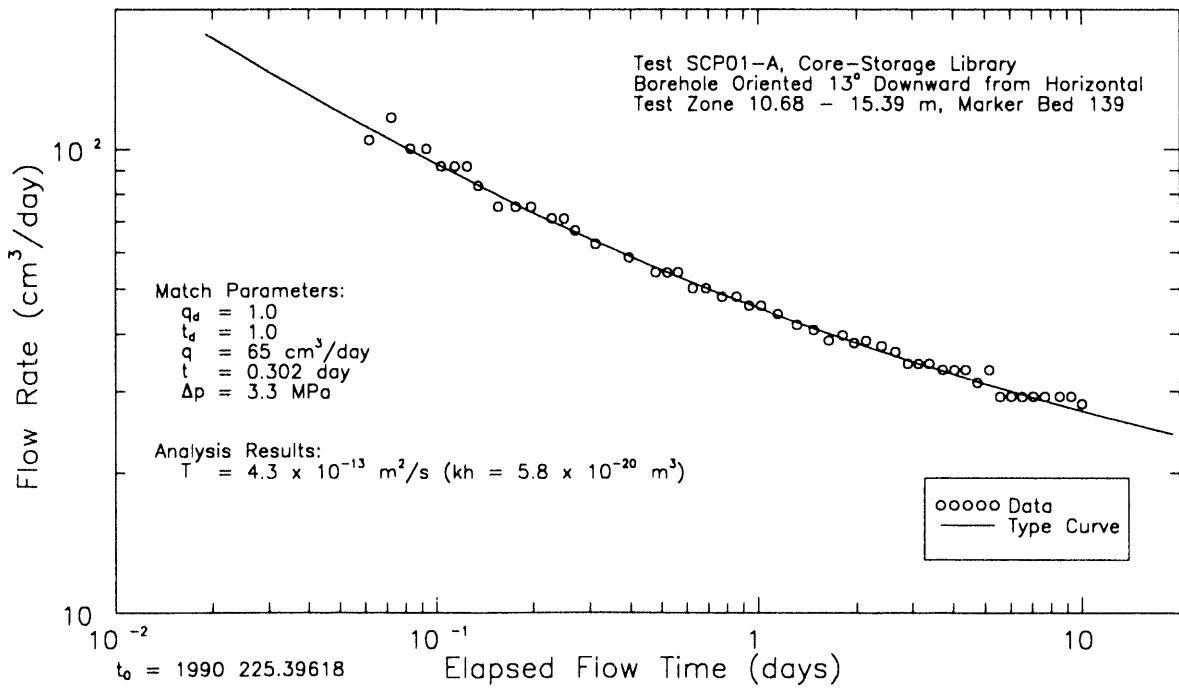
Figure 7-60. Log-log type-curve match to flow rates during SCP01-A constant-pressure withdrawal test #2.

As discussed above, the SCP01-A test zone was completely depressurized and the test tool was repositioned twelve days before the second constant-pressure flow test began. At the time the flow test was initiated, the test-zone pressure was still recovering from the depressurization at a rate of about 0.036 MPa/day. While the rate of this recovery should have steadily decreased with time, the recovery was nevertheless superimposed on the pressure responses induced by the constant-pressure flow test. Specifically, the pressure recovery following the flow test was a combination of recoveries from the flow test and from the earlier depressurization. Initial attempts at simulating the post-flow pressure buildup with Interpret/2 without including any compensation for the pre-existing pressure trend showed the pressure recovering faster than would be expected in a radially homogeneous system, as if a no-flow boundary were accelerating the recovery. These simulations showed the recovery proceeding towards a formation pore pressure of 12.40 MPa, over 1 MPa higher than the test-zone pressure at the time the flow test was initiated (11.38 MPa). For the final Interpret/2 simulations, a compensation was made to the pressure data to remove the component of the recovery attributable to the pre-flow test depressurization. This compensation had the effect of converting the pressure response to that which would have been observed had the pressure been fully stabilized at 11.38 MPa when the flow test began.

For the Interpret/2 analysis of the second pressure-buildup test, the second constant-pressure withdrawal test was divided into 13 separate flow periods having constant rates ranging from 140 to 29 cm^3/day. The best fit obtained between log-log pressure and pressure-derivative type curves and the compensated

pressure-buildup data is shown in Figure 7-61. The best dimensionless Horner match is shown in Figure 7-62, and the best linear-linear match is shown in Figure 7-63. All of these matches provided the same estimated parameters: a transmissivity of 3.8×10^{13} m^2/s (permeability-thickness product of 5.1×10^{20} m^3), a formation pore pressure of 11.38 MPa, a wellbore-storage coefficient of 11.8 cm^3/MPa (corresponding to a test-zone compressibility of 1.35×10^9 Pa^{-1}), and a wellbore skin of -0.62. Because of the compensation applied to the pressure-buildup data, the apparent formation pore pressure of 11.38 MPa indicated by the Interpret/2 simulations does not represent the true formation pore pressure. The value of 12.40 MPa indicated by the preliminary Interpret/2 simulations without any pressure-trend compensations probably represents a more accurate estimate of the formation pore pressure. The interpreted wellbore skin of -0.62 implies, by Eq. 6-9, that the effective wellbore radius is about 1.9 times as large as the actual wellbore radius. This effect is probably caused by fractures intersecting the borehole.

Numerical Interpretations. The initial 12-day open-borehole period, the two constant-pressure withdrawal tests, the pressure fluctuation during the first pressure-buildup test, and the pressure increase on September 5, 1990 (Calendar Day 248) were included in GTFM simulations as specified-pressure history sequences. A constant test-zone compressibility of 2.4×10^9 Pa^{-1} was initially used in the GTFM simulations, but a good fit could not be achieved for each of the tests. Therefore, a varying test-zone-compressibility-versus-time function was used for the simulations. The function was developed by fitting the initial pressure buildup with a decreasing compressibility and then using the three test-zone-compressibility values calculated

123
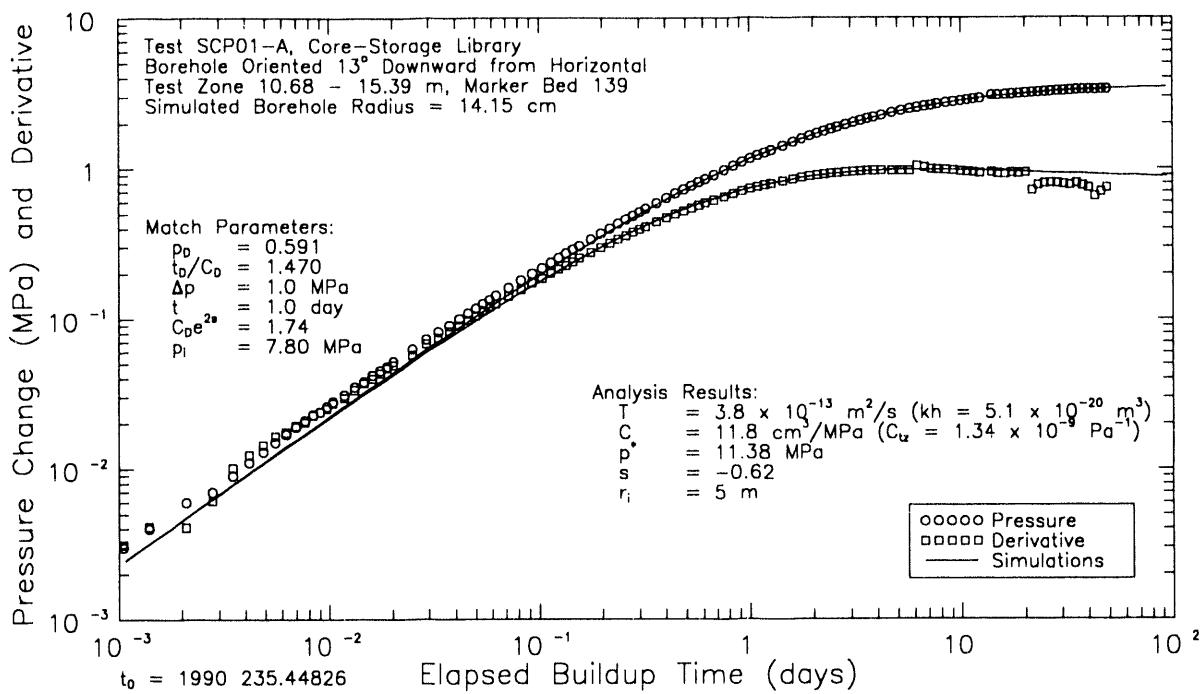
Figure 7-61. Log-log plot of Interpret/2 simulation of SCP01-A pressure-buildup test #2.
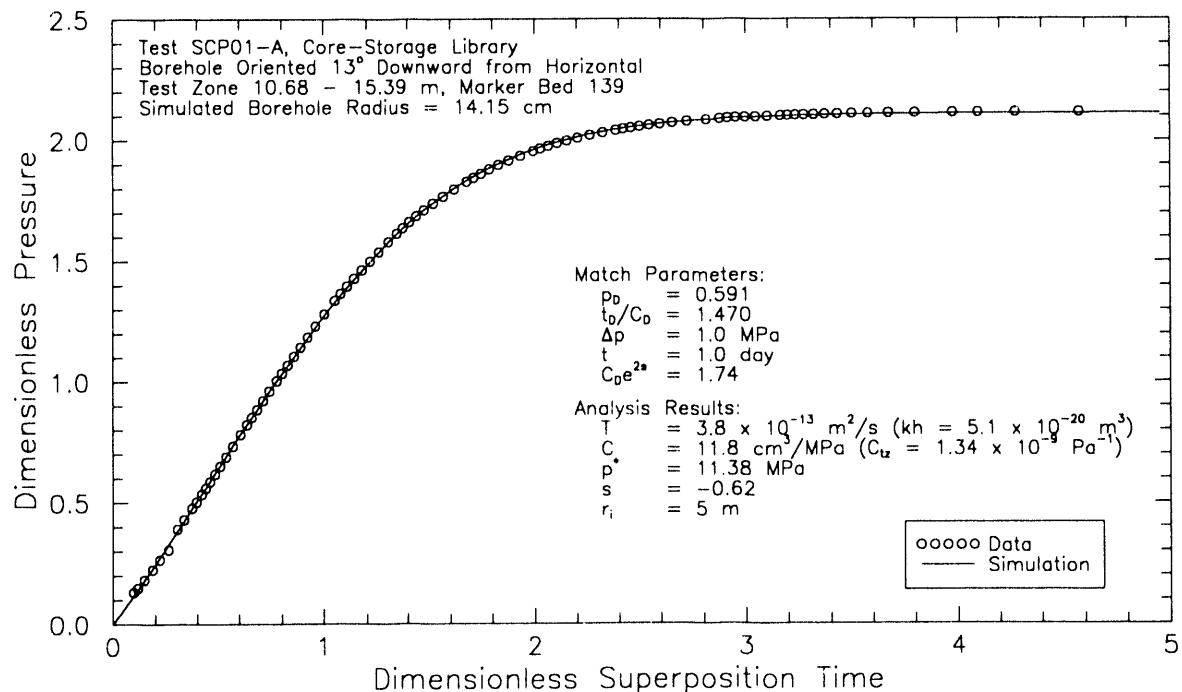
Figure 7-62. Horner plot of Interpret/2 simulation of SCP01-A pressure-buildup test #2.
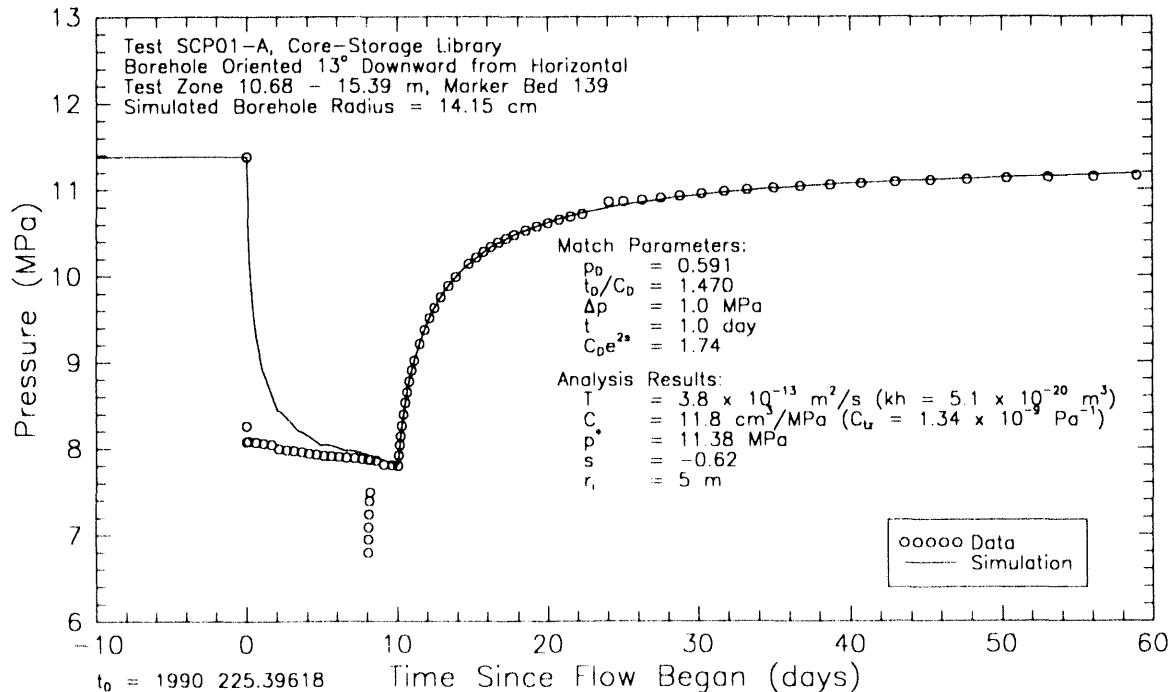
Figure 7-63. Linear-linear plot of Interpret/2 simulation of SCP01-A constant-pressure flow and pressure-buildup tests #2.

at the end of the SCP01-A testing to define the test-zone compressibility for the remainder of the testing period. The test-zone-compressibility function used in the simulations is presented in Figure D-4 of Appendix D. Temperatures measured in the SCP01-A test zone during the monitoring period are shown in Figure E-6 of Appendix E. Also shown is the smoothed representation of the temperature data used as input to GTFM to compensate the simulated pressures for the temperature fluctuations. The specified parameters used in the simulations were a borehole radius of 14.15 cm and a test-zone fluid volume of 8734 cm^3.

Figures 7-64 and 7-65 present semilog plots of pressure versus elapsed time showing the best-fit GTFM simulations for the two pulse-withdrawal tests. The fitted parameters for these simulations were a transmissivity of 5.3 x 10^{-13}

m^2/s (permeability-thickness product of 7.1 x 10^{-20} m^3), a storativity of 1.9 x 10^{-7}, and a formation pore pressure of 12.55 MPa (Table 7-1). The late-time data for the second pulse-withdrawal test show a decrease in the observed test-zone pressure due to pressure leaking by the test-zone packer into the guard zone. This observed decrease in pressure is similar to the decrease that occurred during the first pressure-buildup test. The pressures in the test zone were approximately 10.9 and 10.6 MPa when the first and second suspected leaks occurred, respectively, and these pressures are similar enough to assume that they represent a threshold pressure at which the test-zone pressure forced a break in the seal of the test-zone packer with the borehole wall, causing pressure communication with the guard-zone interval. This pressure communication is evident in the increases in guard-zone pressure at the

125
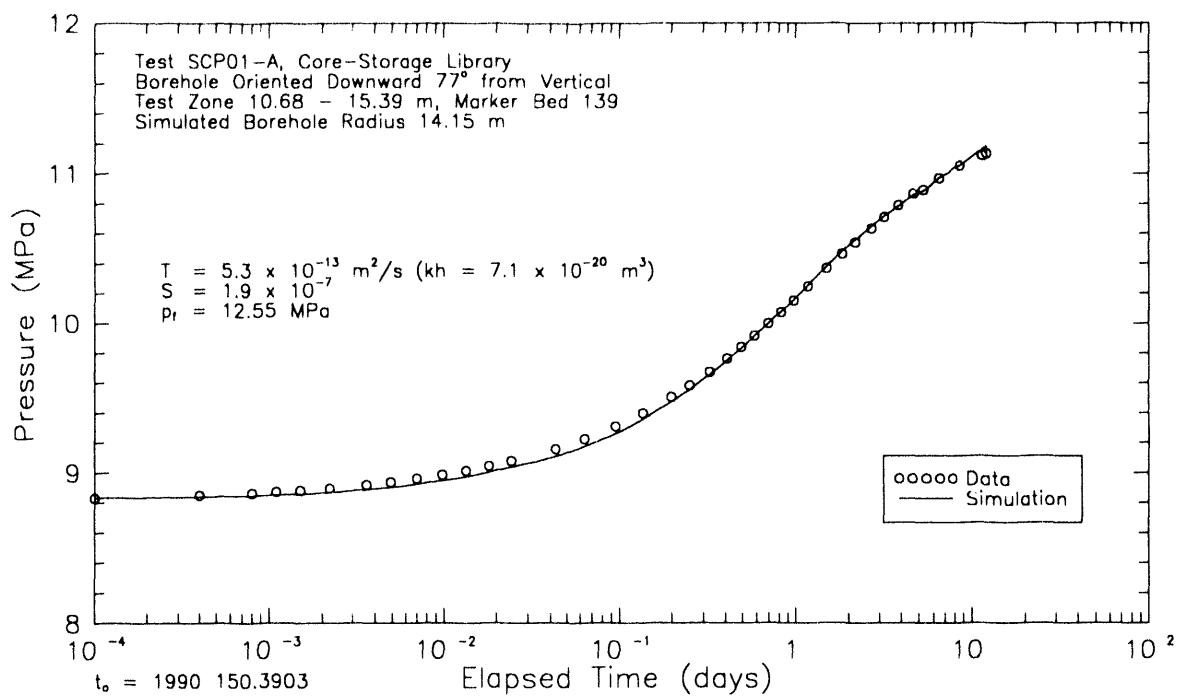
Figure 7-64. Semilog plot of GTFM simulation of SCP01-A pulse-withdrawal test #1.
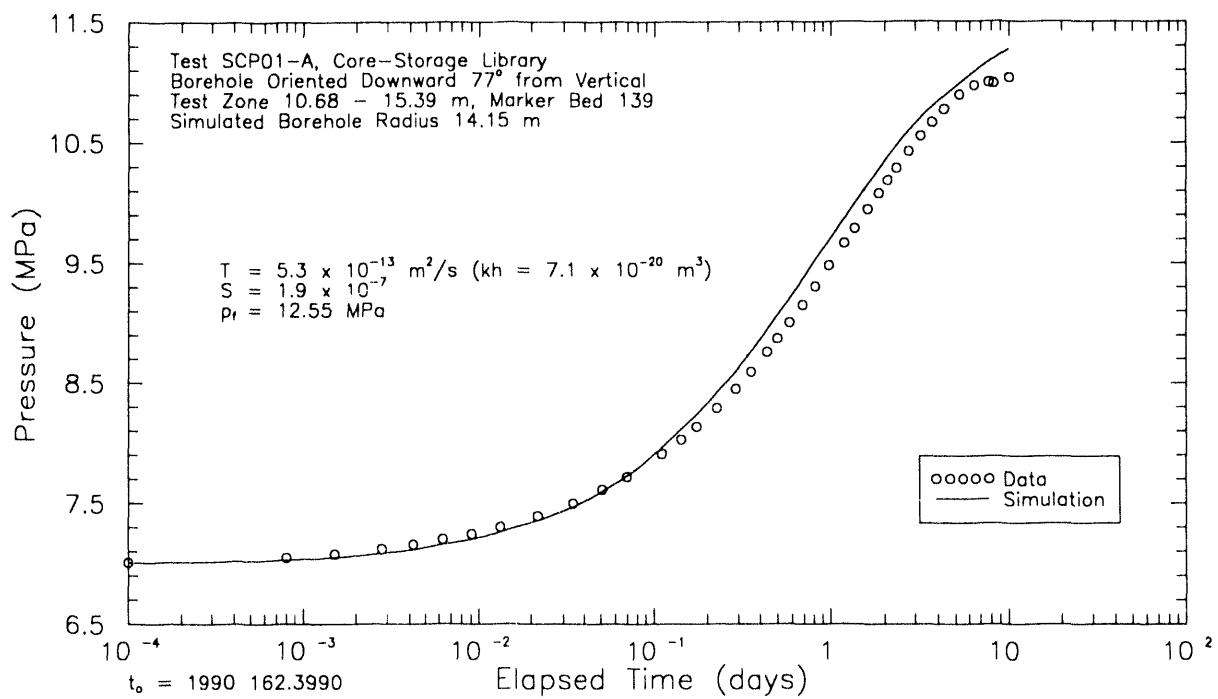

Figure 7-65. Semilog plot of GTFM simulation of SCP01-A pulse-withdrawal test #2.

126

times corresponding to the decreases in test-zone pressure (Figure 7-57).

Figure 7-66 is a plot of the best-fit GTFM simulated and observed cumulative fluid production for the two constant-pressure withdrawal tests. As the test-zone pressure was lowered to initiate the first and second tests, instantaneous production volumes of 38.1 and 31.8 cm^3, respectively, were observed. These volumes were produced from the zone due to test-zone compressibility. On June 25, 1990 (Calendar Day 176), four days after starting the first SCP01-A constant-pressure withdrawal test, the test zone was open to the atmosphere for less than a minute, which resulted in a pressure decrease from 8.2 to 2.7 MPa before the test zone was returned to about 8.1 MPa (Figure 7-57). For five days after the test zone was open to the atmosphere, the fluid-production rate was not consistent (Figure 7-58). However,

production consistent with the first two days of the constant-pressure withdrawal period was measured for the final three days of production. The GTFM analysis of the first SCP01-A constant-pressure withdrawal test does not reproduce the inconsistent data. However, the simulated production rate of 25.81 cm^3/day agrees with the measured flow rate of 25.83 cm^3/day for the late-time period of the test. Figures 7-67 and 7-68 present Horner plots for the first and second pressure-buildup tests, respectively, and Figure 7-69 shows the GTFM simulation of the entire SCP01-A testing sequence. The radius of influence determined from the GTFM simulations, using a one-percent pressure-change criterion, was about 12 m.

Summary. The analytical and numerical interpretations of the SCP01-A tests provided estimates of transmissivity ranging from 3.8 x 10^{-13} to 5.3 x 10^{-13} m^2/s (permeability-thickness
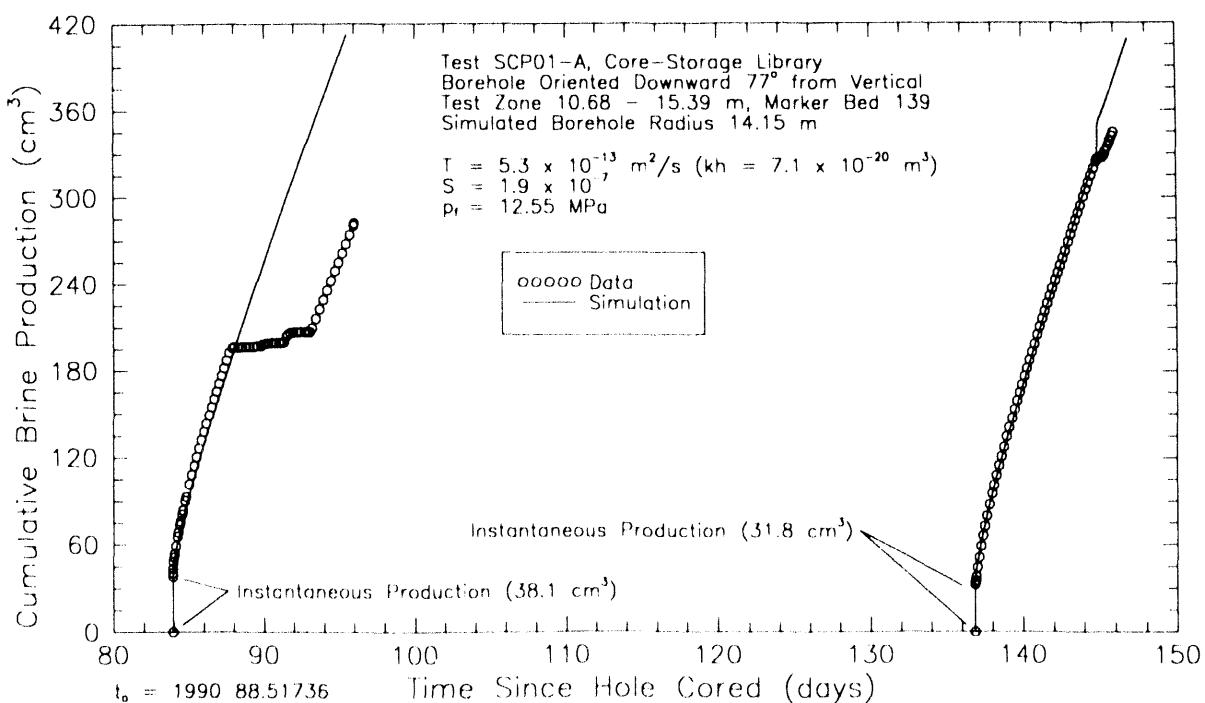

Figure 7-66. Linear-linear plot of GTFM simulation of brine production during SCP01-A constant-pressure withdrawal tests.

127
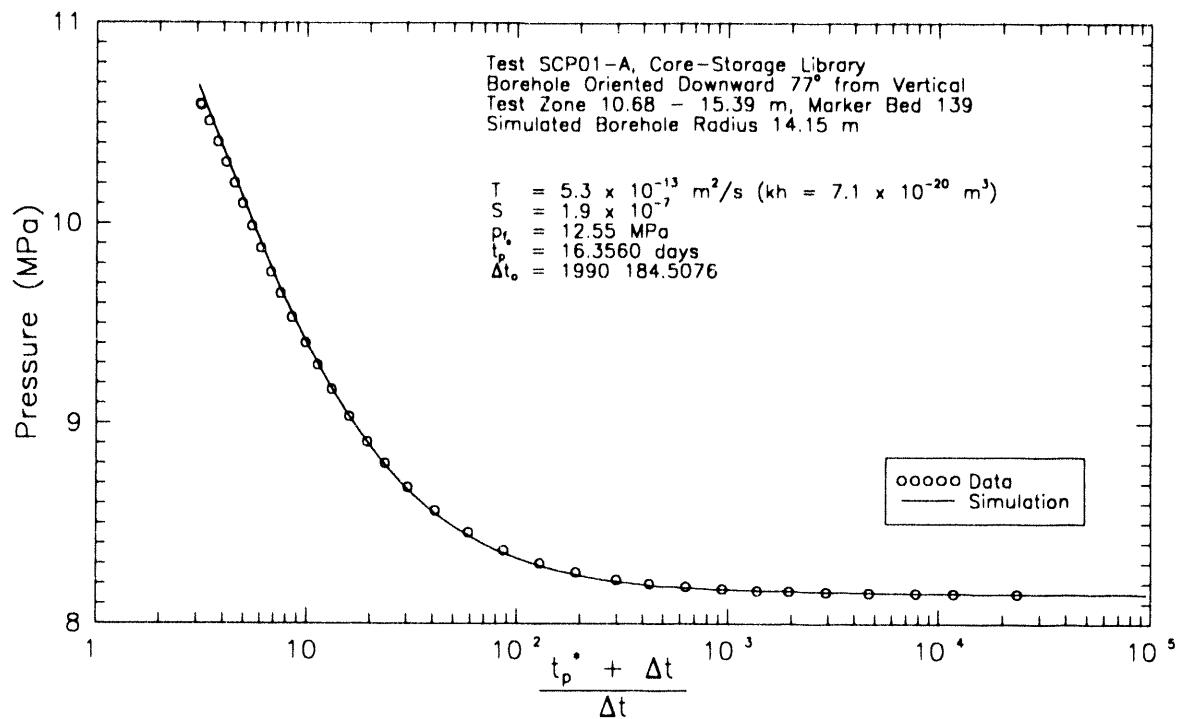
Figure 7-67. Horner plot of GTFM simulation of SCP01-A pressure-buildup test #1.
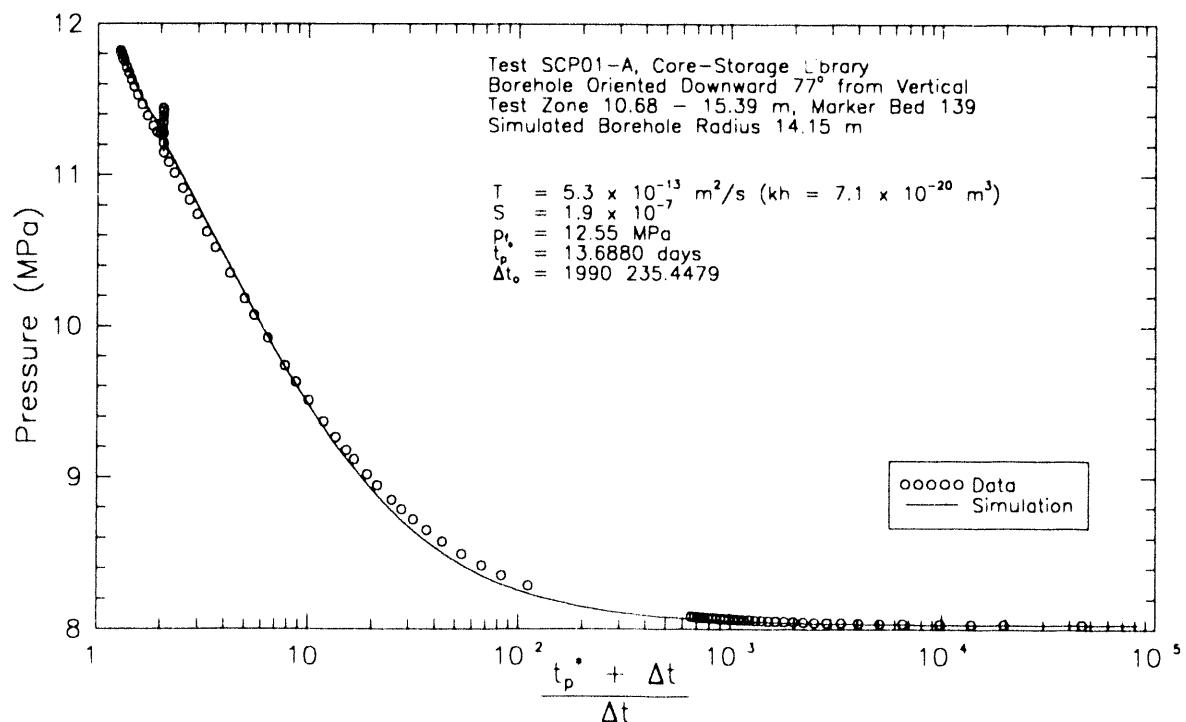

Figure 7-68. Horner plot of GTFM simulation of SCP01-A pressure-buildup test #2.

128
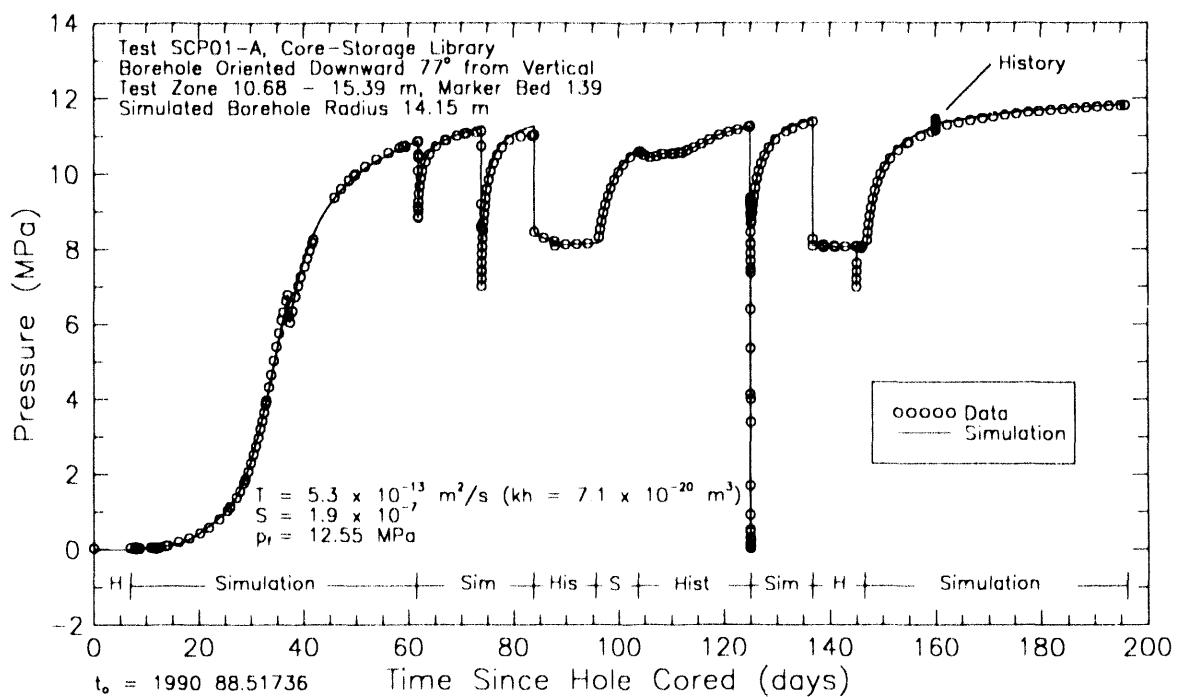
Figure 7-69. Linear-linear plot of GTFM simulation of entire SCP01-A testing sequence.

products of 5.1×10^{-20} to 7.1×10^{-20} m³) for Marker Bed 139. The formation pore pressure was estimated as 12.40 MPa in Interpret/2 simulations and as 12.55 MPa in GTFM simulations. GTFM provided good simulations of all of the tests using a storativity of 1.9×10^{-7}.

Using this value of storativity (expressed as total system compressibility), Interpret/2 calculates a radius of influence for the constant-pressure withdrawal and pressure-buildup tests of about 5 m. A radius of influence for the entire SCP01-A testing sequence of about 12 m was determined from the GTFM simulations using a one-percent pressure-change criterion. Neither Interpret/2 nor GTFM simulations indicated the presence of significant wellbore skin. No non-radial flow effects caused by the inclination of the borehole were evident, indicating that the vertical permeability of the anhydrite is insignificant.

Vertically averaged values of hydraulic conductivity (permeability) and specific storage can be calculated for the SCP01-A test zone by assuming that flow to the hole was horizontal only and that the flow was produced only by the 0.96-m vertical interval containing Marker Bed 139 and clay E. The average hydraulic conductivity of this interval is 4.0×10^{-13} to 5.5×10^{-13} m/s (permeability of 5.3×10^{-20} to 7.4×10^{-20} m²) and the specific storage is 1.95×10^{-7} m⁻¹.

7.1.8.2 Guard Zone. The guard zone in SCP01-A was shut in on April 10, 1990 (Calendar Day 100). After 17 days of apparently no pressure buildup, a pulse injection was performed on April 27, 1990 (Calendar Day 117) by raising the pressure to approximately 0.62 MPa. A pressure buildup to 0.98 MPa was then observed until July 11, 1990 (Calendar Day 192), at which time the guard-zone pressure started

129

increasing at a substantially higher rate (Figure 7-57). The rapid increase in pressure was attributed to leakage from the test zone to the guard zone past the test-zone packer (Section 7.1.8.1). After observing the pressure communication between the test and guard zones, the test and guard zones and test- and guard-zone packers were depressurized and the test tool was rotated on August 1, 1990 (Calendar Day 213). The test-zone and guard-zone packers were then reinflated and brine was injected into the guard zone to increase the pressure to 0.70 MPa. After observing a pressure buildup to only 0.83 MPa in the guard zone, a pulse injection was conducted on September 5, 1990 (Calendar Day 248) by raising the guard-zone pressure to approximately 2.95 MPa. After an initial decline, the pressure in the guard zone increased to 2.96 MPa by the end of the testing period 36 days later.

Guard-zone compressibility values were determined before removing the test tool at the end of the testing period. Guard-zone compressibility values of 1.65×10^{-8}, 4.35×10^{-8}, and 3.12×10^{-7} Pa^{-1} were determined for pressure decreases from 2.26 to 1.47 MPa, from 1.48 to 0.78 MPa, and from 0.78 to 0.12 MPa, respectively (Table 6-2).

GTFM simulations were performed to attempt to match the pressure behavior observed in the SCP01-A guard zone, but no defendable interpretations could be obtained. The small pressure changes observed during the tests do not provide any basis for estimating the true formation pore pressure around the hole. The observed data could probably be matched for any assumed value of formation pore pressure above 3 MPa by modifying the estimated transmissivity, storativity, and guard-zone-compressibility-versus-pressure function.

Reliable, defendable quantification of the transmissivity of the SCP01-A guard zone would require pressure responses more definitive (i.e., of higher magnitude) than those observed. These might be obtained by either having test durations of several years or by significantly reducing the guard-zone compressibility.

7.2 Discussion of Results

Beauheim et al. (1991) discussed how the disturbed-rock zone (DRZ) that forms around underground excavations might affect the parameters interpreted from hydraulic testing in the Salado Formation. They identified a number of factors relating to DRZ development, and sought to establish relationships among those factors and hydraulic properties based on the limited data available at that time. Those factors and relationships can be re-examined with the additional data provided by this report. Other aspects of the test interpretations, such as the assumption of Darcian flow and the treatment of slanted wells, can also be evaluated by examining and comparing interpretations of different tests.

7.2.1 EFFECTS OF DISTURBED-ROCK ZONE.

Beauheim et al. (1991) discussed current hypotheses about the formation of disturbed-rock zones (DRZs) around underground excavations and how hydraulic properties might be affected within a DRZ. They related the results of permeability testing completed at that time to factors identified by Borns and Stormont (1988) as affecting the amount of rock disturbance occurring around excavations in response to stress relief. These factors include the distance at which a test was conducted from an excavation, the size and age of the excavation, and the orientation of the test hole with respect to the excavation. In general, Beauheim et al. (1991) found possible correlations between

increasing proximity to an excavation and increasing permeability and decreasing formation pore pressure, subject to several complicating factors. Properties appear to be disturbed more by large excavations than by sm?!: excavations, and the amount of disturbance appears to increase as excavations age. In addition, they found lower permeability and higher formation pore pressure when a unit was tested beneath the rib or pillar of an excavation than when the same unit was tested directly beneath the excavation, indicating that the position of a test interval with respect to an excavation is also an important factor affecting hydraulic properties and conditions.

7.2.1.1 Relationship Between Hydraulic Conductivity and Distance From an Excavation. Figure 7-70 presents a plot of average hydraulic conductivity versus test-interval distance from an excavation from GTFM

simulations of the tests discussed both in this report and in Beauheim et al. (1991). The tests discussed in this report were, for the most part, conducted at greater distances from the excavations than the tests discussed by Beauheim et al. (1991). A wider variety of test-hole orientations is also considered in this report than in the previous report.

The current report adds only one value of halite hydraulic conductivity (from the S1P72-A guard zone) to the data base established by Beauheim et al. (1991). Compared to the other values of halite hydraulic conductivity shown on Figure 7-70, the value from the S1P72-A guard zone seems anomalously low given that zone's close proximity to an excavation. However, the S1P72-A measurement was made in the rib of an excavation whereas all the other halite measurements were made in the floor As noted by Beauheim et al. (1991), no consistent
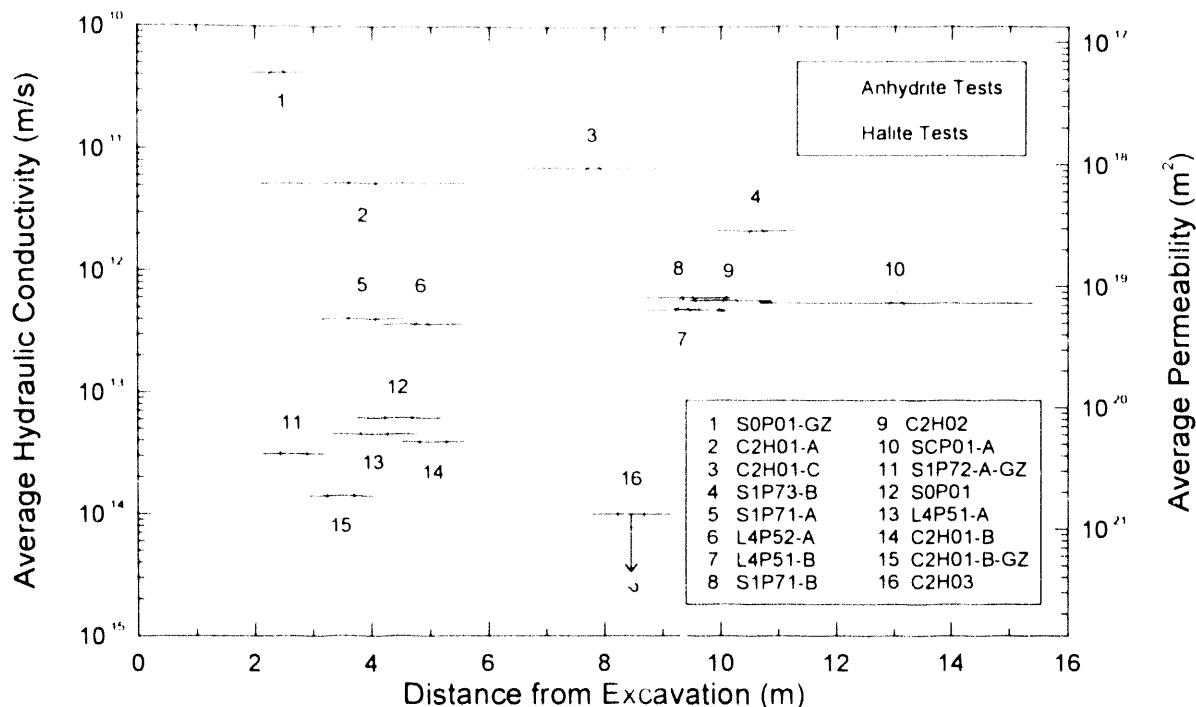

Figure 7-70. Interpreted average hydraulic conductivities versus distances from excavations to the tested intervals.

131

correlation is evident on Figure 7-70 between halite hydraulic conductivity and distance from an excavation. The lack of a correlation may be due, in part, to the fact that halite has not as yet been tested over a great range of distances from the excavations. In addition, the halite tests completed to date have not all been of strata with the same impurity compositions or contents.

Therefore, mineralogic differences could be contributing to the apparent nonsystematic relationship between halite hydraulic conductivity and distance from an excavation. A detailed study involving tens of tests of halite intervals at different orientations and distances from excavations, combined with careful mineralogic description of core samples, would probably be necessary to define how halite hydraulic conductivity is affected by nearby excavations.

Based on only three measurements of the hydraulic conductivity of Marker Bed 139, Beauheim et al. (1991) noted a correlation between increasing hydraulic conductivity and increasing proximity to an excavation. The current report adds five values of anhydrite hydraulic conductivity to the data base of Beauheim et al. (1991). The hydraulic conductivity of anhydrite has not been found to be lower than about 4×10^{-13} m/s (permeability of about 5×10^{-20} m^2) in any interval tested, regardless of distance from or orientation with respect to an excavation (Figure 7-70). The lowest values observed appear to occur in the ribs of excavations (C2H02, L4P52-A, and SCP01-A) or 9 m or more into the floor of excavations (L4P51-B and S1P71-B). Higher values are found directly above excavations (S1P73-B) and less than 8 m into the floor of excavations (C2H01-C and S0P01-GZ). Thus, any correlation between anhydrite hydraulic conductivity and distance from an excavation

appears to be limited to short distances from an excavation, and to be strongly affected by position with respect to the excavation.

A cautionary note is necessary, however, when discussing the hydraulic conductivity (or permeability) of anhydrite. The hydraulic conductivity values presented in this report and in Beauheim et al. (1991) represent average values assuming that the anhydrites are vertically homogeneous. Video observations in boreholes and examination of core specimens indicate that flow and hydraulic conductivity are concentrated in bedding-plane fractures that occupy variable, but small, percentages of the total thicknesses of the anhydrites. If a single fracture was present in a given anhydrite, occupying 1% of the total bed thickness, then the hydraulic conductivity of the fracture would be 100 times higher than the overall average. Variations in the number and apertures of fractures in different anhydrite interbeds at different locations make determination and comparisons of fracture hydraulic conductivities difficult.

7.2.1.2 Relationship Between Formation Pore Pressure and Distance From an Excavation.

At equilibrium, pore pressures around an excavation should reflect steady flow toward the excavation driven by the difference between the far-field pore pressure in the formation and the pressure in the excavation. The time required for this equilibrium condition to be established after an excavation is opened is dependent on the mechanical and hydraulic properties of the rock. When an excavation is first opened, a disequilibrium condition is created between the atmospheric pressure in the excavation and the pore pressure initially present in the surrounding rock. This disequilibrium leads to flow from the rock into the excavation, causing the pore pressure in the rock to decrease. With time, the

pore pressure in the rock is decreased to greater and greater distances from the excavation. In addition to the changes in pore pressure caused by flow, the mining of an excavation also changes pore pressures by changing the state of stress in the surrounding rock mass. The change in the stress in the rock causes an instantaneous change in pore pressure throughout the affected volume of rock. The pore-pressure change is given by Skempton's (1954) coefficient as some fraction of the stress change. The change in stress is a time-dependent process and, therefore, changes in pore pressures have two transient components: one arising from the evolution of the flow field and one arising from the evolution of the stress field. Which, if either, of these components dominates the pore-pressure response at a given time and place depends on the hydraulic and mechanical properties of the medium.

In a medium such as halite that is not linearly elastic, pore pressures may also change during deformation caused by creep, which is itself a time-dependent process. Thus, the evolution of pore pressures in halite is dependent on multiple processes, most of which are affected to some degree by distance from an excavation, but on different time scales. Developing a full understanding of those processes is beyond the scope of the work discussed in this report.

Figure 7-71 presents a plot of formation pore pressure versus test-interval distance from an excavation from GTFM simulations of the tests discussed both in this report and in Beauheim et al. (1991). The current report adds four values of halite pore pressure to the data base of Beauheim et al. (1991). The pore pressure in the S1P72-A guard zone was higher than in many other halite intervals at similar or greater
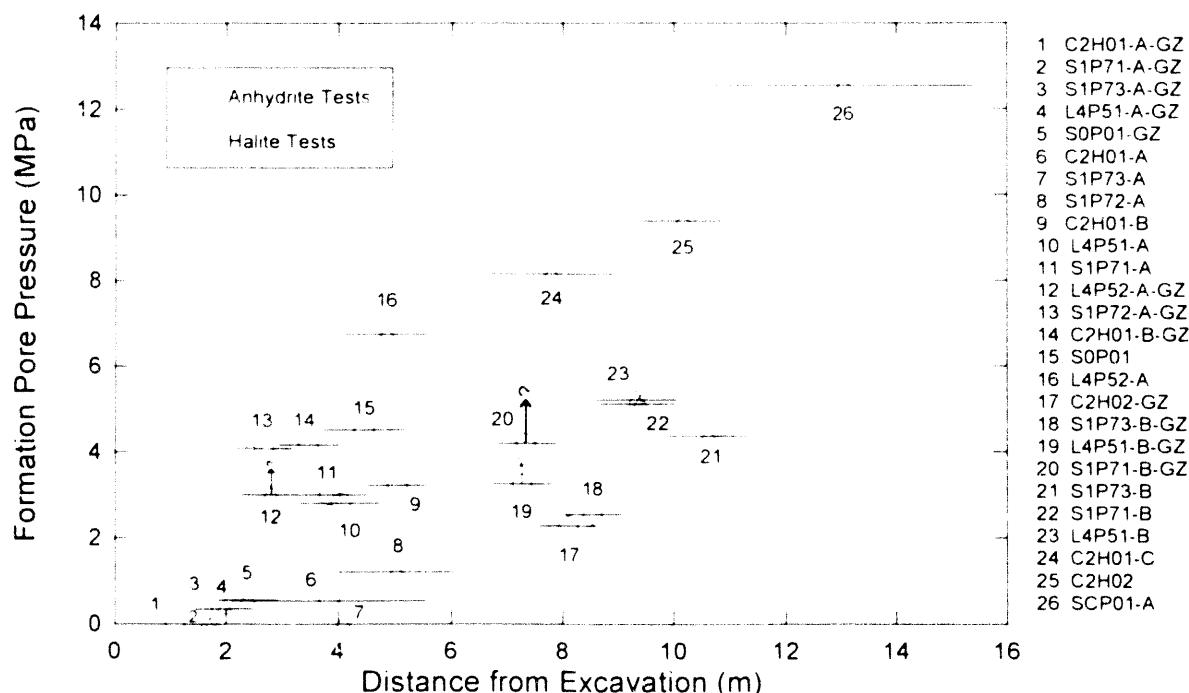

Figure 7-71   Interpreted formation pore pressures versus distances from excavations to the tested intervals

distances from an excavation (Figure 7-71), perhaps indicating less stress relief near the corner of a room than in the floor. In contrast, the pressure in the S1P73-B guard zone, which was farther from but directly above an excavation, was relatively low. Conditions above excavations are affected by gravity pulling down and tending to separate strata along planes of weakness such as bedding planes.

The new data on anhydrite pore pressures from nine locations generally support the observation of Beauheim et al. (1991) of increasing anhydrite pore pressure with increasing distance from an excavation (Figure 7-71), with one major qualification. Pore pressures tend to be lower directly above excavations (S1P73-A test zone and guard zone and S1P73-B) than at comparable distances in other directions from excavations. Comparing pore pressures between test zones and guard zones in individual

boreholes in Figure 7-71, we see that, with the exceptions of S1P72 and C2H01, pore pressures in test zones are higher than pore pressures in guard zones. This observation supports the hypothesis that the Salado becomes progressively depressurized with closer proximity to the repository. Figure 7-72 shows formation pore pressures from L4P51 and S1P71, where two sets of tests have been conducted at different depths, plotted as a function of depth. The pressures and pressure gradients observed in the two holes are very similar, perhaps indicating that DRZs beneath Rooms L4 and 7, which have the same width and were of similar ages at the times of testing, have developed in similar ways. Clear pressure gradients toward the excavations are evident at both locations.

During S1P72-A testing, the highest pressure observed in Marker Bed 139 in the test zone, 4.40 to 6.00 m from Room 7, was about 1.2
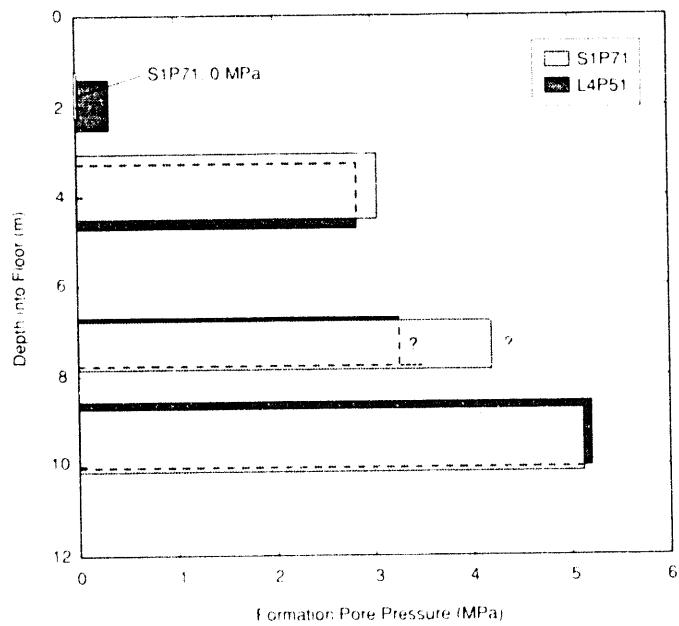

Figure 7-72. Interpreted formation pore pressures versus depth in boreholes L4P51 and S1P71.

134

MPa, while the apparent formation pore pressure in the halite guard zone, 2.15 to 3.18 m from Room 7, was about 4.1 MPa. The pressure in Marker Bed 139 at this location is low and continually decreasing because, we believe, of flow towards the excavation. As discussed in Section 7.1.5.1, Marker Bed 139 is at atmospheric pressure beneath the floor of Room 7 at borehole S1P71. The higher permeability of Marker Bed 139 relative to that of the halite in the S1P72-A guard zone allows more flow toward the excavation and, hence, faster depressurization.

Beauheim et al. (1991) noted that the pore pressure in the C2H01-B test zone, 4.50 to 5.58 m below Room C2, was about 1 MPa lower than that in the guard zone, 2.92 to 4.02 m below the room. They hypothesized that time-dependent deformation processes coupled with vertical heterogeneity in the mechanical properties of the rock might cause localized changes in pore pressure on a time scale shorter than the time required for fluid flow to re-equilibrate the pressures.

7.2.1.3 Comparison of Tests of the Same Strata.
Two of the tests discussed in this report were of the same stratigraphic interval in the same position relative to similarly sized excavations of similar ages at the times of testing. These tests were the L4P51-B and S1P71-B tests of anhydrite "c". The interpreted transmissivities and storativities from these tests were identical (4.8 x 10^{-14} m^2/s and 1.0 x 10^{-8}, respectively) and the formation pore pressures were nearly the same (5.21 and 5.12 MPa; Table 7-1). These results indicate a low degree of heterogeneity in the hydraulic properties of anhydrite "c", and that the history of disturbance at these two locations was probably similar.

7.2.2 EVALUATION OF EVAPORITE FLOW REGIME.
To determine whether or not the hydraulic gradient created during a test affected the transmissivity interpreted from Darcy-flow models such as Interpret/2 and GTFM, different starting pressure differentials were used for successive pressure-pulse tests at individual locations. For instance, the first pulse-withdrawal test at L4P51-B had an initial pressure differential of about 1.09 MPa and the initial pressure differential for the second pulse-withdrawal test was about 2.05 MPa (Table 6-2). At SCP01-A, the initial pressure differentials for the first and second pulse-withdrawal tests were about 2.03 and 4.12 MPa, respectively. For all test sequences, good GTFM simulations of each test phase were obtained using the same hydraulic parameters. The magnitude of the initial pressure differential appeared to have no effect on the hydraulic properties interpreted from a test. The nature of the test performed also appeared to have no influence on the interpreted hydraulic properties. That is, pressure-pulse tests, constant-pressure flow tests, and pressure-buildup tests of individual strata could all be simulated using the same hydraulic properties.

However, as discussed in Section 6.2, the existence of Darcy flow under conditions of low hydraulic gradients and low hydraulic conductivities has not been demonstrated. Success in applying a Darcy-flow model to the interpretation of the Salado hydraulic tests conducted under high-gradient conditions does not necessarily imply that that model would provide a valid description of flow through the Salado under natural low-gradient conditions. The available data suggest that a Darcy-flow model should adequately describe flow in the near-field around the WIPP repository where gradients are high, but the far-field boundary conditions that should be applied to the model

are uncertain. Sensitivity studies should be performed using a numerical model to determine the effects that different boundary conditions might have on flow to or from the repository and whether or not *in situ* definition of those boundary conditions is important.

Uncertainty about hydraulic properties being independent of hydraulic gradient is associated with uncertainty in how test-zone compressibility varies during test sequences. In some instances (e.g., SCP01-A), the simulation parameters for successive test phases were not entirely identical because test-zone compressibility was allowed to vary. As discussed in Section 6.3.2, these variations are considered to have a valid empirical basis, but the fact remains that the exact variations used were fitted to the simulations, not measured. However, as shown in the figures in Appendix D, the imposed variations in test-zone compressibility during individual testing sequences after the initial pressure-buildup period were typically less than an order of magnitude. Any potential variations in transmissivity being masked by the imposed variations in test-zone compressibility would, therefore, be considerably less than an order of magnitude. In the case of the L4P51-B tests, test-zone compressibility was held constant for all of the simulations and good matches were obtained to the data from each of the test phases after the initial buildup period using the same hydraulic properties (Figures 7-11 through 7-15).

In addition to providing evidence on the existence of Darcy flow, other objectives of the test interpretations relating to the nature of flow through evaporites were to determine: (1) whether or not hydraulic boundaries were evident on the scale of testing; (2) whether individual strata behaved as if they were hydraulically confined or leaky; and (3) whether fractured anhydrites behaved hydraulically as single-porosity or double-porosity media. No hydraulic boundaries were evident during any of the tests discussed in this report. On the scale of the tests, which had calculated radii of influence ranging from about 2 to 20 m, the tested strata behaved as though they were infinite. Leakage and/or double-porosity responses were also not observed during any of the tests. Leakage was considered most likely to be evident during tests of anhydrite beds which are bounded above and below by halite beds having lower permeability than the anhydrite. Double-porosity behavior was also considered a possibility for fractured anhydrite beds. Leakage and double-porosity affect pressure-buildup data in similar ways (Gringarten, 1984), causing a temporary stabilization of pressure (or a minimum in the pressure derivative) when the leaky bed or matrix porosity begins contributing flow to the permeable bed or fractures. The two effects can be difficult to tell apart, but neither effect was evident in any of the tests discussed in this report. The absence of these effects may imply that the vertical permeability of halite and/or the permeability of the anhydrite matrix is several orders of magnitude lower than that of the fractures in the anhydrite and that longer duration flow and buildup tests would be required to see a response from the low-permeability component(s) of the system.

As discussed in Section 6.2, slanted holes were treated as vertical cylindrical holes for test interpretation. From a theoretical standpoint, this treatment is thought to provide an accurate interpretation of tests provided that the ratio of vertical to horizontal permeability in the tested intervals is less than 0.1. No direct measurements of hydraulic anisotropy in either halite or anhydrite have yet been performed. Qualitative information is available, however,

from observation of the rock. Considering the method of formation of halite beds and the cubic symmetry of halite crystals, no reason is apparent for permeability to differ vertically and horizontally within a single bed in an isotropic stress field. Mineralogic differences between beds, such as the presence of clay, could create anisotropy on the multibed scale. Anisotropic stresses in the near field around the repository could also result in anisotropic permeability in halite. However, for the single halite test discussed in this report, that of the S1P72-A guard zone which spanned portions of two beds, the presence or absence of hydraulic anisotropy must be considered unknown. Therefore, as discussed in Section 7.1.5.2, we remain uncertain as to whether this test is better interpreted in terms of radial flow to a slanted hole or in terms of horizontal flow to an equivalent vertical hole.

The evidence for hydraulic anisotropy in anhydrite is less equivocal. Video examinations of brine and gas flow from anhydrite layers into boreholes as well as examinations of core all indicate that most of the permeability of anhydrite comes from subhorizontal bedding-plane fractures. No high-angle fractures, which might provide significant vertical permeability, have been observed. While no direct measurements of the matrix permeability of anhydrite are available as yet, we believe that the permeability of the fractures in anhydrite must be several orders of magnitude higher than that of the matrix, and that flow through anhydrites is almost entirely through the subhorizontal fractures. In the absence of significant vertical flow, the tests of anhydrite in slanted holes can be reliably interpreted in terms of horizontal flow to equivalent vertical holes. The good match between the constant-pressure flow data from

the SCP01-A test of Marker Bed 139 and a radial-flow type curve (Figure 7-60) provides an indication that flow through the anhydrite is exclusively horizontal. Laboratory measurements on anhydrite core samples are planned to address the question of hydraulic anisotropy in anhydrite directly.

Beauheim et al. (1991) estimated values for the specific storage of halite and anhydrite based on laboratory measurements of the material properties of those types of rocks (Table 6-1). They then treated specific storage as a fixed or specified parameter in their GTFM simulations of pressure-pulse tests because pressure-pulse tests alone provide little information on specific storage. In this report, specific storage (or storativity) was treated as a fitting parameter in GTFM simulations because the combination of constant-pressure flow tests with pressure-pulse and pressure-buildup tests allows more reliable definition of its value.

Only one value for the specific storage of halite is provided by this report. That value, from the S1P72-A guard-zone test of map unit 0 and polyhalitic halite 4, is 2.1×10^{-7} m^{-1}. This value falls within the range of 2.8×10^{-8} to 3.5×10^{-7} m^{-1} estimated prior to testing (Table 6-1). The values of anhydrite specific storage interpreted from the tests discussed in this report also agree well with the estimates made prior to testing, despite the fact that the anhydrites are fractured, which increases their compressibility to an uncertain extent. All of the interpreted values of anhydrite specific storage fall within the estimated range of 9.7×10^{-8} to 2.3×10^{-7} m^{-1} except for the value of 1.0×10^{-5} m^{-1} from the S1P73-B test of Marker Bed 138. The only explanation that can be given for this high value is that, because of roof sag directly above Room

7, the fractures in Marker Bed 138 at S1P73 may be more highly compressible than fractures in other anhydrite layers or in other positions with respect to the excavations.

8. SUMMARY AND CONCLUSIONS

This report presents interpretations of hydraulic tests conducted in bedded evaporites of the Salado Formation from mid-1989 through mid-1992. The report supplements a report by Beauheim et al. (1991) on tests conducted from 1988 through early 1990. The tests discussed in this report were conducted on nine intervals in six boreholes drilled from the underground WIPP facility. A summary of the test-interpretation results and conclusions about the hydraulic properties and behavior of the Salado Formation are presented below.

8.1 Results of Testing

The primary objectives of the hydraulic tests were to estimate the transmissivities, storativities, and formation pore pressures of different stratigraphic intervals in the Salado Formation around the WIPP facility. Pressure-pulse, constant-pressure withdrawal, and/or pressure-buildup tests of five stratigraphic units were successfully conducted in six intervals. Interpreted transmissivities range from 3.8×10^{-14} to 5.3×10^{-13} m^2/s for anhydrite intervals, with vertically averaged hydraulic conductivities ranging from 3.8×10^{-13} to 2.2×10^{-12} m/s (permeabilities of 5.1×10^{-20} to 2.9×10^{-19} m^2). The transmissivity of a halite interval tested was about 7.4×10^{-15} m^2/s, with an average hydraulic conductivity of either 1.4×10^{-14} or 7.2×10^{-15} m/s (permeability of 1.8×10^{-21} or 9.6×10^{-22} m^2), depending on whether flow was horizontal or radial toward the slanted test interval. The transmissivity of another halite interval in the SCP01-A guard zone was apparently too low to measure over a six-month period. The lack of interpretable responses in this interval is believed to reflect a combination of low transmissivity

($<10^{-14}$ m^2/s) and high guard-zone compressibility.

The storativities of the anhydrite intervals tested range from 1.0×10^{-8} to 1.7×10^{-6}, with vertically averaged specific storage values ranging from 1.0×10^{-7} to 1.0×10^{-5} m^{-1}. The only calculated specific storage greater than 2.0×10^{-7} m^{-1} was from Marker Bed 138 above Room 7 of Waste Panel 1 (test S1P73-B). Roof sag at this location may have increased the compressibility of fractures in Marker Bed 138. The halite interval tested had an interpreted storativity of 5.0×10^{-8}, with a corresponding specific storage of either 9.2×10^{-8} or 1.0×10^{-7} m^{-1}, depending on whether flow was horizontal or radial toward the slanted test interval.

The formation pore pressures of the anhydrite intervals tested range from zero (or atmospheric) in anhydrites "a" and "b" directly above Room 7 of Waste Panel 1 to 12.55 MPa in Marker Bed 139 beyond the westernmost extreme of the core-storage library. Pore pressures in halite intervals range from about 2.55 MPa to greater than 4.2 MPa. Pore pressures in halite may be decreased more by stress relief around the excavations than those in anhydrite because of the different mechanical and rheological responses of the two rock types.

Another objective of the test interpretations was to determine the radii of influence of the tests. The calculated radii of influence of the anhydrite tests range from 2 to 20 m and the radius of influence of the one successful halite test was about 4 m. Stormont et al. (1991) found that borehole excavation (drilling) in halite resulted in

139

increased permeability around the borehole, but only to a distance of about three borehole radii. Therefore, the calculated radii of influence are all great enough to lend confidence that the interpreted hydraulic properties have not been significantly affected by disturbed zones around the boreholes.

The results of the hydraulic tests discussed both in this report and by Beauheim et al. (1991) were used to evaluate how the presence of the WIPP facility has affected hydraulic conductivities and formation pore pressures in the surrounding rock. No firm conclusions can be drawn about possible changes in hydraulic conductivity around the repository. Within approximately 2 to 3 m of the excavations, the rock appears to be significantly destressed and fractured. This zone may be larger vertically above than laterally around an excavation, as reported by Stormont (1990). Too few halite tests have been performed to determine if, beyond 3 m, additional distance from an excavation has an effect on hydraulic conductivity. The average hydraulic conductivity of anhydrite has not been found to be lower than about 4×10^{-13} m/s in any interval tested, regardless of distance from or orientation with respect to an excavation (Figure 7-70). The lowest values observed occur in the ribs of excavations or 9 m or more into the floor of excavations. Higher values are found directly above excavations and less than 8 m into the floor of excavations. Thus, any correlation between anhydrite hydraulic conductivity and distance from an excavation appears to be limited to 8 m or less from an excavation, and to be strongly affected by position with respect to the excavation.

Pore pressures tend to increase with distance from the excavations, although the orientation of a test interval with respect to an excavation also influences the pressures observed. In particular, pressures tend to be lower directly above excavations and higher in the ribs of excavations than at similar distances directly below excavations. Also, pore pressures in halite appear to be decreased more by stress relief around the excavations than those in anhydrite, probably because of the different mechanical responses of the two rock types. The highest formation pore pressure yet encountered was observed in an anhydrite interval that was both farther from the excavations than any other interval tested and also in the rib of an excavation. This pressure was 12.55 MPa in Marker Bed 139 in borehole SCP01, 10.5 to 14.8 m from the excavations. Whether this pressure represents the undisturbed far-field pressure or has been lowered by excavation effects is uncertain. Pressures 3 MPa or more lower (i.e., 9.3 MPa and less) have been observed in anhydrite layers at distances of about 10 m from the excavations (Figure 7-71), indicating that the depressured zone around the excavations extends to at least that distance. In contrast, the highest pore pressure measured to date in a halite interval during this testing program is only 4.5 MPa, observed in the S0P01 test zone 3.7 to 5.2 m below an excavation (Beauheim et al., 1991; corrected for elevation head).

The assumption of Darcy flow through evaporites was evaluated by performing successive pressure-pulse tests with initial pressure differentials differing by a factor of two. For pulse-withdrawal tests, the magnitude of the induced pressure differential had no apparent effect on the interpreted hydraulic parameters. Pressure-pulse tests, however, create a short-lived, localized change in pore pressure and may not adequately represent flow under conditions of long-term, wide-spread changes in gradient. A series of constant-pressure flow tests performed

at different driving pressures, both injection and withdrawal, might provide a better determination of the sensitivity of hydraulic properties to hydraulic gradient. The available data show, however, that models that assume Darcy flow are able to replicate the flow and pressure behavior of entire testing sequences involving different types of tests, from which we conclude that an assumption of Darcy flow provides a reasonable approach to understanding flow through evaporites, at least under high-gradient conditions. The applicability of Darcy's law to flow under the low gradients naturally existing in the Salado Formation remains uncertain.

No evidence was detected of hydraulic boundaries, leakage, or double-porosity effects in the tests discussed in this report. Radial-flow models fit all of the test data well, even when the tests were conducted in slanted holes. The presence or absence of hydraulic anisotropy in halite is uncertain. Flow in anhydrite interbeds appears to be controlled by subhorizontal bedding-plane fractures, which provide horizontal hydraulic conductivity much higher than the vertical hydraulic conductivity provided by the unfractured anhydrite matrix.

8.2 Future Testing Plans and Considerations

Both compliance testing and testing in boreholes have shown that test-zone compressibility decreases as a function of increasing test-zone pressure (Figure 6-6). The tests of the S1P71-B test zone (Figure 7-27) and SCP01-A guard zone (Figure 7-57) showed that initial pressure buildups can take impractically long times when the zone compressibility at low pressures is greater than about 10^{-8} Pa^{-1}. As demonstrated during the S1P71-B test, the pressure buildup

can be accelerated by injecting fluid to increase the zone pressure to a level at which the zone compressibility is lower. This procedure will be employed during all future tests when the initial rate of pressure buildup is low.

In addition to affecting the time required to complete tests, the dependence of test-zone compressibility on test-zone pressure also affects the interpretation of tests. The interpretations presented in this report have shown that defendable estimation of hydraulic parameters from tests in low-permeability systems requires knowledge of test-zone compressibility throughout the testing sequence. For future tests, test-zone compressibility will be measured as continuous functions of decreasing and increasing pressure at the end of each testing sequence. Consideration will also be given to modifying the test tools so as to allow measurement of test-zone compressibility at any time during a testing sequence without significantly disturbing the tests.

While this report was being prepared, tests of six additional intervals were initiated. These include tests of Marker Bed 140 (L4P51-C), halite above Marker Bed 140 (L4P51-C guard zone), anhydrite "a" (S1P74-A), anhydrite "b" (S1P74-A guard zone), Marker Bed 138 (L4P52-B), and clay J (L4P52-B guard zone). The potential pressure-dependence of the transmissivity of Marker Bed 138 in borehole L4P52 is being investigated by performing, first, a constant-pressure withdrawal test, followed by constant-pressure injection tests using different injection pressures. This experimental program is currently scheduled to conclude with additional tests of Marker Bed 138 (S1P74-B), clay J (S1P74-B guard zone), and argillaceous halite

below Marker Bed 140 (L4P51-D), where little or no excavation-induced changes in either pore pressure or permeability are expected.

Hydraulic testing of Marker Beds 139 and 140 is also being performed in Room C1 (Figure 5-1) in conjunction with hydraulic fracturing studies of anhydrite interbeds (Beauheim et al., 1993). Constant-pressure injection and/or withdrawal tests are being performed before and after hydraulic fracturing of the interbeds. Observation holes 3 to 10 m from the main test holes are used to assess the effects of the hydraulic fracturing on the transmissivity and storativity of the interbeds. The results of the pre-hydraulic fracturing tests will be summarized in the third and final interpretive report in this series.

8.3 Conclusions

Pressure-pulse, constant-pressure flow, and pressure-buildup tests have been performed in bedded evaporites of the Salado Formation at the WIPP site to evaluate the hydraulic properties controlling brine flow through the Salado. Transmissivities ranging from about 7×10^{-15} to 5×10^{-13} m²/s have been interpreted from six sequences of tests conducted on five

stratigraphic intervals within 15 m of the WIPP underground excavations. The corresponding vertically averaged hydraulic conductivities of the intervals range from about 1×10^{-14} to 2×10^{-12} m/s (permeabilities of 2×10^{-21} to 3×10^{-19} m²). Storativities of the tested intervals range from about 1×10^{-8} to 2×10^{-6}, and values of specific storage range from 9×10^{-8} to 1×10^{-5} m⁻¹. Pore pressures in eight stratigraphic intervals range from about 2.5 to 12.5 MPa, and appear to be affected by stress relief around the excavations. Anhydrite interbeds appear to be one or more orders of magnitude more permeable than the surrounding halite, primarily because of subhorizontal bedding-plane fractures present in the anhydrites. Interpretations of the tests revealed no apparent boundaries within the radii of influence of the tests, which were calculated to range from about 2 to 20 m from the test holes. An assumption of Darcy flow through the evaporites is thought to be a reasonable interpretive approach because Darcy-flow models are able to replicate the flow and pressure behavior observed during entire testing sequences involving different types of tests performed with different hydraulic gradients.

9. REFERENCES

Abbaszadeh, M., and P.S. Hegeman. 1990. "Pressure-Transient Analysis for a Slanted Well in a Reservoir with Vertical Pressure Support," *SPE Formation Evaluation*. Vol. 5, no. 3, 277-284.

Beauheim, R.L., G.J. Saulnier, Jr., and J.D. Avis. 1991. *Interpretation of Brine-Permeability Tests of the Salado Formation at the Waste Isolation Pilot Plant Site: First Interim Report*. SAND90-0083. Albuquerque, NM: Sandia National Laboratories.

Beauheim, R.L., W.R. Wawersik, and R.M. Roberts. 1993. "Coupled Permeability and Hydrofracture Tests to Assess the Waste-Containment Properties of Fractured Anhydrite," *International Journal of Rock Mechanics and Mining Sciences*. In press.

Bechtel National, Inc. 1986. *Interim Geotechnical Field Data Report, Fall 1986*. DOE-WIPP 86-012. Carlsbad, NM: US DOE.

Borns, D.J., and J.C. Stormont. 1988. *An Interim Report on Excavation Effect Studies at the Waste Isolation Pilot Plant: The Delineation of the Disturbed Rock Zone*. SAND87-1375. Albuquerque, NM: Sandia National Laboratories.

Bourdet, D., J.A. Ayoub, and Y.M. Pirard. 1989. "Use of Pressure Derivative in Well-Test Interpretation," *SPE Formation Evaluation*. Vol. 4, no. 2, 293-302.

Bredehoeft, J.D., and S.S. Papadopulos. 1980. "A Method for Determining the Hydraulic Properties of Tight Formations," *Water Resources Research*. Vol. 16, no. 1, 233-238.

Cinco, H., F.G. Miller, and H.J. Ramey, Jr. 1975. "Unsteady-State Pressure Distribution Created by a Directionally Drilled Well," *Journal of Petroleum Technology*. Vol. 27, no. 11, 1392-1400.

Cooper, H.H., Jr., and C.E. Jacob. 1946. "A Generalized Graphical Method for Evaluating Formation Constants and Summarizing Well-Field History," *Transactions, American Geophysical Union*. Vol. 27, no. IV, 526-534.

Darcy, H. 1856. *Les Fontaines Publiques de la Ville de Dijon*. Paris, France: Victor Dalmont; Ann Arbor, MI: University Microfilms International.

Davis, P.A., N.E. Olague, and M.T. Goodrich. 1992. "Application of a Validation Strategy to Darcy's Experiment," *Advances in Water Resources*. Vol. 15, no. 3, 175-180.

Deal, D.E., R.J. Abitz, D.S. Belski, J.B. Case, M.E. Crawley, R.M. Deshler, P.E. Drez, C.A. Givens, R.B. King, B.A. Lauctes, J. Myers, S. Niou, J.M. Pietz, W.M. Roggenthen, J.R. Tyburski, and M.G. Wallace. 1989. *Brine Sampling and Evaluation Program 1988 Report*. DOE/WIPP 89-015. Carlsbad, NM: US DOE.

Deal, D.E., R.J. Abitz, D.S. Belski, J.B. Clark, M.E. Crawley, and M.L. Martin. 1991. *Brine Sampling and Evaluation Program 1989 Report*. DOE/WIPP 91-009. Carlsbad, NM: US DOE.

Earlougher, R.C., Jr. 1977. *Advances in Well Test Analysis*. Monograph Volume 5. Dallas, TX: Society of Petroleum Engineers of AIME. 264 p.

Ehlig-Economides, C.A. 1979. "Well Test Analysis for Wells Produced at a Constant Pressure". PhD dissertation. Palo Alto, CA: Dept. of Petroleum Engineering, Stanford University. 117 p.

Ehlig-Economides, C.A., and H.J. Ramey, Jr. 1981. "Transient Rate Decline Analysis for Wells Produced at Constant Pressure". *Society of Petroleum Engineers Journal*. Vol. 21, no 1, 98-104.

Fetkovich, M.J. 1980. "Decline Curve Analysis Using Type Curves," *Journal of Petroleum Technology*. Vol. 32, no. 6. 1065-1077.

Gringarten, A.C. 1984. "Interpretation of Tests in Fissured and Multilayered Reservoirs with Double-Porosity Behavior: Theory and Practice," *Journal of Petroleum Technology*. Vol. 36, no. 4, 549-564.

Gringarten, A.C., D.P. Bourdet, P.A. Landel, and V.J. Kniazeff. 1979. "A Comparison Between Different Skin and Wellbore Storage Type Curves for Early-Time Transient Analysis," *54th Annual SPE Technical Conference and Exhibition, Las Vegas, NV, September 1979*. SPE 8205. Richardson, TX: Society of Petroleum Engineers.

Holt, R.M., and D.W. Powers. 1990. *Geologic Mapping of the Air Intake Shaft at the Waste Isolation Pilot Plant*. DOE/WIPP 90-051. Carlsbad, NM: US DOE.

Horner, D.R. 1951. "Pressure Build-Up in Wells," *Proceedings Third World Petroleum Congress, The Hague, Netherlands, May 29, 1951*. Leiden: E.J. Bill. Sec. II:503-523.

Hsieh, P.A., S.P. Neuman, and E.S. Simpson. 1983. *Pressure Testing of Fractured Rocks--A Methodology Employing Three-Dimensional Cross-Hole Tests*. NUREG/CR-3213. Washington, DC: US NRC.

Jacob, C.E., and S.W. Lohman. 1952. "Nonsteady Flow to a Well of Constant Drawdown in an Extensive Aquifer," *Transactions, American Geophysical Union*. Vol. 33, no. 4, 559-569.

Jensen, A.L. 1990. *Borehole Closure and Test Zone Volume Determination Program for Brine-Permeability Test Results Within the Waste Isolation Pilot Plant Underground Facility*. SAND90-0228. Albuquerque, NM: Sandia National Laboratories.

Jones, C.L., C.G. Bowles, and K.G. Bell. 1960. *Experimental Drill Hole Logging in Potash Deposits of the Carlsbad District, New Mexico*. USGS Open-File Report 60-84. Washington, DC: US GPO. 25 p.

Kucûk, F., and W.E. Brigham. 1981. "Unsteady-State Water Influx in Elliptic and Anisotropic Reservoir/Aquifer Systems," *Society of Petroleum Engineers Journal*. Vol. 21, no. 3, 309-314.

McTigue, D.F., S.J. Finley, J.H. Gieske, and K.L. Robinson. 1991. Appendix A: "Compressibility Measurements on WIPP Brines," *Preliminary Comparison with 40 CFR Part 191, Subpart B for the Waste Isolation Pilot Plant, December 1991, Volume 3: Reference Data*. Eds. R.P. Rechard, A.C. Peterson, J.D. Schreiber, H.J. Iuzzolino, M.S. Tierney, and J.S. Sandha. SAND91-0893/3. Albuquerque, NM: Sandia National Laboratories. A-81 through A-98.

Neuzil, C.E. 1982. "On Conducting the Modified 'Slug' Test in Tight Formations," *Water Resources Research*. Vol. 18, no. 2, 439-441.

Neuzil, C.E. 1986. "Groundwater Flow in Low-Permeability Environments," *Water Resources Research*. Vol. 22, no. 8, 1163-1195.

Oliver, D.S. 1990. "The Averaging Process in Permeability Estimation from Well-Test Data," *SPE Formation Evaluation*. Vol. 5, no. 3, 319-324.

Pascal, H. 1981. "Nonsteady Flow Through Porous Media in the Presence of a Threshold Gradient," *Acta Mechanica*. Vol. 39, no. 3-4, 207-224.

Pickens, J.F., G.E. Grisak, J.D. Avis, D.W. Belanger, and M. Thury. 1987. "Analysis and Interpretation of Borehole Hydraulic Tests in Deep Boreholes: Principles, Model Development, and Applications," *Water Resources Research*. Vol. 23, no. 7, 1341-1375.

Powers, D.W., and B.W. Hassinger. 1985. "Synsedimentary Dissolution Pits in Halite of the Permian Salado Formation, Southeastern New Mexico," *Journal of Sedimentary Petrology*. Vol. 55, no. 5, 769-773.

Pruess, K. 1991. *TOUGH2 -- A General-Purpose Numerical Simulator for Multiphase Fluid and Heat Flow*. LBL-29400. Berkeley, CA: Lawrence Berkeley Laboratory.

Reeves, M., D.S. Ward, N.D. Johns, and R.M. Cranwell. 1986. *Theory and Implementation for SWIFT II, The Sandia Waste-Isolation Flow and Transport Model for Fractured Media, Release 4.84* NUREG/CR-3328, SAND83-1159. Albuquerque, NM: Sandia National Laboratories.

145

Remson, I., and S.M. Gorelick. 1982. "Hydrologic Issues in Repository Siting," *The Technology of High-Level Nuclear Waste Disposal.* Ed. P.L. Hofmann. DOE/TIC-4621. Washington, DC: US DOE. Vol. 2, 46-52.

Skempton, A.W. 1954. "The Pore-Pressure Coefficients *A* and *B*," *Géotechnique.* Vol. IV, 143-147.

Sterns, N.D. 1927. *Laboratory Tests on Physical Properties of Water-Bearing Materials.* USGS Water Supply Paper 596. 121-176.

Stensrud, W.A., T.F. Dale, P.S. Domski, J.B. Palmer, R.M. Roberts, M.D. Fort, G.J. Saulnier, Jr., and A.L. Jensen. 1992. *Waste Isolation Pilot Plant Salado Hydrology Program Data Report #2.* SAND92-7072. Albuquerque, NM: Sandia National Laboratories.

Stormont, J.C. 1990. "Discontinuous Behaviour Near Excavations in a Bedded Salt Formation," *International Journal of Mining and Geological Engineering.* Vol. 8, no. 1, 35-56.

Stormont, J.C., C.L. Howard, and J.J.K. Daemen. 1991. *In Situ Measurements of Rock Salt Permeability Changes Due to Nearby Excavation.* SAND90-3134. Albuquerque, NM: Sandia National Laboratories.

Swartzendruber, D. 1962. "Non-Darcy Flow Behavior in Liquid-Saturated Porous Media," *Journal of Geophysical Research.* Vol. 67, no. 13, 5205-5213.

Theis, C.V. 1935. "The Relation Between the Lowering of the Piezometric Surface and the Rate and Duration of Discharge of a Well Using Ground-Water Storage," *Transactions, American Geophysical Union.* Vol. 16, 519-524.

Uraiet, A.A., and R. Raghavan. 1980. "Unsteady Flow to a Well Producing at a Constant Pressure," *Journal of Petroleum Technology.* Vol. 32, no. 10, 1803-1812.

Westinghouse Electric Corporation. 1989. *Geotechnical Field Data and Analysis Report, July 1987-June 1988, Volume II.* DOE/WIPP 89-009. Carlsbad, NM: US DOE.

Westinghouse Electric Corporation. 1990. *Geotechnical Field Data and Analysis Report, July 1988-June 1989, Volume II.* DOE/WIPP 90-006. Carlsbad, NM: US DOE.

APPENDIX A

STRATIGRAPHIC UNITS (MAP UNITS) NEAR THE WIPP FACILITY HORIZON

Figure A-1. Detailed Stratigraphy Near the WIPP Underground Facility.

Table A-1. Description of Generalized Stratigraphy*

Approximate Distance From Clay G (Meters)	Stratigraphic Unit	Description
20.1 to 21.2	Polyhalitic halite (PH-7)	Clear to moderate reddish orange/brown, fine to coarsely crystalline, <1-3% polyhalite.
19.3 to 20.1	Halite (H-9)	Clear to light moderate reddish orange, medium to coarsely crystalline, 1% polyhalite. May contain 1% brown and gray clay.
17.5 to 19.3	Polyhalitic halite (PH-6)	Clear to moderate reddish orange/brown, medium to coarsely crystalline, <1-3% polyhalite. May contain traces of gray clay and/or scattered anhydrite.
16.8 to 17.5	Argillaceous halite (AH-4)	Clear to moderate brown, medium to coarsely crystalline. <1 to 3% brown clay. Intercrystalline and discontinuous breaks. In one core hole, consists of a 2.54 centimeter thick clay seam. Unit can vary up to 1.2 meters in thickness. Contact with lower unit is gradational.
14.2 to 16.8	Halite (H-8)	Clear to moderate reddish orange and moderate brown, coarsely crystalline, some medium. 1% brown clay, locally argillaceous (clays M-1 and M-2). Scattered anhydrite stringers locally.
13.0 to 14.2	Polyhalitic halite (PH-5)	Clear to moderate reddish orange, some moderate brown, coarsely crystalline. <1 to 3% polyhalite. None to 1% brown and some gray clay. Scattered anhydrite locally. Contact with unit below is fairly sharp.
11.6 to 13.0	Argillaceous halite (AH-3)	Clear to moderate brown, medium to coarsely crystalline, some fine. <1 to 5% brown clay. Locally contains 10% clay. Intercrystalline and scattered breaks. Locally contains partings and seams. Contact with lower unit is gradational based on increased clay content. Average range of unit is 11.6 to 13.0 meters above clay G but does vary from 10.3 to 14.0 meters.
10.4 to 11.6	Halite (H-7)	Clear to moderate brown, some moderate reddish brown, coarsely crystalline, some fine and medium. 1% brown clay, trace gray clay locally. Scattered breaks. Locally argillaceous. <1% polyhalite. Contact with unit below is gradational based on clay and polyhalite content.

---

*From *Brine Sampling and Evaluation Program 1988 Report*, DOE/WIPP 89-015, Deal et al. (1989).

Table A-1. Description of Generalized Stratigraphy (Continued)

Approximate Distance From Clay G (Meters)	Stratigraphic Unit	Description
9.2 to 10.4	Halite (H-6)	Clear to moderate reddish orange, coarsely crystalline. <1 to 3% polyhalite. Commonly polyhalitic. Scattered anhydrite stringers with anhydrite layers up to 1.27 centimeters thick locally. Scattered brown clay locally. Contact with MB-138 below is sharp.
9.0 to 9.2	Anhydrite (MB-138)	Light to medium gray, microcrystalline. Partly laminated. Scattered halite growths. Clay seam K found at base of unit.
7.6 to 9.0	Argillaceous halite (AH-2)	Clear to moderate brown, some light moderate reddish orange. Medium to coarsely crystalline. <1 to 3% brown clay, some gray. Locally up to 5% clay. Clay is intercrystalline with scattered breaks and partings present. <1/2% dispersed polyhalite. Contact with lower unit is gradational based on clay content. Upper contact with clay K is sharp.
7.0 to 7.6	Halite (H-5)	Clear, some light moderate brown, coarsely crystalline. <1/2% brown clay. Contact with clay J below varies from sharp to gradational depending if clay J is a distinct seam or merely an argillaceous zone.
6.4 to 7.0	Argillaceous halite (clay J; AH-1)	Usually consists of scattered breaks or argillaceous zone containing <1 to 3% brown clay. In C&SH shaft, it is a 1.27 centimeters thick brown clay seam.
5.1 to 6.4	Halite (map unit 15)	Clear, coarsely crystalline, scattered medium. Up to 1% dispersed polyhalite and brown clay. Scattered anhydrite. Lower contact is sharp with clay I.
4.8 to 5.1	Halite (map unit 14)	Clear to grayish orange-pink, coarsely crystalline, some medium. <1/2% dispersed polyhalite. Scattered discontinuous gray clay stringers. Clay I is along upper contact. Contact with lower unit is diffuse.
3.5 to 4.8	Halite (map unit 13)	Clear to moderate reddish orange and moderate brown, medium to coarsely crystalline, some fine. 1% brown clay, locally up to 3%. Trace of gray clay. Scattered discontinuous breaks. <1% dispersed polyhalite and polyhalite blebs. Contact with unit below is gradational based on clay and polyhalite content.

Table A-1. Description of Generalized Stratigraphy (Continued)

Approximate Distance From Clay G (Meters)	Stratigraphic Unit	Description
2.3 to 3.5	Polyhalitic halite (map unit 12)	Clear to moderate reddish orange, coarsely crystalline. 1 to 3% dispersed polyhalite and polyhalite blebs. Scattered anhydrite stringers. Contact is sharp with unit below.
2.1 to 2.3	Anhydrite ("a" - map unit 11)	Light to medium gray, light brownish gray and sometimes light moderate reddish orange. Microcrystalline. Halite growths within. Partly laminated. Clear, coarsely crystalline halite layer up to 5.1 centimeters wide, found within exposures in waste experimental area. Thin gray clay seam H at base of unit.
1.7 to 2.1	Halite (map unit 10)	Clear to moderate reddish orange/brown, fine to coarsely crystalline. 1% brown and/or gray clay and dispersed polyhalite. Discontinuous clay stringers locally. Contact with lower unit is diffuse based on crystal size and varying amounts of clay and polyhalite.
0.1 to 1.7	Halite (map unit 9)	Clear to light moderately reddish orange, coarsely crystalline, some medium. None to <1% polyhalite. Trace of gray clay locally. Scattered anhydrite stringers. Contact with unit below is sharp.
0.0 to 0.1	Anhydrite ("b" - map unit 8)	Light to medium gray, microcrystalline anhydrite. Scattered halite growths. Thin gray clay seam G at base of unit.
0.0 to -0.7	Halite (map unit 7)	Clean to light/medium gray, some moderate reddish orange/brown. Coarsely crystalline, some fine and medium. 1% brown and gray clay. Locally up to 2% clay. <1% dispersed polyhalite. Upper contact is sharp with clay G. Contact with lower unit is gradational.
-0.7 to -2.1	Halite (map unit 6)	Clear, some moderate reddish orange, coarsely crystalline, some fine to medium locally. <1/2% gray clay and polyhalite. Contact with lower unit gradational and/or diffuse.
-2.1 to -2.7	Halite (map unit 5)	Clear, coarsely crystalline. <1/2% gray clay. Contact with lower unit usually sharp with clay F.

Table A-1. Description of Generalized Stratigraphy (Continued)

Approximate Distance From Clay G (Meters)	Stratigraphic Unit	Description
-2.7 to -3.5	Argillaceous halite (map unit 4)	Clear to moderate brown and moderate reddish brown, coarsely crystalline. <1% polyhalite. <1 to 5% argillaceous material; predominantly brown, some gray, locally. Intercrystalline and discontinuous breaks and partings common in upper part of unit. Decreasing argillaceous content downward. Contact with lower unit is gradational.
-3.5 to -4.2	Halite (map unit 3)	Clear to moderate reddish orange, coarsely crystalline. 1% dispersed polyhalite and polyhalite blebs. Locally polyhalitic. Scattered gray clay locally. Contact with lower unit is sharp.
-4.2 to -4.3	Argillaceous halite (map unit 2)	Moderate reddish brown to medium gray, medium to coarsely crystalline. <1 to 3% argillaceous material. Contact with lower unit is usually sharp.
-4.3 to -4.4	Halite (map unit 1)	Light reddish orange to moderate reddish orange, medium to coarsely crystalline. 1% dispersed polyhalite. Contact with lower unit is sharp.
-4.4 to -6.7	Halite (map unit 0)	Clear to moderate reddish orange/brown, moderate brown and grayish brown. Medium to coarsely crystalline. <1 to 5% argillaceous material. Predominantly brown, some gray, intercrystalline argillaceous material and discontinuous breaks and partings. Upper 0.6 meters of unit is argillaceous halite decreasing in argillaceous material content downward. None to <1% polyhalite. Contact with lower unit is gradational based on polyhalite content.
-6.7 to -7.7	Polyhalitic halite (PH-4)	Clear to moderate reddish orange. Coarsely crystalline, some medium locally. <1 to 3% polyhalite. Scattered anhydrite. Scattered gray clay locally. Contact with lower unit (MB-139) is sharp, but commonly irregular and undulating. Trace of gray locally present along this contact.

153

Table A-1. Description of Generalized Stratigraphy (Continued)

Approximate Distance From Clay G (Meters)	Stratigraphic Unit	Description
-7.7 to -8.6	Anhydrite (MB-139)	Moderate reddish orange/brown to light and medium gray, microcrystalline anhydrite. "Swallowtail" pattern, consisting of halite growths within anhydrite, common in upper part of unit. Locally, hairline, clay-filled, low-angle fractures found in lower part of unit. Thin halite layer common close to lower contact. Clay seam E found at base of unit. Upper contact is irregular, undulating and sometimes contains <0.16 centimeters gray clay.
-8.6 to -9.5	Halite (H-4)	Clear to moderate reddish orange, and light gray. Coarsely crystalline, some fine and medium. 1% polyhalite and intercrystalline gray clay. Contact with lower unit is gradational based on increased polyhalite content.
-9.5 to -11.0	Polyhalitic halite (PH-3)	Clear to moderate reddish orange, coarsely crystalline. <1 to 3% polyhalite. Contact with lower unit is usually sharp along clay D.
-11.0 to -11.5	Halite (H-3)	Clear to moderate reddish orange, some light gray. Medium to coarsely crystalline. 1% polyhalite and gray clay. Contact with lower unit is gradational based on increased polyhalite content.
-11.5 to 13.0	Polyhalitic halite (PH-2)	Clear to moderate reddish orange/brown, coarsely crystalline. <1 to 3% polyhalite. Trace of clay locally. Scattered anhydrite locally. Contact with lower unit is gradational, based on decreased polyhalite content.
-13.0 to 14.4	Halite (H-2)	Clear to moderate reddish orange, medium to coarsely crystalline. <1% dispersed polyhalite. <1% brown and/or gray clay. Contact with lower unit is gradational and/or diffuse.
-14.4 to -16.2	Polyhalitic halite (PH-1)	Clear to moderate reddish orange. Coarsely crystalline with some medium sometimes present close to lower contact. <1 to 3% polyhalite. Scattered anhydrite especially common close to anhydrite "c". Lower contact is sharp with anhydrite "c".

Table A-1. Description of Generalized Stratigraphy (Concluded)

Approximate Distance From Clay G (Meters)	Stratigraphic Unit	Description
-16.2 to -16.3	Anhydrite ("c")	Light to medium gray, microcrystalline anhydrite. Scattered halite growths. Faintly laminated locally. Clay seam B found at base of unit.
-16.3 to -20.0	Halite (H-1)	Clear to medium gray and moderate brown. Medium to coarsely crystalline, some fine locally. 1% polyhalite, locally polyhalitic. <1 to 3% clay, both brown and gray. Intercrystalline clay with discontinuous breaks and partings. Zones of argillaceous halite found within unit. Seams of clay mixed with halite crystals present locally. Upper contact of this unit is sharp with clay B.

APPENDIX B

DERIVATION OF ANALYTICAL SOLUTIONS FOR HYDRAULIC-TEST INTERPRETATION

APPENDIX B

DERIVATION OF ANALYTICAL SOLUTIONS FOR HYDRAULIC-TEST INTERPRETATION

Groundwater and petroleum literature use different terminology and symbols to represent the same physical parameters. The analytical solutions discussed below will be presented using the same symbols and units used by the authors who derived the solutions. After the initial presentation, however, all groundwater terminology and symbols will be converted to their petroleum equivalents because the petroleum terms are more conducive to the use of SI units and calculation of intrinsic permeability than are the groundwater terms.

B.1 Pressure-Pulse Tests

Bredehoeft and Papadopulos (1980) described the response of a shut-in test interval to an instantaneous pressure pulse as a boundary value problem given by:

$$\frac{\partial^2 h}{\partial r^2} + \frac{1}{r}\frac{\partial h}{\partial r} = \frac{S}{T}\frac{\partial h}{\partial t} \tag{B-1}$$

$$h(r,0) = 0 \tag{B-2}$$

$$h(\infty,t) = 0 \tag{B-3}$$

$$h(r_s,t) = H(t) \tag{B-4}$$

$$H(0) = H_0 \tag{B-5}$$

$$2\pi r_s T \frac{\partial h}{\partial r}(r_s,t) = V_w C_w \rho_w g \frac{\partial H}{\partial t}(t) \tag{B-6}$$

where:

h	=	head change in the tested formation resulting from pulse, L
r	=	radial distance from center of well, L
S	=	storativity, dimensionless
T	=	transmissivity, L^2/T
t	=	time since pressure pulse, T
r_s	=	radius of well, L
H	=	head change in the well at time t, L
H_0	=	head change in the well caused by pressure pulse, L
V_w	=	volume of water within shut-in interval, L^3

C_w = compressibility of water, LT^2/M

ρ_w = density of water, M/L^3

g = gravitational acceleration, L/T^2

Their solution to this problem is:

$$\frac{H}{H_0} = F\left[\frac{\pi r_s^2 S}{V_w C_w \rho_w g}, \frac{\pi T t}{V_w C_w \rho_w g}\right] \tag{B-7}$$

Substituting dummy variables α and β for the first and second parameters of the function in Eq. B-7, the function can be defined as:

$$F(\alpha,\beta) = \frac{8\alpha}{\pi^2} \int_0^\infty e^{-\beta u^2/\alpha} \frac{1}{u\, f(u,\alpha)}\, du \tag{B-8}$$

where:

$$f(u,\alpha) = [uJ_0(u) - 2\alpha J_1(u)]^2 + [uY_0(u) - 2\alpha Y_1(u)]^2 \tag{B-9}$$

and: J_0 = Bessel function of first kind and zero order

J_1 = Bessel function of first kind and first order

Y_0 = Bessel function of second kind and zero order

Y_1 = Bessel function of second kind and first order

Neuzil (1982) pointed out that the correct compressibility term to be used in Eqs. B-6 and B-7 was not the compressibility of water, but the compressibility actually observed for the test zone. By knowing the volume of water added to or removed from the shut-in interval to create the pressure pulse, the volume of water within the shut-in interval, and the pressure change caused by the pulse, the test-zone compressibility can be calculated as:

$$C_{tz} = \frac{1}{V}\frac{dV}{dp} \tag{B-10}$$

Bredehoeft and Papadopulos (1980) used Eq. B-7 to construct a family of type curves to be used for pulse-test interpretation (Figure 6-1). Each type curve represents a plot of β on a logarithmic x-axis versus H/H_0 on a linear y-axis for a specific value of α. Pulse-test data are plotted as elapsed time (t) on a logarithmic x-axis versus H/H_0 on a linear y-axis. If the analysis is to be performed manually, the data plot is placed over the type-curve plot and translated in the x direction, while keeping the x-axes overlapping, until the best possible match between the data and one of the type curves is obtained. In this position, an arbitrary match point is chosen and the corresponding values of t and β are read from the data and type-curve plots, respectively. The curve-matching procedure can also be carried out on a computer. The transmissivity (T) of the tested interval is calculated from the following equation, using the t and β values from the match point:

$$T = \frac{V_w C_{tz} \rho_w g \beta}{\pi t}$$ (B-11)

Using petroleum terminology for consistent SI units, Eq. B-11 can be written as:

$$kh = \frac{V_w C_{tz} \mu \beta}{\pi t}$$ (B-12)

where: k = permeability, L^2

μ = fluid viscosity, M/LT

and other symbols are as defined above.

Transmissivity is the main parameter to be obtained from pulse tests. While storativity is theoretically obtainable from the σ value of the type curve providing the best match to the data and Eq. B-7, data rarely show a unique match to one particular type curve. That is, the data may be equally well matched by several type curves having similar shapes with σ values differing by one or more orders of magnitude. Papadopulos et al. (1973) determined that an error in σ (and hence storativity) of two orders of magnitude resulted in an error in transmissivity of less than 30 percent. Thus, while transmissivity can be determined with acceptable accuracy from pulse tests, storativity cannot.

B.2 Constant-Pressure Flow Tests

Jacob and Lohman (1952) provided the first analytical solution to onstant-pressure flow tests in the field of groundwater hydrology. The initial condition, boundary , and governing equation they considered are as follows:

Initial condition:

$$h(r,0) = h_0$$ (B-13)

Boundary conditions:

$$h(\infty,t) = h_0$$ (B-14)

$$h(r_w,t) = h_0 - \jmath_w$$ (B-15)

Governing equation:

$$\frac{\partial^2 h}{\partial r^2} + \frac{1}{r}\frac{\partial h}{\partial r} = \frac{S}{T}\frac{\partial h}{\partial t}$$ (B-16)

where: h = head in the tested formation, L

r = radial distance from center of well, L

161

h_0	=	initial head in the formation, L
t	=	time elapsed since flow began, T
r_w	=	radius of well, L
s_w	=	drawdown of the well, L
S	=	storativity, dimensionless
T	=	transmissivity, L^2/T

Their solution is:

$$Q = 2\pi T \, (h_0 - h) \, G(a) = 2\pi T \, s_w \, G(a) \qquad \text{(B-17)}$$

where: $\quad Q \quad = \quad$ discharge of the well, L^3/T

The function $G(a)$ is given by:

$$G(a) = \frac{4a}{\pi} \int_0^\infty x e^{-ax^2} \left[\frac{\pi}{2} + \tan^{-1} \left[\frac{Y_0(x)}{J_0(x)} \right] \right] dx \qquad \text{(B-18)}$$

where:

$$a = \frac{Tt}{Sr_w^2} \qquad \text{(B-19)}$$

and: $\quad Y_0 \quad = \quad$ Bessel function of second kind and zero order

$\quad\quad\quad J_0 \quad = \quad$ Bessel function of first kind and zero order

In the petroleum literature (e.g., Fetkovich, 1980; Uraiet and Raghavan, 1980; Ehlig-Economides and Ramey, 1981), Q is represented by q, $G(a)$ is represented by q_D, and a is represented by t_D.

To create a type curve, t_D is plotted versus q_D on a log-log graph (Figure 6-2). Test data are then plotted as elapsed flow time, t, versus flow rate, q, on a similarly scaled graph. The data can be matched to the type curve manually by placing the data plot on top of the type-curve plot, and shifting the data plot, keeping both sets of axes parallel, until the data overlie the type curve as much as possible. The curve-fitting procedure can also be carried out on a computer. Once a match is obtained, an arbitrary point is selected and the coordinates of that point are read on both plots. The permeability-thickness product (transmissivity) of the tested interval is calculated from the following rearrangement of Eq. B-17, written for SI units using petroleum symbols:

$$kh = \frac{q_m \, \mu}{2\pi q_{Dm}(p_i - p_{wf})} \qquad \text{(B-20)}$$

where: $\quad k \quad = \quad$ permeability, L^2

$\quad\quad\quad h \quad = \quad$ thickness of tested interval, L

$\quad\quad\quad q_m \quad = \quad$ flow rate at match point on data plot, L^3/T

μ	=	fluid viscosity, M/LT
q_{Dm}	=	dimensionless flow rate at match point on type curve
p_i	=	initial pressure before flow began, M/LT^2
p_{wf}	=	constant pressure at which well flowed, M/LT^2

B.3 Pressure-Buildup Tests

Many authors in the fields of groundwater hydrology and petroleum reservoir engineering have studied the buildup of pressure in a well following a constant-rate flow period. The early studies of Theis (1935), Cooper and Jacob (1946), and Horner (1951) considered only the behavior of a well acting as a line source, with no wellbore storage or skin. Gringarten et al. (1979) included wellbore storage and skin in their analytical solution when they devised a new set of type curves for flow- and buildup-test interpretation.

In defining their type curves, Gringarten et al. (1979) relied on the analytical solution developed by Agarwal et al. (1970) to describe the pressure response of a well with wellbore storage and skin during a constant-rate flow period. This solution is written in terms of dimensionless parameters defined as follows:

$$p_D = \frac{2\pi kh}{q\mu} \Delta p \tag{B-21}$$

$$t_D = \frac{kht}{\mu\phi c_t hr_w^2} \tag{B-22}$$

$$C_D = \frac{C}{2\pi\phi c_t hr_w^2} \tag{B-23}$$

$$r_D = \frac{r}{r_w} \tag{B-24}$$

where:	p_D	=	dimensionless pressure change
	k	=	permeability, L^2
	h	=	test-interval thickness, L
	Δp	=	pressure change, M/LT^2
	q	=	flow rate, L^3/T
	μ	=	fluid viscosity, M/LT
	t_D	=	dimensionless elapsed time
	t	=	elapsed flow time, T
	ϕ	=	porosity
	c_t	=	total system compressibility, LT^2/M
	r_w	=	radius of well, L
	C_D	=	dimensionless wellbore-storage coefficient
	C	=	wellbore-storage coefficient, L^4T^2/M

$$r_D = \text{dimensionless radius}$$

$r_D \quad = \quad$ dimensionless radius

$r \quad = \quad$ radial distance from center of well, L

The problem considered by Agarwal et al. (1970) and Gringarten et al. (1979) is given by:

Initial condition:

$$p_D(r_D,0) = 0 \tag{B-25}$$

Boundary conditions:

$$p_D(\infty,t_D) = 0 \tag{B-26}$$

$$C_D \frac{dp_{wD}}{dt_D} - \left[\frac{\partial p_D}{\partial r_D}\right]_{r_D = 1} = 1 \tag{B-27}$$

$$p_{wD} = \left[p_D - s\left(\frac{\partial p_D}{\partial r_D}\right)\right]_{r_D = 1} \tag{B-28}$$

Governing equation:

$$\frac{\partial^2 p_D}{\partial r_D^2} + \frac{1}{r_D}\frac{\partial p_D}{\partial r_D} = \frac{\partial p_D}{\partial t_D} \tag{B-29}$$

where: $\quad p_{wD} \quad = \quad$ dimensionless pressure change within the wellbore

$s \quad = \quad$ skin factor (dimensionless)

The Laplace transform for the dimensionless wellbore pressure change is given by:

$$L\{p_{wD}\} = \frac{K_0(\sqrt{p}) + s\sqrt{p}\, K_1(\sqrt{p})}{p\left[\sqrt{p}\, K_1(\sqrt{p}) + C_D p\left\{K_0(\sqrt{p}) + s\sqrt{p}\, K_1(\sqrt{p})\right\}\right]} \tag{B-30}$$

where: $\quad K_0 \quad = \quad$ modified Bessel function of second kind and zero order

$K_1 \quad = \quad$ modified Bessel function of second kind and first order

$p \quad = \quad$ Laplace parameter

Inversion of Eq. B-30 gives:

$$p_D = \frac{4}{\pi^2}\int_0^\infty \frac{1 - e^{-u^2 t_D}}{u^3\left\{\left[uC_D J_0(u) - (1 - C_D s u^2)J_1(u)\right]^2 + \left[uC_D Y_0(u) - (1 - C_D s u^2)Y_1(u)\right]^2\right\}}\, du \tag{B-31}$$

Using this solution, Gringarten et al. (1979) devised a set of type curves. Each type curve is characterized by a distinct value of $C_D e^{2s}$ and is plotted as p_D versus t_D/C_D on log-log paper (Figure 6-3). Test data are plotted as pressure change, Δp, versus elapsed flow time, t, on similarly scaled paper. The data can be matched to a type curve manually by placing the data plot on top of the type-curve plot and shifting the data plot, keeping both sets of axes parallel, until the best match possible is obtained between the data and one of the type curves. After a match is obtained, an arbitrary point is selected and the coordinates of that point are read on both plots. Using the ordinate values for the match point (the pressure match), the permeability-thickness product (transmissivity) of the tested interval is calculated from the following rearrangement of Eq. B-21:

$$kh = \frac{q\mu}{2\pi} \frac{p_D}{\Delta p} \tag{B-32}$$

The wellbore-storage coefficient can then be calculated from the abscissa values of the match point (the time match) by combining Eqs. B-22 and B-23 as:

$$C = \frac{2\pi kht}{\mu(t_D/C_D)} \tag{B-33}$$

If the porosity-compressibility product (specific storage) of the formation is known, the wellbore skin factor can be calculated by combining Eq. B-33 with the value of $C_D e^{2s}$ for the type curve that the data matched.

Although the solution of Gringarten et al. (1979) was developed for the drawdown response of a well producing at a constant rate, it can be extended to analysis of the pressure buildup following a constant-rate flow period through linear superposition of the buildup response on the continuing drawdown response. The solution can be further extended to apply to the buildup response following a constant-pressure flow test by subdividing the constant-pressure flow period into a number of shorter periods having constant, but different, rates and using superposition to combine the effects of all of the flow periods. This approach was verified theoretically by Ehlig-Economides (1979).

Bourdet et al. (1989) added the pressure derivative to the analytical procedure of Gringarten et al. (1979) by constructing a family of type curves of the semilog slope of the dimensionless pressure response versus the dimensionless time group, t_D/C_D. The semilog slope of the dimensionless pressure response is defined as:

$$\frac{dp_D}{d \ln(t_D/C_D)} = \frac{t_D}{C_D} \frac{dp_D}{d(t_D/C_D)} = \frac{t_D}{C_D} p_D' \tag{B-34}$$

where: p_D' =   dimensionless pressure derivative

These curves are plotted on the same log-log graphs as the type curves of Gringarten et al. (1979), with the vertical axis now also labeled $(t_D/C_D)p_D'$ (Figure 6-3). Again, each individual type curve is characterized by a distinct value of $C_D e^{2s}$. Pressure-derivative type curves begin with an initial segment with unit slope corresponding to early-time wellbore storage and skin effects. This segment reaches a maximum that is

165

proportional to the amount of wellbore storage and skin, and then the curve declines and stabilizes at a dimensionless pressure/semilog slope value of 0.5 corresponding to late-time, infinite-acting, radial-flow effects.

Pressure-derivative data in combination with pressure data are much more sensitive indicators of double-porosity effects, boundary effects, nonstatic antecedent test conditions, and other phenomena than are pressure data alone. For this reason, pressure-derivative data are useful in choosing between conflicting phenomenological models that often cannot be differentiated on the basis of pressure data alone. Pressure-derivative data are also useful in determining when infinite-acting, radial-flow conditions occur during a test, because these conditions cause the pressure derivative to stabilize at a constant value.

For any given point, the pressure derivative is calculated as the linear-regression slope of a semilog line fit through that point and any chosen number of neighboring points on either side. The equation for the derivative is:

$$p' = \frac{n \sum_{i=1}^{n} x_i y_i - \sum_{i=1}^{n} x_i \sum_{i=1}^{n} y_i}{n \sum_{i=1}^{n} x_i^2 - \sum_{i=1}^{n} x_i^2} \tag{B-35}$$

where, for a single constant-rate flow period:

n	=	number of points to be fitted
x_i	=	$\ln \Delta t_i$
y_i	=	Δp_i
Δt_i	=	elapsed test time at point i, T
Δp_i	=	pressure change at Δt_i, M/LT^2

For a multi-rate flow period or a recovery period, the time parameter is a superposition function calculated as:

$$x_i = \left[\sum_{i=1}^{n-1} (q_i - q_{i-1}) \log \left[\left[\sum_{j=1}^{n-1} \Delta t_j \right] + \Delta t \right] \right] + (q_n - q_{n-1}) \log \Delta t \tag{B 36}$$

where:

q	=	flowrate, L^3/T
Δt	=	elapsed time during a flow period, T

with subscripts:

i	=	individual flow period
j	=	individual flow period
n	=	number of flow periods considered

In general, the fewer the number of points used in calculating the derivative, the more accurate it will be. Three-point derivatives, calculated using only the nearest neighbor on either side of a point, usually provide enough resolution to distinguish most important features. However, excessive noise in the data sometimes makes it necessary to use five- or seven-point derivatives, or various "windowing" procedures, to obtain a smooth curve. Unfortunately, this may also smooth out some of the features sought.

Horner (1951) provided a method of obtaining permeability and static formation pore pressure values independent of log-log type-curve matching, although his method is best used in conjunction with log-log methods. Horner's method applies to the recovery of pressure after a constant-rate flow period in a well that fully penetrates a homogeneous, isotropic, horizontal, infinite, confined, single-porosity or double-porosity reservoir. For a recovery after a single flow period, Horner's solution is:

$$p(t) = p^* - \frac{q\mu}{4\pi kh} \ln\left[\frac{t_p + \Delta t}{\Delta t}\right] \tag{B-37}$$

where:

$p(t)$	=	pressure at time t, M/LT^2
p^*	=	static formation pore pressure, M/LT^2
t_p	=	duration of previous flow period, T
Δt	=	time elapsed since end of flow period, T

and other terms are as defined above under Eq. B-24. For a recovery after multiple flow periods, the time group in Eq. B-37 is replaced by the superposition function given in the right-hand side of Eq. B-36.

The permeability-thickness product (kh) is obtained by (1) plotting $p(t)$ versus log $[(t_p + \Delta t)/\Delta t]$ (or the superposition function), (2) drawing a straight line through the data determined from the log-log pressure-derivative plot to be representative of infinite-acting radial flow, and (3) measuring the change in $p(t)$ on this line over one log cycle of time (m). Eq. B-37 can then be rearranged and reduced to:

$$kh = \frac{2.30 \ q\mu}{4\pi m} \tag{B-38}$$

Static formation pore pressure is estimated by extrapolating the radial-flow straight line to the pressure axis where log $[(t_p + \Delta t)/\Delta t] = 1$, representing infinite recovery time. In the absence of reservoir boundaries, the pressure intercept at that time should equal the static formation pore pressure.

Horner analysis can also be performed using dimensionless parameters. Once type-curve and match-point selections have been made through log-log analysis, this technique allows the $C_D e^{2s}$ type curves to be superimposed on a normalized semilog plot of the data. Logarithmic dimensionless times for the data are calculated using:

$$\frac{q_{n-1}-q_n}{|q_{n-1}-q_n|}\left[\sum_{i=1}^{n-1}\frac{q_i-q_{i-1}}{q_{n-1}-q_n}\log\left(\sum_{j=i}^{n-1}\Delta t_j + \Delta t\right) - \log \Delta t\right] \tag{B-39}$$

where all parameters are as defined above. The dimensionless times calculated using Eq. B-39 are plotted on a linear scale. Dimensionless pressures for the data are calculated using:

$$\frac{p_D}{\Delta p} \, [p^* - p(t)] \tag{B-40}$$

where p_D and Δp are the log-log match-point coordinates, and the other parameters are as defined above. Dimensionless pressures are also plotted on a linear scale.

The type curves are plotted on the same axes with dimensionless time defined as:

$$\frac{q_{n-1}-q_n}{|q_{n-1}-q_n|} \left[\sum_{i=1}^{n-1} \frac{q_i-q_{i-1}}{q_n-q_{n-1}} \, p_D \left(\sum_{j=1}^{n-1} \Delta t_j + \Delta t \right) - \log \Delta t \right] \tag{B-41}$$

and dimensionless pressure defined as:

$$\frac{q_{n-1}-q_n}{|q_{n-1}-q_n|} \left[\sum_{i=1}^{n-1} \frac{q_i-q_{i-1}}{q_n-q_{n-1}} \, \log \left(\sum_{j=1}^{n-1} \Delta t_j + \Delta t \right)_D - p_D(\Delta t)_D \right] \tag{B-42}$$

The dimensionless Horner plot is a very sensitive indicator of inaccuracies in type-curve, match-point, and formation-pore-pressure selections (Gringarten, 1986). By iterating between dimensionless Horner and log-log plots, very accurate hydraulic parameters can be obtained.

All of the techniques discussed above for pressure-buildup analysis are included in the Interpret/2 well-test-interpretation code developed by Scientific Software-Intercomp.

REFERENCES

Agarwal, R.G., R. Al-Hussainy, and H.J. Ramey, Jr. 1970. "An Investigation of Wellbore Storage and Skin Effect in Unsteady Liquid Flow: I. Analytical Treatment," *Society of Petroleum Engineers Journal.* Vol. 10, no. 3, 279-290.

Bourdet, D., J.A. Ayoub, and Y.M. Pirard. 1989. "Use of Pressure Derivative in Well-Test Interpretation," *SPE Formation Evaluation.* Vol. 4, no. 2, 293-302.

Bredehoeft, J.D., and S.S. Papadopulos. 1980. "A Method for Determining the Hydraulic Properties of Tight Formations," *Water Resources Research.* Vol. 16, no. 1, 233-238.

Cooper, H.H., Jr., and C.E. Jacob. 1946. "A Generalized Graphical Method for Evaluating Formation Constants and Summarizing Well-Field History," *Transactions, American Geophysical Union.* Vol. 27, no. IV, 526-534.

Ehlig-Economides, C.A. 1979. "Well Test Analysis for Wells Produced at a Constant Pressure". PhD dissertation. Palo Alto, CA: Dept. of Petroleum Engineering, Stanford University. 117 p.

Ehlig-Economides, C.A., and H.J. Ramey, Jr. 1981. "Transient Rate Decline Analysis for Wells Produced at Constant Pressure," *Society of Petroleum Engineers Journal.* Vol. 21, no. 1, 98-104.

Fetkovich, M.J. 1980. "Decline Curve Analysis Using Type Curves," *Journal of Petroleum Technology.* Vol. 32, no. 6, 1065-1077.

Gringarten, A.C. 1986. "Computer-Aided Well Test Analysis", *Proceedings of the International Meeting on Petroleum Engineering, Beijing, China, March 17, 1986.* SPE 14099. Dallas, TX: Society of Petroleum Engineers.

Gringarten, A.C., D.P. Bourdet, P.A. Landel, and V.J. Kniazeff. 1979. "A Comparison Between Different Skin and Wellbore Storage Type Curves for Early-Time Transient Analysis," *54th Annual SPE Technical Conference and Exhibition, Las Vegas, NV, September 23, 1979.* SPE 8205. Richardson, TX: Society of Petroleum Engineers.

Horner, D.R. 1951. "Pressure Build-Up in Wells," *Proceedings Third World Petroleum Congress, The Hague, Netherlands, May 29, 1951.* Leiden: E.J. Bill. Sec. II:503-523.

Jacob, C.E., and S.W. Lohman. 1952. "Nonsteady Flow to a Well of Constant Drawdown in an Extensive Aquifer," *Transactions, American Geophysical Union.* Vol. 33, no.4, 559-569.

Neuzil, C.E. 1982. "On Conducting the Modified 'Slug' Test in Tight Formations," *Water Resources Research.* Vol. 18, no. 2, 439-441.

Papadopulos, S.S., J.D. Bredehoeft, and H.H. Cooper, Jr. 1973. "On the Analysis of 'Slug Test' Data," *Water Resources Research.* Vol. 9, no. 4, 1087-1089.

Theis, C.V. 1935. "The Relation Between the Lowering of the Piezometric Surface and the Rate and Duration of Discharge of a Well Using Ground-Water Storage," *Transactions, American Geophysical Union.* Vol. 16, 519-524.

Uraiet, A.A., and R. Raghavan. 1980. "Unsteady Flow to a Well Producing at a Constant Pressure," *Journal of Petroleum Technology.* Vol. 32, no. 10, 1803-1812.

APPENDIX C

MODELING STUDY OF SLANTED BOREHOLES

APPENDIX C

MODELING STUDY OF SLANTED BOREHOLES

C.1 Introduction

Permeability testing is being performed in boreholes drilled from within the WIPP repository to determine the hydrologic properties of halite and anhydrite beds of the surrounding Salado Formation. For testing purposes, boreholes are drilled not only vertically but also inclined towards the horizontal at various degrees. Because bedding within the Salado is nearly horizontal, the slanted boreholes penetrate beds at acute angles to the bedding.

The permeability tests performed in the WIPP underground have been interpreted using the well-test interpretation code GTFM (Graph Theoretic Field Model; Pickens et al., 1987). GTFM assumes horizontal, radial flow into a vertical, fully penetrating borehole from a horizontal, homogenous, and fully confined formation. These assumptions are considered to be reasonable for interpretation of tests in vertically oriented boreholes. In order to interpret the test results from an angled borehole using GTFM, the geometry of the angled borehole is transformed to that of an equivalent vertical borehole. This transformation is accomplished by treating the angled borehole as if it were a vertical cylindrical borehole with a diameter equal to the average length of the axes of the ellipse that is created by the intersection of a horizontal plane and the angled borehole (see Section 6.2). The length of the tested interval is assumed to be equal to its vertical thickness. The actual fluid volume in the angled test interval is specified in GTFM for the equivalent vertical test interval. For tests in angled boreholes, however, the assumption made in GTFM of no vertical flow towards the wellbore may not be appropriate.

To evaluate the conditions under which an equivalent-vertical-borehole approximation is appropriate for interpretation of permeability tests in angled boreholes, a grid preprocessor for the finite-difference flow model SWIFT II (Reeves et al., 1986) was developed. This preprocessor is the SWIFT II Transmissibility Generator for Angled Boreholes (STAB). The function of STAB is to modify the transmissibilities and pore volumes in the grid blocks surrounding an angled borehole in a way that allows the angled borehole to be modeled by SWIFT II using a simplified grid system appropriate for a vertical hole. The term STAB will be used throughout the remainder of this appendix to refer to simulations generated using both the STAB preprocessor and SWIFT II. The term SWIFT II will be used to refer to equivalent-vertical-borehole simulations generated using only SWIFT II. The theory underlying STAB and verification of the code by comparison to an analytical solution are presented in Appendix H.

This appendix presents the results of permeability-test simulations generated by STAB showing the effects of varying the borehole angle and of introducing differences between vertical and horizontal hydraulic conductivity (anisotropy). SWIFT II and GTFM simulations were performed to compare the results of the equivalent-vertical-borehole methodology to the STAB-generated results.

C.2 STAB and SWIFT II Configuration

The system of interest was discretized into a 10 x 10 x 10 grid. The output from the preprocessor contains grid-block-transmissibility and pore-volume modifiers which are input into the SWIFT II code. This grid-block modification enables the user to simulate an angled borehole using a vertical borehole discretization, thus allowing for a substantial decrease in grid size and simulation time.

A Carter-Tracy (1960) boundary approximation is coupled to the outer boundary of the grid system. The distance to this outer boundary is calculated in the preprocessor as the radius of influence (ROI). If the ROI was less than 15 m, a default value of 15 m was used. The default distance was selected based on the results of sensitivity simulations designed to determine how close to the wellbore the Carter-Tracy boundary could be placed without adversely affecting the pressure response.

The basic system configuration used in the angled STAB simulations consisted of a 10.16-cm (4-in) diameter borehole intersecting and fully penetrating a 1-m-thick test interval at angles ranging from 0° to 75° from the vertical in 15° increments. The upper and lower surfaces of the tested interval were treated as no-flow boundaries. Table C-1 presents the STAB input parameters that were used for all of the different angled simulations. Table C-2 presents the input parameters specific to each angled simulation. The angle-specific parameters are the borehole angle measured from vertical, the equivalent vertical borehole radius, and the borehole fluid volume. The system parameters included a radial (horizontal) hydraulic conductivity (K_r) of 5.0×10^{-13} m/s, a specific storage of 1.8×10^{-7} m^{-1}, a brine density of 1220 kg/m^3, a test-zone compressibility of 1.52×10^{-9} Pa^{-1}, and a formation pore pressure of 2.0 MPa. Anisotropy in hydraulic conductivity was obtained by assigning vertical hydraulic conductivities (K_z) of 5.0×10^{-13}, 5.0×10^{-14}, and 5.0×10^{-15} m/s to different simulations.

C.3 Sensitivity Simulations

Pulse-withdrawal, constant-pressure withdrawal, and pressure-buildup tests were simulated using STAB for borehole slant angles of 0°, 15°, 30°, 45°, 60°, and 75° from vertical, and for anisotropy ratios (K_r/K_z) of 1, 10, and 100. The scenario for the pulse-withdrawal-test simulations consisted of decreasing the pressure in the borehole from 2.0 MPa (formation pressure) to 0.5 MPa over a period of 100 seconds and then allowing the pressure to recover for 35 days. The constant-pressure-withdrawal-test scenario entailed decreasing the borehole pressure from 2.0 MPa to 0.5 MPa and holding that lower pressure for 20 days while simulating the volume of fluid produced to the borehole. The pressure-buildup-test scenario involved simulation of pressure recovery for 30 days following the constant-pressure withdrawal test.

C.3.1 STAB SIMULATIONS OF PULSE-WITHDRAWAL TESTS. The effects of borehole slant angle on pressure responses observed during pulse-withdrawal tests for anisotropies of 1, 10, and 100 are shown in Figures C-1, C-2, and C-3, respectively. Relative to the pressure recovery in a vertical borehole, pressure recoveries are increasingly delayed as the slant angle increases. This occurs because the fluid volume in the test interval increases as the slant angle increases (Table C-2), requiring more flow from the formation to increase the test-interval pressure a given amount. The differences between the responses in vertical
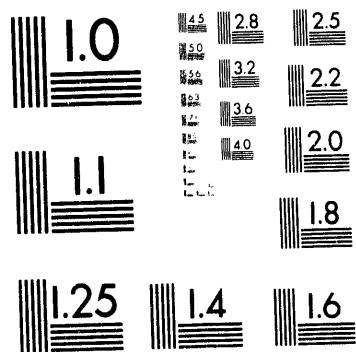
3 of 3

Table C-1. STAB Input Parameters for All Angled Simulations

Parameter	Value
Number of Radial Grid Nodes	10
Number of Theta Grid Nodes	10
Number of Vertical Grid Nodes	10
Formation Thickness	1 m
Radial Hydraulic Conductivity	5.0 E-13 m/s
Vertical Hydraulic Conductivity	5.0 E-13, 5.0 E-14, or 5.0 E-15 m/s
Specific Storage	1.8 E-7 m^{-1}
Formation Pore Pressure	2.0 MPa
Fluid Density	1220 kg/m^3
Test-Zone Compressibility	1.52 E-9 Pa^{-1}
Borehole Radius	0.0508 m

Table C-2. STAB Input Parameters for Specific Angled Simulations

Parameter	Values				
Borehole Angle	15°	30°	45°	60°	75°
Equivalent Vertical Borehole Radius (m)	0.0517	0.0547	0.0618	0.0785	0.1347
Half Borehole Volume (E-3 m^3)	4.197	4.681	5.733	8.107	15.660
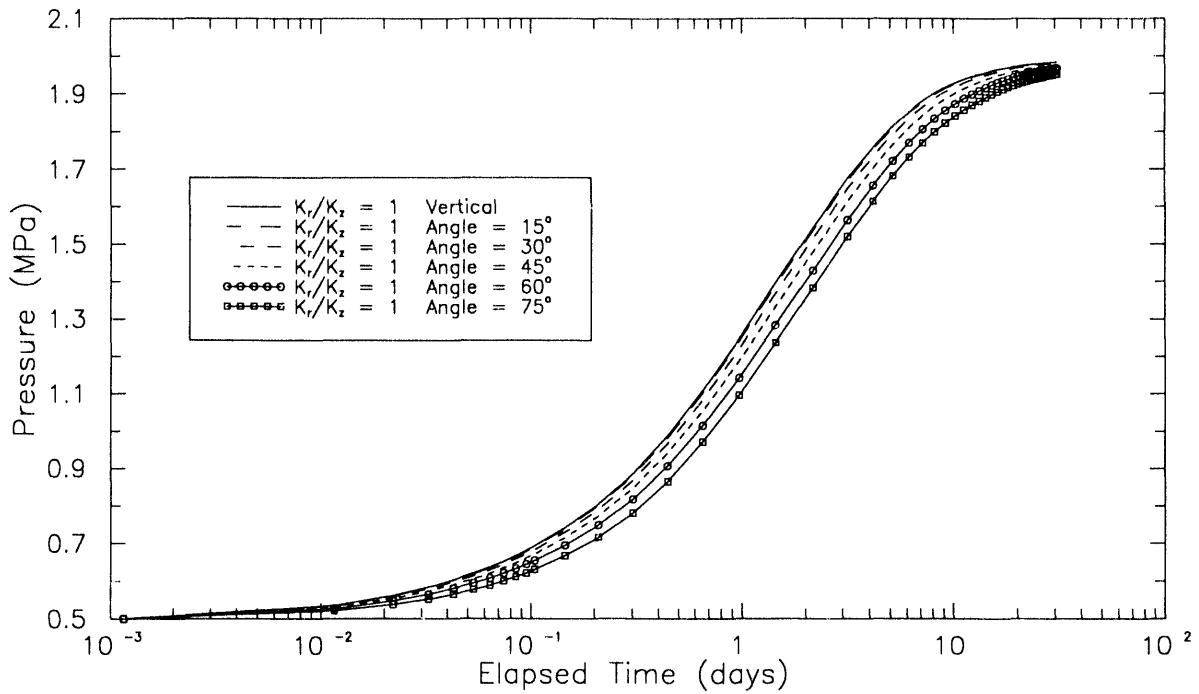
Figure C-1.   The effects of borehole slant angle on pressure responses observed during pulse-withdrawal tests for an anisotropy of 1.
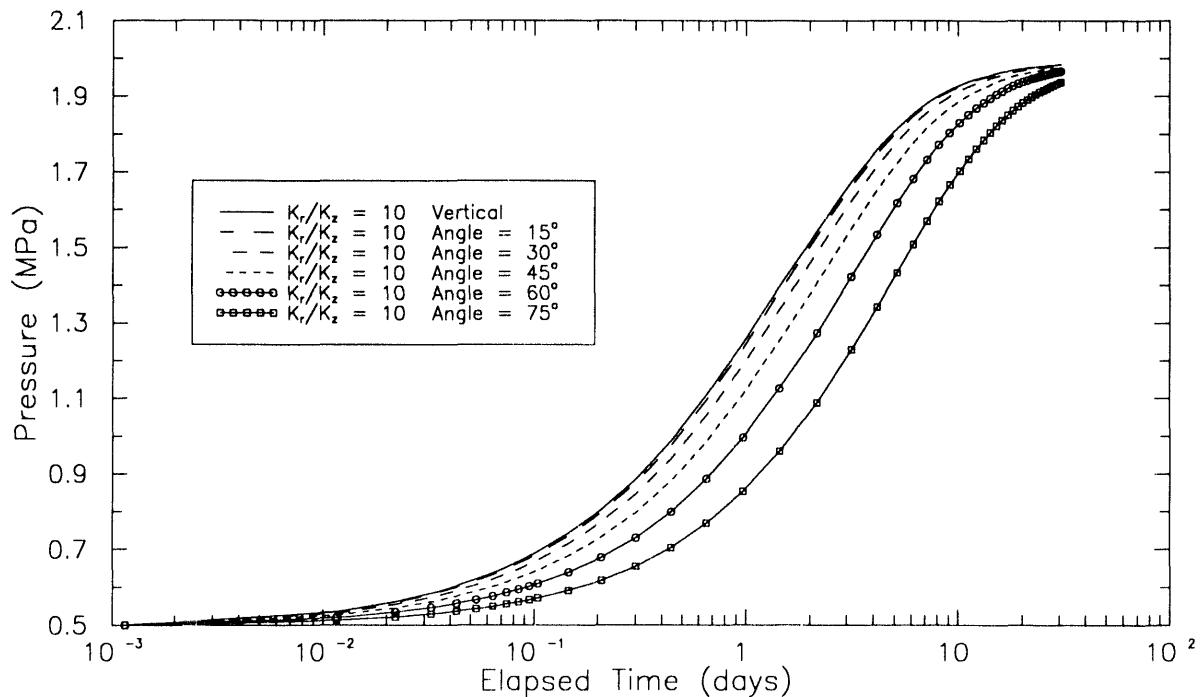
Figure C-2.   The effects of borehole slant angle on pressure responses observed during pulse withdrawal tests for an anisotropy of 10.
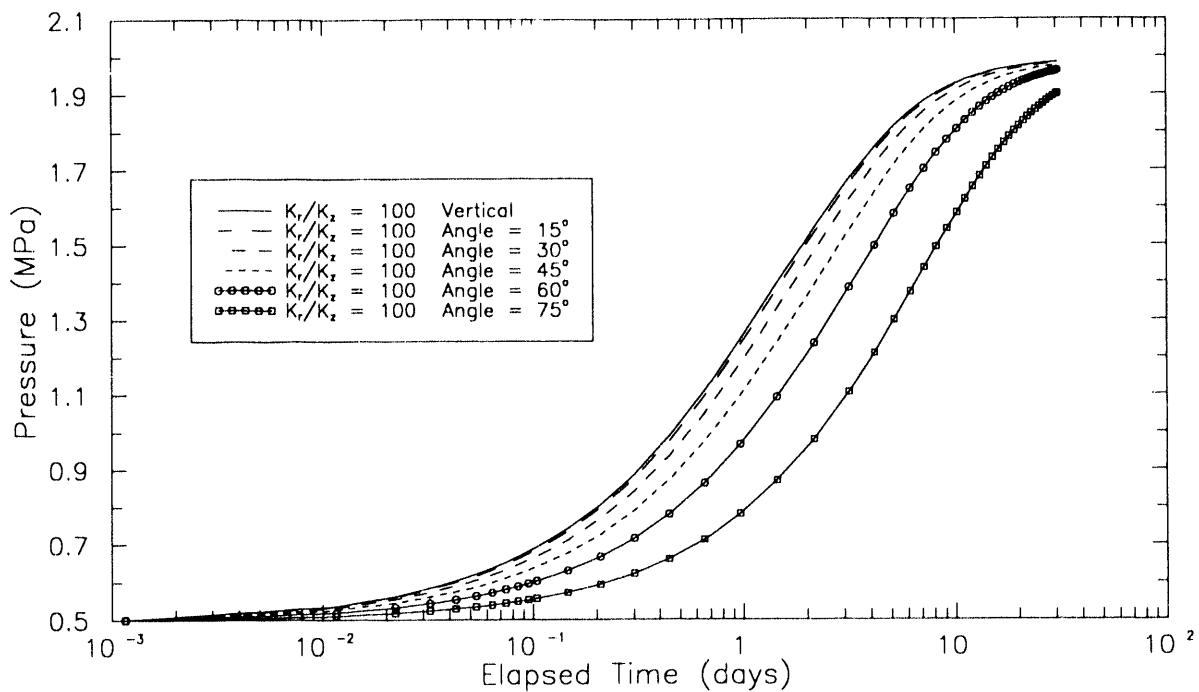
Figure C-3. The effects of borehole slant angle on pressure responses observed during pulse-withdrawal tests for an anisotropy of 100.

boreholes and boreholes slanted only 15° are insignificant for all values of anisotropy. Figures C-4 through C-8 show the effects of anisotropy for slant angles of 15°, 30°, 45°, 60°, and 75°. Pressure recoveries are also increasingly delayed as anisotropy increases, because increasing anisotropy decreases the vertical component of flow to the hole. An anisotropy change from 1 to 10 has a greater effect on the simulated responses than does a change from 10 to 100. Differences between simulations with anisotropies of 10 and 100 are insignificant for slant angles up to 45°.

C.3.2 STAB SIMULATIONS OF CONSTANT-PRESSURE WITHDRAWAL TESTS. The effects of borehole slant angle on the amount of brine produced during a constant-pressure withdrawal test for anisotropies of 1, 10, and 100 are shown in Figures C-9, C-10, and C-11, respectively. The amount of brine produced increases as the slant angle increases because of the accompanying increase in surface area of the borehole. This effect diminishes as anisotropy increases, decreasing vertical flow to the hole. As was the case for the simulated pulse-withdrawal tests, the differences between the responses in vertical boreholes and boreholes slanted only 15° are insignificant for all values of anisotropy. Figures C-12 through C-16 show the effects of anisotropy on brine production for slant angles of 15°, 30°, 45°, 60°, and 75°. An anisotropy change from 1 to 10 has a greater effect on the simulated responses than does a change from 10 to 100.
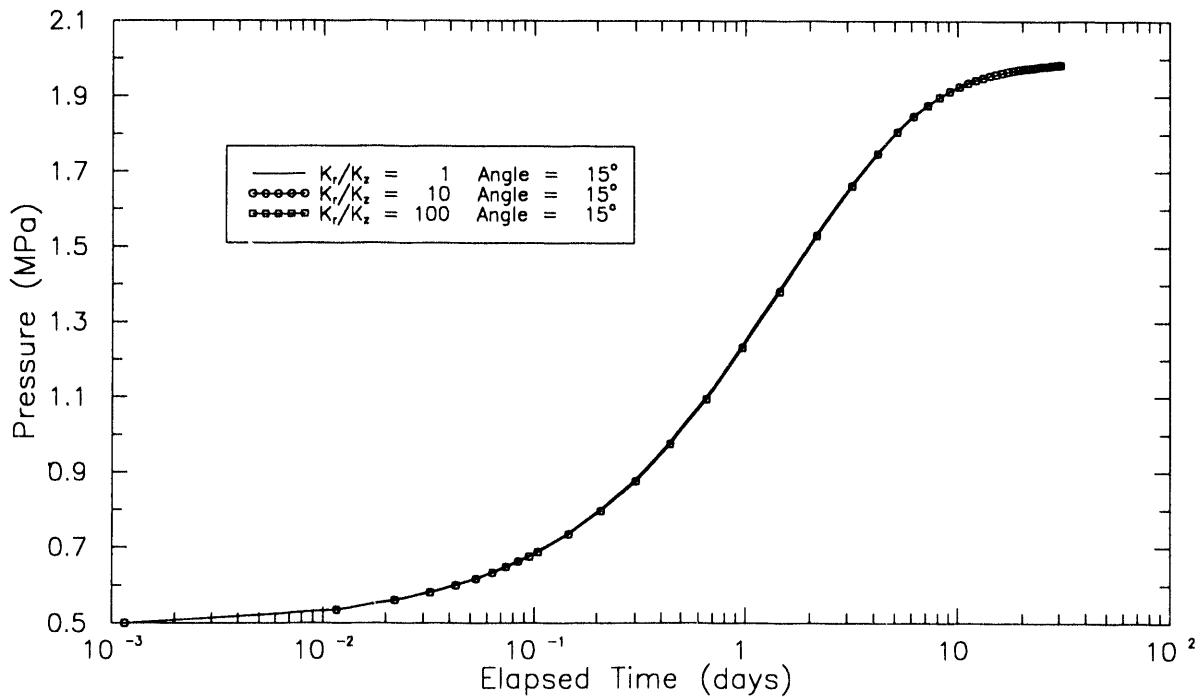
Figure C-4.   The effects of anisotropy on pressure responses observed during pulse-withdrawal tests for a borehole slant angle of 15°.
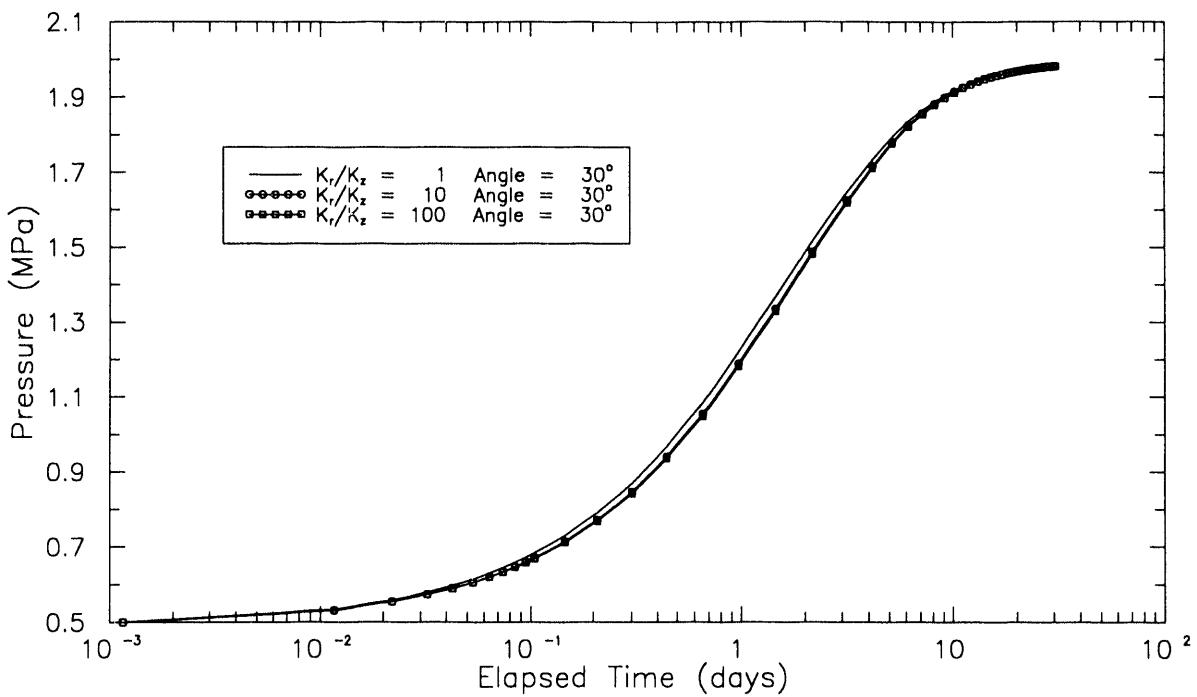
Figure C-5.   The effects of anisotropy on pressure responses observed during pulse-withdrawal tests for a borehole slant angle of 30°.

178

Figure C-7.   The effects of anisotropy on pressure responses observed during pulse-withdrawal tests for a borehole slant angle of 60°.
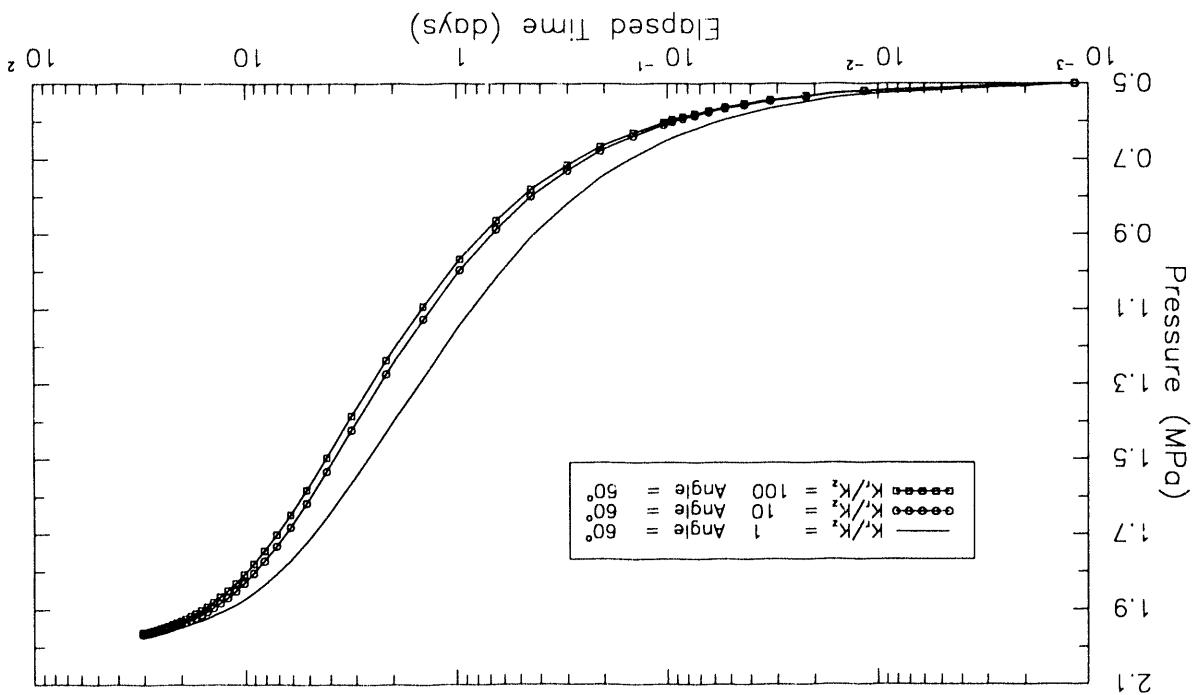
Figure C-6.   The effects of anisotropy on pressure responses observed during pulse-withdrawal tests for a borehole slant angle of 45°.
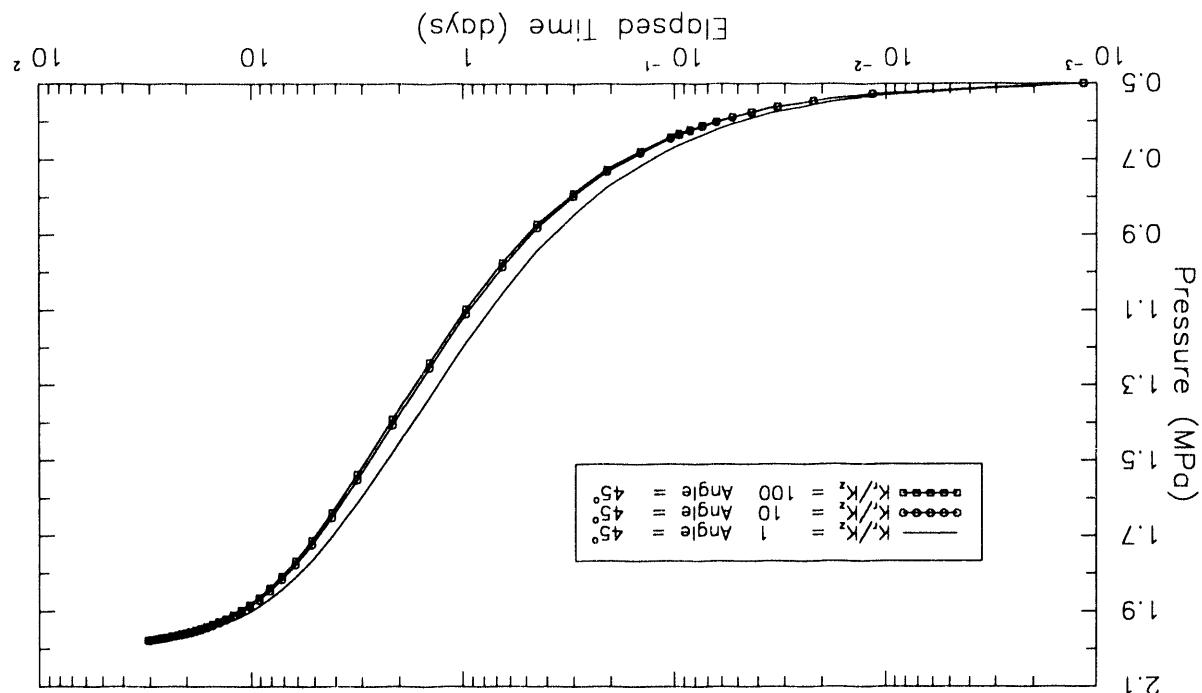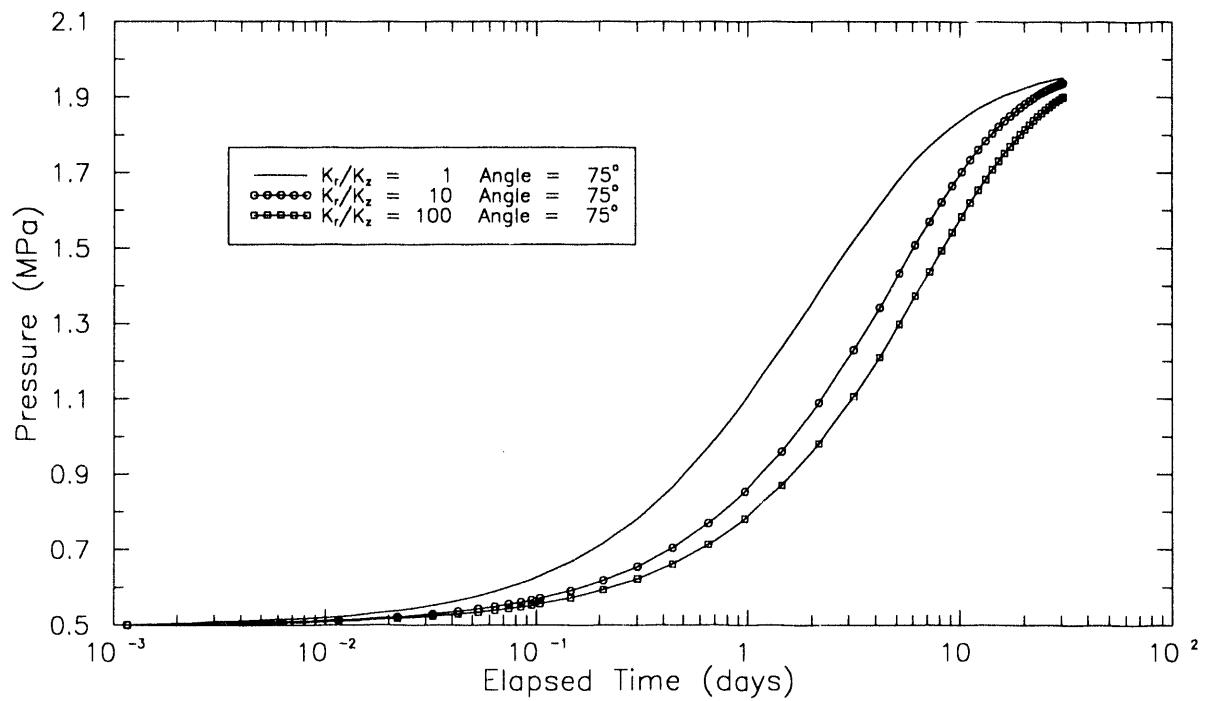
Figure C-8.   The effects of anisotropy on pressure responses observed during pulse-withdrawal tests for a borehole slant angle of 75°.
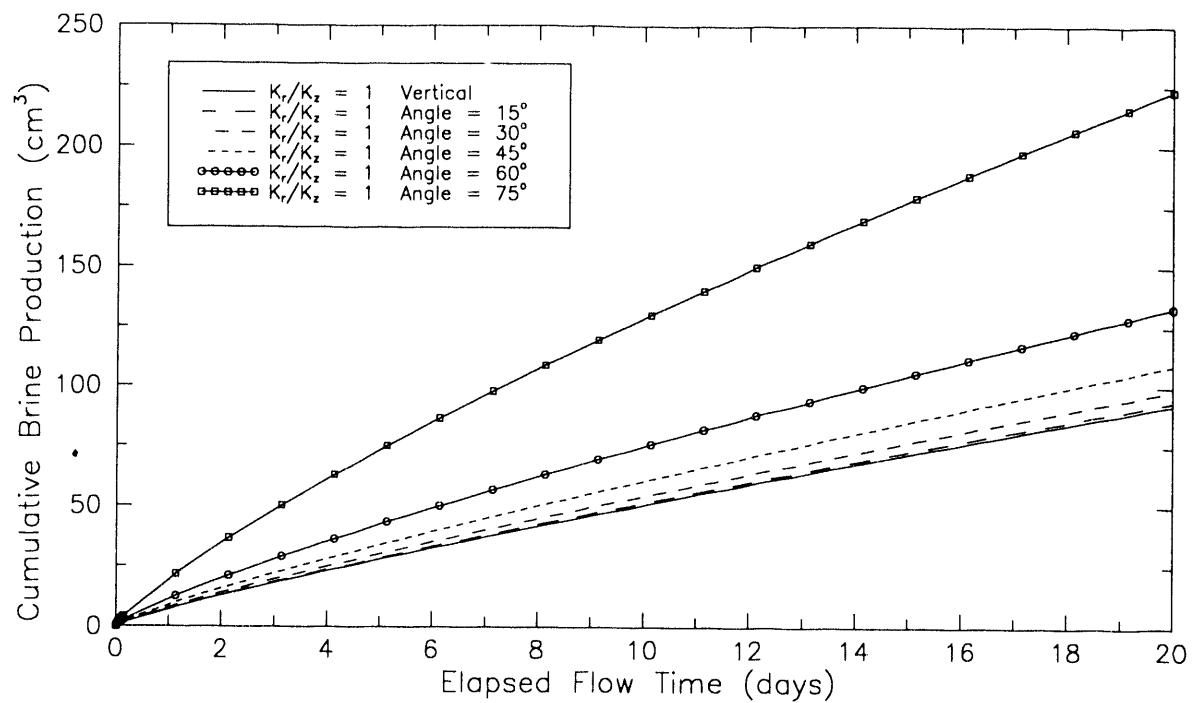
Figure C-9.   The effects of borehole slant angle on the amount of brine produced during a constant-pressure withdrawal test for an anisotropy of 1.
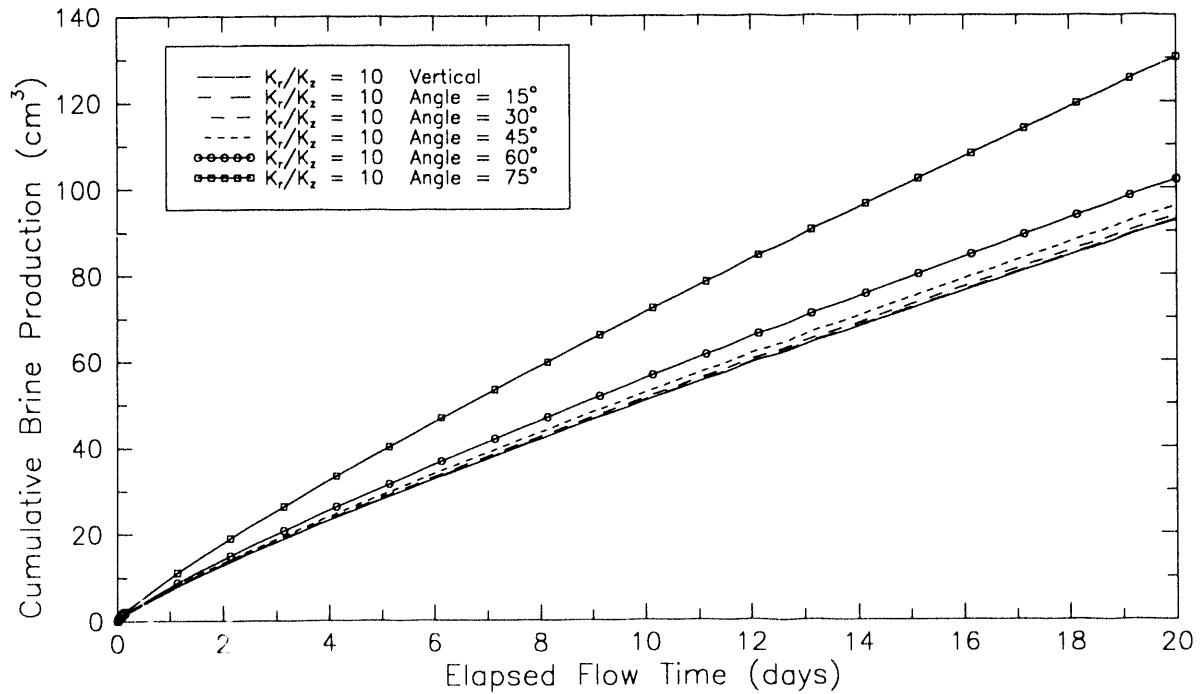
Figure C-10.   The effects of borehole slant angle on the amount of brine produced during a constant-pressure withdrawal test for an anisotropy of 10.
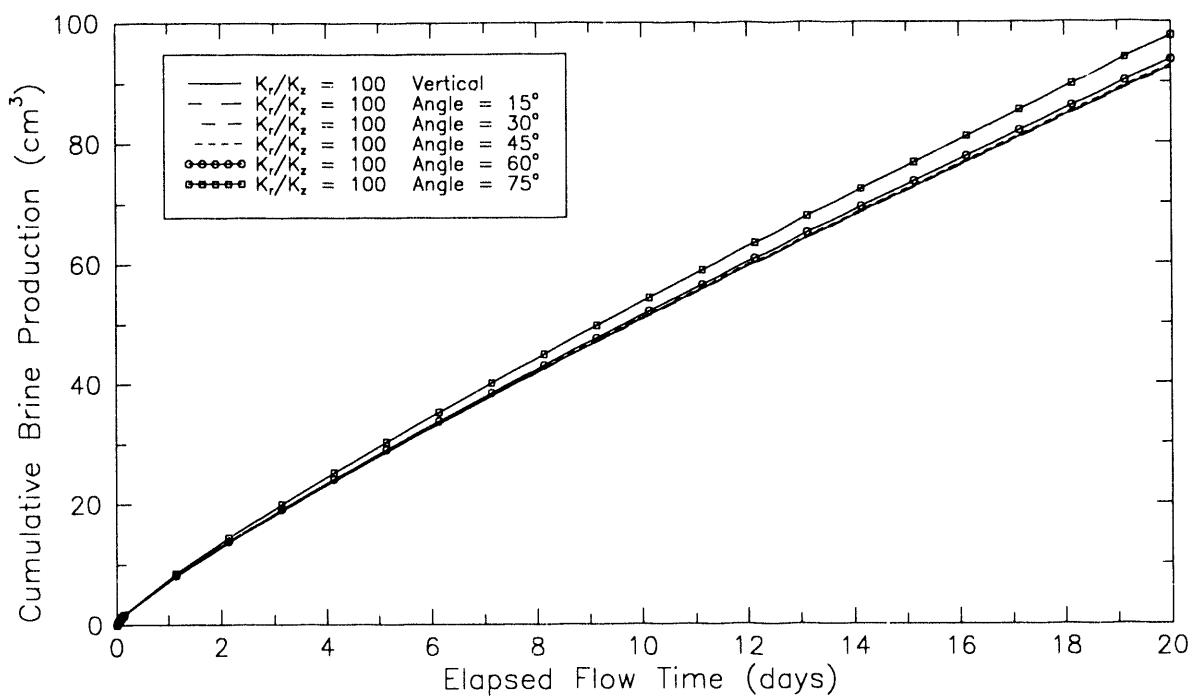
Figure C-11.   The effects of borehole slant angle on the amount of brine produced during a constant-pressure withdrawal test for an anisotropy of 100.
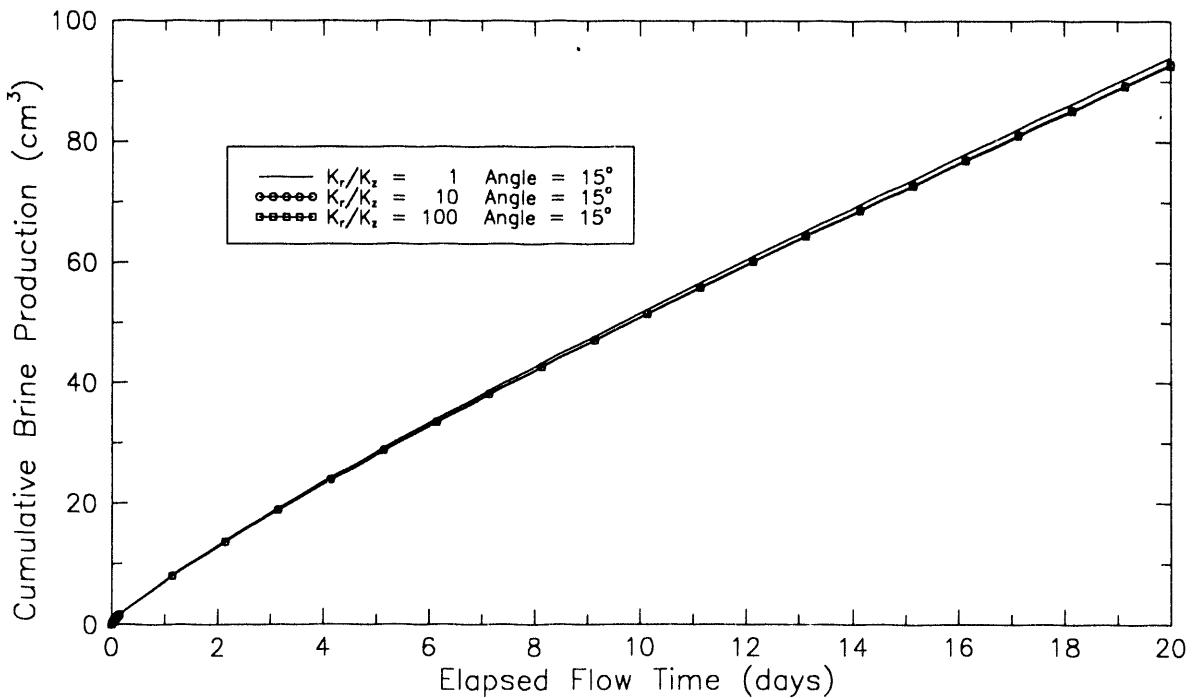
Figure C-12.   The effects of anisotropy on brine production during constant-pressure withdrawal tests for a borehole slant angle of 15°.
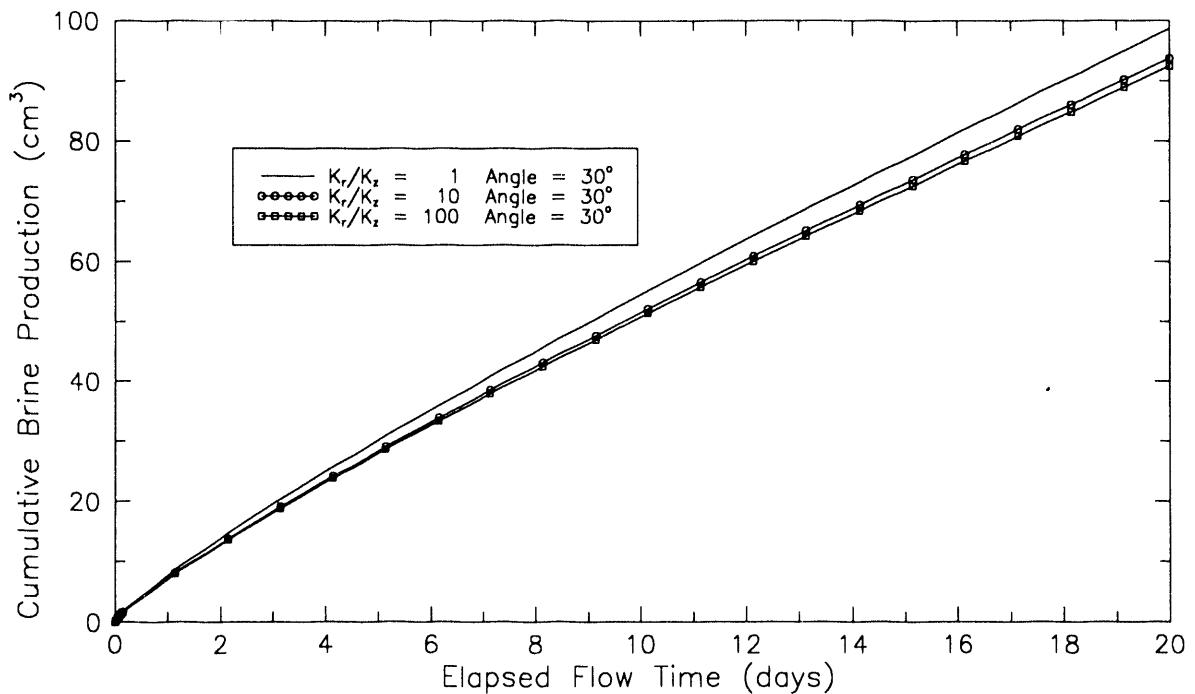

Figure C-13.   The effects of anisotropy on brine production during constant-pressure withdrawal tests for a borehole slant angle of 30°.
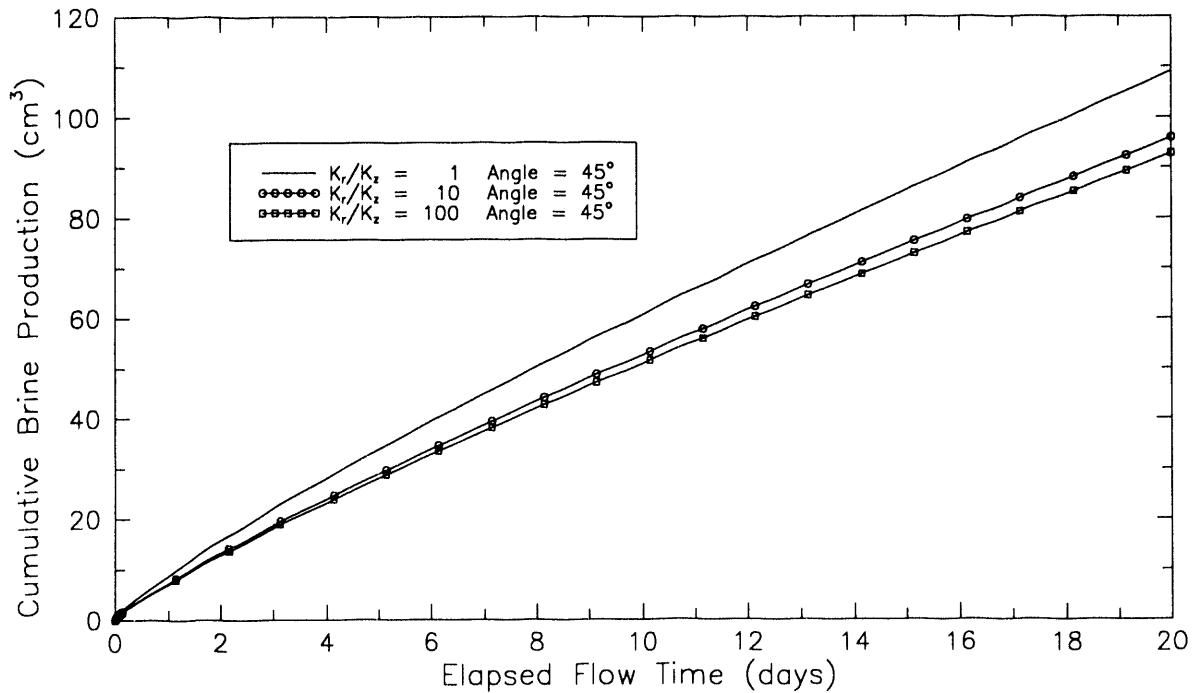
Figure C-14.   The effects of anisotropy on brine production during constant-pressure withdrawal tests for a borehole slant angle of 45°.
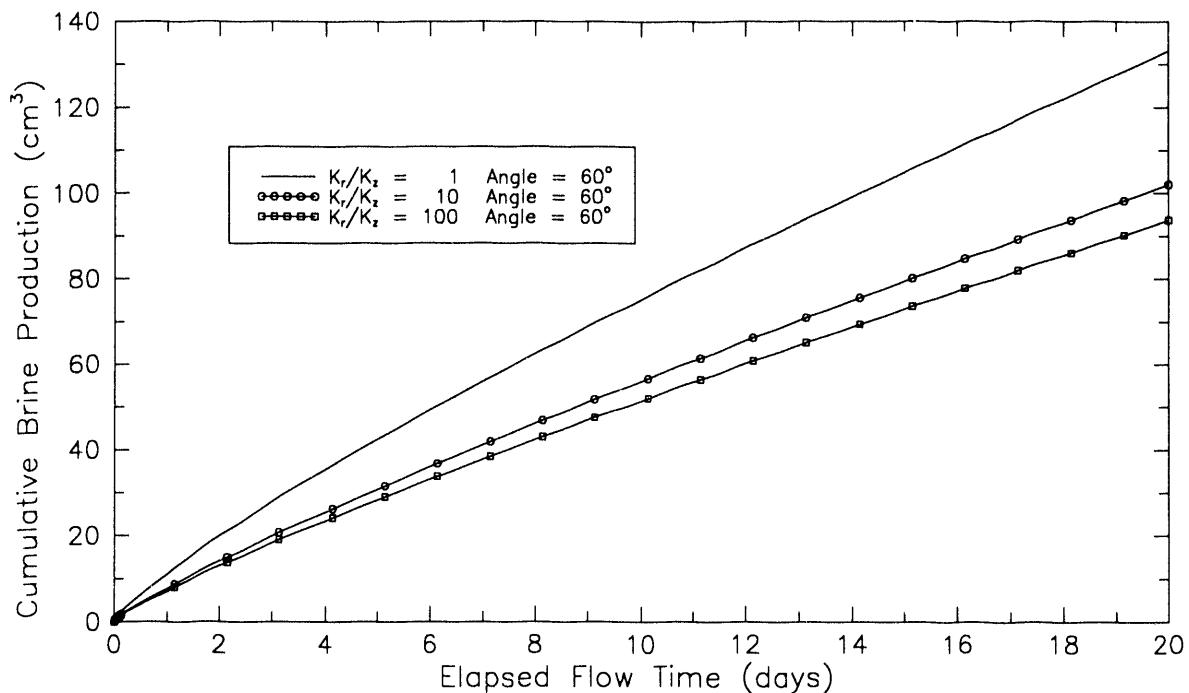
Figure C-15.   The effects of anisotropy on brine production during constant-pressure withdrawal tests for a borehole slant angle of 60°
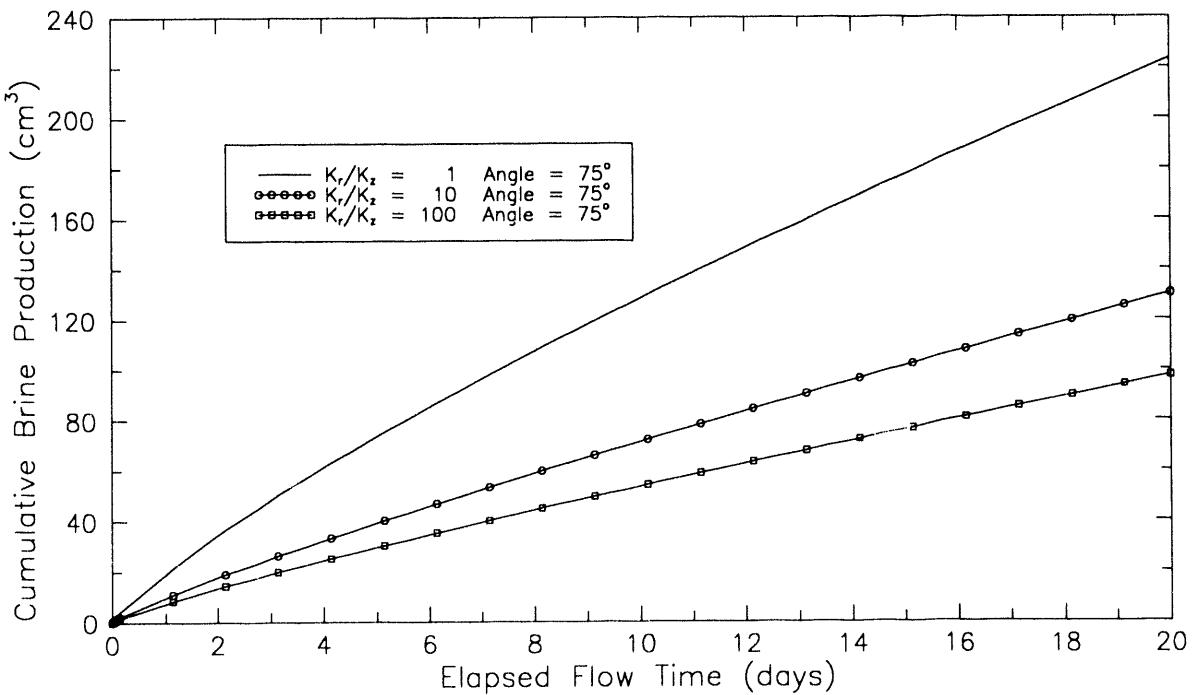
Figure C-16.   The effects of anisotropy on brine production during constant-pressure withdrawal tests for a borehole slant angle of 75°.

C.3.3 STAB SIMULATIONS OF PRESSURE-BUILDUP TESTS. The effects of borehole slant angle on pressure buildup following a constant-pressure withdrawal test for anisotropies of 1, 10, and 100 are shown in Figures C-17, C-18, and C-19, respectively. The amount of pressure recovery at any given time decreases as the slant angle and/or anisotropy increases, for the reasons discussed above in Sections C.3.1 and C.3.2. Figures C-20 through C-24 show the effects of anisotropy on pressure buildup for slant angles of 15°, 30°, 45°, 60°, and 75°. As was the case for the simulations of the other types of tests, the differences between the responses in vertical boreholes and boreholes slanted only 15° are insignificant, regardless of anisotropy. The pressure-buildup responses in boreholes slanted 30° are insensitive to anisotropy (Figure C-21). In general, an anisotropy change from 1 to 10 has a greater effect on the simulated responses than does a change from 10 to 100.

For the boreholes slanted 60° and 75°, the simulated pressure-buildup curves for the different values of anisotropy cross after 5 to 20 days of recovery. That is, the pressure-buildup curves for the higher values of anisotropy, which initially show less recovery than the curves for lower values of anisotropy, show more recovery at late time. This occurs because the upper and lower no-flow boundaries influence the simulations sooner as anisotropy decreases. For the isotropic case, flow is radial towards the borehole at the start of the buildup period and changes to horizontal as the upper and lower no-flow boundaries come into play, reducing the rate of buildup. For anisotropic cases, less flow is contributed vertically to begin with and the effects of the boundaries are felt later than in the isotropic case.

184
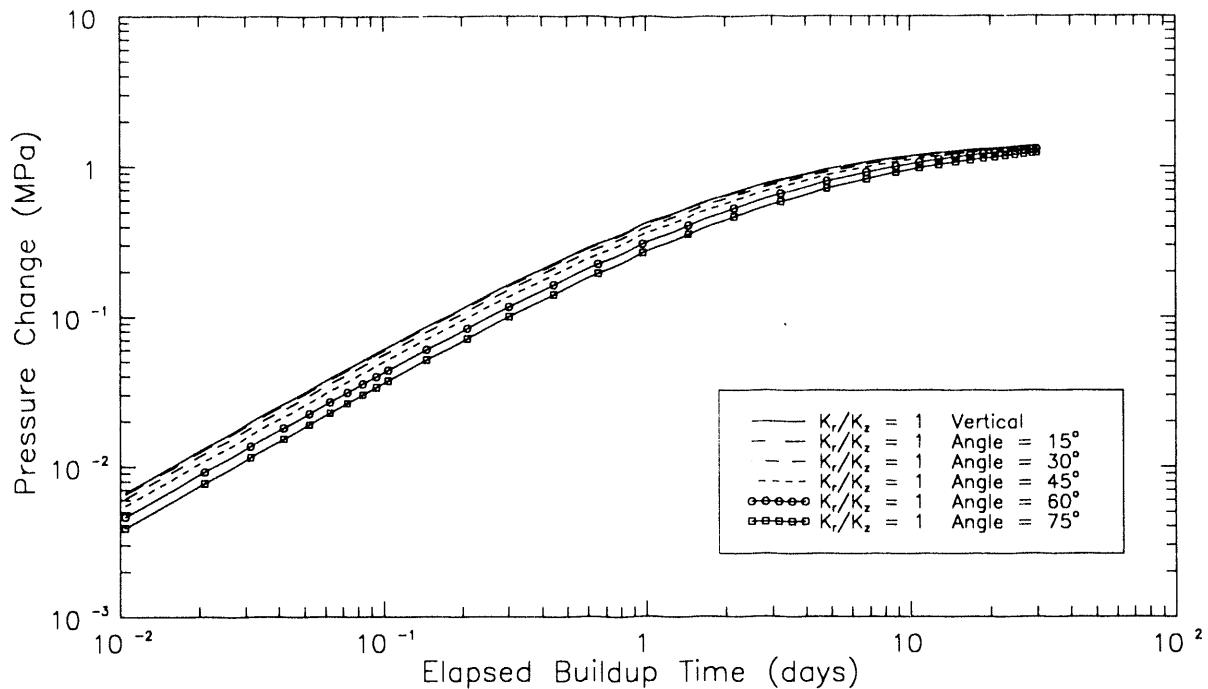
Figure C-17.   The effects of borehole slant angle on pressure buildup following a constant-pressure withdrawal test for an anisotropy of 1.
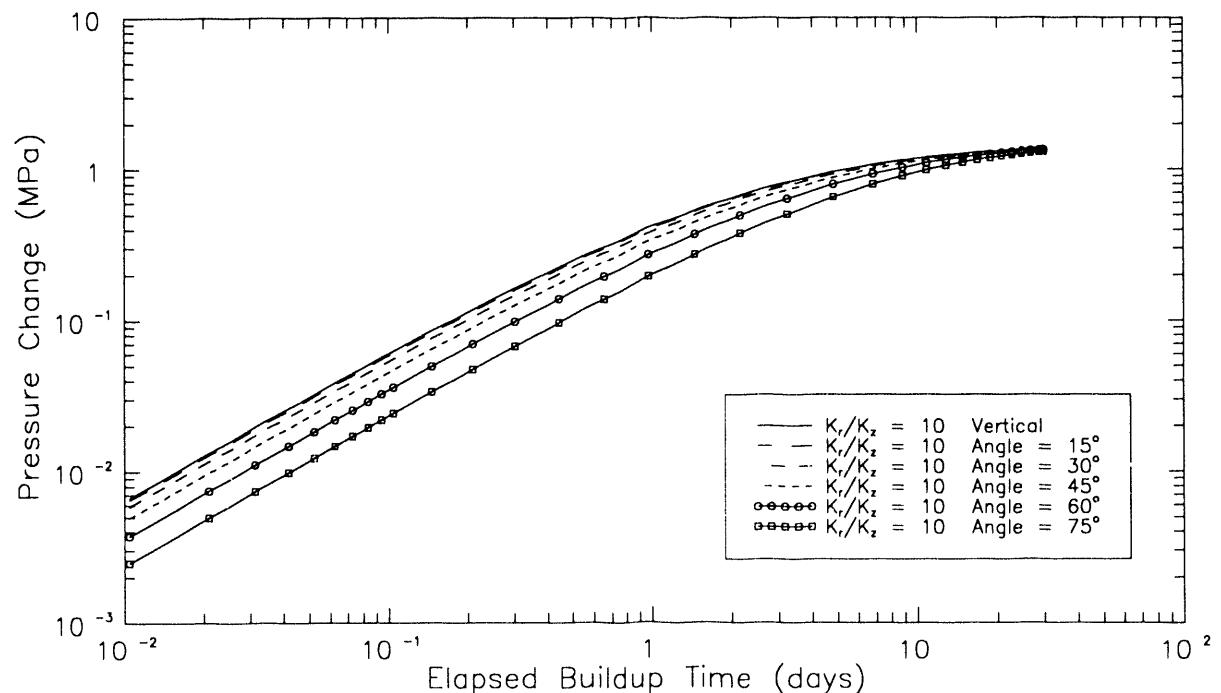
Figure C-18.   The effects of borehole slant angle on pressure buildup following a constant-pressure withdrawal test for an anisotropy of 10.

185
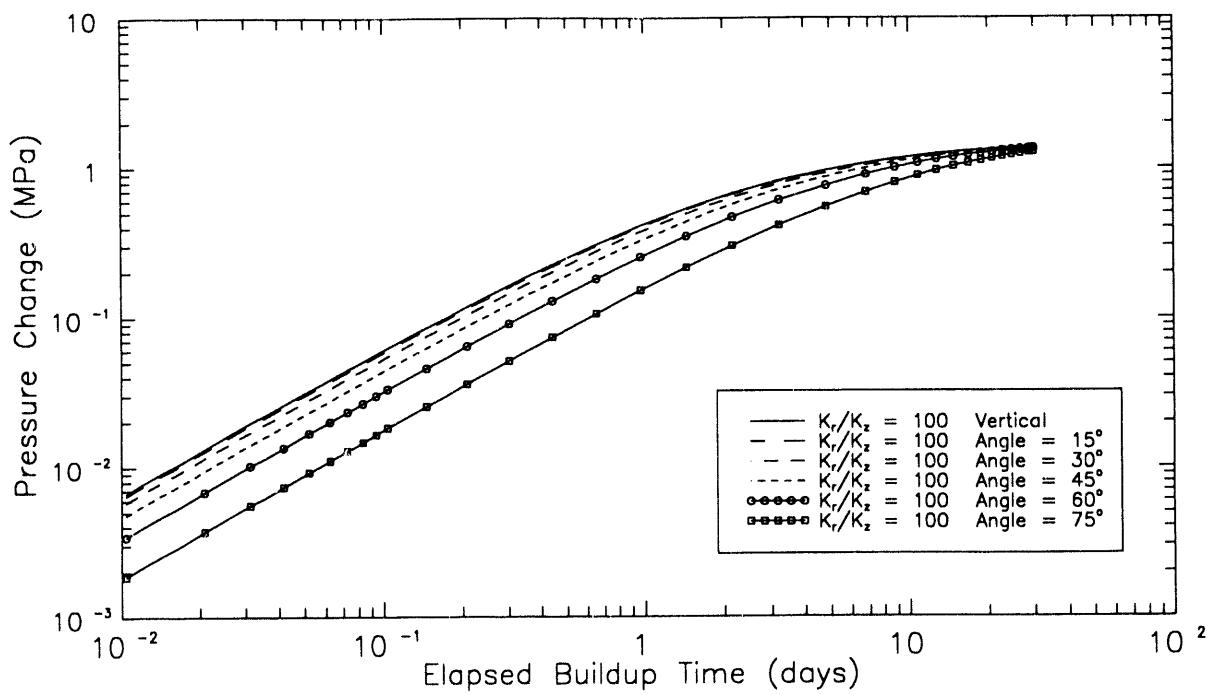
Figure C-19. The effects of borehole slant angle on pressure buildup following a constant-pressure withdrawal test for an anisotropy of 100.
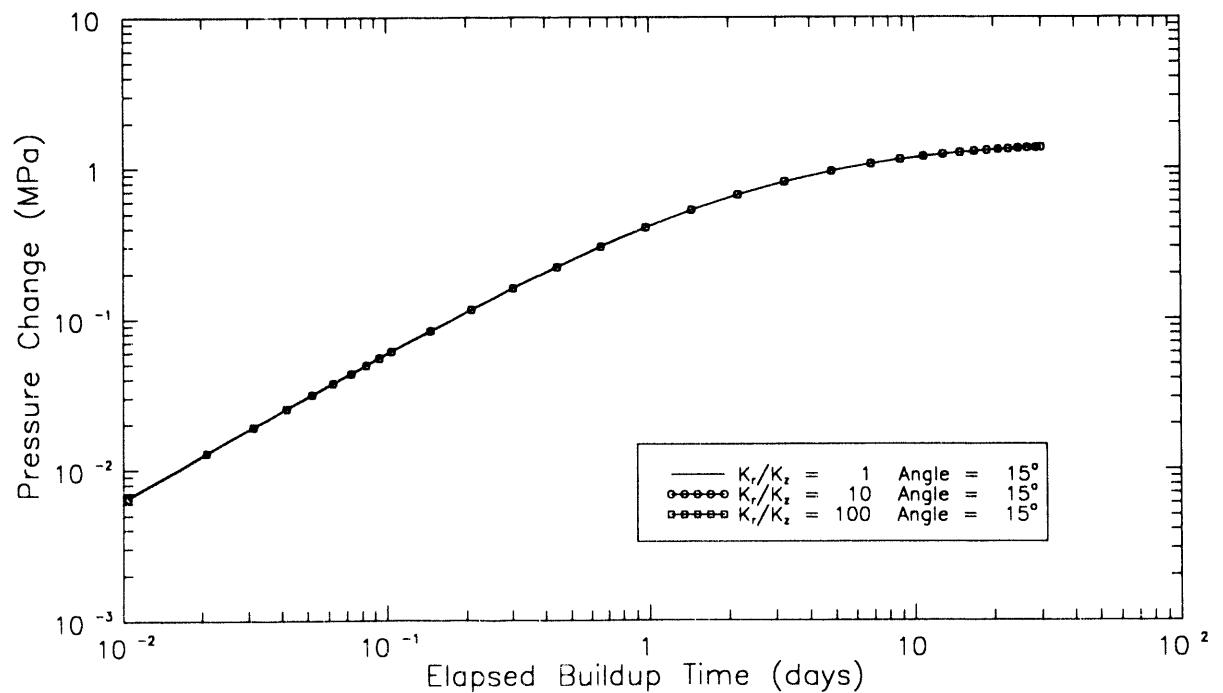
Figure C-20. The effects of anisotropy on pressure buildup following a constant-pressure withdrawal test for a borehole slant angle of 15°.
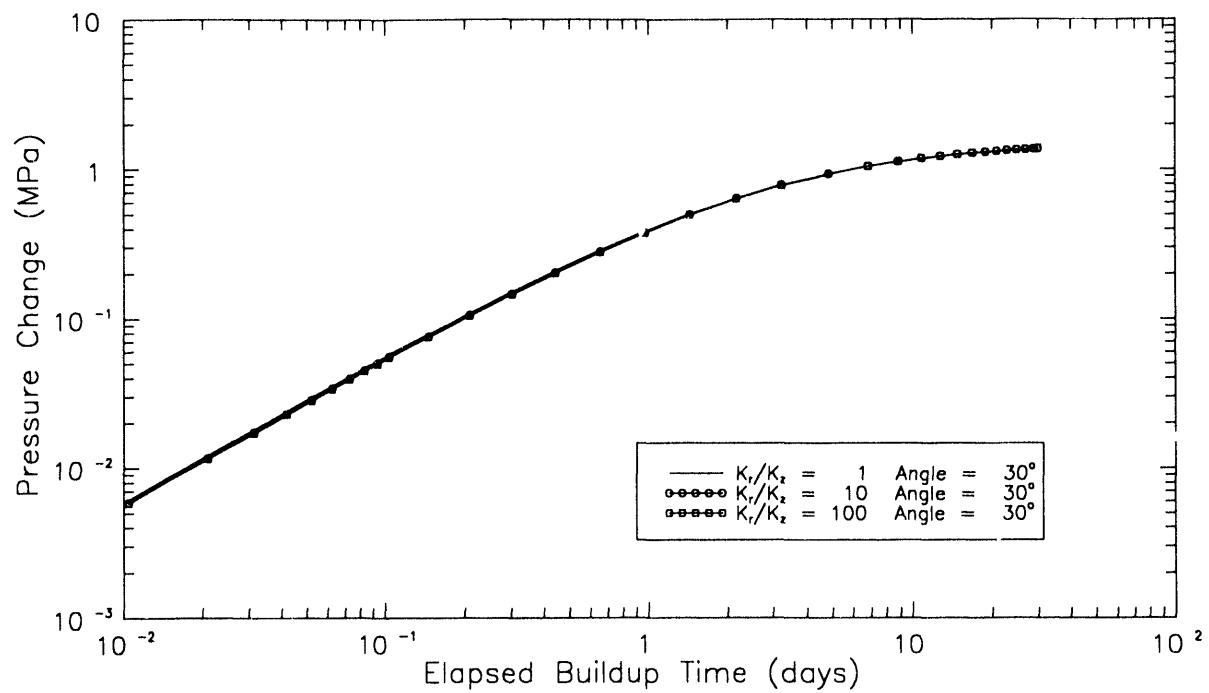
Figure C-21.   The effects of anisotropy on pressure buildup following a constant-pressure withdrawal test for a borehole slant angle of 30°.
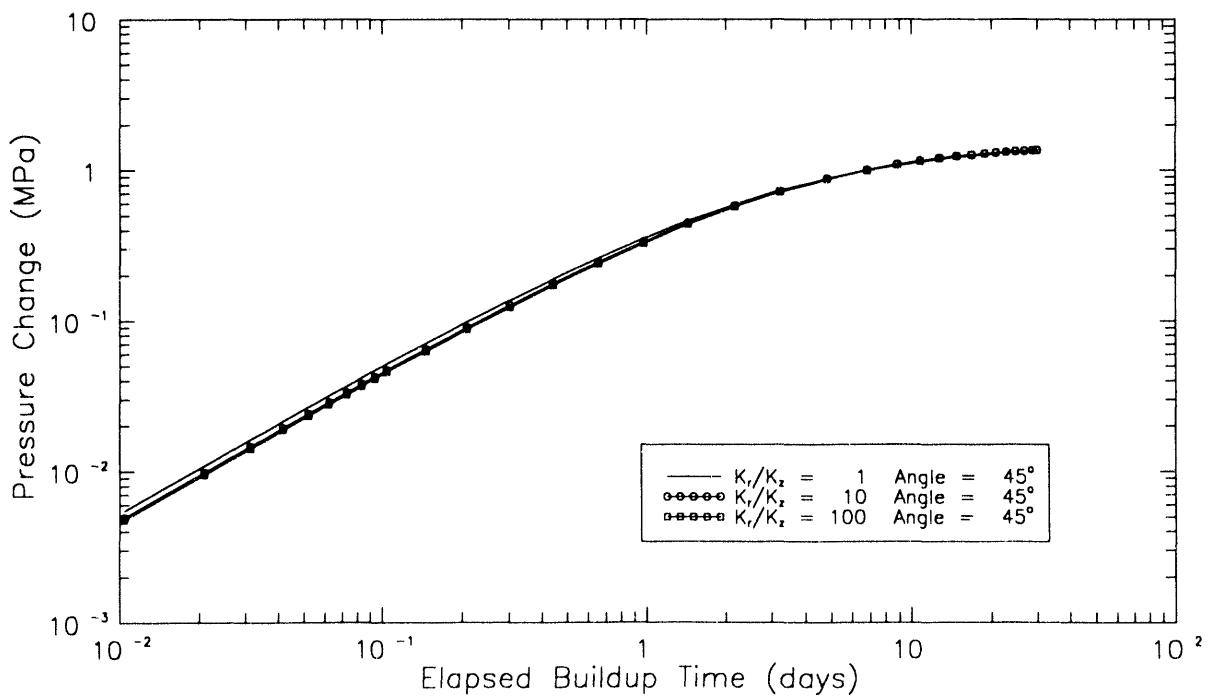
Figure C-22.   The effects of anisotropy on pressure buildup following a constant-pressure withdrawal test for a borehole slant angle of 45°.
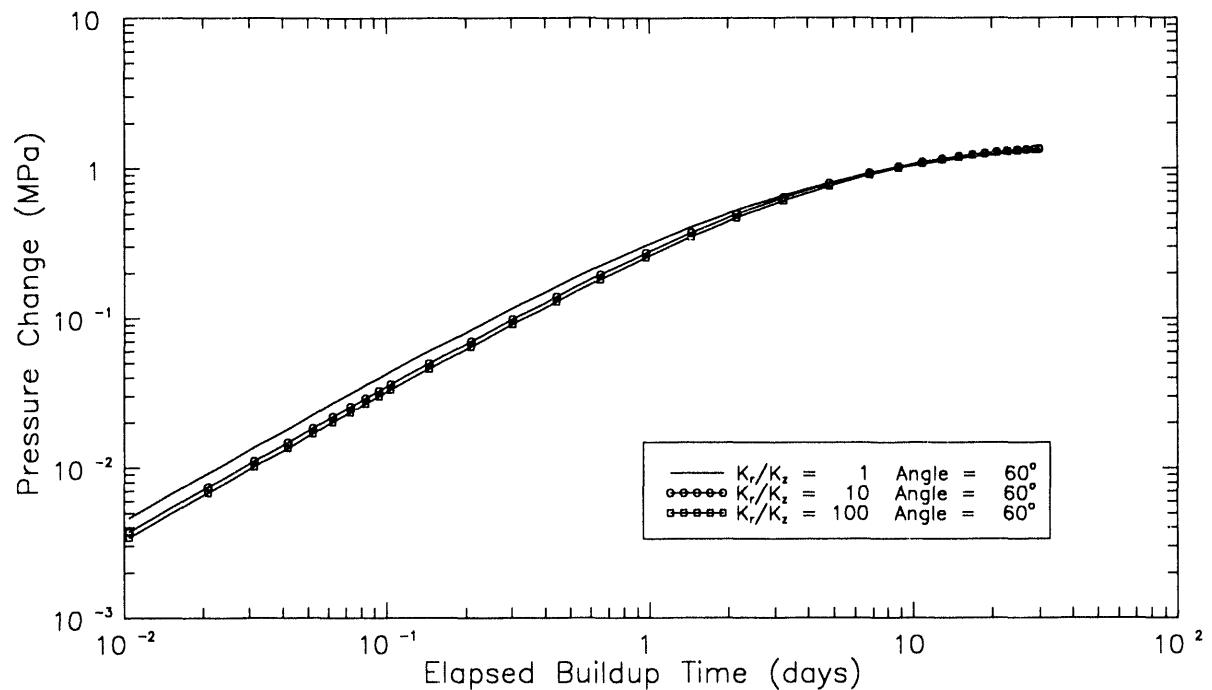
Figure C-23.   The effects of anisotropy on pressure buildup following a constant-pressure withdrawal test for a borehole slant angle of 60°.
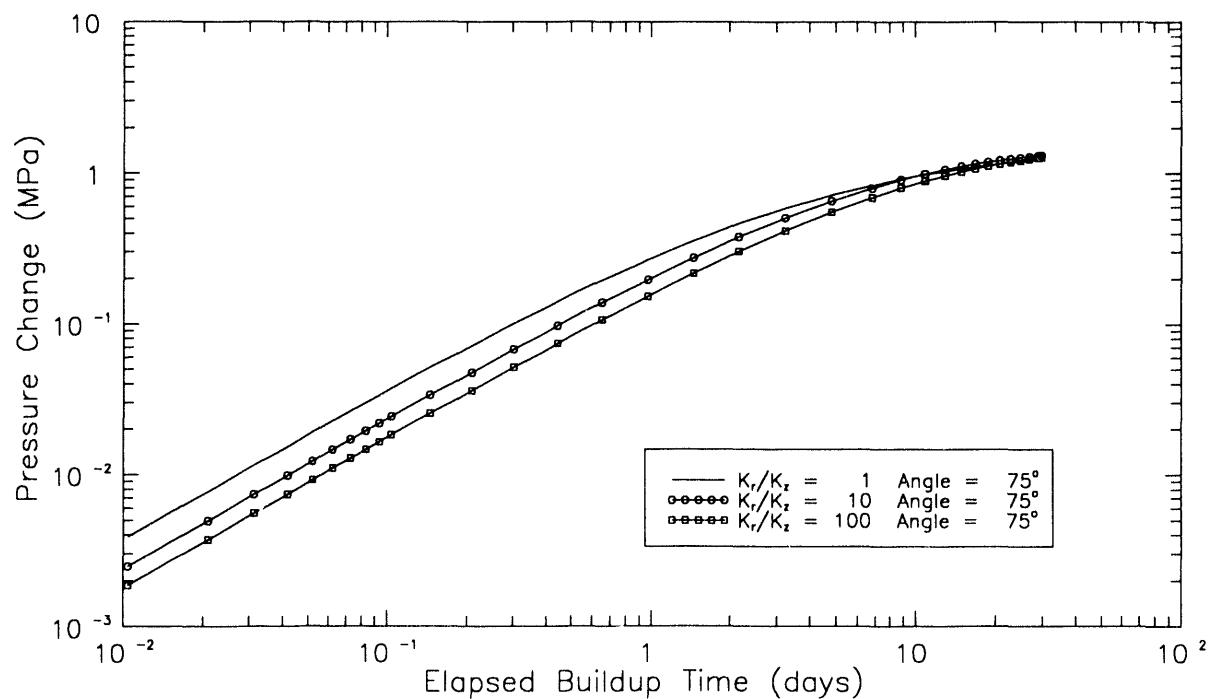
Figure C-24.   The effects of anisotropy on pressure buildup following a constant-pressure withdrawal test for a borehole slant angle of 75°.

188

C.4   Comparison of STAB Simulations with SWIFT II and GTFM Equivalent-Vertical-Borehole Simulations

Figures C-25, C-26, and C-27 show comparisons of STAB simulations of pulse-withdrawal tests for different anisotropies and slant angles of 15°, 45°, and 75°, respectively, with SWIFT II and GTFM simulations for equivalent vertical boreholes. For a slant angle of 15° (Figure C-25), all of the simulations are in good agreement. For a slant angle of 45° (Figure C-26), the SWIFT II and GTFM simulations generally fall between the STAB simulations with anisotropies of 1 and 10. For a slant angle of 75°, the SWIFT II and GTFM simulations are closest to the STAB simulation using an anisotropy of 10, but both show more recovery at early time and less recovery at late time than the STAB simulation. In all cases, the SWIFT II and GTFM equivalent-vertical-borehole simulations are in good agreement.

Figures C-28 through C-30 show comparisons of brine production during a constant-pressure withdrawal test between STAB, SWIFT II, and GTFM simulations for slant angles of 15°, 45°, and 75°. Figure C-28 shows that all of the simulations are in good agreement for a slant angle of 15°. For slant angles of 45° and 75° (Figures C-29 and C-30), the SWIFT II and GTFM simulations are best matched by the STAB simulation using an anisotropy of 10. In all cases, the SWIFT II simulations show slightly more brine production than the GTFM simulations.

Figures C-31 through C-33 show comparisons between STAB, SWIFT II, and GTFM simulations of the pressure buildup following a constant-pressure withdrawal test for slant angles of 15°, 45°, and 75°. Figure
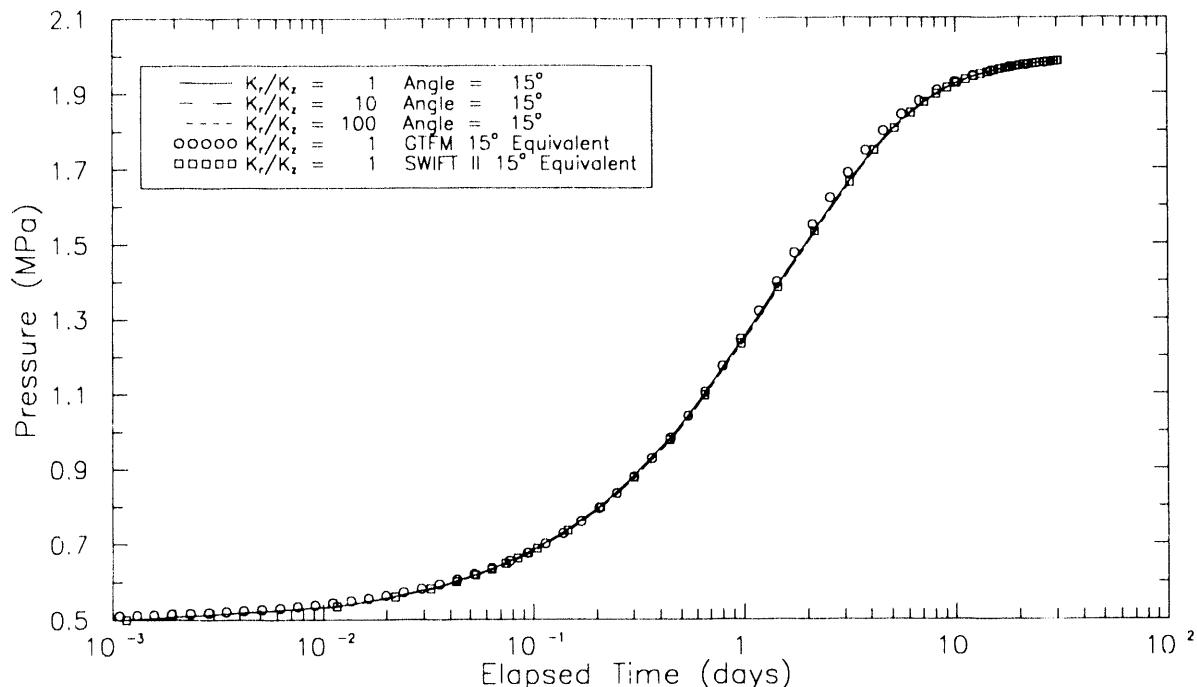

Figure C-25.   Comparisons of STAB simulations of pulse-withdrawal tests for different anisotropies and a borehole slant angle of 15° with SWIFT II and GTFM simulations for equivalent vertical boreholes.
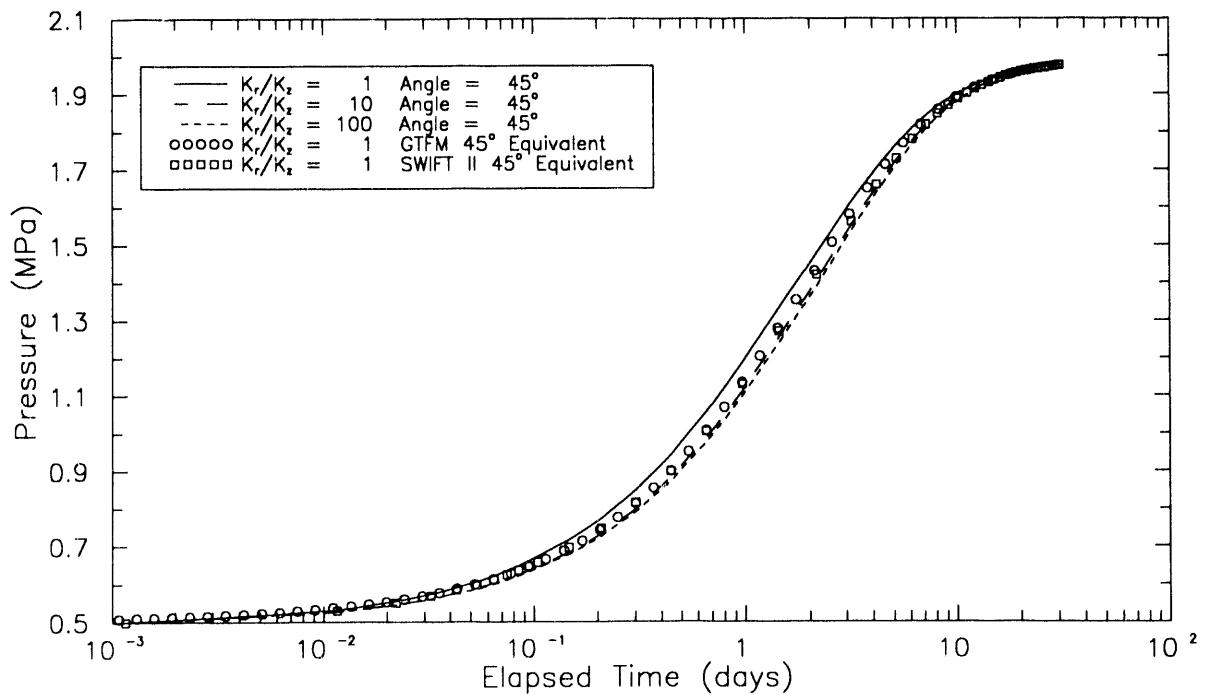
Figure C-26.   Comparisons of STAB simulations of pulse-withdrawal tests for different anisotropies and a borehole slant angle of 45° with SWIFT II and GTFM simulations for equivalent vertical boreholes.
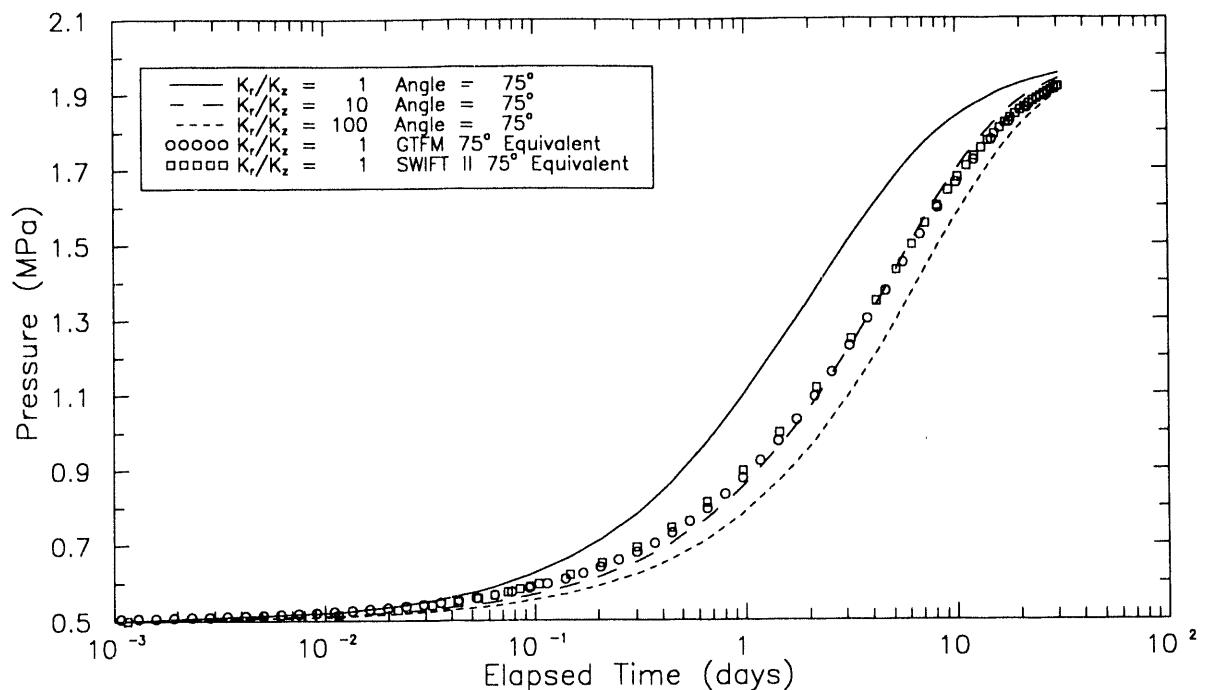
Figure C-27.   Comparisons of STAB simulations of pulse-withdrawal tests for different anisotropies and a borehole slant angle of 75° with SWIFT II and GTFM simulations for equivalent vertical boreholes.
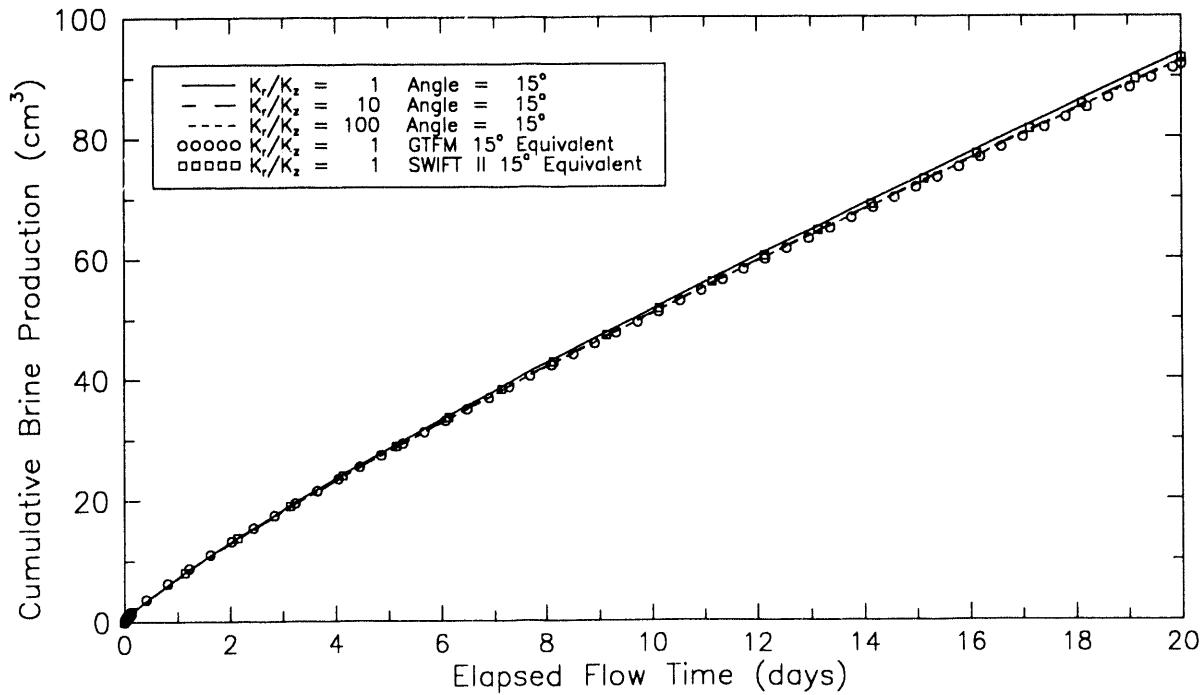
Figure C-28.   Comparisons of brine production during a constant-pressure withdrawal test between STAB, SWIFT II, and GTFM simulations for a borehole slant angle of 15°.
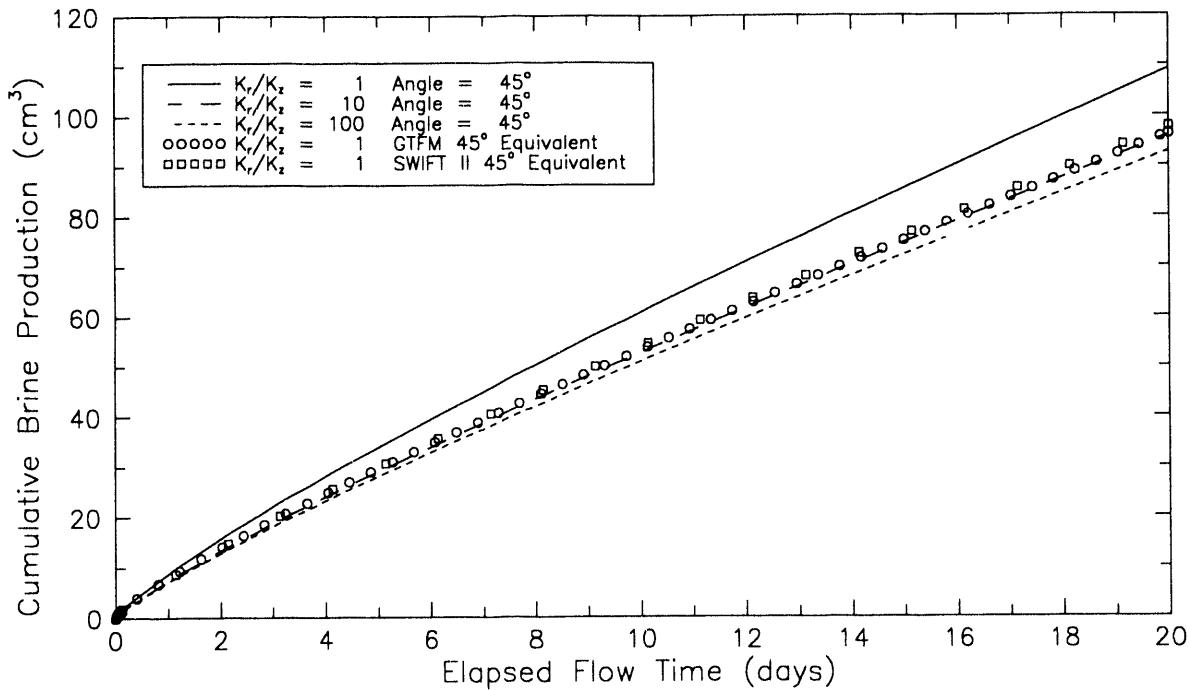
Figure C-29.   Comparisons of brine production during a constant-pressure withdrawal test between STAB, SWIFT II, and GTFM simulations for a borehole slant angle of 45°.
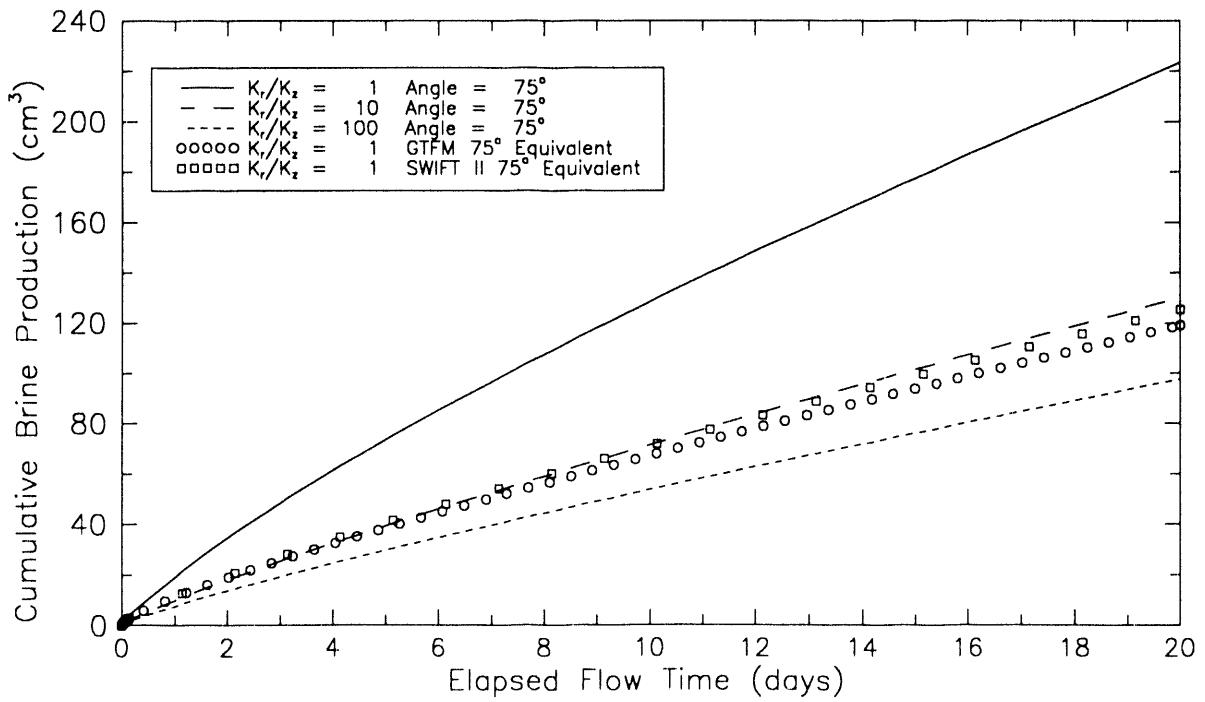
Figure C-30.   Comparisons of brine production during a constant-pressure withdrawal test between STAB, SWIFT II, and GTFM simulations for a borehole slant angle of 75°.
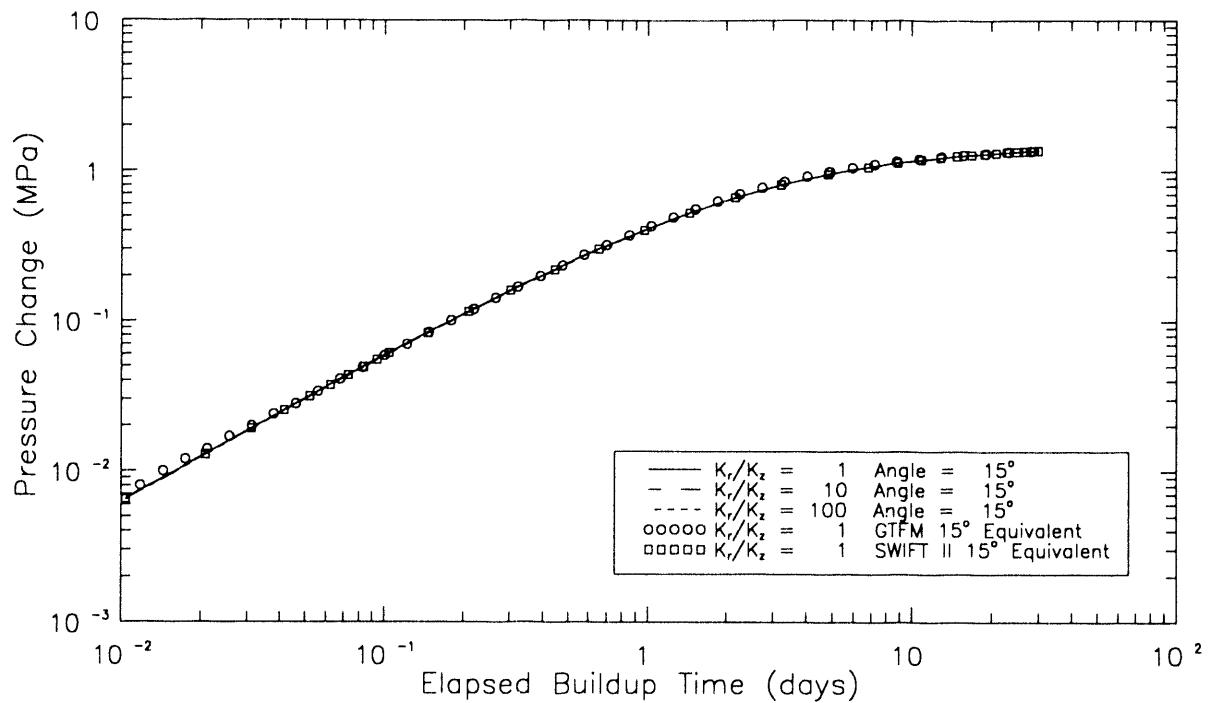
Figure C-31.   Comparisons between STAB, SWIFT II, and GTFM simulations of the pressure buildup following a constant-pressure withdrawal test for a borehole slant angle of 15°.
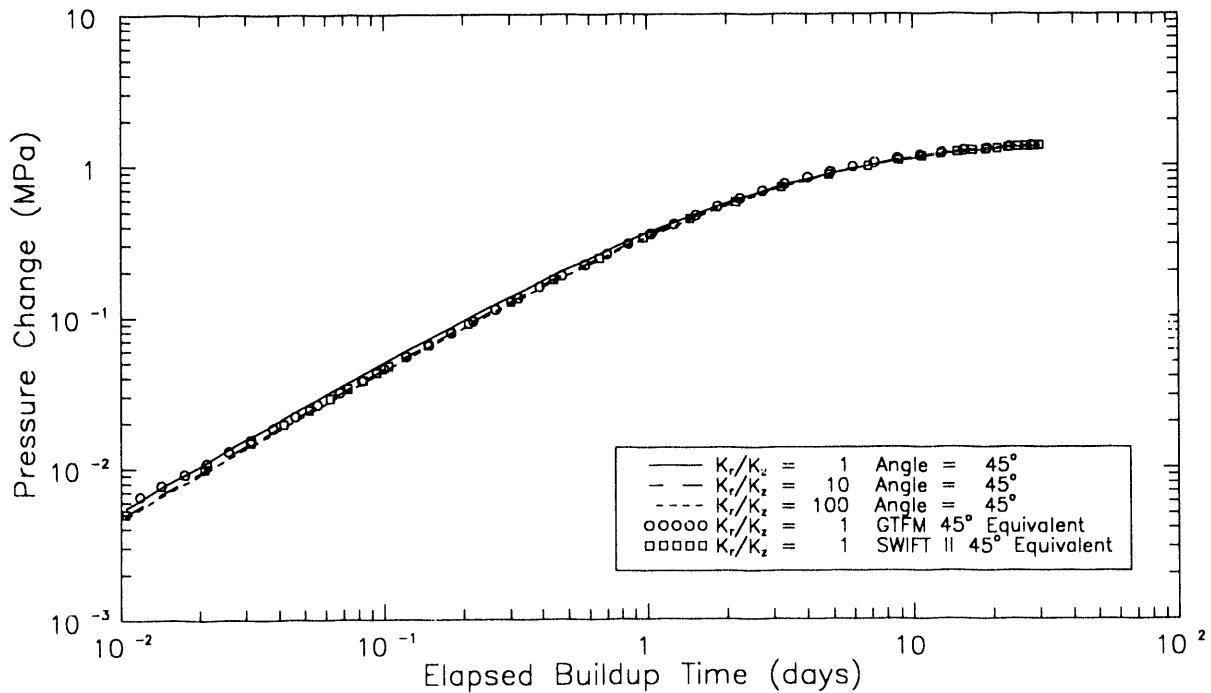
Figure C-32.   Comparisons between STAB, SWIFT II, and GTFM simulations of the pressure buildup following a constant-pressure withdrawal test for a borehole slant angle of 45°.
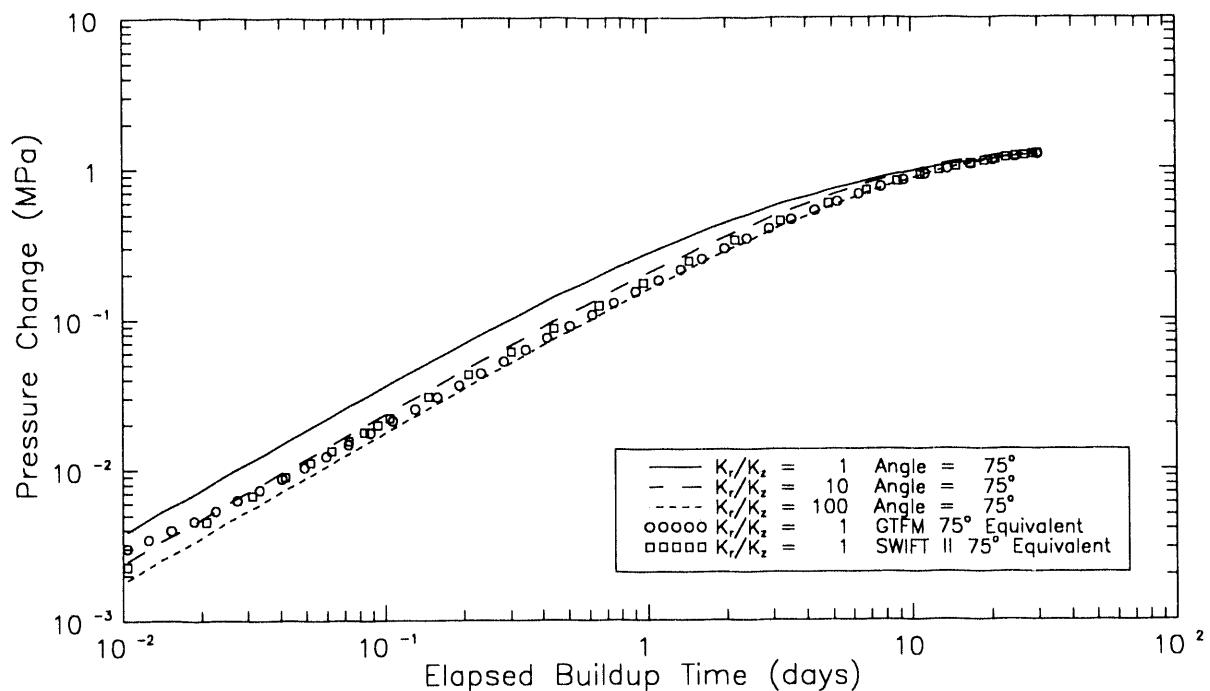
Figure C-33.   Comparisons between STAB, SWIFT II, and GTFM simulations of the pressure buildup following a constant-pressure withdrawal test for a borehole slant angle of 75°.

193

C-31 shows that all of the simulations are in good agreement for a slant angle of 15°. For a slant angle of 45° (Figure C-32), the SWIFT II and GTFM simulations are best matched by the STAB simulation using an anisotropy of 10, although the differences between the three anisotropic STAB simulations are slight. For a slant angle of 75° (Figure C-33), the SWIFT II and GTFM simulations fall between the STAB simulations using anisotropies of 10 and 100.

C.5 Type-Curve Analysis of STAB Simulations of Constant-Pressure Withdrawal Tests

To evaluate how borehole slant angle and anisotropy might affect type-curve analysis of constant-pressure withdrawal tests, STAB simulations were interpreted as if they were actual tests. The flow-rate data corresponding to the STAB simulations of brine production to holes slanted 15°, 45°, and 75° shown in Figures C-12, C-14, and C-16, respectively, were first plotted versus elapsed flow time on a log-log graph. The type curve of Jacob and Lohman (1952; Figure 6-2) was then fit to the data as described in Section 6.1.2, and a value of transmissivity was calculated.

The STAB simulations and type-curve matches for slant angles of 15° and 45° and anisotropies of 1, 10, and 100 are shown in Figures C-34 through C-39. In all cases, a good match was found between the late-time data and the type curve, and the interpreted transmissivity was between 4.9×10^{-13} and 5.1×10^{-13} m^2/s. The actual vertical transmissivity value used in the STAB simulations was 5.0×10^{-13} m^2/s.

Anisotropy had a significant effect on the simulated flow rates for the borehole slanted 75°. Figure C-40 shows the flow-rate data from the 75° borehole with isotropic conditions. Instead of an asymptotic decline in flow rate as typified by the Jacob-Lohman type curve, the flow rate decreased more rapidly after approximately the first 0.5 day of the simulated test. This accelerated decline in the flow rate probably reflects the influence of the no-flow boundaries at the top and bottom of the test interval, as discussed above in Section C.3.3. The Jacob-Lohman type curve was fitted to the early-time data in Figure C-40, when flow should have been largely radial towards the borehole. This type-curve match provides a transmissivity estimate of 1.7×10^{-12} m^2/s. Dividing this transmissivity by the "actual" slanted length of the borehole, 3.86 m, provides an estimated hydraulic conductivity of 4.4×10^{-13} m/s. The isotropic hydraulic conductivity used in the STAB simulation was 5.0×10^{-13} m/s. Good matches between the late-time STAB data and the Jacob-Lohman type curve were obtained for the 75° angle and anisotropies of 10 and 100 (Figures C-41 and C-42). The interpreted transmissivity was 7.1×10^{-13} m^2/s for an anisotropy of 10, and 5.3×10^{-13} m^2/s for an anisotropy of 100.
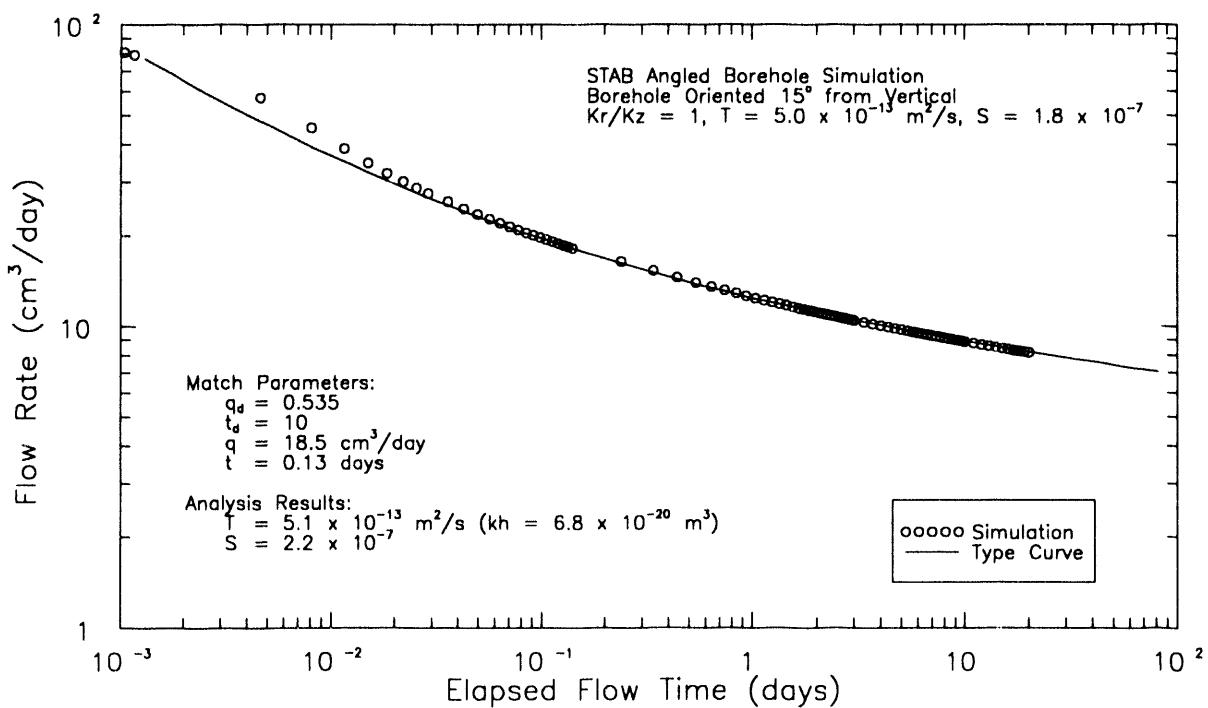
Figure C-34.   The Jacob-Lohman type-curve match to the STAB simulation for a borehole slant angle of 15° and an anisotropy of 1.
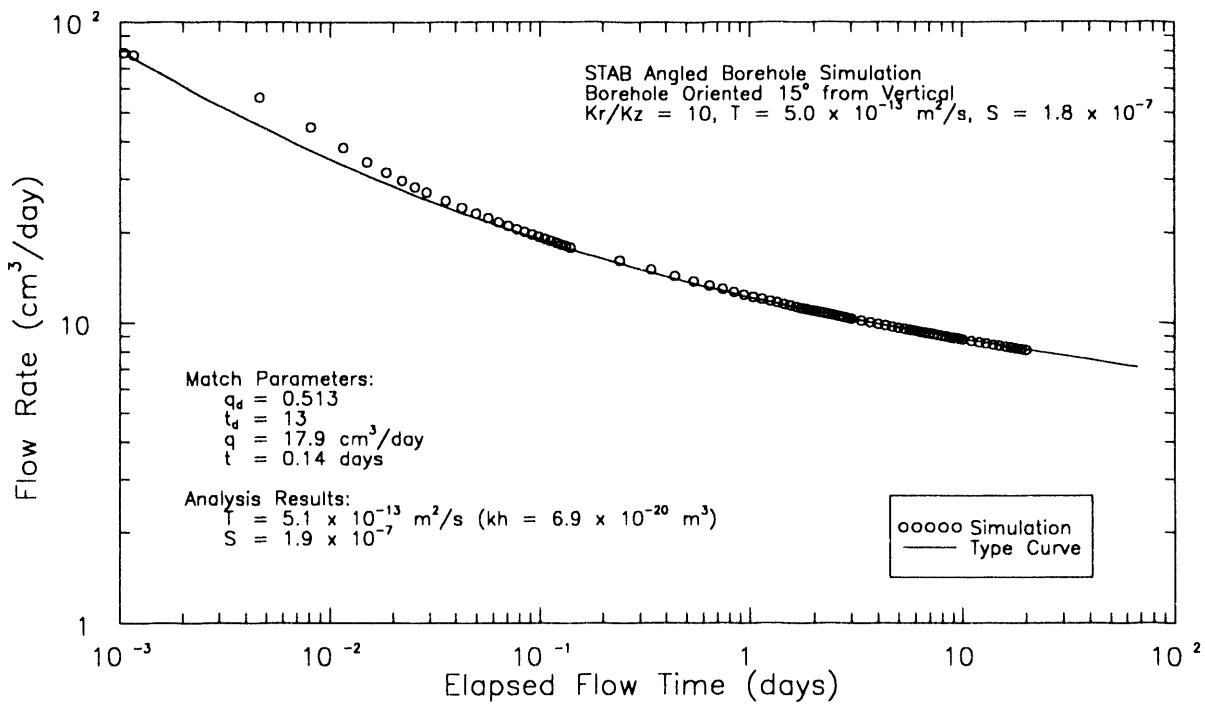

Figure C-35.   The Jacob-Lohman type-curve match to the STAB simulation for a borehole slant angle of 15° and an anisotropy of 10.
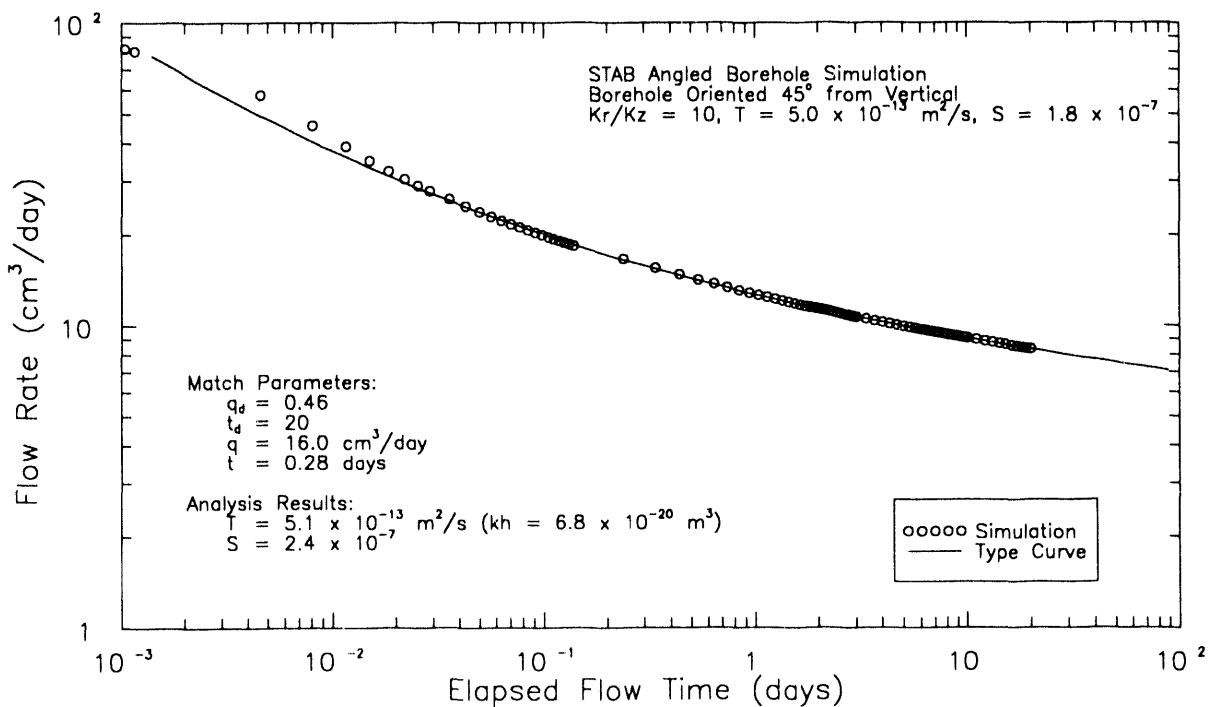
Figure C-36.   The Jacob-Lohman type-curve match to the STAB simulation for a borehole slant angle of 15° and an anisotropy of 100.
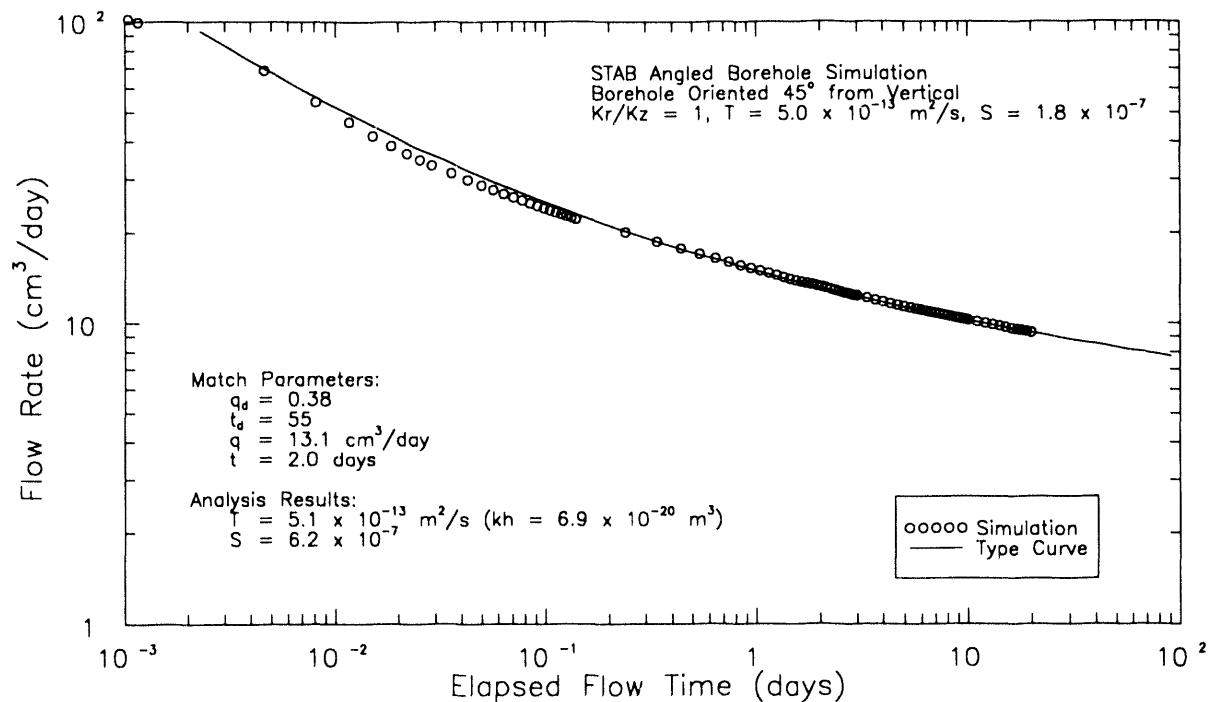
Figure C-37.   The Jacob-Lohman type-curve match to the STAB simulation for a borehole slant angle of 45° and an anisotropy of 1.
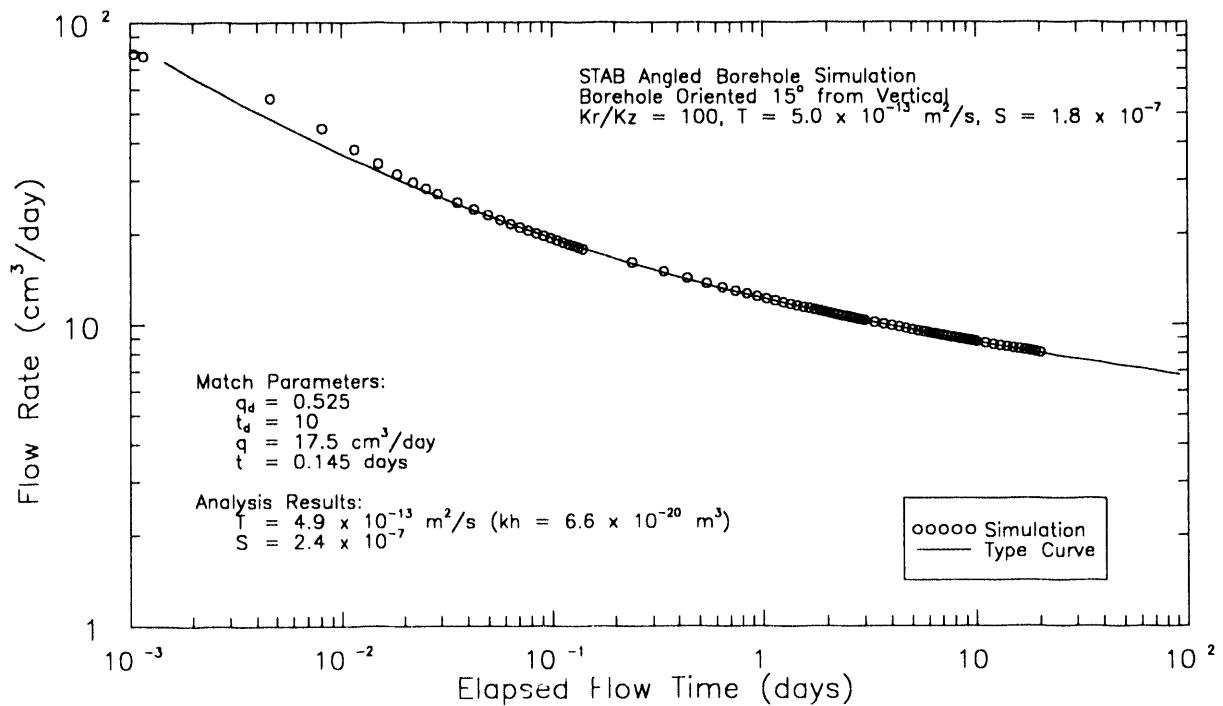
Figure C-38.   The Jacob-Lohman type-curve match to the STAB simulation for a borehole slant angle of 45° and an anisotropy of 10.
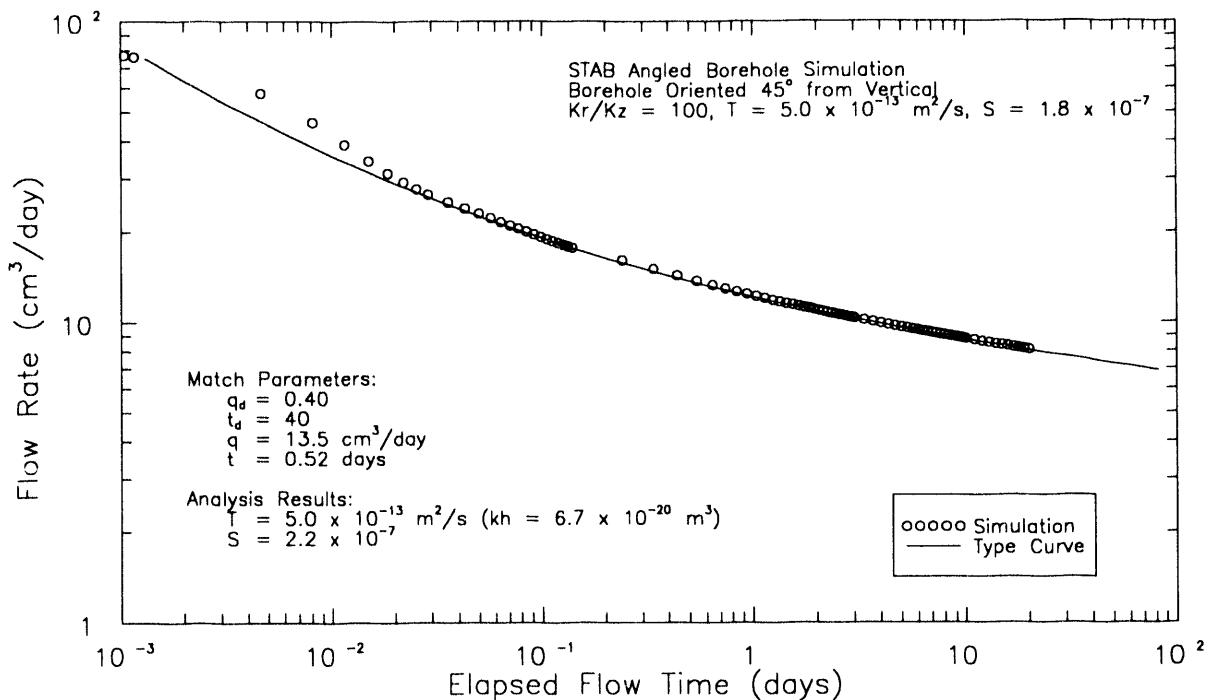

Figure C-39.   The Jacob-Lohman type-curve match to the STAB simulation for a borehole slant angle of 45° and an anisotropy of 100.
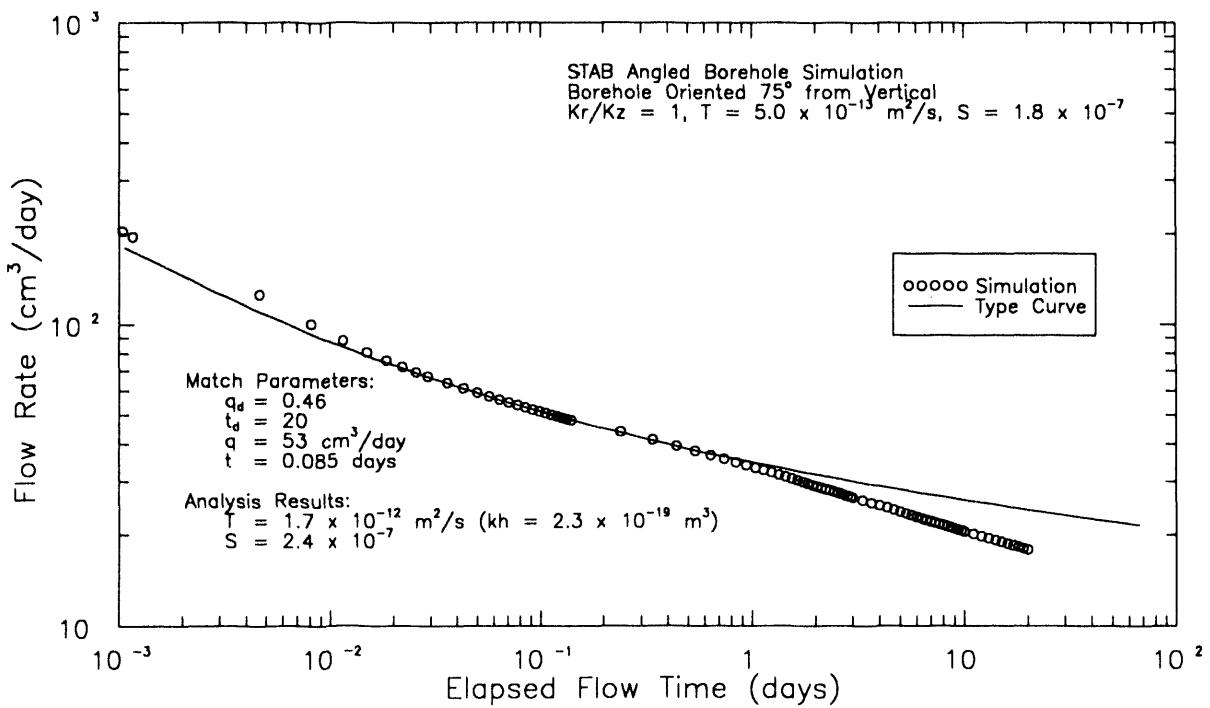
Figure C-40.   The Jacob-Lohman type-curve match to the STAB simulation for a borehole slant angle of 75° and an anisotropy of 1.
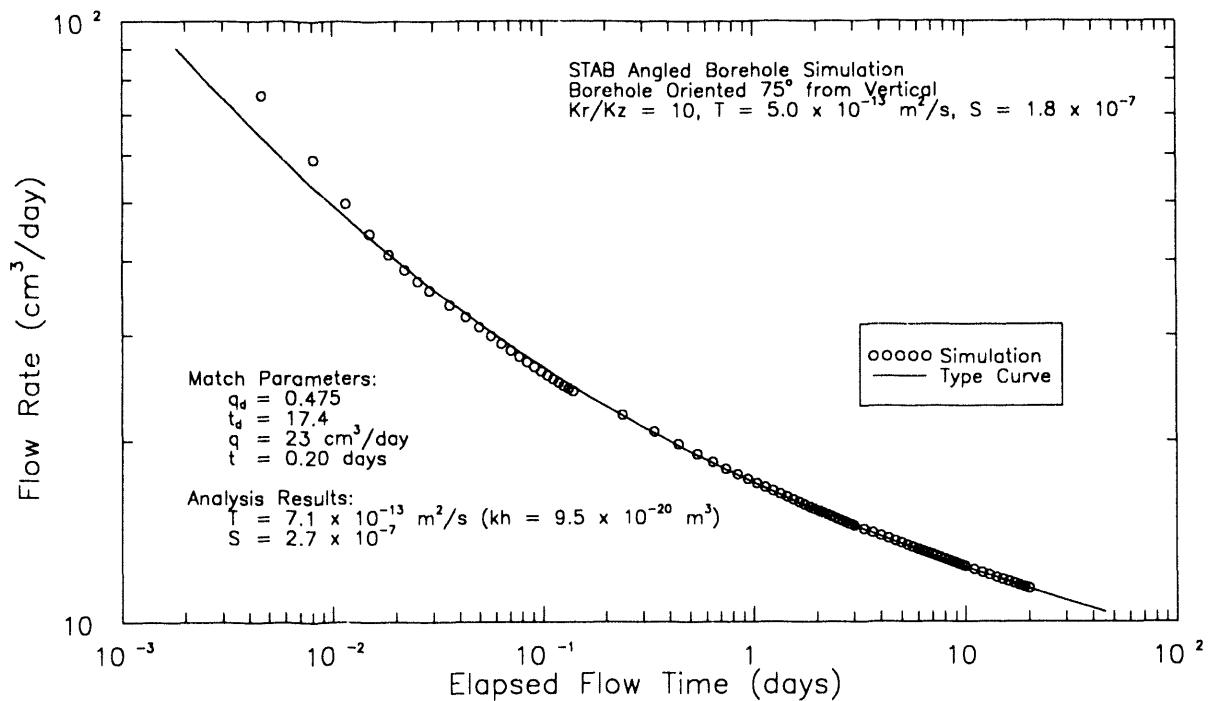
Figure C-41.   The Jacob-Lohman type-curve match to the STAB simulation for a borehole slant angle of 75° and an anisotropy of 10.

198
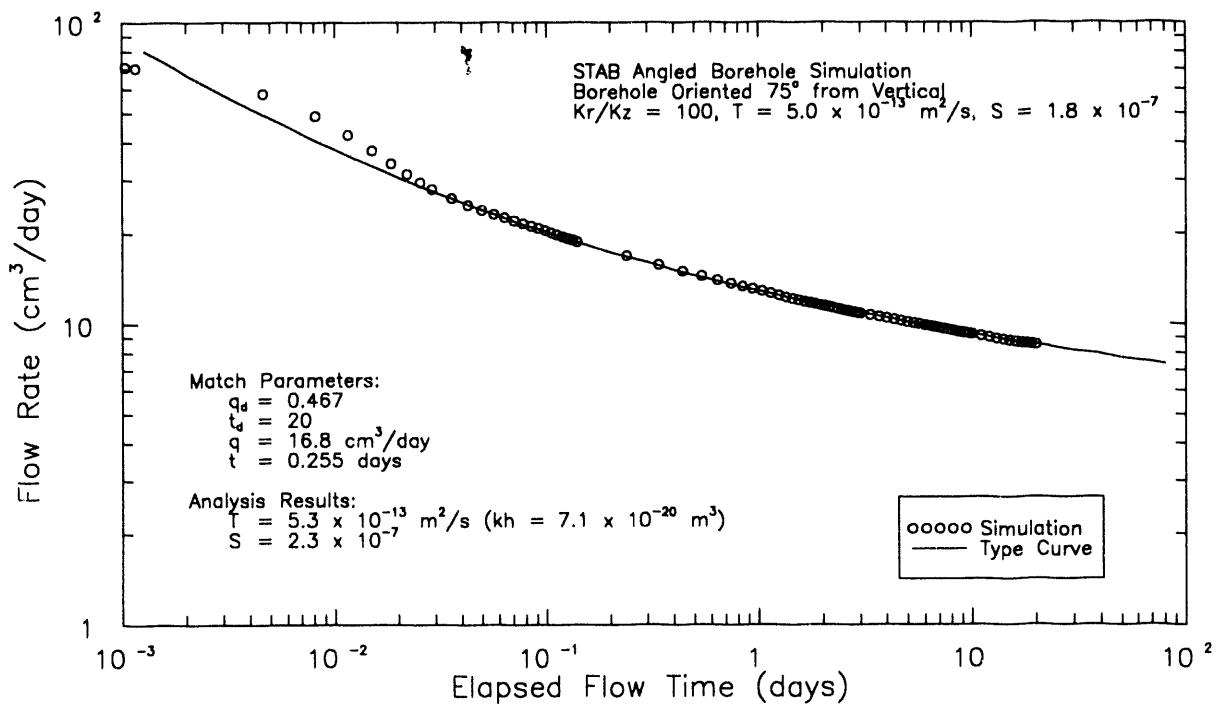
Figure C-42. The Jacob-Lohman type curve match to the STAB simulation for a borehole slant angle of 75° and an anisotropy of 100.

C.6 Conclusions

Sensitivity studies of the effects of borehole slant and anisotropy on responses to permeability tests have shown the following:

1) test responses in boreholes slanted only 15° from vertical are not significantly different from responses in vertical boreholes.

2) pressure responses are increasingly delayed as slant angle increases because of the associated increase in borehole fluid volume.

3) brine production increases as slant angle increases because of the associated increase in borehole surface area.

4) increasing anisotropy slows pressure responses and decreases brine production.

5) changing anisotropy from 1 to 10 has a larger effect than changing it from 10 to 100.

6) upper and lower no-flow boundaries affect responses more as slant angles increase and as anisotropy decreases.

199

Comparisons of angled-borehole STAB simulations with SWIFT II and GTFM equivalent-vertical-borehole simulations show the following:

1) equivalent-vertical-borehole simulations match angled-borehole behavior reasonably well when slant angles are 30° or less.

2) equivalent-vertical-borehole simulations match angled-borehole behavior reasonably well when slant angles are greater than 30° if anisotropy is at least 10.

Type-curve analyses of STAB simulations of constant-pressure withdrawal tests show that:

1) accurate transmissivity estimates can be obtained from tests in boreholes slanted as much as 45° regardless of anisotropy.

2) accurate transmissivity estimates can be obtained from holes slanted 75° if anisotropy is at least 100.

REFERENCES

Carter, R.D., and C.W. Tracy. 1960. "An Improved Method for Calculating Water Influx," *Transactions of the Society of Petroleum Engineers.* Vol. 219, 415-417.

Jacob, C.E., and S.W. Lohman. 1952. "Nonsteady Flow to a Well of Constant Drawdown in an Extensive Aquifer," *Transactions, American Geophysical Union.* Vol. 33, no.4, 559-569.

Pickens, J.F., G.E. Grisak, J.D. Avis, D.W. Belanger, and M. Thury. 1987. "Analysis and Interpretation of Borehole Hydraulic Tests in Deep Boreholes: Principles, Model Development, and Applications," *Water Resources Research.* Vol. 23, no. 7, 1341-1375.

Reeves, M., D.S. Ward, N.D. Johns, and R.M. Cranwell. 1986. *Theory and Implementation for SWIFT II, The Sandia Waste-Isolation Flow and Transport Model for Fractured Media, Release 4.84.* NUREG/CR-3328, SAND83-1159. Albuquerque, NM: Sandia National Laboratories.

APPENDIX D

PLOTS OF TEST- AND GUARD-ZONE COMPRESSIBILITY FUNCTIONS USED IN GTFM SIMULATIONS
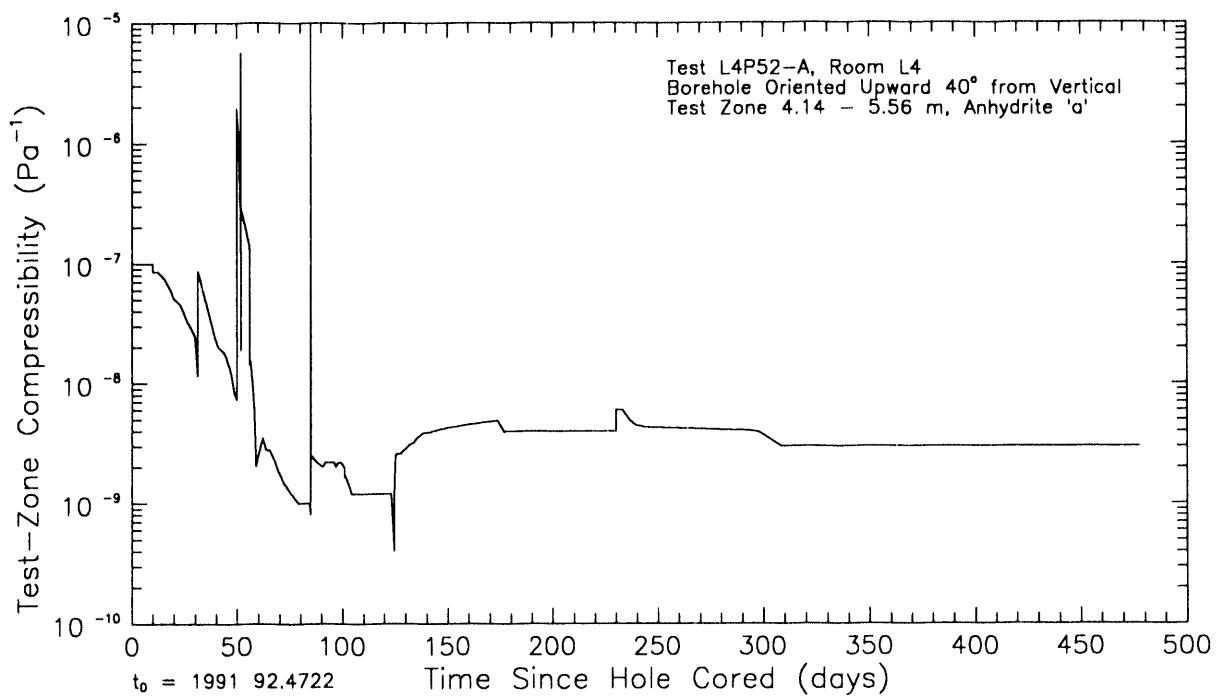
Figure D-1.   The test-zone-compressibility-versus-time function used in the L4P52-A GTFM simulations.
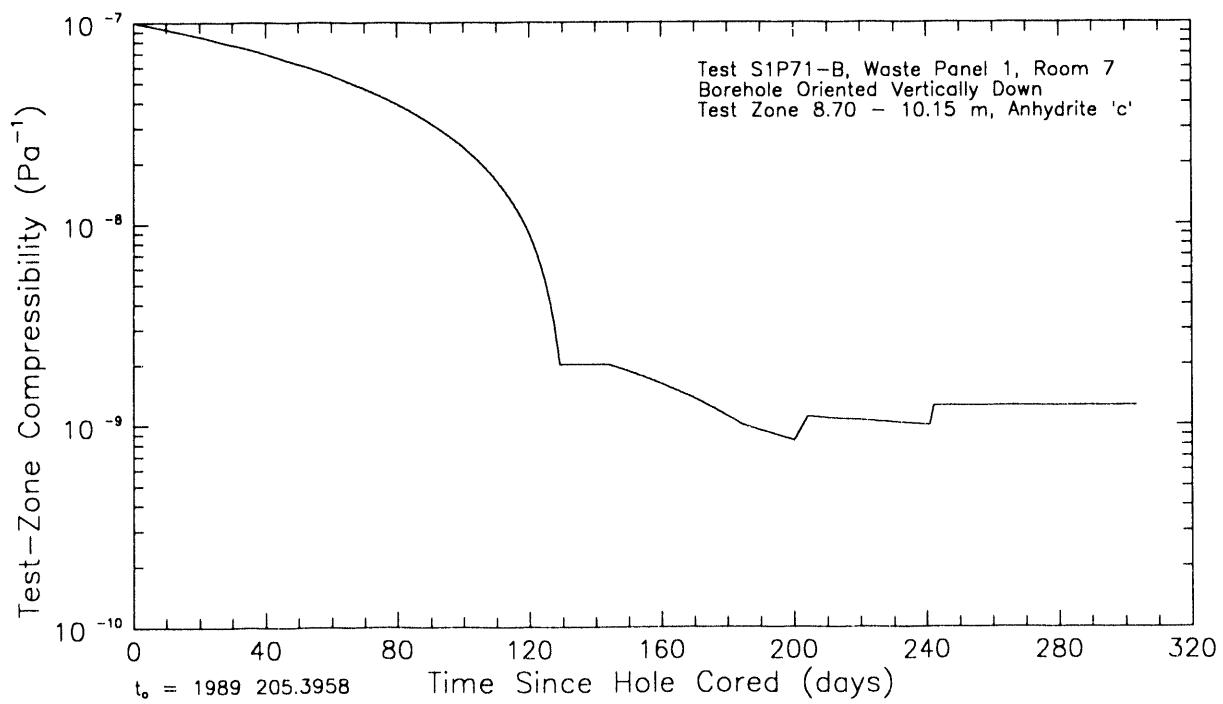

Figure D-2.   The test-zone-compressibility-versus-time function used in the S1P71-B GTFM simulations.
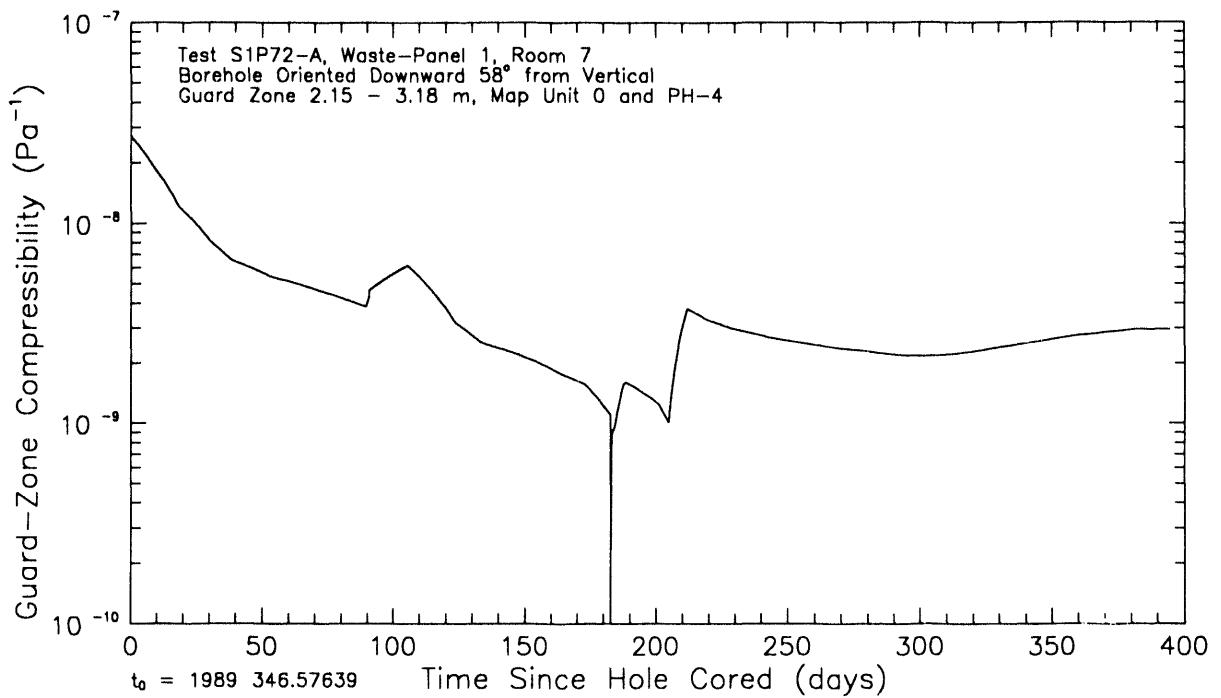
Figure D-3. The guard-zone-compressibility-versus-time function used in the S1P72-A GTFM simulations.
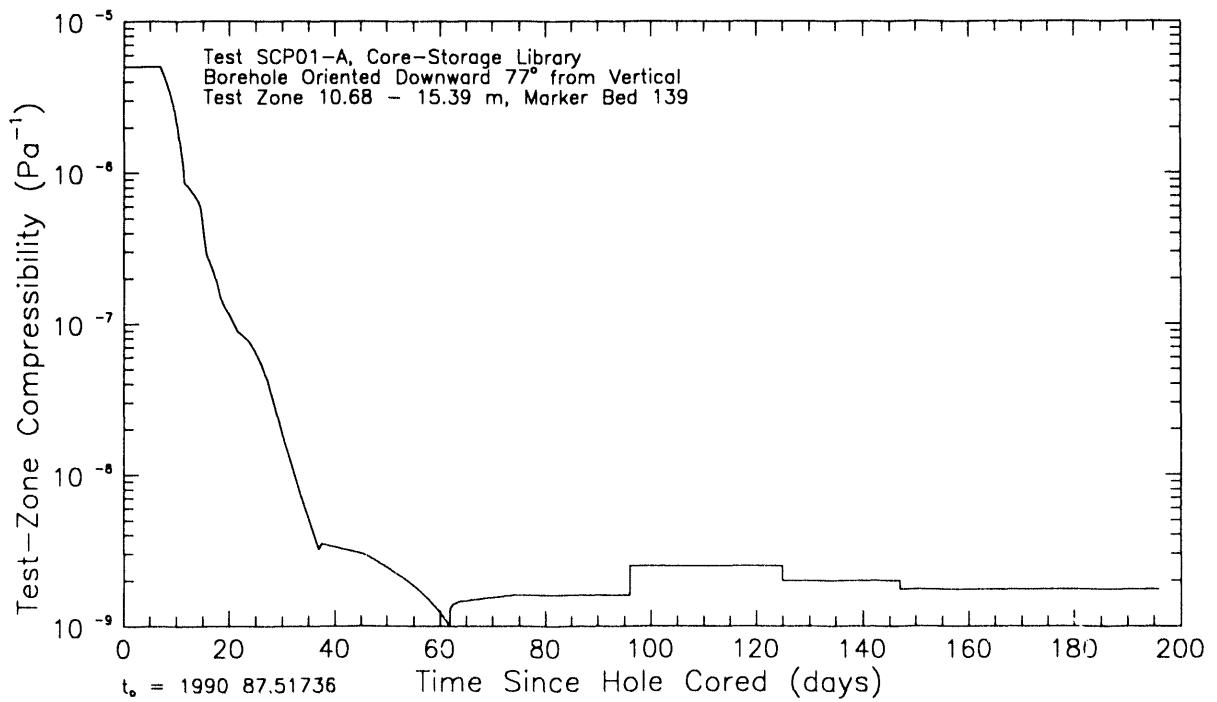
Figure D-4. The test-zone-compressibility-versus-time function used in the SCP01-A GTFM simulations.

206

APPENDIX E

# PLOTS OF TEST- AND GUARD-ZONE TEMPERATURES DURING TEST SEQUENCES
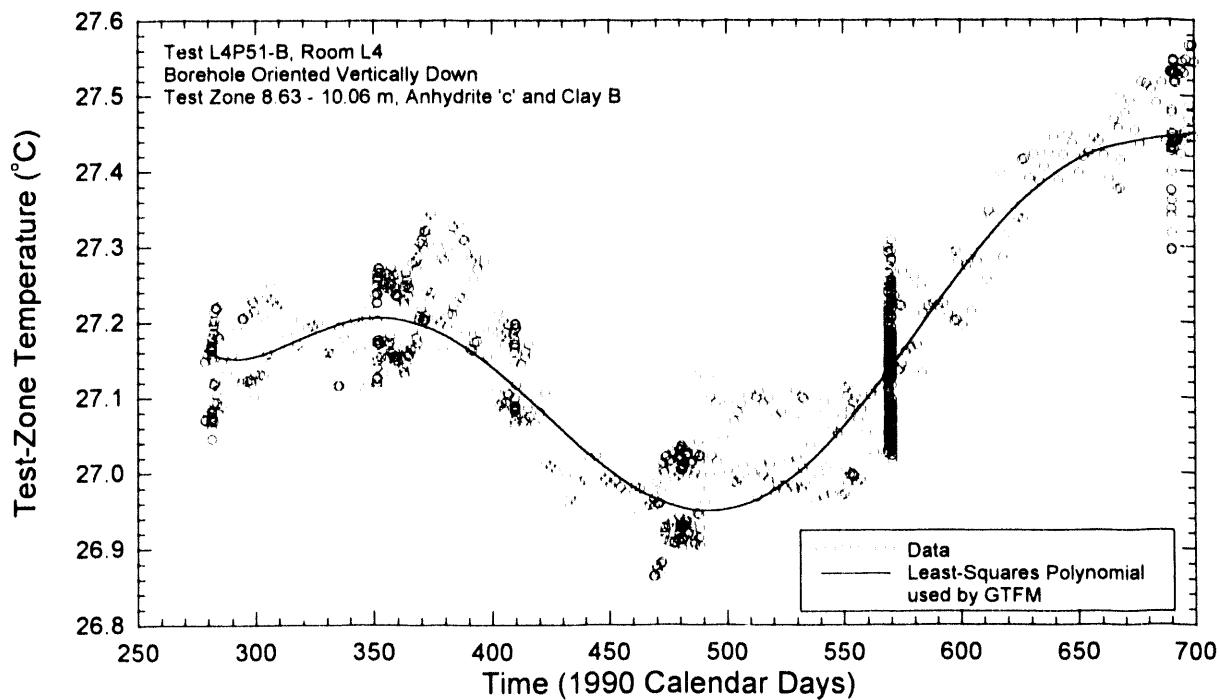
Figure E-1.   Temperatures measured in the L4P51-B test zone during the monitoring period and the temperature-versus-time function used in the GTFM simulations.
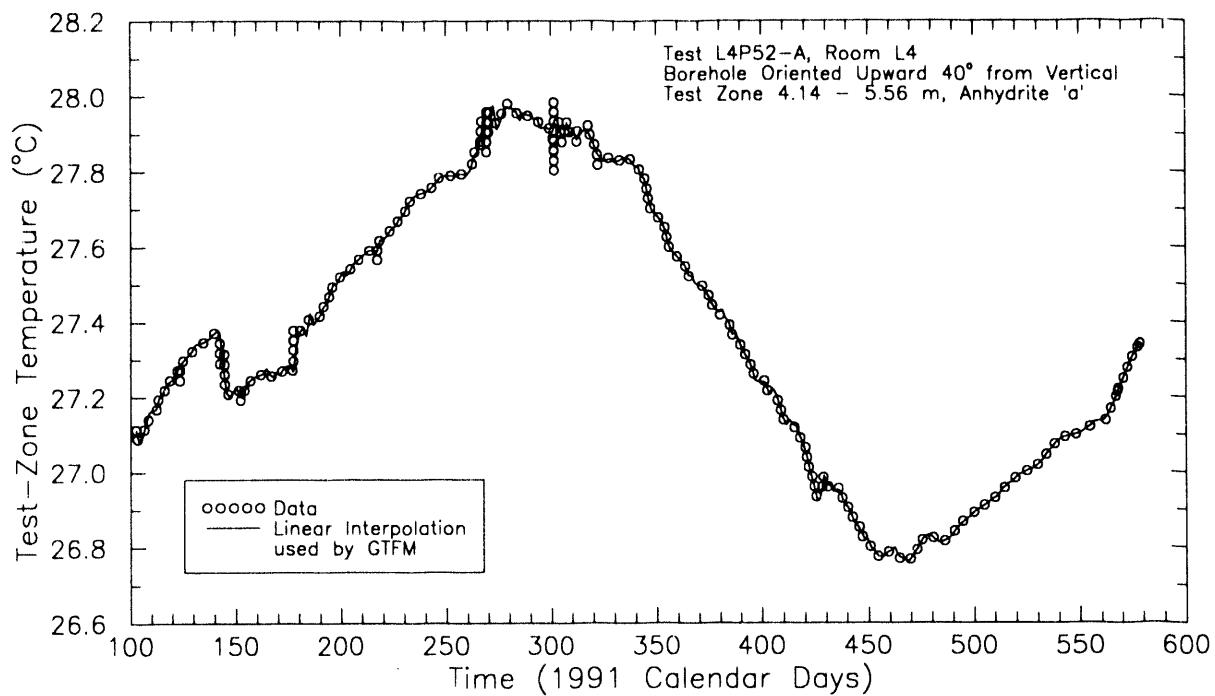

Figure E-2.   Temperatures measured in the L4P52-A test zone during the monitoring period and the temperature-versus-time function used in the GTFM simulations.

209
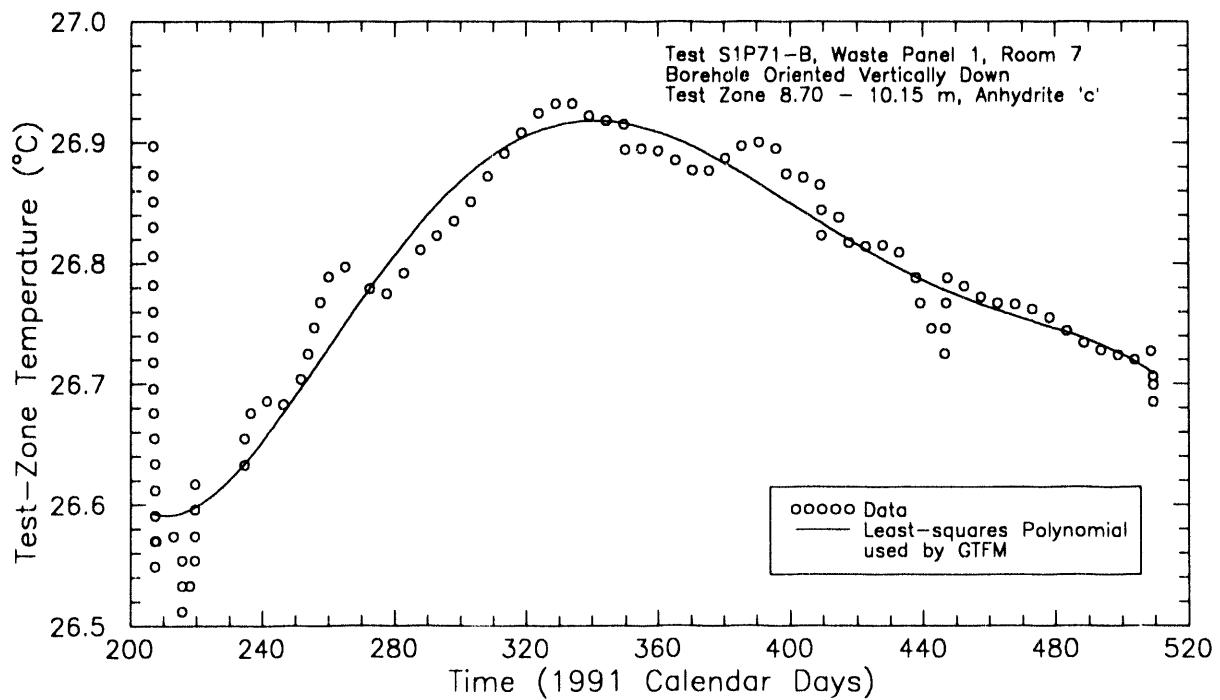
Figure E-3. Temperatures measured in the S1P71-B test zone during the monitoring period and the temperature-versus-time function used in the GTFM simulations.
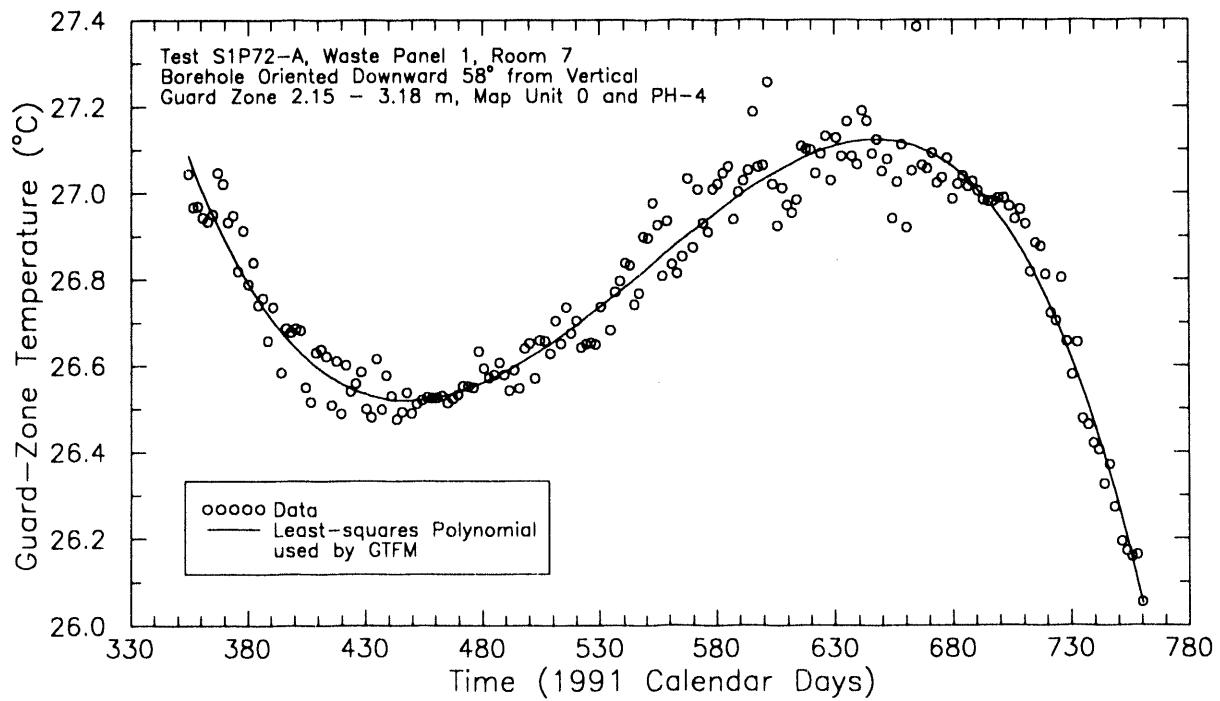
Figure E-4. Temperatures measured in the S1P72-A guard zone during the monitoring period and the temperature-versus-time function used in the GTFM simulations.

210
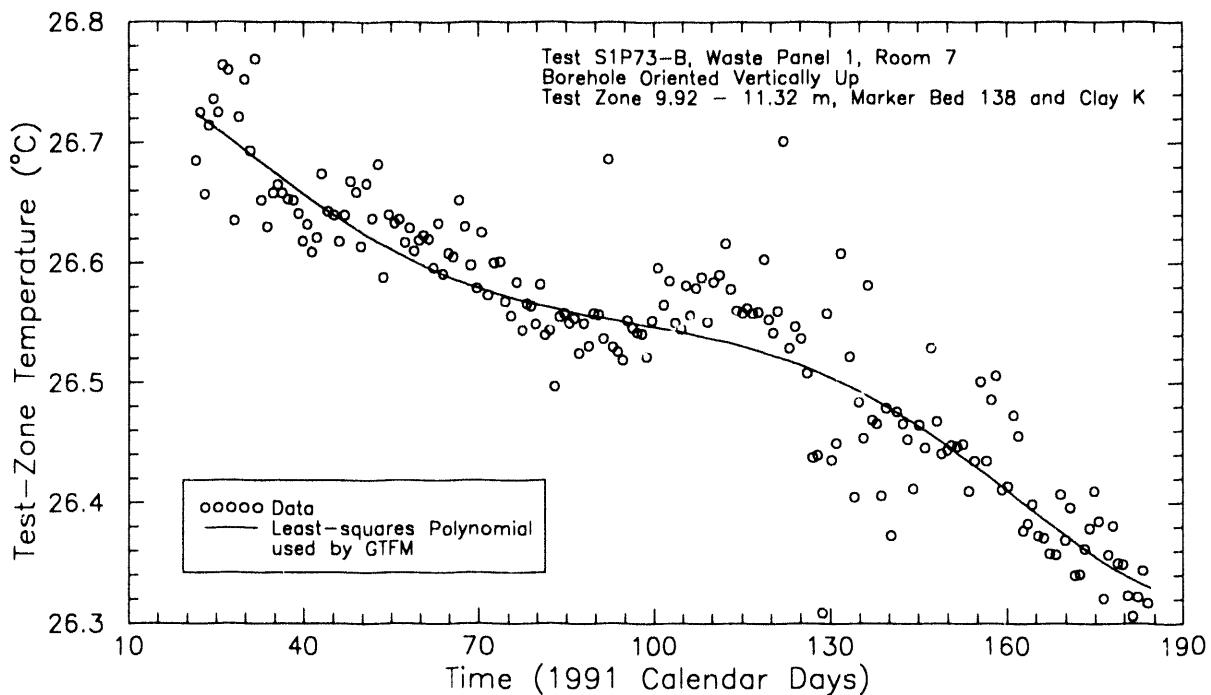
Figure E-5.   Temperatures measured in the S1P73-B test zone during the monitoring period and the temperature-versus-time function used in the GTFM simulations.
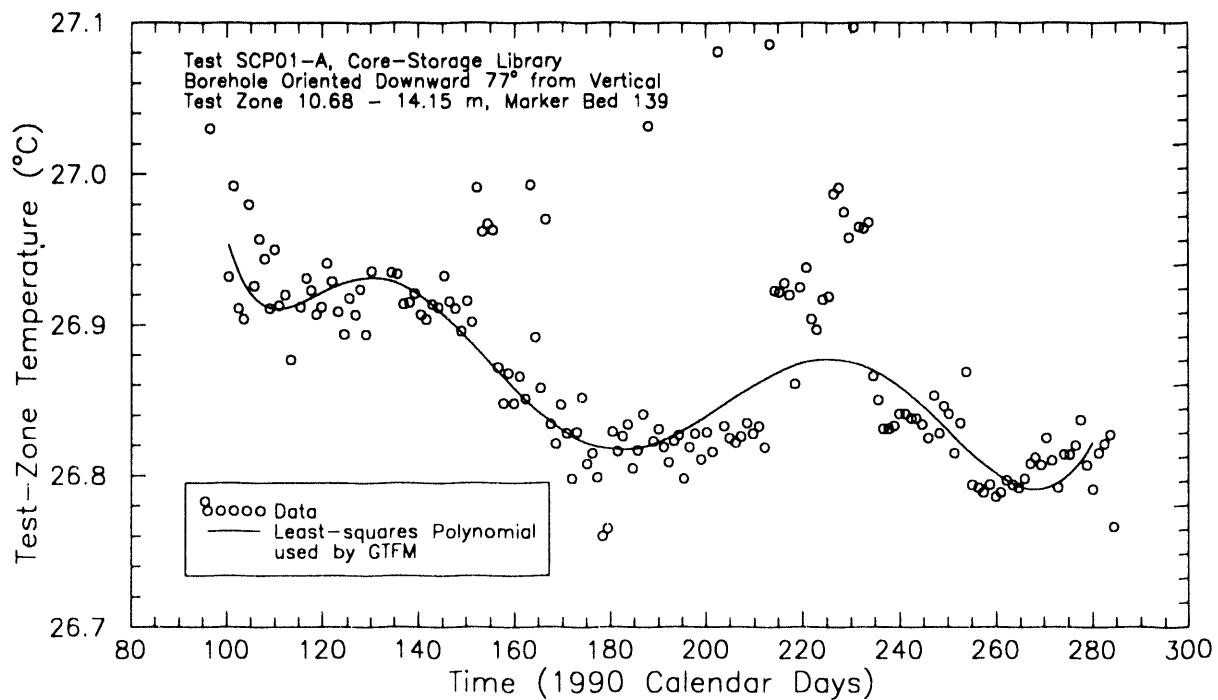
Figure E-6.   Temperatures measured in the SCP01-A test zone during the monitoring period and the temperature-versus-time function used in the GTFM simulations.

APPENDIX F

PLOTS OF PACKER PRESSURES DURING TEST SEQUENCES
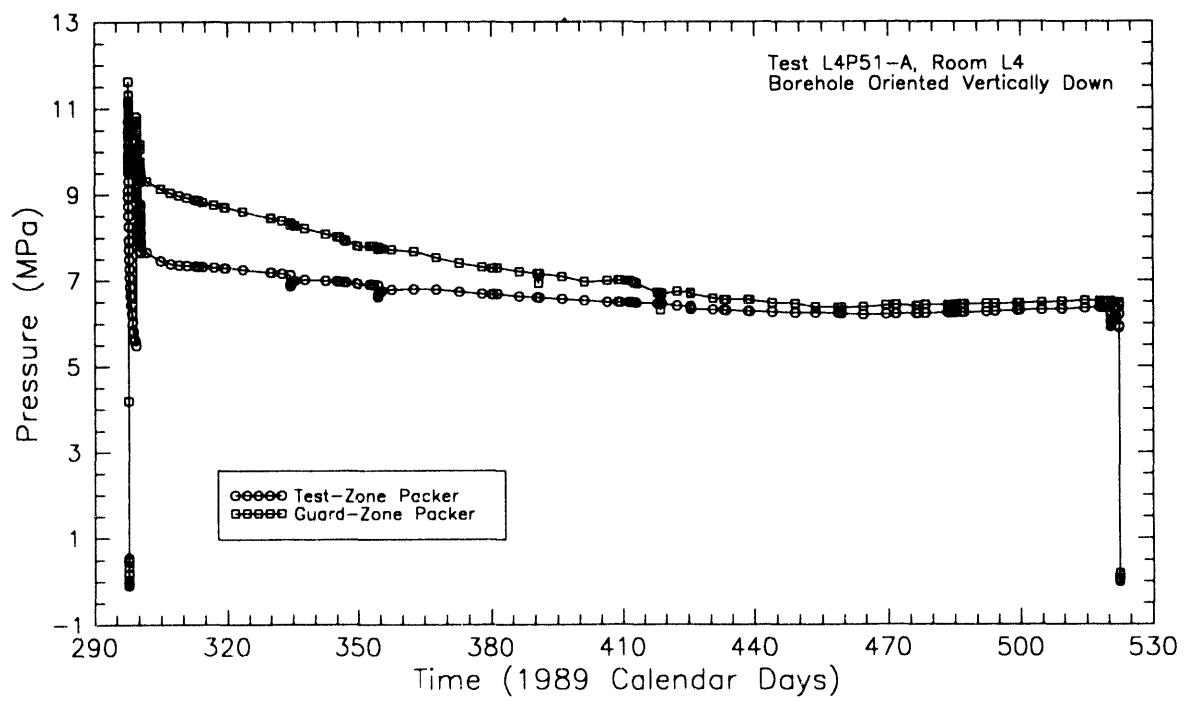
Figure F-1. Test- and guard-zone packer-inflation pressures during L4P51-A testing.
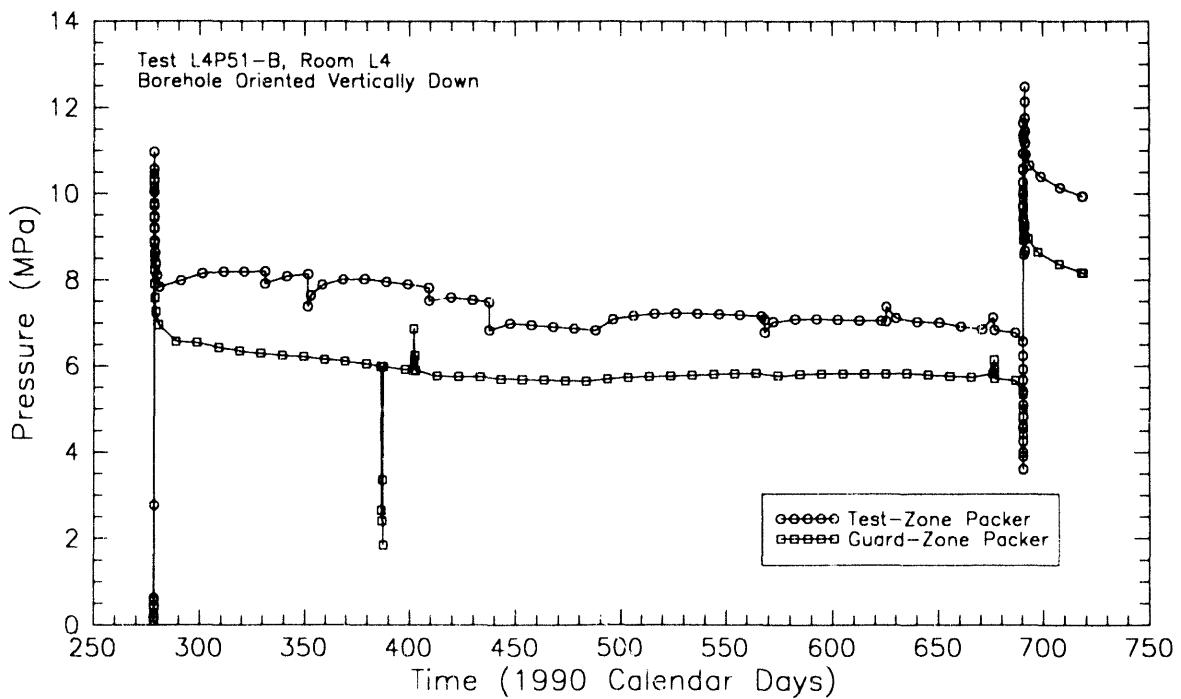
Figure F-2. Test- and guard-zone packer-inflation pressures during L4P51-B testing.
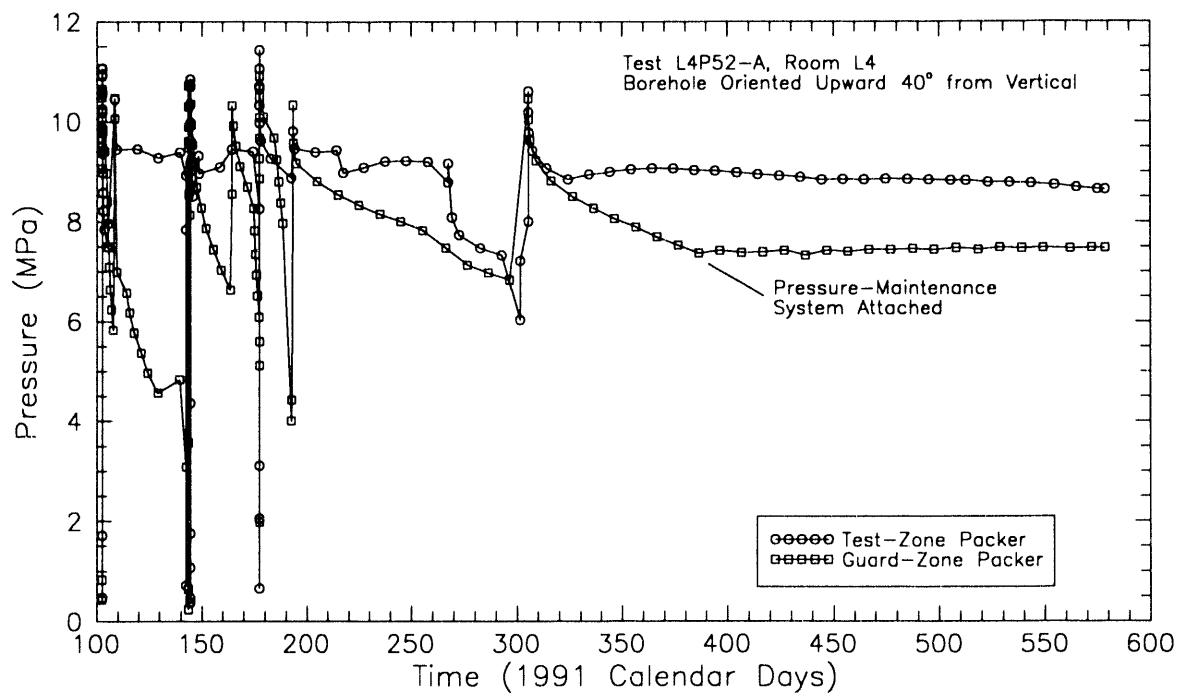
Figure F-3. Test- and guard-zone packer-inflation pressures during L4P52-A testing.
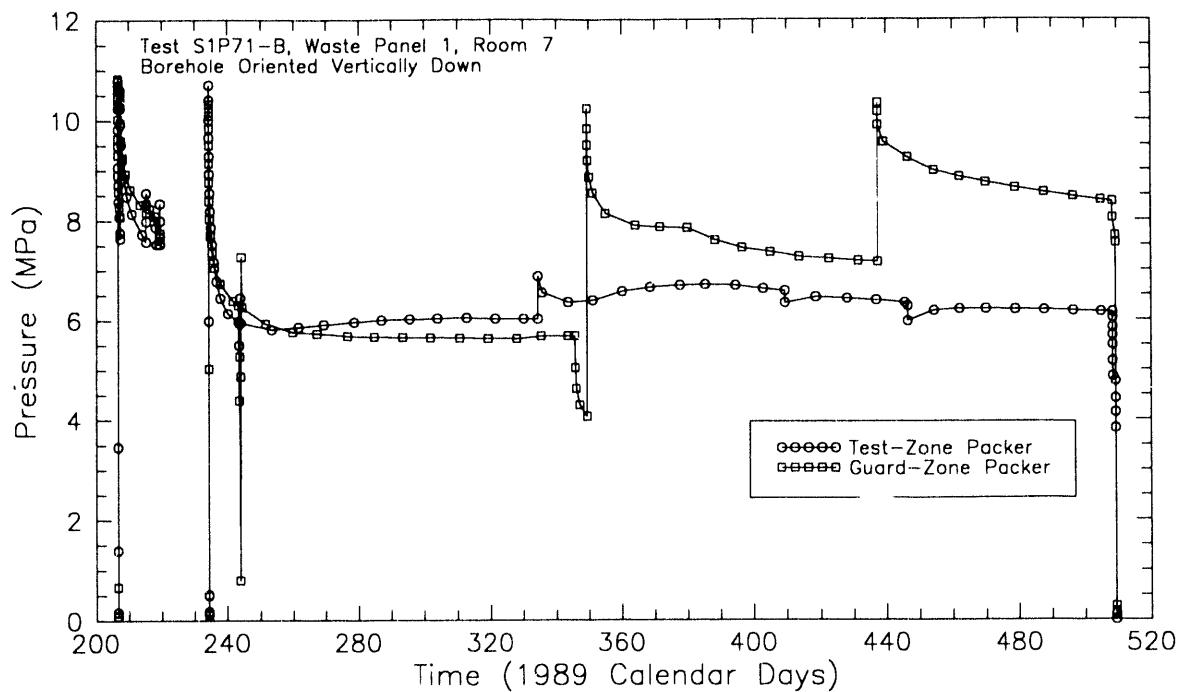
Figure F-4. Test- and guard-zone packer-inflation pressures during S1P71-B testing.

216
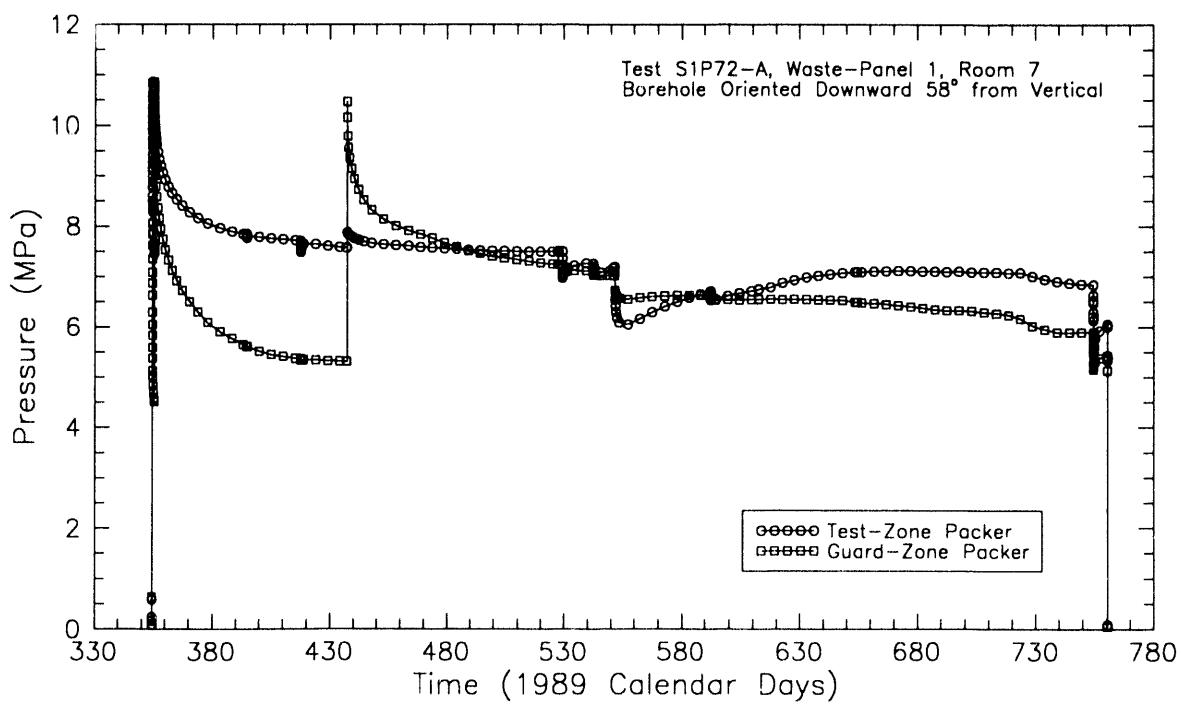
Figure F-5. Test- and guard-zone packer-inflation pressures during S1P72-A testing.
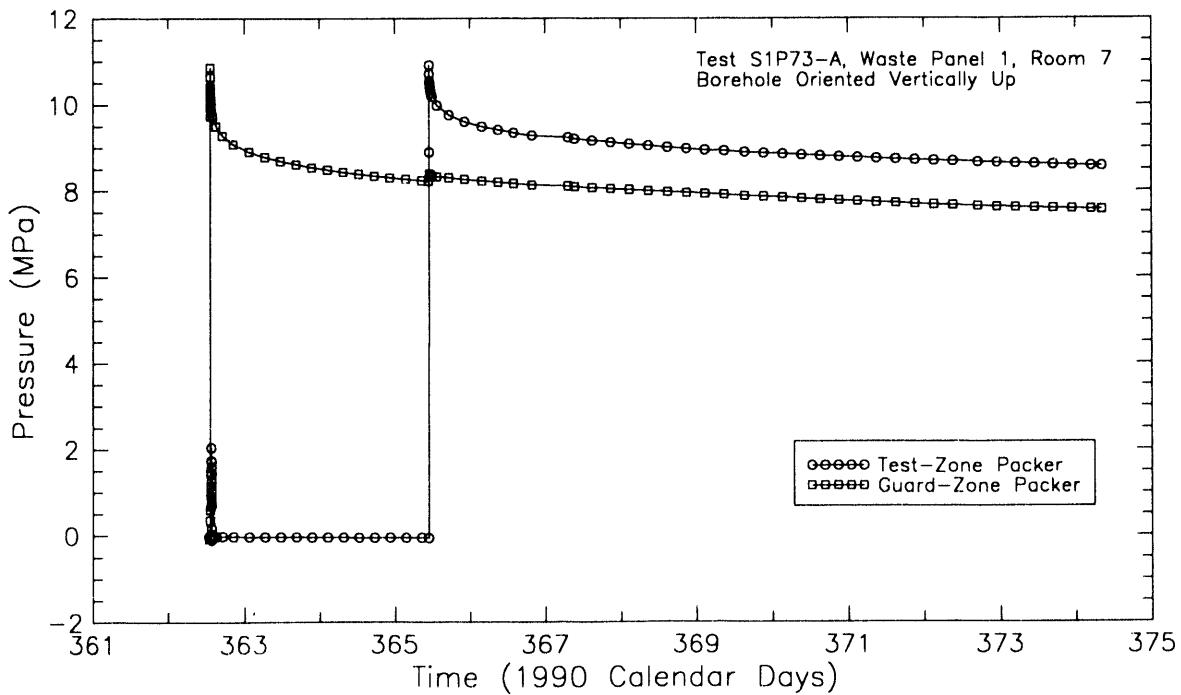
Figure F-6. Test- and guard-zone packer-inflation pressures during S1P73-A testing.

217
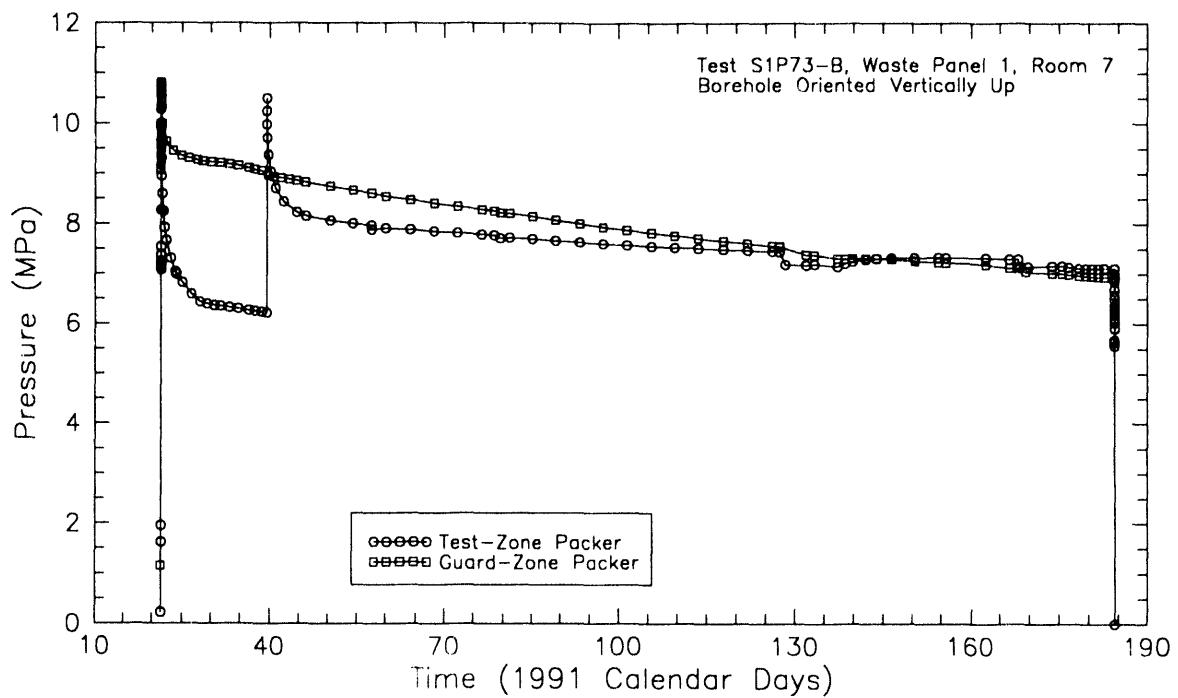
Figure F-7. Test- and guard-zone packer-inflation pressures during S1P73-B testing.
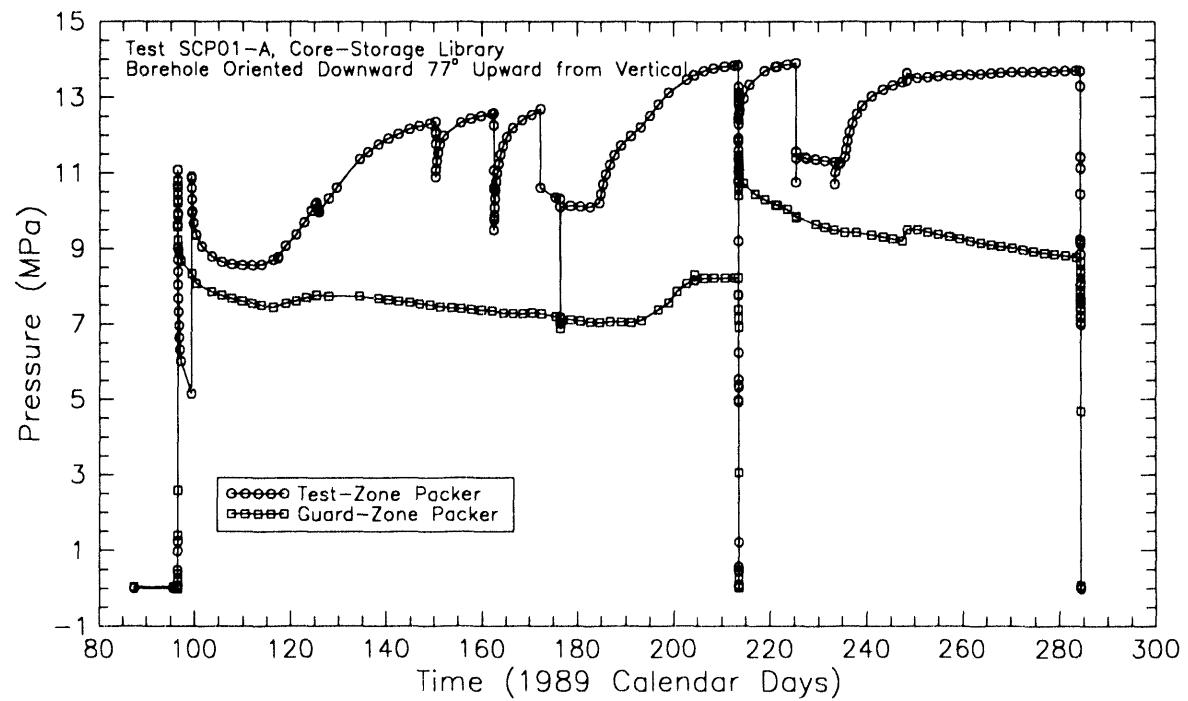
Figure F-8. Test- and guard-zone packer-inflation pressures during SCP01-A testing.

218

APPENDIX G

TWO-PHASE EVALUATION OF THE TEST-ZONE PRESSURE
RESPONSES DURING TESTING SEQUENCE S1P72-A

APPENDIX G

TWO-PHASE EVALUATION OF THE TEST-ZONE PRESSURE RESPONSES DURING TESTING SEQUENCE S1P72-A

by Toya L. Jones, INTERA Inc.

G.1 Introduction

Section 7.1.5.1 of this report describes the test-zone pressure responses for testing sequence S1P72-A conducted in borehole S1P72. The testing sequence in the test zone consisted of an initial buildup period, two pulse-withdrawal tests, two constant-pressure withdrawal tests, and two pressure-buildup tests (Figure 7-32). A seven-day open-hole period following drilling preceded the testing sequence. The pressure response during testing shows recovery to approximately 1.25 MPa during the two pulse-withdrawal tests, recovery to approximately 0.95 MPa during the first pressure-buildup test (PB1), and recovery to approximately 0.73 MPa during the second pressure-buildup test (PB2). The decrease in the pressure to which the test zone recovered could be the result of (1) the continued equilibration between atmospheric pressure in Room 7 of Waste Panel 1 and the far-field pressure in the formation and/or (2) the exsolution of gas from the brine and the subsequent depletion of free gas from the vicinity of borehole S1P72 through the test zone. Support for the theory of pressure equilibration includes the decline in pressure observed during the second pulse-withdrawal test (PW2) and the second pressure-buildup test (PB2). Support for the theory of gas depletion consists of the fact that fluid removed for the first pulse-withdrawal test (PW1) was white and cloudy in nature signifying exsolution of gas from the brine under atmospheric pressure and the fact that both free gas and brine were produced from the borehole during pressure reduction for the second pulse-withdrawal test and during the two constant-pressure withdrawal tests.

This appendix presents studies conducted using the multi-phase simulator TOUGH2 to investigate the effects of formation depressurization due to room excavation and the effects of free gas on the test-zone pressure response. The simulations presented here are not intended to reproduce the pressure responses observed during S1P72-A testing rigorously, but are instead an attempt to determine whether or not excavation-related depressurization and the presence of free gas can reproduce the general trend observed in the test zone (i.e., the successive decrease in the pressure to which the test zone recovered).

G.2 TOUGH2 Code Description

The effects of formation depressurization due to room excavation and the effects of the presence of free gas on pressure responses during permeability testing in borehole S1P72 were examined using the TOUGH2 code, a more general version of the TOUGH (Transport of Unsaturated Groundwater and Heat) code. TOUGH2 was selected because it can be easily adapted to a variety of problem types. TOUGH2 and TOUGH are closely related in methodology and architecture. The theory and implementation of the code and a guide to the input data are provided in Pruess (1987 and 1991).

TOUGH2 is a multi-dimensional, integral finite-difference numerical model that solves the coupled fluid and heat, flow and transport equations of multiphase, multicomponent fluid mixtures. The phases considered by TOUGH2 are liquid and gas. A number of multicomponent equation-of-state (EOS) modules, which describe fluid properties for various mixtures, are included with TOUGH2 making the code applicable to a variety of flow systems such as groundwater aquifers, unsaturated zones, and geothermal reservoirs. Because TOUGH2 is an integral finite-difference code, it can handle regular and irregular flow geometries in one, two, and three dimensions. In addition, single- and multiple-porosity systems can be specified.

Pruess (1987) describes the following physical processes taken into account by the two-component air/water system in TOUGH.

> "Fluid flow in both liquid and gaseous phases occurs under pressure, viscous, and gravity forces according to Darcy's law, with interference between the phases represented by means of relative permeability functions. In addition we consider binary diffusion in the gas phase. However, no account is presently made of Knudsen diffusion... Capillary and phase adsorption effects are taken into account for the liquid phase, but no allowance is made for vapor pressure lowering... Also, no allowance is made for hysteresis in either capillary pressure or relative permeability. All thermophysical properties of liquid water and vapor are obtained within experimental accuracy from steam table equations (International Formulation Committee, 1967). Air is treated as an ideal gas, and additivity of partial pressures is assumed for air/vapor mixtures. Air dissolution in water is represented by Henry's law. However, because air solubility in water is very small, we felt justified in neglecting the temperature dependence of Henry's constant ...

> The governing equations used in TOUGH, and their numerical implementation, are applicable to one-, two-, and three-dimensional anisotropic porous or fractured media. TOUGH does not perform stress calculations for the solid skeleton, but it allows for porosity changes in response to changes in pore pressure (compressibility) and temperature (expansivity)."

The EOS3 (air/water) module of TOUGH2 used for the simulations presented here is identical to TOUGH, as described above. The water properties in the EOS3 module were modified to approximate brine for these simulations.

G.3 Simulation Parameters

A two-dimensional horizontal representation of Marker Bed 139 was simulated using TOUGH2 from the time Room 7 of Waste Panel 1 was excavated through the time when the S1P72-A testing sequence was completed. The modeled region extended from 1.5 m inside the room to a distance of 31.5 m in the easterly direction and was centered about S1P72 in the north-south direction (Figure G-1). The eastern edge of the modeled region was considered to be the far field. In the horizontal plane of Marker Bed 139, the distance from the western edge of the model to the center of the test interval in S1P72 is 5.9 m. The test zone was
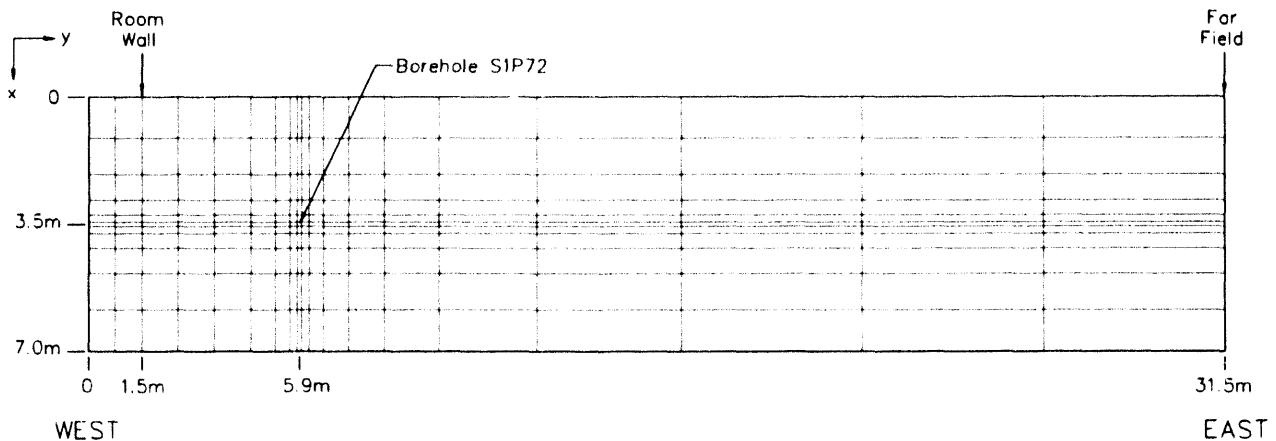
Figure G-1. Model grid.

assumed to be an equivalent vertical test interval at this location. At the western model edge and at the far field, constant-pressure boundaries were maintained. A constant pressure of 0.1 MPa (atmospheric pressure) was assigned at the western edge and a constant pressure of 12.6 MPa was assigned to the far field.

Intrinsic permeabilities of 10^{-18} and 10^{-20} m^2 were assigned at the western model edge and at the far field, respectively. The remainder of the modeled region was assigned an intrinsic permeability distribution as described below in Section G.4.1. The specific storage distribution assigned in the model is also discussed in Section G.4.1. The model assumed Marker Bed 139 is vertically homogeneous with a porosity of 0.01 and a thickness of 0.85 m.

Site-specific data for the relative-permeability and capillary-pressure curves for Marker Bed 139 are not available. In the absence of site-specific data, two-phase properties were based on data from actual measurements on roughly analogous materials. A "tight" gas sand core discussed in Morrow et al. (1986) was selected as an analogue material to define the relative-permeability and capillary-pressure characteristics of Marker Bed 139. The relative-permeability and capillary-pressure curves assumed for the simulations (Figures G-2 and G-3, respectively) are those used by Davies et al. (1992) for sensitivity studies of gas pressurization in the WIPP repository and gas migration from the WIPP repository into interbeds.
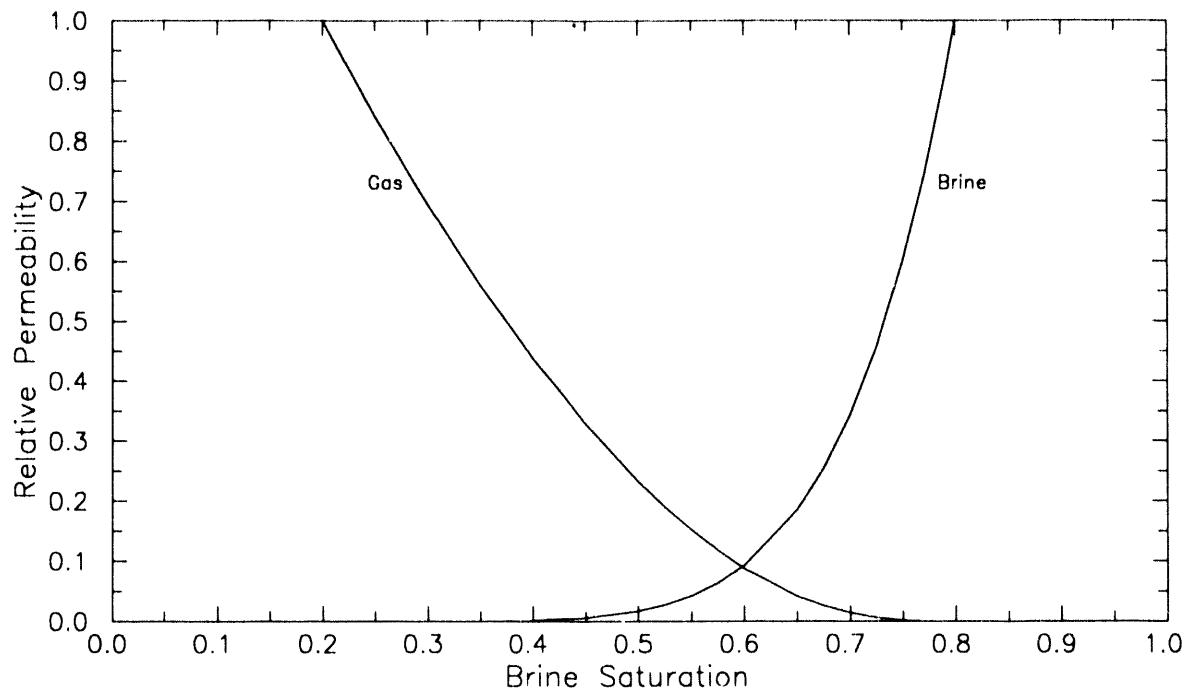
Figure G-2.   Relative permeabilities assigned to Marker Bed 139 for TOUGH2 simulations of the test-zone pressure response during testing sequence S1P72-A.
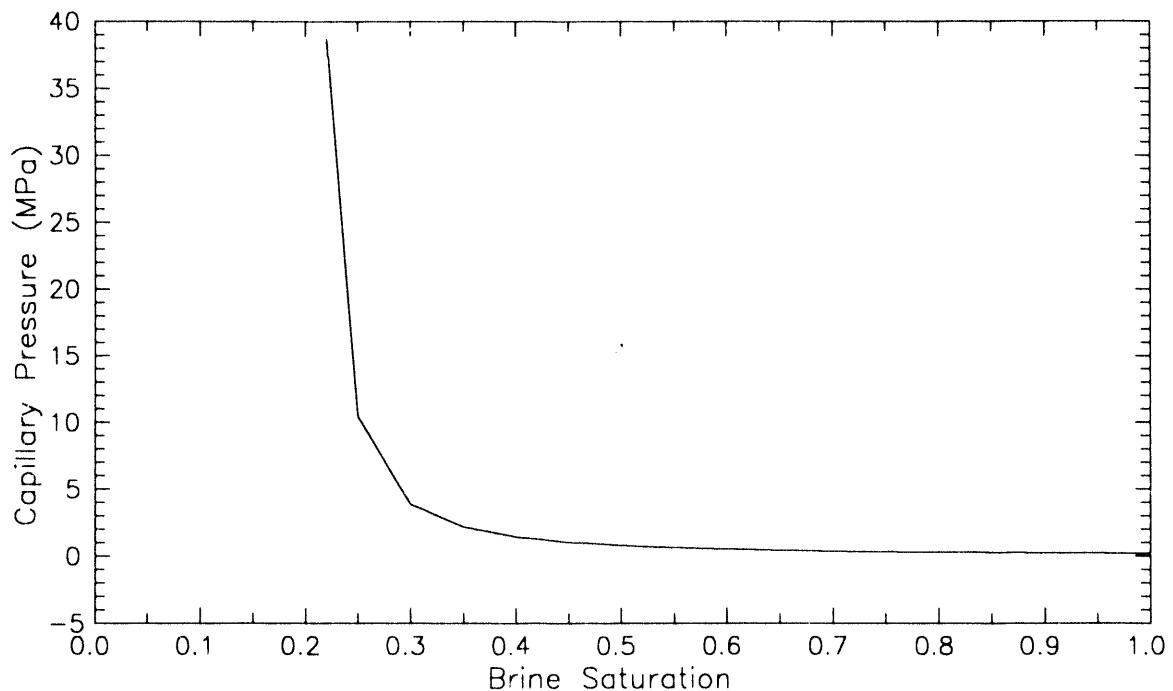

Figure G-3.   Capillary-pressure curve assigned to Marker Bed 139 for TOUGH2 simulations of the test-zone pressure response during testing sequence S1P72-A.

The simulations assumed the test zone was a vertical borehole represented by a single element having a perimeter equivalent to the circumference of the ellipse formed by the intersection of S1P72 and the horizontal marker bed. The circumference of an ellipse is calculated as:

$$C = \pi \sqrt{2(a^2 + b^2) - \frac{(a - b)}{2.2}} \qquad \text{(G-1)}$$

where: a   =   half-length of the major axis; and

            b   =   half-length of the minor axis.

For S1P72, the values for a and b are 9.93 and 5.27 cm, respectively, which yield a circumference of 48.96 cm. The element used in the simulation to represent the borehole had assigned side lengths of 12.24 cm. This modeling representation of the borehole is not entirely consistent with the technique used for GTFM simulations, as discussed in Section 6.2, which would produce a circumference of 47.75 cm using an axis-averaging approach. The conclusions drawn from the TOUGH2 modeling study should not, however, be affected by small changes in the simulated hole circumference.

The fluid volume in the test zone during the S1P72-A testing sequence was 5009 cm^3. The borehole element in the model was assigned a porosity of 1.0 and a volume of 5009 cm^3 during the testing sequence to maintain that volume.

G.4   Simulation Approach and Results

Simulations designed to reproduce the general trend of the pressure responses observed during S1P72-A testing were conducted in two stages. The first stage assumed single-phase flow and simulated from the time of room excavation through the time of testing in borehole S1P72. The presence of S1P72 and the testing sequence were ignored during this stage. The purpose of the first stage was to determine the distribution of intrinsic permeability and specific storage in the y-direction that would allow depressurization of Marker Bed 139, due to the presence of the room, that was consistent with the pressure observed immediately before the first pulse-withdrawal test was initiated. In other words, the function of this stage was to determine the formation parameters that would be used to set up the initial-pressure conditions in Marker Bed 139 prior to the start of permeability testing in borehole S1P72. The second stage used the distribution of permeability and specific storage determined during stage one and simulated the S1P72-A testing sequence in the test zone. In order to include the effects of room excavation on the pressure responses observed during the test sequence, time zero for the second stage simulations corresponded to excavation of the room. Stage two simulations considered both single and two-phase conditions. The purpose of stage two was to reproduce the general pressure responses observed during permeability testing in S1P72-A.

G.4.1   STAGE ONE; DETERMINATION OF MARKER BED 139 INTRINSIC PERMEABILITY AND SPECIFIC STORAGE DISTRIBUTION. Little is known about the effects of excavation in the WIPP underground on the lateral distribution of intrinsic permeability and specific storage in Marker Bed 139. During stage one of the TOUGH2 simulations, different spatial distributions of these two parameters were used to simulate formation depressurization caused by excavation of the room. Intrinsic permeability and

specific storage in Marker Bed 139 were varied linearly, exponentially, and a combination of linearly and exponentially in the y-direction. As constraints, the permeability at the western model edge was held at 10^{-18} m^2 and the permeability of the far field was held at 10^{-20} m^2. The constraints for specific storage were 10^{-5} and 10^{-7} m^{-1} at the western model edge and in the far field, respectively. The values at the western edge of the model were assumed to be excavation-enhanced and the values for the far field were assumed to be undisturbed.

Simulated pressures at the location of S1P72 during the time period of the permeability testing were sensitive to the permeability distribution. Figure G-4 shows the pressure profile in the y-direction through the location of S1P72 at the end of the simulation (1045 days) and Figure G-5 shows pressure with time at the location of S1P72 for a linearly varying permeability distribution, an exponentially varying permeability distribution, and a permeability that was constant everywhere except at the east and west boundaries of the model domain. The three permeability distributions are illustrated in Figure G-6. For all cases shown in Figures G-4 and G-5, the specific storage varied linearly in the y-direction (Figure G-7). The simulation that used a constant permeability of 7×10^{-18} m^2 for Marker Bed 139 produced simulated pressures that matched the observed initial buildup pressure at S1P72 most closely. Neither of the simulations with varying permeability with distance in the y-direction yielded pressures that matched the observed data. Although no simulations were conducted to address this point, the observed pressures could probably be matched using a changing permeability with distance if the distance to the far field was increased.
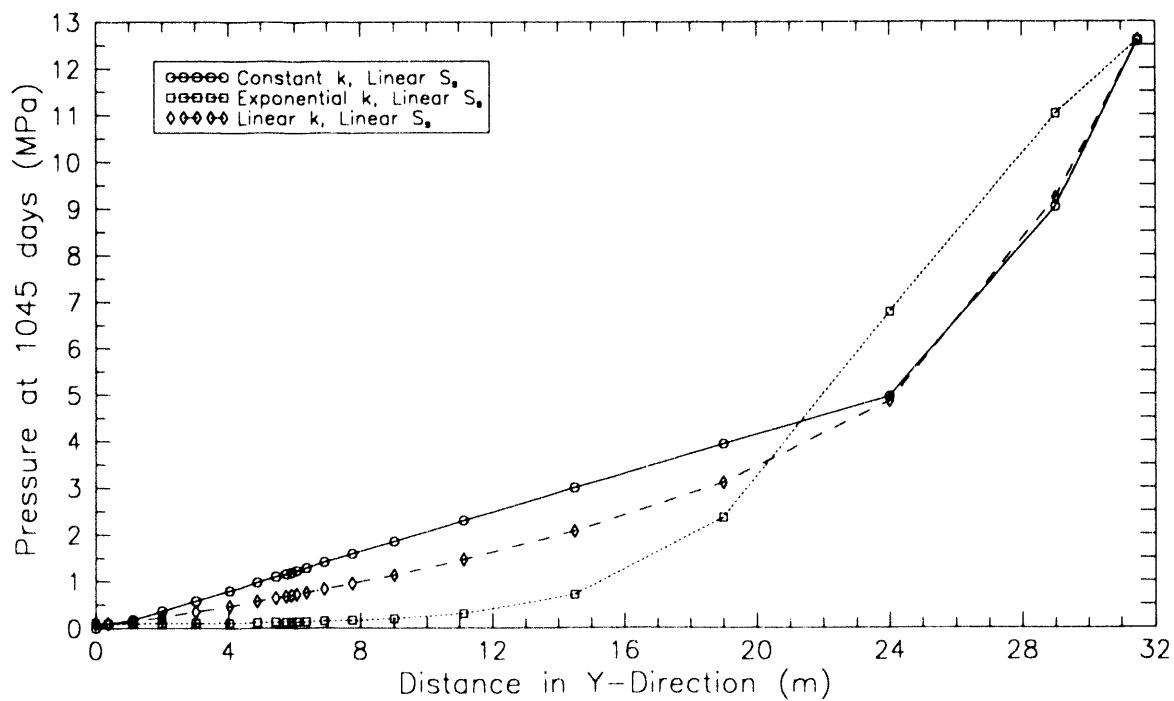
Figure G-4.   Pressure profile in Marker Bed 139 for a constant intrinsic permeability, an exponentially varying intrinsic permeability, and a linearly varying intrinsic permeability.
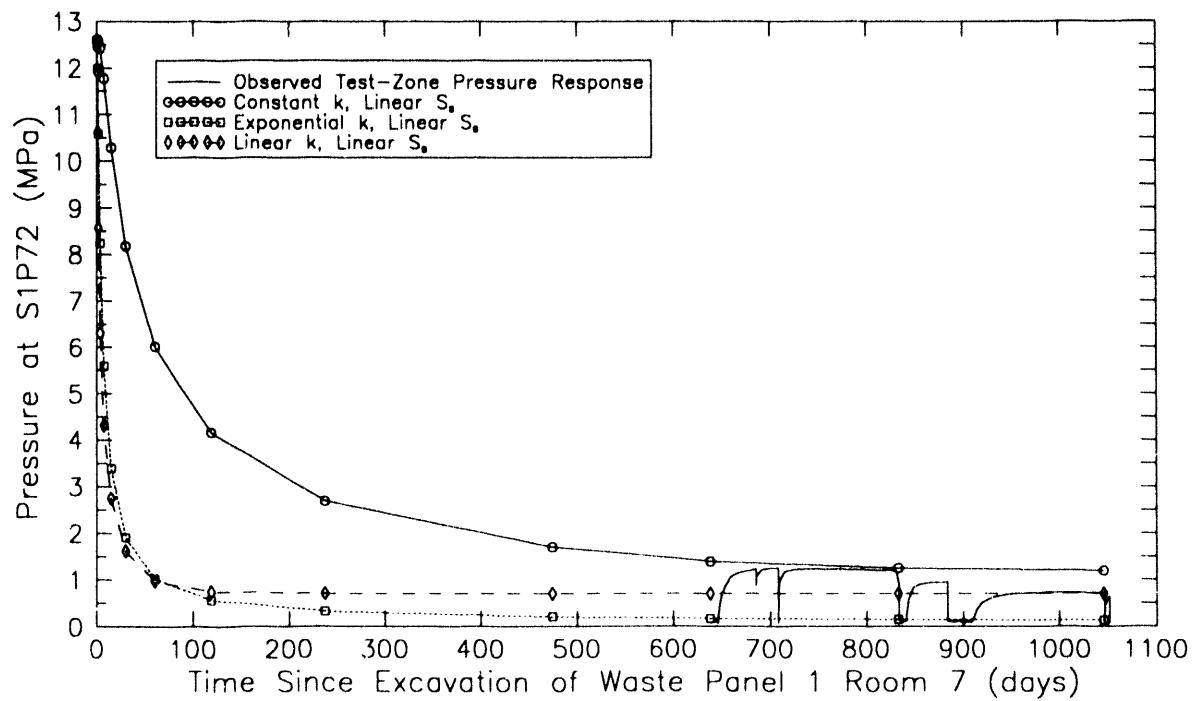
Figure G-5. Pressure with time at the location of S1P72 for a constant intrinsic permeability, an exponentially varying intrinsic permeability, and a linearly varying intrinsic permeability.
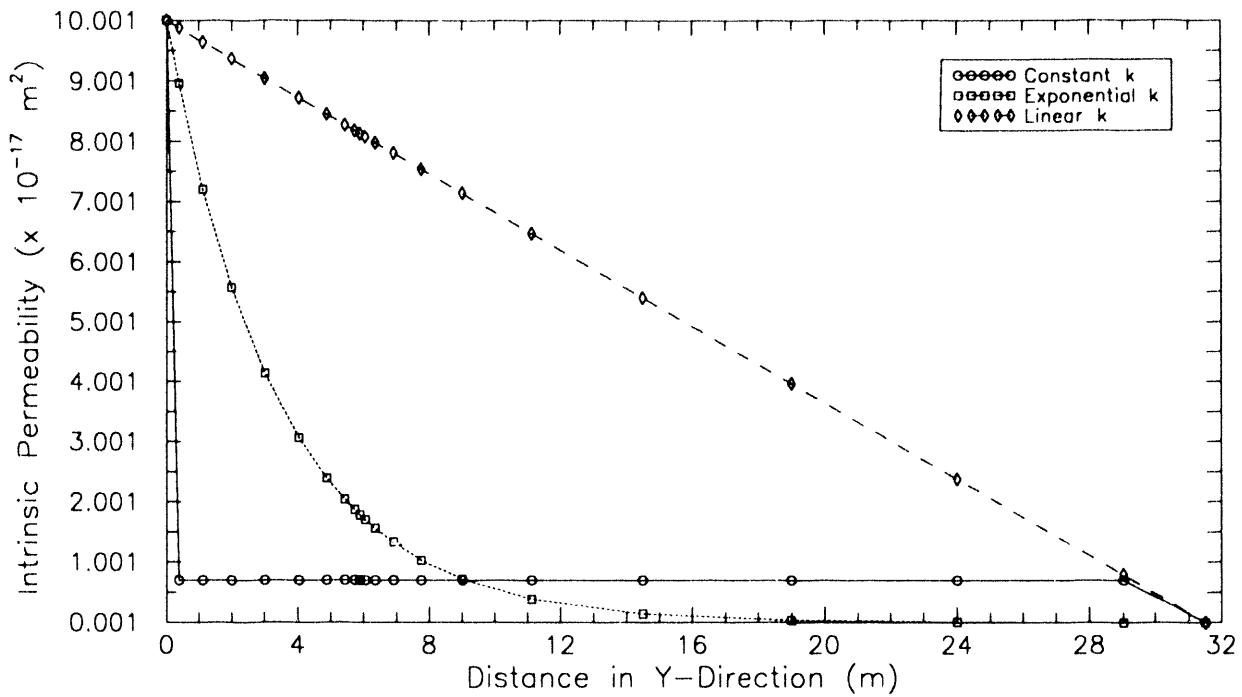
Figure G-6. Intrinsic permeability distribution.
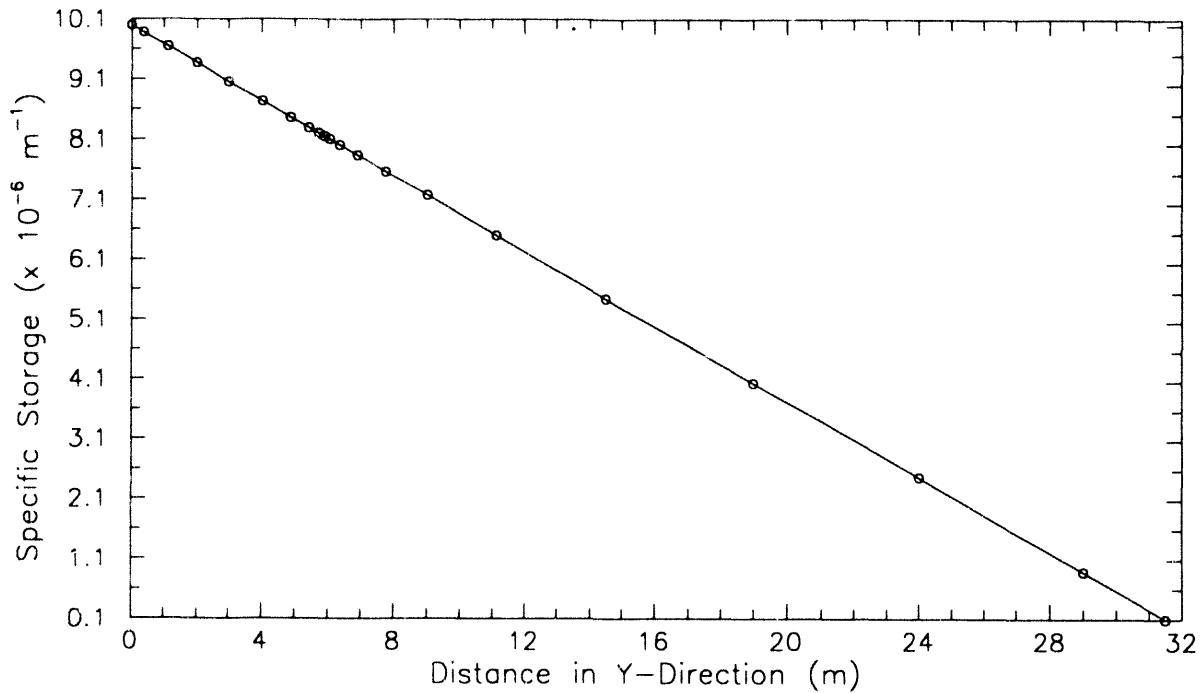
Figure G-7.   Specific storage assigned to Marker Bed 139 for TOUGH2 simulations of the test-zone pressure response during testing sequence S1P72-A.

The distance over which a constant permeability of 7×10^{-18} m^2 was assigned was varied to evaluate its effect on the simulations. The distances considered were 19, 24, and 29 m from the western model edge. These simulations assumed that the permeability was 10^{-20} m^2 beyond the region with a permeability of 7×10^{-18} m^2. The results are illustrated in Figures G-8 and G-9. As the distance decreased, the pressure at the location of S1P72 decreased. The closest match to the initial pressures observed at S1P72 was obtained assuming a distance of 29 m.

Changes to the distribution of specific storage affected the pressure at the location of S1P72 less than did changes to the distribution of intrinsic permeability. Because of this relative insensitivity to specific storage, the specific storage was assigned a linear distribution from 10^{-5} m^{-1} at the western model edge to 10^{-7} m^{-1} at the far field (Figure G-7).

Based on the simulations conducted for stage one, a constant permeability of 7×10^{-18} m^2 out to a distance of 29 m (Figure G-10) and a linear distribution of specific storage (Figure G-7) were selected for subsequent simulations. These parameters produced the closest match between the simulated pressures and the observed pressures in the test zone prior to pulse-withdrawal testing. The selected combination of intrinsic-permeability distribution, specific-storage distribution, and distance to the far field does not, however, represent a unique solution. In addition, the degree to which the selected parameter distributions match the actual distributions is unknown. However, without additional constraints on these parameters, the
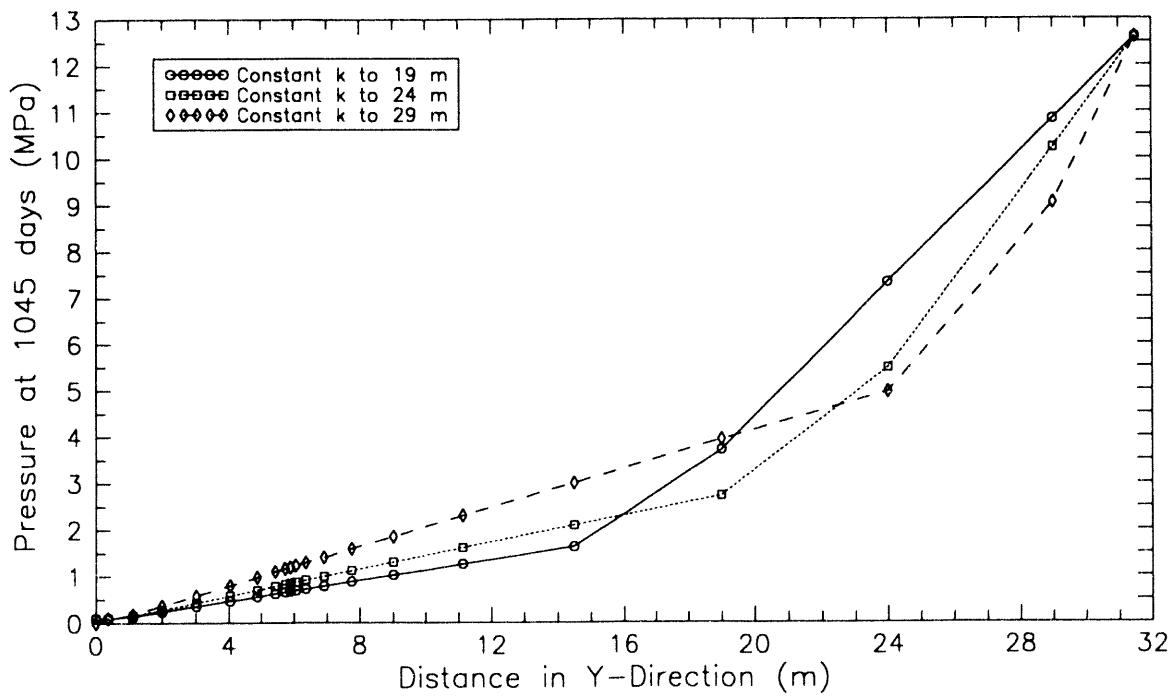
Figure G-8.   Pressure profile in Marker Bed 139 for variable extent of constant intrinsic permeability.
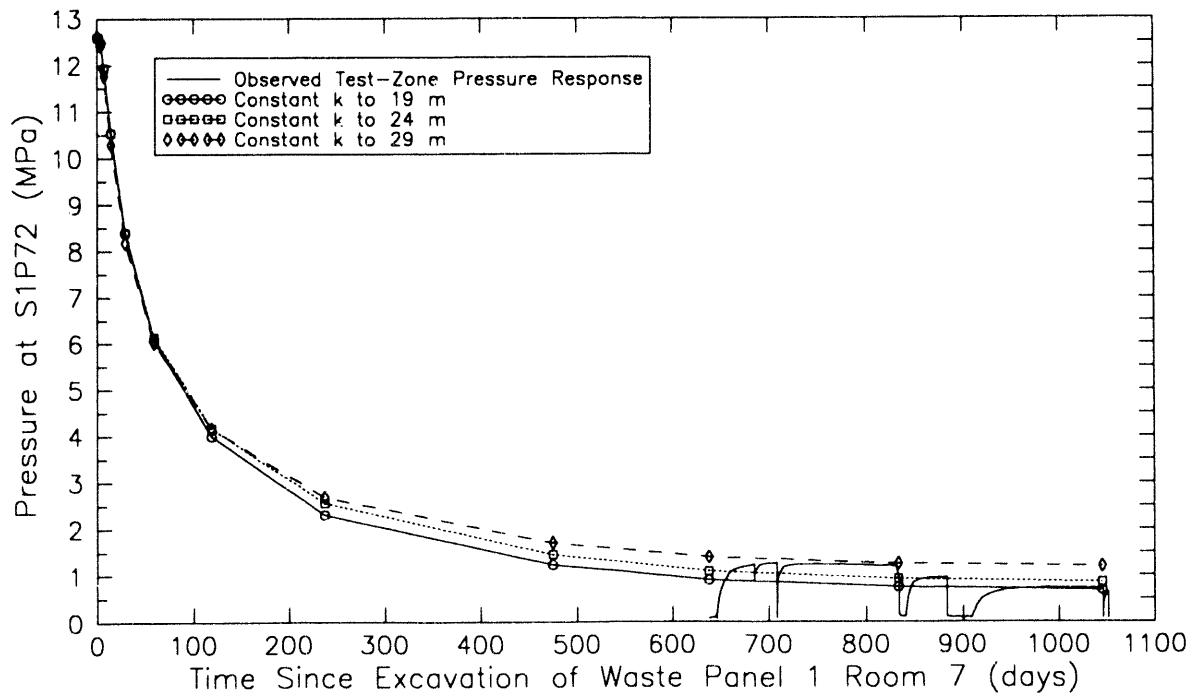
Figure G-9.   Pressure with time at the location of S1P72 for variable extent of constant intrinsic permeability.
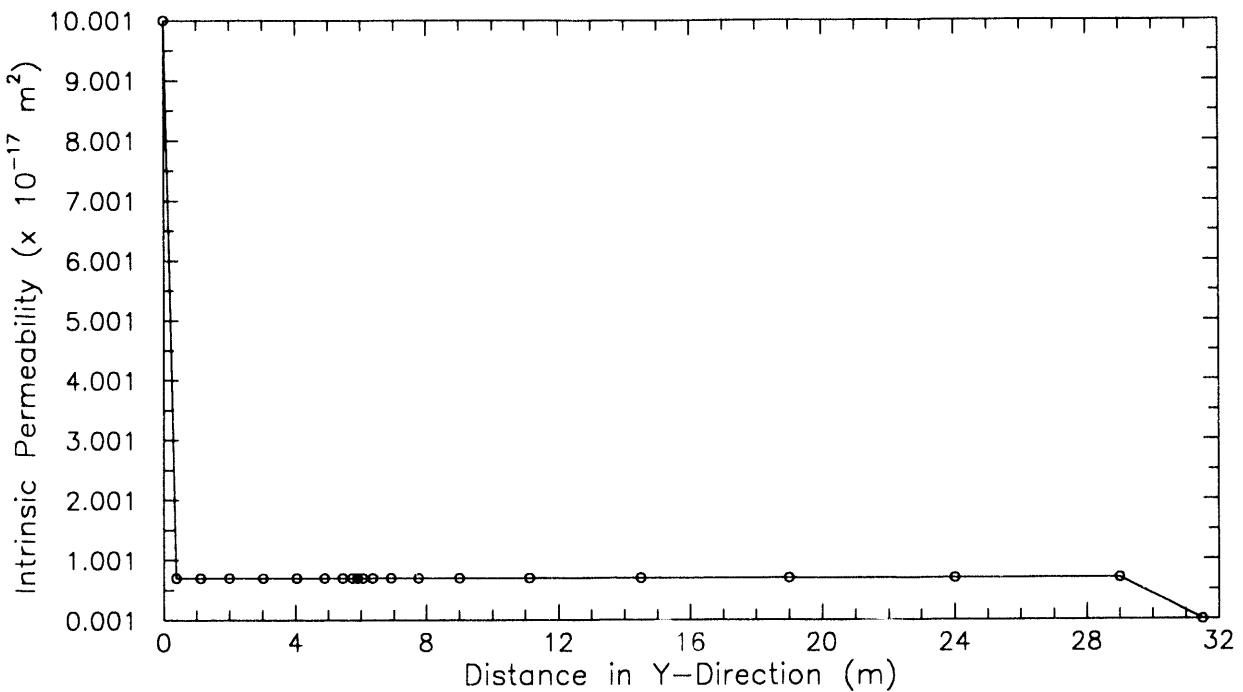
Figure G-10.   Intrinsic permeability assigned to Marker Bed 139 for TOUGH2 simulation of the test-zone
pressure response during testing sequence S1P72-A.

possibility of determining a unique and representative parameter combination is limited. Determination of
the selected parameter distributions ignored the effects of the seven-day open-hole period prior to testing
and also ignored the temporal variations in intrinsic permeability and specific storage caused by room
excavation.

G.4.2   STAGE TWO: SINGLE- AND TWO-PHASE SIMULATIONS OF THE TEST-ZONE PRESSURE
RESPONSE DURING TESTING SEQUENCE S1P72-A. The purpose of the stage two simulations was to
reproduce the general trend of the pressure responses observed during the S1P72-A testing sequence.
Because of the lack of site-specific data on parameters such as intrinsic permeability, specific storage,
undisturbed formation pressure, distance to the undisturbed formation, gas saturation and/or dissolved gas
in the formation, relative-permeability curves, and capillary-pressure curves, no attempt was made to fit the
observed data exactly. The goals of the simulations were to determine whether the decrease in the pressure
to which the test zone recovered after each of the constant-pressure withdrawal tests was due to free gas
in the system and/or was due to continued formation depressurization resulting from room excavation.
Stage two simulated from the time the room was excavated to the end of the S1P72-A testing sequence.
Section 6.3.2 discusses the dependence of test-zone compressibility on pressure and time. The simulations
presented here used test-zone compressibility as a fitting parameter.

Figure G-11 shows the results of simulations that assumed single-phase flow; neither free nor dissolved gas was present in the system. Note that the model test-zone compressibility was changed for each buildup period and each pulse-withdrawal test. During the initial buildup period, the simulated pressures rise more rapidly and level off more quickly than the observed data. For the two pulse-withdrawal tests, the simulated pressures closely match the observed pressures. In addition, the simulated response rises to a maximum and then begins to decline during the late-time portion of PW2 as do the observed data. This decline is attributed to continued depressurization of the formation due to room excavation. Two simulated curves are shown in Figure G-11 for the two pressure-buildup tests. Different va: :es of test-zone compressibility were used for the two simulations. These curves show that for single-phase conditions with the properties used here, the decrease in the pressure to which the test zone recovered following the two constant-pressure withdrawal tests could not be reproduced. Using a lower test-zone compressibility (the dashed curves in Figure G-11), the simulated data matched the early-time portion of the observed buildup curves but recovered to a higher ending pressure. Using a higher test-zone compressibility (the solid curves in Figure G-11), the simulated data matched the ending pressure but recovered much slower than the observed data and were recovering to a higher pressure. The poor comparison between the simulated and observed pressures during the pressure-buildup tests for single-phase conditions suggests that the observed pressure responses could have been affected by the presence of free gas.

The series of simulations presented in Figure G-12 assume no free or dissolved gas in the system from the time the room was excavated until the mid-point of S1P72 drilling. During the open-hole period, a gas
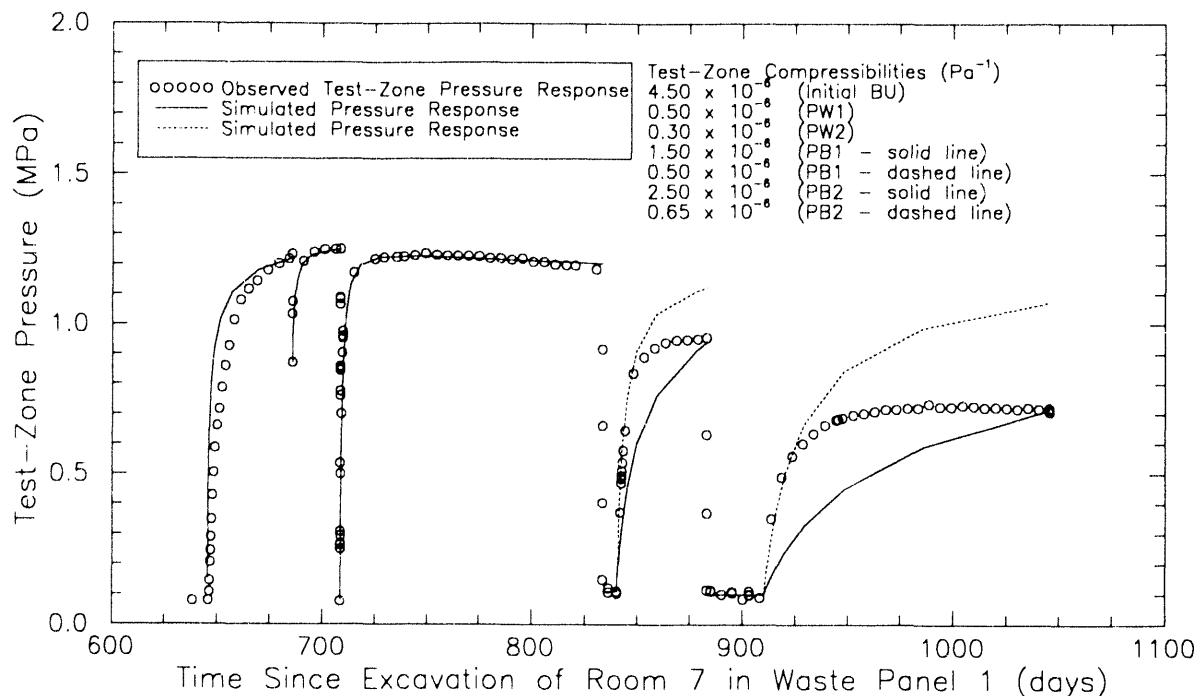
Figure G-11. Single-phase TOUGH2 simulation of test-zone pressure response during testing sequence S1P72-A.
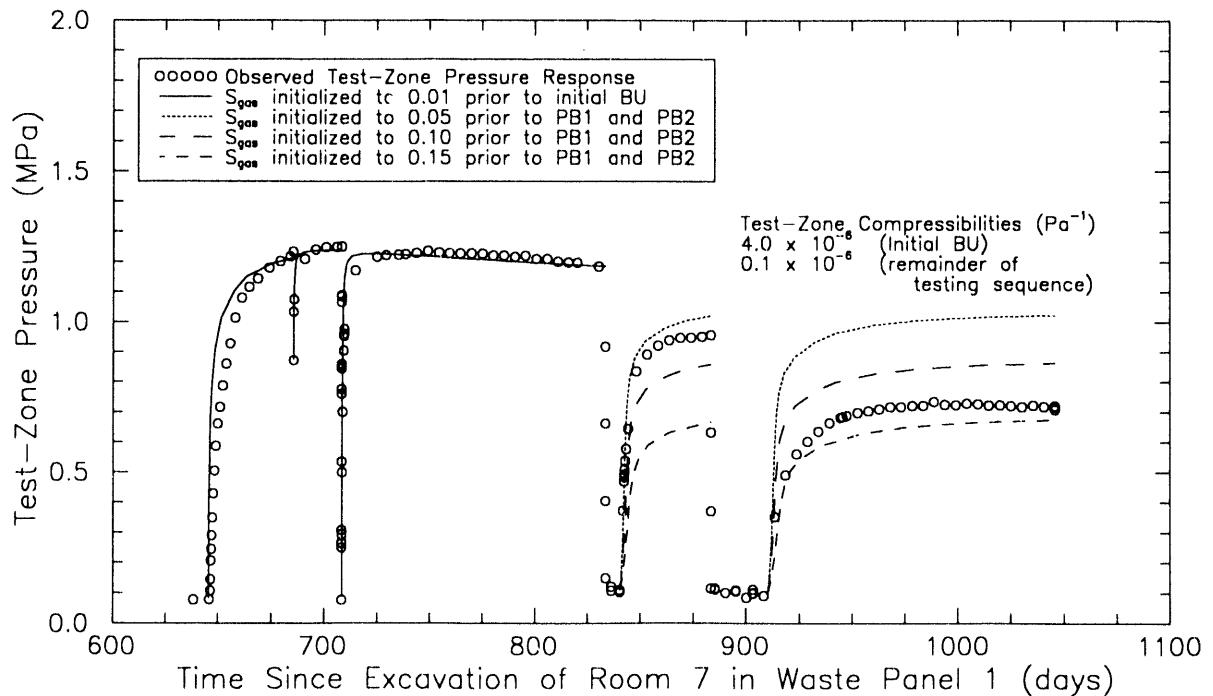
Figure G-12.   Multi-phase TOUGH2 simulations with gas saturation initialized to 0.01 prior to the initial buildup period and initialized to 0.05, 0.10, and 0.15 prior to PB1 and PB2.

saturation of 0.99 was assigned in the borehole. Marker Bed 139 was assigned a gas saturation of 0.01 at the start of the initial pressure-buildup period. Simulated responses during the initial buildup period and the two pulse-withdrawal tests show more rapid pressure recovery than the observed data. Three simulated curves are presented in Figure G-12 for each of the pressure-buildup tests. The differences between the three curves are due to the gas saturations assigned to Marker Bed 139 at the start of the buildup periods. Specific gas saturations were assigned to Marker Bed 139 at the beginning of PB1 and then again at the beginning of PB2. The short-dashed, long-dashed, and medium-dashed lines are results for initial gas saturations of 0.05, 0.10, and 0.15, respectively. These initial gas saturations were selected because they produced results which bound the measured data using the two-phase and formation properties assumed for the simulations. The degree to which these gas saturations represent actual formation values is dependent upon the degree to which the assumed two-phase properties used in the simulations represent the site-specific properties. Arbitrary assignment of gas saturation was necessary because site-specific hydrologic parameters and initial conditions are unknown and because no gas-saturation data are available for model calibration. All simulations of the pressure-buildup tests assumed a test-zone compressibility of 10^{-7} Pa^{-1}. These results illustrate that (1) the pressure recovery is reduced as the amount of free gas is increased and (2) the simulated pressures increased more rapidly at the end of the buildup periods than did the observed pressure.

An estimate of the amount of free gas in the system prior to the two pressure-buildup tests can also be made based on the bounding results presented in Figure G-12. However, the degree to which those

estimates represent actual conditions in Marker Bed 139 is unknown since they are based on relative-permeability curves for an analogue material that may not be representative of Marker Bed 139 (see Section G.3). The simulated results in Figure G-12 show the best agreement with the observed data for an initial gas saturation near 0.05 prior to PB1 and an initial gas saturation near 0.15 prior to PB2. This indicates that the amount of free gas in the system prior to PB2 was probably higher than the amount of free gas in the system prior to PB1. For the simulations presented in Figure G-12, free gas in the system was initialized prior to both buildup periods. Therefore, the effect of CPW2 on increasing or decreasing the gas saturation in the formation surrounding the borehole was not evaluated.

The simulation presented in Figure G-13 initialized the gas saturation in Marker Bed 139 to 0.10 at the end of CPW1 and then let the model calculate changes to that saturation during the remainder of the testing sequence based on the conditions imposed at the borehole. Comparing Figures G-12 and G-13, the main conclusion from this simulation is that, for the assumed relative-permeability curves and gas solubility, the borehole conditions during CPW2 are such that little additional gas comes out of solution over the course of the test. The gas saturation at the start of PB1 was similar to the gas saturation at the start of PB2 and the simulated responses showed recovery to approximately the same pressure.

The sensitivity of the response during PB1 to test-zone compressibility is shown in Figures G-14, G-15, and G-16 for gas saturations initialized to 0.05, 0.10, and 0.15, respectively, prior to PB1. The values of test-zone compressibility considered for the sensitivity analysis were 10^{-5}, 10^{-6}, 10^{-7}, and 10^{-8} Pa^{-1}. As the test-zone compressibility is decreased from 10^{-5} to 10^{-7} Pa^{-1}, the pressure recovers more quickly and to a higher
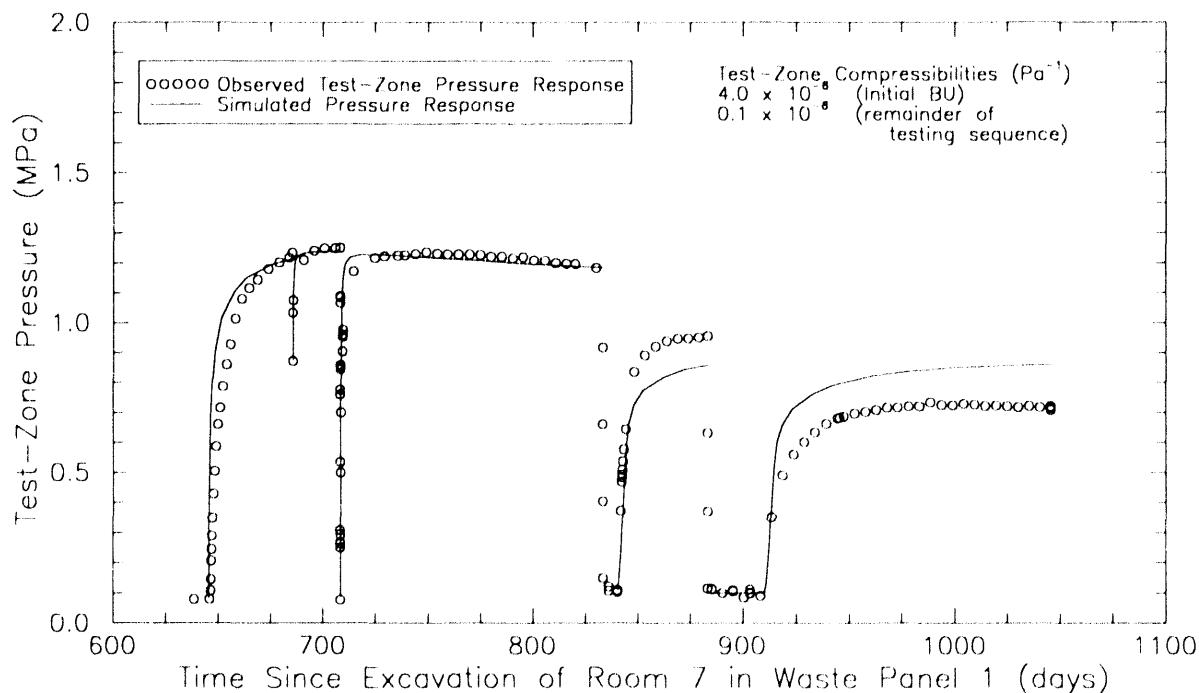
Figure G-13.   Multi-phase TOUGH2 simulations with gas saturation initialized to 0.01 prior to the initial buildup period and initialized to 0.10 prior to PB1.
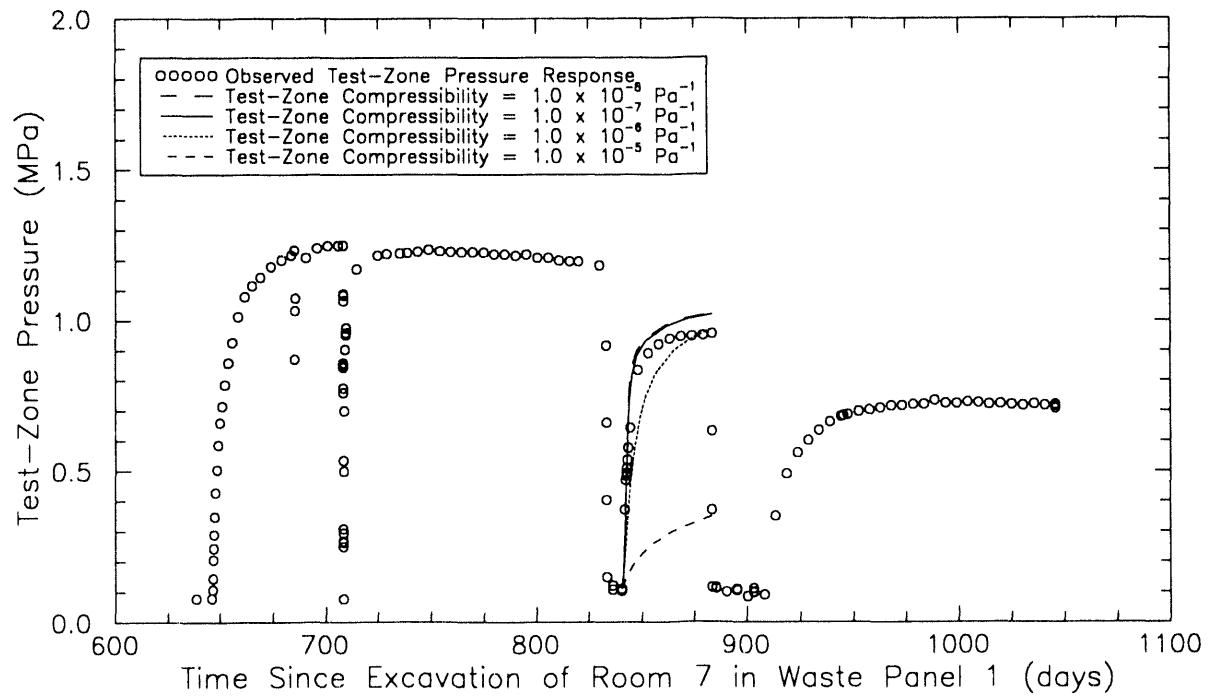
Figure G-14. Sensitivity of simulated PB1 to test-zone compressibility for TOUGH2 simulation with gas saturation initialized to 0.05 at the end of CPW1.
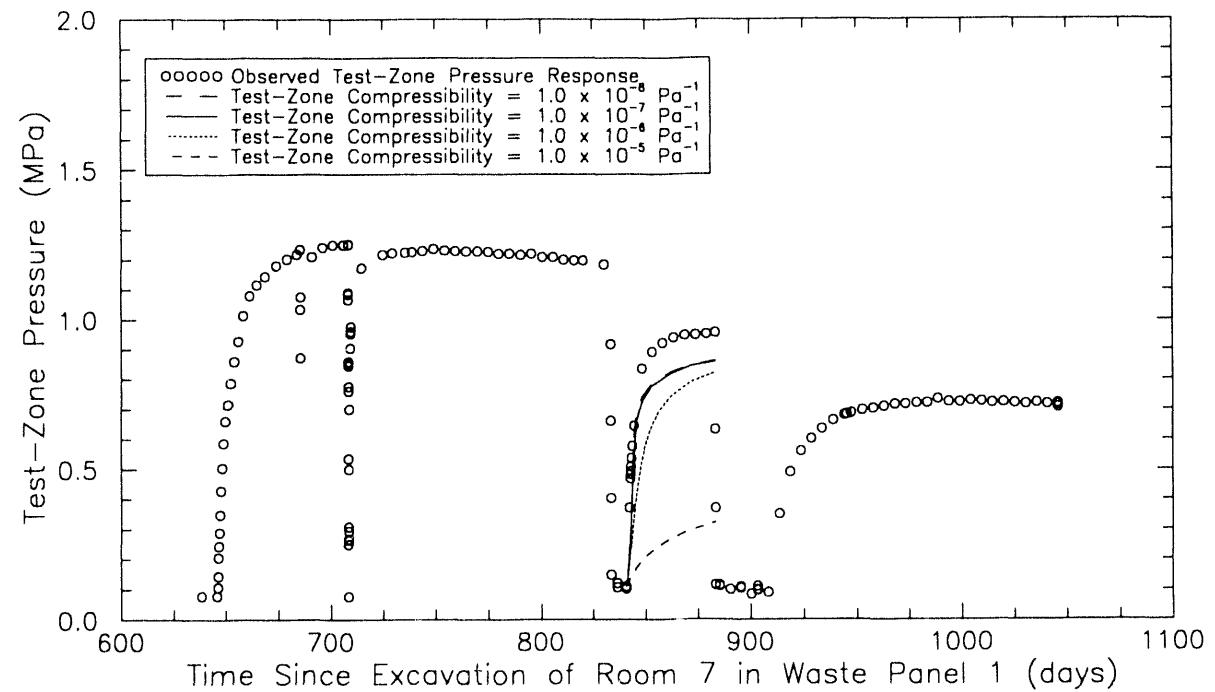
Figure G-15. Sensitivity of simulated PB1 to test-zone compressibility for TOUGH2 simulation with gas saturation initialized to 0.10 at the end of CPW1.
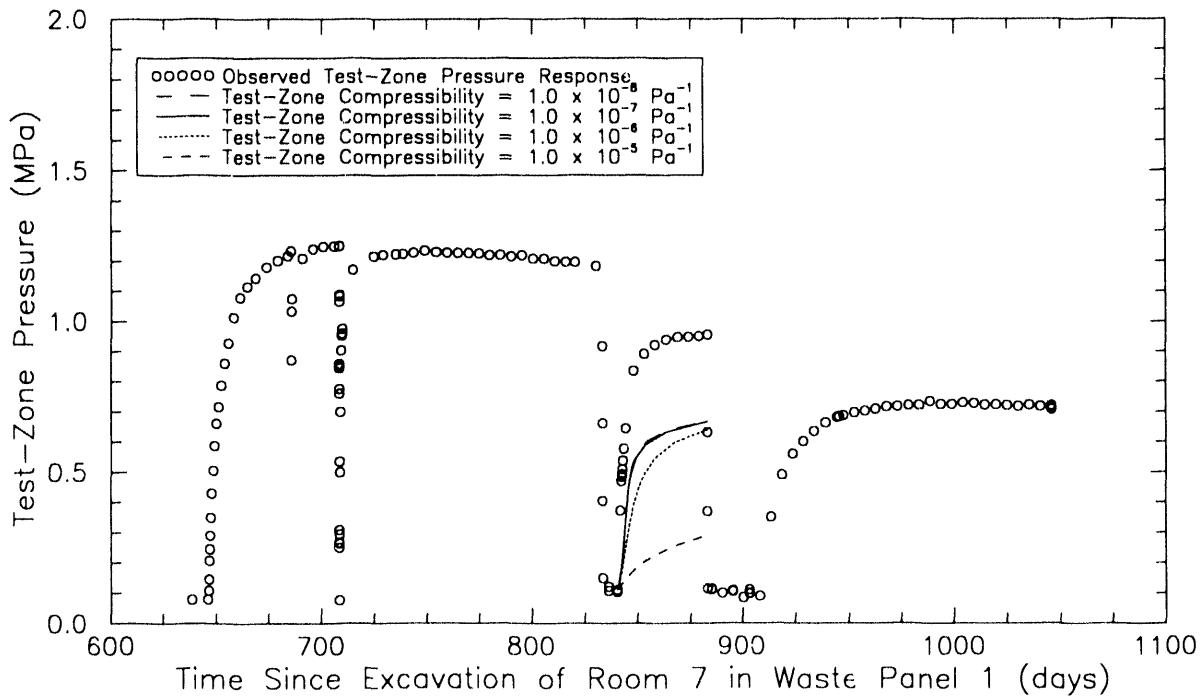
Figure G-16.   Sensitivity of simulated PB1 to test-zone compressibility for TOUGH2 simulation with gas saturation initialized to 0.15 at the end of CPW1.

pressure over the length of the buildup period. The pressure recovery was insensitive to a decrease in the test-zone compressibility from 10^{-7} to 10^{-8} Pa^{-1}.

The simulations of PB1 shown in Figure G-12 initialized the gas saturation in Marker Bed 139 prior to the start of the buildup period. A sensitivity analysis was conducted to examine the effect of initializing the gas saturation at the start of CPW1 rather than at the end. A comparison of the pressure recovery curves for initialization of gas saturation at the beginning and at the end of CPW1 is presented in Figure G-17. Pressure recovery is slower during the early time and steeper during the late time when gas saturation is initiated at the end of CPW1 rather than at the beginning.

The model element representing borehole S1P72 was established as a boundary condition with a constant pressure and a constant gas saturation during the constant-pressure withdrawal tests. For all of the simulations discussed above, a constant gas saturation of 0.50 was assumed during CPW1 and CPW2. Figure G-18 shows little sensitivity of the simulated pressure response during PB1 to constant gas saturations of 0.01, 0.50, and 0.99 assigned to the borehole element during CPW1.

The simulated volumes of brine and gas produced from the test zone during the two constant-pressure withdrawal tests were compared to the volumes collected during testing. The model predicted brine production of approximately 2,500 to 3,500 cm^3 during CPW1 and 9,000 to 10,000 cm^3 during CPW2 compared to observed volumes of about 10,350 and 22,000 cm^3, respectively. The model simulations did not produce gas from the test zone during either constant-pressure withdrawal test because the gas
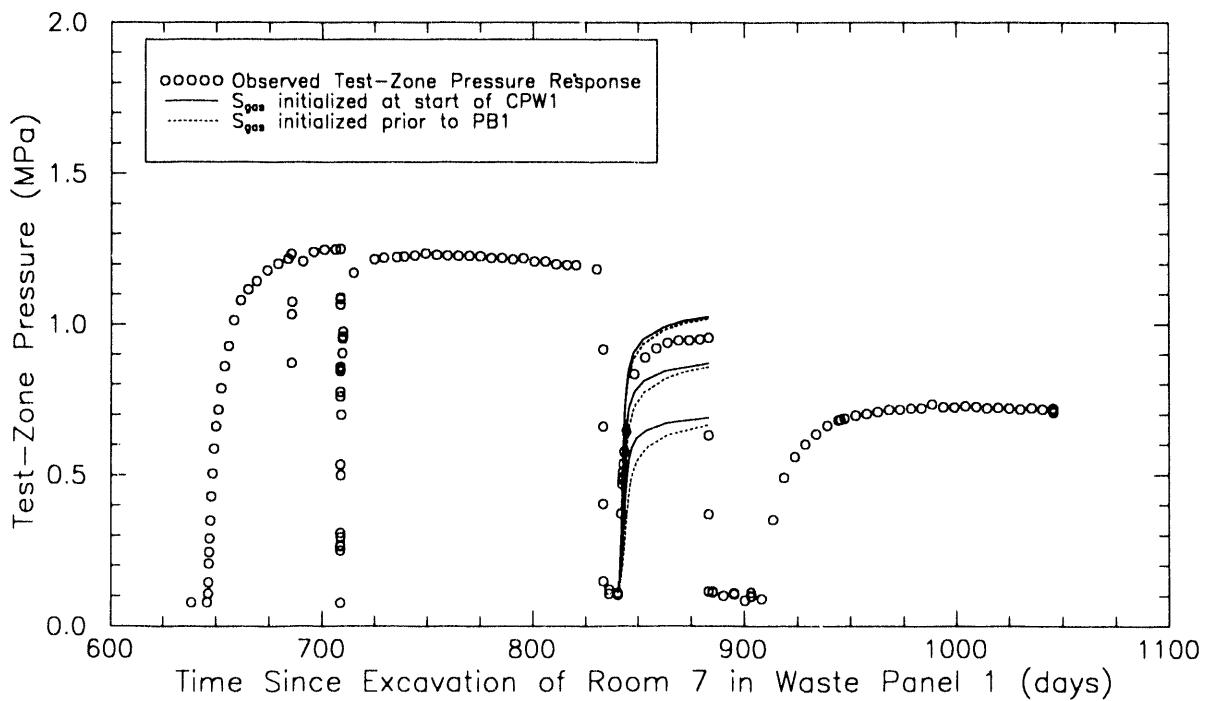
Figure G-17. Multi-phase TOUGH2 simulations of PB1 for gas saturations of 0.05 (top curves), 0.10 (middle curves), and 0.15 (bottom curves) initialized at the start of CPW1 and initialized prior to PB1.
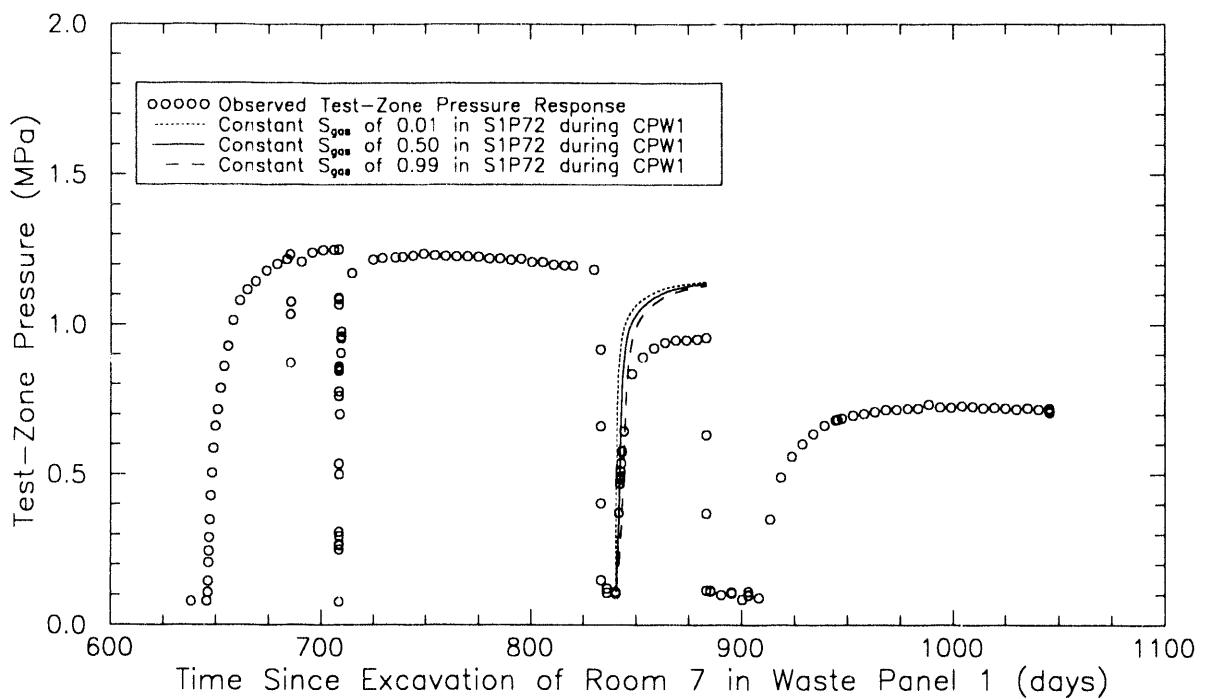
Figure G-18. Multi-phase TOUGH2 simulations of PB1 for constant gas saturations of 0.01, 0.50, and 0.99 in S1P72 during CPW1.

236

saturation never reached the critical saturation. The observed gas production at atmospheric pressure was approximately 124,400 cm^3 during CPW1 and 343,000 cm^3 during CPW2. The apparatus and technique used to measure these gas volumes are discussed in Section 3.7. The poor match between the simulated and observed production rates of brine and gas during the constant-pressure withdrawal tests suggests that the intrinsic permeability and the relative-permeability curves used for the simulations may not be representative of Marker Bed 139 in the vicinity of borehole S1P72.

G.5 Summary of Unknown Site-Specific Hydrologic Parameters

A quantitative interpretation of the test-zone pressure response during testing sequence S1P72-A was not possible because of a lack of necessary data. Major limitations of the simulations presented here are: (1) the uncertainty in the spatial and temporal distributions of the formation properties (intrinsic permeability and specific storage); (2) the uncertainty in the two-phase properties (relative permeability and capillary pressure) of Marker Bed 139; and (3) the uncertainty in the initial conditions of the formation prior to testing (pressure and pressure history, gas saturation, and dissolved gas).

Excavation activities in the WIPP underground have created conditions in the Salado that cause the hydrologic parameters to change in time and space (Stormont et al., 1991). The time dependence of intrinsic permeability, relative permeability, specific storage, and formation pore pressure is unknown. The TOUGH2 simulations presented here examined a time period of 1050 days, or almost three years. Over that length of time, significant changes in the hydrologic properties of Marker Bed 139 probably occurred. Until a better understanding of the time dependence of key parameters is achieved, our ability to simulate complex testing situations such as that at S1P72 and obtain realistic results is limited.

To date, no comprehensive study on the variation of hydrologic parameters within a single anhydrite interbed with time and distance from an excavation has been performed. In addition, uncertainties also exist with respect to the distance beyond which hydrologic parameters have not been modified by excavation effects and the values of those undisturbed parameters. Using numerical models to obtain this information when observations are only available from a single location for calibration is not ideal because the uniqueness of the interpreted results cannot be confirmed. Some quantitative understanding of the spatial distribution of hydrologic properties within the area disturbed by the excavation and of far-field conditions is necessary in order to model the physical system with confidence.

Measured data from an analogue material were used to develop the relative-permeability and capillary-pressure curves used for the simulations. The extent to which these curves are representative of the tested interval is uncertain. A quantitative interpretation of the test-zone pressure response is not possible without site-specific data on the relative permeability and capillary pressure in Marker Bed 139. This information, which can be obtained for unfractured systems from laboratory tests on core samples, is important for two-phase interpretations of permeability tests and for prediction of gas migration from the underground facility after waste disposal. The gas saturation and/or the amount of gas dissolved in the brine prior to conducting the permeability tests must also be known to interpret the tests quantitatively. Without this information, the initial conditions of the system are unknown and any interpretation is uncertain.

Our understanding of formation conditions prior to the start of testing could be improved by modifying the testing procedures. The pretest formation pore pressure could be determined by reducing the open-hole period to a few hours and then allowing the test interval to recover to a stable pressure before beginning testing. The pressure could also be monitored for several months before testing began. This would not only give a better estimate of the formation pore pressure but would also define the rate of formation depressurization due to the room excavation prior to testing. A brine sample collected at near-formation pressure and temperature could be analyzed to determine the amount of dissolved gas contained in the brine prior to testing. A better understanding of the solubility of gas in the brine could be obtained by determining the geochemistry of the brine and by conducting a chemical analysis of the gas.

G.6 Summary and Conclusions

The pressure responses observed during permeability-testing sequence S1P72-A show a decrease in the pressure to which the test zone recovered after each of the constant-pressure withdrawal tests. The simulations presented here examined the effect of continued formation depressurization due to excavation effects and the effect of free gas in the formation on the pressure response. The goal of the simulations was to reproduce the general trend of the observed responses. Exact reproduction of the observed pressure responses was not attempted because the values for intrinsic permeability, specific storage, undisturbed formation pressure, distance to the undisturbed formation, formation gas saturation and/or solubility, and relative-permeability and capillary-pressure curves are unknown.

The first stage of the simulation process determined a non-unique combination of intrinsic-permeability distribution, specific-storage distribution, and distance to the far field that yielded a pressure distribution in Marker Bed 139 that was consistent with the pressure responses observed during the initial buildup period and the two pulse-withdrawal tests. The non-uniqueness of the combination results from a lack of knowledge concerning the actual spatial and temporal distributions for these three parameters. The stage one simulations ignored the effect of the seven-day open-hole period of S1P72 on the formation pressures and gas saturations.

The second stage of the simulation process was designed to reproduce the general trend of the pressure responses observed during permeability testing in S1P72. All conclusions obtained from the simulations of the testing sequence are speculative because of the uncertainty in the relative-permeability and capillary-pressure curves for Marker Bed 139 and because of the uncertainty in the amount of free and dissolved gas in the brine. Based on the good match between the single-phase simulations and the observed data, it appears that there was little effect from free gas on the pressure increase during the initial buildup period and on the responses during the two pulse-withdrawal tests. The effect of continued formation depressurization due to room excavation on the observed and simulated pressure response is illustrated by the decline in pressure during the late-time portion of PW2 (Figure G-11).

The poor match between the single-phase simulations and the observed data from the pressure-buildup tests indicates that factors other than continued formation depressurization and the reduction of formation pressure in the vicinity of the borehole during the constant-pressure withdrawal tests caused recovery to successively lower pressures. Simulations with gas saturations initialized to 0.05, 0.10, and 0.15 prior to the

238

pressure-buildup tests indicate that the pressure to which the test zone recovers decreases as the gas saturation increases. The simulations also suggest a higher gas saturation prior to PB2 than prior to PB1. For the relative-permeability curves used here, the simulations indicate that the conditions during CPW2 do not produce a substantial increase in gas saturation over the saturation present at the end of CPW1.

The simulations presented in this appendix assumed that the pressure to which the test zone recovered during the two pulse-withdrawal tests was representative of pressure conditions resulting from room excavation. In other words, the simulations assumed that the seven-day open-hole period prior to permeability testing had no effect on the formation pressure or gas saturation in the vicinity of the borehole. An alternative conceptualization is that if the formation pressure and gas saturation in the vicinity of the borehole were modified by the two constant-pressure withdrawal tests, then they would have also been modified by the open-hole period. This latter assumption was not considered by the simulations because data on the distribution of pressure and gas saturation in the vicinity of S1P72 prior to drilling do not exist.

In summary, the TOUGH2 simulations demonstrated that continued formation depressurization due to room excavation and the presence of free gas in Marker Bed 139 could have affected the pressure responses in the S1P72-A test zone during permeability testing. The effects could not be quantified because the conditions in Marker Bed 139 prior to drilling S1P72 are unknown, as are many of the formation properties. For the parameters and assumptions used here, the pressure responses during the initial buildup period and the two pulse-withdrawal tests do not appear to have been significantly affected by free gas. The decline in pressure during the late-time portion of PW2 is the result of formation depressurization. The pressure responses during the pressure-buildup tests appear to have been affected by free gas. In addition, the amount of free gas in the formation at the end of the second constant-pressure flow test (prior to PB2) appears to have been greater than the amount of free gas in the formation at the end of the first constant-pressure flow test (prior to PB1).

REFERENCES

Davies, P.B., L.H. Brush, and F.T. Mendenhall. 1992. "Assessing the Impact of Waste-Generated Gas From the Degradation of Transuranic Waste at the Waste Isolation Pilot Plant (WIPP): An Overview of Strongly Coupled Chemical, Hydrologic, and Structural Processes," *Proceedings: NEA Workshop on Gas Generation and Release From Radioactive Waste Repositories, Aix-en-Provence, France, September 23-26, 1991.* Paris, France: Nuclear Energy Agency, Organisation for Economic Co-Operation and Development. 54-74.

International Formulation Committee. 1967. *A Formulation of the Thermodynamic Properties of Ordinary Water Substance.* Dusseldorf, Germany: IFC Secretariat.

Morrow, N.R., J.S. Ward, and K.R. Brower. 1986. *Rock Matrix and Fracture Analysis of Flow in Western Tight Gas Sands. 1985 Annual Report.* DOE/MC/21179-2032 (DE86001055). Morgantown, WV: U.S. Department of Energy.

Pruess, K. 1987. *TOUGH User's Guide.* NUREG/CR-4645, SAND86-7104, LBL-20700. Berkeley, CA: Lawrence Berkeley Laboratory; Albuquerque, NM: Sandia National Laboratories.

Pruess, K. 1991. *TOUGH2 -- A General-Purpose Numerical Simulator for Multiphase Fluid and Heat Flow.* LBL-29400. Berkeley, CA: Lawrence Berkeley Laboratory.

Stormont, J.C., C.L. Howard, and J.J.K. Daemen. 1991. "Changes in Rock Salt Permeability Due to Nearby Excavation," *Rock Mechanics as a Multidisciplinary Science, Proceedings: 32nd U.S. Symposium on Rock Mechanics, Norman, OK, July 10-12, 1991.* Ed. J.-C. Rogiers. SAND91-0269C. Brookfield, VT: A.A. Balkema. 899-907.

APPENDIX H

THEORY AND VERIFICATION FOR STAB, THE SWIFT II TRANSMISSIBILITY GENERATOR FOR ANGLED BOREHOLES

APPENDIX H

THEORY AND VERIFICATION FOR STAB, THE SWIFT II TRANSMISSIBILITY GENERATOR FOR ANGLED BOREHOLES

by Mark Reeves, William H. Statham, and Toya L. Jones, INTERA Inc.

H.1   Introduction

Bedded evaporites of the Salado Formation at the Waste Isolation Pilot Plant (WIPP) site have been tested to evaluate the hydraulic properties controlling brine flow through the Salado (Beauheim et al., 1991 and this report). Testing in the underground facility has consisted of pressure-pulse, constant-pressure withdrawal, and pressure-buildup tests performed in boreholes drilled from drifts and rooms into the adjacent formation. Four of the tested boreholes were drilled vertically downward, one was drilled vertically upward, one was drilled horizontally, three were drilled downward at angles of 45°, 58°, and 77° from vertical, and one was drilled upward at a 40° angle from vertical. The interpretations of tests performed in the slanted boreholes presented in Section 7 were conducted using the Graph Theoretic Field Model (GTFM; Pickens et al., 1987) assuming radial flow to an equivalent vertical borehole with an idealized test-zone geometry. The angled test zones were modeled as vertical cylindrical boreholes with a diameter equal to the average of the major and minor axes of an ellipse formed by the intersection of the slanted borehole and a horizontal plane and with a height equal to the vertical thickness of the permeable unit contained within the test interval.

In order to evaluate the validity of assuming radial flow into an equivalent vertical borehole, simulations of the field tests were performed using the three-dimensional, finite-difference flow model SWIFT II (Reeves et al., 1986a,b). The SWIFT II results were then compared to the GTFM results. A second objective for simulating with SWIFT II was to perform a sensitivity analysis to evaluate the pressure response during testing in slanted boreholes for a range of permeabilities (horizontally and vertically), storativities, test-zone compressibilities, borehole angles, and test types. In order for SWIFT II to perform in an optimal fashion a grid preprocessor, STAB, was developed. After constructing an appropriate grid, STAB calculates pore volumes and transmissibilities which are the basic quantities needed by SWIFT II to perform the flow calculation. The function of STAB is to construct a grid which conforms to the geometry of the problem and minimizes the number of required grid blocks. Such a geometry recognizes that, near the borehole, flow is radial with respect to the borehole but that, at the radius of influence (defined below), flow becomes radial with respect to a vertical axis passing through the geometric center of the borehole. Beyond the radius of influence, the flow field behaves as if it emanated from a vertical borehole, and the Carter-Tracy (1960) facility in SWIFT II can be used to match the gridded region onto an infinite aquifer using an analytic solution for the external region. Recognizing this, STAB generates a grid only within the region extending from the borehole center to the radius of influence.

Ideally, one would employ a natural coordinate system for a slanted borehole with coordinate surfaces aligned with pressure contours and streamlines. Unfortunately, exact expressions for natural-coordinate surfaces cannot be known until the flow solution has been obtained. The present version of STAB estimates the location of pressure contours and spaces its radial grid accordingly. For a borehole fully penetrating a permeable layer, this appears to be the most important aspect of a natural system in determining the pressure response at the well. For a partially penetrating borehole, streamlines should become equally important.

The radius of influence for a slanted borehole, r_i, varies in accordance with an elliptical shape, the semi-major axis of which is given as (Cinco, 1974):

$$r_I = 5ah \tan \varphi_w \qquad \text{(H-1)}$$

where:

a	=	$(k_r/k_z)^{\frac{1}{2}}$
k_r	=	radial permeability,
k_z	=	vertical permeability,
φ_w	=	angle of borehole slant from vertical, and
h	=	formation thickness.

H.2   Determination of a Finite-Difference Grid for a Slanted Borehole

In a conceptualization inspired by the Green's function method for developing analytic solutions, Figure H-1 shows pressure pulses emanating from a slanted borehole. The effects of pressure reflecting off of the upper and lower boundaries of the test interval are accounted for through image borehole completions. Figure H-1 illustrates a situation in which point A, located in the top layer of the completion interval, experiences pressure pulses initiated from the borehole segments located in three separate layers, including one from the upper image region. Based on the pressure response experienced at point A, the slanted-borehole segments of these layers cannot be separately identified as sources. The response at point A is indistinguishable from that which would have resulted from three segments of a vertical borehole. This vertical borehole is referred to as the apparent borehole and represents the apparent sources of the pressure pulses. The location of the apparent borehole is determined with an algorithm that relies on an averaging process as the main component. Placement of each radial node in each modeled layer is based on the location of the apparent source of its pressure response (i.e., the apparent borehole).

The first step in developing the geometry appropriate for a slanted borehole is to develop a radial grid from the geometric center of the slanted borehole to the radius of influence. This grid is referred to as the reference grid. In the layer representing the center of the test interval, the reference grid extends from the center of the borehole to the radius of influence. The grid is developed such that the distances between nodes are equal in log space. The first node, r_1, is positioned inside the borehole and the second node, r_2, is positioned outside the borehole with the well radius, r_w, providing the interface between block 1 and block 2. Outside of the borehole there are $N_r - 1$ grid blocks that cover the region $r_w' \leq r \leq r_I$ where N_r is the total number of radial grid blocks. The radius r_w' refers to a radius on the ellipse created by the intersection of
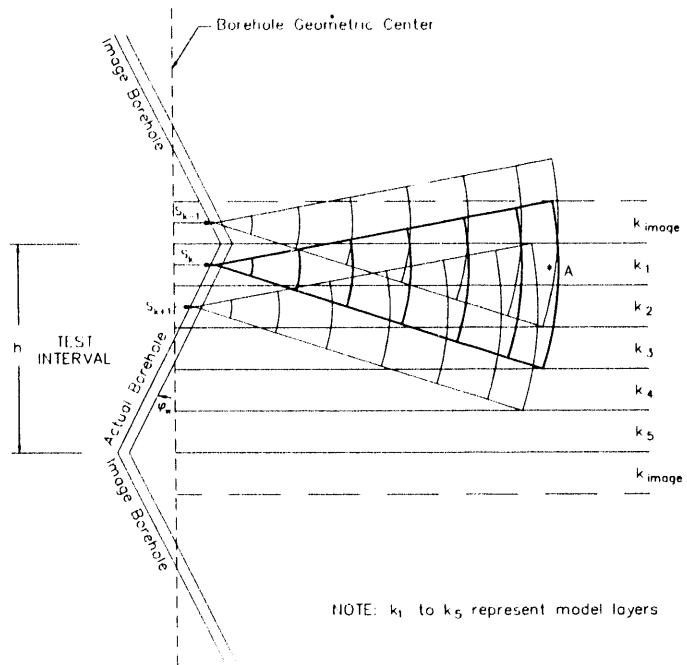
Figure H-1. Conceptualization of slanted borehole for development of SWIFT II mesh geometry.

a horizontal plane with the slanted borehole (Figure H-2). The line of interest on Figure H-2 is the center of an angular grid block along which radial nodes are located. The expression for r_w' is:

$$r_w' = \frac{r_w}{\cos\varphi_w \left(1 + \tan^2\varphi_w \sin^2\theta'\right)^{1/2}} \tag{H-2}$$

where: r_w = actual radius of the slanted borehole,

φ_w = angle of borehole slant from vertical, and

θ' = angle from the major axis of the borehole ellipse to the line of interest.

The appropriate logarithmically varying reference grid is obtained by setting:

$$r_I = A^{N_I-1} \, r_w' \quad \text{or} \quad A = \left(\frac{r_I}{r_w'}\right)^{\frac{1}{N_I-1}} \tag{H-3}$$

This gives grid-block radii of:

$$r_1 = \frac{r_w'}{A^{1/2}}, \quad r_2 = Ar_1, \quad \ldots, \quad r_{N_I} = A^{N-1}r_1 = \frac{r_I}{A^{1/2}} \tag{H-4}$$

245
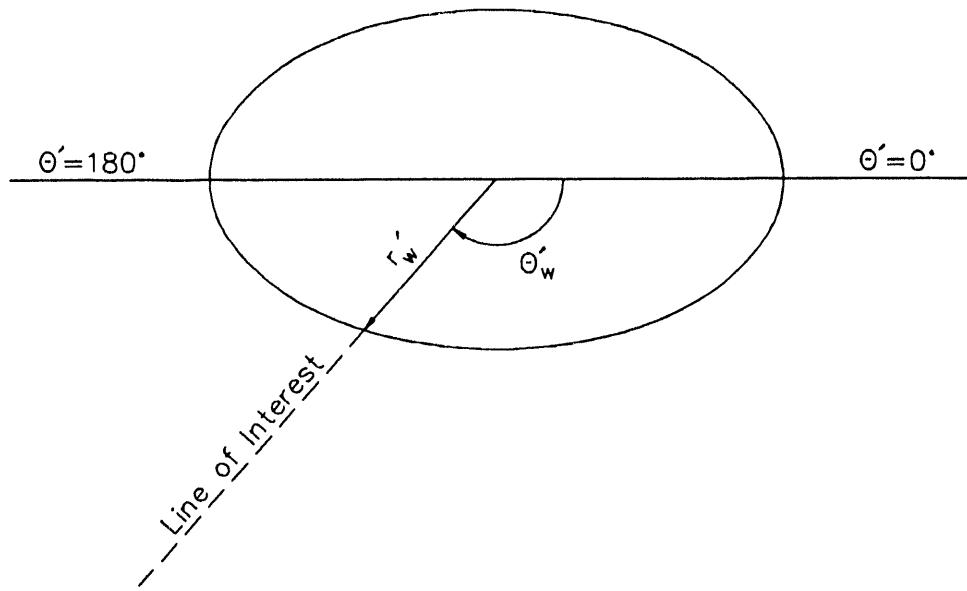
Figure H-2. Ellipse created by the intersection of a horizontal plane with a slanted borehole.

At the center of the test interval, the reference grid fits exactly from the center of the borehole to the radius of influence. Above and below the center of the test interval, the reference grid with the first node placed in the center of the borehole is too long or too short with respect to the radius of influence. Therefore, the reference grid must be either shortened or lengthened. This is accomplished by modifying the node locations of the reference grid in the model layers above and below the layer positioned at the center of the test interval through adjustment of the apparent source of the pressure pulses.

The process conducted by STAB first divides the completion zone into layers of equal thickness, Δz, thus dividing the borehole into segments. Each layer is then divided into sectors of equal angular extent, $\Delta\theta$, assuming the origin of the sectors is coincident with the centroid of the borehole segment.

For each layer k and angular sector j, the radial gridding algorithm used to modify the node locations of the reference grid is as follows:

(1)   The node located in the center of the borehole segment in layer k is set equal to the reference-grid value $r_1 = r_w'/A^{\frac{1}{2}}$. Assuming that within each sector the elliptical borehole may be adequately approximated by a circular borehole, r_w' is evaluated at the center of the borehole sector using Eq. H-2.

246

(2)   Node positioning involves a prediction step and a correction step. The predicted value of r_2 is taken from the reference grid (i.e., calculated with Eq. H-4) using the actual borehole as the origin. For $i>2$, the correction step (described below) will have been applied at node i-1 to yield an apparent-borehole segment. The location of the apparent-borehole segment is a distance $s_{i-1,k}$ from the geometric center of the actual borehole (Figure H-1). The approximate radial location of r_i is taken from the reference grid (i.e., calculated with Eq. H-4) using the center of this apparent-borehole segment as the origin.

(3)   The correction step involves relocating the apparent-borehole segment to a position appropriate for node i. As the distance to node i increases, pressure pulses released from actual-borehole segments in neighboring layers cause the location of the apparent borehole to move to a new position s_{ik}. The new position is closer to the geometric center of the actual borehole than was the location of the apparent borehole for node i-1. Correcting the apparent-borehole location involves computing weights for layer k and neighboring layers and then performing a weighted average.

Using the Green's function for an infinite system as a guide (Carslaw and Jaeger, 1959), the following empirical relation was adapted for the weighting function:

$$W_{ik}(z) = \exp\left[-\frac{1}{2}\left(\frac{z-z_k'}{\sigma(r_i')}\right)^2\right] \qquad \text{(H-5)}$$

where:

$$\sigma(r_i') = \frac{\beta r_i'}{a}, \qquad a = \left(\frac{k_r}{k_z}\right)^{\frac{1}{2}} \qquad \text{(H-6)}$$

and: z_k' =   point in the actual (slanted) borehole from which the pressure pulse originates,

z =   vertical depth from the top of the test interval in the actual borehole,

r_i' =   distance from the actual borehole to grid-node i,

W =   weighting factor,

β =   grid diffusion parameter,

i =   radial-node index, and

k =   vertical-node index.

The grid diffusion parameter is an empirical constant with a value of:

$$\beta = 1 - 0.007\varphi_w \qquad \text{(H-7)}$$

Eqs. H-5 and H-6 are used to calculate weighting factors for each layer contributing to the pressure experienced at node i. As the node of interest moves further from the borehole, the number of layers contributing non-negligible weighting factors increases. For point A in Figure H-1, weighting factors are calculated for three layers: the layer containing point A and the layers above and below point A. Based on the weighting factors, the apparent borehole is positioned according to:

$$\overline{s}_k = \frac{\sum_{k'} W_{k'} s_{k'}}{\sum_{k'} W_{k'}} \qquad (H-8)$$

where: $\overline{s}_k$ = distance from the borehole geometric center to the apparent-borehole location,

$W_{k'}$ = weighting factor based on Eqs. H-5 and H-6,

$s_{k'}$ = distance from the borehole geometric center to the actual borehole location, and

k' = model layer.

Although many of the weighting factors are negligible for $r_i \ll r_i$, STAB sums over all layers of the completion zone and all layers of the upper and lower image zones. Theoretically there would be an infinite number of image zones, the effects of which would decrease rapidly with distance from the completion zone. STAB considers only the two nearest-neighbor image zones. Neglecting other image zones does not introduce significant errors.

(4) In the correction step, the radial location of node i is positioned according to the reference grid (i.e., calculated with Eq. H-4) using the corrected location of the apparent borehole as the origin of the grid. Therefore, the numerical value for r_i in layer k is identical to that of r_i in the reference grid. The difference between the two node locations lies solely in the location of the apparent borehole which is used as the origin of the grid.

As the distance to the radial-node location increases (i.e., with larger and larger radii from the well), the averaging process positions the apparent borehole farther from the actual borehole and closer to the borehole geometric center. For the radial node in grid bock N_r, the averaging process causes the apparent borehole to coincide with the geometric center of the actual borehole as desired. The locations of actual and apparent boreholes are identical for instances when there are no contributions from image layers. In other words, the apparent borehole located using Eq. H-8 will deviate from the actual borehole only when a weighting factor from an image layer becomes non-negligible.

Figure H-3a shows a vertical grid generated by STAB. Near the slanted borehole, the grid-block interfaces are aligned approximately parallel to the borehole. As distance from the borehole increases, the interfaces approach a vertical alignment. Figure H-3b shows a radial one-layer grid generated by STAB. The radial grid centers on the actual borehole and not on the geometric center of the borehole. Therefore, the radial grid is asymmetrical about the borehole geometric center.
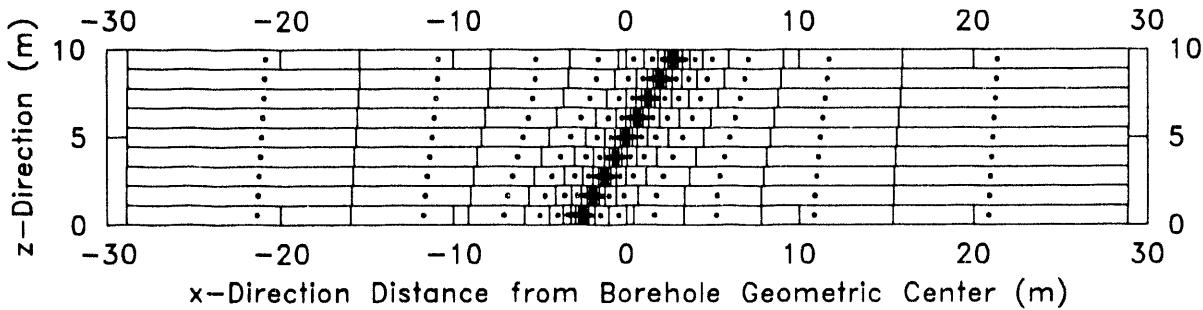
Figure H-3a. Example of generated vertical grid using STAB.
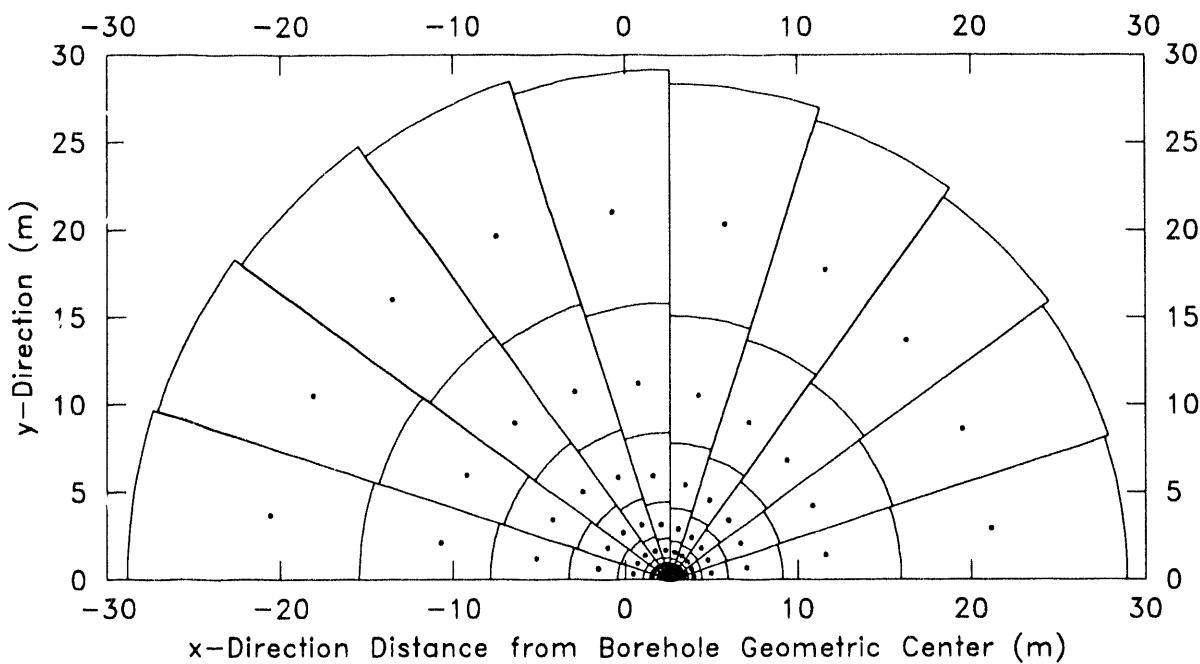
Figure H-3b. Example of generated radial grid using STAB.

STAB specifies nodal coordinates (r',θ') with respect to the location of the actual borehole. This requires that radial distances from the apparent borehole as determined in step 3 be converted to radial distances from the actual borehole. Figure H-4 conceptualizes the conversion process. The known parameters are θ', r'', $\bar{s}$, and s. The first parameter, θ', is specified in the gridding, the second parameter, r'', is a reference-grid value, the third parameter, $\bar{s}$, comes from the averaging procedure using Eq. H-8, and the fourth parameter, s, is calculated from the angle of the borehole slant, φ_w. The law of cosines gives:

$$r'^2 = r''^2 + (s-\bar{s})^2 - 2r''(s-\bar{s})\cos\theta'' \qquad \text{(H-9)}$$
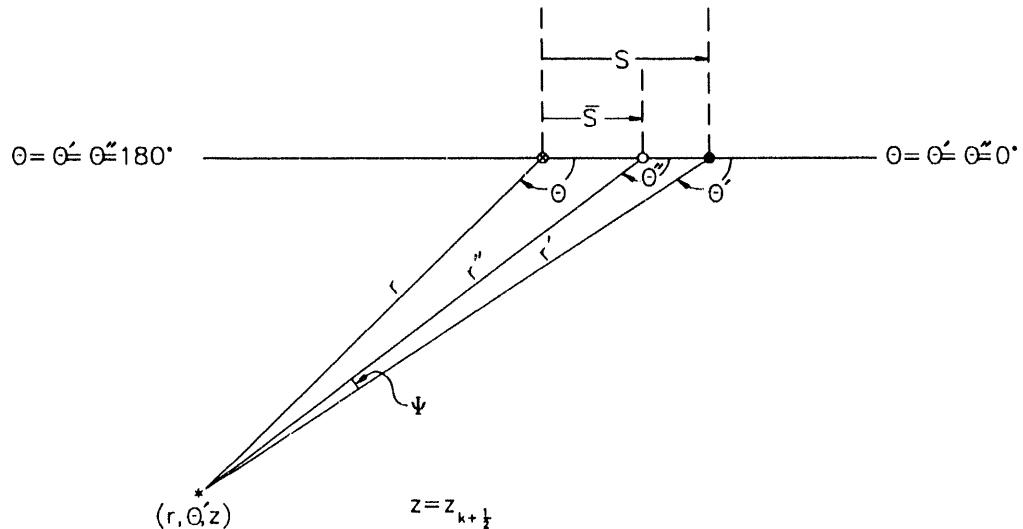
- • Cen.er of actual borehole in layer k.
- o Center of apparent borehole in layer k.
- ⊛ Borehole geometric center projected to layer k.
- ＊ Center of an arbitrary radial grid block in layer k.

Figure H-4.   Relationship between actual borehole, apparent borehole, borehole geometric center, and radial mode locations.

with the two unknowns r' and θ''. The law of sines gives:

$$\frac{s - \bar{s}}{\sin\psi} = \frac{r''}{\sin(180 - \theta')} \tag{H-10}$$

Since plane geometry relates ψ to θ'' according to $\theta'' = \theta' - \psi$, Eq. H-10 can be solved for θ''. That result, when substituted in Eq. H-9, gives the desired value of r'.

STAB also specifies nodal coordinates (r,θ) with respect to the geometric center of the actual borehole. The values of r and θ are obtained through analogous applications of the laws of sines and cosines.

The algorithm discussed above determines nodal locations. Block-interface locations are taken as the logarithmic mean of nodal-location pairs r_{i-1} and r_i and are calculated by:

$$r_{i-1/2} = \frac{r_i - r_{i-1}}{\ln(r_i/r_{i-1})} \tag{H-11}$$

H.3 Determination of the Transmissibilities and Pore Volumes for a Slanted Borehole

The transmissibility in the radial direction connecting blocks (i-1,j,k) and (i,j,k) for a vertical borehole is:

$$T_{r,i-\frac{1}{2},j,k} = \left[\frac{\Delta\theta_j^{'} \, r_{i-\frac{1}{2},j,k}^{'} \, \Delta z_k}{r_{i,j,k}^{'} - r_{i-1,j,k}^{'}} \right] k_r \qquad \text{(H-12)}$$

$$i = 2, \ldots, N_r$$

and

$$T_{r,\frac{1}{2},j,k} = T_{r,N_r+\frac{1}{2},j,k} = 0 \qquad \text{(H-13)}$$

Quantity k_r is the radial permeability, the subscript k denotes the layer, and the prime indicates that the parameter corresponds to the actual borehole. Eq. H-12 calculates radial transmissibility using the vertical interface length between grid blocks for its area calculation. For a slanted borehole, this length is not applicable because grid-block interfaces from one model layer to another are not aligned in the vertical direction. The appropriate area for cases when the vertical permeability is equal to the radial permeability is determined based on the straight-line distances between the centers of the grid-block interfaces of adjacent model layers (Figure H-5). Therefore, the radial transmissibility between blocks i-1,j,k and i,j,k in Figure H-5 is calculated by:

$$T_{r,i-\frac{1}{2},j,k} = \left[\frac{\Delta\theta_j^{'} \, r_{i-\frac{1}{2},j,k}^{'} \, \Delta z_k}{r_{i,j,k}^{'} - r_{i-1,j,k}^{'}} \right] k_r \cdot$$

$$\frac{1}{2\Delta z} \left[\left(\Delta z^2 + \Delta r_{i-\frac{1}{2},k-\frac{1}{2}}^2 \right)^{1/2} + \left(\Delta z^2 + \Delta r_{i-\frac{1}{2},k+\frac{1}{2}}^2 \right)^{1/2} \right] \qquad \text{(H-14)}$$

where: Δz = layer thickness, and

Δr = radial distance from the grid-block interface in layer k to the grid-block interface in the layer above (k-1) or the layer below (k+1).

Note that the calculation of radial transmissibility requires all layers to be of equal thickness.

For cases in which the vertical permeability is less than the radial permeability, the apparent distance to the overlying and underlying layers is greater than the actual distance (Figure H-6). The apparent distance, Δl, is defined as:

$$\Delta l = \left[\Delta r^2 + (\sigma\Delta z)^2 \right]^{1/2} \qquad \text{(H-15)}$$

251

- Grid-block center
- - Actual grid-block interface
— Interface length used for transmissibility calculation
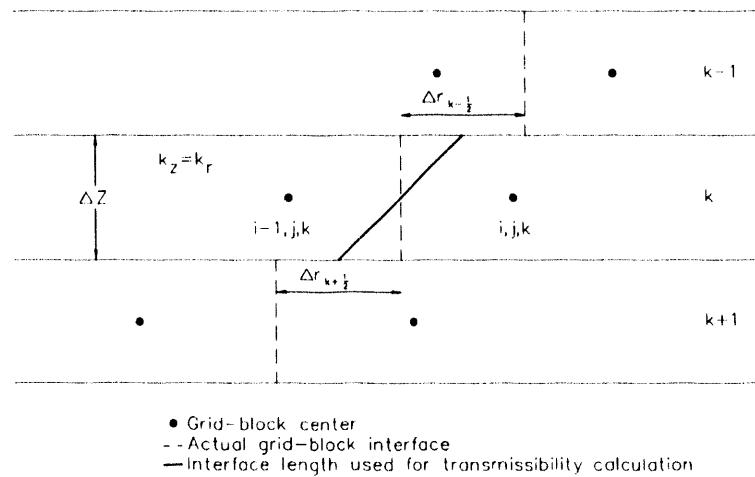
Figure H-5. Grid-block interface length used for calculation of radial transmissibility for cases when the vertical permeability is equal to the radial permeability.

- Grid-block center
- - Actual grid-block interface
Δl   Apparent distance to underlying layer
Δl*   Segment of Δl used for transmissibility calculation
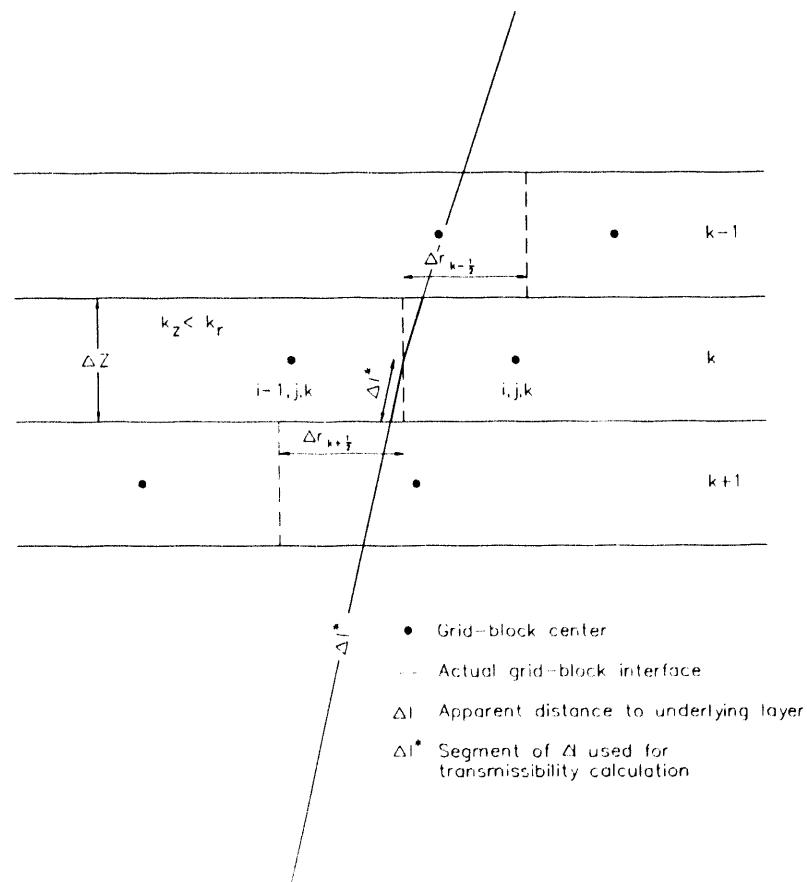
Figure H-6. Grid-block interface length used for calculation of radial transmissibility for cases when the vertical permeability is less than the radial permeability.

where: $\quad a \quad = \quad (k_r/k_z)^{1/2}$.

The appropriate area for calculation of the radial transmissibility requires the segment of the apparent distance that is located in layer k or length Δl^* in Figure H-6. Using the relationship:

$$\frac{\Delta l^*}{\Delta l} = \frac{\Delta z/2}{a\Delta z} \tag{H-16}$$

length Δl^* is defined as:

$$\Delta l^* = \frac{1}{2a}\left[\Delta r^2 + (a\Delta z)^2\right]^{1/2} \tag{H-17}$$

Rearranging Eq. H-17 yields:

$$\Delta l^* = \frac{\Delta z}{2}\left[1 + \left(\frac{\Delta r}{a\Delta z}\right)^2\right]^{1/2} \tag{H-18}$$

The surface area required for the transmissibility calculation when $k_z < k_r$ is based on the area of a cylinder and is given as:

$$\Delta A^* = \Delta\theta' r' \Delta l^* \tag{H-19}$$

Substituting Eq. H-18 into Eq. H-19 yields:

$$\Delta A^* = \Delta\theta' r' \frac{\Delta z}{2}\left[1 + \left(\frac{\Delta r}{a\Delta z}\right)^2\right]^{1/2} \tag{H-20}$$

Altering the equation for the transmissibility of a vertical borehole (Eq. H-12) based on the area given in Eq. H-20 yields the appropriate equation for calculation of the transmissibility for a slanted borehole when $k_z < k_r$, which is:

$$T_{r,i-\frac{1}{2},j,k} = \left(\frac{\Delta\theta_j' \, r_{i-\frac{1}{2},j,k}' \, \Delta z_k}{r_{i,j,k}' - r_{i-1,j,k}'}\right) k_r \cdot$$

$$\left(\frac{1}{2}\left[1 + \left(\frac{\Delta r_{i-\frac{1}{2},k-\frac{1}{2}}}{a\Delta z}\right)^2\right]^{1/2} + \frac{1}{2}\left[1 + \left(\frac{\Delta r_{i-\frac{1}{2},k+\frac{1}{2}}}{a\Delta z}\right)^2\right]^{1/2}\right) \tag{H-21}$$

Note that for $k_z = k_r$ (i.e., $a = 1$), Eq. H-21 reduces to Eq. H-14.

For the azimuthal direction, interface areas are given by:

$$a_{\theta,i,j(-),k} = \left(r'_{i+\frac{1}{2}} - r'_{i-\frac{1}{2}}\right)\Delta z_k \qquad \text{(H-22)}$$

Rather than using j-½, the notation j(-) is used in order to distinguish between the j-½ side of block i,j,k and the j+½ side of block i,j-1,k. In general, the values for these two areas will differ (Figure H-7). The transmissibilities for the azimuthal direction are given by:

$$T_{\theta,i,j-\frac{1}{2},k} = \frac{2}{\left[\dfrac{r'\Delta\theta'}{a_\theta}\right]_{i,j(-),k} + \left[\dfrac{r'\Delta\theta'}{a_\theta}\right]_{i,j-1(+),k}} (k_r)_{i,j-\frac{1}{2},k} \qquad \text{(H-23)}$$

$$j = 2, \ldots, N_\theta$$

and

$$T_{\theta,i,\frac{1}{2},k} = T_{\theta,i,N_r+\frac{1}{2},k} = 0 \qquad \text{(H-24)}$$

N_θ denotes the last grid block in the azimuthal direction.

x = area for j− ½ side of block i,j,k
y = area for j+ ½ side of block i,j−1,k
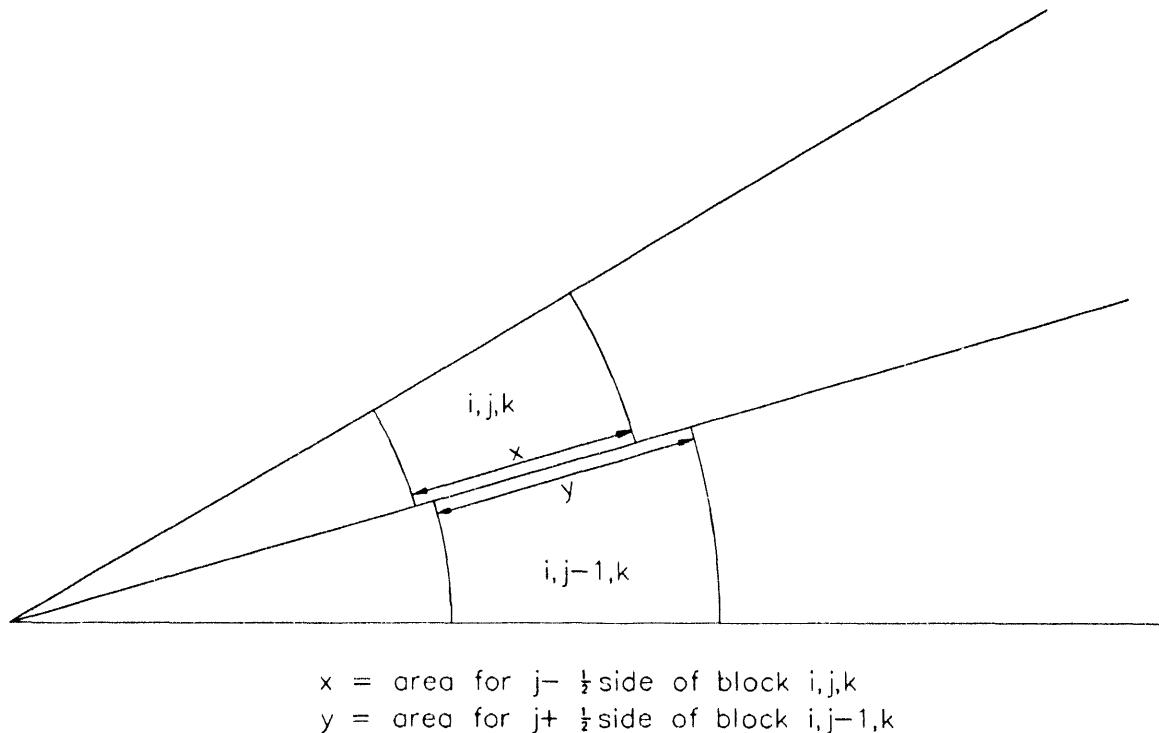
Figure H-7. Areas of interest for calculation of azimuthal-direction transmissibilities.

For the z direction, the interface areas are given by:

$$a_{z,i,j,k(-)} = \frac{\Delta\theta_j'\left[\left(r_{i+\frac{1}{2}}'\right)^2 - \left(r_{i-\frac{1}{2}}'\right)^2\right]}{2}$$

(H-25)

The interface area for block k may differ from that of block k-1; therefore, a notation distinction is again required. The z-direction transmissibilities are taken as:

$$T_{z,i,j,k-\frac{1}{2}} = \frac{2}{\left[\dfrac{\Delta z}{k_z a_z}\right]_{i,j,k-1} + \left[\dfrac{\Delta z}{k_z a_z}\right]_{i,j,k}}$$

(H-26)

$$k = 2, \ldots, N_z$$

and

$$T_{z,i,j,\frac{1}{2}} = T_{z,i,j,N_z+\frac{1}{2}} = 0$$

(H-27)

N_z denotes the last grid block in the z direction.

The pore volume for block i,j,k is given by:

$$V = \frac{\phi\,\Delta z\,\Delta\theta'\left[\left(r_{i+\frac{1}{2}}'\right)^2 - \left(r_{i-\frac{1}{2}}'\right)^2\right]}{2}$$

(H-28)

where: ϕ =   porosity.

H.4 Comparison to an Analytic Solution

Pressure transients predicted by SWIFT II using STAB-generated transmissibilities and pore volumes were compared to the results of an analytic solution for borehole angles of 30°, 45°, 60°, and 75° from vertical. The analytic solution considered was developed by Cinco (1974) to examine the transient pressure response caused by constant-rate production to a slanted well. The comparison between the two results is presented in Figure H-8. The STAB/SWIFT II results are identical to the analytic results for a borehole angle of 30°. As the slant of the borehole increases with respect to vertical, STAB/SWIFT II overestimates the pressure response slightly with respect to the analytic results, particularly at early time. The overestimation of the early-time pressure response is roughly equivalent to a 5° underestimation of the borehole slant.

Figure H-9 shows STAB/SWIFT II results for a vertical borehole with $k_r/k_z = 1$ (solid line) and for a borehole slanted 60° from vertical with $k_r/k_z = 1, 2, 5, 10, 20,$ and 100 (dashed lines). For the slanted borehole, the
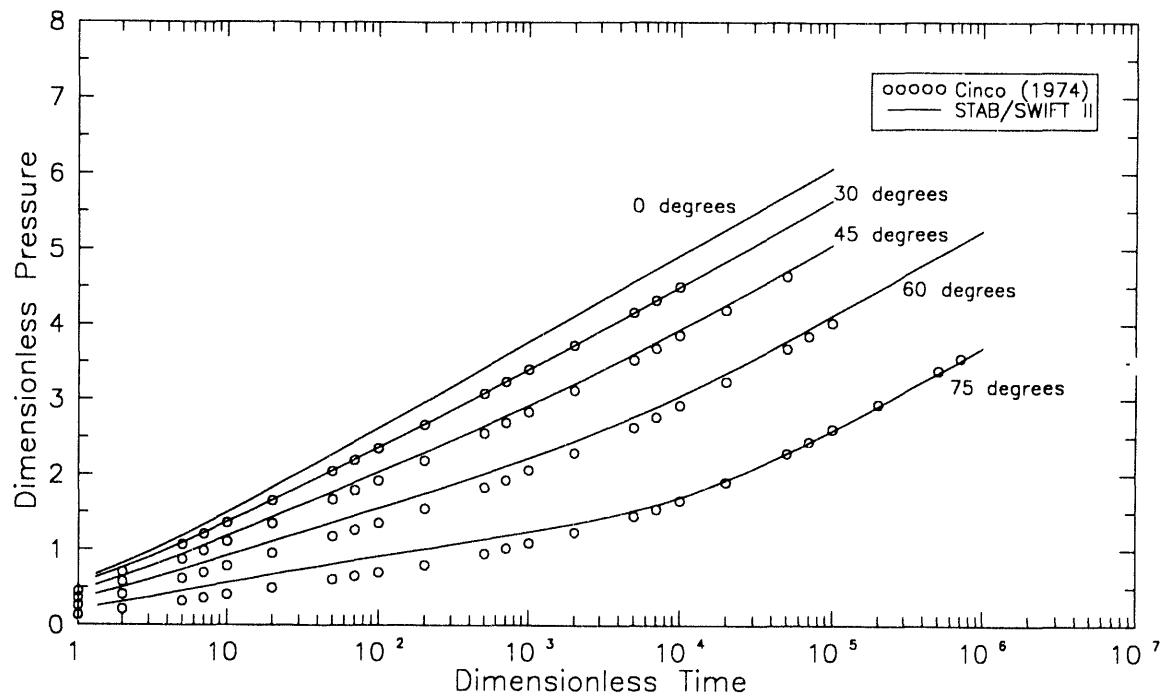
Figure H-8.   Comparison of STAB/SWIFT II results with analytical solution of Cinco (1974) for various slant angles.
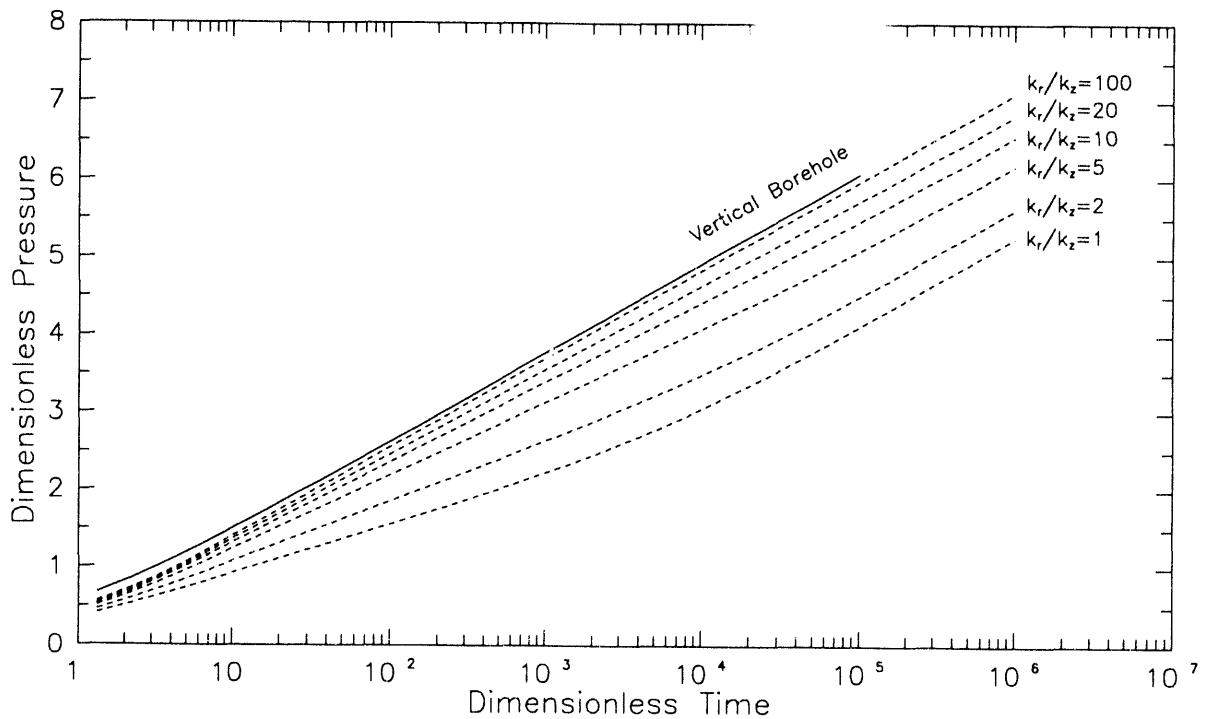
Figure H-9. Effect of anisotropy on STAB/SWIFT II results for a borehole slanted 60°.

256

predicted pressure response approaches the predicted response for a vertical borehole as k_r/k_z increases due to a decrease in the pressure contribution from neighboring layers.

H.5   Summary

STAB is a pre-processor for SWIFT II that first calculates nodal positions consistent with a slanted borehole and then calculates transmissibilities across grid-block interfaces and grid-block pore volumes. Application of STAB for simulating tests in slanted boreholes is desirable because (1) it eliminates the need for a very finely discretized rectangular grid, (2) it closely conforms to the actual geometry by letting the origin of the coordinate system lie along the slanted borehole and letting the coordinate system gradually evolve into a near-cylindrical coordinate system, and (3) grid-block interface lengths more appropriate for a slanted-borehole geometry are used to calculate the radial-direction transmissibilities.

Use of STAB instead of a rectangular grid can reduce the number of grid blocks by an order of magnitude. For some implementations, this can reduce the run time from hours to minutes. Adequate agreement was obtained from a comparison of results from STAB/SWIFT II and the analytical solution of Cinco (1974) for unsteady-state pressure distributions for a slanted borehole.

REFERENCES

Beauheim, R.L., G.J. Saulnier, Jr., and J.D. Avis. 1991. *Interpretation of Brine-Permeability Tests of the Salado Formation at the Waste Isolation Pilot Plant Site: First Interim Report.* SAND90-0083. Albuquerque, NM: Sandia National Laboratories.

Carslaw, J.S., and J.C. Jaeger. 1959. *Conduction of Heat in Solids.* 2nd ed. Oxford, UK: Oxford University Press.

Carter, R.D., and C.W. Tracy. 1960. "An Improved Method for Calculating Water Influx." *Transactions of the Society of Petroleum Engineers.* American Institute of Mining Engineers, Vol. 219, 415-417.

Cinco, H. 1974. "Unsteady-State Pressure Distributions Created by a Slanted Well, or a Well with an Inclined Fracture." Petroleum Engineering Department, Ph.D. dissertation. Stanford, CA: Stanford University.

Pickens, J.F., G.E. Grisak, J.D. Avis, D.W. Belanger, and M. Thury. 1987. "Analysis and Interpretation of Borehole Hydraulic Tests in Deep Boreholes: Principles, Model Development, and Applications," *Water Resources Research.* Vol. 23, no. 7, 1341-1375.

Reeves, M., D.S. Ward, N.D. Johns, and R.M. Cranwell. 1986a. *Theory and Implementation for SWIFT II, The Sandia Waste-Isolation Flow and Transport Model for Fractured Media, Release 4.84.* SAND83-1159, NUREG/CR-3328. Albuquerque, NM: Sandia National Laboratories.

Reeves, M., D.S. Ward, N.D. Johns, and R.M. Cranwell. 1986b. *Data Input Guide for SWIFT II, The Sandia Waste-Isolation Flow and Transport Model for Fractured Media, Release 4.84.* SAND83-0242, NUREG/CR-3162. Albuquerque, NM: Sandia National Laboratories.

DISTRIBUTION

Federal Agencies

US Department of Energy (6)
Office of Civilian Radioactive Waste
Management
Attn: Deputy Director, RW-2
    Associate Director, RW-10/50
      Office of Program and
      Resources Management
      Office of Contract Business
      Management
    Director, RW-22
      Analysis and Verification
      Division
    Associate Director, RW-30
      Office of Systems and
      Compliance
    Associate Director, RW-40
      Office of Storage and
      Transportation
    Director, RW-4/5
      Office of Strategic Planning
      and International Programs
      Office of External Relations
Forrestal Building
Washington, DC 20585

US Department of Energy
Albuquerque Operations Office
Attn: National Atomic Museum Library
PO Box 5400
Albuquerque, NM 87185-5400

US Department of Energy (4)
WIPP Project Integration Office
Attn: W.J. Arthur III
    L.W. Gage
    P.J. Higgins
    D.A. Olona
PO Box 5400
Albuquerque, NM 87115-5400

US Department of Energy (2)
WIPP Project Integration Satellite
Office
Attn: R. Batra
    R. Becker
PO Box 3090, Mail Stop 525
Carlsbad, NM 88221-3090

US Department of Energy
Research & Waste Management Division
Attn: Director
PO Box E
Oak Ridge, TN 37831

US Department of Energy (3)
WIPP Project Site Office (Carlsbad)
Attn: V. Daub
    J. Lippis
    J.A. Mewhinney
PO Box 3090
Carlsbad, NM 88221-3090

US Department of Energy
Attn: E. Young
Room E-178
GAO/RCED/GTN
Washington, DC 20545

US Department of Energy
Office of Environmental Restoration
  and Waste Management
Attn: J. Lytle, EM-30,
    Trevion II
Washington, DC 20585-0002

US Department of Energy (3)
Office of Environmental Restoration
  and Waste Management
Attn: M. Frei, EM-34,
    Trevion II
Washington, DC 20585-0002

US Department of Energy
Office of Environmental Restoration
  and Waste Management
Attn: S. Schneider, EM-342,
    Trevion II
Washington, DC 20585-0002

US Department of Energy (2)
Office of Environment, Safety
  and Health
Attn: C. Borgstrom, EH-25
    R. Pelletier, EH-231
Washington, DC 20585

US Department of Energy (2)
Idaho Operations Office
Fuel Processing and Waste
  Management Division
785 DOE Place
Idaho Falls, ID 83402

US Environmental Protection
Agency (2)
Radiation Protection Programs
Attn: M. Oge
ANR-460
Washington, DC 20460

US Geological Survey (2)
Water Resources Division
Attn: R. Livingston
4501 Indian School NE
Suite 200
Albuquerque, NM 87110

U. S. Geological Survey (2)
Water Resources Division
Attn: P. Hsieh
      A. F. Moench
345 Middlefield Rd.
Menlo Park, CA 94025

US Nuclear Regulatory Commission
Division of Waste Management
Attn: H. Marson
Mail Stop 4-H-3
Washington, DC 20555

Boards

Atomic Energy Control Board
Waste Management Division
Attn: D. Metcalfe
PO Box 1046, Station 'B'
Ottawa, Ontario
K1P 5S9 CANADA

Defense Nuclear Facilities Safety
Board
Attn: D. Winters
625 Indiana Ave. NW, Suite 700
Washington, DC 20004

Nuclear Waste Technical Review
Board (2)
Attn: Chairman
      S.J.S. Parry
1100 Wilson Blvd., Suite 910
Arlington, VA 22209-2297

Advisory Committee on Nuclear
Waste
Nuclear Regulatory Commission
Attn: R. Major
7920 Norfolk Ave.
Bethesda, MD 20814

State Agencies

Environmental Evaluation Group (3)
Attn: Library
7007 Wyoming NE
Suite F-2
Albuquerque, NM 87109

NM Bureau of Mines and Mineral
  Resources
Socorro, NM 87801

NM Energy, Minerals, and Natural
  Resources Department
Attn: Library
2040 S. Pacheco
Santa Fe, NM 87505

NM Environment Department (3)
Secretary of the Environment
Attn: J. Espinosa
1190 St. Francis Drive
Santa Fe, NM 87503-0968

NM Environment Department
WIPP Project Site
Attn: P. McCasland
PO Box 3090
Carlsbad, NM 88221

Laboratories/Corporations

Battelle Pacific Northwest
Laboratories
Attn: R.E. Westerman, MSIN P8-44
Battelle Blvd.
Richland, WA 99352

Golder Associates
Attn: T.W. Doe
4104 148th Ave. NE
Redmond, WA 98052

INTERA, Inc. (9)
Attn: P.S. Domski
      M.D. Fort (2)
      G.A. Freeze
      M.B. Kloska
      K. Larson
      D.T. Upton
      R.M. Roberts (2)
1650 University Blvd. NE, Suite 300
Albuquerque, NM 87102-1732

INTERA, Inc. (8)
Attn: G.E. Grisak
      J.F. Pickens
      G.J. Saulnier
      T.F. Dale (2)
      T.L. Jones
      V.A. Kelley
      Library
6850 Austin Center Blvd., Suite 300
Austin, TX 78731

INTERA, Inc. (6)
Attn: W.A. Stensrud (2)
F. Holzmer
J.B. Palmer
R. King
D. Chace
PO Box 2123
Carlsbad, NM 88221

IT Corporation (3)
Regional Office
Attn: R.F. McKinney
M.E. Crawley
J. Myers
5301 Central NE
Suite 700
Albuquerque, NM 87108

IT Corporation (2)
Attn: D. Deal
PO Box 2078
Carlsbad, NM 88221

L. Lehman and Associates, Inc.
Attn: L. Lehman
1103 W. Burnsville Parkway
Suite 209
Minneapolis, MN 55337

Los Alamos National Laboratory
Attn: B. Erdal, INC-12
PO Box 1663
Los Alamos, NM 87544

National Ground Water Information
Center
Attn: J. Bix
6375 Riverside Dr.
Dublin, OH 43017

RE/SPEC, Inc.
Attn: W. Coons
4775 Indian School NE
Suite 300
Albuquerque, NM 87110-3927

RE/SPEC, Inc.
Attn: J.L. Ratigan
PO Box 725
Rapid City, SD 57709

Southwest Research Institute (2)
Center for Nuclear Waste
  Regulatory Analysis
Attn: P.K. Nair
6220 Culebra Road
San Antonio, TX 78228-0510

SAIC
Attn: D.C. Royer
101 Convention Center Dr.
Las Vegas, NV 89109

SAIC
Attn: H.R. Pratt
10260 Campus Point Dr.
San Diego, CA 92121

SAIC (2)
Attn: M. Davis
J. Tollison
2109 Air Park Rd. SE
Albuquerque, NM 87106

S.S. Papadopulos and Associates, Inc.
Attn: J.W. Anthony
12596 W. Bayard Ave., Suite 290
Lakewood, CO 80228

Tech Reps Inc. (3)
Attn: J. Chapman
C. Crawford
T. Peterson
5000 Marble NE, Suite 222
Albuquerque, NM 87110

TRW Environmental Safety Systems
Attn: L. Wildman
2650 Park Tower Dr., Suite 1300
Vienna, VA 22180-7306

Westinghouse Electric Corporation (5)
Attn: C. Cox
L. Fitch
B.A. Howard
R. Kehrman
Library
PO Box 2078
Carlsbad, NM 88221

Westinghouse-Savannah River
Technology Center (4)
Attn: N. Bibler
J.R. Harbour
M.J. Plodinec
G.G. Wicks
Aiken, SC 29802

**National Academy of Sciences,
WIPP Panel**

Howard Adler
Oak Ridge Associated Universities
Medical Sciences Division
PO Box 117
Oak Ridge, TN 37831-0117

Ina Alterman
Board on Radioactive
  Waste Management, GF456
2101 Constitution Ave.
Washington, DC   20418

Fred M. Ernsberger
1325 NW Tenth Ave.
Gainsville, FL   32605

John D. Bredehoeft
Western Region Hydrologist
Water Resources Division
US Geological Survey (M/S 439)
345 Middlefield Road
Menlo Park, CA   94025

Rodney C. Ewing
Department of Geology
University of New Mexico
Albuquerque, NM   87131

Charles Fairhurst, Chairman
Department of Civil and
  Mineral Engineering
University of Minnesota
500 Pillsbury Dr. SE
Minneapolis, MN   55455-0220

B. John Garrick
PLG Incorporated
4590 MacArthur Blvd.
Suite 400
Newport Beach, CA   92660-2027

Leonard F. Konikow
US Geological Survey
431 National Center
Reston, VA   22092

Peter B. Myers
National Academy of Sciences
Board on Radioactive
  Waste Management
2101 Constitution Ave.
Washington, DC   20418

Jeremiah O'Driscoll
Jody Incorporated
505 Valley Hill Drive
Atlanta, GA 30350

Christopher G. Whipple
ICF Kaiser Engineers
1800 Harrison St., 7th Floor
Oakland, CA   94612-3430

Individuals

P. Drez
8816 Cherry Hills Rd. NE
Albuquerque, NM 87111

D.W. Powers
Star Route Box 87
Anthony, TX   79821

Universities

New Mexico Tech (4)
Department of Geoscience
Attn: J. Wilson
      F. Phillips
      R. Bowman
      C.S. Chen
Socorro, NM   87801

Texas A&M University
Department of Geology
Attn: P.A. Domenico
College Station, TX   77843

University of Arizona
Department of Hydrology
Attn: S.P. Neuman
Tucson, AZ   85721

University of California (3)
Lawrence Berkeley Laboratory
Earth Sciences Division
Attn: K. Kara aki
      J.C. Long
      C.F. Tsang
1 Cyclotron Road
Berkeley, CA   94720

University of Kansas
Kansas Geological Survey
Attn: J. Butler
1930 Constant Ave.
Campus West
Lawrence, KS   66046

University of New Mexico
Geology Department
Attn: Library
Albuquerque, NM   87131

University of Virginia
Department of Environmental Sciences
Attn: G.M. Hornberger
Clark Hall
Charlottesville, VA   22903

University of Washington
College of Ocean and Fishery Sciences
Attn: G.R.Heath
583 Henderson Hall   HN-15
Seattle, WA   98195

University of Wisconsin-Madison (2)
Department of Geology and Geophysics
Attn: M. P. Anderson
     H.F. Wang
1215 W. Dayton St.
Madison, WI   53706

Libraries

Thomas Brannigan Library
Attn: D. Dresp
106 W. Hadley St.
Las Cruces, NM   88001

Government Publications Department
Zimmerman Library
University of New Mexico
Albuquerque, NM   87131

New Mexico Junior College
Pannell Library
Attn: R. Hill
Lovington Highway
Hobbs, NM   88240

New Mexico State Library
Attn: N. McCallan
325 Don Gaspar
Santa Fe, NM   87503

New Mexico Tech
Martin Speere Memorial Library
Campus Street
Socorro, NM   87810

WIPP Public Reading Room
Carlsbad Public Library
Attn: Director
101 S. Halagueno St.
Carlsbad, NM   88220

Foreign Addresses

Studiecentrum Voor Kernenergie
Centre D'Energie Nucleaire
Attn: A. Bonne
SCK/CEN   Boeretang 200
B-2400 Mol, BELGIUM

Atomic Energy of Canada, Ltd. (5)
Whiteshell Laboratories
Attn: B. Goodwin
     M. Stevens
     D. Wushke
     C. Davison
     E. Kozak
Pinewa, Manitoba, CANADA ROE 1L0

Environment Canada
National Water Research Institute
Canada Centre for Inland Lakes
Attn: K.S. Novakowski
867 Lakeshore Road
PO Box 5050
Burlington, Ontario, CANADA L7R 4A6

Technical Research Center of Finland
Nuclear Engineering Laboratory
Attn: V. Taivassalo
PO Box 169
SF-00181 Helsinki, FINLAND

ANDRA (2)
Attn: Francois Chenevier
Route du Panorama Robert Schumann
B.P. 38
92266 Fontenay-aux-Roses, Cedex
FRANCE

OECD Nuclear Energy Agency
Attn: Jean-Pierre Olivier
Division of Radiation Protection
and Waste Management
38, Boulevard Suchet
75016 Paris, FRANCE

Centre D'Etudes Nucleaires
De La Vallee Rhone
Attn: Claude Sombret
CEN/VALRHO
S.D.H.A.   B.P. 171
30205 Bagnols-Sur-Ceze, FRANCE

Centre de Géotechnique et
d'Exploitation du Sous-Sol
Attn: A. Aït-Chalal
35, Fue Saint-Honoré
F-77305 Fontainebleau, Cedex
FRANCE

Bundesanstalt für Geowissenschaften
und Rohstoffe (3)
Attn: M. Langer
      P. Vogel
      K. Schelkes
Postfach 510 153
D-30631 Hannover, GERMANY

Bundesministerium für Forschung und
Technologie
Attn: Rolf-Peter Randl
Postfach 200 706
5300 Bonn 2, GERMANY

Gesellschaft für Anlagen- und
Reaktorsicherheit (GRS) (3)
Attn: B. Baltes
      P. Bogorinski
      W. Muller
Schwertnergasse 1
D-50667 Cologne, GERMANY

Golder Associates Umwelttechnik
Attn: L. Ostrowski
Vorbruch 3
D-3100 Celle, GERMANY

Institut für Tieflagerung (2)
Attn: K. Kuhn
Theodor-Heuss-Strasse 4
D-3300 Braunschweig, GERMANY

Physikalisch-Technische Bundesanstalt
Attn: P. Brenneke
Postfach 3345
D-3300 Braunschweig, GERMANY

Japan Atomic Energy Research Inst.
Attn: Shingo Tashiro
Tokai-Mura, Ibaraki-Ken, 319-11
JAPAN

National Institute of Public Health
and Environmental Protection
Attn: S.M. Hassanizadeh
Antonie von Leeuwenhoeklaan 9
PO Box 1
3720 BA Bilthoven, THE NETHERLANDS

Netherlands Energy Research
Foundation ECN
Attn: L.H. Vons
3 Westerduinweg
PO Box 1
1755 ZG Petten, THE NETHERLANDS

Utrecht University (2)
Institute of Earth Sciences
HPT Lab/ Department of Geology
Attn: C.J. Peach
      C.J. Spiers
Budapestlaan 4
PO Box 80.021
3508 TA Utrecht, THE NETHERLANDS

Conterra AB
Attn: A. Winberg
Krokslätts Fabriker 30
S-431 37 Mölndal, SWEDEN

Svensk Kärnbränsleforsorjning AB (3)
Attn: F. Karlsson
      A. Ström
      K. E. Almén
Project KBS (Kärnbränslesakerhet)
Box 5864
S-102 48 Stockholm, SWEDEN

Geosigma AB
Attn: P. Andersson
PO Box 894
S-751 08 Uppsala, SWEDEN

Statens Kärnkraftinspektion
Attn: J. Andersson
Box 27106
S-102 52 Stockholm, SWEDEN

Kemakta Konsult AB
Attn: L. Birgersson
Box 12655
S-112 93 Stockholm, SWEDEN

Colenco Ltd.
Attn: S. Löw
Mellingerstrasse 207
CH-5405 Baden
SWITZERLAND

SolExperts Ltd.
Attn: E. Wyss
Ifangstrasse 12
CH-8603 Schwerzenbach
SWITZERLAND

Nationale Genossenschaft für die
Lagerung radioaktiver Abfälle (2)
Attn: S. Vomvoris
        P. Zuidema
Hardstrasse 73
CH-5430 Wettingen, SWITZERLAND

AEA Technology
Attn: J.H. Rees
D5W/29 Culham Laboratory
Abington, Oxfordshire OX14 3DB
UNITED KINGDOM

AEA Technology
Attn: W.R. Rodwell
O44/A31 Winfrith Technical Centre
Dorchester, Dorset DT2 8DH
UNITED KINGDOM

AEA Technology
Attn: J.E. Tinson
B4244 Harwell Laboratory
Didcot, Oxfordshire OX11 ORA
UNITED KINGDOM

Golder Associates
Attn: J.H. Black
Landmere Lane, Edwalton
Nottingham
NG12 4DE, UNITED KINGDOM

British Nuclear Fuels, plc
Attn: D.R. Knowles
Risley, Warrington
Cheshire WA3 6AS
1002607 UNITED KINGDOM

Internal

MS	Org.	
0827	1502	P.J. Hommert
0127	4511	D.P. Garber
0724	6000	D.L. Hartley
1324	6115	P.B. Davies
1324	6115	R.L. Beauheim (10)
1324	6115	Staff (15)
1320	6119	E.J. Nowak
1320	6119	Staff (7)
1332	6121	J.R. Tillerson
1332	6121	Staff (7)
1337	6300	D.E. Ellis
1335	6302	L.E. Shephard
1335	6303	S.Y. Pickering
1335	6303	W.D. Weart
1335	6305	S.A. Goldstein
1335	6305	A.R. Lappin
1341	6306	A.L. Stevens
1341	6307	P.A. Davis
1328	6342	D.R. Anderson
1328	6342	Staff (20)
1328	6343	V. Harper-Slaboszewicz
1328	6343	Staff (2)
1341	6345	R.C. Lincoln
1341	6345	Staff (9)
1341	6347	D.R. Schafer
1341	6348	J.T. Holmes
1341	6348	Staff (4)
1343	6351	R.E. Thompson
1330	6352	S.E. Sharpton
1330	6352	WIPP Central Files (10)
0899	7141	Technical Library (5)
0619	7151	Technical Publications
1119	7613-2	Document Processing for DOE/OSTI (10)
	8523-2	Central Technical Files

END

DATE FILMED

3 / 9 / 94